Development, characterization, and first field deployments of a novel aerosol mass spectrometer combining laser ablation and flash vaporization techniques for aircraft application at high altitudes

Dissertation

zur Erlangung des Grades

„Doktor der Naturwissenschaften“

im Promotionsfach Chemie

am Fachbereich Chemie, Pharmazie und Geowissenschaften

der Johannes Gutenberg-Universität

in Mainz

Andreas Hünig

geboren in Immenstadt im Allgäu

Mainz, Juli 2020

Dekan:

1. Berichterstatter:

2. Berichterstatter:

Tag der mündlichen Prüfung: 23.11.2020

D77

“For, in the final analysis, our most basic common link is that we all inhabit this small planet. We all breathe the same air. We all cherish our children's future. And we are all mortal.”

John F. Kennedy, American University speech, 10.6.1963

Abstract

Aerosol particles are affecting human health and the environment. To estimate the effects, a detailed characterization of these particles is required. Particles can be characterized according to their size, shape, and chemical composition. The latter property can be determined by mass spectrometry. Two main types of mass spectrometers are currently used for in-situ chemical analysis of aerosol particles from the ambient atmosphere. One uses a pulsed laser to vaporize and ionize submicron to micrometer sized single particles before injecting ions into the mass spectrometer. The other uses thermal vaporization and electron impact ionization to analyze small particle ensembles. These ions are also detected by a mass spectrometer. In the here presented novel aerosol mass spectrometer ERICA (acronym for: ERc Instrument for Chemical composition of Aerosols) the two techniques were combined to obtain complementary chemical information about the aerosol. Such an instrumental design is unique. The first part is called ERICA-LAMS (ERICA Laser Ablation Mass Spectrometer) and the second part ERICA-AMS (ERICA Aerosol Mass Spectrometer). After being focused by an aerodynamic lens, the sampled ambient aerosol particles enter a high vacuum chamber, where they are detected by two laser light scattering units, namely the detection units, before they reach the laser ablation region. Here, the particles are vaporized and ionized by a pulsed, frequency quadrupled Nd:YAG laser. The ions are then measured by a bipolar Time-of-Flight mass spectrometer. Particles which are too small to be detected by the detection unit or are missed by the ablation laser continue their travel to the ERICA-AMS section of the instrument, within which they are flash-vaporized on a heated tungsten surface and ionized by electron impact ionization. The resulting positive ions are guided into a Compact Time-of-Flight mass spectrometer.

The goal of this work was to set up, characterize, and deploy the ERICA instrument. To characterize the focused detection laser and ablation laser beams, dedicated experiments as well as the particle beam comprehensive laboratory measurements were conducted. For the laser beam characterization, the so-called knife-edge technique was adopted. The detection efficiency of the particle detection units was measured for various aerodynamic lens positions with PSL and ammonium nitrate particles in various sizes (91 nm – 5,145 nm, vacuum aerodynamic diameter). An adopted curve fitting procedure provided the particle beam parameters, such as the particle beam width, the effective detection radius, the particle beam divergence, and the transmission efficiency of the aerodynamic lens. Furthermore, two different particle size calibration functions were compared and validated. In addition, pure chemical substance particles (sodium chloride, ammonium nitrate, gold-spheres, and benz[a]anthracene) were sampled to validate the ERICA-LAMS mass spectra evaluation. By that it was found that the erosion of gold fragments from the gold-plated aircraft inlet is sufficiently low and the inlet reliably deployable. The dimensions of the instrument are 600 mm x 740 mm x 1,400 mm (height x width x length) with a total weight of around 200 kg.

The first field deployment of ERICA took place during a test campaign in Kalamata, Greece, from August to September 2016 aboard the Russian high-altitude research aircraft M-55 Geophysica. This was the first aircraft phase of the StratoClim (acronym for: Stratospheric and upper tropospheric processes for better Climate predictions) project. Here, positive and negative ion mass spectra of single particles were concurrently measured in the lower stratosphere for the first time. The results of the data evaluation show that the ERICA-LAMS is capable of measuring elemental carbon and meteoric dust particles in altitudes where these particle types were expected besides organic and inorganic particle types. However, some improvements needed to be implemented to be enable measuring the mass

concentration of particulate sulfate, nitrate, ammonium, and organic content quantitatively with the ERICA-AMS.

The second aircraft phase was performed in Kathmandu, Nepal, from July to August 2017, where single particle and particle ensemble mass spectra were recorded in altitudes of up to 20 km. Here, nitrate-containing single particles and an enhanced nitrate mass concentration were observed in an aerosol layer that was previously identified as particulate nitrate-consisting layer by a remote sensing instrument. For the first time an AMS type of instrument was operated at such altitudes. By means of ERICA, answers concerning the long- standing scientific question about the chemical composition of ATAL (Asian Tropopause Aerosol Layer) aerosol could be provided and were published 2019 in Nature Geoscience. Furthermore, the data set was investigated for metal-containing particles.

Overall, this work documents the high quality of the ERICA instrument and its reliable performance. The field campaigns have shown that the instrument is able to operate continuously under demanding conditions like heat, vibration, and turbulences aboard an aircraft covering an altitude range from mean sea level to 20,477 m above mean sea level, an ambient temperature range from -87 °C to 32 °C, and an ambient pressure range from 55 hPa to 1015 hPa. Thus, design, implementation, and fully autonomous flight operation, especially on a high-altitude aircraft, of ERICA can be considered as veritable experimental success.

Zusammenfassung

Aerosolpartikel beeinflussen die menschliche Gesundheit und die Umwelt. Um diesen Einfluss abschätzen zu können, ist eine detaillierte Charakterisierung dieser Partikel erforderlich. Die Partikel können nach ihrer Größe, Form und chemischen Zusammensetzung charakterisiert werden. Die letztere Eigenschaft kann durch Massenspektrometrie bestimmt werden. Derzeit werden zwei Haupttypen von Massenspektrometern für die chemische in-situ-Analyse von Aerosolpartikeln aus der Umgebungsatmosphäre verwendet. Der erste Typ verwendet einen gepulsten Laser, um einzelne Partikel von Submikron- bis Mikrometergröße zu verdampfen und zu ionisieren, bevor die Ionen in das Massenspektrometer eingespeist werden. Der andere verwendet thermische Verdampfung und Elektronenstoßionisation zur Analyse kleiner Partikelensembles. Diese Ionen werden ebenfalls mit einem Massenspektrometer nachgewiesen. In dem hier vorgestellten neuartigen Aerosol-Massenspektrometer ERICA (Akronym für: ERc Instrument for Chemical composition of Aerosols) wurden die beiden Techniken kombiniert, um komplementäre chemische Informationen des Aerosols zu erhalten. Ein solches instrumentelles Design ist einzigartig. Der erste Teil wird als ERICA-LAMS (ERICA Laser Ablations Mass Spectrometer) und der zweite Teil als ERICA-AMS (ERICA Aerosol Mass Spectrometer) bezeichnet. Nach der Fokussierung durch eine aerodynamische Linse gelangen die beprobten Aerosolpartikel aus der Umgebung in eine Hochvakuumkammer, wo sie von zwei Laserlichtstreuungseinheiten, den Detektionseinheiten, erfasst werden, bevor sie den Laserablationsbereich erreichen. Hier werden die Partikel durch einen gepulsten, frequenzvierfachen Nd:YAG-Laser verdampft und ionisiert. Die so erzeugten Ionen werden mit einem bipolaren Flugzeitmassenspektrometer gemessen. Partikel, die zu klein sind, um von der Detektionseinheit erfasst zu werden, oder die vom Ablationslaser verfehlt werden, gelangen zum ERICA-AMS-Abschnitt des Instruments, wo sie auf einer erhitzten Wolframoberfläche verdampft und durch Elektronenstoßionisation ionisiert werden. Die resultierenden positiven Ionen werden in ein kompaktes Flugzeitmassenspektrometer geleitet.

Ziel dieser Arbeit war es das ERICA-Instrument aufzubauen, zu charakterisieren und einzusetzen. Zur Charakterisierung des fokussierten Detektionslasers und der Ablationslaserstrahlen wurden sowohl entsprechende Experimente als auch umfangreiche Labormessungen des Teilchenstrahls durchgeführt. Für die Charakterisierung des Laserstrahls wurde die sogenannte Rasierklingenmethode verwendet. Die Detektionseffizienz der Partikeldetektionseinheiten wurde für verschiedene aerodynamische Linsenpositionen mit PSL- und Ammoniumnitratpartikeln verschiedener Größe (91 nm - 5145 nm, vakuumaerodynamischer Durchmesser) gemessen. Mittels Kurvenanpassungs-verfahren wurden die Partikelstrahlparameter, wie z.B. die Partikelstrahlbreiten, die effektiven Detektionsradii, die Partikelstrahldivergenz und die Transmissionseffizienz der aerodynamischen Linse bestimmt. Darüber hinaus wurden zwei verschiedene Partikelgrößenkalibriermethoden verglichen und validiert. Des Weiteren wurden Partikel reiner chemischer Substanzen (Natriumchlorid, Ammoniumnitrat, Goldpartikel und Benz[a]anthracen) zur Validierung der ERICA-LAMS-Massenspektrenauswertung gemessen. Dabei wurde festgestellt, dass die Freisetzung der Goldfragmente vom vergoldeten Flugzeugeinlass ausreichend gering ist und der Einlass somit zuverlässig einsetzbar ist. Die Abmessungen des Instruments betragen 600 mm x 740 mm x 1.400 mm (Höhe x Breite x Länge) bei einem Gesamtgewicht von rund 200 kg.

Der erste Feldeinsatz von ERICA fand während einer Testkampagne in Kalamata, Griechenland, von August bis September 2016 an Bord des russischen Höhenforschungsflugzeugs M-55 *Geophysica* statt. Dies war die erste Flugzeugphase des StratoClim-Projekts (Akronym für: Stratospheric and upper

tropospheric processes for better Climate predictions). Dabei wurden zum ersten Mal simultan positive und negative Massenspektren einzelner Partikel in der unteren Stratosphäre gemessen. Die Ergebnisse der Datenauswertung zeigen, dass das ERICA-LAMS in der Lage ist, neben organischen und anorganischen Partikeltypen auch elementare Kohlenstoff- und Meteoritenstaubpartikel in den Höhenbereichen zu messen, in denen diese Partikeltypen erwartet wurden. Es mussten jedoch noch einige Verbesserungen vorgenommen werden, um die Massenkonzentration von partikulärem Sulfat, Nitrat, Ammonium und organischen Stoffen mit dem ERICA-AMS quantitativ messen zu können.

Die zweite Flugzeugphase fand von Juli bis August 2017 in Kathmandu, Nepal, statt, wobei Einzelpartikel- und Partikelensemblemassenspektren in Höhen von bis zu 20 km aufgenommen wurden. Dabei wurden nitrathaltige Einzelpartikel und eine erhöhte Nitratmassenkonzentration in einer Aerosolschicht gemessen, die zuvor mit einem Fernerkundungsinstrument als partikelförmige nitrathaltige Schicht identifiziert worden war. Zum ersten Mal wurde ein Instrument vom AMS-Typ in solchen Höhen betrieben. Mit Hilfe von ERICA konnten Antworten auf die langjährige wissenschaftliche Frage nach der chemischen Zusammensetzung des ATAL-Aerosols (Asian Tropopause Aerosol Layer) gegeben und 2019 in Nature Geoscience veröffentlicht werden. Darüber hinaus wurde der Datensatz auf metallhaltige Partikel untersucht.

Insgesamt belegt diese Arbeit die hohe Qualität des ERICA-Instruments und dessen zuverlässige Leistungsfähigkeit. Die Feldkampagnen haben gezeigt, dass das Instrument unter anspruchsvollen Bedingungen wie Hitze, Vibrationen und Turbulenzen an Bord eines Flugzeugs kontinuierlich in einem Höhenbereich von mittlerer Meereshöhe bis 20.477 m über dem Meeresspiegel, einem Umgebungs-temperaturbereich von -87 °C bis 32 °C und einem Umgebungsdruckbereich von 55 hPa bis 1015 hPa betrieben werden kann. Daher können Design, Implementierung und vollständig autonomer Flugbetrieb, insbesondere auf einem Höhenflugzeug, von ERICA als wahrer experimenteller Erfolg angesehen werden.

Contents

Abstract iii
Zusammenfassung v
Contents vii
1 Introduction 1
1.1 Aerosols and aerosol measurement techniques 1
1.2 Motivation for the experimental concept 3
1.3 Structure of the thesis 5
2 Methodology 6
2.1 Particle beam focusing by aerodynamic lenses 6
2.2 Particle sizing 8
2.2.1 Particle acceleration by an aerodynamic lens 8
2.2.2 Light scattering on particles 9
2.3 Laser desorption and –ionization technique for the ERICA-LAMS 10
2.4 Particle flash vaporization and electron ionization technique for the ERICA-AMS 14
2.5 Ion detection by time-of-flight mass spectrometry 18
3 Instrumental overall design of ERICA 20
3.1 General description 20
3.2 Inlet and vacuum system 23
3.3 Particle detection and sizing by the detection units 25
3.4 Single particle laser ablation 27
3.4.1 Ablation laser and optics 27
3.4.2 Ion detection with bipolar time-of-flight mass spectrometer 28
3.5 Particle flash vaporization and electron impact ionization 29
3.5.1 Motivation to combine flash vaporization/electron impact ionization with the laser ablation technique 29
3.5.2 Ionizer and time-of-flight mass spectrometer for positive ions 29
3.6 Power supply requirements and distribution to the ERICA sub-systems for safe aircraft operation 31
3.7 Instrument control and data acquisition 31
3.7.1 Safety systems and basic control of the instrument 32
3.7.2 Single particle detection and ablation laser trigger 34
3.7.3 Data acquisition of ion mass spectra 37
3.8 Design considerations for aircraft operation aboard the M-55 *Geophysica* 39

3.8.1 Satellite communication link 39
3.8.2 Low power mode (LPM) 39
3.8.3 Pressurized container and aircraft inlet for ERICA on the M-55 *Geophysica* 40
3.8.4 Acquisition of data from the aircraft systems and avionics 41
4 Instrumental characterization 42
4.1 Characterization of the laser beams 42
4.1.1 Experimental setup 42
4.1.2 Detection laser 43
4.1.3 Ablation laser 45
4.1.4 UV light fraction of the ablation laser 47
4.1.5 Summary of the characterization of the laser beams 48
4.2 Characterization of the detection unit and the particle beam 49
4.2.1 Experimental setup 49
4.2.2 Aerodynamic sizes based on particle flight times 54
4.2.3 Method for particle detection efficiency and mass concentration detection efficiency determination in the laboratory 60
4.2.4 Evaluation and results of the curve fits for the detection efficiency 70
4.2.5 Particle beam properties 77
4.2.6 Summary of the detection unit and particle beam characterization 84
4.3 Ablation efficiency 87
4.4 Mass spectrometer performance of the ERICA-LAMS 89
4.4.1 Exemplary single particle mass spectra from laboratory tests 89
4.4.2 Resolution of the ERICA-LAMS mass spectra 93
4.4.3 Summary of the mass spectrometer performance of the ERICA-LAMS 94
4.5 Mass spectrometer performance of the ERICA-AMS 96
4.5.1 Determination of mass concentration by the ERICA-AMS 96
4.5.2 Ionization efficiency of the ERICA-AMS 99
4.5.3 Resolution of the ERICA-AMS mass spectra 100
4.5.4 Interaction between the ERICA-LAMS and the ERICA-AMS 101
4.5.5 Summary of mass spectrometer performance of the ERICA-AMS 102
5 In-field performance during first aircraft measurements 104
5.1 Proof of concept: StratoClim mid-latitude phase in August/September 2016 104
5.1.1 Data preparation and particle type identification for the ERICA-LAMS by the clustering algorithm method 107
5.1.2 Results of mid-latitudes phase using the clustering algorithm method 112

5.1.3 Improvements on the instrumental design and particle losses inside ERICA 115
5.2 StratoClim Asian monsoon phase in July/August 2017 117
5.2.1 Data preparation and particle type identification for the ERICA-LAMS by the clustering algorithm method 120
5.2.2 Results of Asian monsoon phase using the clustering algorithm method 129
5.2.3 ERICA-LAMS results from application of the ion marker method: tungsten, mercury, and gold 136
5.2.4 Interaction of the ERICA-LAMS and the ERICA-AMS in StratoClim 145
6 Summary and outlook 150
6.1 Summary of the ERICA instrumental properties 150
6.2 Summary of selected results from the StratoClim aircraft campaign 152
6.3 Outlook 155
References 157
Acronyms 179
Variables, symbols, and units 183
Appendix A: Supplementary information for Chapter 3 190
A.1 Diagram of the ERICA-LAMS mass spectrometer ion optics 190
A.2 Diagram of the ERICA-AMS mass spectrometer ion optics 191
A.3 Temperature sensors and cooling fans 192
A.4 UCSE parameters 193
Appendix B: Supplementary information for Chapter 4 194
B.1 Uncertainty analysis 194
B.1.1 Detection laser and ablation laser characterization 194
B.1.2 Ablation laser characterization 194
B.1.3 UV light fraction of the ablation laser 194
B.1.4 Particle size 194
B.1.5 Particle size calibration 195
B.1.6 Detection efficiencies determined by aerodynamic lens scans 195
B.1.7 Overlap parameter for detection units 197
B.1.8 Overlap parameter for ablation region 197
B.1.9 Particle beam divergence 198
B.1.10 Ablation efficiency, number of spectra and number of shots 198
B.2 Particle size calculation 199
B.3 Determination of the best position for the aerodynamic lens 201
B.4 Geometry and distance ratios in the ERICA instrument 202

B.5 Particle detection efficiency measurements for PSL particles at the detection units DU1 and DU2 by aerodynamic lens scans 204
B.6 Calculation of the relative Mie scattered light intensity 207
B.7 Calculation of the effective laser radius for PSL particles of d_{va} = 108 nm 208
B.8 Particle detection efficiency measurements for ammonium nitrate particles at the detection units DU1 and DU2 by aerodynamic lens scans 211
B.8.1 Scans from Series Of Measurements (SOM) A 212
B.8.2 Scans from Series Of Measurements (SOM) B 219
B.9 Determination of the electrical mobility Z 222
B.10 Determination of the parameters f_{SC} and f_{DC} 223
B.11 Calculation of the effective laser radius for ammonium nitrate particle sizes d_{va} = 138 nm and d_{va} = 91 nm 224
B.11.1 Calculation of the effective laser radius for ammonium nitrate particles of d_{va} = 138 nm 224
B.11.2 Calculation of the effective laser radius for ammonium nitrate particles of d_{va} = 91 nm 225
B.12 Particle detection efficiency measurements for ammonium nitrate particles at the ERICA-AMS vaporizer by aerodynamic lens scans 226
B.12.1 Scans from Series Of Measurements (SOM) A 227
B.12.2 Scans from Series Of Measurements (SOM) B 229
B.13 Determination of maximum detection efficiency DE_{max} and the detection efficiency for the field deployment in Kathmandu DE_{KTM} 231
B.14 Determination of ion peak area threshold for stick spectra 232
Appendix C: Supplementary information for Chapter 5 233
C.1 Mid-latitude phase – flight profiles and flight tracks 233
C.2 Uncertainty calculation for vertical profiles and size distribution 236
C.2.1 Rate of recorded mass spectra 236
C.2.2 Number of spectra 236
C.2.3 Particle number fraction 236
C.3 Parameters for m/z calibration and clustering 237
C.3.1 Mid-latitude flights from Kalamata, Greece 237
C.3.2 Subtropical flights from Kathmandu, Nepal 238
C.3.3 Case studies from Kathmandu, Nepal 239
C.4 Ion marker peaks identification 240
C.5 Mid-latitude phase – mean spectra 242
C.6 Mid-latitude phase – data overview in pie charts 245

C.7 Mid-latitude phase – vertical profiles 246
C.8 Asian monsoon phase – flight profiles and flight tracks 248
C.9 Asian monsoon phase – mean spectra 256
C.10 Asian monsoon phase – size distributions 273
C.11 Asian monsoon phase – vertical profiles 278
Publications 290
External contributions to the thesis work 292
Danksagung 293
Curriculum Vitae 295
Declaration 296

1 Introduction

1.1 Aerosols and aerosol measurement techniques

An aerosol is defined as a suspension of solid particles or liquid droplets in air or another gas and its particles/droplets are between 1 nm and 100 µm in size (Hinds, 1999). Depending on their size and the meteorological conditions the residence time in the atmosphere can range from a few hours to several weeks (Jaenicke, 1981). The sources can be either natural or anthropogenic (Seinfeld and Pandis, 2016). Furthermore, atmospheric aerosol particles have bearing on the earth's climate and human health (Dockery, 2009; IPCC, 2013; Fuzzi et al., 2015).

Aerosol particles affect the human body after inhalation and/or deposition onto the skin immediately (Roed et al., 1998; Lelieveld et al., 2013). Particles in the submicron size range can enter the pulmonary tract efficiently and can cause negative health effects (Pöschl, 2005; Thomas, 2013; Sánchez-Soberón et al., 2015). Due to its high surface-to-volume ratio, within this size range they are especially harmful (Lippmann et al., 1980). The chemical composition of the entered particle is decisive to the effect on the human's body. There is an increased health risk if the particle consists of carcinogenic substances (Tie et al., 2009). Furthermore, these particles can cause a wide variety of health impacts, such as asthma, bronchitis, COPD (Chronic Obstructive Pulmonary Disease), and cardiovascular diseases (Anderson et al., 2012). Therefore, particle size physical properties and chemical composition are crucial parameters for assessing health effects.

Aerosol particles have direct and indirect effects on the climate (Lohmann and Feichter, 2005). They influence the climate directly by scattering, absorbing and emitting solar and terrestrial radiation (IPCC, 2013) and indirectly by serving as cloud condensation nuclei or as ice nucleating particles, e.g., according to their chemical composition (Hiranuma et al., 2013; Hiranuma et al., 2019). In this way, aerosol particles change the occurrence frequency of cloud formation and the properties of clouds resulting in a change of the earth's energy budget (IPCC, 2013).

The individual behavior of aerosol particles is not only depending on the optical and physical, but also on the chemical properties. Particles between 100 nm and 1 µm play a major role in atmospheric particle chemistry due to its long residence time and high concentration (Jaenicke, 1981). Events such as smoke plumes of biomass burning (Haslett et al., 2019) can propagate to effect an area as large as a continent.

To characterize the number and size of aerosol particles, various measurements methods are available, such as Condensation Particles Counters (CPCs; Hinds (1999)), Optical Particle Counters (OPCs), and Ultra-High Sensitivity Aerosol Spectrometers (UHSAS; Cai et al. (2008)). It is also important to conduct detailed measurements of the chemical composition of the particles (Fuzzi et al., 2015).

Remote sensing experiments such as satellite measurements are performed to determine aerosol types that cover a high spatial range and resolution by optical extinction or backscatter experiments. For instance, a spatial resolution of 5 km x 5 km can be achieved by CALIOP (Cloud-Aerosol Lidar with Orthogonal Polarization) onboard the CALIPSO (Cloud-Aerosol Lidar and Infrared Pathfinder Satellite Observations) satellite (Winker et al., 2009).

Offline methods, which involve particle sampling by impactors or filters on suitable substrates are followed by a-posteriori chemical analysis in the laboratory. Desorption of moisture, adsorption of gases and vapors from the air stream, evaporation of volatile or semi-volatile materials and particle bounce effects can bias the sample (Kulkarni et al., 2011). In addition, storage and transport of the

sample on the filter substrate might lead to aging effects. Such disadvantages can be avoided by in-situ online measurement methods such as the aerosol mass spectrometry. However, online methods also suffer from various drawbacks.

The particle size and the chemical composition can be simultaneously determined online based on single particle analyses (single particle mass spectrometry, SPMS) and analyses of particle ensembles (bulk aerosol mass spectrometry). Thus, aerosol mass spectrometry is suitable for cloud research (e.g., Schneider et al. (2017), Drewnick et al. (2007), Kamphus et al. (2010), Schmidt et al. (2017)) as well as for air quality measurements (e.g., Wittig et al. (2004), Brands et al. (2011), Fachinger et al. (2018); Haslett et al. (2019)). The chemical composition can provide information, for instance on particle sources, e.g., natural or anthropogenic, and on the state of chemical and physical processing of the particles (IPCC, 2013; Seinfeld and Pandis, 2016). In-situ online aerosol particle mass spectrometry is a widespread established tool (Suess and Prather, 1999). Compact built aerosol mass spectrometers can be deployed on mobile platforms such as trucks (e.g., Mobile Laboratory (MoLa) of the Max Planck Institute for Chemistry (Drewnick et al., 2012) or the PSI (Paul Scherrer Institute) mobile laboratory (Bukowiecki et al., 2002)) or onboard research aircraft (e.g., HALO (High Altitude and Long Range research aircraft; Wendisch et al. (2016)) or NASAs DC-8 (Brock et al., 2019)) to measure particle chemical composition at sufficient temporal and spatial resolution (e.g., Cziczo et al. (2006), Schneider et al. (2006), Bahreini et al. (2009), Pratt et al. (2009), Morgan et al. (2010), Schmale et al. (2010), Brands et al. (2011), Zelenyuk et al. (2015), Vu et al. (2016), Willis et al. (2016), Köllner et al. (2017), Willis et al. (2017), Brito et al. (2018), Goetz et al. (2018), Schulz et al. (2018), and Haslett et al. (2019)). Research aircraft can reach altitudes as high as 21 km (Borrmann et al., 1995; Murphy et al., 1998; Stefanutti et al., 1999; Borrmann et al., 2000; Murphy et al., 2003; Murphy et al., 2006).

For in-situ online aerosol particle mass spectrometry, two complementary measurement techniques are commonly deployed. The first, the SPMS, is based on Laser Desorption and Ionization technique (LDI), also called laser ablation technique, where a pulsed laser vaporizes and ionizes submicron to micrometer sized single particles before the created ions are injected into a time-of-flight mass spectrometer (Sinha, 1984; McKeown et al., 1991; Murphy and Thomson, 1995; Hinz et al., 1996; Zelenyuk and Imre, 2005; Brands et al., 2011). The second method, the bulk aerosol mass spectrometry, is based on thermal flash vaporization and electron impact ionization (Davis, 1973; Jayne et al., 2000; Jimenez et al., 2003c; Allan et al., 2004; Drewnick et al., 2005; Canagaratna et al., 2007) to analyze small particle ensembles (commonly referred to as “bulk aerosol”).

1.2 Motivation for the experimental concept

Both, the LDI and the thermal vaporization/electron impact ionization technique, have their strengths and weaknesses that are presented in this section. By building a novel instrument in a hybrid design, the weaknesses of one technique are reduced by the strengths of the other and vice versa to obtain complementary information delivered by the LDI technique and the thermal vaporization/electron impact ionization technique. Therefore, both techniques were combined in one single instrument. The name of the here presented aerosol mass spectrometer is ERICA (acronym for ERc Instrument for Chemical composition of Aerosols). The aim was to build a compact, autonomously running instrument with properties comparable to other well-known aircraft-based online aerosol mass spectrometers. Instruments using the LDI technique are for instance PALMS (Murphy et al., 1998; Cziczo et al., 2006), A-ATOFMS (Pratt et al., 2009), ALABAMA (Brands et al., 2011) and miniSPLAT (Zelenyuk et al., 2015). The thermal vaporization and electron impact ionization technique is deployed for instance by the C-ToF-MS (Schneider et al., 2006; Bahreini et al., 2009; Morgan et al., 2010) and the mAMS (Vu et al., 2016; Goetz et al., 2018). In the ERICA instrument the LDI part is named ERICA-LAMS (ERICA Laser Ablation Mass Spectrometer) and the other ERICA-AMS (ERICA Aerosol Mass Spectrometer). The abbreviation AMS is adopted from the AMS provided by Aerodyne Inc., Billerica, MA, USA. The ERICA-AMS is linearly connected to the ERICA-LAMS and terminates the particle beam.

The sampled aerosol particles are focused by an aerodynamic lens (see Sections 2.1 and 3.2) to a narrow particle beam. For calculating the point in time for the ablation, the particle has to be detected first by two consecutive detection units (DUs). The particle detection is based on the light scattering principle (Hinds, 1999), where the detected light signal depends on particle size, particle shape, and complex refractive index (Bohren and Huffman, 1998). However, the particle has to be large enough to create a detectable signal. Typically, this particle size is larger than roughly 80 nm (geometric diameter d_{geo}, see Section 4.2.2) depending on the properties of the particle and the optics of the instrumental setup.

The LDI technique of the ERICA-LAMS is able to measure a wide range of components by ablation, ionization, and bipolar mass spectrometric ion analysis. Thus, refractory and non-refractory substances can be analyzed (see Table 1). Due to their low ionization energy, elements, like sodium and potassium, can be detected easily (Murphy et al., 1998). The LDI mechanism is complex and not fully understood yet (e.g., Suess and Prather (1999), Drewnick (2000), Murphy (2007)). The LDI process is a non-linear multi photon process that prevents a linear calibration. Different absorption characteristics and ionization efficiencies of the analyte's matrix, possible reactions within the micro-plasma and charge transfer effects in the ionization region limit this technique to qualitative analysis (Suess and Prather, 1999; Zelenyuk et al., 2009). The charge transfer reactions in the ablation plume can cause suppressions of ion signals from major compounds by less concentrated compounds (e.g., Reilly et al. (2000), Zhou et al. (2006) and Köllner (2019)). Furthermore, substances that are transparent to the ablation laser light, like pure sulfuric acid, cannot be analyzed by this technique (Murphy, 2007). In addition, the ablation laser is idle for 120 ms to recover from the previous laser pulse and to stay in a stable condition (e.g., to be able to deliver constant pulse energies over many shots). During this idle time, no single particle mass spectra can be recorded. Considering a pulse duration of 6 ns and approximately 8 pulses in maximum per second (see Section 3.4.1), the laser ablation part is idle for more than 99 % of its operation time. Nonetheless, ERICA-LAMS is capable of simultaneously delivering positive and negative ion mass spectra from each detected and ablated particle (Table 1). Thus, the ERICA-LAMS provides bipolar spectral information of a single particle.

The ERICA-AMS can measure the chemical composition of aerosol particles quantitatively, due to the thermal vaporization/ionization technique at a particle beam terminating vaporizer. For this, a quantitative calibration with known substances is necessary and possible (Jayne et al., 2000). In this way, particles that vaporize below the set vaporizer temperature of 600 °C can be measured (see Table 1). These non-refractory substances are for instance ammonium nitrate (Jayne et al., 2000), sulfuric acid (Jimenez et al., 2003c), or volatile organics (e.g., IEPOX-SOA, Schulz et al. (2018)). Typically, from AMS instruments the amounts of particulate ammonium, sulfate, nitrate, chloride, and organics are provided in absolute amounts of microgram per cubic meter of air (Jayne et al., 2000). However, refractory particle components like pure mineral dust or fresh soot particles cannot be measured by this technique, neither quantitatively nor qualitatively. Due to the recording of the mass spectra at a frequency of 50 Hz a large amount of spectral data is acquired. This data then is averaged over one second (see Section 3.7.3.2) to be able to send this data to the main computer. The obtained mean spectrum provides only particle ensemble information. Furthermore, by the electron impact ionization technique only mass spectra with positive polarity can be detected and the chemical information is limited to cation spectra (see Table 1). This technique is not dependent on a previous particle light scattering detection. Thus, it is principally possible to measure smaller particles than by the LDI technique (see Table 1).

Table 1 summarizes the characteristics of both described techniques implemented in the ERICA instrument. The characteristics are valued as advantages (+) or disadvantages (-). The disadvantages of the ERICA-AMS, such as the fact that only particle ensembles, cations and non-refractory compounds are capable to be measured, are partially compensated by the ERICA-LAMS. If the LAMS were a quantitative method the two techniques would be fully complementary. On the other hand, the ERICA-AMS enlarges the size and time range of the particle analysis and enables a quantitative aerosol analysis.

For mobile operation, the instrument has to be compact, lightweight, and suitably controlled by a computer for fully autonomous deployment. Both instrument components share one power distribution, one main control computer, one inlet, and one vacuum system that leads to a compact recipient (see Chapter 3). Furthermore, during the idle time of the ablation laser of the ERICA-LAMS part, the ERICA-AMS part is able to continue measuring.

Table 1: Summary of the properties of the two instrument parts of ERICA: ERICA-LAMS (left) and ERICA-AMS (right). Advantages of the part is marked in the cell as (+), disadvantages as (-).

ERICA-LAMS	ERICA-AMS
Single particle (+)	Particle ensemble (-)
Cations and anions (+)	Cations (-)
Non-refractory and refractory compounds (+)	Non-refractory compounds (-)
Small particle size range (-)	Larger particle size range (+)
Qualitative only (-)	Quantitative and qualitative (+)
Long idle times (-)	Continuous measurement (+)

Another advantage of the combination especially for aircraft operation is the fact that if one part fails, the other part might still be able to continue its measurement. For some aircraft measurement campaigns, only a few opportunities such as appropriate aircraft or meteorological conditions are given. Here, the loss of the recording of one part would not result in a total loss of data collecting. The

instrument was designed for fully automated operation (Dragoneas et al., 2020) aboard the Russian high altitude research aircraft M-55 *Geophysica* which is capable of reaching 20 to 21 km altitude (Borrmann et al., 1995; Stefanutti et al., 1999).

The ERICA prototype was deployed for the first time during the aircraft-based measurement campaigns of the StratoClim (acronym for: Stratospheric and upper tropospheric processes for better Climate predictions) project (Rex et al., 2016). The first phase took place in August and September 2016 at the Kalamata International Airport (KLX; see Section 5.1) in Kalamata, Greece, while the tropical research flights were performed at the Tribhuvan International Airport (KTM; see Section 5.2) in Kathmandu, Nepal, during July and August 2017.

1.3 Structure of the thesis

Within the scope of this thesis work, the ERICA instrument was designed, assembled, adjusted, and characterized by laboratory experiments, as well as implemented into the aircraft and deployed during the StratoClim field missions. In addition, the data sets were processed and first technical and scientific results are presented in this thesis.

The instrument was assembled in steps. The gradually added components (introduced in Chapter 3) had to be tested and some of them, e.g., the detection units and the ablation laser beam, optically and mechanically adjusted. With the preconditioned instrument, first characterization measurements were performed (Section 4.1). After the first aircraft-based field deployment in Kalamata, Greece, technical improvements had to be made (Section 5.1). These improvements allowed the characterization measurements of the detection units and the particle beam (Section 4.2). By these characterization measurements, the particle beam width, the effective radius of the detection unit, and the transmission efficiency of the aerodynamic lens were determined dependent of particle size and type. In addition, the particle size calibration for the ERICA-LAMS was conducted. Furthermore, the ablation efficiency (Section 4.3) was determined in a ground-based field experiment and defined chemical substances were sampled (Section 4.4) to establish the ERICA-LAMS performance. The performance of the ERICA-AMS is presented in Section 4.5. Aerosol particle mass spectra could be successfully recorded at all altitudes from the ground up to 20 km. For the data evaluation, the author's focus was on the ERICA-LAMS part. The data set was evaluated using two different methods: the clustering method and the ion marker method. The overall operational capabilities of the ERICA instrument could be successfully demonstrated from the laboratory experiments and the field deployments in Kalamata and Kathmandu. For the development and the data evaluation the background and the long standing experience within the working group (e.g., Brands (2009), Klimach (2012), and Köllner (2019)) were of essential help. Parts of this thesis have contributed to two peer-reviewed publications and four publications in review or in preparation: Höpfner et al. (2019), Molleker et al. (2020), Schneider et al. (2019), Hünig et al. (2020), Clemen et al. (2020), and Dragoneas et al. (2020).

2 Methodology

In this chapter the methods of particle focusing, particle sizing, laser desorption and ionization, flash vaporization and electron impact ionization, as well as time-of-flight mass spectrometry are introduced.

2.1 Particle beam focusing by aerodynamic lenses

To measure the chemical composition of particles by a mass spectrometer, the particles have to be directed to the ion source in a defined way. Therefore, two different techniques are commonly in use: capillaries and aerodynamic lens arrays. Named in the following as aerodynamic lens, the latter technique is deployed in ERICA. This aerodynamic lens consists of six concentric apertures (see Section 3.2). Contrary to capillaries aerodynamic lenses do not clog and permit aerodynamic sizing due to size dependent exit velocities (Kulkarni et al., 2011).

The principle of particle focusing by an aerodynamic aperture is shown in Figure 1. The particle containing air sample is drawn through an axial-symmetric aperture where the particles are separated from the fluid (air) due to their mass dependent inertia. As the fluid and particles approach the aperture, both the fluid streamlines and the particle trajectories bend toward the center-axis and radial acceleration occurs. Due to the smaller cross-section of the aerodynamic aperture, both the fluid and the particles accelerate as they flow past the constriction. The trajectories of the particles overshoot relative to the fluid streamlines due to the higher inertia of the particles and thus the particles are pushed closer to the axis. Thereon, the particles exit the aperture. The higher inertia of the particles (relative to the fluid) prevents the particles from readily changing their direction of motion. This fact causes the particles to follow a path that remains closer to the centerline than the fluid streamline on which they initially were moving along. Repeating this procedure several times also with smaller diameters of the apertures the particle trajectories come step by step closer to the axis of the lens. Characteristic for the flow properties of an aperture and therefore for the particle focusing are the dimensionless Stokes number Stk and the stop distance s_p.

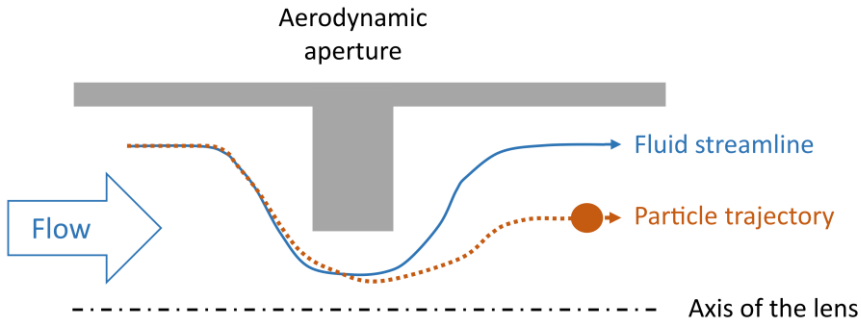

Figure 1: Scheme of the particle focusing mechanism in an aerodynamic lens aperture. The figure is redrawn according to Peck et al. (2016).

To adjust the particle velocity to the new condition of forces it takes the relaxation time τ (Hinds, 1999). The relaxation time is given in Equation (1), where m_p is the particle mass, C_c is the Cunningham slip correction factor, μ is the fluid viscosity, and d_p is the particle diameter (Seinfeld and Pandis, 2016).

$$\tau = \frac{m_p \cdot C_c}{3 \cdot \pi \cdot \mu \cdot d_p} \quad (1)$$

For spherical particles, m_p is given as:

$$m_p = \frac{\pi}{6} \cdot {d_p}^3 \cdot \rho_p \tag{2}$$

Here ρ_p is the particle density. Combining both equations, the relaxation time for ideal spherical particles given as follows (Hinds, 1999):

$$\tau = \frac{\rho_p \cdot {d_p}^2 \cdot C_c}{18 \cdot \mu} \tag{3}$$

Non-spherical particles are inferior to focus, such as NH_4NO_3 particles, due to additional radial velocity components caused by lift forces (Liu et al., 1995a; Huffman et al., 2005; Liu et al., 2007).

The Cunningham slip correction factor C_c is given by Equation (4), which includes the empirically determined coefficients and the mean free path of the air λ_{mfp}. The mean free path λ is defined as the average distance travelled by a molecule before it encounters any other molecule (Seinfeld and Pandis, 2016).

$$C_c = 1 + \frac{2 \cdot \lambda_{mfp}}{d_p}\left[\alpha + \beta\, exp\left(-\frac{\gamma \cdot d_p}{2 \cdot \lambda_{mfp}}\right)\right] \tag{4}$$

The parameters that are valid for solid particles are: $\alpha = 1.142$, $\beta = 0.558$, $\gamma = 0.999$ (Allen and Raabe, 1985).

Values of C_c as a function of the particle diameter d_p in nitrogen, as major fraction of the air, at 298 K and at 1,013 hPa (λ_{mfp} = 6.68·10^{-8} m, calculated according to Atkins and De Paula (2006)) range from 1.030 (d_p = 5.0 µm) to 5.077 (d_p = 50 nm). The Knudsen number Kn is given by Equation (5) (Seinfeld and Pandis, 2016).

$$Kn = \frac{2 \cdot \lambda_{mfp}}{d_p} \tag{5}$$

In case the particle diameter d_p is in the same order of magnitude as of the mean free path λ_{mfp} of the suspending fluid, e. g., air (for Kn is larger 1), the drag force F_{drag} to the particle is reduced by the slip correction factor. Equation (6) is taking this fact into account. Here u_∞ is the undisturbed velocity of the fluid upstream of the particle body (Seinfeld and Pandis, 2016).

$$F_{drag} = \frac{3 \cdot \pi \cdot \mu \cdot d_p \cdot u_\infty}{C_c} \tag{6}$$

The stop distance s_p is the product of the relaxation time τ and the particle velocity v_p.

$$s_p = \tau \cdot v_p \tag{7}$$

The stop distance s_p describes the distance that the particle travels within the relaxation time τ (Kulkarni et al., 2011). The particles will not impact onto the aperture body and adjust fast enough to the changed conditions, in case the diameter of the aperture is designed larger than the stop distance of the particle (Ettner-Mahl, 2006). The dimensionless Stokes number Stk (Equation (8)) describes the ratio of the stop distance s_p to the characteristic length of the flow L (Seinfeld and Pandis, 2016).

$$Stk = \frac{s_p}{L} \tag{8}$$

For aerodynamic lenses, L is the diameter of a lens aperture (Wang and McMurry, 2006). When $Stk \ll 1$, particles follow the fluid stream lines, when $Stk \gg 1$ the particles continue moving in a straight line when the gas molecules follow a curvature (Hinds, 1999).

For the design of an aerodynamic lens it has to be considered that the particles have to be small enough to follow the stream lines and do not impact on the aperture surface. However, the particles have to be large enough, i.e., inert, to get focused into a beam. Thus, multiple apertures are combined consecutively with decreasing inner diameters. Since small particles follow the fluid stream lines after the aperture relatively well, multiple apertures are necessary to focus these small particles to a narrow beam (Brands, 2009). The aerodynamic lens deployed in ERICA consists of six such apertures (see Section 3.2).

2.2 Particle sizing

To determine the aerodynamic size of particles that exit the aerodynamic lens, the flight time between two detection units (DU) is measured. The following two sub-sections briefly introduce the principles of particle acceleration and light scattering on particles.

2.2.1 Particle acceleration by an aerodynamic lens

At the transition from the aerodynamic lens to the high vacuum in the recipient of the instrument the particles are accelerated. According to Stokes' law, particles moving in a fluid undergo a drag force F_{drag} following Equation (6). Stokes' law is derived from the solution of continuum fluid mechanics and the Navier-Stokes equations and is applicable to the limit $Kn \to 0$. The nonslip condition used as a boundary condition is not applicable for high Kn values (Seinfeld and Pandis, 2016).

The slip correction factor C_c can be parameterized according to Equation (4). For the condition $Kn \gg 1$, C_c can be approximated as (Ettner-Mahl, 2006):

$$C_c \approx \frac{\lambda_{mfp} \cdot (\alpha + \beta)}{d_p} \tag{9}$$

Considering Newton's second law,

$$F = m_p \cdot a \tag{10}$$

where m_p is the mass of the spherical particle and a its acceleration, and Newton's third law $F = F_{drag}$, the acceleration a can be calculated as:

$$a = \frac{18 \cdot \mu \cdot u_\infty}{\rho_p \cdot \lambda_{mfp} \cdot (\alpha + \beta)} \cdot \frac{1}{d_p} \tag{11}$$

Thus, the acceleration in flight direction of the spherical particles is inversely proportional to d_p. After this acceleration the particle travels with approximately constant velocity in the high vacuum regime of the recipient. The terminal velocity additionally depends on the size dependent acceleration time.

The calculation of the terminal velocity would require deep analysis of fluid dynamics and cannot be done without simplifying approximations (in comparison with Klimach (2012)). However, the size dependence of the velocity can be used for a particle size determination after a suitable calibration (see Section 4.2.2). The particle density ρ_o is then assumed as 1.00 g cm^{-3}. Per definition this is the vacuum aerodynamic diameter d_{va} (Equation (12)), since it is determined in the free molecular regime (Jimenez et al., 2003b, a; DeCarlo et al., 2004; Brands, 2009):

$$d_{va} = d_p \cdot \frac{\rho_p}{\rho_o} \tag{12}$$

2.2.2 Light scattering on particles

The particle flight time is determined by two light scattering units at known distance. Two continuous wave diode lasers function as light source by emitting laser light at a wavelength λ = 405 nm. Each unit detects the light scattered by the individual particles. The time difference between both signals is measured.

The intensity of scattered light is depending on the optical cross-sectional area of the particle. According to ambient size distribution measurements, the major number fraction of the ambient aerosol is smaller than 1 µm (Seinfeld and Pandis, 2016). The background signal has to be reduced and a largest possible fraction of scattered light has to be collected to decrease the minimum detectable particle size. To increase the detected scattered light signal, the detection units of ERICA features an ellipsoidal reflector, which collects the light over a wide angular range and focuses it on the detector (see Section 3.3).

Since the wavelength of the ERICA detection lasers (λ = 405 nm) is in the order of the particle size, the scattered light intensities can be calculated by Mie theory, which is based on the solution of the Maxwell equations for scattering of electromagnetic waves on spherical particles (Mie, 1908; Wriedt, 1998). By interference of single waves, a characteristic intensity distribution around the particle emerges. Figure 2 presents the generic intensity distribution of spherical, non-absorbing PolyStyrene Latex (PSL) particles with different sizes d_p (100 nm, 300 nm, 600 nm, 2,000 nm, and 6,000 nm) and with a refractive index (real part) $n_{D,PSL}$ of 1.65 (Galpin et al., 2017). The relative scattered light intensity I_{sc} was calculated for this thesis using the program *BH-Mie-Rechner* (from Vetter (2004), based on Bohren and Huffman (1998)). The graph shows that the light is scattered in a wide angular range.

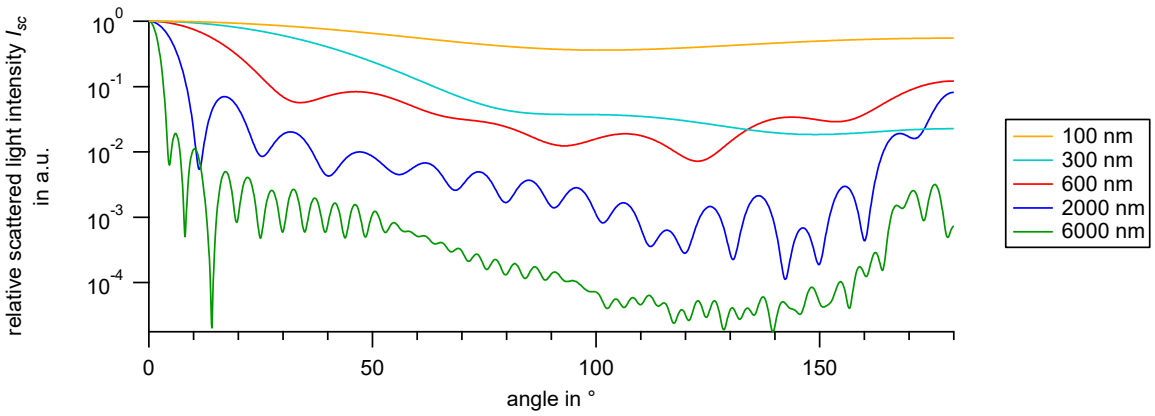

Figure 2: Calculation of relative light scattering intensity I_{sc} (in arbitrary units) versus the angle (in degrees) of polystyrene latex (PSL) particles of five sizes d_p (100 nm, 300 nm, 600 nm, 2,000 nm, and 6000 nm) at a wavelength of 405 nm.

2.3 Laser desorption and –ionization technique for the ERICA-LAMS

Laser desorption denominates the ablation of surface material of a body by an intense laser beam. For the ERICA-LAMS this is the ablation of material from individual aerosol particles by means of an UV (Ultra Violet) laser. For the desorption and the simultaneous ionization of the resulting vapor of atoms and molecules, flux densities between 10^6 and 10^{12} W cm^{-2} are necessary (Suess and Prather, 1999). For such flux densities commonly these lasers are used: CO_2 laser (λ = 10.6 µm), frequency quadrupled (λ = 266 nm) Nd:YAG laser (neodymium-doped yttrium aluminum garnet; Nd:$Y_3Al_5O_{12}$; λ = 1,064 nm), or excimer laser (often used λ = 193 nm) with pulse duration of ~1 µs (CO_2) or ~10 ns (excimer and Nd:YAG). The laser beam can be focused down to a spot size of 1 µm in diameter (Heinen, 1981; Suess and Prather, 1999).

The LDI process depends on the laser wavelength, i.e., the energy of the photons, and the pulse duration of the laser. However, further parameters, such as the component's ionization potential and lattice energy, play an important role during the LDI process. Complex thermal, photochemical and photo-mechanic effects affect the ionization process (Schoolcraft et al., 2000). Hereby the thermal effect is most important (Heinen, 1981). The process can solely be explained qualitatively, because the interaction of non-linear effects (Kissel and Krueger, 1987) is still not amenable for mathematical description. In addition, different ionization efficiencies of the analytes limit this technique to qualitative analysis, as well as possible reactions within the micro-plasma and charge transfer effects in the ionization region (e.g., Suess and Prather (1999) and Zelenyuk et al. (2009), see Section 1.2).

During a laser pulse, the energy of photons is transmitted to the electrons and from the electrons to the lattice of the solid body. By that, the lattice starts to vibrate and the body heats up. If the laser fluence exceeds a certain threshold, the heat cannot be dissipated from the surface anymore due to insufficient heat conduction (Ready, 1965; Schoolcraft et al., 2000). As a result, the particle begins to evaporate. The fraction of a particle that will be vaporized depends on the laser fluence and the particle size (Zhigilei et al., 1998; Schoolcraft et al., 2000), i.e., particle volume and mass. Furthermore, the morphology of the particle is important. Figure 3 shows computer simulated (molecular dynamics simulation) laser shots (pulse duration 15 ps) to visualize the particle evaporation process on two different particle types, of 110 nm in size, with two different laser pulse energies. The homogeneous particle (a) that consists completely of laser light absorbing material, gets partially evaporated at low pulse energy (laser fluence 25 eV nm^{-1}) and completely at high pulse energy (laser fluence 300 eV nm^{-1}). The heterogeneous particle (b) consists of a laser light transparent core and a laser light absorbing coating. The pictures show the particle 20 ps, 50 ps, and 400 ps after the laser shot. At low energy, solely the coating gets evaporated but not the core. To evaporate also the core, more energy is needed. The simulation clearly demonstrates the difficulty of the LDI technique. Since it is a two-dimensional model of a relatively small particle and a relatively low laser fluence, the model can only be considered as a qualitative measure and cannot be directly compared to the conditions in the ERICA instrument. Incomplete ablation processes can lead to misinterpretation of the particle composition, since it is possible that parts of a particle are not detected. The absorption coefficient of the single components of an aerosol particle and their binding energy are decisive for the vaporization properties.

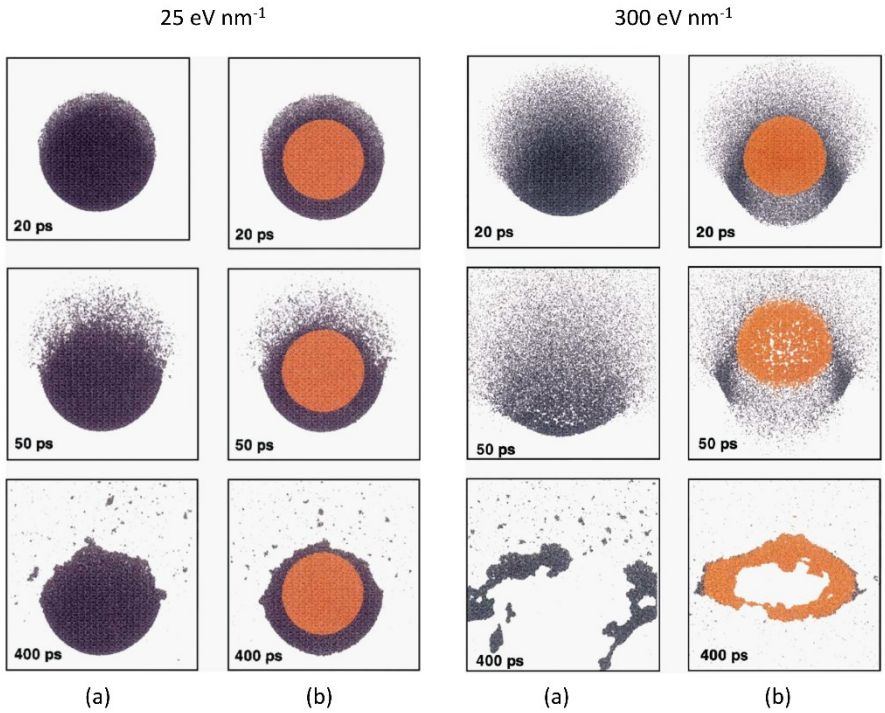

Figure 3: Simulation of laser shots (pulse duration 15 ps) on two particles (size 110 nm) of two different types and two different laser pulse energies (laser fluence of 25 eV nm^{-1} and 300 eV nm^{-1}). The single pictures show the particle 20 ps, 50 ps and 400 ps after the laser shot. (a) Homogenous absorbing (black) particle. (b) Transparent (red marked) core coated by absorbing material. Reprinted/adapted from Molecular dynamics simulations of laser disintegration of amorphous aerosol particles with spatially nonuniform absorption, 180, Tracy A. Schoolcraft, Gregory S. Constable, Bryan Jackson, Leonid V. Zhigilei, Barbara J. Garrison, Nuclear Instruments and Methods in Physics Research Section B: Beam Interactions with Materials and Atoms, 245 - 251, Copyright (2001), with permission from Elsevier (https://doi.org/10.1016/S0168-583X(01)00424-4).

Besides the ablation, ionization of the resulting vapor is an important process at high laser power density. The excitation is performed by photo and thermal ionization in a multi photon process. By collision with photons of the laser light or with neutral fragments, electrons from vapor atoms/molecules are emitted and the atom/molecule gets ionized. Hereby a plasma is created at flux densities typically $\sim 10^8 - 10^9$ W cm^{-2} (Zhou et al., 2006; Kamphus et al., 2008; Brands, 2009). This is also the case for ERICA with a value of $1.36 \cdot 10^9$ W cm^{-2} (see Section 4.1.3). Besides the flux density of the laser beam, the emitted wavelength λ is also relevant, since the ionization process is a complex multi-photon process (Bläsner, 2001; Wollny, 2002). For example, pure sulfuric acid droplets are transparent at λ = 266 nm and will not ablate, while at λ = 193 nm ablation, ionization and detection of these droplets occurs (Murphy, 2007).

The absorption of a UV light photon ($h\nu$; h is the Planck constant and ν the frequency) by a neutral molecule M can lead to electronic excited states M^* that relax either by emission of light (fluorescence or phosphorescence) or emit an electron (Photo Ionization, PI; Gross (2013), and Atkins and De Paula (2006)), according to Equation (13):

$$M + h\nu \rightarrow M^{+\bullet} + e^- \tag{13}$$

In this equation, the emitted positive fragment ion $M^{+\bullet}$ stands for an odd-electron ion (radical ion) that has lost (not added) one electron, indicated by "$+\bullet$". The radical symbol "$\bullet$" indicates the remaining unpaired electron after the ionization process (Gross, 2011).

Figure 4 depicts the energy of a single photon E_{photon} as function of the wavelength λ according to Equation (14):

$$E_{photon} = \frac{h \cdot c}{\lambda} \tag{14}$$

Here, h is the Planck constant and c is the speed of light. The wavelengths that are emitted by the ablation laser in ERICA are marked (λ = 1,064 nm, λ = 532 nm, and λ = 266 nm). A UV photon (λ = 266 nm) possesses an energy of 4.66 eV. The first ionization energies are between 3.9 eV for cesium and 24.6 eV for helium (Atkins and De Paula, 2006). Single bond-dissociation energies for carbon-hydrogen (e.g., H_3C-H) carbon-carbon (e.g., H_3C-CH_3), and carbon-oxygen (e.g., H_3C-OH) bonds are in the order of 4 eV (Blanksby and Ellison, 2003). Lattice energies are typically higher (e.g., NaCl: 8 eV; MgCl: 26 eV; MgO: 40 eV (Atkins and De Paula, 2006)).

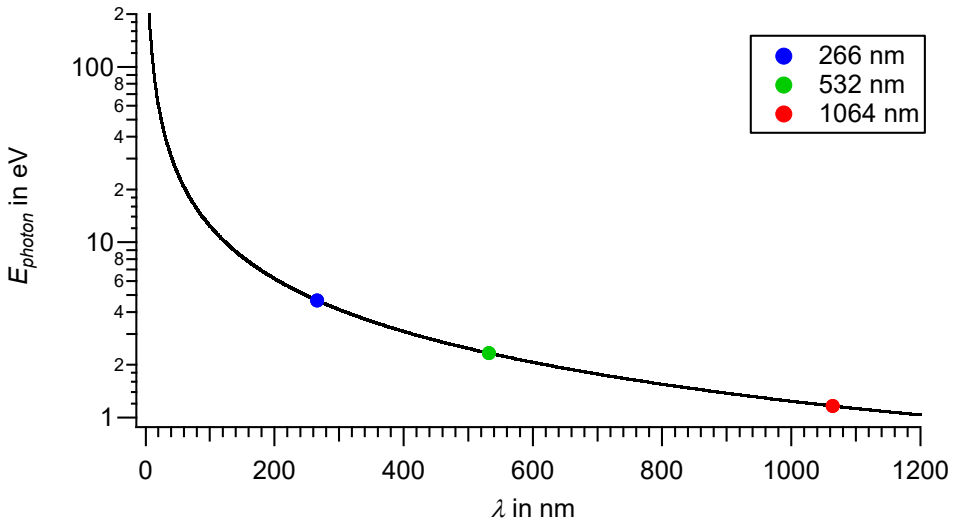

Figure 4: Energy of a photon E_{photon} as function of the wavelength λ. The wavelengths that are emitted by the ERICA ablation laser are marked with dots.

The absorption of energy needs not to be a single-photon process. A stepwise accumulation of energy from energy-poor photons can also lead to photo ionization. This process is called MUlti-Photon Ionization (MUPI; Gross (2013)). The Resonance-Enhanced Multi-Photon Ionization (REMPI) process is orders of magnitudes more effective than the non-resonance-enhanced MUPI (see Figure 5; Gross (2013) and Streibel and Zimmermann (2014)). The resonance absorption of the first photon in the ground state (S_0) leads to an excited intermediate state (S_1) from which the molecule can be excited by an additional photon that possesses the same wavelength λ_1 into the continuum by exceeding the ionization energy $E_{ionization}$. This process is termed (1+1) REMPI. In case, two photons (of the same wavelength λ_2) are needed to reach the S_1 state, the process is termed (2+1) REMPI. The (2+1') REMPI process describes the ionization by using photons possessing different wavelengths. In the ERICA-LAMS, three different wavelengths are involved in the LDI process.

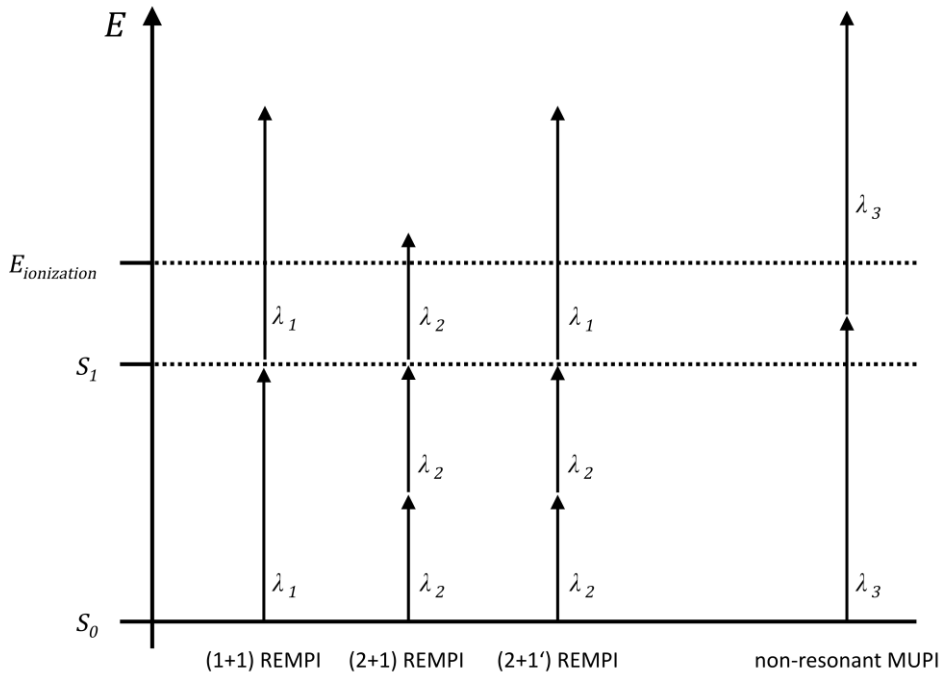

Figure 5: Schemes for ionization by Resonance-Enhanced Multi-Photon Ionization (REMPI) and non-resonant MUPI. See text for details.

The minimum energy to ionize a particle decreases systematically with shorter wavelengths (Thomson et al., 1997). In parallel, the degree of fragmentation in the mass spectra increases for shorter wavelengths at same laser intensity and also increases for higher laser intensities at the same wavelength (Murphy and Thomson, 1995; Roth, 2009). As a consequence, the higher degree of fragmentation can impede the identification of the aerosol particles initial chemical composition. Considering a Gaussian laser beam profile, the flux density in the center of the beam is higher than off-center, where still the ablation threshold might be exceeded. This fact leads to an unpredictable location dependent fragmentation effect that also cannot be calibrated.

To calculate the fraction of ionized fragments (also called degree of ionization) of one particular species the Saha–Eggert equation (Equation (15)) is applied assuming a local thermodynamic equilibrium in the plasma. It is derived from the law of mass action (Drawin, 1963).

$$\frac{n_i}{n_0} = \frac{2 \cdot Q(T)}{Q_0(T) n_e} \frac{(2 \cdot \pi \cdot m_e \cdot k_B \cdot T)^{\frac{3}{2}}}{h^3} \, exp\left(-\frac{E_{ip} - \Delta E}{k_B \cdot T}\right) \tag{15}$$

Here n is the atoms/molecules/fragments number density (indices: i, ions; 0, neutral atoms/molecules/fragments; e, electrons), $Q(T)$ the partition function of the ions, $Q_0(T)$ the partition function of the neutral atoms/molecules/fragments, m_e the electron mass, k_B the Boltzmann constant, T the temperature, h the Planck constant, E_{ip} the ionization energy of the atoms and ΔE the Coulomb depression. The equation describes the temperature T dependent equilibrium between neutral particles n_0, ions n_i, and free electrons n_e in the plasma for one particular species. An ambient particle might consist of multiple different species. The number of ions n_i in the plasma increases for higher temperature T and lower ionization energy E_{ip} of the atoms. Since charge carriers create an electrical micro field in the plasma, electrons can be separated from the atoms easier in the plasma than without this field. The ionization energy reduction is called Coulomb depression ΔE (Ettner-Mahl, 2006). However, the assumption of a thermodynamic equilibrium might not always be justified,

especially not for high flux densities, since the degree of ionization in the ablation region depends besides other parameters on the intensity distribution of the ablation laser in time and space, the ablation laser pulse duration, size width of the ablation spot and on the properties of the analyte such as particle size, light absorption coefficient, and the surface condition (Vertes et al., 1988; Wieser et al., 1991; Drewnick, 2000). Very short laser pulses, in the time range of femto-seconds, can cause a Coulomb explosion. Here, the high energetic electrons are emitted by the solid body before their energy is transmitted to the lattice. The remaining positive ions are pushed out by repelling Coulomb forces (Hashida et al., 2009). Up to a particle diameter of $\sim$ 1 µm, the ion yield correlates linearly with the particle size (Wieser et al., 1991; Brands, 2009). Larger particles are not fully ablated, so the ion yield decreases. Furthermore, higher laser power does not increase the ion yield, since the plasma around the particle absorbs the laser light and shields the residual particle. Thus, such particles are not fully ablated and ionized.

Due to this multitude of parameters influencing the ionization and the non-constant ablation process, the LDI technique cannot deliver quantitative single particle mass spectra. In contrast with the particle flash vaporization and Electron Ionization (EI) technique explained in the following Section 2.4, the integral over a spectral line in the time-of-flight mass spectrum cannot be used to infer the absolute mass of the compound within the aerosol particle. Only the presence (qualitative) of the detected elements or molecule fragments in the aerosol particle can be stated but not the amounts (quantitative). Quantitative estimations can solely be made with simplified assumptions (e.g., Jeong et al. (2011), Healy et al. (2013), Shen et al. (2019)) or by taking simultaneous measurements with other instruments into account (e.g., Qin et al. (2006), Brock et al. (2019), and Froyd et al. (2019)).

2.4 Particle flash vaporization and electron ionization technique for the ERICA-AMS

The precondition for the Electron Ionization (EI) technique is a gaseous analyte. Therefore, the aerosol particles have to be vaporized first. Since the temperature of the vaporizer inside ERICA-AMS is set to 600 °C, only non-refractory components that evaporate at this or below this temperature can be detected. Typically, the Aerodyne-AMS (Aerodyne Inc.) is capable of quantitatively measuring the particulate nitrate, sulfate, ammonium, organics, and chloride mass concentration. This also is the case for the ERICA-AMS. Of particular interest for this thesis work is ammonium nitrate (NH_4NO_3) among others, which can be measured at 600 °C for the vaporizer setting (Canagaratna et al., 2007). The in that way generated neutral gas molecules are exposed to an electron beam for ionization. A heated tungsten filament emits electrons with an energy of 70 eV (6.8 MJ mol^{-1}) by thermionic emission (Kellner, 2004). Compared to single photon energy (see Section 2.3), this value is more than one order of magnitude higher. The major part of the emitted electrons is elastically scattered. Some emitted electrons cause electronic excitation of the analyte molecule. In that way, the electrons are absorbed by the analyte molecule's electron cloud (Suess and Prather, 1999; Kellner, 2004). Typical values for the ionization energy of the analyte is between 6 and 10 eV (0.6 – 1 MJ mol^{-1}). Equation (16) shows a molecule M absorbing approximately 10 eV. The excess energy causes the molecule M to emit an electron of less energy (here exemplarily 60 eV) besides a thermal electron.

$$M + e^-(70\ eV) \rightarrow\ M^{+\bullet} + e^-(60\ eV) + e^-(thermal) \tag{16}$$

The in this equation emitted positive fragment ion $M^{+\bullet}$ stands for an odd-electron ion (radical ion) that has lost (not added) one electron, indicated by "$+\bullet$". The radical symbol "$\bullet$" indicates the remaining unpaired electron after the ionization process (Gross, 2011). The electron fulfills the same role as

photons during the PI process (see Section 2.3, Equation (13)). In ERICA, the voltage difference between the electron emitting filament and the ionization region is set to 70 V, resulting in an electron energy of 70 eV (see Section 3.5.2). There are three major reasons why the ionization energy of 70 eV is used. First, almost all atoms or molecules can be ionized at 70 eV. Second, the plateau of the ionization cross section is from around 60 – 80 eV. Thus, small deviations of the electron energy towards higher or lower values are negligible. Third, it allows comparisons of spectra from databases or other mass spectrometers using the EI technique (Gross, 2011).

The Franck-Condon principle states that electronic transitions are so fast ($2 \cdot 10^{-16}$ s) that the distance of the nuclei (r_0 and r_1 in Figure 6) does not change during these processes. The time period of the vibrational frequency of the cores is orders of magnitude slower, e.g., $1.1 \cdot 10^{-14}$ s for a C-H stretching vibration. These so-called vertical electron transitions hit the potential curve of the excited state not in the vibrational ground state but in the higher vibrational levels. To visualize this principle Figure 6 shows the potential energy curves of the ground, i.e., neutral (M), and excited state, i.e., ionic state ($M^{+\bullet}$), for a diatomic molecule. Electron ionization can be described by a vertical transition that is represented in the diagram as a vertical line. The minimum of the potential energy curve of the neutral, which is assumed to be in its vibrational ground state, is located at shorter bond length r_0 than the minimum of the ion in its ground state, r_1 (Gross, 2011). Thus, the ionization is accompanied by a vibrational excitation, due to the vertical transition (Gross, 2019).

The Franck-Condon factors f_{FC} describe the probabilities of the electronic transition from the electron and vibrational ground state to a certain vibrational level of the excited state, i.e., the ion. The probability of a transition is at a maximum, where the overlap of the electronic wave function of the ground state and the excited state is at a maximum. For the ground state the maximum is at the equilibrium position and for wave functions of higher vibrational states their maxima are at the turning points of the motion. The ionization leads to a weakening of the bonds within the ion that accompanied with a higher tendency towards dissociation of the bonds. The larger the value of r_1 compared to the value of r_0, the more probable is the generation of excited ions, which can be above the dissociative energy D illustrated by the dissociative hyper surface in Figure 6 (Gross, 2013). Ions having internal energies below the dissociation energy D remain stable, whereas molecules $M^{+\bullet}$ possessing an internal energy above D will fragment (see Equation (17)). These fragment ions can be identified in the mass spectrum. AE_{frag} is the appearance energy that is characteristic for every fragmentation reaction (Gross, 2013). Adiabatic ionization, the counterpart of the vertical ionization, is the process where ionization of the neutral in its vibrational ground state results in an ion also in the vibrational ground state (a so-called (0 ← 0) transition). This process, visualized by a slanted line, does not occur within EI conditions (Gross, 2019).

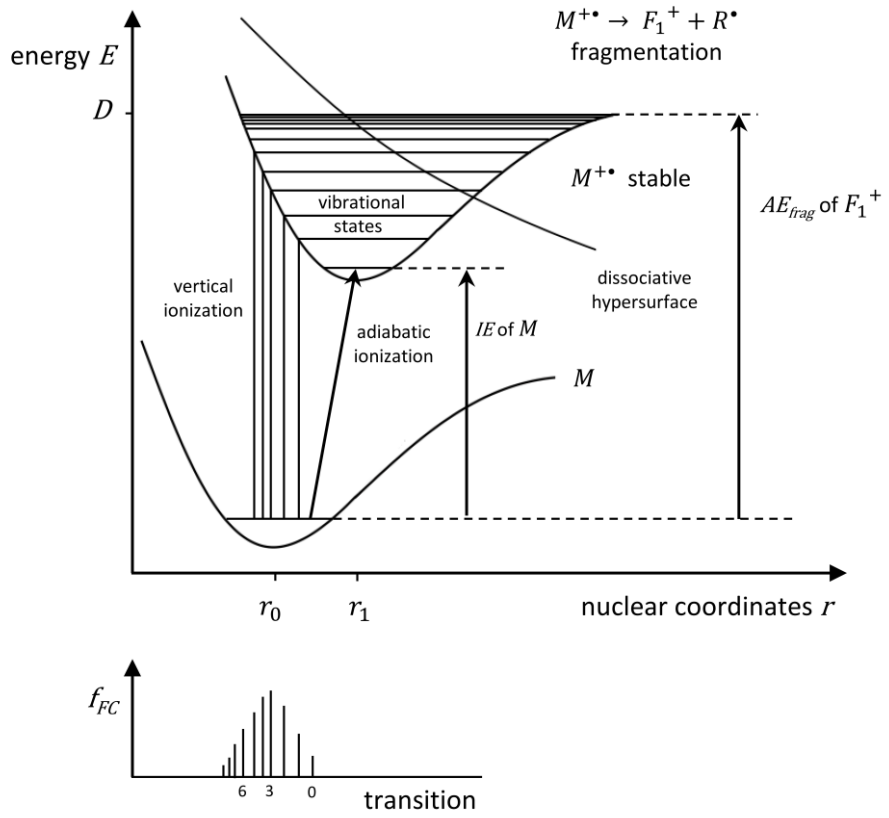

Figure 6: Transitions from the neutral to the ionic state for a diatomic molecule. The figure is adapted and redrawn according to Gross (2013). See text for details.

The excess internal energy and the radical character (unpaired electron) of the cation can give rise to unimolecular dissociations resulting in fragment ions F_n^{+}. These are unique for different structures. Typically the reaction mechanism ends up in radicals $R_n^{\bullet}$ or neutral fragments N (Equations (17) to (19) from Kellner (2004)).

$$M^{+\bullet} \rightarrow F_1^{+} + R_1^{\bullet} \quad (17)$$

$$M^{+\bullet} \rightarrow F_2^{+\bullet} + N \quad (18)$$

$$F_2^{+\bullet} \rightarrow F_3^{+} + R_2^{\bullet} \quad (19)$$

The electron of lower energy (here the 60-eV electron in Equation (16)) excites in turn a further analyte molecule. The fragmentation pattern is highly dependent on the initial electron energy (Suess and Prather, 1999). Besides a singly charged ion also multiply charged ions can possibly be generated. Electron attachment processes are unlikely with electrons that possess an energy of 70 eV due to the fact that electron capture is a resonance process (Gross, 2011, 2013).

The '*even-electron rule'* states that ions containing an odd number of electrons (such as $M^{+\bullet}$ and $F_2^{+\bullet}$) may eliminate either a radical (such as $R_1^{\bullet}$ and $R_2^{\bullet}$) or an even-electron neutral species (N). Even electron ions (such as F_1^{+} and F_3^{+}) will usually not lose a radical to form a cation that consists of an odd number of electrons, i.e., the successive loss of radicals is forbidden (Gross, 2011). The internal energy leads from $M^{+\bullet}$ to further fragmentation. Figure 7 (Gross, 2011) exemplifies the various possibilities of a hypothetical analyte consisting of four atoms ($ABYZ^{+\bullet}$) obeying the '*even-electron rule'*. The figure exemplarily shows that species $Y^{+\bullet}$ and YZ^{+} can be formed in different pathways via

$AYZ^{+\bullet}$ or $ABY^{+\bullet}$ and BYZ^{+}, respectively. Also, the same fragment can be formed with different electron configuration ($Y^{+\bullet}$ odd electron number and Y^{+}even electron number).

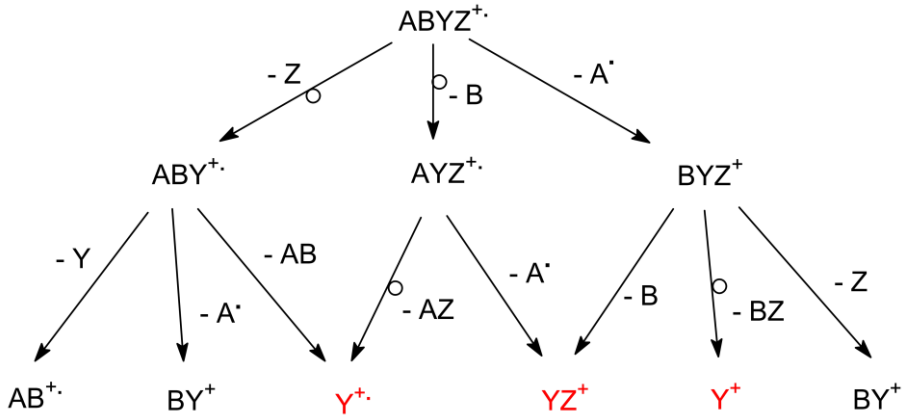

Figure 7: Possible fragmentation pathways for a hypothetical molecular ion ($ABYZ^{+\bullet}$) that contains internal energies in the range for electron impact ionization. Species $Y^{+\bullet}$ and YZ^{+} can be formed in different pathways originated from $ABYZ^{+\bullet}$. The odd electron number species $Y^{+\bullet}$ and the even electron number species $YZ^{+}$and Y^{+} are highlighted in red. Reprinted/adapted by permission from © Springer-Verlag Berlin Heidelberg 2011: Springer Nature, Mass Spectrometry by Gross (2011).

In addition to the generation of a molecule ion, other occurrences can result from interactions between electron and neutral molecule (Figure 8). The excitation of a neutral molecule into an excited state without ionization is a less effective interaction. With increasing energy of the primary electron, the frequency and the diversity of the other processes increase. The electron ionization can proceed in various ways whereby each process leads to a generation of characteristic ionized and neutral products: molecule ions, fragment ions, multiply charged ions, meta-stable ions, rearranged ions and ion pairs (Gross, 2013). The reaction that is equivalent to Equation (16) is highlighted in red.

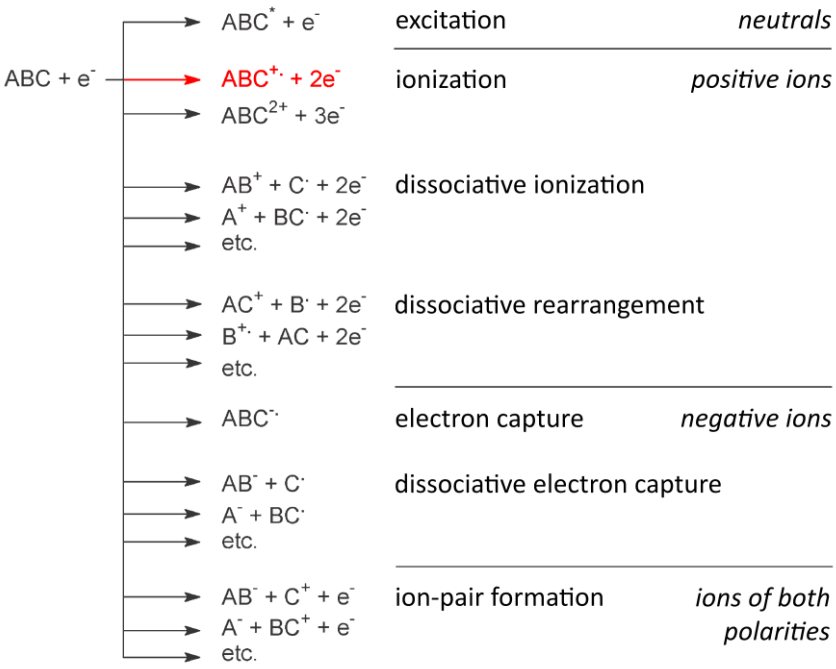

Figure 8: Processes under electron ionization conditions. Reprinted/adapted by permission from © Springer-Verlag Berlin Heidelberg 2011: Springer Nature, Mass Spectrometry by Gross (2011); originally from Schröder (1991).

2.5 Ion detection by time-of-flight mass spectrometry

The Time-of-Flight Mass Spectrometry (ToF-MS) is based on the principle of ion separation due to the different ion velocities. The criterion for the separation is the mass-to-charge ratio (m/z) of the ions. In an electric field, the ions are accelerated according to their m/z and the ions get separated in a field-free path according to their velocities and arrive at the detector at different times, a Multi-Channel-Plate (MCP). The arrival time is recorded by an oscilloscope. In case the ToF-MS is coupled with LDI (i.e., ERICA-LAMS), the laser trigger sets the starting time for the recording of the spectra and for the ToF-MS coupled with the EI (i.e., ERICA-AMS) the extractor defines the starting time.

In the ionization region the ions get extracted and accelerated by an electric field into the drift tube of the ToF-MS. The electric field energy is converted to kinetic energy of one ion (Equation (20)).

$$z \cdot U = \frac{1}{2} \cdot m \cdot v^2 \tag{20}$$

Here z is the charge of the ions, U the voltage of the electric field, m is the mass of an ion and v its velocity. Since the ion flight path length s_{tof} (tube length) is known and constant, v only depends on the time of flight t_{tof}. Thus $\frac{m}{z}$ can be expressed as Equation (21).

$$\frac{m}{z} = \frac{2 \cdot U \cdot {t_{tof}}^2}{{s_{tof}}^2} \tag{21}$$

This leads to a flight time t_{tof} defined in Equation (22).

$$t_{tof} = s_{tof} \cdot \sqrt{\frac{m}{2 \cdot z \cdot U}} \tag{22}$$

The constant parameters such as the acceleration voltage U (electric field) and the tube length s_{tof} can be combined to a single constant B_{tof}. With an additional time offset A_{tof}, Equation (22) can be re-written as Equation (23) that is used for m/z calibration (Hings, 2006).

$$t_{tof} = A_{tof} + B_{tof} \cdot \sqrt{\frac{m}{z}} \tag{23}$$

The flight times for lighter ions is shorter than for heavier ions of the same charge and thus the lighter ions reach the detector first.

When an evaporated particle is ionized, an ion plume is generated. The point in time and the location of the ion generation in this plume vary as well as the modulus and the direction of the kinetic energy that is transferred to the created ions during the ionization process. Therefore, ions of the same m/z can reach the detector by a time shift Δt (Brands, 2009). To detect ions of different masses (m/z) separately, the signal's width of Δt should not overlap with other signals (Gross, 2011). According to Equation (22), a Δm can be calculated from Δt, assuming a single charge (Brands, 2009).

The resolution in mass spectrometry is defined by IUPAC as $R_{MS} = \frac{M}{\Delta M}$ (IUPAC, 1997), where M is the mass of the peak, in the unit of the m/z –value, and ΔM is the resolving power. Commonly ΔM is the full width at half maximum (FWHM) of mass M. The resolution is influenced by the size of the ionization region volume, the pulse length, and the variation of the initial energy distribution of the ions with the same value for m/z during the ionization process. The initial energy distribution of the ions in turn depends on laser energy, pulse length and particle properties (Ettner-Mahl, 2006).

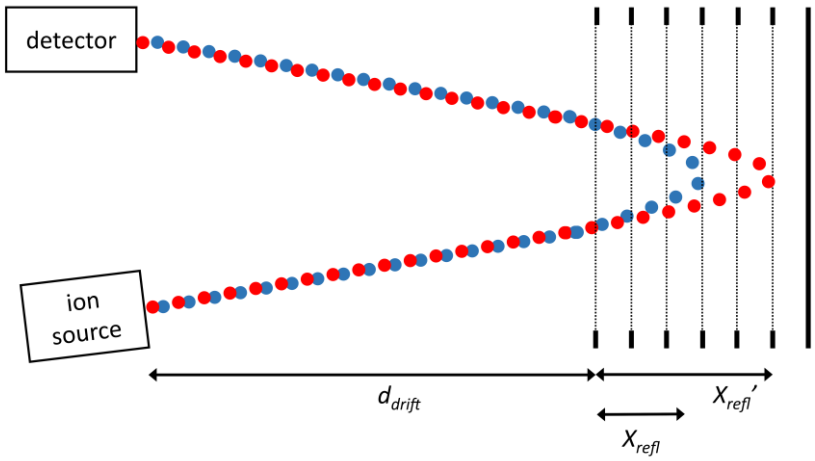

Figure 9: Scheme of the design of a reflectron. Two ions of the same m/z value but different start velocities are first moderated in an electric field and then accelerated in the opposite direction (reflection). The duration of stay is longer for the faster (red) ion than for the slower (blue) one. The figure is redrawn according to Ettner-Mahl (2006).

To increase the resolution, a reflectron can be used for cations as well as for anions. It extends the travel path of the ions and improves the separation of different ion velocities of a particular m/z (Figure 9). In the ion source, the ions are created with different initial velocities and travel directions. The path in the drift tube d_{drift} is field-free. Here, the ions of the same m/z values but different start velocities are first decelerated in an electric field and then accelerated in the opposite direction (reflection). The duration of stay in the reflectron is longer for the faster (red) ion than for the slower (blue) one, since it enters the reflectron deeper (X_{refl}') than the slower one (X_{refl}). A sufficient adjustment of the voltages in the reflectron can partially compensate for small initial velocity differences of ions at the same m/z, but not for different starting points and travel directions of the ions within the ionization plume (see Section 2.3). Currently, reflectrons are commonly deployed in mass spectrometers coupled to LDI technique (e.g., Brands et al. (2011), Cziczo et al. (2006), and Pratt et al. (2009)) or to EI techniques (e.g., Drewnick et al. (2005), Canagaratna et al. (2007), and Vu et al. (2016)). Reflectrons are implemented in each ToF-MS of the ERICA, such as the ERICA-AMS for positive ions and the ERICA-LAMS for positive and negative ions.

3 Instrumental overall design of ERICA

3.1 General description

The here presented novel aerosol particle mass spectrometer ERICA (as shown in Figure 10) is a combination of a single particle laser ablation bipolar mass spectrometer (ERICA-LAMS) with a particle ensemble mass spectrometer (ERICA-AMS), adopting the thermal flash vaporization and electron impact ionization technique.

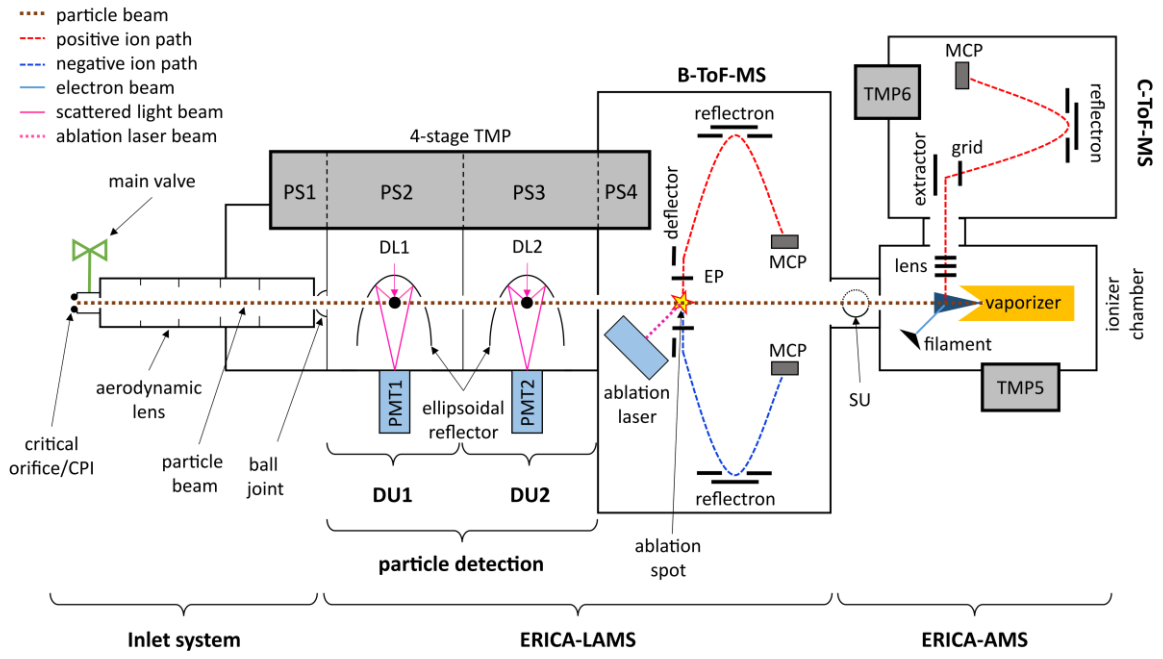

Figure 10: Instrumental design of the ERICA instrument (CPI – Constant Pressure Inlet, DL – Detection Laser, DU – Detection Unit, EP – Extraction Plate, MCP – Multi Channel Plate, PMT – PhotoMultiplier Tube, PS – Pumping Stage, SU – Shutter Unit, TMP – Turbo Molecular Pump).

A critical orifice as part of the Constant Pressure Inlet (CPI) serves as continuous mass flow entry providing sample air with the suspended aerosol particles. The orifice consists of a silicone rubber O-ring that changes its inner diameter by being compressed. A controller unit connected to pressure sensors regulates the O-ring compression and thus the mass flow into the instrument according to ambient pressure. The controller keeps the pressure on the vacuum side of the O-ring constant. Thus, the compression unit is called CPI as described by Molleker et al. (2020). A main plug valve interrupts the sample flow into the instrument and seals the vacuum chamber in case the instrument is not in measuring mode.

The sampled particles are focused by the aerodynamic lens to a narrow beam and accelerated into a vacuum chamber (see Section 3.2) with the particle detection unit of the single particle Time-of-Flight (ToF) mass spectrometer (ERICA-LAMS). The particle detection is realized by a flight time measurement from two light scattering modules, named Detection Units (DU; see Section 3.3). Here two parallel lasers are focused onto the particle beam. The scattered light is focused on PhotoMultiplier Tubes (PMTs) by means of ellipsoidal reflectors. These DUs are essential for particle flight time determination (see Section 3.7.2.2). After calibration, the vacuum aerodynamic diameter d_{va} can be determined (see Section 4.2.2). In addition, the particle flight time is used to determine the point in time when the particle detected by the DUs arrives in the ablation spot. At this ablation spot, the particle gets

evaporated and ionized by a triggered UV laser pulse (λ = 266 nm) emitted by a Nd:YAG laser (see Section 3.4.1). The resulting positive and negative ions, or more accurately the charged molecule fragments, are accelerated into a Bipolar ToF Mass Spectrometer (B-ToF-MS), where they are detected by Multi-Channel Plates (MCPs). Some particles are not ablated by the laser either because (1) the laser is forced to idle condition and cannot fire, (2) the particles are too small to be detected by the DUs, and/or (3) the particles are detected by only one DU. If the number density of particles within the focused particle beam is sufficiently high, most particles, however, pass by the ablation laser unablated, because the laser is capable only of firing at a repetition rate of 8 times per second. These unablated particles pass through the B-ToF-MS region of the ERICA-LAMS and enter the continuous ionization aerosol particle ToF mass spectrometer of the ERICA-AMS, where they hit the vaporizer surface. This surface essentially terminates the particle beam. The flash vaporization at the vaporizer is followed by electron impact ionization. The so generated positive ions are accelerated into the C-ToF-MS (C-shaped Time-of-Flight Mass Spectrometer) and detected by MCPs along the Aerodyne Inc. Aerosol Mass Spectrometer (AMS) principle. The ERICA instrument is suitable to measure particles in a size range between 80 nm and 5 µm (see size calibration in Section 4.2.2). Single particles are detected with an efficiency above 50 % between 174 nm and 3,173 nm (see Section 4.2.4).

The single particle mass spectrometer is a thoroughly modified LAAPTOF (Laser Ablation Aerosol Particle Time-Of-Fight mass spectrometer) that was provided by AeroMegt GmbH (Gemayel et al., 2016; Marsden et al., 2016; Shen et al., 2018). The ERICA-AMS is very similar to the Aerosol Mass Spectrometer (AMS) from Aerodyne Inc. (Davis, 1973; Jayne et al., 2000; Jimenez et al., 2003c; Drewnick et al., 2005; Canagaratna et al., 2007). A major modification for ERICA-AMS is the substitution of the chopper with a shutter (see Section 3.7.3.2).

The ERICA-LAMS is capable of measuring simultaneously positive and negative ions of a single particle. It detects refractory and non-refractory particle types like soot, salt, mineral and meteoric dust particles as well as metal-containing particles qualitatively (e.g., Suess and Prather (1999), Zelenyuk and Imre (2005), Murphy (2007), Schneider et al. (2019)). Like the AMS of Aerodyne Inc. the ERICA-AMS provides quantitative mass concentration of non-refractory particulate sulfate, nitrate, ammonium, chloride and organic compounds (Canagaratna et al., 2007).

Since the two instruments share one vacuum chamber, weight and space is saved. Otherwise, additional chamber volume and additional units like pumps would be necessary. Also, only one Main Control Computer (MCC) is required. This results in a compact design of ERICA. The dimensions of the final implemented design (see Figure 11) in an aircraft capable rack (Dragoneas et al., 2020) are 600 mm x 740 mm x 1,400 mm (height x width x length) with a total weight of around 200 kg. For the first field deployments during the StratoClim campaign in Kalamata, Greece, and Kathmandu, Nepal (see Section 5) the instrument was implemented in an in-house built rack, the so called *Geophysica*-rack, which in turn was inserted into a cylindrical pressurized barrel (Section 3.8.3). The overall weight of this aircraft ready configuration was 360 kg.

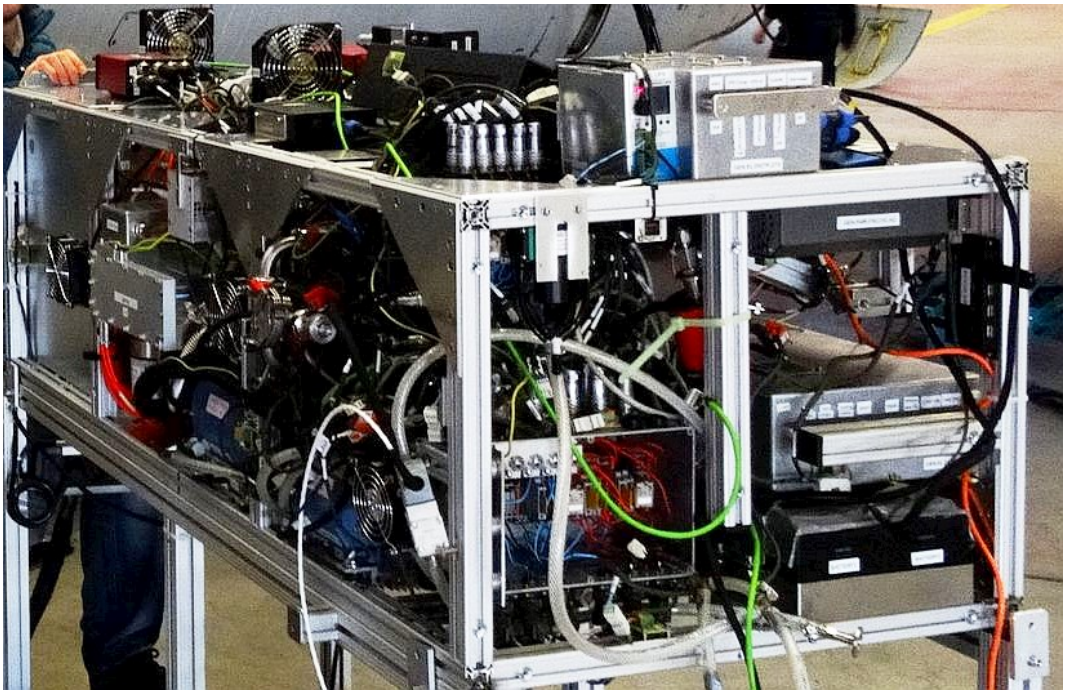

Figure 11: ERICA mounted in the Geophysica-rack for the StratoClim campaign (picture: S. Molleker, MPIC, Mainz, Germany).

To visualize the orientation of the major components, Figure 12 shows a three-dimensional drawing of the instrument body including the Turbo Molecular Pumps (TMP) in dark red. The particle entry includes the CPI (dark green) which is mounted to the aerodynamic lens (bright red) that intrudes the detection unit recipient (light gray). The detection laser units (orange) are oriented perpendicular (y-direction) to the particle beam (z-direction) and to the PMTs (dark blue, x-direction). The ablation laser head (black) is mounted on top of the B-ToF-MS (light blue) and emits the laser beam towards a dichroitic mirror that reflects the laser beam in the same direction as the detection lasers (-y-direction). A plano-convex lens focuses the laser beam on the particle beam. Hence, all lasers are oriented parallel onto the particle beam. The Shutter Unit (SU, purple) of the ERICA-AMS is located between the B-ToF-MS and the ionizer chamber of the ERICA-AMS (yellow). The C-ToF-MS (light green) juts the B-ToF-MS (light blue).

The instrument layout had to be designed that ERICA geometrically and electrically meets the boundary conditions imposed by the implementation on the Russian M-55 *Geophysica*. The dimensions of the instrument were limited to the space inside a container that was mounted on the airframe of the aircraft and was able to be pressurized during operation (see Section 3.8.3).

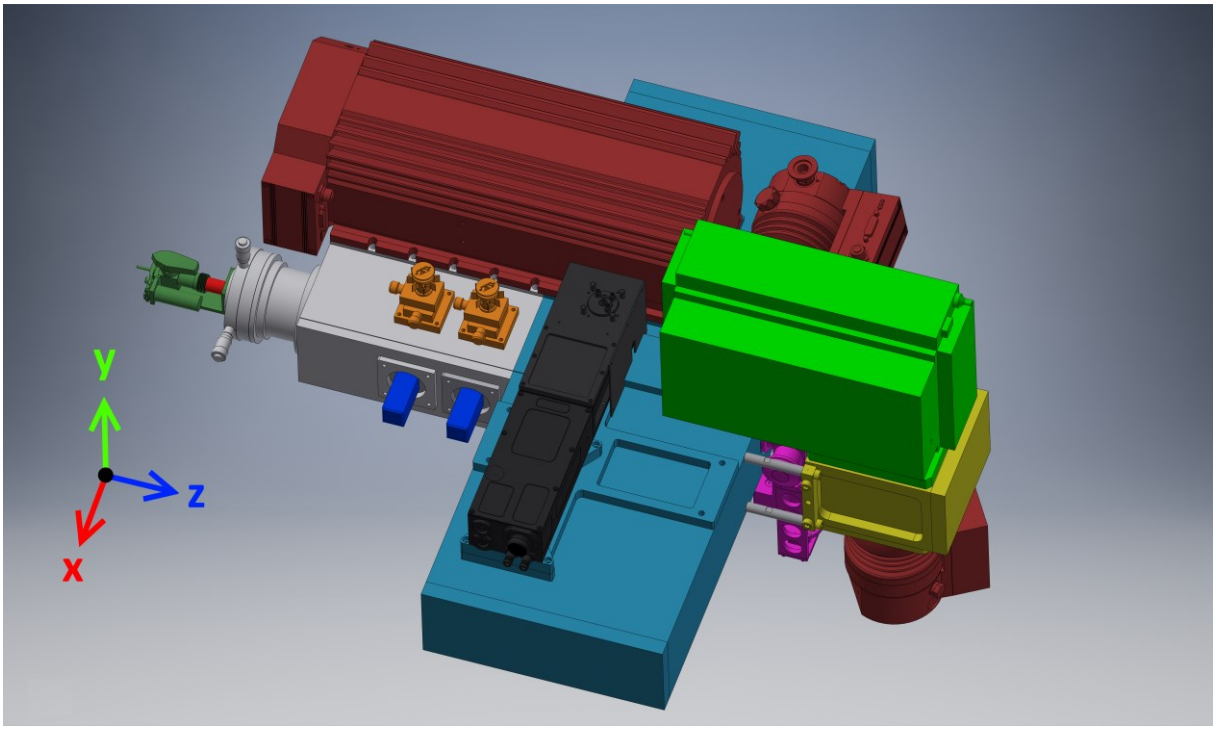

Figure 12: Three-dimensional drawing of the instruments body showing the major components of the ERICA-LAMS and the ERICA-AMS color coded (see text). The Three-dimensional drawings of the turbo molecular pumps (dark red; Pfeiffer Vacuum GmbH) and the ablation laser head (black; Quantel) were provided by the manufacturers.

3.2 Inlet and vacuum system

The continuous flow of sample air contains the particles that enter the instrument via a critical orifice. For ground measurements at standard pressure 1,013 mbar the pinhole diameter of the orifice is 100 µm to establish a pressure ratio of 0.0045 behind the critical orifice, since the pressure inside the aerodynamic lens is 4.53 mbar. This ratio is below 0.53 and thus the flow into the instrument can be assumed to be constant (Hinds, 1999). The volume flow rate into the instrument is (1.476 ± 0.015) $cm^3\ s^{-1}$. For keeping the mass flow rate constant during flight operation under varying ambient pressure (for flights with *Geophysica* from roughly 1,013 mbar to 55 mbar) a newly developed setup consisting of a controlled compressible in-house built silicone (polymerizing silicon rubber ZA 50 LT, Zhermack, shore-hardness of 50) O-ring is utilized instead of a fixed diameter critical orifice (e.g., Brands et al. (2011), Roth et al. (2016), and Schneider et al. (2017)). The setup is described in detail in Molleker et al. (2020). To focus the particles into a narrow beam for hitting a distant target like the ERICA-AMS vaporizer 76 cm downstream of the O-ring, a Liu-type aerodynamic lens (IPL-013 manufactured by Aerodyne Inc., bright red) is used (Liu et al., 1995a, b). Its 50 % transmission efficiency lower diameter (d_{50}) is approximately 120 nm (Peck et al., 2016; Xu et al., 2017) for 4.53 mbar lens pressure. The aerodynamic lens itself consists of six apertures (excluding the above described critical orifice/CPI) with decreasing diameter (from 5 mm to 2.9 mm; Peck et al. (2016)). The aerodynamic lens accelerates the particles to velocities up to 200 m s^{-1}. Figure 13 shows a detailed three-dimensional cross section scheme of the CPI, the aerodynamic lens, and the detection units (DUs, see Figure 10). The lens tube pervades a holder plate through a radially sealed feed-through and is attached to a ball joint inside the first pumping stage (PS1 in Figure 10; ball joint not shown in Figure 13). Four fine threaded screws, two of them with tics, enable the operator to tilt the lens precisely in two dimensions (dark gray) for adjusting and fine-tuning the particle beam.

The vacuum recipient (light gray) is the same as used by the LAAPTOF instrument and was purchased from AeroMegt GmbH. Flanges in the second and third pumping stages were centered to the inlet line and two also centered side flanges were added. For operation in a laboratory or during ground-based measurements, a scroll pump (model SH-110, Agilent Technologies, 1.8 $m^3\ h^{-1}$) provides a backing pressure of $1{\cdot}10^{-1}$ mbar. During mobile operation on aircraft, two membrane pumps (MD 1 VARIO SP, VACUUBRAND GmbH + Co KG, 1.8 $m^3\ h^{-1}$) yield 3 mbar for the backing pressure. As in the AeroMegt LAAPTOF, the four-stage turbo molecular pump (SplitFlow 270, Pfeiffer Vacuum GmbH) is utilized for pumping down the entire single particle mass spectrometer (ERICA-LAMS) with a flow rate of $3.0{\cdot}10^4\ cm^3\ s^{-1}$ in the first pumping stage (PS1). The first pumping stage of the 4-stage-TMP is separated from the second (PS2) by a conically shaped 2.0 mm skimmer (purple left, in Figure 13). The second pumping stage (PS2 in Figure 10) is the first detection stage DU1 (pressure $3{\cdot}10^{-4}$ mbar, flow rate $1.55{\cdot}10^5\ cm^3\ s^{-1}$). A pinhole of 1.8 mm (purple middle, in Figure 13) separates this second from the third pumping stage. The third pumping stage (PS3 in Figure 10) is the second detection stage DU2 (pressure $8{\cdot}10^{-7}$ mbar, flow rate $1.55{\cdot}10^5\ cm^3\ s^{-1}$). The particle detection and the mass spectrometer chambers are connected through a 4 mm pinhole (purple right). The fourth pumping stage (PS4 in Figure 10) is attached to the B-ToF-MS chamber. Finally, a pressure of $4{\cdot}10^{-7}$ mbar with a flow rate of $2.00{\cdot}10^5\ cm^3\ s^{-1}$ is reached in the B-ToF-MS chamber. All presented pressures were measured during operational mode with an open inlet in the laboratory.

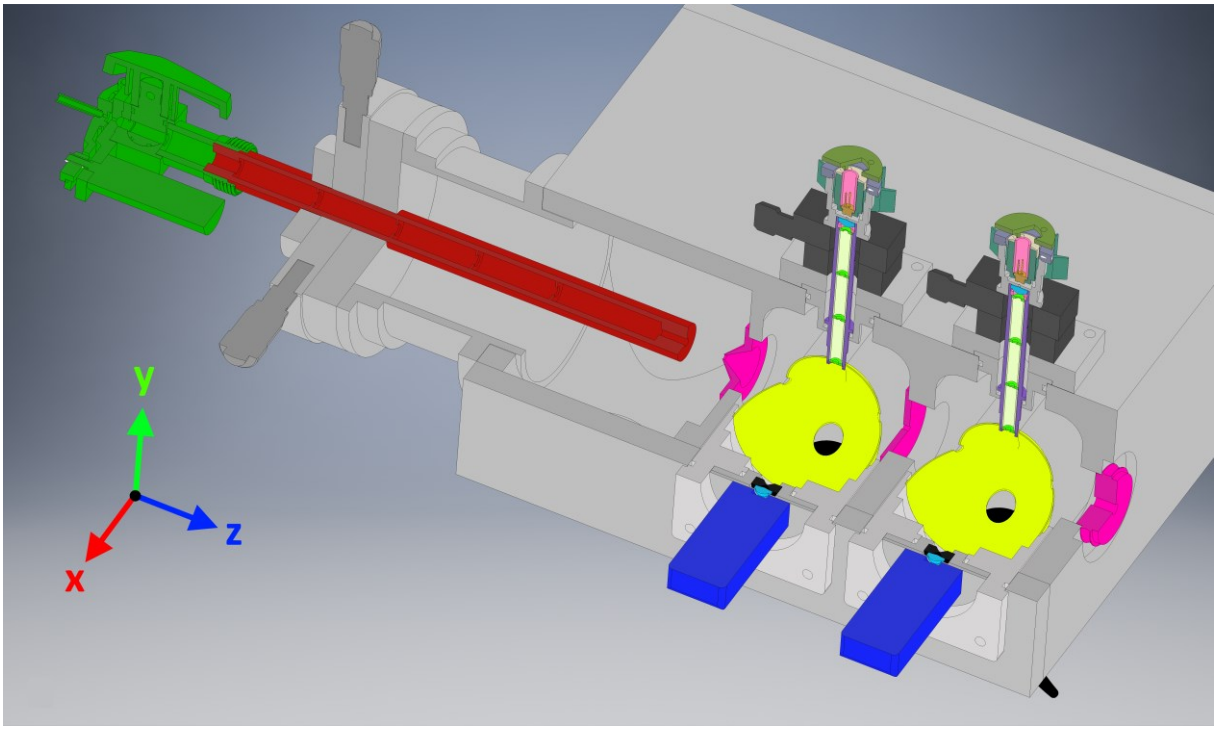

Figure 13: Cross sectional view of the CPI (green), the aerodynamic lens (red) and the detection units including the ellipsoidal reflectors (yellow) and PMTs (blue). The components are described in the text.

Between the B-ToF-MS chamber and the ERICA-AMS ionizer chamber the shutter unit (SU) is placed (see Figure 10 (SU) and Figure 12, purple). The shutter unit and the ionizer chamber of the ERICA-AMS are connected by a milled centering ring with an inner diameter of 7 mm. A turbo molecular pump (TMP5 in Figure 10, HiPace® 80, Pfeiffer Vacuum GmbH; $6.7{\cdot}10^4\ cm^3\ s^{-1}$) is attached to the ionizer chamber keeping it at a chamber pressure of $1{\cdot}10^{-7}$ mbar. Another turbo molecular pump (TMP6 in Figure 10, HiPace® 30, Pfeiffer Vacuum GmbH; $2.2{\cdot}10^4\ cm^3\ s^{-1}$) supports a high pumping rate in the

C-ToF. The operational pressure in the C-ToF mass spectrometer is $2 \cdot 10^{-7}$ mbar. Both HiPace® pumps, TMP5 and TMP6, are backed by the third pumping stage (PS3) of the SplitFlow pump. The Pump and Pressure Controller (PPC, see Section 3.7.1.4) controls the MD 1 VARIO SP pumps and the TMPs and additionally monitors seven pressure sensors.

3.3 Particle detection and sizing by the detection units

The setup of the detection unit for the ERICA-LAMS is similar to the one implemented in the ALABAMA (Brands et al., 2011). The particle detection stage (Figure 14) consists of two units, each containing a laser, an ellipsoidal reflector (yellow), and a PhotoMultiplier Tube (PMT; dark blue) as detector. The two laser beams are parallel. The lasers are 150 mW UV-laser diodes (model SF-AW210, provided by Insaneware-Deluxe, brown) mounted in a heatsink (dark green). The emitted continuous wave laser light (wavelength of 405 nm) is focused by a plano-convex lens (Aspheric Collimator Lens A 671 A, G317005000, Qioptiq Photonics GmbH & Co. KG; light blue, top half of Figure 14) with a focal length of 4.02 mm to a $1/e^2$-radius of 30 µm (see Section 4.1.2). To reduce disturbances like diffraction fringes, the laser beam passes a baffle of four pinhole diaphragms (lens – 1.6 mm – 1.6mm – 0.8 mm – 1.0 mm, with 19.55 mm spacing between them; light green) before the beam enters the detection region. To adjust the beam through these apertures, the diode can be moved with respect to the lens. The holder (dark green) can be tilted in two dimensions and also moved towards the lens. The entire laser unit is mounted within a micro adjustment stage (setting sensitivity 1 µm, model MKT 30-D10-EP, Owis GmbH; dark gray in Figure 14) and can be tilted in two dimensions in order to adjust the laser focus onto the particle beam. At an operating current of 75 mA a laser power of approximately 58 mW remains at the laser unit output (after the forth pinhole). The laser beam is dumped after passing focal point F1 in a black coated and curved glass cone (Figure 14, left).

To focus the scattered light to the detectors, ellipsoidal reflectors (model E50NV-01 anti-fingerprint coated, Optiforms, Inc.) were used (Figure 14, yellow). The first focal point F1 (Figure 14, left) matches the axis of the particle beam as well as the focal point of the laser unit and focuses the scattered light to the second focal point F2. The reflector has an inner diameter of 50.8 mm and a F1-F2 distance of 49.78 mm. Four openings in the reflector allow the particle beam and the orthogonal laser beam pass into the inner volume of the reflector and reduce the maximum collectable light. Figure 14 (right, bottom) shows the ellipsoidal reflector including the taper angles (blue, green, and red taper) not contributing to the scattered light signal recorded by the PMT, i.e., only light that is reflected on the reflector surface (yellow in Figure 14, right top) is collected in F2. Thus, light that is scattered into a taper angle of 180° to 164.8° and 14.0° to 0° with respect to the laser beam axis (y-axis, green taper) and into a taper angle of 180° to 175° and 5.0° to 0° with respect to the particle beam axis (z-axis, blue taper) is not detected. In addition, scattered light that is emitted in a taper angle of 44.4° with respect to the F1-F2 axis (x-axis, red taper) is not reflected by the ellipsoidal reflector and thus not detected (see example B3 in Figure 14, right top). F2 is designed to be within a spatial filter (diameter 0.2 mm; black) to separate the particle scattering light from background scattering light. This design collects approximately 75 % of the total scattered light, not considering the losses at the described pinholes (personal communication: T. Klimach, MPIC, 2019). A plano-convex lens (model 352330-A, Thorlabs, Inc.; light blue) collimates the scattered light towards the PMT (model H10721-210, Hamamatsu Photonics Deutschland GmbH) and seals the vacuum chamber. The distance from the exit of the aerodynamic lens to the first detection point (F1 of DU1) is 58.8 mm and from the first to the second

detection point (F1 of DU2) the distance is 66.5 mm. The acquired signals are processed by an in-house built Trigger Card (TC, see Section 3.7.2.2).

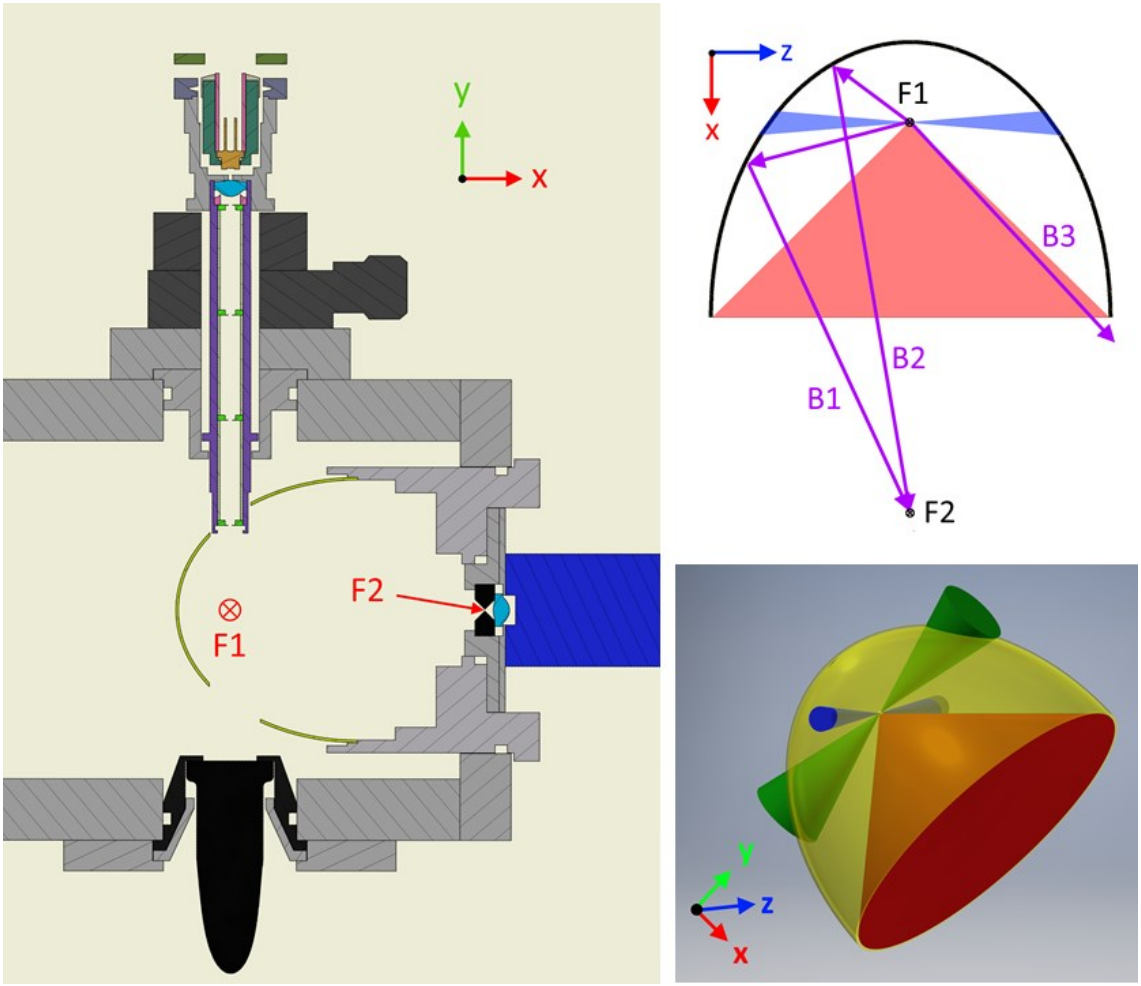

Figure 14: Left: Cross section (xy-plane) of one detection unit. F1 and F2 are the focal points of the ellipsoidal reflector. The red cross in the circle indicates the particle flight direction perpendicular into the drawing plane. The color code is the same as in Figure 13. Right, top: Scheme of the ellipsoidal reflector in the xz-plane with various beam paths of light scattered by a particle. The beams B1 and B2 are reflected to F2 and thus detected by the PMT, beam B3 is not detected. Right, bottom: Ellipsoidal reflector (yellow) including the taper angle ranges (blue, green, and red; see text) not contributing to the scattered light signal recorded by the PMT.

For the determination of the particle flight time, both detection units are needed. From the velocity between the two DU focal points, the TC computes the arrival time of the particle at the ablation spot on hardware level. The measured particle flight time is multiplied by an adjustable constant factor (termed *Multiplier*, typically 1.815 with a maximum value of 2, see Section 3.7.2.2) to timely trigger the ablation laser Q-switch. The laser flash lamp is constantly pre-triggered 145 µs before the Q-switch. By calibration with various particle size standards (see Section 4.2.2), also the vacuum aerodynamic diameter d_{va} of each sampled particle can be calculated from the particle flight times. The distance from the second detection unit to the ablation region is 120.7 mm and the distance from the exit of the aerodynamic lens to the ablation spot is 246 mm. This leads to particle flight times of around 1.5 ms from aerodynamic lens exit to the ablation spot (see Section 4.2.2 for a d_{va} of 200 nm).

3.4 Single particle laser ablation

3.4.1 Ablation laser and optics

In the ablation region a single particle is vaporized and ionized in one step by a multi-photon process induced by a pulsed laser (see Section 2.3). The laser pulses come from a frequency quadrupled Nd:YAG laser (model Ultra 50, Quantel SA) with 266 nm wavelength, 6 ns pulse duration and 10.9 mJ (UV fraction, in total 44 mJ) pulse energy. The maximum repetition rate of the ablation laser is specified to be 10 s^{-1}, for ERICA the maximum operational rate, however, is 8 s^{-1}, since the laser is idle for at least 120 ms (laser gate) after a pulse to keep the output energy constant. This leads to a maximum capable repetition rate of approximately 8 s^{-1}. The simultaneously emitted additional light by the laser at wavelengths of 1,064 nm and 532 nm is not filtered by a wavelength separator inside the laser head.

The manufacturer of the ablation laser provides a wavelength separator to pass only UV light. This wavelength separator would be additionally mounted to the ablation laser head. The over-all combined length of such an equipped laser head would have exceeded the permissible dimensions of the ERICA instrument inside the container (see Section 3.8.3). As shown in Figure 15, the emitted laser beam is oriented orthogonal to the particle flight direction and focused by a plano-convex lens (anti-reflective coated model L-11612, Laseroptik GmbH). It is directed towards the mass spectrometer chamber by dichroitic mirror DM1 (model G340722000, Qioptiq Photonics GmbH & Co. KG) that separates the UV-light from the other wavelengths by reflecting > 99.5 % of its intensity. Only 12.6 % of the other wavelengths (see Section 4.1.4) are reflected. The transmitted light is dumped in an in-house built beam trap with a neutral density filter (model 1-NF-05-0254, Altechna). An uncoated and 3° tilted quartz glass windows (model S-00028, Laseroptik GmbH) allows the laser beam to enter and exit the vacuum chamber. The tilting reduces back-reflections into the laser head, which could cause damages at the laser head's optics. Two apertures (6.6 mm and 5.8 mm) provide additional reduction of reflections. The exiting beam is directed by a second dichroitic mirror DM2 (same model as DM1) towards an energy meter (EnergyMax™-USB, model J-25MB-LE, Coherent, Inc.) for monitoring the primary UV energy of each pulse. To keep the energy meter sensor head within its specified damage threshold, an UV attenuating filter (model UG11, Qioptiq Photonics GmbH & Co. KG) is installed in front of the energy meter.

The focal length of the focusing lens is chosen to generate a high intensity ablation spot (see Figure 10) within the ionization region between the two time-of-flight mass spectrometers. In order to adjust the UV focal point (focal length z_0 = 76 mm and ablation laser beam width with a $\frac{1}{e^2}$ beam waist diameter $w_{0,dia}$ of 250 µm, see Section 4.1.3) onto the particle beam, the mirror is mounted on a moveable holder. This holder allows the mirror to be tilted with two degrees of freedom. Furthermore, the lens can be moved in the direction towards the vacuum chamber. Hence, the diameter in the region of the particle beam can be enlarged up to approximately 740 µm by defocusing. By this way, the energy density at the ablation spot can be intentionally varied. A reduced energy density will lead to larger, less destroyed molecule fragments in the mass spectra on one hand, but will miss particle types with high specific ionization energies on the other (Brands et al., 2011).

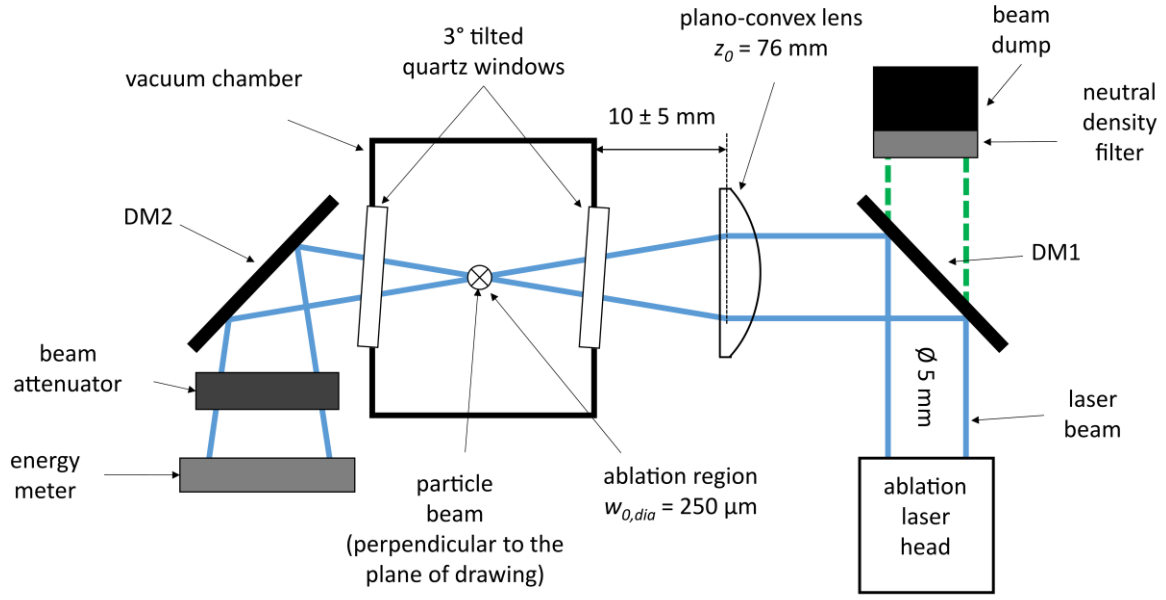

Figure 15: Schematic of the ablation laser unit of the ERICA-LAMS and corresponding optical dimensions (z_0: focal length; $w_{0,dia}$: ablation spot $\frac{1}{e^2}$ −diameter). The particle beam is pointing perpendicular to the plane of the drawing. The dichroitic mirrors are labelled as DM1 and DM2.

3.4.2 Ion detection with bipolar time-of-flight mass spectrometer

To analyze ablated single particles for chemical composition, the generated ions are accelerated into the Bipolar Time-of-Flight Mass Spectrometer (model B-ToF-MS, Tofwerk AG, Thun, Switzerland; see Figure 10).

The ions are accelerated into the mass spectrometer by an electric field originating from electrodes, i.e., Extraction Plates (EP in Figure 10), supplied with a potential difference of 10 kV and deflected by a charged plate (deflector in Figure 10; 2.1 kV) towards the reflectron. The ion path is surrounded by a grid that is set to a potential of 2.8 kV for shielding the ion flight path. After the ions are reflected in the reflectron to the opposite direction, they reach the Multi-Channel Plate (MCP; model MCP 40/12/10/8 D 46:1, Photonis USA Inc., Sturbridge, MA, USA), where the ions generate an electrical current from an avalanche of secondary electrons. This current is picked up and conditioned by an amplifier unit (provided by Tofwerk AG) that transforms the current to a measurable voltage, which is recorded by a digital oscilloscope (model Picoscope 6404C, Pico Technology). The diagram of the ion optics in the mass spectrometer and the pre-set voltages are shown in Appendix A.1.

The acceleration field at the EP (see Figure 10) is generated only for the short time interval during the ion extraction by fast High Voltage (HV) transistor switches (HV-switches, model HTS 61-03-C, Behlke Power Electronics). These switches are triggered by the TC 1.2 µs before the laser pulse trigger (Q-switch), they respond within 18 ns, and apply the electric field between the extraction plates for 2 µs duration. The extraction plates are electrically grounded when no detected particles are present. The electric field decay is designed for a RC (Resistor-Capacitor) time constant of 10 ms, although the real value could not be measured with standard equipment. Without this unit , which means for a constant electric field, charged aerosol particles are deflected from their straight flight direction by the electric fields reaching into the particle beam (Chen et al., 2020) during the idle time of the ablation laser and might not hit the vaporizer in the ERICA-AMS. For this reason, the particle path through the ERICA-

LAMS part is shielded by grounded tubes and plates. During the first flights of ERICA in Kalamata, the problem of charged aerosol particles not reaching the ERICA-AMS vaporizer became apparent and was solved by these measures (see Section 5.1). It is possible to set the time of extraction, i.e., the trigger to provide the HV at the extraction plates, after the Q-switch pulse trigger (so-called delayed extraction) to improve resolution by reducing space charge effects (Wiley and McLaren, 1955; Clemen et al., 2020). However, this delayed extraction mode is already implemented (*DelayExtr*, see Section 3.7.2.2), but not characterized and not deployed for ERICA yet.

3.5 Particle flash vaporization and electron impact ionization

3.5.1 Motivation to combine flash vaporization/electron impact ionization with the laser ablation technique

Both techniques have advantages and disadvantages, as explained in Section 1.2. For example, small particles below 100 nm in diameter are rarely detected by the DUs and are as such not hit by the UV laser in the ablation region. Aerosol particles that are detected by the DUs during the idle time of the UV laser pass the ablation region while being not ablated. This is the major fraction of the sampled particles due to the laser idle time. In case the ambient particle concentration (e.g., during a flight at high altitudes) is 100 cm^{-3}_{Std}, only 5.4 % of the detected particles are ablated by the laser at the maximum at the given instrumental flow rates and settings (see also Section 4.5.4). Laboratory measurements with ERICA-AMS support this observation. Furthermore, particles that are transparent for the wavelength of 266 nm, such as pure sulfuric acid, are not ionized (Murphy, 2007). ERICA was originally developed specifically for the purpose of sampling inside the Asian Monsoon Anticyclone (AMA) at altitudes between 12 km and 20 km (Upper Troposphere/Lower Stratosphere, UT/LS). An UV laser emitting light with 266 nm wavelength was implemented, because a large fraction of particles consisting not only of pure sulfuric acid-water solution droplets was expected based on the meteorological and transport phenomena in connection with the AMA (Vernier et al., 2015). For applications in the free stratosphere with a higher proportion of H_2SO_4/H_2O particles (Junge and Manson, 1961; Murphy et al., 2007), a UV laser emitting light with 193 nm wavelength can be implemented in the future.

All the non-ablated particles, either caused by their small size or their optical properties, continue their travel towards the ERICA-AMS heater and are measured when the shutter is open (see Section 3.5.2). Although the ERICA-AMS is also affected by limitations (see Section 1.2), the ERICA-AMS can provide information about the non-ablated particles by the instrumental design.

3.5.2 Ionizer and time-of-flight mass spectrometer for positive ions

All those particles, which are not ablated, reach the vaporizer of the ERICA-AMS. Here, the particles are flash vaporized by a porous tungsten vaporizer on a molybdenum heater body (surface diameter 3.8 mm) operating at a surface temperature of 600 °C. The resulting vapor molecules and fragments are ionized to positive ions by an electron beam emitted by a filament. The emission current of the filament is set to 1.6 mA and the voltage difference between the filament and the vaporizer surface results in an electron acceleration to 70 eV. The ions are guided through an electrostatic lens stack and extracted by periodic pulses at a frequency of 50 kHz perpendicularly into the C-ToF-MS (see Figure 10) from Tofwerk AG. These extractions define the starting points for the mass spectra. This vaporization/ion generation unit was manufactured by Aerodyne Inc. and is identical to the commonly used Aerodyne Inc. Aerosol Mass Spectrometer (AMS). A detailed description is published by Drewnick

et al. (2005) and Canagaratna et al. (2007). The ions reach the multi-channel plates (model MCP 40/12/10/8 D 46:1, Photonis USA Inc., Sturbridge, MA, USA) and generate a signal that is recorded by a data acquisition card (DAQ card; model ADQ1600 USB3, Teledyne Signal Processing Devices Sweden AB). The diagram of the ion optics in the mass spectrometer and the pre-set voltages are shown in Appendix A.2.

For quantitative measurements the background signal, which originates from residual organic gases and air in the chamber, has to be subtracted from the sampling signal. For this purpose, the particle beam is periodically blocked in the commercial Aerodyne AMS by a chopper in a low vacuum stage close to the aerodynamic lens. In the commercial Aerodyne AMS it is possible to distinguish between different particle sizes based on the particles' vacuum aerodynamic diameters by means of the chopper. The particle flight time between passing the (open) chopper and arriving at the vaporizer is size dependent. However, this flight time – and the corresponding flight distance between chopper and vaporizer – need to be long enough to achieve such size resolved sampling. This corresponds to a flight distance in the range of 39.7 cm between the chopper and the vaporizer (Jayne et al., 2000). For ERICA-AMS the distance from the SU position to the vaporizer (see Figure 10) is too short (9.5 cm). This would not be the case if the chopper would have been placed directly behind the ball joint of the aerodynamic lens (see Figure 10). However, by periodically blocking the particle beam with a chopper at this position the detection frequency of the ERICA-LAMS would have been reduced accordingly. For this purpose, a simple shutter is used instead downstream the ablation spot of the ERICA-LAMS.

The shutter, a high vacuum magnetically coupled feed-through (Pfeiffer Vacuum GmbH), is made of non-outgassing metal components on the high vacuum side. A C-shape metal profile (Figure 10), mounted on the shutter rod, blocks the particle beam for 5 seconds to measure the background signal by rotating the profile 90° into the axis of the particle beam. For another 5 seconds the shutter opens and particles can pass by to reach the vaporizer. The servo motor (model Savöx SA-1283SG Servo, savox) is located outside the vacuum chamber. The open-closed cycles of the shutter are controlled by the DAQ card and can be set in the user interface of the acquisition software (*TofDAQ Recorder* by Tofwerk AG). The position of the shutter is read out by a position sensor (model Magnepot 6150, TT electronics plc). The acquired values of the shutter position are transmitted to the DAQ card and stored by the acquisition software such that the times at which the shutter was open, closed, or in-between are precisely known (see Section 3.7.3.2). During the field deployments on the aircraft the selected values for the settings for vaporizer temperature, electron beam energy, shutter cycle duration (see Section 3.7.3.2) turned out to be useful choices.

3.6 Power supply requirements and distribution to the ERICA sub-systems for safe aircraft operation

All design decisions concerning the power management of ERICA has to comply with aircraft safety and aircraft operator regulations (MDB). The instrument is powered by a 27 V DC (model RSP-750-27, MeanWell delivering 750 W) power supply and two additional 230 V AC/DC converter power supplies (model VIPAC™ VP-C2884813 (24VDC, 600 W at 50 Hz) and model VIPAC™ VP-A2885244 (12 VDC and 24 VDC, 450 W at 50 Hz), Vicor). The total power consumption during operation is 1.2 kW, at stand-by 600 W and during start-up in maximum 1.8 kW. All power is distributed via in-house built distribution boxes to the different instrument units, such that each unit can be switched automatically or manually by the MCC (Dragoneas et al., 2020), or if necessary by manual switches at the distribution boxes. The critical sub-systems for safe flight operation, like the basic control and safety systems (see Section 3.7.1), and the MCC are backed by a 24 VDC uninterruptible power supply unit (UPS, model DCU20, Nextys, see Section 3.7.1.1), which is capable of providing power from a battery pack for several minutes up to one hour depending on the preset values in the UPS control. The battery pack provides a maximum electric charge of 12 Ah, a feature which secures the safe and reliable operation of the system during temporary aircraft power losses. To protect the DC lines from power spikes, a DC/DC converter (model Traco Power THN 30-2415, Traco Electronic AG) is used as a noise and spike filter and transforms the 27 VDC to 24 VDC. The power supplies for the ToF-MS (ToF Power Supplies (TPS); Tofwerk AG) of the mass spectrometers and the ablation laser Power Supply (PS; Quantel SA) run on 230 VAC (50 Hz), the main control computer and the sub-units on 27 VDC. The input current lines are fused with a 25 A fuse in the DC line and with a 15 A (phase A) and a 16 A (phase B) fuse in the AC line. Leaded PTC (Positive Temperature Coefficient) resettable fuses (Littlefuse Inc., Chicago, IL, USA) are used for this purpose. This type of fuses recovers automatically when the current falls back below the limiting current value. In addition to the main lines, the secondary lines are also fused as required.

The described fuses are beside all other fuses and current limiting units in the instrument part of the aircraft safety concept. The aircraft power lines are fused to ensure safe operation according to the specifications of the operating company MDB. However, additional fuses in the instrument are necessary to protect individual lines from overload and overheating. Otherwise, this could cause a fire, which would be a severe danger for the research aircraft.

3.7 Instrument control and data acquisition

The ERICA instrument is based on a modular design with several sub-units, which carry out different tasks. These hardware sub-systems communicate with the Main Control Computer (MCC) running Windows® 7 (64-bit) as operating system. The MCC was built upon a quad-core processor (i7-4790K, Intel Corporation, Santa Clara, CA) operating at 4 GHz and was in-house assembled out of off-the-shelf, high-end components (16 GB RAM, 512 GB SSD). The Graphic User Interface (GUI) control software was written in *LabView* (National Instruments Corp.) and extends to 18 virtual instruments (Table 2) that are described in the following sub-sections. The trigger card controller is a virtual V25 embedded controller system, technically based on the hardware controller design of the ALABAMA (Brands et al., 2011). The ERICA control was developed by Dragoneas et al. (2020). Names of variables and virtual instruments are highlighted in italic print.

Table 2: Graphic user interface (GUI) control programs for 18 virtual LabView instruments running on the MCC to control autonomously or manually ERICA operation. For acronyms, abbreviations, and meaning see text of the following sections or sub-sections referenced in the third column.

name of the virtual instrument	description	see Section
Detection unit control	Controls detection lasers (Section 3.3) and HV-switches (Section 3.7.2.4)	3.7.2.1
Energy meter monitor	Records ablation laser energy from the energy meter	3.7.3.1
Fail-safe control	Controls the Fail-Safe Controller (FSC)	3.7.1.3
Iridium messenger	Sends SBD message via *Iridium* antenna	3.8.1
LAAP data acquisition	Records LAMS raw spectra	3.7.3.1
LAAP spectrum batch converter	Converts LAMS raw spectra into CRISP readable format	3.7.3.1
LAAP spectrum file viewer	Views LAMS raw spectra on demand	3.7.3.1
Logged Status Viewer	Views logged operating status	3.7.1.6
Pfeiffer control	Controls Pfeiffer TMPs (Section 3.2)	3.7.1.4
Pressure control	Controls PPC	3.7.1.4
Quantel control	Controls ablation laser power supply (Section 3.4.1)	3.7.2.3
Remote command composer	Creates SBD message for *Iridium* messenger that is sent by the operator on ground as remote-control command	3.8.1
SBD message merger	Creates SBD message for *Iridium* messenger that is sent by the instrument during research flight deployment	3.8.1
Supervision local	Records and views current operating status	3.7.1.6
Temperature control	Controls Temperature Control (TEMPCTRL)	3.7.1.5
TofDaqRec monitor	Monitors TPS (Section 3.4.2 and 3.5.2) values	3.7.1.6
Trigger control	Controls TC	3.7.2.2
UCSE decoder	Decodes UCSE information	3.8.4

3.7.1 Safety systems and basic control of the instrument

The critical operations of the system, especially during autonomous operation during flight are: the vacuum system control PPC that includes the safety interlocks of the high voltage system and the inlet pressure control, the temperature control, the CPI control that includes the control of the main valve, and the Fail-Safe Controller (FSC). All of these are handled by stand-alone embedded systems, which are backed by the UPS. The safety interlocks monitor the high vacuum pressure. The GUI software *Supervision local* accumulates all instrument system information.

3.7.1.1 Uninterruptable Power Supply (UPS)

The Uninterruptable Power Supply (UPS) unit (see also Section 3.6) is a commercially available apparatus that is capable of supplying battery power to the main computer and other critical sub-systems (see Sections 3.7.1.2 to 3.7.1.5). During a power-failure (expected or unexpected, especially while aircraft operation) these components are powered by two lead-acid 12 V batteries (model NP7-12FR, Yuasa) connected in series (12 Ah). This allows a controlled and secure shut-down of the MCC to prevent data losses. This is the case for instance after each completed research flight during StratoClim, when the pilot switched off the engine power.

3.7.1.2 Constant Pressure Inlet Control (CPICTRL)

The Constant Pressure Inlet (CPI, see Section 3.2) is required to provide stable conditions in front of the aerodynamic lens to assure the operation under a constant lens pressure. This is necessary mainly during flight operation, because the ambient pressure drops with increasing altitude. Unstable pressure conditions would lead to changes in the lens transmission, to varying particle acceleration, and consequently to inaccurate particle sizing. The design and characterization of the used CPI is described in detail in Molleker et al. (2020). The main advantage compared to previously adopted systems (Bahreini et al., 2008; Schmale et al., 2010) is saving space and power consumption due to less tubing and less pumping. The Constant-Pressure Inlet ConTRoL (CPICTRL) unit is an in-house built component. It employs a PID (Proportional-Integral-Derivative) control system for the regulation of the aerodynamic lens pressure via a compressible rubber ring. Also, it serves for controlling the main valve (see Figure 10) of the instrument.

3.7.1.3 Fail-safe Controller (FSC)

The Fail-Safe Controller (FSC) secures the stability of the MCC by serving as an external watchdog timer. In case of a failed response of the observed programs it induces a hardware reboot of the MCC and thus a restart of the data acquisition. The timer can be set in a GUI program (*Fail-safe control*). More details and functions of the FSC can be found in Dragoneas et al. (2020).

3.7.1.4 Pump and Pressure Controller (PPC)

The Pump and Pressure Controller (PPC) unit plays a central role for the autonomous and safe operation of the ERICA instrument. To protect the instrument from critical damage, additional emergency features were installed. Three pressure sensors that measure the pressures in the high vacuum regime (B-ToF, ERICA-AMS ionizer chamber, and C-ToF) are read out at a frequency below 100 Hz. However, this is still fast enough to respond to rapid pressure changes. The pressure sensor attached to the B-ToF-MS chamber (PS4 in Figure 10) serves as primary pressure sensor, the pressure sensor attached to the ERICA-AMS ionizer chamber (PS6 in Figure 10) as backup sensor, in case the primary fails. Thus, the high vacuum regime is monitored. For pressures above $5.5 \cdot 10^{-6}$ mbar in the high vacuum regime, the main inlet valve will be closed and the high voltages will be switched off immediately. After recovering (below the pressure threshold of $3.5 \cdot 10^{-6}$ mbar) the MCC will be restarted and the instrument will turned be back into Auto Mode, i.e., measuring mode.

The PPC also starts and stops the TMPs via their embedded control software (*Pfeiffer control*) and controls the pre-pumps (see Section 3.2) keeping both within the limits of pre-set pressure values. The TMPs are started as the pressure in the high vacuum chamber drops below 5 mbar and are stopped above 15 mbar. Additional features include the opening and (also automatic emergency) closing of the main inlet valve via the CPICTRL depending on pre-set values, as well as detecting power cuts. A positive chamber pressure check (chamber pressure < $4.5 \cdot 10^{-6}$ mbar) leads the PPC to command the CPICTRL to open the main inlet valve. The main inlet valve is by the same control automatically closed for a chamber pressure above $8.0 \cdot 10^{-6}$ mbar.

The PPC contains a multiplexer, which reads out the analogue voltage output of seven pressure sensors that monitors the pressure of the B-ToF, the ERICA-AMS ionizer chamber, the C-ToF, the aerodynamic lens, the backing line, the pressurized container (see Section 3.8.3), and the ambient air outside the container. In total, it can accommodate up to 13 pressure sensors. The pressure sensor values and the additional operating status data are transmitted via serial connection to the respective control interface, running on the MCC. Settings of the parameter values are accessible through the graphical user interface (GUI) program *Pressure control* running on the MCC and the default start-up values are

stored in a look up table on the embedded EEPROM (Electrically Erasable Programmable Read-only Memory). Further details of that unit are described in Dragoneas et al. (2020). The PPC successfully operated during all laboratory, as well as field experiments.

3.7.1.5 Temperature Control (TEMPCTRL)

A network of up to 64 temperature sensors can be installed within the entire instrument to monitor the temperature distribution. During the first deployment of ERICA (StratoClim, see Section 5) 12 sensors were mounted at the main frame bars (*Geophysica*-rack) to monitor the surrounding temperature and another 32, four of them outside the instrument containing pressurized barrel (see Section 3.8), to monitor the temperature of certain surfaces (see Appendix A.3, in total: 44 temperature sensors). Furthermore heating cartridges and Resistance Temperature Detectors (RTDs) were implemented at the outer inlet at the aircraft (Dragoneas et al., 2020) to prevent icing when flying under supercooled cloud conditions. The TEMPerature ConTRoL (TEMPCTRL) unit reads out all values of the sensors and controls the cartridges automatically, or manually upon user demand by a GUI software (*Temperature control*). In addition, this unit powers and controls six evenly distributed fans that transfer the heat to the cold container (see Section 3.8.3) walls for cooling the instrument (see Appendix A.3).

3.7.1.6 Operating status data

The operating status data is used for performance monitoring and failure analysis. All GUI programs report their status to the GUI program S*upervision local*. Here, all statuses and selected parameter values, for instance pressures, temperatures, number of spectra, and detected particles, are collected, stored, and comprehended to an overall status every five seconds. Furthermore, the high voltages and currents of the TPSes are observed by the program *TofDaqRec monitor*. The program *Logged status viewer* can display the recorded binary file.

3.7.2 Single particle detection and ablation laser trigger

The particle detection and ablation are controlled by the following units. As for the other control units all are accessible through individual GUIs.

3.7.2.1 Detection Card (DETC)

The DETection Card (DETC, running at 12 VDC power) provides the current to the laser diodes as well as the gain voltages and driving voltages of the PMTs (see Section 3.3). Two separate current sources are incorporated in this board, each providing a maximum current of 200 mA to the laser diodes (DL in Figure 10). The DETC is controlled by the GUI program *Detection unit control*. Here the values, such as diode current and gain voltage can be set as default startup settings and stored on the board at an EEPROM. By this way, the detection unit independently commences operation immediately after power is applied.

3.7.2.2 Trigger card (TC)

The ablation trigger unit is a modification of a previous single particle mass spectrometer development at the Max Planck Institute of Chemistry, including ALABAMA's instrumental control unit based on *NEC V25* chipset (µPD70320, NEC Corporation; Brands et al. (2011)). It connects the detection and the ablation unit as it measures the particle flight time, computes the time when the particle arrives in the ablation laser focus (ablation spot in Figure 10; see Section 3.3), and provides the trigger signals for the ablation laser and the HV switches (see below). In the GUI software panel (*Trigger control*), a virtual memory map of the control computer of the ALABAMA is displayed. Furthermore, in the *Trigger control* panel the pre-set values for different parameters (see Table 3) can be set, such as the PMT

signal thresholds (*Thresh0* and *Thresh1*), the *Multiplier* value, the extraction delay time (*DelayExtr*), i.e., the time interval between Q-switch and HV switch (see Section 3.4.2), the particle gate (*PartGate*), the pre-trigger (*PreTrigger*) and the laser gate (*LaserGate*). The particle flight time is given by the IC (Integrated Circuit), a FPGA (Field Programmable Gate Array), in clock cycles. A clock cycle equals a time t_{TC} of 40 ns. The clock starts counting, when a scattered light signal of a passing particle exceeds the threshold *Thresh0* at DU1 and stops, when this particle causes the corresponding signal at DU2. This means that the signal at PMT2 need to exceed *Thresh1*. This particle flight time is the *Upcount* value that provides particle size information after an appropriate calibration (see Section 4.2.2). The thresholds can be set between a minimum of 0 Volts and a maximum of 2.5 V and can be adjusted in 10 mV steps. If *Thesh0* and *Thesh1* were exceeded within a defined time interval (*TriggTMin* and *TriggTMax*), the particle is counted as a so-called coincidence (*Coincid*). In the case the ablation laser is not idle at that time, a Q-switch trigger is sent to fire a UV laser pulse for particle ablation. The variable *LaserGate* is the minimum idle time of the laser in ms (usually set to 120 ms).

The timing of events between the first signal delivered by DU1 for a successful particle detection and the actual firing of the ablation laser shot is shown in Figure 16. The following variables and parameters are of relevance: The *Multiplier* describes the ratio of the particle flight time between DU1 and DU2 and the flight time between DU2 and the ablation spot (max. ratio 2 equals the value 65,535 in the GUI setting). The *PartGate* is the time interval in which the number of detected particles is summed up and usually set to 1,000 ms. Thus, in the GUI, the recorded and displayed particle number counts are given in particles per second. The pre-trigger (*PreTrigger*) defines the point in time to trigger the ablation laser Flash Lamp (FL trigger) before the Q-switch trigger (see Figure 16). The ablation laser PS expects a trigger for the Flash Lamp (FL) for internal processing 500 µs in advance (FL delay). After the UV laser flash, it takes another 145 µs to reach the maximum peak in excitation (Flash Lamp Q-switch Delay, FLQS delay). Longer FLQS delay times can be set resulting in a decreasing output energy. Thus, the pre-trigger is the sum of 500 µs and the FLQS delay and cannot be set below 645 µs. From the reception of the QS trigger signal to the actual UV laser flash at the ablation spot, another 70 ns elapse.

All values (settings and parameters, see Table 3) are recorded with a rate of 1 s^{-1} and are stored in a text file on the hard disk drive. For every particle for which a Q-switch trigger was sent, the *Upcount* value is sent to the *LAAP data acquisition* and stored. If the information does not arrive within 70 ms after the Q-switch trigger, the value “0” is stored instead to ensure a *Upcount* value to the corresponding single particle mass spectrum. In addition, the *Upcount* value is stored consecutively in a separate text file. Thus, for each coincidence for that the ablation laser was triggered the *Upcount* value is available for post-processing such as determining the overall ablation efficiency (see Section 4.3).

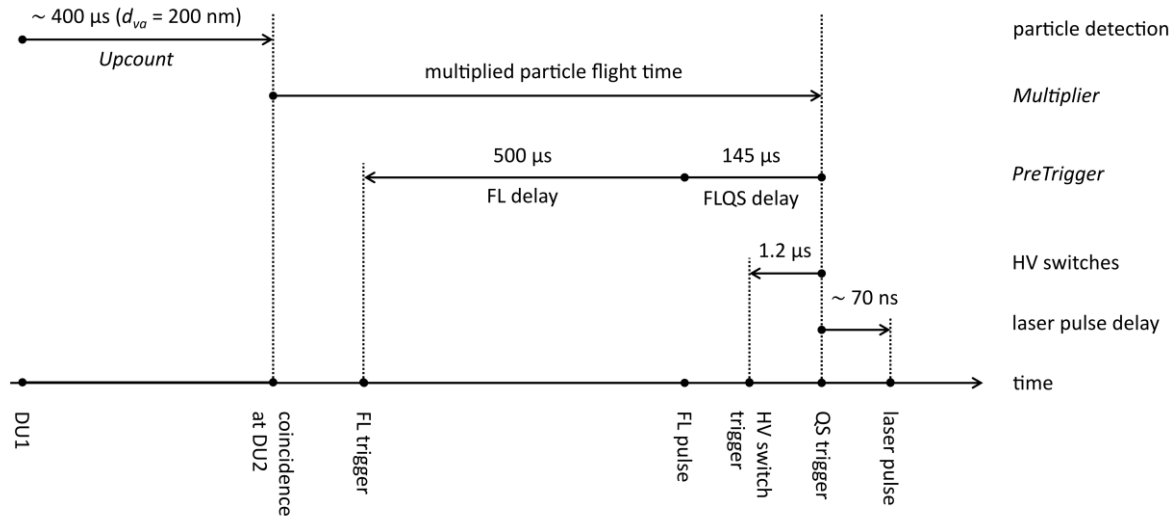

Figure 16: Timing scheme of various trigger signals on the trigger card (not to scale).

Table 3: Parameters of Trigger control program implemented in the Trigger Control card (TC). See text for explanation of terms and acronyms.

Parameter	**Additional description**	**Unit**	**Standard value**
Upcount	Particle flight time counts	FPGA clock ticks x 40ns	-
Counts0	Detected particle counts at DU1	number per *PartGate* value	-
Counts1	Detected particle counts at DU2	number per *PartGate* value	-
Coincid	Coincidences	number per *PartGate* value	-
LaserGate	Laser idle time	ms	120
PartGate	Time interval to acquire particle counts	ms	1,000
Multiplier	Timing factor	dimensionless	1.815 (59,478)
TriggTMax	Maximum time interval for signals at DU1 and DU2 to be counted as valid particle	FPGA clock ticks x 40ns	30,000
TriggTMin	Minimum time interval for signals at DU1 and DU2 to be counted as valid particle	FPGA clock ticks x 40ns	5,000
DelayExtr	Time interval between Q-switch and HV switches (before or after Q-switch; synchronized with Q-switch: 2030)	FPGA clock ticks x 40ns	2,000
Thresh0	Threshold at DU1	x 10 mV	5
Thresh1	Threshold at DU2	x 10 mV	20
PreTrigger	Delay between flash lamp and Q-switch	FPGA clock ticks x 40ns	16,125

3.7.2.3 Ablation laser control

The ablation laser is controlled by the program *Quantel control*. For this, a graphical interface was developed adapting the controller device that was provided by the manufacturer with the laser power supply. Furthermore, a routine was added that allows automatic firing of the UV laser pulses during measurement operation (auto mode) being triggered by the TC.

3.7.2.4 High Voltage switches (HV switches)

The HV switches were added to the initial design of the AeroMegt GmbH LAAPTOF instrument. It comprises two solid-state high voltage switches that get triggered by the TC 1.2 µs before the Q-Switch trigger (see Figure 16) for the ablation laser (see Section 3.4). It can be enabled at the *Detection control* panel, where also the status is indicated. The value for *DelayExtr* is set in *Trigger control* to 2,000 that equals a HV switch trigger 1.2 µs before the Q-switch trigger. To trigger the HV switches synchronized to the Q-switch the variable has to be set to 2,030.

3.7.3 Data acquisition of ion mass spectra

3.7.3.1 ERICA-LAMS

The single particle mass spectra are recorded by a compact computer-based oscilloscope (model Picoscope 6404C, Pico Technology), which provides four channels at 8-bit vertical resolution and a total sampling performance of up to $5 \cdot 10^9$ samples per second. The time resolution is set to 1.6 ns per sample. Each of the two detector outputs (anions and cations) are sampled simultaneously by two separate channels of different input voltage ranges (cations ±2 V and ±100 mV, anions ±2 V and ±50 mV). This approach broadens the dynamic range in the data acquisition. The acquisition trigger signal is provided by the trigger output of the ablation laser unit (QS trigger, see Figure 16) and starts recording the spectrum. A GUI application (*LAAP acquisition software*) was developed for the control of the oscilloscope and the export of raw data to binary files. To store a spectrum, the signal has to exceed a defined threshold (usually set to 25,500 bits which corresponds to 12 mV for cations and 6 mV for anions, respectively) of either the cations or the anions (or both). The first 100 samples are not regarded. Within these 100 samples (i.e., the first 160 ns), only the systematic peak signal of the ablation laser pulse is present. Furthermore, in the anion spectra the electron peak, but no other mass spectral line, is present within the time period of the first 100 samples. In addition to the recording of the spectra, the *Upcount* value, i.e., the particle size information (after an appropriate calibration, see Section 4.2.2), is read out from *Trigger control* (see Section 3.7.2.2) and added to the mass spectra file. Furthermore, the recording time (in UTC: Coordinated Universal Time) of each spectrum is added as a time stamp to the file. All the stored files (one file for each bipolar spectrum) have to be converted to a format that is compatible to the in-house developed evaluation software CRISP (Concise Retrieval of Information from Single Particles) by Klimach (2012). This offline file conversion is performed a-posteriori by means of another dedicated GUI program *LAAP spectrum batch converter*. Here also the polarity of the spectra can be swapped and the time stamps adjusted, if necessary. The single raw spectra can be viewed by *LAAP spectrum file viewer* without any changes of the file structure. Another GUI program (*Energy meter monitor*) reads out the energy meter (see Section 3.4.1) and records the pulse energy of every shot regardless of whether the particle generated a spectrum or not. Thus, a degradation of the flash lamp and the laser optics can be monitored. An energy value can be assigned to a certain mass spectrum a-posteriori.

Table 4: Provided parameters together with a single particle mass spectrum (UTC: Coordinated Universal Time)

parameter	**unit**	**used for**
Time stamp	UTC time	correlation to other data
Upcount value	FPGA clock ticks x 40 ns	particle size information after an appropriate calibration
Laser pulse energy	mJ	monitoring ablation laser performance on a single particle

All parameters that are provided with a single particle spectrum are listed in Table 4. The time stamp of each recorded particle enables a comparison of the mass spectra to other data, e.g., ERICA-AMS data or aircraft altitude, e.g., Section 5.1.2 and 5.2.2, recorded by ERICA or from external instruments, e.g., ozone mixing ratio (see Section 5.2.3.2).

3.7.3.2 ERICA-AMS

A digitizer (DAQCard, model ADQ1600, SP Devices) serves for both, the generation of trigger pulses for the ion extraction pulser and the acquisition of ion-generated electrical signals from the MCPs. This device samples at 1.6 GS/s with a high vertical resolution of 14 bits. Thus, the stored raw spectra have a time resolution of 0.625 ns per sample. The ion extraction pulser operates typically at a frequency of 50 kHz. These consecutive spectra are processed on hardware level over a time period of user-selectable length and finally streamed via a USB 3.0 connection as one averaged raw spectrum to the MCC (averaged in real-time over 400 ms, defined and termed 1 *buff*). The averaged spectra are recorded by the software *TofDAQ Recorder*, as part of the software kit *TofDAQ Suite* (Tofwerk AG, Switzerland, version 1.99), where also acquisition rules can be set. Usually the parameters are set as follows: One measurement cycle (1 *write*) is defined as 10 s (25 *buffs*). In total, 30 *writes* (750 *buffs*) are accumulated in one output file covering a measurement interval of 5 minutes. The files are in HDF5 (Hierarchical Data Format, version 5) format and can be used for evaluation by the software *Tofware* (Tofwerk AG, Switzerland, version 2.5.6). Basics of the software are described by Stark et al. (2015), Timonen et al. (2016), and Cubison and Jimenez (2015).

During the a-posteriori data evaluation the first *buff* is discarded, because the shutter changes its state from closed to open, resulting in an undefined position within this *buff* (termed *switch buff*). At an undefined position no quantitative information can be retrieved. The following 12 *buffs* (4.8 s) represent the “open” measurement, followed by a *switch buff* again, where the shutter is driven to the closed position and blocking the particle beam. Another 11 *buffs* (4.4 s) represent the gas phase background measurement at shutter closed. The position of the shutter is controlled with a signal sent by the digitizer to the shutter controller unit, where also the exact position of the shutter is monitored and recorded. More details of the SU can be found in Dragoneas et al. (2020). During operator supervised operation the ERICA-AMS acquisition can be controlled by means of the *TofDAQ viewer* software (Tofwerk AG, Switzerland, version 1.2.99).

In the Aerodyne AMS community it is common to use the acquisition software *ToF-AMS DAQ* (Kimmel, 2011) together with the evaluation software SQUIRREL (SeQUential Igor data RetRiEvaL; based on the principle described in Allan et al. (2004)). Since *ToF-AMS DAQ* cannot handle the serial input signal of the shutter position sensor the sole use of the software package *TofDAQ Suite* is necessary. This leads to the need to use *Tofware*, since the *TofDAQ Recorder* output files are not compatible with SQUIRREL.

The measuring mode of the ERICA-AMS is based on the “MS mode” of common Aerodyne AMSes (Drewnick et al., 2005). Furthermore, the ERICA-AMS data acquisition card supports another mode, the “event trigger mode”, where single non-refractory particles could be measured by the ERICA-AMS quantitatively. This mode has not been applied and characterized yet, but is available for future studies.

3.8 Design considerations for aircraft operation aboard the M-55 *Geophysica*

The instrument was developed for the first deployment aboard the Russian research aircraft M-55 *Geophysica* (Borrmann et al., 1995; Stefanutti et al., 1999). It reaches a ceiling height of 20 – 21 km and can operate for up to six hours. This makes it similar to other high altitude research aircraft like the NASA research aircraft ER-2 (NASA, 2002) and the WB-57F (NASA, 2017). The aircraft is single seated, i.e., only the pilot and no other operators are on-board. Therefore, the instrument has to be designed as totally autonomous. An *Iridium* (Iridium communication system, Iridium Satellite LLC) satellite link has been implemented within ERICA to enable ground operators to monitor the instrument's performance and to access the instrument by limited remote control while the aircraft is flying.

3.8.1 Satellite communication link

For remote control of the instrument during flight operation, an antenna for satellite communication (Iridium communication system, Iridium Satellite LLC) was implemented and the GUI software for message generating, transmitting, and receiving was programmed. The *Iridium Messenger* acquires the status information from all ERICA components every two minutes and transmits this information to the ground via an *Iridium* modem (9602 SBD, Geoborders) in a binary coded file. The data are received by the operator on ground as an attachment of an e-mail. The *SBD Message Merger* (Short Burst Data) running on the MCC combines multiple binary files into one single file that contains the information of the entire flight. This file can be read out by the *Logged Status Viewer* to observe the instrumental behavior on-line during flight. To control the instrument remotely from ground, a command file can be exported by the GUI program *Remote command composer*. Commands can be sent from ground to ERICA to control the FSC (e.g., resetting the data acquisition card, ablation laser power supply, and TPS relays in case of failures), the TEMPCTRL (e.g., switching fans and heating cartridges) and the PPC (e.g., resetting pump relays and the take-off timer, see Section 3.8.2). The unit is part of the UPS backed systems.

The need to interfere with ERICA from the ground via the *Iridium* link occurred three times during the StratoClim field campaigns, when the ERICA-LAMS data acquisition software suddenly failed (see Section 5.2). The first two incidences happened in flight KTM05. After the MCC was remotely powered down and up again the acquisition resumed operation with about 30 minutes of flight data loss. In flight KTM07 the same failure occurred. Here, the data acquisition software was reset without restarting the MCC. Thus, only 9 minutes of data were lost. After the corresponding software modules were remotely restarted by the ground operators, ERICA-LAMS and ERICA-AMS resumed normal operation. This way the flight data loss could be limited to a total of only 39 minutes. Thus, the design of the redundancy and safety control features proved to be reliable and highly effective.

3.8.2 Low power mode (LPM)

To reach a sufficiently high vacuum (see Section 3.7.1.4) for a research flight, the pumps have to be switched on a few hours before the planned aircraft take-off. To reduce power consumption and heat production of the instrument during this time, only the essential components, like the pumps, the MCC, the PPC and the ion source of the ERICA-AMS, are powered. This mode is named Low-Power Mode (LPM), as a kind of stand-by mode. All other components are switched-off by relay switches. A restart of the MCC turns the instrument from LPM into automatic measurement mode (auto mode), by starting the GUI programs automatically. The default values of the parameters are stored either as text files (for instance the mass spectra voltages for the TPSes), internally (ERICA-LAMS data acquisition and TC control) in the GUI software, or on EEPROMs (PPC, TC and DETC). For a restart after aircraft

take-off, two independent parameters can be set on the PPC. Either preset values for a timer or an altitude have to be exceeded – whichever occurs at first – to trigger a restart the MCC, then in autonomous flight operation mode (Dragoneas et al., 2020).

3.8.3 Pressurized container and aircraft inlet for ERICA on the M-55 *Geophysica*

The M-55 *Geophysica* has no pressurized compartments for the instruments such that the instruments need to be functional at ambient pressures (as low as 55 hPa), or – like ERICA – are installed in pressurized containers. For this purpose, the aircraft company MDB (Myasishchev Design Bureau, Moscow Region, Russia) had built a pressure tight cylindrical container, where full diameter lids on both sides are sealed by rubber O-Rings (outer diameter 816 mm, length 1,428 mm, Figure 17). The container can sustain up to 1.6 bar over-pressure, but no under-pressure. A pressurized environment is necessary, because electrical units, especially the high voltage power supplies, cannot operate at ambient pressures below 700 mbar. To avoid effects of ambient humidity (especially in the Asian monsoon phase in Kathmandu, Nepal), the sealed barrel was flushed and pressurized to 1.2 bars with dry nitrogen before each flight. That prevents water condensation inside the container during flight. The heat production of the instrument keeps the temperature inside the barrel above 7 °C. The gaseous medium inside the container is well mixed by six fans (see Appendix A.3). If necessary, additional heating fans could be turned on automatically or remotely. A 5-liter gas cylinder with a pressure of 200 bar was installed inside the container to compensate for possibly occurring pressure drops during flight due to leakages or defective sealing. Based on an in-house built mechanical differential pressure regulator, the valve keeps the container pressure within acceptable limits, acting automatically and independently from electrical units such as the MCC or the PPC. The valve opens at container pressures below 0.75 bar. During 11 test and research flights within the StratoClim project the pressure loss inside the barrel was at most from 1.15 bar to 0.85 bar.

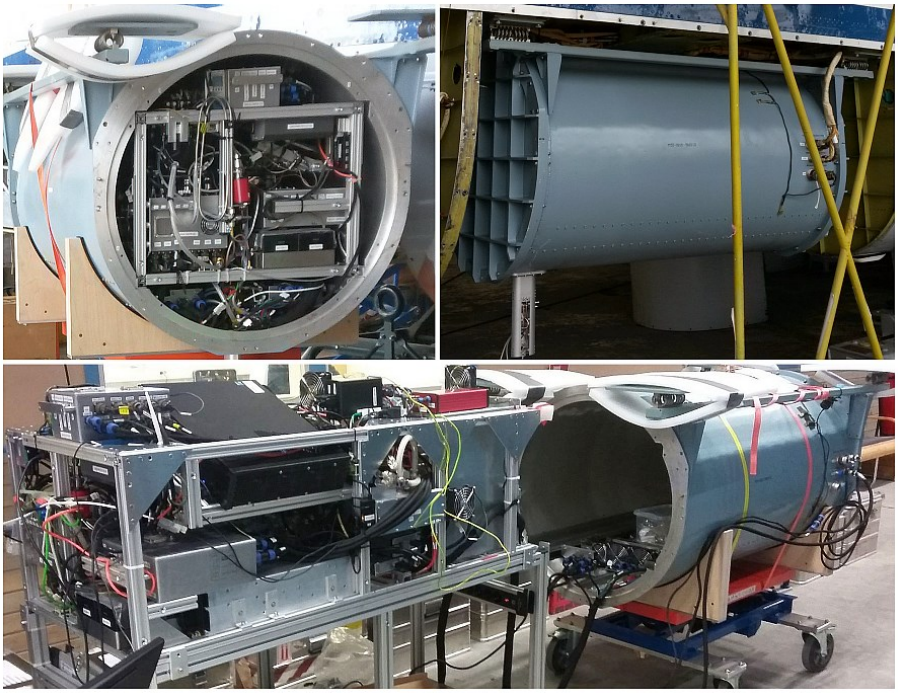

Figure 17: ERICA inside the container manufactured by MDB with opened front lid (left, top). ERICA inside the container with closed lids and mounted on the aircraft. The shaft of the inlet for sampling the ambient air can be seen protruding at the bottom left of the barrel directly adjacent to the lid (right, top). ERICA in front of the container in its rack frame before sliding onto the rails into the container (bottom). Photographs by the author, except bottom picture from S. Molleker, MPIC, Mainz, Germany.

Figure 18 shows gold-plated aircraft inlet that was mounted directly before each research flight to prevent damages on the inlets' body and to check for clogging or damages from the previous flight. The gold layer has a thickness of a few micrometers and is used not only to chemically inert the surface but also to identify particles that had wall contact during sampling (see Section 5.2.3.3). The design of the inlet is described in detail in Dragoneas et al. (2020).

Figure 18: Gold-plated aircraft inlet.

3.8.4 Acquisition of data from the aircraft systems and avionics

The aircraft provides flight data, such as time, altitude, and GPS (Global Positioning System) position (a complete list is provided in Appendix A.4) to all payload instruments by the UCSE (Unit for Connection with Scientific Equipment). The interface to the MCC is the UCSE ConTRoL unit (UCSECTRL) as part of the ERICA instrument. It receives the flight parameters and transmits them via a serial connection to the MCC, where a GUI program (*UCSE decoder*) records them. In the opposite direction it transmits the status of the instrument to the pilot's control panel to provide the pilot with information during the flight: measuring mode (green indicator), overheat failure (yellow indicator), and stand-by mode (LPM; white indicator).

4 Instrumental characterization

Knowledge about the instrumental behavior, its' limits and possibilities are essential obtaining reliable measurements from complex instruments like ERICA. For this purpose, characterization measurements on the detection units, the detection and ablation lasers and the particle beam were conducted. Some of the results are part of the forthcoming publication Hünig et al. (2020), but presented here in more detail. The ERICA-AMS measurements were performed and evaluated by O. Appel (MPIC).

4.1 Characterization of the laser beams

Two key units in the instrument, the detection unit (see Section 3.3) and the ablation unit (see Section 3.4), are laser based. The detection and ablation laser have to overlap with the particle beam to work sufficiently well such that the particles intercept all three foci. Therefore, the dimensions like the beam waist radius and the focal length play an important role. Furthermore, the determination of the fraction of UV light in the ablation laser flash is important for the ionization process optimization (Suess and Prather, 1999).

4.1.1 Experimental setup

For characterization of the laser beam profiles of the detection lasers and the ablation laser, a razor blade was moved manually stepwise into the respective laser beam. The procedure, also called knife-edge experiment, is well known (e.g., Skinner and Whitcher (1972), Araújo et al. (2009), and Eichler et al. (2016)) and was conducted as described for instance in Hünig (2014). In this experiment, the laser unit was mounted on an optical bench and the laser beam spotted on a bolometer (model High sensitivity thermal sensor 3A, Ophir Optronics Solutions Ltd) in case of the diode lasers. For the pulsed UV ablation laser an energy meter (model EnergyMax-USB, J-25MB-LE, Coherent, Inc.) was used instead. The razor blade was glued on a bracket and mounted on a translation stage (resolution 0.01 mm) perpendicular to the laser beam. All measurements were performed with the focusing lens implemented. The sensors (bolometer and energy meter) were positioned in a distance of 30 cm to the focal point to reduce the energy density on the sensor's surface in order to prevent damage on the sensor head.

The determination of various parameters via user-defined functions (Equations (24) and (25)) was performed by means of a curve fitting routine using the software *IGOR Pro* (version 6.3.7.2, WaveMetrics Inc. Lake Oswego, OR, USA). The curve fitting routine is based on the Levenberg-Marquardt algorithm (least-squares fitting algorithm).

Since no additional wavelength separator (see Section 3.4.1) is deployed, a mixture of infra-red (λ = 1,064 nm), green (λ = 532 nm) and UV light (λ = 266 nm) is emitted. To quantify the UV fraction, both dichroitic mirrors (termed here as M and are the same as used in the ERICA instrument, see Section 3.4.1) were used in two different set-ups without the focusing lens (see Section 3.4.1). Figure 19 (left) depicts all possible positions of the mirrors in the beam path (M1, M2 and M3). The numbers in circles indicate the position of the energy meter to record the pulse energy. In Figure 19 (right) the measurement at position 4 (mirrors at position M1 and M2) and position 6 (mirrors at position M1 and M3) are shown exemplarily. Position 4 reflects the position of the energy meter in ERICA during particle measurements. The particle ablation is performed between the two mirrors, corresponding to position 3. To determine the fraction of UV light, the reflectivity of the mirrors have to be determined first. Therefore, at all 7 positions the pulse energy was measured.

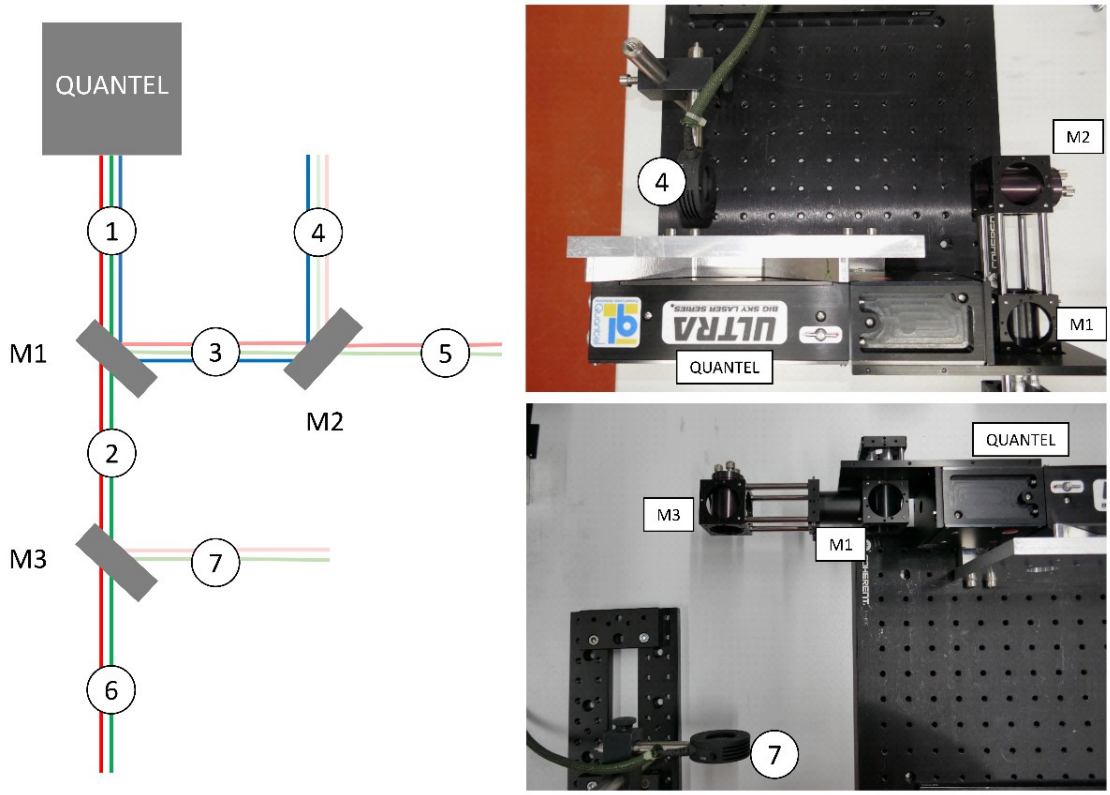

Figure 19: Left: Possible positions of dichroitic mirrors (M) and the energy meter sensor (numbers in circles) during the UV light quantification experiment. Right: Dichroitic mirrors at position M1 and M2 to measure at position 4 (top) and dichroitic mirrors at position M1 and M3 to measure at position 7 (bottom; both pictures are reconstructed).

4.1.2 Detection laser

The beam waist radius w_0 (1/e²-radius; see Figure 20) of the focused detection laser beam (see Section 3.3) was characterized by positioning the razor blade directly at the focal point of the optical axis and moving it stepwise into the beam. The focal point was determined by a black sheet of paper that smolders in the focal point.

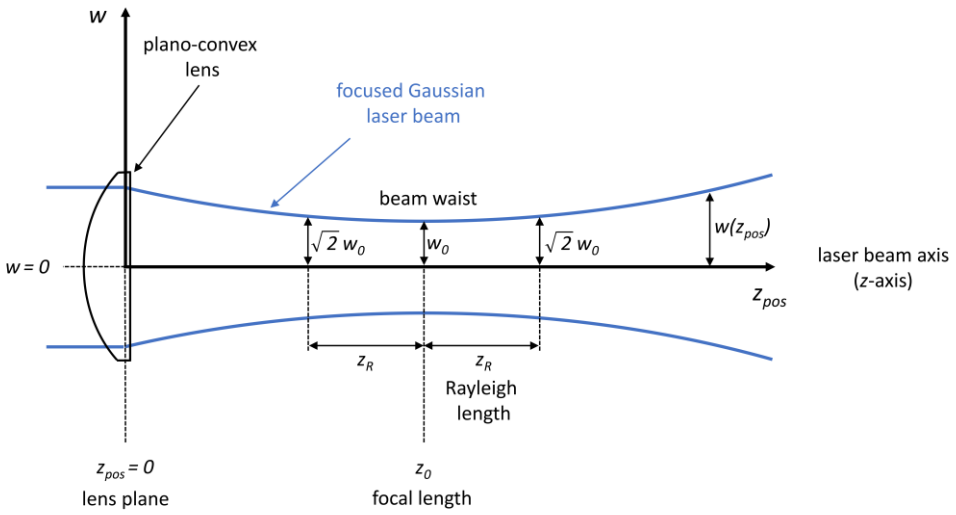

Figure 20: Gaussian beam width w (1/e²-radius) as function of the distance z along the laser beam axis (z-axis). z_{pos} = 0 is defined as the lens plane and the laser beam z-axis corresponds to the y-axis in Figure 12. w_0: beam waist; z_R: Rayleigh length; z_0: focal length. The figure was redrawn according to Eichler et al. (2016)).

The power of the laser beam (λ = 405 nm) was detected by a bolometer that was positioned in a distance of 30 cm from the focal point. The remaining power P was observed for 10 seconds and noted down. The fluctuations of the value were considered as uncertainties. The measurement was performed in two dimensions. After the first run (27 data points, here termed *x*-direction) the detection unit was rotated by 90° (28 data points, *y*-direction, perpendicular to *x*). The axis titles in this section do not refer to the instrumental axis definition shown in Figure 12 (see Section 3.1). The results are shown in Figure 21. Both data sets were curve fitted (using *IGOR Pro*, see Section 4.1.1) by the Gaussian error function (Equation (24)) with P_0 for the offset of the power for the fitting routine baseline subtraction, P_{max} the maximum power, pos_0 the central point of the Gaussian profile (in *x*- and *y*-direction), pos the position of the blade (in *x*- and *y*-direction), and w_0 the beam waist radius (1/e²-radius of intensity) of the Gaussian profile (Araújo et al., 2009).

$$P(pos) = P_0 + \frac{P_{max}}{2} \cdot \left(1 - \mathrm{erf}\left(\frac{\sqrt{2} \cdot (pos - pos_0)}{w_0}\right)\right) \tag{24}$$

All parameters P_0, P_{max}, pos_0, and w_0 and their respective uncertainties are results from the fitting algorithm (see text boxes in Figure 21).

The results for w_0 of the measurements in *x*- and *y*-direction slightly differ and indicate an oval cross-sectional focal spot profile. In *x*-direction, w_0 (1/e²-radius) was determined to 30.3 µm and in y-direction to 20.0 µm, respectively for $w_{0,dia} = 2w_0$, a 1/e²-diameter, 60.6 µm (*x*-direction) and 40.0 µm (*y*-direction). Due to the identical design of the detection laser units this measurement is considered to be representative for all detection laser units: DL1, DL2 (see Figure 10), and the spare detection laser unit.

The determined values are in the order of magnitude of other well described single particle mass spectrometers such as LAAPTOF with a 1/e²-diameter of 51.2 µm (Marsden et al., 2016). LAAPTOF uses laser light with a wavelength of λ = 405 nm for light scattering (Gemayel et al., 2016; Marsden et al., 2016).

The instruments PALMS, LAMPAS2, and A-ATOFMS use detection lasers with a wavelength of λ = 532 nm for particle detection. For PALMS, the dimensions of the spot size of 100 µm x 25 µm (Cziczo et al., 2006) are given in FWHM that can be recalculated into a 1/e²-diameter. The result of this calculation is a spot size of 170 µm x 34 µm. Trimborn et al. (2000) report for LAMPAS2 a detection spot size of ~30 µm and Su et al. (2004) for A-ATOFMS 300 µm. The method adopted for spot size determination for the latter two instruments was not specified by the authors. Thus, the presented values are not directly comparable with the values of the other instruments.

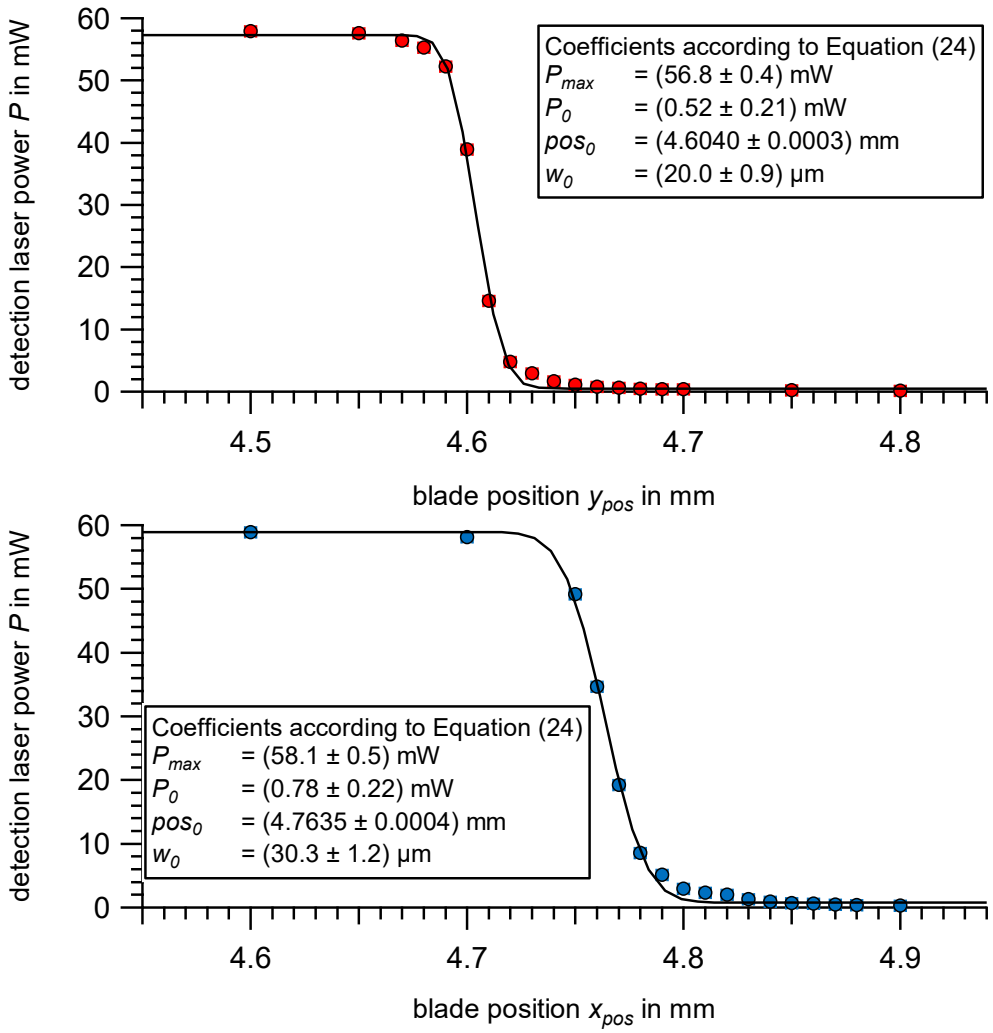

Figure 21: Detection laser beam characterization measurement in the focal point of the optical setup (x-direction top, y-direction bottom. The axis titles do not refer to the instrumental axis definition in Figure 12) curve fitted with Equation (24), where P is the measured power, P_0 is the offset of the power for the fitting routine baseline subtraction, P_{max} the Gaussian area of the intensity profile, pos_0 the central point, pos the horizontal position of the blade, and w_0 the beam waist radius ($1/e^2$-radius) of the Gaussian profile. The uncertainties of the detection laser power P reflect the fluctuation of the value at the bolometer display and the uncertainty of the blade position (x_{pos} and y_{pos}) is based on the reading error of the micrometer positioning system (see Appendix B.1.1). The uncertainty bars are smaller than the symbols. The boxes present the values and uncertainties of the parameters from the curve fitting.

4.1.3 Ablation laser

The procedure of the characterization of the ablation laser is similar to the one for the detection lasers. Instead of the bolometer, an energy meter was used to measure the energy of the focused laser pulse by observing 20 shots at Position 3 (Figure 19). Position 3 reflects the position of the ablation spot in the instrument (see Figure 10). These measurements were repeated eight times at different positions along the laser beam beams' optical z-axis with respect to the lens' focal plane ($z_{pos} = 0$; see Figure 20). Therefore, the $\frac{1}{e^2}$ −radii $w(z_{pos})$ were plotted versus the value of the razor blade to lens distance z_{pos} (Figure 22). The optical z-axis corresponds to the y-axis of the instrument (see Figure 12).

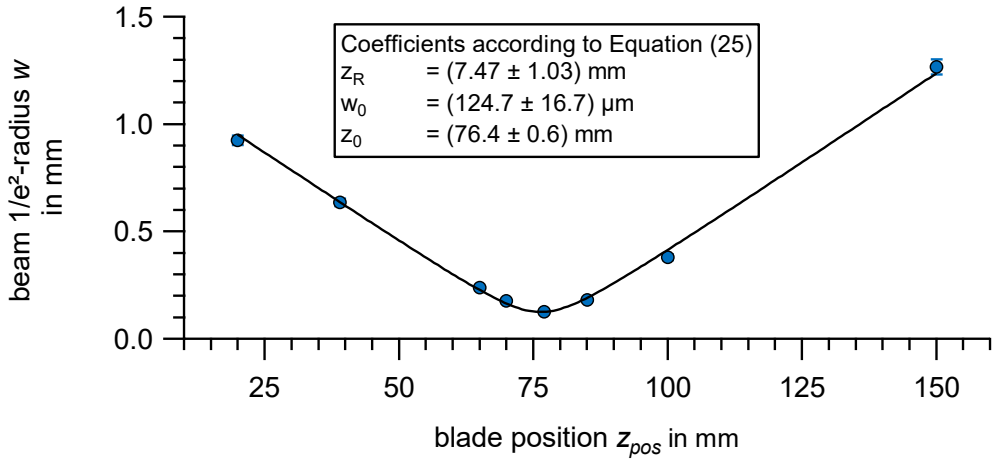

Figure 22: Ablation laser beam characterization along the laser beam curve fitted with Equation (25), where z_R is the Rayleigh range, z_0 the focal length and w_0 is the beam waist radius ($\frac{1}{e^2}$ –radius). The uncertainties of the ablation laser energy E reflect the fluctuation of the value at the energy meter display and the uncertainty of the blade position z_{pos} is based on the reading error of the used caliper (see Appendix B.1.2). The uncertainty bars are smaller than the symbols. The box presents the values and uncertainties of the parameters from the curve fitting.

The data points were curve fitted (using *IGOR Pro*, see Section 4.1.1) with the Gaussian near field equation (Equation (25), Siegman (1986)) to determine the focal length z_0, the Rayleigh range z_R and the beam waist radius w_0 at the position $z_{pos} = z_0$:

$$w(z_{pos}) = w_0 \cdot \sqrt{1 + \left(\frac{z_{pos} - z_0}{z_R}\right)^2} \tag{25}$$

Since the reflections of the laser beam profile appeared symmetrical when firing on white paper, this measurement was only done along one cross sectional direction. The curve fitting results in a Rayleigh range z_R of z_R = 7.5 mm, focal length z_0 of z_0 = 76.4 mm and a beam waist radius (1/e²-radius) w_0 of w_0 = 124.7 µm. The beam waist diameter $w_{0,dia}$ (1/e²-diameter, $w_{0,dia} = 2w_0$) is approximately $w_{0,dia}$ = 250 µm and provides an irradiance E_e of E_e = 3.73 · 10^9 W cm^{-2}, considering a laser pulse duration τ_p of τ_p = 6 ns and a laser pulse energy E_{UV} of E_{UV} = 11 mJ, which corresponds to a radiant fluence H_e of H_e = 2.24 · 10^4 mJ cm^{-2}. The determination of z_0 is crucial for adjusting the highest possible flux density – occurring at z_0 – onto the particle beam at the ablation spot.

The values obtained for the focal spot size and the flux density are similar to other single particle mass spectrometers, which are well described in the literature. Of the following particle mass spectrometers, the one most similar to ERICA is ALABAMA. It contains the same ablation laser type as the ERICA-LAMS (λ = 266 nm). The ablation laser beam is focused to a spot size of 200 µm with an irradiance of 3 · 10^9 W cm^{-2} at a pulse energy of 7 mJ and a pulse duration of 6 ns (Brands, 2009; Brands et al., 2011; Köllner, 2019). The A-ATOFMS also contains an ablation laser that emits a laser beam with a wavelength of λ = 266 nm (Pratt et al., 2009). The ablation spot size of 400 µm (Gard et al., 1997) is slightly larger and the irradiance of 3 · 10^8 W cm^{-2} (Su et al., 2004) with a pulse duration of 5 ns (Gard et al., 1997) and a pulse energy of 2 mJ (Su et al., 2004) one order of magnitude lower than the corresponding values of the parameters of the ERICA-LAMS.

Another commonly adopted laser wavelength for particle ablation is λ = 193 nm provided by excimer lasers such as it is used in the PALMS (Cziczo et al., 2006) and the LAAPTOF (Ahern et al., 2016; Gemayel et al., 2016) single particle mass spectrometers. However, different ablation spot sizes are in use. In

the PALMS the FWHM ablation spot size is 150 µm (Cziczo et al., 2006) that equals a 1/e²-diameter of 255 µm with an irradiance of up to $5 \cdot 10^9$ W cm^{-2} and at a pulse duration of 2.5 ns (Lee et al., 2002). The ablation spot size in the LAAPTOF is 800 µm x 600 µm (Reitz et al., 2016) and thus much larger than the ablation spot of the ERICA-LAMS. However, the irradiance of $\sim 10^9$ W cm^{-2} (Reitz et al., 2016) is in the same order than for the ERICA-LAMS (pulse energy of 4 mJ and pulse duration of 8 ns; Ahern et al. (2016)).

The value of the irradiance of $\sim 10^9$ W cm^{-2} (0.25 mJ, 3 ns; Trimborn et al. (2000)) in the ablation spot of the LAMPAS2 is similar to the irradiance in the ablation spot in the ERICA-LAMS. However, the spot size in the dimensions of ~30 µm (Trimborn et al., 2000) is approximately one order smaller than the spot size in the ERICA-LAMS. In addition, another ablation laser wavelength (λ = 337 nm) is used (Trimborn et al., 2000).

The method for determining the values for the listed parameters of the A-ATOFMS, the LAAPTOF, and the LAMPAS2 is not described in the publications. Therefore, the values may not be directly comparable with those determined here. Furthermore, the laser type and the laser wavelength of the LAAPTOF and the LAMPAS2 differ from the setup in ERICA. However, they provide qualitive information for comparing the various single particle mass spectrometer with each other.

The repetition rates f_{rep} of the ablation lasers are different. While the ablation laser of the ERICA is set to a maximum of f_{rep} = 8 s^{-1} (see Section 3.4.1), the repetition rates in the ALABAMA and the A-ATOFMS is in maximum f_{rep} = 20 s^{-1} (Su et al., 2004; Köllner, 2019), in the PALMS f_{rep} = 50 s^{-1} (Cziczo et al., 2006), and in the LAAPTOF it is set to f_{rep} = 10 s^{-1} (Ahern et al., 2016).

4.1.4 UV light fraction of the ablation laser

For the ablation and ionization process, UV light photons play a major role (see Section 2.3). Thus, the amount of UV light emitted by the ablation laser has to be adjusted to the maximum. In the following determination of the UV fraction, the energy of the focused laser beam was determined by averaging over 20 ablation laser shots.

To quantify the fraction of UV light in the emerging laser pulses, the reflectivity of the mirrors has to be determined first, due to lack of specification information from the manufacturer for wavelengths larger λ = 440 nm. The reflectivity for the λ = 266 nm is given as 99.5 %. To measure the reflectivity for the green (λ = 532 nm) and Infra-Red (IR, λ = 1,064 nm) part of the laser light, the sensor was positioned, according to Figure 19, at Position 2 and 7 (Figure 19, left). Here, less than 0.5 % UV light and thus only the residual wavelengths are present. The measurements lead to a reflectivity of 12.6 % for the IR/green mixture at one mirror (Position 3 in Figure 19, left). After two reflections (Position 4, Figure 19, left) only 1.6 % of the initial IR/green light remains. Thus, the sum of the remaining IR/green light fraction at Position 5 and 2 amounts to 98.5 %. At the sensor position in the instrument (Position 4) 99.0 % of the emitted UV light remains. Based on these two values, it can be assumed that at Position 4 the pure UV fraction was measured and the sum of Position 2 and 5 can be counted as the pure IR/green light fraction.

The output energy of a laser pulse can be adjusted by the FLQS delay (see Section 3.7.2.2). A specific set of experiments was performed to explore this further and Figure 23 shows the laser pulse energy as function of the FLQS delay for the UV light E_{UV} and the IR/green light $E_{IR/green}$. The FLQS delay value at the highest UV fraction (29 % of the total laser energy output) equals the value at the highest laser pulse output energy of 12 mJ at a FLQS delay value of 145 µs. The maximum measured UV light energy value confirms the manufacturer's specification of the ablation laser.

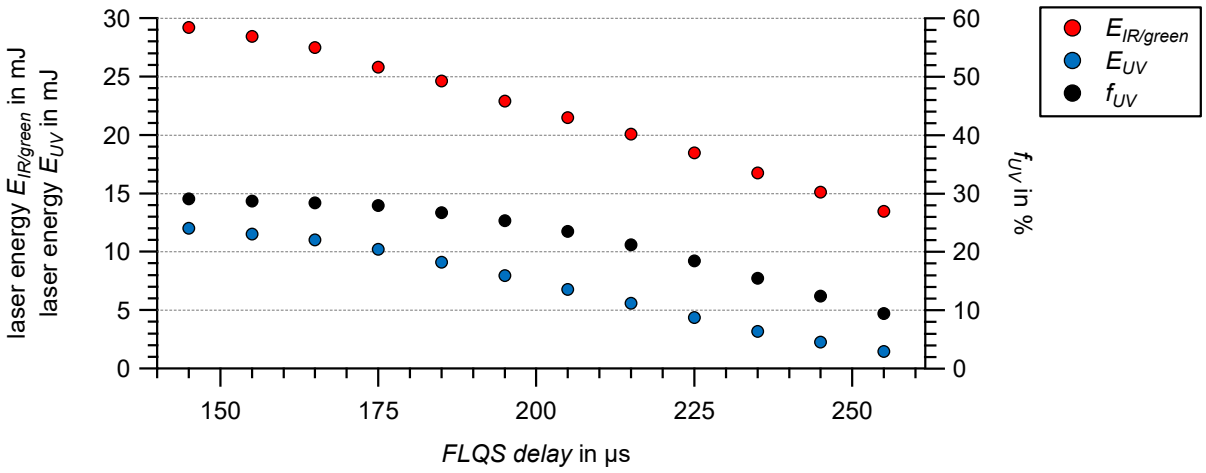

Figure 23: Laser pulse energy as function of the FLQS delay for the UV light E_{UV} (blue) and the IR/green light $E_{IR/green}$ (red) and the fraction of UV light f_{UV} (black). The uncertainties of the laser energy E_{UV} and $E_{green/IR}$ reflect the reading errors of the energy meter display and are used as basis for uncertainty propagation of the UV fraction f_{UV} and $E_{green/IR}$ (see Appendix B.1.3). The uncertainty bars are smaller than the symbols.

The UV light photons possess the highest photon energy emitted by the ablation laser in ERICA. However, the green and IR photons might assist the LDI process in terms of particle evaporation with their lower single photon energy (see Section 2.3, Figure 4).

4.1.5 Summary of the characterization of the laser beams

The aerosol particles are detected by two focused laser beams (λ = 405 nm). The 1/e²-diameter $w_{0,dia}$ of the investigated focal spot were determined as 60.3 µm (*x*-direction) and 40.0 µm (*y*-direction). The ablation laser beam (λ = 266 nm) is focused down to a 1/e²-diameter spot size $w_{0,dia}$ of 250 µm. The calculation of the radiant fluence results in $8.15 \cdot 10^3$ mJ cm^{-2}. In addition, the UV light energy of the laser pulse is 12 mJ which amounts to a fraction of 29 % of the total laser pulse energy.

4.2 Characterization of the detection unit and the particle beam

The characterization of the detection unit and the particle beam is necessary to understand the mutual dependencies and necessities for adjustments. Two different types of aerosols were used to characterize the particle beam. First, the PolyStyrene Latex NIST certified size standard (PSL) particles, which are established as calibration standard in aerosol science (Brockmann et al., 1988; Zelenyuk and Imre, 2005; Kamphus et al., 2008; Brands et al., 2011) and second, the atmospheric relevant substance ammonium nitrate that is used for calibration in the Aerodyne Inc. AMS community (Jayne et al., 2000; Canagaratna et al., 2007). The experiments presented in this section were conducted right after the Asian monsoon phase. By that, the results represent the instrumental behavior during this campaign phase. Because a different type of O-ring in the CPI and a different aerodynamic lens were used during the mid-latitude phase (see Section 5.1.3), the results shown here cannot be applied to this mid-latitude phase.

4.2.1 Experimental setup

To perform the particle size calibration measurement at the light scattering units DU1 and DU2 (see Section 4.2.2), and to characterize the particle beam (see Sections 4.2.3, 4.2.4, and 4.2.5), a laboratory configuration with a nebulizer, dryers and, for some measurements, particle size selecting equipment was set up (e.g., Brands (2009), and Hünig (2014)). Before any meaningful measurement can be conducted, the instrument has to be prepared by various adjustments.

4.2.1.1 Measurement setups for laboratory experiments

The following characterization measurements in Section 4.2 consist of two parts. In the first part, the particle size calibration procedure was performed and investigated (see Section 4.2.2). Subject of the second part is the particle beam (see Sections 4.2.3, 4.2.4, and 4.2.5).

The measurement set-up for the particle size calibration measurements consisted of a nebulizer (TSI 3076, TSI Inc., St. Paul, Minnesota, USA) that generated the particles out of a solution or suspension. The aerosol was directed through two diffusion dryers filled with silica gel (orange gel, Carl Roth GmbH & Co. KG) into ERICA (*Setup A* in Figure 24). The used PSL particle sizes (Polysciences Europe GmbH) are listed in Table 5 in Section 4.2.1.2. For validating the PSL calibration, ammonium nitrate (Merck KGaA, Darmstadt) particles were used (see markers in Table 6 in Section 4.2.1.2). Particles of this particle type, were additionally charge neutralized by an X-ray bipolar charger (TSI 3087, TSI Inc., St. Paul, Minnesota, USA) and size selected by a DMA (Differential Mobility Analyzer, Minnesota Type 5.5-900, GRIMM Aerosol Technik Ainring GmbH & Co. KG). After passing the DMA, the line with the aerosol output is split into two lines. One leads to ERICA and the other to a Condensation Particle Counter (CPC, Series 5.400 CPC, GRIMM Aerosol Technik Ainring GmbH & Co. KG) for number concentration measurements (*Setup B* in Figure 24).

For the particle beam characterization, the detection efficiencies of the ERICA-LAMS detection units at DU1 and DU2 (detection efficiency of PSL particles: DE_{PSL}, detection efficiency of ammonium nitrate particles DE_{AN}; definitions see Section 4.2.3) or of the ERICA-AMS (detection efficiency of ammonium nitrate particles at the ERICA-AMS: DE_{AMS}; definition see Section 4.2.3) were determined. Therefore, measurements performed either by a CPC or by an OPC that serve as a reference device, depending on the measured particle sizes and types. For measurements with ammonium nitrate particles (see marker in Table 6) and PSL particles smaller than $d_{va} \leq 834$ nm in diameter, the set-up including the bipolar charger and the DMA was deployed (*Setup B* in Figure 24). Table 7 in Section 4.2.1.2 lists the PSL particle sizes for the particle beam characterization. For PSL particle sizes between d_{va} = 834 nm and d_{va} = 3,150 nm (see Table 5) an OPC (model Sky-OPC, Series 1.129, GRIMM Aerosol Technik

Ainring GmbH & Co. KG) was used as reference device without bipolar charger and DMA for the particle beam characterization measurements (*Setup C* in Figure 24). The particle size d_{va} = 834 nm was measured with both reference methods (*Setup B* and *Setup C* in Figure 24). The OPC reference measurements were conducted and evaluated by S. Molleker (MPIC). The detailed experimental setup and the evaluation procedure for these OPC reference measurements are described in Molleker et al. (2020), where also the here presented results are included. The measurements with the OPC were only evaluated for DU1.

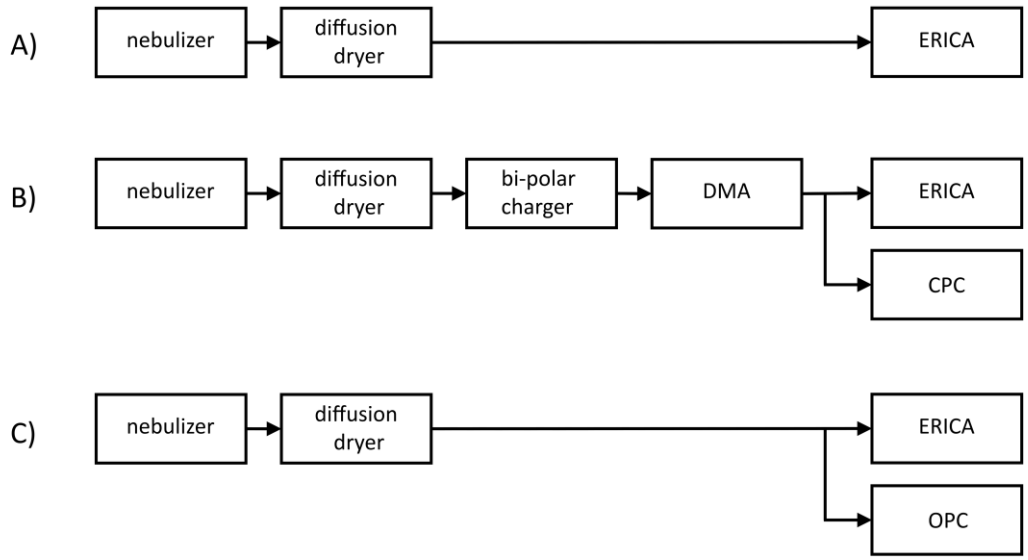

Figure 24: Scheme of the various measurement setups for the characterization measurements.

The measurements with the OPC (*Setup C* in Figure 24) were conducted after the size calibration and particle beam characterization measurements with the CPC as a reference device. Before the measurements with the OPC could be performed, the aerodynamic lens accidentally was rotated around its z-axis (see Figure 13) of estimated 90°. Since the overall particle beam cross-sectional area does not describe a circle (see Section 4.2.4) the rotation of the aerodynamic lens might partially influence these results. These influences are discussed individually for each determined parameter (see Section 4.2.5). However, the aerodynamic lens was rotated after the field deployment in Kathmandu, Nepal (see Section 5.2). Thus, the following characterization measurements with the CPC reflect the conditions during the field deployment.

4.2.1.2 Deployed chemical substances and particle sizes

Table 5 shows the different PSL particle sizes, which were used for the size calibration measurements. The different particle sizes are listed in geometric diameters d_{geo} (NIST certified) and nominal diameters d_{nom} (Hinds, 1999; Jimenez et al., 2003b, a; DeCarlo et al., 2004). The vacuum aerodynamic diameters d_{va} were calculated from d_{geo}. The particle density $\rho_{p,PSL}$ was assumed as 1.05 g cm^{-3} (Jayne et al., 2000). The equations adopted for conversion are listed in Appendix B.2.

Table 5: Measured PSL NIST size standards for particle size calibration measurements and particle beam characterization measurements. Listed are the particle sizes in nominal diameters d_{nom}, geometric diameters d_{geo} (NIST certificate), their absolute uncertainties $\Delta^{abs}d_{geo}$, the calculated vacuum aerodynamic diameters d_{va}, and their absolute uncertainties $\Delta^{abs}d_{va}$, and their relative uncertainties $\Delta^{rel}d_{va}$.

PSL particle sizes						Used for	
d_{nom} in nm	d_{geo} in nm	$\Delta^{abs}d_{geo}$ in nm	d_{va} in nm	$\Delta^{abs}d_{va}$ in nm	$\Delta^{rel}d_{va}$ in %	Size calibration	Particle beam characterization with OPC
80	76	11	80	11	14	X	
100	100	5	105	5	5	X	
150	150	9	158	9	6	X	
200	198	7	207	8	3.7	X	
300	288	14	302	15	5	X	
350	356	14	374	15	4	X	
400	401	12	421	13	3	X	
600	599	10	629	11	1.7	X	
800	794	24	834	25	3	X	X
1,000	990	30	1,040	31	3	X	X
1,500	1,540	39	1,617	40	2.5	X	X
2,000	1,990	60	2,090	63	3	X	X
2,500	2,580	65	2,709	68	2.5	X	X
3,000	3,000	60	3,150	63	2	X	X
5,000	4,900	25	5,145	26	0.5	X	X

Ammonium nitrate particles are detectable with the ERICA-LAMS as well as with the ERICA-AMS and serve as non-refractory particle species during the aerodynamic lens adjustment. Table 6 shows the assignment of the different ammonium nitrate particle sizes for the size calibration validation (Section 4.2.2), particle beam characterization (see Sections 4.2.3, 4.2.4, and 4.2.5) and aerodynamic lens adjustment (Section 4.2.1.3). To calculate d_{va} from the electric mobility particle diameter d_{mob} (see Appendix B.2) the ammonium nitrate particle density $\rho_{p,AN}$ was assumed as $\rho_{p,AN}$ = 1.725 g cm^{-3} (Zapp et al., 2000) and the Jayne shape factor as S = 0.8 (Jayne et al., 2000). The uncertainty of all sizes is conservatively estimated as $\Delta^{rel}d_{va}$ = 14 %, because the uncertainty for PSL particles in that size range (d_{va} = 80 nm to d_{va} = 834 nm) is between 1.7 % and 14 % (see Table 5 and Table 6).

Table 6: Ammonium nitrate particle sizes used for size calibration measurements, particle beam characterization measurements and aerodynamic lens adjustment. Listed are the particle sizes in electric mobility particle diameters d_{mob} and the calculated vacuum aerodynamic diameters d_{va}. The uncertainty of all sizes is 14 %. X: not used for evaluation of DE_{AN} at the detection units DU1 and DU2 (see Section 4.2.4); X**: not used for evaluation of DE_{AMS} at the ERICA-AMS vaporizer (see Section 4.2.4).*

Ammonium nitrate particle diameter		Used for		
d_{va} in nm	d_{mob} in nm	Size calibration	Particle beam characterization and detection efficiency determination with DMA	Aerodynamic lens adjustment
91	66		X*	
138	100	X	X*	X
177	128	X		
207	150			X
213	154	X	X	
276	200	X		X
297	215	X	X	
335	243	X	X	
414	300			X
483	350	X	X**	X
548	397	X	X**	
552	400			X
814	590	X	X**	

Table 7 shows the sizes of the PSL NIST size standards, which were used for the particle beam characterization measurements (see Sections 4.2.3, 4.2.4, and 4.2.5). The values of d_{va} were calculated from d_{geo} values (see Appendix B.2). Also, the d_{mob} values are listed to which the DMA was set during the measurements.

Table 7: PSL NIST size standards for particle beam characterization measurements. Particle sizes in nominal diameter d_{nom}, electric mobility particle diameters d_{mob}, geometric diameters d_{geo} (NIST certificate), their absolute uncertainties $\Delta^{abs}d_{geo}$, the calculated vacuum aerodynamic diameters d_{va}, and their absolute $\Delta^{abs}d_{va}$ and relative uncertainties $\Delta^{rel}d_{va}$. Also, the electric mobility diameters values d_{mob} to which the DMA was set are listed.

d_{nom} in nm	d_{geo} in nm	$\Delta^{abs}d_{geo}$ in nm	d_{va} in nm	$\Delta^{abs}d_{va}$ in nm	$\Delta^{rel}d_{va}$ in nm	d_{mob} in nm
100	103	14	108	15	14	105
200	208	7	218	8	4	225
400	390	12	410	13	3	405
600	599	12	629	13	2	585
800	794	27	834	28	3	795

For further laboratory studies also an aqueous solution of sodium chloride (Merck KGaA, Darmstadt) as well as a gold sphere suspension containing spheres of d_{geo} = 200 nm (Sigma-Aldrich, Inc.; particle size selection see Appendix B.2) were nebulized, the generated aerosol dried and measured (*Setup A* in Figure 24). Furthermore, measurements were conducted out of an alcoholic (isopropanol, Carl Roth GmbH & Co. KG) solution of benz[a]anthracene (Sigma-Aldrich, Inc.) via an X-ray bipolar charger and a

DMA (*Setup B* in Figure 24). These substances were used to demonstrate the satisfactory performance of ERICA-LAMS, as well as the applied evaluation software (see Section 4.4.1).

4.2.1.3 Preparation of the instrument for deployment by various adjustments

Prior to any successful measurement various adjustments had to be performed. Since the particle beam emerging from the aerodynamic lens has a certain beam spread, i.e., divergence (Huffman et al., 2005), during its propagation through the vacuum chamber, adjustment procedures had to be developed and applied to avoid the particle beam missing the ERICA-AMS vaporizer, or that it is only partially intercepted by the vaporizer, or not detected by both detection units (DU1 or DU2). Also, a certain probability exists that particles, which are detected by DU1, arrive off-center at DU2, or miss DU2 completely.

For the instrument adjustment, first, the aerodynamic lens to ERICA-AMS vaporizer axis has to be determined (see Figure 10). Second, the scattered light signal at the detection units (DU1 and DU2, see Figure 13) has to be maximized. Third, the focal point F1 of the ellipsoidal reflectors (see Section 3.3) has to be shifted such that it coincides with the previously determined particle beam axis. Fourth, to maximize the ablation efficiency (AE; definition see Section 4.3) the ablation laser beam has to be tilted onto the particle beam axis and the *Multiplier* value has to be adjusted. These four adjustments are described the following sub-section.

At first, the particle beam axis has to be centered onto the vaporizer of the ERICA-AMS (adjustment results see Appendix B.3). Therefore, size selected ammonium nitrate particles (sizes see Table 6, experimental set-up see Figure 24, *Setup B*) were sampled by the ERICA-AMS. By tilting the aerodynamic lens stepwise for each particle size, the signal intensity profile of the nitrate mass concentration was recorded. All profiles were compared to determine a position with high signals for all sizes. This procedure was performed in x- and y-direction, perpendicular to the particle beam axis (see Figure 12). The adjusted lens position in x-direction (scan perpendicular to the detection laser beam) was determined as x_{pos} = 10.55 mm, in y-direction (scan parallel to the detection laser beam) as y_{pos} = 10.80 mm. The result of the compromise was a position close to the optimum of the measurement with vacuum aerodynamic diameter d_{va} = 276 nm. Ammonium particles of this size are small, but still sufficiently detectable (DE of the detection units in the ERICA-LAMS $>$ 60 %, definition of DE see Section 4.2.4), but as consequence the detection unit adjustment was done with PSL particles (d_{va} = 218 nm, see Table 7) with respect to the determined particle axis.

In the second step the laser diodes of the detection unit were adjusted/tilted to maximize the scattered light signal intensity at the PMTs. For this purpose, the PMT signals were grounded via a 10 kΩ resistor. The voltage drop at this resistor was measured by scope probes (P2220 voltage probe, Tektronix Inc.) and recorded by an oscilloscope (model Picoscope 4424, Pico Technology). As particle source for the scattering light signal a PSL suspension (d_{va} = 207 nm) was used without further narrowing the size range by a DMA.

To maximize the counting rate at the detection units (DU1 and DU2) the aerodynamic lens was tilted in x-direction (see Figure 13). The procedure is similar to the above described procedure to determine the maximum ERICA-AMS signal intensity (see Appendix B.3). Here the particular aerodynamic lens position was determined from which the highest output in terms of count rate results. The difference of the x-position of the maximum signal from the aerodynamic lens scan at the ERICA-AMS vaporizer (see above) and the scans at each DU were compensated for by inserting metal spacers of appropriate

thickness under the ellipsoidal reflector holders (see Figure 13). By that, the detection unit was adjusted to the determined optimum aerodynamic lens position.

The next step to prepare the instrument for measurements was the adjustment of the ablation laser beam onto the particle beam (z-axis, see Figure 10 and Figure 12). Therefore, the dichroitic mirror DM1 (see Figure 15) was tilted to maximize the ablation efficiency AE (definition see Section 4.3). For this adjustment, PSL particles of d_{va} = 421 nm in diameter were used. Also, the *Multiplier* value (see Section 3.7.2.2) was adjusted to enhance the AE to its maximum (~50 %).

4.2.2 Aerodynamic sizes based on particle flight times

As described in Section 3.7.2.2, the particle flight time is determined at the detection unit by the TC and correlates with the vacuum aerodynamic diameter d_{va} directly (Brands et al., 2011). First, the particle flight time is needed to derive the particle arrival time in the ablation region to trigger the ablation laser at the right instant. Furthermore, it can be used as a particle size information after a suitable calibration. To determine the particle flight time the time between DU1 and DU2 (see Figure 10) is measured in clock cycle counts (*Upcount*, abbreviated as upc), where one clock cycle equals a time t_{TC} of 40 ns (see Section 3.7.2.2).

For the particle size calibration 15 different PSL size NIST standards in the range from d_{nom} = 80 nm to d_{nom} = 5,000 nm nominal diameter were used (see Table 5). For the measurements, *Setup A* was used and the aerodynamic lens was set to the optimal position (see Section 3.2.1). Figure 25 shows the combined histograms of the PSL calibration measurements, where the different sizes can be clearly distinguished. Only the results from the measurement of the PSL particles with d_{va} = 105 nm in diameter overlaps with the measurement of the PSL particles with d_{va}= 80 nm in diameter and cannot be well differentiated. The probability density functions underly the histograms of the individual particle sizes. To find the calibration value upc for each particle size, the ordinates $f(upc)$, i.e., the number of detected particles, of each histogram was curve fitted with upc as the independent counter variable to the normal distribution (Gaussian function) of Equation (26):

$$f(upc) = y_0 + A \cdot exp\left[-\left(\frac{upc - upc_0}{\sqrt{2}\sigma}\right)^2\right] \tag{26}$$

Here y_0 is the y-offset for baseline subtraction, A the amplitude, upc_0 the value of the abscissa at the mode maximum, and σ designates the standard deviation. The determination of these parameters via the user-defined function (Equation (26)) was performed by a curve fitting routine using the software *IGOR Pro* (version 6.3.7.2, WaveMetrics Inc. Lake Oswego, OR, USA). The curve fitting routine is based on the Levenberg-Marquardt algorithm (least-squares fitting algorithm).

The bin widths of the histograms (Figure 25) were chosen for each particle size such that they were smaller than the single standard deviation σ resulting from the curve fitting.

The data-set provides the basis for the following fitting procedures to obtain an empirical function (see following sub-section), which uniquely relates particle sizes (d_{va}) to *Upcount* values and thus to particle flight times (t_{ptof}, see Section 4.2.2.1).

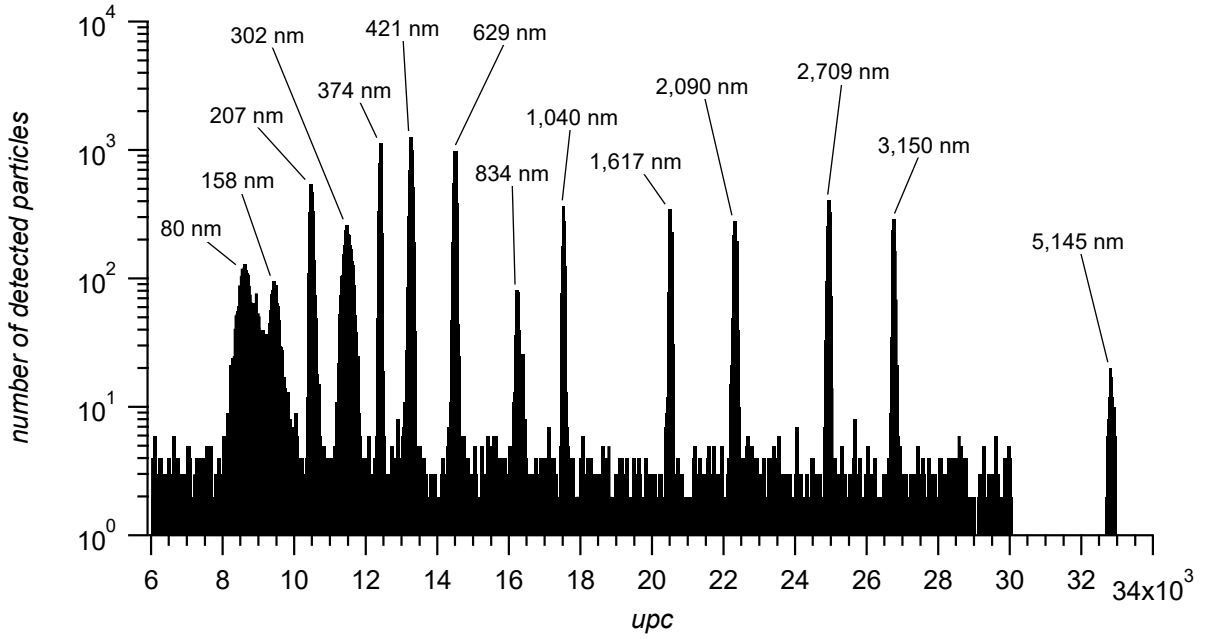

Figure 25: Combined histograms of the PSL calibration measurements (particle sizes provided as d_{va}). The histogram of d_{va} = 105 nm overlaps the broad histogram of d_{va} = 80 nm.

Beside PSL particles, also ammonium nitrate particles were measured using a bipolar charger and a DMA for size selection (*Setup B*, see Figure 24). For each particle size a histogram was generated in the same way as it was conducted for the PSL particles. The upc_0 and σ values were also determined by curve fitting each histogram using Equation (26). Figure 26 shows the resulting fitting curves that were normalized to the maximum value of the amplitude A for each particle size. The labels show the vacuum aerodynamic diameters d_{va} (see Table 6).

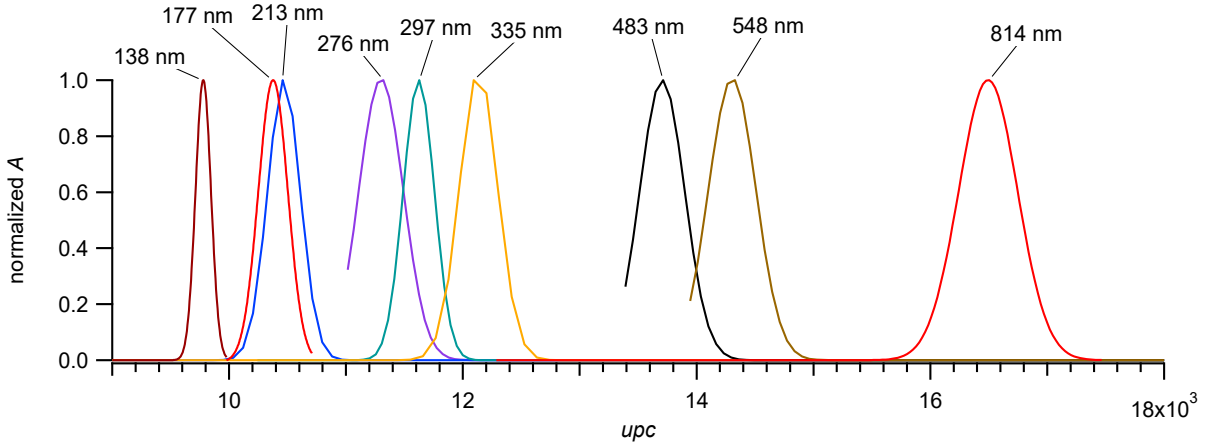

Figure 26: Combined fitting curves according to Equation (26) for the particle size calibration measurements with ammonium nitrate particles. The amplitude A was normalized to the maximum value for each particle size (provided as d_{va}).

4.2.2.1 Particle size calibration procedure according to Brands et al. (2011)

Four different fit functions have been applied to the particle size calibration measurements. The first one described here follows the procedure used by Brands et al. (2011). For calibration the value upc_0 of the mode maximum is used for each particle size (Equation (26)). Considering the clock cycle time of the trigger card of 40 ns and the density of the PSL the vacuum aerodynamic diameter d_{va} (Jimenez et al., 2003b, a; DeCarlo et al., 2004) can be plotted versus the particle time-of-flight t_{ptof} (Figure 27, left).

To create a calibration curve, a polynomial fit of second order was used:

$$d_{va}(t_{ptof}) = K0 + K1 \cdot t_{ptof} + K2 \cdot {t_{ptof}}^2 \quad (27)$$

The fitting routine was performed with *IGOR Pro* (version 6.3.7.2, WaveMetrics Inc. Lake Oswego, OR, USA). The results for the parameters $K0$, $K1$ and $K2$ of the fit are shown in the legend of the left panel in Figure 27.

In Figure 27, right panel, the relative deviation DVI_{rel} from the fitting curve $d_{va,fit}$, i.e., the calibration curve, calculated according to Equation (28), is depicted in x-direction for each measured particle size $d_{va,particle}$ (plotted in y-direction).

$$DVI_{rel} = \frac{d_{va,fit} - d_{va,particle}}{d_{va,particle}} \quad (28)$$

For particle sizes larger than d_{va} = 421 nm the deviation from the calibration curve is lower than 4 %. For smaller particles the deviation is up to 17 % at a particle size of d_{va} = 158 nm.

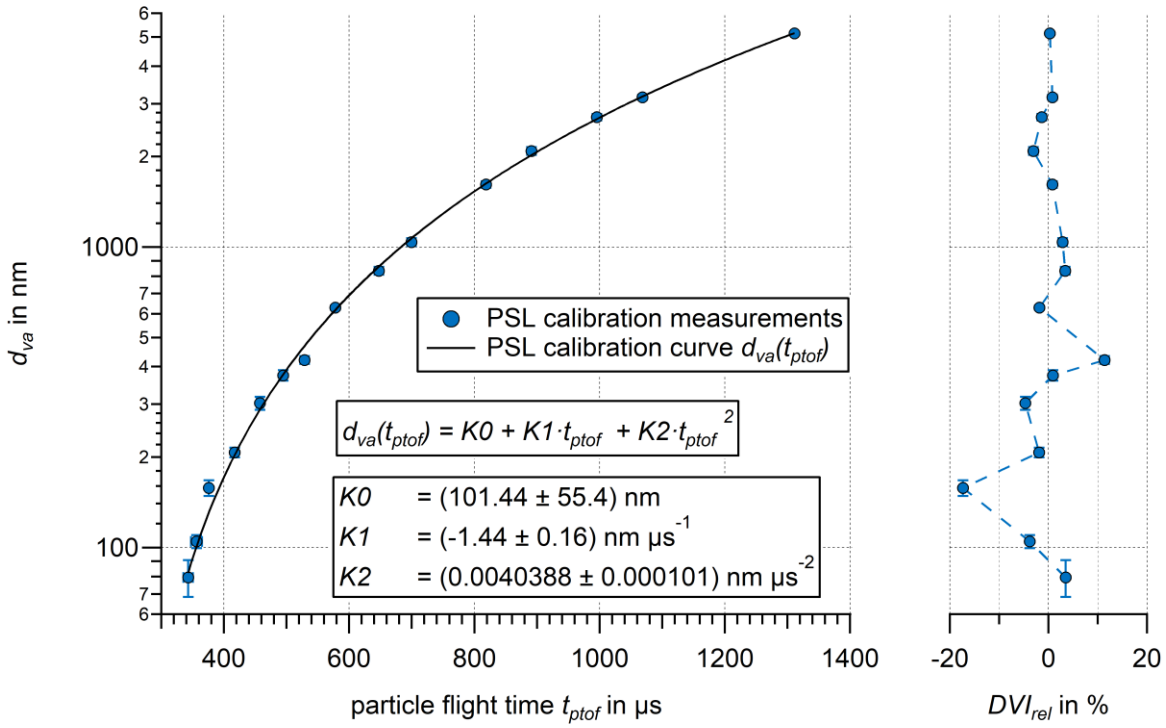

Figure 27: Calibration curve (d_{va} against t_{ptof}) for size calibration with PSL particles (left) and the relative deviation of the particle size fitting curve from the NIST particle size standard DVI_{rel} in % as function of the particle sizes d_{va} (right). The uncertainty of d_{va} along the ordinate is given by NIST certificates (values from Table 5; see also Appendix B.1.4). The uncertainty of the particle flight time can be estimated by Gaussian propagation of uncertainties (see Appendix B.1.5). K0, K1, and K2 are coefficients from the polynomial function used for the size calibration according to Equation (27). The uncertainty bars are in some cases smaller than the symbol.

To compare the PSL calibration curve with ammonium nitrate particles, the ammonium nitrate particle sizes (listed in Table 6) are plotted against the measured particle flight times t_{ptof} in Figure 28, left. The relative deviation from the PSL calibration curve (right) was calculated according to Equation (28) and is less than 10 % for ammonium nitrate particles between d_{va} = 213 nm and d_{va} = 548 nm in diameter. As result, within this size range the PSL size calibration is also valid for pure ammonium nitrate particles.

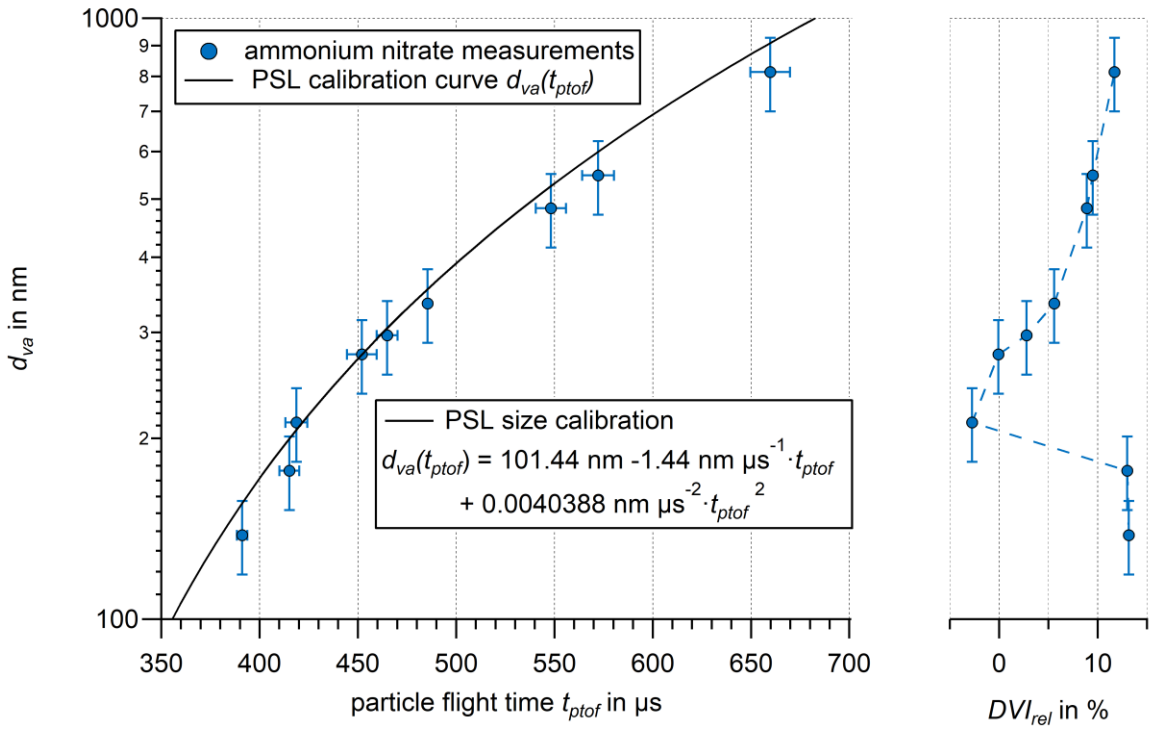

Figure 28: Different ammonium nitrate particle sizes and their respective aerodynamic diameters d_{va} as function of the particle flight time t_{ptof} compared with the PSL size calibration curve (left). Right panel: The relative size deviation of ammonium nitrate particles to the PSL calibration curve in % (right). The uncertainty of d_{va} is conservatively estimated to 14 % (see Appendix B.1.4). The uncertainty of the particle flight time can be estimated by Gaussian propagation of uncertainties (see Appendix B.1.5). The uncertainty bars are in some cases smaller than the symbol.

The polynomial function $d_{va}(t_{ptof})$ indicated in the legend of the left panel in Figure 27 was implemented in the evaluation software CRISP (see Section 3.7.3) and can be applied in a-posteriori analysis (see Section 3.7.3.1). The validity of the calibration curve should not be extrapolated beyond the given size range of the measured particle sizes from d_{va} = 80 nm to d_{va} = 5,145 nm as it is only applied within these limits.

4.2.2.2 Particle size calibration procedure according to Klimach (2012)

The evaluation software CRISP was developed by Klimach (2012) and used for data evaluation of several data sets from different field and laboratory measurement campaigns (e.g., Roth et al. (2016); Köllner et al. (2017); Schmidt et al. (2017)). Before the implementation of the polynomial-fit function (see Section 4.2.2.1) the software used only Equation (33) for size calibration.

The calibration method is based on the fact that aerosol particles have an enhanced inertia compared to the surrounding gas molecule. The enhanced inertia leads to a different velocity change during an acceleration of the gas. The temporal change of the particle velocity v_p is linked to the gas molecules' velocity v_g via the relaxation time τ. This can be described by Klimach (2012):

$$\frac{dv_p(t)}{dt} = \frac{v_g - v_p(t)}{\tau} \tag{29}$$

Considering the free molecular regime (Kn ~1,000 for $d_{mob} = 100$ nm) in the aerodynamic lens and the fluid as an ideal gas, τ is given as (Klimach, 2012):

$$\tau = k_G \cdot d_{va} \tag{30}$$

The constant k_G contains the gas constant R, the temperature T and the gas pressure p_g.

A detailed derivation of Equation (30) can be found in Klimach (2012). Combining τ from Equation (30) and the differential Equation (29) leads to Equation (31).

$$\frac{dv_p(t)}{dt} = \frac{v_g - v_p(t)}{k_G\, d_{va}} \tag{31}$$

The solution of this differential equation is:

$$v_p(d_{va}, t) = v_g - (v_g - v_0) \cdot exp\left(-\frac{t}{k_G\, d_{va}}\right) \tag{32}$$

The variable v_0 is the particles' starting velocity at the end of the aerodynamic lens and t the time. The velocity of the gas v_g can be considered as independent from particle size and the term $\frac{t}{k_G}$ can be combined to a new constant k, thus the size calibration function is given as:

$$d_{va}(v_p) = \frac{k}{\ln\left(\frac{v_g - v_0}{v_g - v_p}\right)} \tag{33}$$

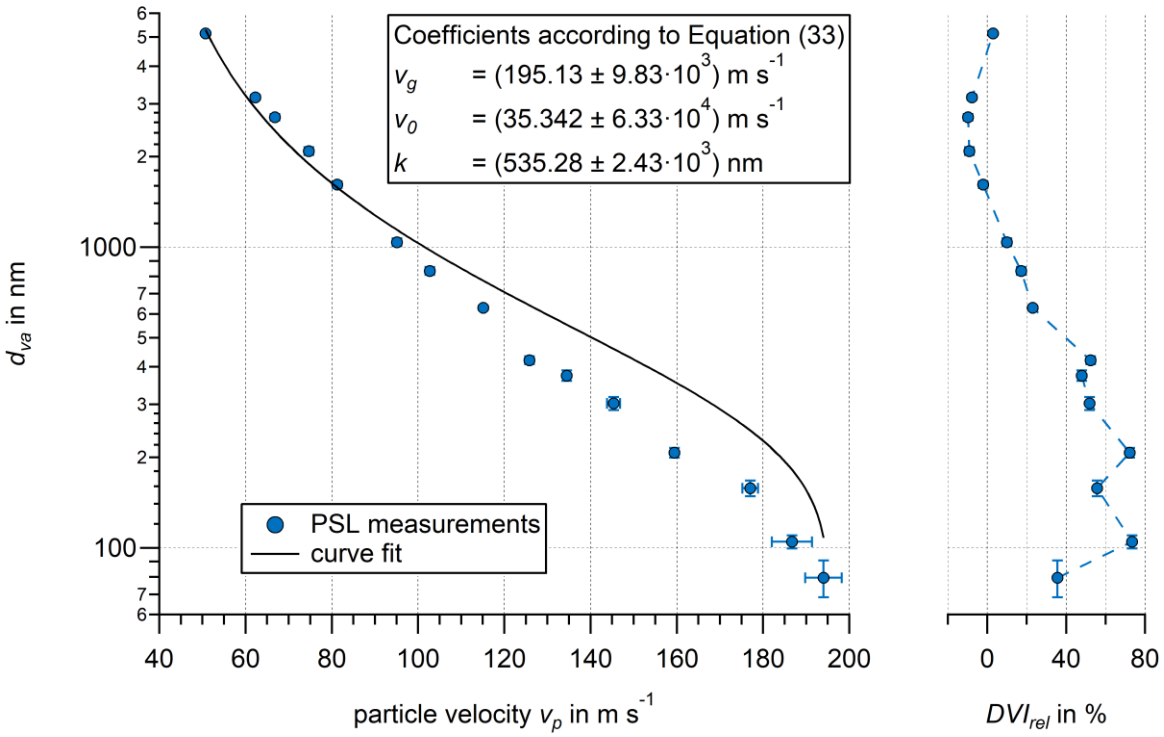

Figure 29: Calibration curve (d_{va} against v_p) for size calibration with PSL particles (left) and the relative deviation of the particle size fitting curve from the NIST particle size standard DVI_{rel} in % as function of the particle sizes d_{va} (right). The uncertainty of d_{va} along the ordinate is given by NIST certificates (values from Table 5; see also Appendix B.1.4). The uncertainty of the particle velocity can be estimated by Gaussian propagation of uncertainties (see Appendix B.1.5). v_g, v_0 and k are coefficients from the function used for the size calibration according to Equation (33). The uncertainty bars are in some cases smaller than the symbol.

The applied size calibration according to Equation (33) to the PSL measurements and the relative deviation (to d_{va}) from the NIST particle size standard DIV_{rel} is shown in the left and right panel of Figure 29, respectively. The deviation is unaccepably high ($DIV_{rel} \gg 14$ %) up to PSL particle sizes of d_{va} = 629 nm, since the maximum relative uncertainty for the NIST particle sizes is 14 % (see Table 5).

The gas velocity v_g is calculated to be 195 m s^{-1}. This value is close to the v_p of the smallest measured particles (d_{va} = 80 nm). Therefore, the behavior of the size calibration was investigated taking two different size ranges of the PSL measurements into account. Both approaches are displayed in Figure 30. Firstly, the fitting procedure was executed for PSL particle sizes between d_{va} = 80 nm and d_{va} = 2,090 nm (*Approach A*; solid line) and secondly considering only particle sizes between d_{va} = 158 nm and d_{va} = 5,145 nm (*Approach B*; dashed line). The excluded data points are highlighted by red boxes (excluded in *Approach A*) and circles (excluded in *Approach B*). It is obvious that the smallest by calibration determinable size depends on the smallest size of the used data set. Excluding small particle sizes, here d_{va} = 80 nm and d_{va} = 105 nm (marked by red circles) for the calibration with large particle sizes (*Approach B*), leads to a smaller v_g compared to *Approach A*. It follows that particles with d_{va} < 158 nm cannot be reliably sized, i.e., it is not attempted to extrapolate to smaller sizes than this lowest limit in the data set.

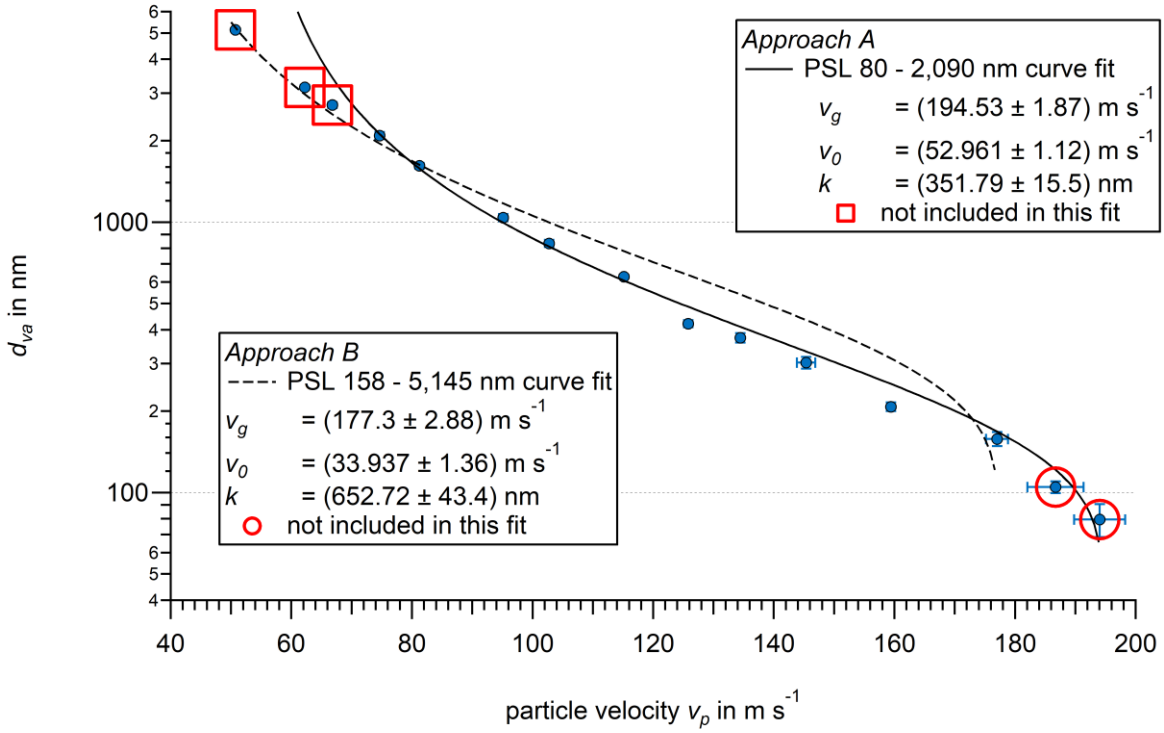

Figure 30: Two different approaches for size calibration (d_{va} against v_p) with PSL according to the size calibration method by Klimach (2012) using Equation (33) and the described two different data sets as bases. The first data set includes PSL particles in the size range of 80 nm – 2,090 nm (Approach A; calibration curve solid line; not included values marked by red squares) and the second data set covering the size range from 158 nm to 5,145 nm (Approach B; calibration curve dashed line; not included values marked by red circles). The resulting fit parameters are provided in the text box. The uncertainty of d_{va} along the ordinate is given by NIST certificates (values from Table 5; see also Appendix B.1.4). The uncertainty of the particle velocity can be estimated by Gaussian propagation of uncertainties (see Appendix B.1.5). The uncertainty bars are in some cases smaller than the symbol.

In Figure 31, the relative deviation from PSL size (d_{va}) DVI_{rel} (Equation (28)) of the described two different curve fitting approaches is presented and the ±14 % margin marked by two horizontal lines. The value of the relative deviation for d_{va} = 5,145 nm, 540 %, is more than 38 times higher than the ±14 % margin. This data point is far outside of the range of the ordinate of Figure 31, and not shown. Except for four outliers (d_{va} = 80 nm, (21 %), d_{va} = 105 nm, (16 %), d_{va} = 207 nm, (22 %), and d_{va} = 421 nm, 16 %) all points are within the ±14 % margin for *Approach A*. Therefore, the size calibration method is applicable, but only in the range of values covered by the fit, extending from

d_{va} = 80 nm to d_{va} = 2,090 nm for the abscissa. The excluded sizes of d_{va} = 2,709 nm and d_{va} = 3,150 nm (marked by red squares) are above 14 %.

In *Approach B*, regarding the large particle sizes d_{va} = 158 nm to d_{va} = 5,145 nm, DVI_{rel} values are not determinable for $d_{va} \leq$ 105 nm, as shown above. The calibration curve (see Figure 30) results from the fact that for the smallest particles v_g and v_p are too close to each other. This is considered for the curve fitting routine, so particles of smaller sizes cannot be determined, however the relative deviations for $d_{va} \geq$ 1,040 nm are within the ±14 % margin.

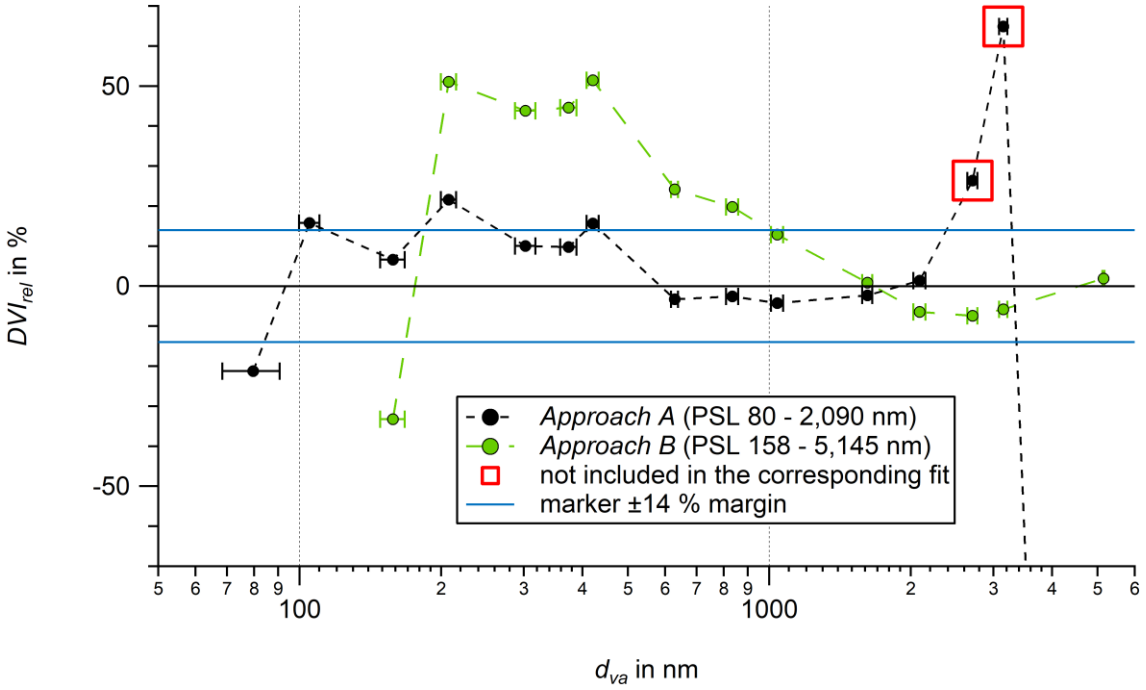

Figure 31: Relative deviation of the particle size calibration fitting curve (d_{va}) from the NIST particle size standard DVI_{rel} according to the size calibration method by Klimach (2012) applying Equation (33) for Approach A (black markers; PSL particles with $d_{va} \leq$ 2090 nm; value for d_{va} = 5145 nm is out of display range) and Approach B (green markers; PSL particles with $d_{va} \geq$ 157 nm; values for $d_{va} \leq$ 105 nm cannot be determined). The ±14 % margin is marked by blue horizontal lines. The visible excluded values are marked by red squares. The uncertainties of d_{va} are given by NIST certificates from the provider. The uncertainty bars are in some cases smaller than the symbol.

Neither *Approach A* nor *Approach B* perform sufficiently well as a calibration method for particle size determination in an overall size range between d_{va}= 80 nm to d_{va} = 5,145 nm. Also, extrapolations are not applicable. Although the parameterization provided by Klimach (2012) has the advantage of being based on the underlying physics, it proved here as too limited for the size range of the ERICA-LAMS. Consequently, the empirical method by Brands et al. (2011) has been adopted for the CRISP software evaluating the particle size measurements.

4.2.3 Method for particle detection efficiency and mass concentration detection efficiency determination in the laboratory

The overall detection efficiency is one of the key parameters of aerosol mass spectrometers. This overall detection efficiency is the fraction of the number of those particles which generated valid mass spectra and the number of encountered ambient aerosol particles in the size range of detection.

Several factors, or partial efficiencies affect this overall efficiency. For ERICA-LAMS these are for instance the efficiency by which particles are detected by one of the detection units DU1 or DU2 and

the efficiency by which detected particles are hit by the UV laser flash and deliver interpretable mass spectra in both, positive and negative ion channels (ablation efficiency). Since for the ERICA-AMS no particle numbers are registered, but instead the masses associated with small groups of particles, as measure for the efficiency the mass measured by the ERICA-AMS divided by the mass detected from the reference instruments is used.

In this section measurements of the following partial detection efficiencies are described: The detection efficiency of the particle counting at the detection units DU1 and DU2 (Section 4.2.3.1 and 4.2.3.2) and the detection efficiency of the mass concentrations at the ERICA-AMS vaporizer (Section 4.2.3.3). The ablation efficiency is subject of Section 4.3. The detection efficiency of the particle counting at each detection unit was conducted with PSL (DE_{PSL}) and ammonium nitrate particles (DE_{AN}). The detection efficiency of the mass concentrations at the ERICA-AMS vaporizer (DE_{AMS}) was conducted with ammonium nitrate particles. For the evaluation, curve fit procedures were used which are based on the Levenberg-Marquardt algorithm using the *IGOR Pro* software (Version 6.32, WaveMetrics Inc.). The curve fit parameters (see equations in the following sub-sections) which were used for the determination of DE_{PSL}, DE_{AN}, and DE_{AMS} are used for the particle beam characterization in Section 4.2.5.

Of particular importance is the precise alignment of the particle beam onto the ERICA-AMS vaporizer by adjusting the aerodynamic lens and the following adjustment of the detection laser and elliptical reflector foci onto the pre-defined axis. These procedures are described in detail in Section 4.2.1.3.

4.2.3.1 PSL particle detection efficiency at the ERICA-LAMS detection units

The detection efficiency of the particle count on both detection units DUs was determined by comparison measurements on the individual detection units (DU1 and DU2) with a reference device (CPC or OPC), which measures the particle number concentrations independently of ERICA. In this way, the particle numbers or indirectly the mass concentrations measured by ERICA can be related to the number concentrations present in the sample air flow. The measured PSL particle sizes and the respective measurement setups that were used (*Setup B* and *Setup C*; Figure 24) are shown in Section 4.2.1.

To determine the maximum detection efficiency at DU1 and DU2 with PSL (DE_{PSL}), this detection efficiency DE_{PSL} was measured at different positions of the aerodynamic lens x_{pos}, whereby the position of the detection laser was always constant. For this purpose, the aerodynamic lens was moved in discrete steps in x-direction (see Figure 13) as a so-called "aerodynamic lens scan" and DE_{PSL} was determined for each lens position x_{pos} according to Equation (34).

$$DE_{PSL}(x_{pos}) = \frac{\overline{cts}_{Det}(x_{pos}) \cdot \Phi_{ERICA}{}^{-1}}{\bar{c}_{ref}} \tag{34}$$

Here, $\overline{cts}_{Det}$ is the value of the number of particles per second counted at the detection units over 30 seconds (*counts0* for DU1 and *counts1* for DU2, see Section 3.7.2.2), Φ_{ERICA} is the volume flow into the ERICA instrument (Φ_{ERICA} = 1.476 cm³ s^{-1}, see Section 3.2 and Appendix B.1.6) and $\bar{c}_{ref}$ is the value of the number of particles per volume unit averaged over 30 seconds at the reference instrument (CPC or OPC), taking the volume flow Φ_{ERICA} into the reference instrument into account.

For each particle size and lens position, measurements were conducted alternately at DU1, DU2 and with both simultaneously by switching on the laser diodes LD1 and LD2 (see Figure 10) for 30 seconds respectively. Thus, an aerodynamic lens scan took about 40 minutes. During this time, the particle

generation was stable. With longer operation of the aerosol generation, the generated particle concentration fluctuates by up to 30 %. To ensure that the measurements within a scan remained comparable, a measuring interval of 30 seconds per data point was adopted. In the following, only the measurements conducted with LD1 and LD2 switched on individually are used. Measuring times longer than 60 minutes increase the probability of clogging of the DMA nozzle. Due to electronic crosstalk, measurements where both laser diodes are switched on simultaneously may show a biased counting on both DUs. For this reason, only those measurements are presented here in which the laser diodes LD1 or LD2 were switched on individually.

Figure 32 shows a typical result of an aerodynamic lens scan (for PSL particles with d_{va} = 834 nm). The results of further scans for other particle sizes can be found in Appendix B.5.

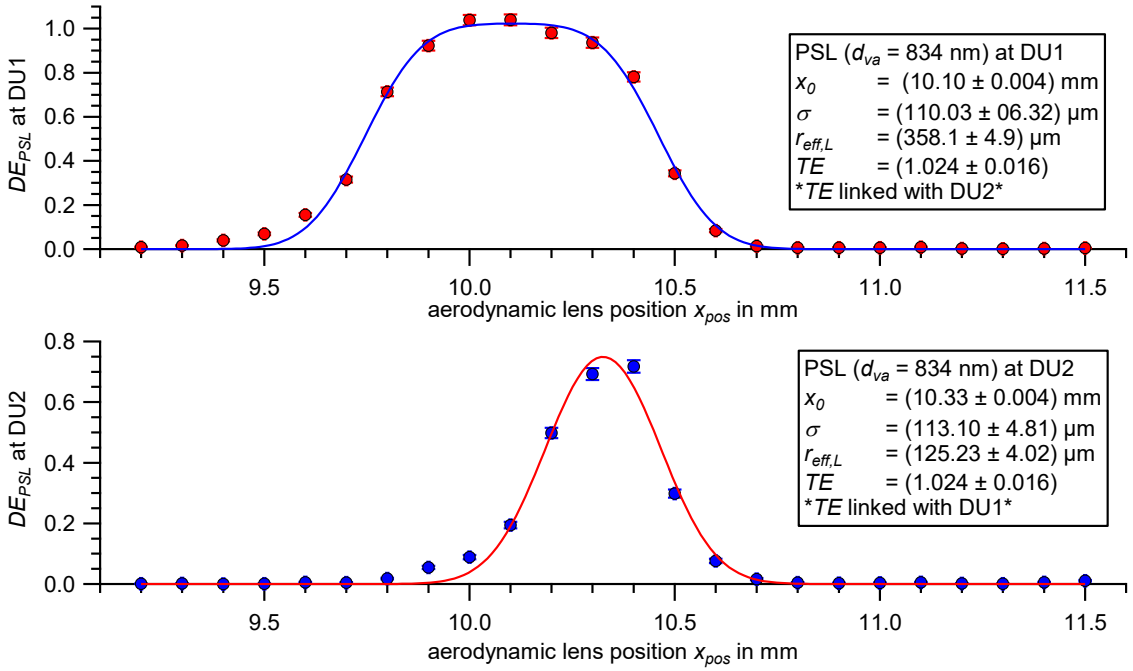

Figure 32: Scan of the aerodynamic lens position (x_{pos}) with PSL particles of d_{va} = 834 nm perpendicular to the laser beam at DU1 (top) and DU 2 (bottom). Displayed are the DE_{PSL} values of the measurement (markers) according to Equation (34) and the curve fit (line) according to Equation (37). The results and constants of the curve fits are shown in the box. The uncertainty of the detection efficiency is based on counting statistics of DU and the CPC. The uncertainty of the lens position results from reading errors (see Appendix B.1.6). The uncertainty bars are in almost all cases smaller than the symbol.

During the scan with the aerodynamic lens the particle beam and the detection laser beam overlap (Figure 33, a)). Usually, the laser beam is much wider than the particle beam such that the particle beam moves across the laser beam during an aerodynamic lens scan. The particle beam profile and the detection laser intensity are normally distributed (Gaussian distribution). Since it is not the light intensity of the scattered light but the particle number above a set limit value that is recorded (see Section 3.7.2.2), the laser beam profile is considered as a rectangular function representing the effective laser width (as radius) $\pm r_{eff,L}$ (Klimach, 2012). The effective laser width is the laser beam width at which a particle can be detected. In this way $\pm r_{eff,L}$ is the spatial volume in which the scattered light intensity is large enough to generate a detectable signal at the respective detection unit (Klimach, 2012). Thus, the curve of the scan corresponds to a convolution of the particle beam profile and the effective laser width (Figure 33, b)). Figure 33 c) schematically shows the described overlap of particle beam and laser beam. All particles within the effective laser beam width $\pm r_{eff,L}$ are detected

(gray shaded). To investigate the detection efficiency and other particle beam properties (see Section 4.2.5), the aerodynamic lens is systematically tilted (x_{pos}) in small steps, thus changing the relative position of the laser beam (x_0) to the particle beam. By that, each area of the particle beam is detected several times.

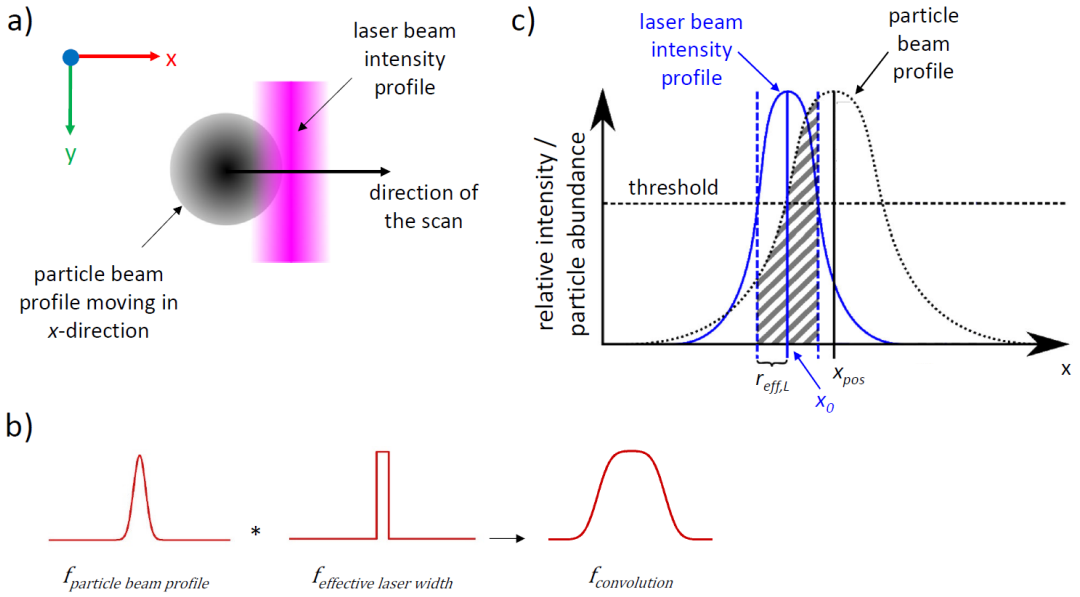

Figure 33: Schematic drawings of the overlap of particle beam and detection laser beam in the detection units: a) The particle beam profile (black) overlaps the laser beam intensity profile (purple; not to scale), both following a Gaussian distribution. The indicated directions correspond to the ordinate axes in Figure 13. The particle beam is pointing perpendicular to the plane of the drawing. b) Since the detection of a particle needs an exceeding of a set threshold, the function of the laser beam profile $f_{laser\ beam\ profile}$ can be assumed as rectangular. Together with the function of the particle beam profile $f_{particle\ beam\ profile}$ the curve fit function results in a convolution function $f_{convolution}$. c) For the determination of the detection efficiencies and other particle beam parameters the relative position of the laser beam (x_0) to the particle beam position (x_{pos}) the aerodynamic lens was systematically tilted stepwise in x-direction (not to scale). All particles within the effective laser width ($\pm r_{eff,L}$; gray shaded area) are detected (Figure adapted from Klimach (2012)).

The following derivation of the fit function is provided by Klimach (2012). The radial Gaussian profile of the particle beam describes the probability $p(x,y)$ of encountering a particle at a certain location x, y in lateral coordinates (Equation (35)).

$$p(x,y) = \frac{1}{2 \cdot \pi \cdot \sigma^2} \cdot exp\left(-\frac{(x - x_{pos})^2 + (y - y_{pos})^2}{2\sigma^2}\right) \tag{35}$$

Here, σ is the standard deviation of the Gaussian distribution and x_{pos} and y_{pos} are the central positions on which the particle beam was set during the scan. From this, the number of particles n_p detected at a certain lens position (x_{pos}, y_{pos}) can be calculated by integrating over the effective laser beam width around the focal point (x_0, y_0) of the laser (Equation (36)). The y-direction corresponds to the laser beam direction, in which the laser in principle has an infinite extension and thus the integration runs from -∞ to +∞. All scans were performed in x-direction (see Figure 33).

$$n_p(x_{pos}) = \int_{x_0 - r_{eff,L}}^{x_0 + r_{eff,L}} \int_{-\infty}^{+\infty} p(x,y)\,dy\,dx \tag{36}$$

The general solution of the integral is the function $DE_{PSL}(x_{pos})$ of Equation (37), which was used to determine the detection efficiency and to determine the particle beam parameters x_0, $r_{eff,L}$, σ, and TE.

$$DE_{PSL}(x_{pos}) = \frac{1}{2} \cdot \left(erf\left(\frac{x_{pos} + r_{eff,L} - x_0}{\sqrt{2}\sigma}\right) - erf\left(\frac{x_{pos} - r_{eff,L} - x_0}{\sqrt{2}\sigma}\right)\right) \cdot TE \qquad (37)$$

The variable σ is a measure for the particle beam width and x_0 corresponds to the value of x_{pos} at the maximum of the amplitude. This value is also called modal value. The parameter TE is the transmission efficiency of the aerodynamic lens and is used as a scaling factor to compensate for particle losses in the aerodynamic lens. This is necessary because ultimately the particle numbers detected by the DUs are related to the OPC and CPC number concentrations from -outside- the ERICA instrument. Consequently, sampling losses induced by the lens itself need to be corrected for. Since the sampling losses, or TE, are not directly measured by dedicated experiments, this variable TE is used as one of the parameters towards which the fit routine optimizes.

For the measurements of the particle sizes d_{va} = 218 nm to d_{va} = 834 nm it was assumed that the particle losses between the detection units DU1 and DU2 are negligible. Therefore, the curve fitting for both detection units was performed simultaneously for each particle size with both data sets (DU1 and DU2). The *Global Fitting* (*IGOR Pro*) process, also known as *Global Analysis*, was chosen for this purpose. This method allows several data sets (here two) to be carried out in a single curve fit. The variable TE was linked for both detection units by determining the value for DU1 and DU2 simultaneously. Thus, only one value for TE per measured particle size was obtained (see Figure 32). This procedure is called *common curve fitting* in the following and was carried out with the *IGOR Pro* software (version 6.32, WaveMetrics Inc.).

For the evaluation of the measurement with PSL particles d_{va} = 108 nm, a different approach was chosen because losses between DU1 and DU2 seemed possible due to the particle beam divergence (Huffman et al., 2005). Therefore, the evaluation was carried out without *common curve fitting* and thus individually for DU1 and DU2. Due to the strong mathematical relation between the variables $r_{eff,L}$ and TE during curve fitting it was not possible to determine both variables by curve fitting at the same time. Therefore, a value for $r_{eff,L}$ was calculated and kept constant during the curve fitting. The value for $r_{eff,L}$ determined for d_{va} = 218 nm was used for this purpose. Considering the size dependence of the scattered light intensity based on Mie scattering (Bohren and Huffman, 1998), a value for $r_{eff,L}$ can be estimated for the measurement at d_{va}= 108 nm. To calculate the scattered light intensity for both particle sizes, the software *BH-Mie-Rechner* (Vetter, 2004) was used (see Appendix B.6). The calculated result for the ratio of the scattered light intensity for particles of d_{va} = 218 nm to particles of d_{va} = 108 nm is 0.955 (see Appendix B.7). In this way, further determination of the variables x_0, TE, and σ is possible by means of the curve fitting routine.

The measurements and the corresponding curve fits with their results are shown in Appendix B.5 and are used in the following sections to calculate the maximum possible detection efficiency DE_{max}, to calculate the detection efficiency during the measurement campaign in Kathmandu, Nepal, DE_{KTM}, (both Section 4.2.4) and for the evaluation of the particle beam characterization (Section 4.2.5). The particle beam characterization includes the discussion of the determined curve fit parameters.

4.2.3.2 Ammonium nitrate particle detection efficiency at the ERICA-LAMS detection units

In addition to PSL particles, the detection efficiency of particle counting at both detection units DUs (DU1 and DU2) was also determined for ammonium nitrate particles (Table 6). A CPC served as reference instrument for the comparison measurement at the individual detection units (DU1 and DU2). The measured particle sizes and the measurement setup used with DMA and CPC (*Setup B* in Figure 24) are shown in Section 4.2.1.

Analogous to Equation (34), Equation (38) is used to determine the detection efficiency of ammonium nitrate particles DE_{AN}.

$$DE_{AN}(x_{pos}) = \frac{\overline{cts}_{Det}(x_{pos}) \cdot \Phi_{ERICA}{}^{-1}}{\bar{c}_{ref}} \tag{38}$$

Here, $\overline{(cts)}_{Det}$ is the value of the number of particles per second counted at the detection units over 30 seconds (*counts0* for DU1 and *counts1* for DU2), Φ_{Det} is the volume flow into the ERICA instrument (Φ_{ERICA} = 1.476 cm³ s^{-1}, see Section 3.2) and $\bar{c}_{ref}$ is the number concentration value averaged over 30 seconds at the CPC. The volume flow of the reference instrument is considered in $\bar{c}_{ref}$. The measurement procedure was adopted from the experiment conducted with PSL particles (see Section 4.2.3.1). Figure 34 shows as an example the measurement with ammonium nitrate particles of size d_{va} = 297 nm at DU1 and the constants used and values obtained for the variables after the curve fitting with Equation (39) below. The results of all measurements and the corresponding curve fits with their results are shown in Appendix B.8.

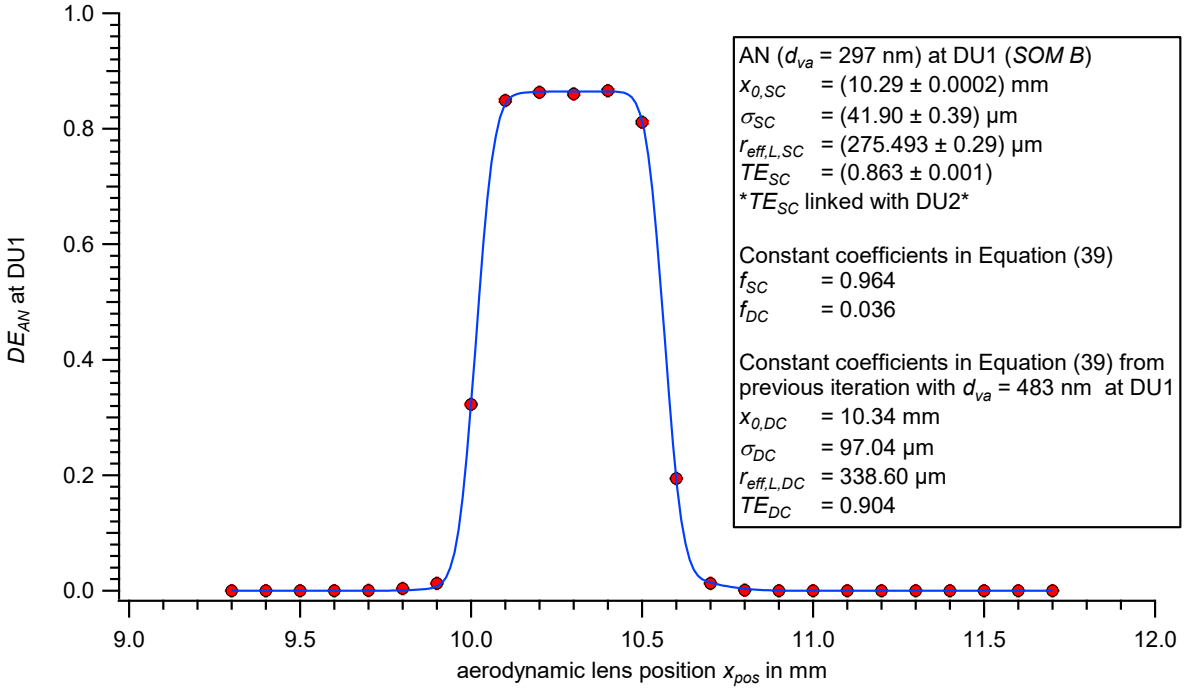

Figure 34: Scan of the aerodynamic lens position (x_{pos}) with ammonium nitrate particles of d_{va} = 297 nm perpendicular to the laser beam at DU1. Displayed are the DE_{AN} values of the measurement (markers) according to Equation (38) and the curve fit (line) according to Equation (39). The results and constants of the curve fits are shown in the box. The uncertainty of the detection efficiency is based on counting statistics of the DU and the CPC and the uncertainty of the lens position results from reading errors (see Appendix B.1.6). The uncertainty bars are in all cases smaller than the symbol.

The main fraction of the particles leaving the DMA bear single electrical charges. However, even larger particles with the same electrical mobility Z (Allen and Raabe, 1985; Seinfeld and Pandis, 2016) exit

the DMA doubly charged. Therefore, both singly charged (SC) and doubly charged (DC) particles must be taken into account. The fraction of particles with more than two charges is negligible in the considered size range (Wiedensohler, 1988). The occurrence of doubly charged particles at a given particle size artificially increases the total number concentration measured by CPC and thus influences DE_{AN} (see Equation (38)). For monodisperse PSL suspensions, it is not necessary to consider doubly charged particles. For salt solutions such as ammonium nitrate solutions, from which polydisperse aerosol is generated, quantification and corresponding correction is essential.

Table 8 shows the measured sizes of the singly charged particles d_{va}, the sizes of the doubly charged particles $d_{va,DC}$, and the corresponding electrical mobility Z. The voltage that must be set for the electric field in the DMA for a given particle size depends on the electrical mobility Z. Example for illustration: When the voltage at the DMA is set to a value corresponding to an electrical mobility of Z = 5.87·10^{-5} cm² V^{-1} s^{-1}, the fraction of singly charged particles with a size of d_{va} = 91 nm is f_{SC} = 88.7% and the fraction of the corresponding doubly charged particles is f_{DC} = 11.3 % ($d_{va,DC}$ = 138 nm). The calculation of Z is shown in Appendix B.9.

Two *Series Of Measurements* (*SOM A* and *SOM B*, Table 8) were carried out with complementary particle sizes. Within a *SOM* the particle size of the species with single charge d_{va}, i.e., d_{va}=138 nm, also corresponds to the particle size of the species with double charge $d_{va,DC}$, i.e., $d_{va,DC}$ =138 nm, for the next smaller species with single charge d_{va}, i.e., d_{va}= 91 nm. This approach enables an iterative procedure for evaluation in the following. The fraction of doubly charged particles depends on the particle size and the deployed nebulizer. The calculation of the used values for f_{SC} und f_{DC} are shown in Appendix B.10. The highest fraction of doubly charged particles can be obtained for a particle size of d_{va}= 138 nm (12.3 %).

Table 8: Electrical mobility Z of the measured ammonium nitrate particles for various particle sizes of singly charged (SC) particles, d_{va}, the corresponding doubly charged (DC) particles $d_{va,DC}$ with the same Z value, and the corresponding fraction of singly f_{SC} and doubly charged f_{DC} particles for the two Series Of Measurements (SOM) A and B.

Z in cm² V^{-1}s^{-1}	d_{va} singly charged (SC) particles in nm	$d_{va,DC}$ doubly charged (DC) particles in nm	f_{SC}	f_{DC}	*Series Of Measurements (SOM)*
5.87·10^{-5}	91	138	0.887	0.113	*A*
2.93·10^{-5}	138	213	0.877	0.123	
1.47·10^{-5}	213	335	0.892	0.108	
7.37·10^{-6}	335	548	0.937	0.063	
3.69·10^{-6}	548	934	1.000	0.000	
8.82·10^{-6}	297	483	0.964	0.036	*B*
4.39·10^{-6}	483	814	0.982	0.018	
2.20·10^{-6}	814	1435	1.000	0.000	

In order to consider the doubly charged particles during the curve fitting, Equation (37) was extended by a term for the doubly charged particles (see Equation (39)). The parameters indexed with SC refer to the singly charged particles, the parameters indexed with DC refer to the doubly charged particles:

$$DE_{AN}(x_{pos}) = \left(\frac{1}{2}\cdot\left(erf\left(\frac{x_{pos}+r_{eff,L,SC}-x_{0,SC}}{\sqrt{2}\ \sigma_{SC}}\right)-erf\left(\frac{x_{pos}-r_{eff,L,SC}-x_{0,SC}}{\sqrt{2}\ \sigma_{SC}}\right)\right)\cdot TE_{SC}\cdot f_{SC}\right) + \left(\frac{1}{2}\cdot\left(erf\left(\frac{x_{pos}+r_{eff,L,DC}-x_{0,DC}}{\sqrt{2}\,\sigma_{DC}}\right)-erf\left(\frac{x_{pos}-r_{eff,L,DC}-x_{0,DC}}{\sqrt{2}\,\sigma_{DC}}\right)\right)\cdot TE_{DC}\cdot f_{DC}\right) \quad (39)$$

The parameters were determined iteratively with the procedure and details comprehended in Figure 35). The iteration series was started at the largest particle size in the respective *SOM* (*A* or *B*). For *SOM A* this is d_{va}= 548 nm, for *SOM B* d_{va}= 814 nm. For the first iteration f_{DC} = 0 is assumed in each case, since it is assumed that particles larger than $d_{va,DC}$ > 1,000 nm are not generated in the nebulizer. Then, analogous to the procedure in Section 4.2.3.1, a common curve fitting, here with Equation (39), is carried out, whereby the parameter of the transmission efficiency TE_{SC} of DU1 is linked with that of DU2 by a *common curve fitting*. This *common curve fitting* is conducted with the *IGOR Pro* software (version 6.32, WaveMetrics Inc.). The parameters $x_{0,SC}$, σ_{SC}, $r_{eff,L,SC}$, and TE_{SC} obtained in each case are used for the next iteration step as constants for the doubly charged species as $x_{0,DC}$, σ_{DC}, $r_{eff,L,DC}$, und TE_{DC} and for determining the detection efficiency at the detection units DE_{max} and DE_{KTM} (Section 4.2.4) and particle beam characterization (Section 4.2.5) for the respective particle size d_{va}. The further results of the measurements described here and the corresponding curve fits with their results are shown in Appendix B.8.

Example for *SOM A*: For the *common curve fitting*, the constants for f_{SC} and f_{DC} in Equation (39) are used for both detection units (DU1 and DU2). This results in the second half of the term in Equation (39) becoming 0. The obtained variables $x_{0,SC}$, σ_{SC}, $r_{eff,L,SC}$, and TE_{SC} are used to evaluate the detection efficiencies DE_{max} and DE_{KTM} (see Section 4.2.4) and to characterize the particle beam (see Section 4.2.5) for the particle size d_{va} = 548 nm (1st iteration). Additionally, these variables, together with the calculated values for f_{SC} and f_{DC}, are the constants $x_{0,DC}$, σ_{DC}, $r_{eff,L,DC}$, and TE_{DC} for the 2nd iteration for the measurement at particle size d_{va} = 335 nm. With the results obtained from this *common curve fitting*, the same procedure is followed for the measurement at d_{va} = 213 nm (3rd iteration). The iteration series of *SOM A* ends with the measurement at d_{va} = 91 nm.

The *common curve fitting* for the measurements with ammonium nitrate particles of d_{va} = 138 nm yielded incomprehensibly high values for both detection units despite the seemingly reasonable curve progression. Therefore, an approach analogous to the measurements with PSL particles with a size of d_{va} = 108 nm was applied (see Section 4.2.3.1). Based on known $r_{eff,L,SC}$ values at DU1 and DU2 when measured with d_{va} = 213 nm, the $r_{eff,L,SC}$ values for the measurements with d_{va} = 138 nm were calculated by a factor using the relative intensity of Mie scattering (see Appendix B.6). The exact value of the refractive index (at λ = 405 nm) is not available for ammonium nitrate particles. However, it turned out that the calculation of the factor is not strongly dependent on the refractive index (see Appendix B.11.1). A new *common curve fitting* (4th iteration of *SOM A*, see Figure 35) yielded values for $x_{0,SC}$, σ_{SC}, and TE_{SC} for the particle size d_{va} = 138 nm, where $r_{eff,L,SC}$ was kept constant. However, the evaluation revealed contradictory results due to a strong dependence on the exact amount of

doubly charged particles (see Appendix B.8.1.1 and B.8.1.2). Thus, the results of these curve fits are not included in the further evaluation in Sections 4.2.4 and 4.2.5.

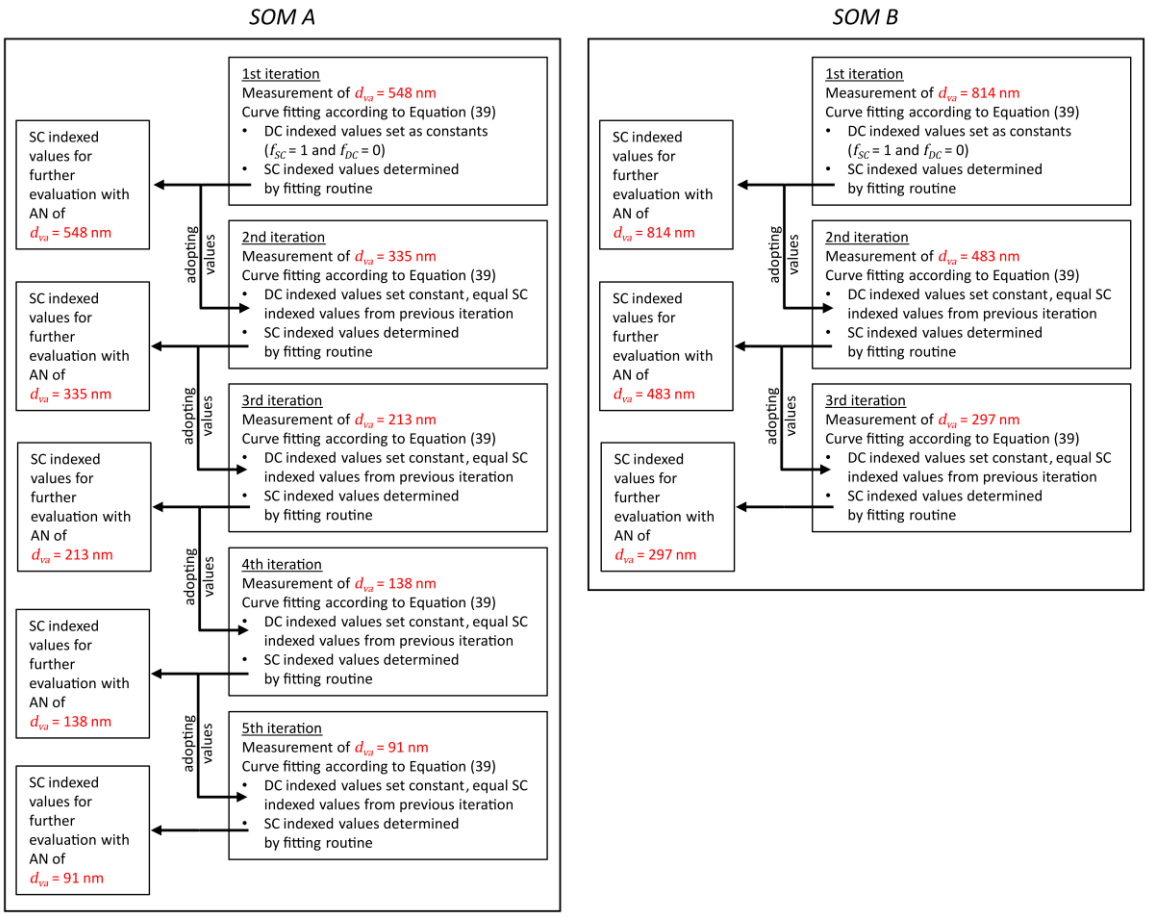

Figure 35: Iteration scheme for Series of Measurements (SOM) A (left) and SOM B (right) using Equation (39) for the common curve fitting. The particle sizes are highlighted in red. AN: Ammonium nitrate; SC: Singly Charged; DC: Doubly Charged.

The values of these four parameters were used in the 5th iteration of the *SOM A* (d_{va} = 91 nm, see Figure 35) in addition to a value for $r_{eff,L,SC}$ (see Appendix B.11.2) which was also obtained using Mie scattering. For this particle size the curve fit was performed individually for the measurement on DU1 and DU2. Since the curve fit on the measurement at DU2 delivered inexplicably high values and the curve of the measurement at DU1 showed three peaks, the results of these curve fits are not included in the further evaluation presented in Sections 4.2.4 and 4.2.5. The origin of the three modes is unknown. However, they could be caused by the increased interaction of the small particles with the gas molecules.

4.2.3.3 Ammonium nitrate particle detection efficiency at the ERICA-AMS vaporizer

In addition to the measurements with ammonium nitrate particles at the detection units DU1 and DU2 on the ERICA-LAMS, the mean mass concentration of ammonium nitrate $\bar{C}_{NO3}$ (determination of mass concentration see Section 4.5.1) was also determined with the ERICA-AMS (*Setup B* in Figure 24; Table 6) and in parallel, as a reference, the mean particle number concentration $\bar{c}_{ref}$ was measured at the CPC (similarly to Liu et al. (2007)). The data of this evaluation were provided by O. Appel (MPIC, 2018).

The detection efficiency of the ERICA-AMS DE_{AMS} is given by:

$$DE_{AMS} = \frac{\bar{C}_{NO3}}{\frac{1}{6} \cdot \pi \cdot \rho_{p,AN} \cdot S \cdot \bar{c}_{ref} \cdot \left(\left({d_{mob}}^3 \cdot f_{SC} \right) + \left({d_{mob,DC}}^3 \cdot f_{DC} \right) \right)} \tag{40}$$

Here, $\rho_{p,AN}$ is the density of ammonium nitrate, S is the Jayne shape factor and d_{mob} is the mobility diameter set at the DMA. This can be converted into the vacuum aerodynamic diameter d_{va} according to Equation (81) (see Appendix B.2), which is used in the following. Furthermore, the fractions of singly (f_{SC}) and doubly (f_{DC}) charged particles are considered (see Table 8).

Analogous to the measurements on the detection units, the particle beam parameters were obtained by curve fittings. For this, Equation (41) was used. Like in Equation (39), the fractions of singly f_{SC} and doubly f_{DC} charged particles are considered. However, the detection efficiency at the ERICA-AMS vaporizer does not depend on an effective laser width ($r_{eff,L,SC}$ and $r_{eff,L,DC}$), but on the effective vaporizer width ($r_{eff,V,SC}$ und $r_{eff,V,DC}$).

$$\begin{aligned} DE_{AMS}(x_{pos}) = \\ \left(\frac{1}{2} \cdot \left(erf\left(\frac{x_{pos} + r_{eff,V,SC} - x_{0,SC}}{\sqrt{2}\,\sigma_{SC}} \right) - erf\left(\frac{x_{pos} - r_{eff,V,SC} - x_{0,SC}}{\sqrt{2}\,\sigma_{SC}} \right) \right) \cdot TE_{SC} \cdot f_{SC} \right) \\ + \left(\frac{1}{2} \cdot \left(erf\left(\frac{x_{pos} + r_{eff,V,DC} - x_{0,DC}}{\sqrt{2}\,\sigma_{DC}} \right) - erf\left(\frac{x_{pos} - r_{eff,V,DC} - x_{0,DC}}{\sqrt{2}\,\sigma_{DC}} \right) \right) \cdot TE_{DC} \cdot f_{DC} \right) \end{aligned} \tag{41}$$

The procedure for determining the individual parameters $x_{0,SC}$, σ_{SC}, $r_{eff,V,SC}$, and TE_{SC} is iterative as for the measurements at the detection units DU1 and DU2 (see Section 4.2.3.2, Figure 35). However, Equation (41) is used for the measurements at the ERICA-AMS vaporizer instead of Equation (39).

Figure 36 shows the measurement with ammonium nitrate particles of size d_{va} = 297 nm on the ERICA-AMS vaporizer and the result of the curve fitting performed according to Equation (41). All results of the here described measurements, the corresponding curve fits, and their results are shown in Appendix B.12. These results will be used in the following sections to calculate the maximum possible detection efficiency DE_{max} and the detection efficiency during the measurement campaign in Kathmandu, Nepal, DE_{KTM}, (both Section 4.2.4), as well as for the evaluation of the particle beam characterization (Section 4.2.5).

The curve fitting of the measurement at the particle size of d_{va} = 91 nm only provided reasonable values if the value for $r_{eff,V,SC}$ = 1.98 mm was kept constant during the curve fitting. This value was determined by averaging the $r_{eff,V,SC}$ values of the measurements with the four larger particle sizes (d_{va} = 138 nm to d_{va} = 335 nm).

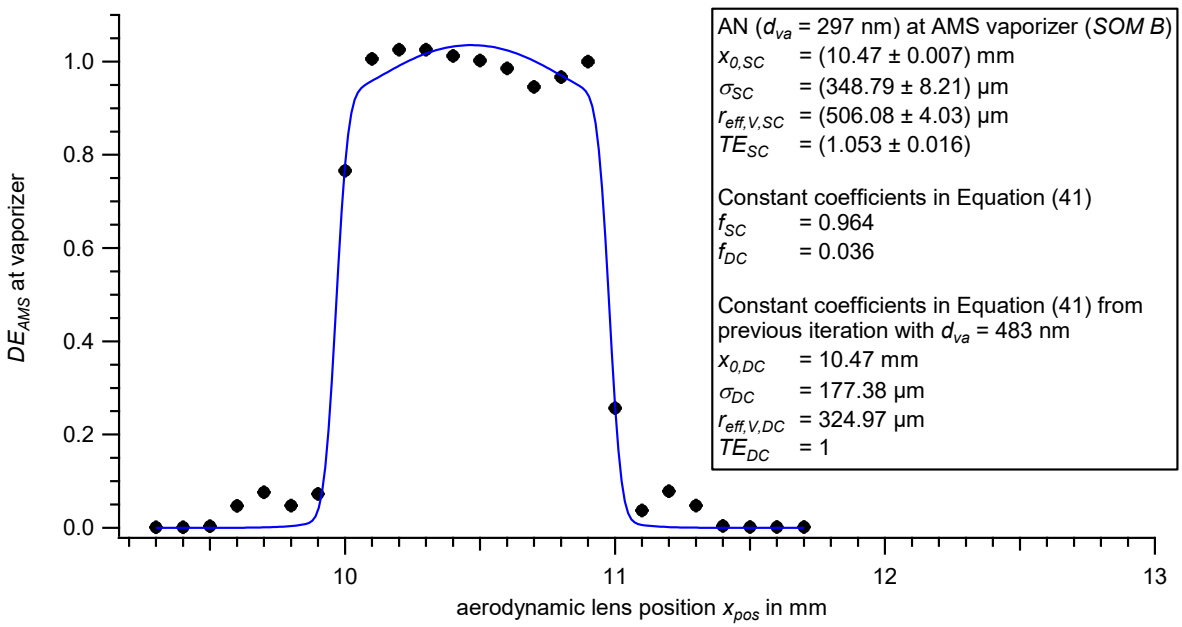

Figure 36: Scan of the aerodynamic lens position (x_{pos}) with ammonium nitrate particles of d_{va} = 297 nm at the ERICA-AMS vaporizer. The detection efficiency DE_{AMS} was evaluated from Equation (40) (markers) and curve fitted with a function according to Equation (41). The results and constants of the curve fits are shown in the box. The uncertainty of the detection efficiency is based on counting statistics of the CPC as well as the estimated counting statistic expected for the ERICA-AMS. The uncertainty of the lens position results from reading errors (see Appendix B.1.6). The uncertainty bars are in all cases smaller than the symbol.

The results of the curve fittings for particle sizes d_{va} > 335 nm are not sufficiently suitable for further evaluation (see Appendix B.12), although the measurements look reasonable in terms of amplitude and shape. As the particle beam emerges into the vacuum chamber from the aerodynamic lens together with a residual air stream the largest beam spread can be expected for the smallest particles, i.e., those sizes which are covered here. In the case the aerodynamic lens scan measurement, either at the detection units or at the ERICA-AMS vaporizer, provided a plateau shaped curve for an aerodynamic lens scan (see Appendices B.5, B.8, and B.12), the parameter TE is strongly correlated either with the effective laser width $r_{eff,L}$ or $r_{eff,L,SC}$ or with the effective vaporizer width $r_{eff,V,SC}$. A plateau indicates a narrow particle beam with respect to the effective widths. In total five aerodynamic lens scans were conducted with PSL particles at DU1 and DU2 and eight with ammonium nitrate particles at DU1, DU2 and the ERICA-AMS vaporizer.

4.2.4 Evaluation and results of the curve fits for the detection efficiency

To determine the detection efficiencies for PSL and ammonium nitrate particles at the detection units DU1 and DU2, and for ammonium nitrate particles at the ERICA-AMS vaporizer, two cases were considered: the maximum possible detection efficiency DE_{max} and the detection efficiency DE_{KTM} for the set aerodynamic lens position (x_{pos} = 10.55 mm) during the deployment in Kathmandu, Nepal (KTM; see Section 5.2). The Equations (37), (39), and (41) show that the detection efficiencies DE_{PSL}, DE_{AN} and DE_{AMS} depend on the parameter x_0 or $x_{0,SC}$ (see Sections 4.2.3.1, 4.2.3.2, and 4.2.3.3). Both, DE_{max} and DE_{KTM}, combine the detection efficiency measurements with PSL and ammonium nitrate particles (see Appendix B.13) described in the previous Section 4.2.3.

The maximum possible detection efficiency DE_{max} was determined for each measurement. Therefore, the determined parameters (see Sections 4.2.3.1, 4.2.3.2, and 4.2.3.3) of each curve fitting (see boxes for each measurement in Appendices B.5, B.8, and B.12) was inserted in the respective equation ((37),

(39), or (41)). In addition, for maximum possible detection efficiency DE_{max}, the variable x_{pos} equals the modal value of the aerodynamic lens scan x_0 or $x_{0,SC}$. For ammonium nitrate particles, only the detection efficiency of the singly charged (SC) particles was considered. The determination of DE_{KTM} followed the same approach as the determination of DE_{max} with the exception that x_{pos} equals 10.55 mm. In the following the results of the determination are presented.

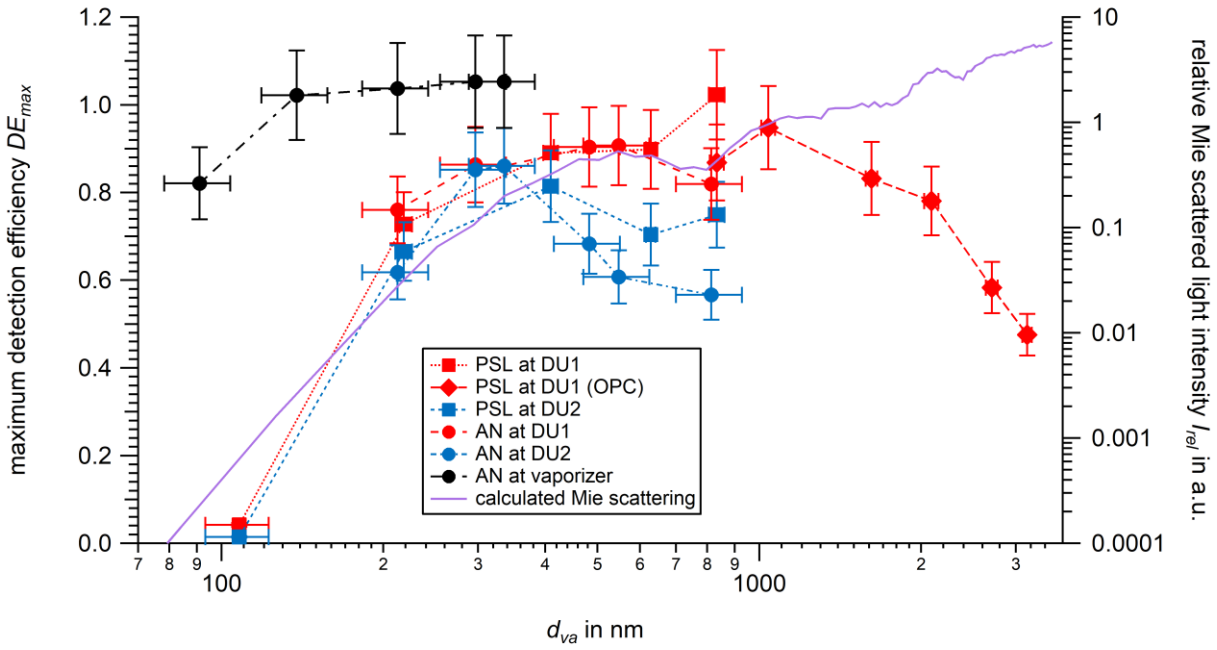

Figure 37: Maximum detection efficiency DE_{max} as function of particle size d_{va} experimentally determined for PSL (squares) and ammonium nitrate (AN; circles) particles measured at the detection units DU1 (red) and DU2 (blue), and the ERICA-AMS vaporizer (black). The reference values for number concentrations were either obtained from the experimental setup with the OPC or the CPC. The purple curve shows the scattered light intensity signal I_{rel} as function of particle size (right ordinate). The uncertainties of DE_{max} reflect the conservatively estimated value of 10 % (see Appendix B.1.6). The uncertainties of the PSL particle sizes result from NIST certificates. For ammonium nitrate particles the uncertainty of all sizes was conservatively estimated as 14 % (see Appendix B.1.4). The uncertainty bars are in some cases smaller than the symbol.

Figure 37 presents the maximum possible detection efficiency DE_{max}, i.e., the amplitude at aerodynamic lens position x_0 (see Equations (37), (39), and (41)). The values of DE_{max} for PSL particles with particle sizes larger d_{va} = 200 nm is above 60 % reaching 100 % for particle sizes of d_{va} = 800 nm at DU1. The particle size d_{50} typically is used as parameter for characterizing detection limits of single particle counting devices. It describes the particle size, here as d_{va}, at which 50 % of the maximum are detected. Principally, there are a lower and an upper d_{50}. Here, d_{50} (low) is between d_{va} = 108 nm and d_{va} = 218 nm. The upper d_{50} size lies between d_{va} = 2,709 nm and d_{va} = 3,150 nm as indicated by the OPC reference measurements. Interpolations for the measurements with PSL particles can be used to estimate the d_{50} values. The results are d_{va} = 184 nm at DU1 and d_{va} = 174 nm at DU2 as lower d_{50} values and d_{va} = 3,173 nm at DU1 as upper d_{50} value, referenced by an OPC. The DU2 appears to be less efficient, which is supported by the ammonium nitrate measurements. The measurement of ammonium nitrate supports this curve progression. The shape of the measurements at DU2 leads to an underestimated DE_{max} result, since the particle beam is broader at this stage than at DU1 due to the particle beam divergence (see Section 4.2.5). This results in a curve progression, where the plateau is less pronounced. Furthermore, the relative Mie scattered light intensity I_{rel} is displayed (Figure 37, right ordinate). It was calculated by the program *BH-Mie-Rechner* (Vetter, 2004) with the parameters from Appendix B.6. The curve progression of the particle measurements up to

d_{va} = 1,000 nm is well explained by Mie theory, especially the inferior DE_{max} for smaller particle sizes. The PSL measurements referenced by the OPC show a decrease with particle size. This decrease indicates the losses in the aerodynamic lens and/or is accounted from by the aerodynamic lens rotation (see Section 4.2.1). The results of the PSL particle measurements with OPC and CPC as reference devices (d_{va} = 834 nm) agree within the scope of the uncertainties.

The DE_{max} values found for the measurements at the ERICA-AMS vaporizer are not comparable in absolute terms with the DE_{max} values found for the ammonium nitrate measurements at DU1 and DU2, since the measurements at the position of the ERICA-AMS vaporizer are analogue to an ionization efficiency calibration measurement (IE calibration, see Section 4.5.2 and Drewnick et al. (2005)). With an IE calibration measurement, as with the determination of DE_{max}, the measured mass concentration at the ERICA-AMS is compared with the mass concentration injected into the measuring instrument. This mass concentration is determined indirectly with a CPC. For an IE calibration measurement, the determined discrepancy is multiplied as a factor by the mass concentration measured at the AMS (see Section 4.5.1). Here, among other losses, the transmission losses in the aerodynamic lens are compensated. For this reason, the values for DE_{max} shown here are overestimated and are not absolutely comparable with the DE_{max} values found for the ammonium nitrate measurements on DU1 and DU2. However, this measurement demonstrates that the decreasing DE_{max} for smaller sizes at DU1 and DU2 are not caused by potential losses in the aerodynamic lens. The scattered light signals decrease with size until the noise level of the detection arrangement is reached.

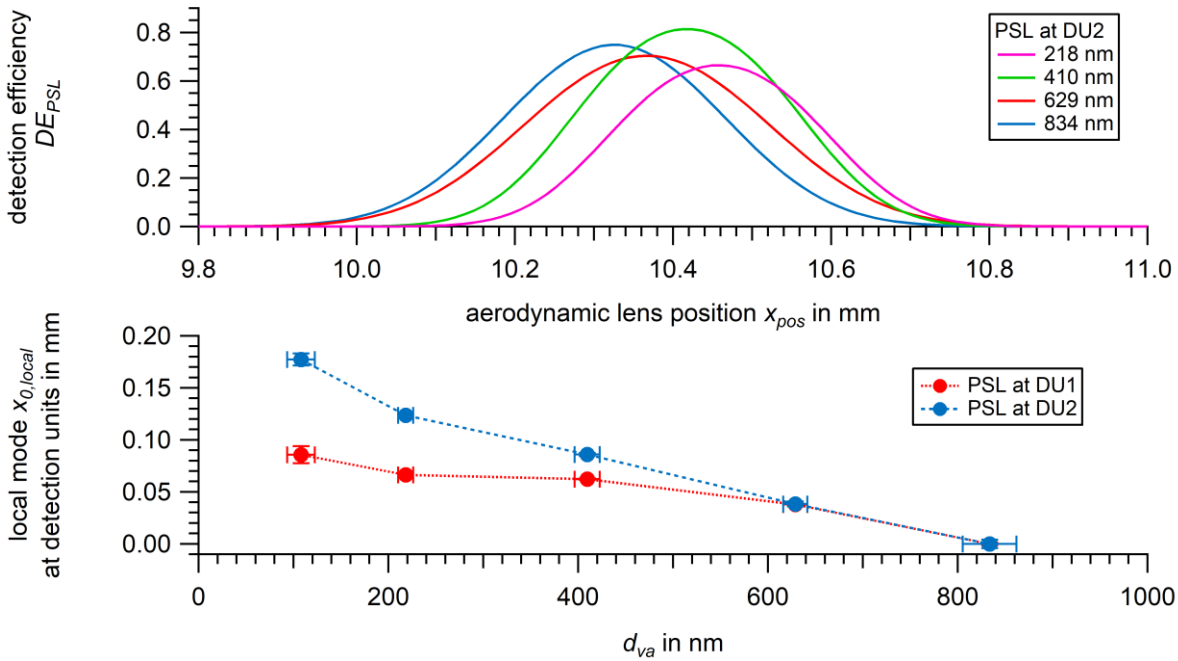

Figure 38: Top: curve fits from aerodynamic lens position x_{pos} scans with various PSL particle sizes (d_{va}) at ERICA-LAMS detection unit DU2. For clarity the individual measured values are not shown. Bottom: local modal values $x_{0,local}$ from the aerodynamic lens scans (see Section 4.2.3.1) as function of PSL particle size d_{va}. The uncertainties of $x_{0,local}$ result from the curve fittings and the uncertainties of the particle sizes result from NIST certificate.

During the development of the instrument it was found that the particle beam cross-sectional profiles for all particle sizes appears as non-concentric indicated by various x_0 values. Figure 38 shows the various curve fit plots (see Section 4.2.3.1 and Appendix B.5) for the PSL measurements at detection unit DU2 (top). Here, a shift to smaller x_{pos} for larger particles is observable. To quantify the deviation

of the various modal values x_0 (see Equation (37)) at the location of the focal points of the ellipsoidal reflectors (termed $x_{0,local}$) of DU1 and DU2, the distance ratios in the geometry of the instrument has to be considered for both locations (see Appendix B.4). In the lower panel of Figure 38, the parameter $x_{0,local}$ is plotted against the PSL particle size d_{va}. The lowest $x_{0,local}$ value for DU1 and DU2 was defined to be zero. The maximum deviation of the different $x_{0,local}$ is up to 0.18 mm at DU2. The maximum detection efficiency DE_{max} is not affected by these shifts, since the respective inserted x_0 value is the modal value. This observation leads to the conclusion that a fixed single setting of the aerodynamic lens will not lead to the same maximum DE_{max} value for the particular particle sizes. Thus, a compromise in aerodynamic lens adjustment for all particle sizes has to be found.

Beside PSL particles also ammonium nitrate particles were measured and the behavior of the $x_{0,SC}$ as function of the particle size investigated. The fitting curves as results of ammonium nitrate particle measurements at the ERICA-AMS vaporizer are shown in Figure 39. These curve fits are based on a convolution function of the Gaussian particle beam profile and the effective laser vaporizer width $r_{eff,V,SC}$ (see Section 4.2.3). The non-concentric behavior is visible, but no tendencies are identifiable. Here, the in Section 4.2.1.3 described adjustment (x_{pos} = 10.55 mm, see also Appendix B.3) marked by a black line, indicates a proper adjustment of the aerodynamic lens as a compromise for all measured particle sizes. The intersections of the individual curves with the marker line indicate the particular detection efficiency value for each particle size (described later in this section using DE_{KTM}). The shapes of the curves are changing. Curve fits of the measurements with particles of d_{va} = 213 nm to d_{va} = 335 nm in diameter show a broad plateau, whereas the other curve fits are round shaped. The reason is a smaller particle beam diameter for these sizes (d_{va} = 213 nm to d_{va} = 335 nm), much smaller than the effective width of the vaporizer (see Section 4.2.5).

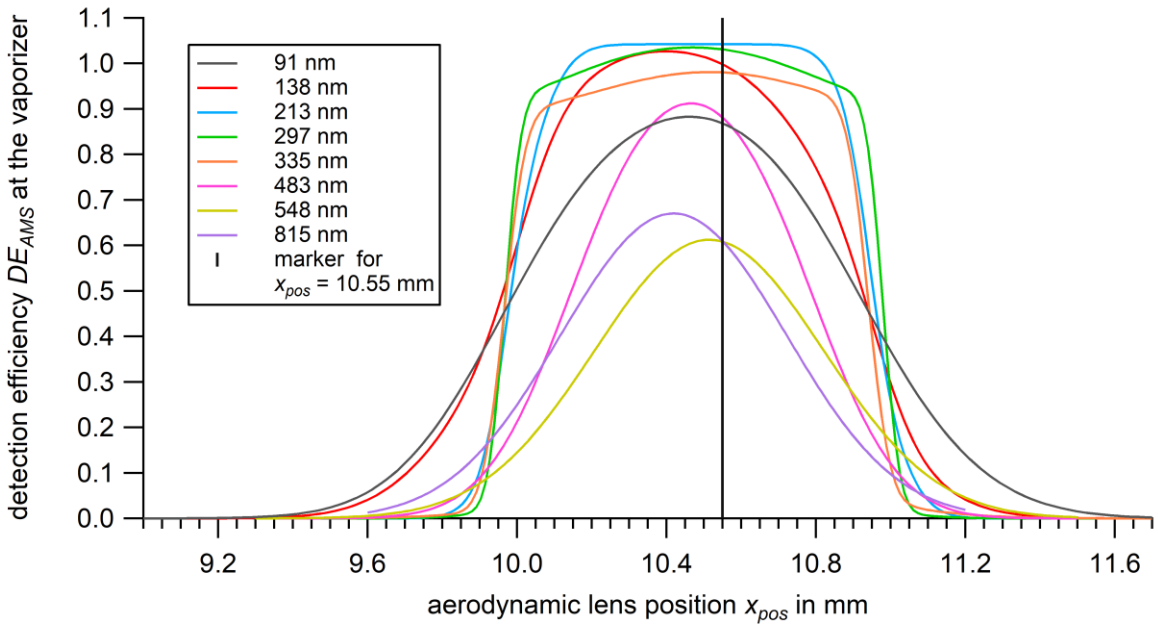

Figure 39: Curve fits from aerodynamic lens position x_{pos} scans with various ammonium nitrate particle sizes (d_{va}) at the ERICA-AMS vaporizer. The black line marks the adjusted aerodynamic lens position at x_{pos} = 10.55 mm (see Section 4.2.1.3 and Appendix B.3).

For direct, visual validation of the non-symmetric shape of the particle beam, an additional experiment was conducted. Therefore, a black adhesive strip glued on the last pinhole between DU2 and the B-

ToF chamber in the high vacuum regime. A dry poly-disperse ammonium nitrate aerosol was sampled for 25 minutes. By that a small amount of ammonium nitrate was deposited on this adhesive strip. The resulting spot was photographed by an optical microscope (model Axiophot, Carl Zeiss Microscopy GmbH) as shown in Figure 40 with a magnification factor of 10). For better visualization, the picture was digitally modified (increased acuity and contrast, negative colors). A non-circular shape is clearly evident. The beam widths are approximately 450 µm and 200 µm. Considering the geometry of the instrument (see Appendix B.4) the dimensions of the deposited spot would be 1,553 µm and 690 µm (full width) and thus within the dimensions of the vaporizer of 3.8 mm (see Section 3.5.2).

Since the aerodynamic lens was rotated from an unknown position (see Section 4.2.1), no estimations for the locations of different particle sizes accumulated on the adhesive strip can be made. Also, the picture was taken after the rotation. Referring to the picture, the detection laser is positioned on the right-hand side and the detector on the bottom side. The true color microscope image is shown in Figure 40 on the righthand side.

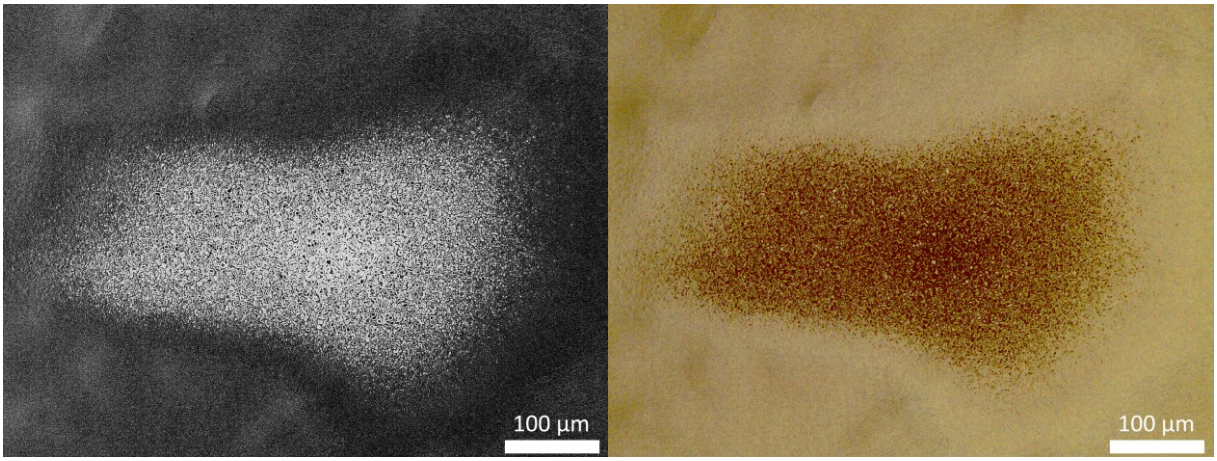

Figure 40: False color (left) and true color (right) digitally modified microscope image (magnification factor 10) of the deposited ammonium nitrate particles on a black adhesive strip, sampled on the last pinhole position between DU2 and the B-ToF chamber in the high vacuum regime. The white structure (left picture) and the brown structure (right picture) are the sampled particles.

Due to the different spatial distributions ($x_{0,local}$) of the maximum detection efficiency for various particle sizes (see Figure 38), a compromise for all particle sizes has to be found. To choose the optimum aerodynamic lens position, ammonium nitrate particles with various sizes were measured with the ERICA-AMS at different aerodynamic lens positions. The position that yields the highest mass concentration signal as compromise for all sizes is defined as the best lens position (see Section 4.2.1, x_{pos} = 10.55 mm and y_{pos} = 10.80 mm) and used during the first field deployment in Kathmandu, Nepal (KTM). Figure 41 shows the detection efficiency during field deployment in KTM DE_{KTM} as function of particle size d_{va} at this appropriate position. The parameter DE_{KTM} was calculated for PSL particle measurements by Equation (37) and for ammonium nitrate particle measurements by Equations (39) and (41) considering only the singly charged particle fraction (see Appendix B.13). The parameter x_{pos} was set to x_{pos} = 10.55 mm. All other parameter values were adopted from the curve fitting results of the individual measurements.

The measurements, where an OPC was used as a reference device, were conducted after a rotation of the aerodynamic lens estimated to 90° (see Section 4.2.1.1). The measurements with the DMA and an CPC as a reference device were performed before the rotation. The lens rotation occurred during a laboratory experiment after the field campaign in Kathmandu, Nepal (see Section 5.2), so all

measurements before the lens rotation reflect the condition during the campaign. It has to be emphasized that for this reason, and the fact that the particle beam profile is non-circular and non-concentric for all particle sizes, the DE_{KTM} values of the measurements using an OPC as reference are not representative in Figure 41.

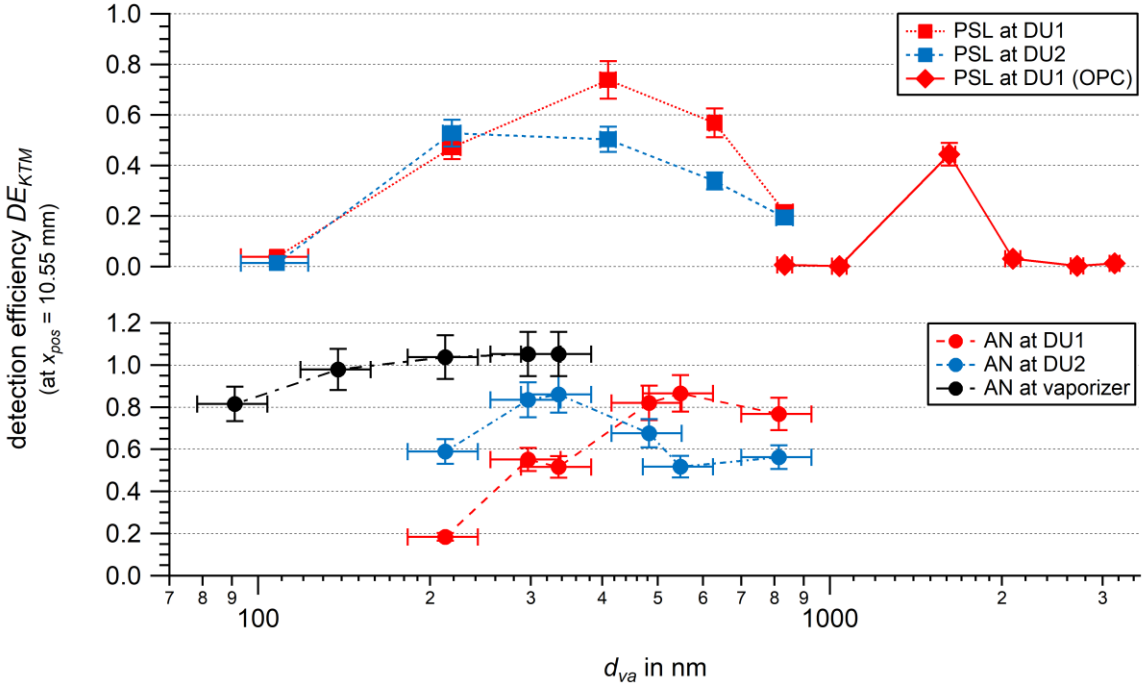

Figure 41: Detection efficiency DE_{KTM} as function of particle size d_{va} experimentally determined for PSL (squares, top) and ammonium nitrate (AN; circles, bottom) particles measured at the detection units DU1 (red) and DU2 (blue), and the ERICA-AMS vaporizer (black) for the aerodynamic lens setting during field deployment in Kathmandu, Nepal. CPC and OPC measurements as for Figure 37. The uncertainties of DE_{KTM} reflect the conservatively estimated value of 10 % (see Appendix B.1.6). The uncertainties of the PSL particle sizes result from NIST certificates. For ammonium nitrate particles the uncertainty of all sizes was conservatively estimated as 14 % (see Appendix B.1.4). The uncertainty bars are in some cases smaller than the symbol.

In Figure 41 (top) the overlap of the PSL measurements for d_{va} = 218 nm at DU1 and DU2 reflects the described adjustment (see Section 4.2.1.3) of the laser diodes of the detection units to maximize the scattered light signal intensity for PSL particles with d_{va} = 207 nm at the PMTs. The reason for the DE_{KTM} increase with particle size to a particle size of d_{va} = 410 nm (maximum DE_{KTM} = 74 %) and the decrease with larger particle sizes can be explained by the scattered light intensity varying with particle size (Figure 37). A sharply defined d_{50} is difficult to determine for the ERICA-LAMS detection units out of the performed measurements. By interpolation d_{50} = 192 nm (DU1) and d_{50} = 159 nm (DU2) can be coarsely estimated as lower d_{50} values and d_{50} = 745 nm (DU1) and d_{50} = 752 nm (DU2) as the upper d_{50} values. Furthermore, this value is divergent for particles with different optical properties from PSL like ammonium nitrate.

Except for the measurement with particle size of d_{va} = 213 nm at DU1, all ammonium nitrate particle measurements result in a DE_{KTM} > 40 % and reach their maximum at d_{va} = 335 nm (DU2) and d_{va} = 548 nm (DU1), both having values around 86 % (Figure 41, bottom). Here a detection limit d_{50} solely can be determined for the measurement with ammonium nitrate particles at DU1 (d_{50} = 269 nm).

For the measurements at the vaporizer no d_{50} values can be determined, because the results are above 50 % of their maximum DE_{KTM} values over the entire size range. The behavior of DE_{KTM} at the vaporizer of around 100 % is mostly due to the IE calibration by ammonium nitrate particles at d_{va} = 483 nm (not presented in Figure 41).

Due to the aerodynamic lens rotation, the measurements with larger particle sizes (with an OPC as reference device) do not reflect the measurement setup during the StratoClim campaign in Kathmandu, Nepal (Section 5.2).

The measurements demonstrated in this section have shown that detection efficiency varies with particle size and type. Overall, the measurements have shown good qualitative agreement with the expected results. Measurements of ambient aerosol usually do not represent the actual composition of the aerosol (Brands, 2009). The different measurements allowed to quantify the detection efficiencies for two different particle types. In the case of measurements of ambient aerosol containing a large number of different particle types with mostly mixed composition, this does not allow for precise quantitative measurements of the composition later on, because there are too many uncharacterized particle types. However, the measurements can provide a rough estimate of the respective occurrence of different particle types (Brands, 2009).

As shown above, the detection unit of the ERICA-LAMS achieves a detection efficiency of up to 100 % for PSL particles and up to 90 % for ammonium nitrate particles. The particle detection efficiency, i.e., the number of detected particles compared to the number of particles determined by an external instrument, was also determined for other single particle mass spectrometers such as the ALABAMA, the A-ATOFMS, the PALMS, and the LAAPTOF. The ALABAMA achieves a maximum detection efficiency of around 35 % during PSL measurements at a particle size of d_{va} = 420 nm (Köllner, 2019). With a newly developed aerodynamic lens it is possible to achieve a detection efficiency of up to 100 % for PSL particles in the particle size range of d_{va} = 350 nm to d_{va} = 1,800 nm (Clemen et al., 2020). Su et al. (2004) measured PSL particles in an aerodynamic diameter d_a (definition for d_a see B.2) range between d_a = 95 nm and d_a = 290 nm and achieved a maximum value of 47.4 % for PSL particles of d_{va} = 290 nm for the A-ATOFMS. A detection efficiency of 10 % is stated for the PALMS by Cziczo et al. (2006) without further information about the particle size. The LAAPTOF in its original design achieves a detection efficiency of 3 % for PSL particles of d_{mob} = 500 nm in diameter up to 4.8 % for PSL particles of d_{mob} = 1,000 nm (Shen et al., 2018). Zawadowicz et al. (2020), conversely, measured detection efficiencies between approximately 0.001 % and 0.02 % with the original LAAPTOF setup in a size range between d_{va} = 500 nm and d_{va} = 2,000 nm, which could be improved by two orders of magnitude by instrumental modifications. For ammonium nitrate particles larger d_{mob} > 500 nm in the size, a detection efficiency of 3 % up to 8 % was determined for the LAAPTOF (Shen et al., 2018). The relatively low values for the detection efficiencies of the PALMS and the LAAPTOF compared with the ERICA-LAMS, the ALABAMA, and the A-ATOFMS might be explained by the design of the detection units. In the ERICA-LAMS, the ALABAMA, and the A-ATOFMS, an ellipsoidal reflector enhances the particle scattering signal (see Section 3.3).

For the ERICA-LAMS, a size range of d_{va} = 174 nm to d_{va} = 3,173 nm was determined in this work by interpolation in which the detection efficiency is above 50 % of the maximum detection efficiency (d_{50}). The detectable size range varies between the single particle mass spectrometers. Whereas for the ALABAMA a size range of d_{va} = 270 nm to d_{va} = 1,900 nm was (d_{50}) published by Köllner (2019). Like for the ERICA-LAMS, for the ALABAMA the d_{50} is used as threshold parameter (Köllner, 2019). With the above mentioned newly developed aerodynamic lens, the detectable size range could be

extended to a size range from d_{va} = 230 nm to d_{va} = 3240 nm (Clemen et al., 2020). For the PALMS, a size range between d_{nom}~150 nm to d_{nom} = 2.0 µm is stated (Cziczo et al., 2006). However, the values are not directly comparable to the values obtained for the ERICA-LAMS, since the design of the inlet and detection unit is different and the methods for determination and the definition of the detectable size range could be different from the here presented one. This also applies to the LAMPAS2, the A-ATOFMS, and the LAAPTOF. Trimborn et al. (2000) found a detectable size range from d_{va} = 200 nm to d_{va} = 5,700 nm for the size calibration measurement with LAMPAS2. For the A-ATOFMS (Pratt et al., 2009) a size range of d_a = 200 nm to d_a = 3.0 µm is stated. These two values can be seen as approximated d_{50} values for the A-ATOFMS (see supplementary information of Pratt et al. (2009)). The detection unit in the LAAPTOF achieves a size range of d_{mob} = 200 nm to d_{mob} = 2,000 nm, where the detection efficiency is above 0.01 % (Shen et al., 2018).

4.2.5 Particle beam properties

Besides determining the values for the detection efficiencies (see Section 4.2.4), also other parameters of the particle beam can be revealed from the performed scans (see Section 4.2.3), which are discussed in this section. The knowledge of the particle beam behavior at the detection units, at the ablation laser area and the vaporizer are essential for interpreting and evaluating measured data.

The parameters r_{eff}, σ, x_0, and TE (including the SC and DC indexed species) were determined by Equations (37), (39), and (41) and are thus in the dimension relative to the aerodynamic lens position x_{pos}. For the following, the parameters were rescaled using the intercept theorem to the dimension of the particle beam at the specific position (DU1, DU2, ablation point, and ERICA-AMS vaporizer, see Appendix B.4). Furthermore, only the SC indexed values $r_{eff,L,SC}$, $r_{eff,V,SC}$, σ_{SC}, $x_{0,SC}$, and TE_{SC} from the ammonium nitrate measurements (Equation (39) and Equation (41)) were used for further presentation in this section. The denomination "SC" is therefore not used in the following.

The curve fitting by means of Equations (37), (39), and (41), deliver the standard deviation σ, which is proportional to the particle beam width at a certain detection unit. Considering 2σ is the $\frac{1}{\sqrt{e}}$-diameter of the Gaussian distribution function, the particle beam width w_{part} can be calculated. In Figure 42, w_{part} is displayed as function of the particle size d_{va}.

The particle beam width w_{part} results in approximately w_{part} = 0.1 mm at the first, and w_{part} = 0.2 mm at the second detection stage for measurements with PSL particle sizes above d_{va} = 200 nm. For PSL particles with d_{va} = 108 nm the beam widths w_{part} are 5 times (7 times) wider at DU1 (DU2) than these values of w_{part} = 0.1 mm and w_{part} = 0.2 mm. For ammonium nitrate particles, a narrower particle beam was found, as the corresponding values for w_{part} at DU1 and DU2 are w_{part} = 0.04 mm and w_{part} = 0.03 mm for d_{va} = 335 nm, respectively. The longer travel distance for the particles results in a broader w_{part} for ammonium nitrate particles at the vaporizer (by about a factor of 3.3) caused by the divergence α of the particle beam (Huffman et al., 2005). The maximum value for w_{part} = 2.2 mm was measured for ammonium nitrate particles of d_{va} = 91 nm in diameter. Taking the extrapolation based on the geometry of the instrument (see Appendix B.4) into account, also the particle beam widths at the ablation point and at the ERICA-AMS vaporizer can be calculated from the ammonium nitrate particle beam width at DU2. The calculation results in a maximum of w_{part} = 0.48 mm at the ablation point and w_{part} = 1.07 mm at the vaporizer, both for d_{va} = 548 nm. This is narrower than the width of the vaporizers' opening (diameter = 3.8 mm) and thus by adjusting the aerodynamic lens properly all particles d_{va} > 91 nm can be intercepted by the vaporizer. The

particle beam widths for d_{va} > 1,000 nm, measured at DU1 with the OPC as reference, is up to w_{part} = 0.20 mm.

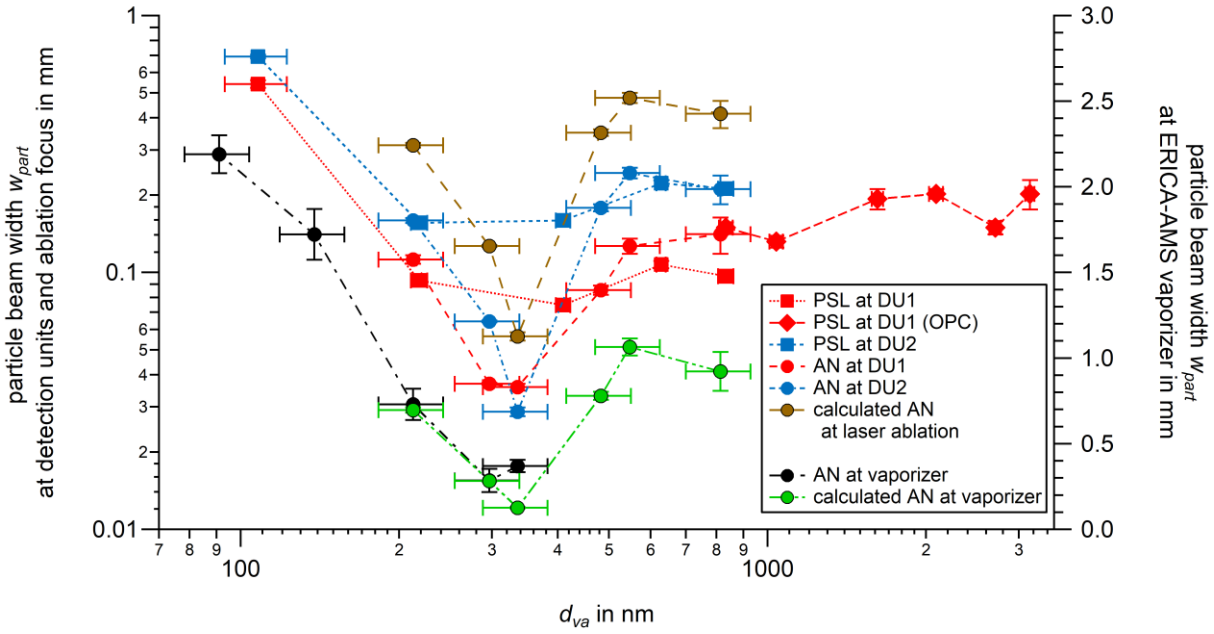

Figure 42: Particle beam widths w_{part} ($\frac{1}{\sqrt{e}}$-diameter) as function of particle size d_{va} for PSL (squares) and ammonium nitrate (circles) particle sizes measured at the detection units DU1 (red, left axis) and DU2 (blue, left axis) and for ammonium nitrate particles measured at the ERICA-AMS vaporizer (right axis, black). The reference values for number concentrations were either obtained from the experimental setup with the OPC or the CPC. The ammonium nitrate particle beam widths at the ablation point (brown, left axis) and the ERICA-AMS vaporizer (green, right axis,) were calculated. The uncertainties of the particle beam widths result from the curve fittings (see Appendix B.1.6). The uncertainties of the PSL particle sizes result from NIST certificates. For ammonium nitrate particles the uncertainty of all sizes was conservatively estimated as 14 % (see Appendix B.1.4). The uncertainty bars are in some cases smaller than the symbol.

The dimension of the particle beam in other single particle mass spectrometers is similar to the here observed dimension. In the LAAPTOF and in the PALMS the particle beam is focused to a diameter of 130 µm (for PSL, d_p = 600 nm; Marsden et al. (2016)) and ~100 µm (no specific particle type or size; Cziczo et al. (2006)) in the plane of the detection laser. In the LAMPAS2 the particle beam width is 800 µm at the detection laser unit (Trimborn et al., 2000). In the ALABAMA the particle beam width is between 300 µm and 700 µm for PSL particle sizes of d_{mob} = 300 nm to d_{mob} = 700 nm (Brands, 2009) that is comparable to the determined values for the ERICA for particle sizes of d_{va} > 400 nm. For the A-ATOFMS a particle beam width between 340 µm and 380 µm is stated for PSL particle sizes between d_a = 100 nm and d_a = 290 nm (Su et al., 2004).

Considering an optical laser beam width $w_{0,dia}$ (1/e²-diameter) of 60 µm for the ERICA (see Section 4.1.2), the particle beam is factor 2 to factor 3 wider (PSL, d_{va} > 200 nm). A different and possibly better measure than the optical laser beam waist diameter $w_{0,dia}$ is the effective beam width $r_{eff,L}$ (effective radius) of the detection laser (see Section 4.2.3).

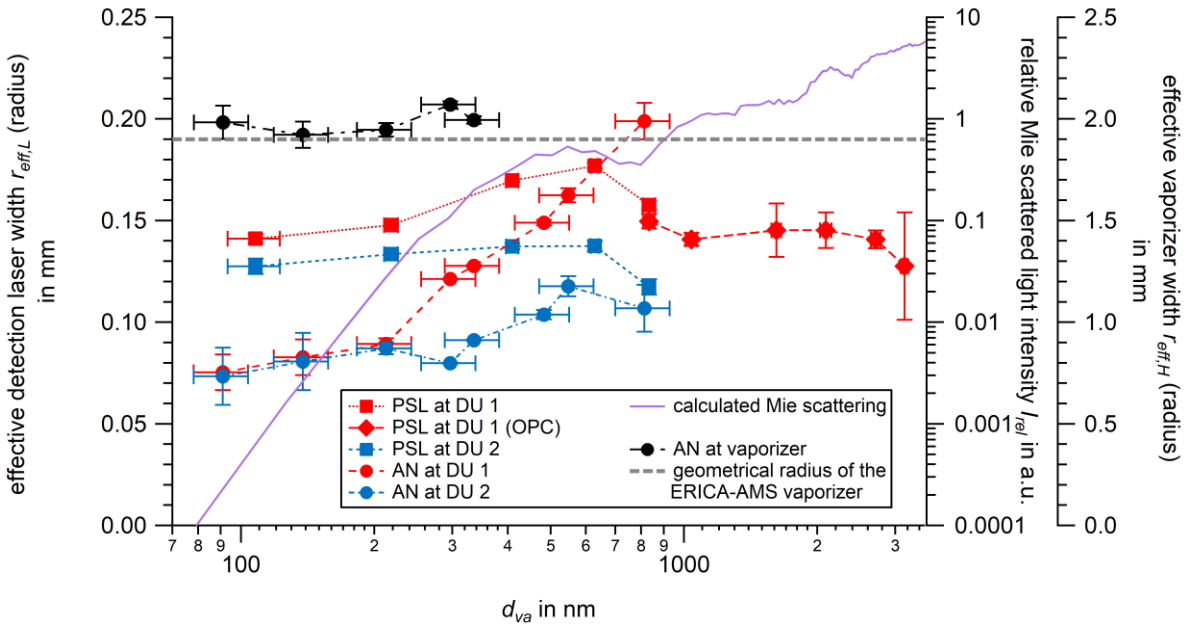

Figure 43: Effective detection laser width $r_{eff,L}$ and effective vaporizer width $r_{eff,V}$ (here in terms of radii) as function of particle size d_{va} for PSL (squares) and ammonium nitrate (circles) particle sizes that are measured at the detection units DU1 (red, left ordinate) and DU2 (blue, left ordinate) and for ammonium nitrate particles measured at the ERICA-AMS vaporizer (right ordinate, black). The calculated relative Mie scattered light intensity I_{rel} (second right ordinate, purple) is displayed. CPC and OPC measurements as for Figure 42. The geometric vaporizer radius is marked by a dashed gray line. The uncertainties of the effective detection laser width result from the curve fitting (see Appendix B.1.6) and uncertainties of the particle size result from NIST certificate (PSL). For ammonium nitrate particles the uncertainty of all sizes was conservatively estimated as 14 % (see Appendix B.1.4). The uncertainty of $r_{eff,L}$ for the PSL measurement with particle size of d_{va} = 108 nm (see Appendix B.7) was estimated as 0.002 mm (DU1) and 0.004 mm (DU2) and the uncertainties of $r_{eff,L}$ for the ammonium nitrate measurements with particle sizes of d_{va} = 138 nm (see Appendix B.11.1) and d_{va} = 91 nm (see Appendix B.11.2) are conservatively estimated as 0.009 mm at DU1 and 0.014 mm at DU2. These values are the rescaled approximated maximum uncertainties of $r_{eff,L}$ in the considered size range of d_{va} = 213 nm to d_{va} = 814 nm at DU1 and DU2. For the ammonium nitrate measurement with particle size d_{va} = 91 nm the uncertainty of $r_{eff,V}$ was estimated as 0.08 mm (rescaled from value in Appendix B.1.6). The uncertainty bars are in some cases smaller than the symbol.

Figure 43 shows the effective laser beam widths $r_{eff,L}$ and the effective vaporizer width $r_{eff,V}$ as function of the particle size d_{va}. The effective laser beam width $r_{eff,L}$ (effective radius) is the laser beam width wherein a particle is registered (see Section 4.2.3). Overall, for PSL particles $r_{eff,L}$ is between 0.1 mm and 0.4 mm. The decrease at d_{va} = 800 nm is caused by a minimum in the light scattering response function of the Mie curve (see Appendix B.6). The parameter $r_{eff,V}$ represents the effective vaporizer width (effective radius) of the ERICA-AMS vaporizer, i.e., the region where particles get vaporized in such a degree that enough ions are accelerated into the mass spectrometer to generate a detectable signal at the MCPs. The resulted values match the physical dimension of the vaporizer body (geometric radius: 1.9 mm).

The shape of the curve of the effective laser beam width depends on the shape of the response function of the scattered light intensity as function of size. This intensity is defined by the angle distribution of the Mie scattering subject to the spherical particle diameter and its trend is reflected in the curve progression of the PSL particle measurements ($d_{va} \leq$ 834 nm). For the measurements with PSL particles of d_{va} = 108 nm and ammonium nitrate particles of d_{va} = 91 nm and d_{va} = 138 nm in diameter, this is obvious, since the calculation of their $r_{eff,L}$ values are based on the Mie scattering (see Sections 4.2.3.1 and 4.2.3.2).

For larger particles, i.e., the measurements with OPC as reference device, an increase with particle size would be expected. The fact that the OPC measurements were performed by Molleker et al. (2020) with various PMT threshold values (increasing with size), $r_{eff,L}$ appears lower than the CPC reference measurements and thus $r_{eff,L}$ for particle sizes above d_{va} > 834 nm is underestimated in this Figure 43. The ammonium nitrate measurement results do not agree with the results of the measurements with PSL particles. This result indicates either a non-spherical shape of the ammonium nitrate particle type and/or is caused by a different refractive index compared to PSL.

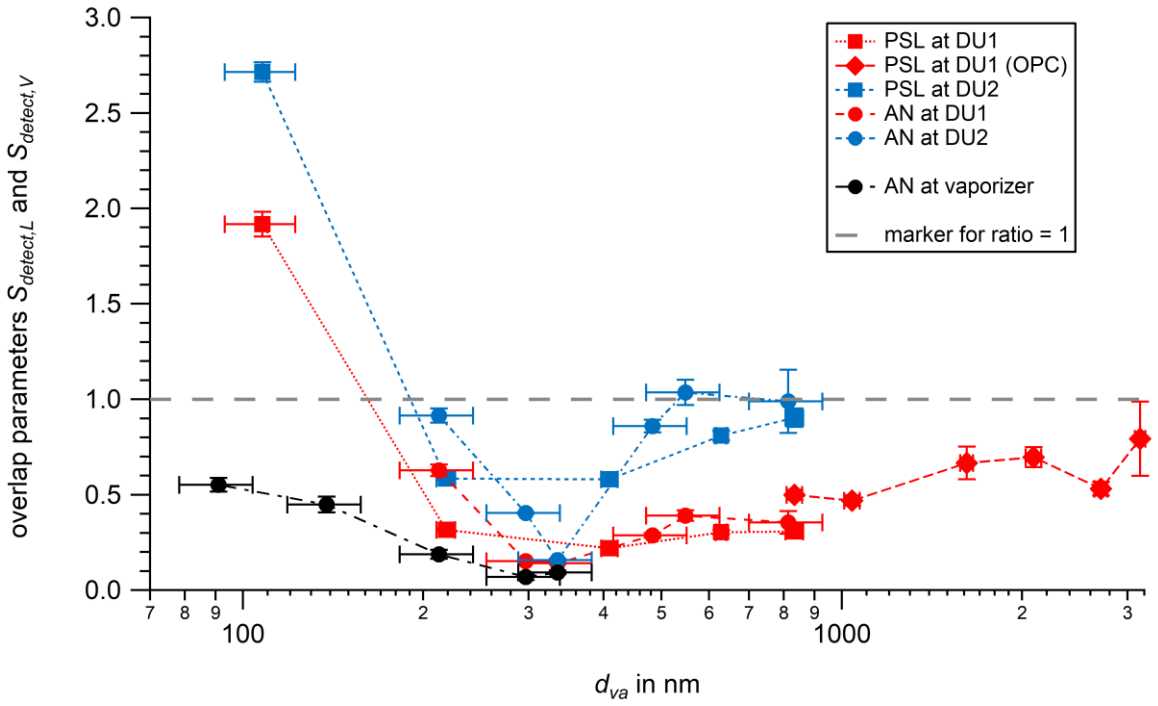

Figure 44: Overlap parameters $S_{detect,L}$ and $S_{detect,V}$ as function of particle size d_{va} for PSL (squares) and ammonium nitrate (circles) particle sizes measured at the detection units DU1 (red) and DU2 (blue) and for ammonium nitrate particles measured at the ERICA-AMS vaporizer (black). CPC and OPC measurements as for Figure 42. The dark gray horizontal line illustrates where the ratio equals 1. The uncertainties of $S_{detect,L}$ and $S_{detect,V}$ result from the curve fitting values (see Appendix B.1.6) as base for the propagation of uncertainties (see Appendix B.1.7). The uncertainties of the effective detection laser width result from the curve fitting. The uncertainties of the PSL particle sizes result from NIST certificates. For ammonium nitrate particles the uncertainty of all sizes was conservatively estimated as 14 % (see Appendix B.1.4). The uncertainty bars are in some cases smaller than the symbol.

To determine the overlap of both beams, the particle beam width (w_{part}) is compared to the effective laser diameter $d_{eff,L} = 2 \cdot r_{eff,L}$, as well as the effective vaporizer diameter $d_{eff,V} = 2 \cdot r_{eff,V}$. Therefore, the $S_{detect,L} = {w_{part}}/{d_{eff,L}}$ was calculated for different particle sizes at the detection units and considers the maximum possible overlap of w_{part} and $d_{eff,L}$ for each measurement at lens position x_{pos} = x_0. The parameter $S_{detect,L}$ serves as a measure of the particle beam and detection laser beam overlap. The same holds for $S_{detect,V} = {w_{part}}/{d_{eff,V}}$. Both are shown in Figure 44. The dark gray horizontal line marks the overlap, where the ratio equals 1. All particle sizes below that line are detected sufficiently within one standard deviation σ of the particle beam width. That is the case, within their uncertainties, for all measurements except for PSL particles of d_{va} = 108 nm in diameter. Behind this is a broad w_{part} for the smallest particles resulting from the interaction with the residual gas molecules simultaneously emerging from the aerodynamic lens. However, as described above the

uncertainty of $r_{eff,L}$ for the measurement with PSL particles of d_{va} = 108 nm in diameter might be underestimated and therefore the uncertainty for $S_{detect,L}$ might be underestimated as well. The values of $S_{detect,L}$ of the measurements with the OPC are overestimated, since the resulting values of $r_{eff,L}$ are underestimated, due to the varying threshold during the measurements. However, the values are below a ratio of 1.

The overlap $S_{ablation}$ of the calculated particle beam width w_{part} ($\frac{1}{\sqrt{e}}$-diameter) of ammonium nitrate particles in the UV ablation laser area (see brown curve in Figure 42) and the determined optical laser beam waist $w_{0,dia}$ = 250 µm (1/e²-diameter, see Section 4.1.3) was calculated and plotted against the particle size as qualitative approximation and is shown in Figure 45 ($S_{ablation} = {}^{w_{part}}/_{w_{0,dia}}$). For ammonium nitrate particles, the calculated fraction of the illuminated area of the UV ablation laser spot is between 23 % (at d_{va} = 335 nm and up to 191 % (d_{va} = 548 nm). This means that the particle beam is 4.3 times smaller for particles of d_{va} = 335 nm in diameter than the ablation laser spot of $w_{0,dia}$ = 250 µm. This is of fundamental importance for the efficiency of the ERICA-LAMS laser ablation arrangement.

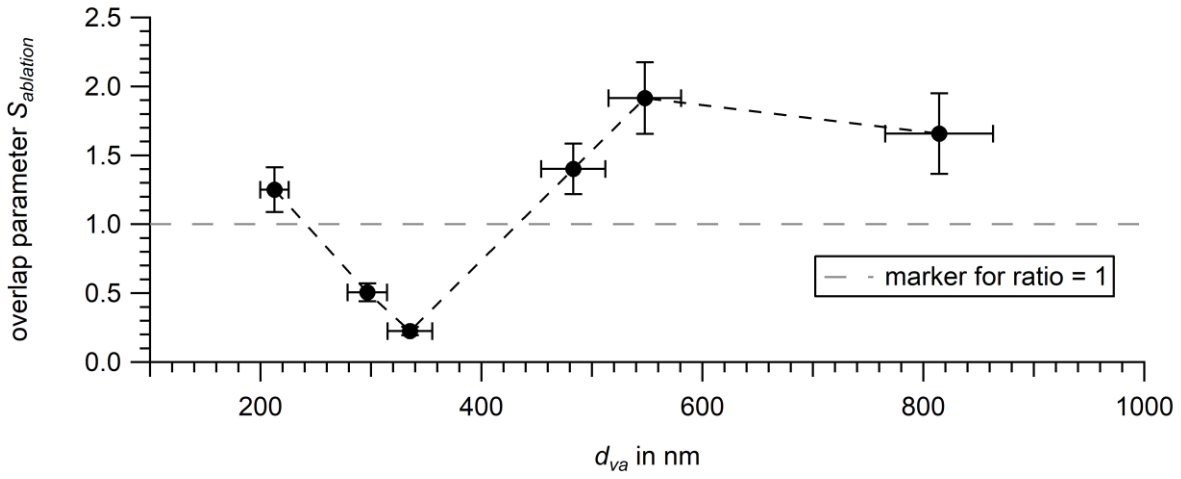

Figure 45: Overlap parameter $S_{ablation}$ as function of particle size (d_{va}) for ammonium nitrate particles in the ablation spot. The uncertainties of $S_{ablation}$ result from the curve fitting values (see Appendix B.1.6) as base for the propagation of uncertainties (see Appendix B.1.8). For ammonium nitrate particles the uncertainty of all sizes was conservatively estimated as 14 % (see Appendix B.1.4). The uncertainty bars are in some cases smaller than the symbol.

The particle beam divergence α is displayed in Figure 46 for various PSL and ammonium nitrate particle sizes, at both detection stages (DU1 and DU2), and ammonium nitrate at the ERICA-AMS vaporizer, calculated from the particle beam width analogue σ defined as:

$$\alpha = \frac{\sigma}{z_{asd}} \tag{42}$$

The parameter σ is in the dimension of a $\frac{1}{\sqrt{e}}$-radius) and z_{asd} the distance from the adjustment screws to the ball joint (z_{asd} = 133.7 mm; see Appendix B.4). It is apparent that the very small particles (d_{va} < 200 nm) diverge into a much wider cone than the other measured sizes. The reason for this is the collisional interaction with the residual air molecules right after critical expansion. The values at DU1 are larger than for the values at DU2 for small particles. One reason is the fact that these particle sizes do not have a common, single starting point but rather a finite starting area within the cross section of the lens's exit. This fact might be caused by turbulence in the aerodynamic lens and leads to

a discrepancy of the different divergence values for the same particle sizes at different distances from the aerodynamic lens's exit. Values of α measured at DU2 are more reliable than those measured at DU1, since the influence of the starting area is higher for measurements closer to the aerodynamic lens, i.e., measurements at DU1, than for measurements further from the aerodynamic lens, i.e., measurements at DU2 and at the vaporizer. This is especially the case for the measurements with PSL particles of d_{va} = 108 nm in diameter. Larger particle sizes (d_{va} > 421 nm) tend to slightly higher α values. For particle sizes between d_{va} = 218 nm and d_{va} = 834 nm, the particle beam divergence α seems to be independent of the particle type. A minimum for α of α = 0.1 mrad can be extracted from the measurements with ammonium nitrate particles of d_{va} = 335 nm in diameter at DU2 and a maximum of α = 4.6 mrad for PSL particles of d_{va} = 108 nm in diameter at DU1. The measurements with the OPC as reference device were measured before the lens rotation (see Section 4.2.1.1). However, considering a rotationally symmetric particle beam profile for each specific particle size, the divergence is unaffected by the rotation. The values for these measurements are between 1.1 mrad and 1.7 mrad. For the PALMS, Cziczo et al. (2006) state a particle beam divergence of 0.5° that equals 8.7 mrad. The difference might result from a different inlet design.

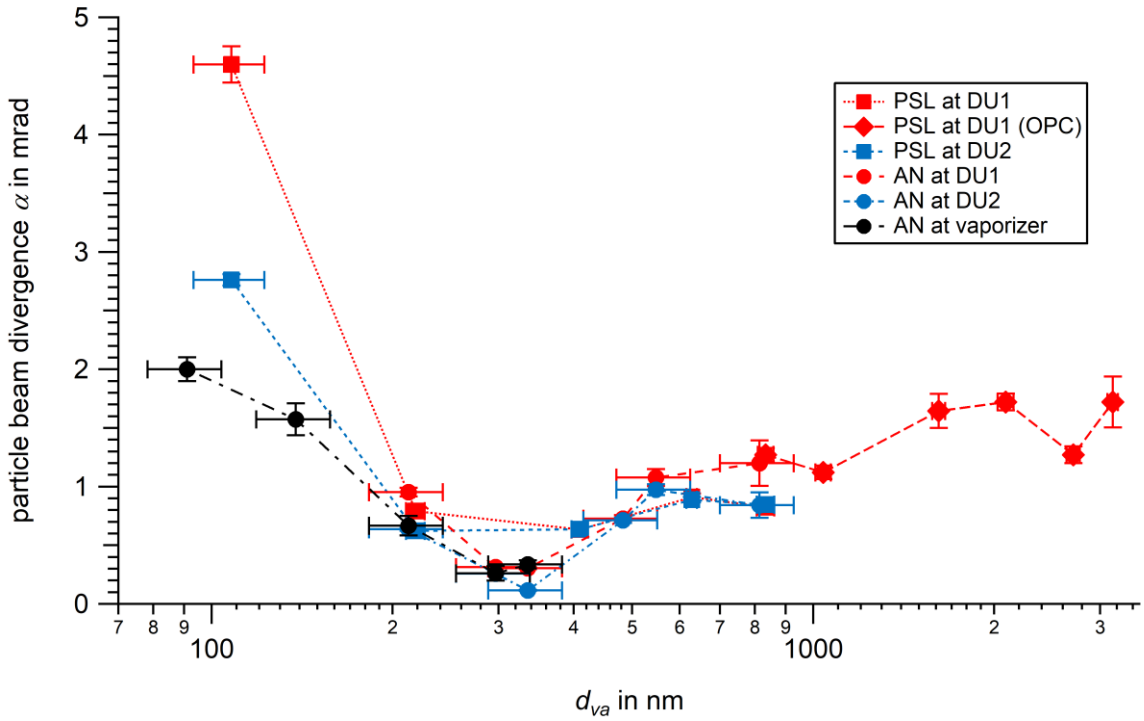

Figure 46: Particle beam divergence α as function of particle size d_{va} for PSL (squares) and ammonium nitrate (circles) particle sizes measured at the detection units DU1 (red) and DU2 (blue) and for ammonium nitrate particles measured at the ERICA-AMS vaporizer (black). CPC and OPC measurements as for Figure 42. Values of α measured at DU2 are more reliable than those measured at DU1 (see text). The uncertainties of α result from the curve fitting (see Appendix B.1.6) and reading errors as base for the propagation of uncertainties (see Appendix B.1.9). The uncertainties of the PSL particle size result from NIST certificates. For ammonium nitrate particles the uncertainty of all sizes was conservatively estimated as 14 % (see Appendix B.1.4). The uncertainty bars are in some cases smaller than the symbol.

Another parameter given in the curve fitting function of Equations (37), (39), and (41) is the aerodynamic lens particle transmission efficiency TE. This is the calculated factor that describes the transmitted particle number concentration divided by the number concentration of the CPC/OPC measurements. Similar efficiency measurements, also for different ambient pressures, were performed by Molleker et al. (2020). The parameter TE describes the efficiency of the transmission of

aerosol particles passing the aerodynamic lens. By that the particle losses in the aerodynamic lens can be estimated.

The resulting TE from all measurement evaluations are shown in Figure 47 as function of the particle size d_{va}. In case of the aerodynamic lens scan measurement provided a plateau shaped curve (see Appendices B.5, B.8, and B.12) the parameter TE is strongly correlated with the effective laser width $r_{eff,L}$ (or $r_{eff,L,SC}$) or with the effective vaporizer width $r_{eff,V,SC}$, as described in Section 4.2.3.3. For such measurements the parameter of the effective width and TE can be estimated sufficiently well with low uncertainty values.

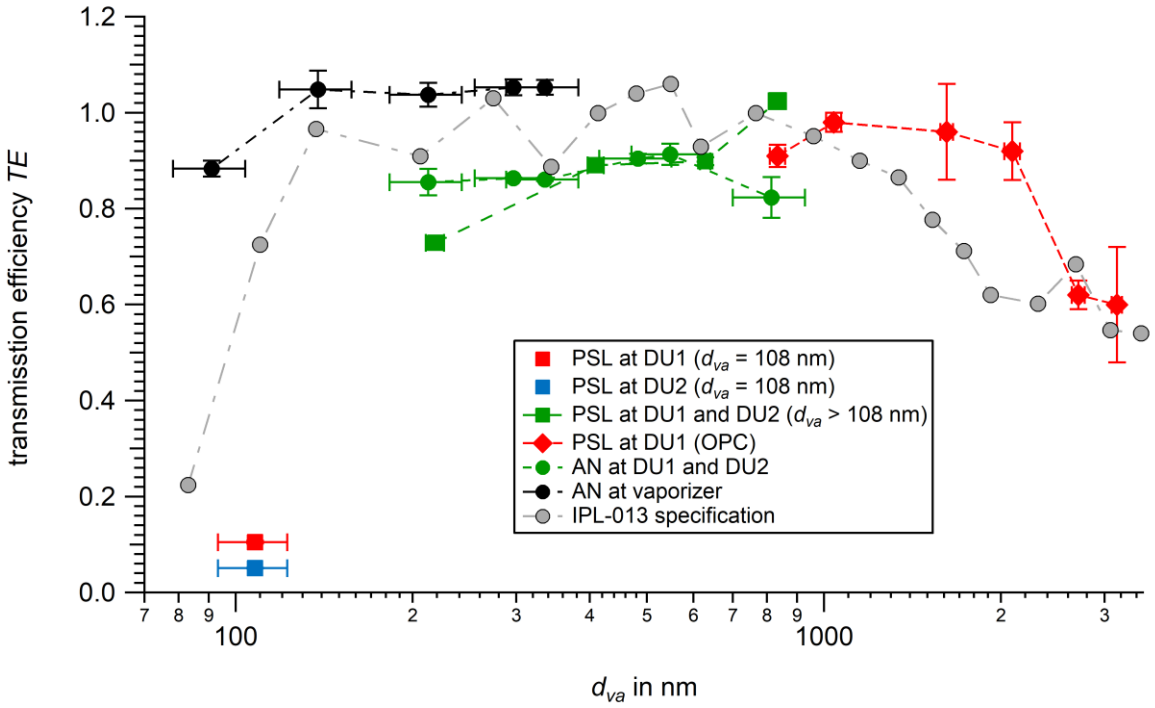

Figure 47: Particle transmission efficiency TE as function of particle size d_{va} for PSL (squares) and ammonium nitrate (circles) particles measured at the detection units DU1 (red), and DU2 (blue) and both (DU1 and DU2, green), ammonium nitrate particles at the ERICA-AMS vaporizer (black). CPC and OPC measurements as for Figure 42. The IPL-013 specification curve (by Aerodyne Inc.) is plotted in dark gray. The PSL particle measurements for d_{va} = 108 nm were evaluated not by a common curve fit procedure, but individually. The uncertainties of TE result from the curve fitting (see Appendix B.1.6). The uncertainties of the PSL particle sizes result from NIST certificates. For ammonium nitrate particles the uncertainty of all sizes was conservatively estimated as 14 % (see Appendix B.1.4). The uncertainty bars are in some cases smaller than the symbol.

Due to the *common curve fitting* analysis procedure as mentioned in Section 4.2.3, only one value of TE is available for each particle type and size. Thus, the value of TE at DU1 equals the value at DU2. This is the case for all ammonium nitrate particle measurements and for all PSL particle measurements for particle sizes above d_{va} > 108 nm. Here, it is assumed that the particle loss between DU1 and DU2 is negligible. Since the evaluation of the measurement with PSL particles of d_{va} = 108 nm was conducted not by a *common curve fitting* routine, two values of TE are available for one PSL particle size (see Section 4.2.3.1). This approach leads to reduced uncertainty values of TE for this particular particle size. For particles of d_{va} = 108 nm, the particle beam width in y-direction might be broader than the effective laser width in y-direction, i.e., along the laser beam axis. Thus, the approximation done in Section 4.2.3.1 where the effective laser beam width in y-direction was approximated by infinity (limits from $-\infty$ to $+\infty$) is not valid for this particular measurement. Since the detected

particles are a fraction of all sampled particles, the particle beam divergence α affects the measurement at DU2 even more and TE cannot assumed to be the same as at DU1.

The parameter TE increases with particle size and reaches an efficiency of 100 % for PSL particles at a particle size of d_{va} = 834 nm. PSL particles with d_{va} = 218 nm were transmitted with an efficiency of 73 %, whereas particles of d_{va} = 108 nm were transmitted with a transmission efficiency TE of 5 % at DU2, and with a TE of 10 % at DU1. These two latter values are underestimated due to the broad particle beam width w_{part} for the measurement with PSL particles of d_{va} = 108 nm, which leads to a particle loss in y-direction. Thus, also the d_{50} values for the transmission efficiency determined by interpolation of 180 nm (at DU1) and 183 nm (at DU2) are overestimated in terms of particle size.

The values of TE measured at the vaporizer of the ERICA-AMS are not directly comparable to the values of the measurements at the detection units due to the freedom of determining the calibration factor at the ERICA-AMS. However, the lower d_{50} cut-off for the ERICA-AMS measurements is below d_{va} = 90 nm. This indicates that the TE values determined by the detection units for PSL particles of d_{va} = 108 nm might be underestimated.

The dark gray curve was provided in the datasheet of the aerodynamic lens by the manufacturer (model IPL-013 from Aerodyne Inc.). The results of the measurements correspond with the values specified for the applied aerodynamic lens by the manufacturer within its fluctuation for particle sizes between d_{va} = 138 nm and d_{va} = 1,040 nm. Furthermore, a smaller lower d_{50} value is achieved for the ERICA-AMS than provided by the datasheet. However, the aerodynamic lens type of the here used lens was comprehensively described by Peck et al. (2016) and Xu et al. (2017). Xu et al. (2017) show that the TE is above 80 % in a size range of d_{va} = 200 nm to d_{va} = 2,000 nm and that TE reaches a maximum of 100% in the size range of d_{va} = 300 nm to d_{va} = 1,000 nm and thus even higher than what was achieved in the here presented measurements. A reason might be the different method for determination of TE. The d_{50} cut-offs are stated for particle sizes between $d_{va} \sim$ 120 nm and d_{va} = 3.5 µm (Xu et al., 2017).

Except for the measurement with PSL particles of d_{va} = 108 nm, the transmission efficiency was determined above 70 % for the size range between d_{va} = 91 nm and d_{va} = 2,090 nm and above 60 % for the size range between d_{va} = 91 nm and d_{va} = 3,150 nm.

The determined values for TE above 70 % in the size range of d_{va} = 91 nm and d_{va} = 2,090 nm can be compared with other single particle mass spectrometers. Referring to the manufacturer of the aerodynamic lens, Shen et al. (2018) state for the aerodynamic lens of the LAAPTOF a value of TE of around 100 % in the size range of d_{va} = 100 nm and d_{va} = 2,000 nm. For the ALABAMA a maximum TE of 100 % was given for particle sizes between d_{va} = 150 nm and d_{va} = 350 nm (Brands, 2009).

4.2.6 Summary of the detection unit and particle beam characterization

For the characterization of the detection unit and the particle beam, PSL particles were used as well as ammonium nitrate particles (for the non-refractory components) covering the size diameter range between d_{va} = 80 nm and d_{va} = 5,145 nm. After adjustment of the aerodynamic lens, vacuum aerodynamic size calibration measurements were performed by using PSL particles. The calibration was conducted by two different methods. The calibration method that uses a polynomial fit was found suitable for the ERICA instrument that was confirmed by ammonium nitrate particle measurements. This method is suitable within the calibration sizes. The d_{va} deviation from the calibration curve was for all particle sizes below 20 %. Furthermore, the detection efficiency of the detection unit was determined by tilting the aerodynamic lens in discrete steps, so called scans. As reference device either

a DMA/CPC set-up or an OPC was used to measure the particle number concentration. The results were curve fitted by a convolution function adopting the Gaussian spatial distribution of the particle density inside the particle beam and a rectangular function for the effective laser width. During the evaluation of the ammonium nitrate particles also the presence and influence of doubly charged particles were considered. The deployed approach determining particle beam characteristic parameters by simultaneously considering doubly charged particles besides singly charged particles by an iterative evaluation for various particle sizes was not described in literature yet.

Hereafter, the results of the different curve fits (x_0, σ, r_{eff}, and TE) were used to calculate the detection efficiency for each particle type at the detection units DU1, DU2, and the ERICA-AMS vaporizer. Therefore, two different values for x_{pos} were considered. First the maximum DE_{max}, where x_{pos} equals x_0 and secondly DE_{KTM}, where the lens position during the deployment in Kathmandu, Nepal was considered (x_{pos} = 10.55 mm).

The maximum detection efficiency DE_{max} is explainable by Mie theory for small particle sizes. By interpolations, the d_{50} values can be estimated to be 174 nm (PSL at DU2, lower value) and to d_{va} = 3,173 nm (OPC reference, upper value). Furthermore, it was found that the particle beam does not consist of an overall concentric beam profile for all particle sizes. That result was validated by a microscopic imaging experiment. The detection efficiency for the aerodynamic lens position during the deployment in Kathmandu DE_{KTM} is lower than DE_{max}. Adopting interpolations, d_{va} = 192 nm (DU1) and d_{va} = 159 nm (DU2) are determined as lower d_{50} values, and d_{va} = 745 nm (DU1) and d_{va} = 752 nm (DU2) as the upper d_{50} values that are valid for the StratoClim field campaign. For the ammonium nitrate particle measurements, solely a d_{50} value for d_{va} = 269 nm can be determined at DU1 (low value).

The results of the curve fit parameters, r_{eff}, TE and σ, or derived parameters like, w_{part}, $S_{detect,L}$, $S_{detect,V}$, $S_{ablation}$ and α, are discussed separately as function of the particle size d_{va}. The particle beam width w_{part} results in approximately 0.1 mm at DU1, and 0.2 mm at DU2 (PSL). The value of w_{part} for d_{va} = 108 nm is roughly up to a factor 7 wider. Calculations for the ablation point and the vaporizer position, results in a maximum of w_{part} = 0.48 mm at the ablation point and w_{part} = 1.07 mm at the vaporizer (d_{va} = 548 nm). The maximum value of w_{part} for ammonium nitrate particles is w_{part} = 2.2 mm (d_{va} = 91 nm). For d_{va} > 1,000 nm, w_{part} is up to 0.2 mm at DU1. A minimum of w_{part} = 0.03 mm can be observed at DU2 during the measurements with ammonium nitrate particles. The effective laser width $r_{eff,L}$ for PSL particles is overall between $r_{eff,L}$ = 0.1 mm and $r_{eff,L}$ = 0.4 mm. The curve progression of $r_{eff,L}$ as function of particle size can be qualitatively explained by the pattern of the scattered light intensity calculated from Mie theory for particle sizes $d_{va} \leq$ 834 nm. The resulted values for $r_{eff,V}$ match the physical dimension of the vaporizer body. A qualitative measure for the overlap of the particle beam width w_{part} and the detection laser beam width $d_{eff,L}$ (diameter) is their ratio $S_{detect,L}$ and $S_{detect,V}$. A value of $S_{detect,L}$ or $S_{detect,V}$ below 1 indicates an overlap (within one standard deviation of the particle beam) and thus a highly likely detection of a particle. That is the case for all measurements (at the DUs and the vaporizer) except for the measurement with PSL particles of d_{va} = 108 nm at DU2, due to the broad divergence of the particle beam for that size. For $S_{ablation}$, a value for d_{eff} is not available, so the value of the beam waist diameter $w_{0,dia}$ of $w_{0,dia}$ = 250 µm, determined by the knife-edge experiment, was used instead. For ammonium nitrate particles the calculated fraction of the area where the particles are exposed to the ablation beam is between 23 % (d_{va} = 335.3 nm) and 191 % (d_{va} = 548 nm). This implies that the smaller particles not

only suffer from losses due to the beam divergence and lower detection efficiency, but also because the particle beam is wider than the illuminated area. The particle beam divergence α evaluation results in a particle type independent behavior between particle sizes of d_{va} = 218 nm and d_{va} = 834 nm. A minimum for α was found for d_{va} = 335 nm (0.1 mrad) and a maximum for d_{va} = 108 nm (4.6 mrad). Larger particle sizes ($d_{va} > 421$ nm) tend to slightly higher α values. The values of α for the OPC referenced measurements are between 1.1 mrad and 1.7 mrad. The aerodynamic lens particle transmission efficiency TE increases with particle size and reaches for PSL particles a transmission efficiency of 100 % at a particle size of d_{va} = 834 nm. Between DU1 and DU2 the particle losses were considered as negligible. The lower d_{50} values of TE is found at d_{va}= 180 nm (at DU1) and d_{va}= 183 nm (at DU2). These values are overestimated due to the broad particle beam width w_{part} and a high $S_{detect,L}$ value. The overall transmission efficiency was determined of over 70 % for the size range between d_{va} = 91 nm and d_{va} = 2,090 nm and of over 60 % was determined for the size range between d_{va} = 91 nm and d_{va} = 3,150 nm, except for the measurement with PSL particles of d_{va} = 108 nm. All in all, these results correspond with the values specified by the aerodynamic lens manufacturer (Aerodyne Inc.).

The results of the determined particle beam's key parameters are summarized in Table 9. All particle sizes including d_{50} values are given in in terms of d_{va}.

Table 9: Key parameters (d_{50} of DE_{max}, DE_{KTM} and TE as well as α, r_{eff} and w_{part}) of the particle beam characterization measurements and resulting values. Non-determined values are noted as n/a and ammonium nitrate as AN. All particle sizes, including d_{50} values, are given in terms of d_{va}.

Parameter			Lowest limit	Highest limit
Range of the particle size calibration			80 nm	5,145 nm
d_{50}	DE_{max}	PSL (DU overall)	174 nm	3,173 nm
		AN at DU	*n/a*	*n/a*
	DE_{KTM}	PSL at DU1 only	192 nm	745 nm
		PSL at DU2 only	159 nm	752 nm
		AN at DU1 only	269 nm	*n/a*
		AN at DU2 only	*n/a*	*n/a*
	TE	PSL at DU1 only	180 nm (overestimated)	*n/a*
		PSL at DU2 only	183 nm (overestimated)	*n/a*
		AN at vaporizer	< 91 nm	*n/a*
α			0.1 mrad (for 335 nm, AN at DU2)	4.6 mrad (for 108 nm, PSL at DU1)
$r_{eff,L}$			0.1 mm (overall)	0.4 mm (overall)
$r_{eff,H}$			1.9 mm	
w_{part}	PSL	at DU1	~0.1 mm (d_{va}> 218 nm)	
		at DU2	~0.2 mm (d_{va} > 218 nm)	
	AN	at ablation spot	0.48 mm (d_{va} = 548 nm)	
		at vaporizer	2.2 mm (d_{va} = 91 nm)	

4.3 Ablation efficiency

Another relevant parameter to describe the performance of a single particle laser ablation mass spectrometer is the ablation efficiency AE. The definition of AE (see Equation (43)), also called hit rate, is the number of acquired spectra $N_{spectra}$, i.e., successfully ionized by the ablation laser and recorded by the oscilloscope, divided by the number of laser shots N_{shots}, i.e., attempts to ionize the particle (Brands et al., 2011). This definition is largely independent of ambient aerosol concentration. For each particle for which the particle size was determined by the TC, a laser shot is triggered (see Section 3.7.2.2).

$$AE = \frac{N_{spectra}}{N_{shots}} \tag{43}$$

With ERICA-LAMS in the laboratory AE values of up to 50 % could be achieved for PSL particles after adjusting the PMT thresholds and the *Multiplier* value according to the procedure described in Section 4.2.1.3. To assess on the smallest detectable particle size (see Section 4.2.4), the detection units DU1 and DU2 were optimized for the following experiment for PSL particle sizes of d_{va} = 218 nm. It has to be mentioned that an AE value of up to 100 % could be artificially generated for a single PSL particle size by adjusting the *Multiplier* value and the PMT thresholds. However, this latter type of adjustment is not suitable for ambient measurements. For other single particle mass spectrometers, values higher than 50 % are stated for valid measurements with PSL particles. The ALABAMA achieves with PSL particles an ablation efficiency of up to 99.5 % (Brands, 2009), the PALMS of ~95 % (Cziczo et al., 2006), the LAAPTOF of up to 94 % (d_{va} = 400 nm; Shen et al. (2018)), and the A-ATOFMS of above 80 % (d_a = 120 nm to d_a = 290 nm, Su et al. (2004)). The high AE values of the PALMS and the LAAPTOF might result from the instrumental design of the mass spectrometer, where the ablation spot is close to the last detection stage. By that, the time delay between detection signal and ablation pulse can be short.

To determine the ablation efficiency for ambient aerosol as proof-of-concept, in July 2018 ambient air from the atrium of the Max Planck Institute for Chemistry building in Mainz, Germany, was sampled. Only spectra for which the size information was available and particle sizes within the range of calibration (Section 4.2.2) were considered. The ablation laser was adjusted to maximum ablation efficiency for ambient aerosol, by varying the *Multiplier* value and adjusting the dichroitic mirror DM1 (Figure 15). Figure 48 shows the ablation efficiency AE as function of the particle size d_{va} from the described experiment. Furthermore, the histograms of $N_{spectra}$ and N_{shots} are plotted. At approximately d_{va} = 230 nm a maximum (AE = 52 %) occurs amongst a high number of sized particles. The reason might be the selected optimization in the adjustment of the detection and ablation units. For larger particles (d_{va} > 1,000 nm) the particle flight time deviates too much from the calculated time (*Multiplier*) due to a high $d_{eff,L}$ combined with a high α, so AE declines for the larger particles.

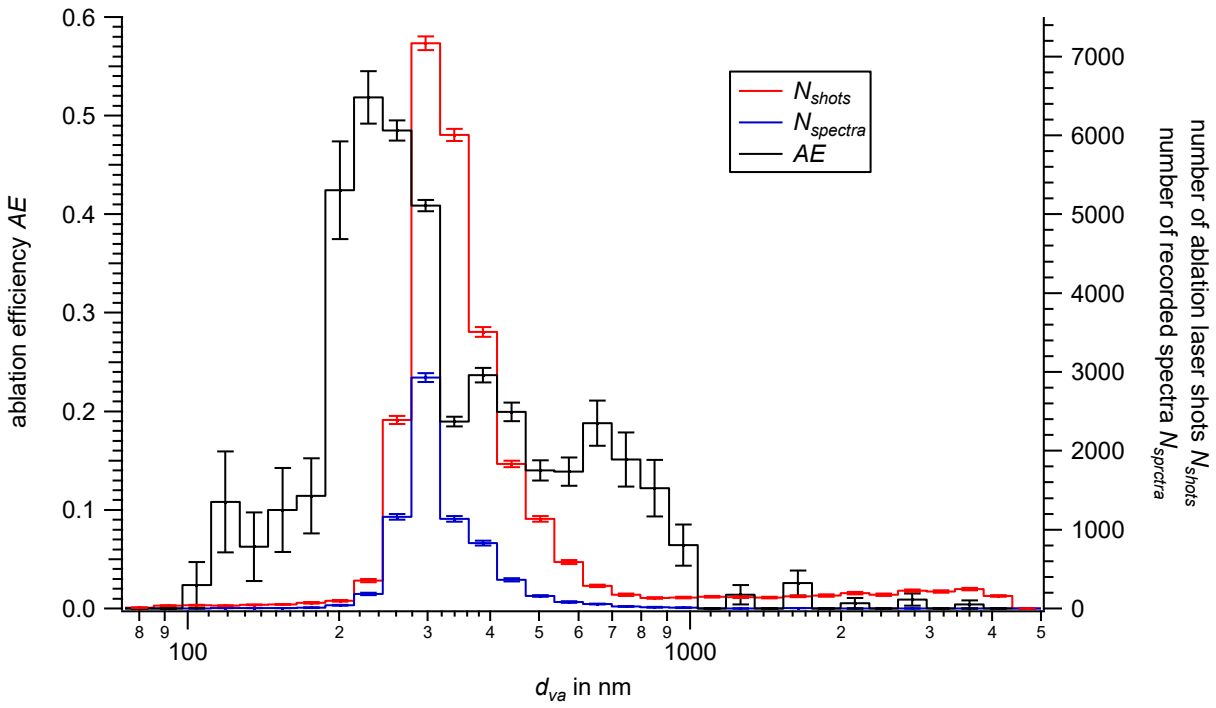

Figure 48: Ablation efficiency AE (black histogram, left axis), number of spectra (blue histogram, right axis) and the number of detected particles (red histogram, right axis) as function of particle size d_{va} for ambient urban aerosol in the city of Mainz, Germany. Only the spectra with size information within the calibrated size range were processed (see Section 4.2.2). Uncertainties of AE, uncertainties of the number of laser shots, and uncertainties of the number of recorded spectra are based on counting statistics (see Appendix B.1.10).

Beside the particle size, AE depends furthermore on the particle shape, charge, and the chemical composition of the particle as well as on the laser intensity of the ablation laser (Su et al., 2004; Moffet and Prather, 2009; Brands et al., 2011). In Brands (2009) the ablation efficiency is presented for various substances with the ALABAMA. Here, maximum ablation efficiencies between 21.5 % for mineral dust and 58.8 % for ammonium nitrate are stated. For ambient measurements the ablation efficiency is on average 10 % (Köllner, 2019).

Ambient measurements were also conducted with the A-ATOFMS and the LAAPTOF. From these, ablation efficiencies of ~30 % for particle sizes between d_a = 75 nm and d_a = 250 nm (Su et al., 2004) and ~58 % for a particle size of d_a = 300 nm (Gemayel et al., 2016) were achieved. These values are comparable with the here presented results.

4.4 Mass spectrometer performance of the ERICA-LAMS

In the following two sub-sections the performance of the ERICA-LAMS is described by presenting laboratory studies from sodium chloride (NaCl), ammonium nitrate (NH_4NO_3), benz[a]anthracene, and gold particle measurements. Single particle mass spectra of NaCl and NH_4NO_3 were used to show the performance of the m/z calibration with the evaluation software CRISP. Furthermore, it was investigated whether it is possible to ablate and ionize gold particles with the deployed ablation laser. Using lead- and tin-containing particles, the resolution of the ERICA-LAMS was determined.

4.4.1 Exemplary single particle mass spectra from laboratory tests

To assess on the performance of the ERICA-LAMS, NaCl, NH_4NO_3, gold particles, and benz[a]anthracene were tested in laboratory experiments. The *Setup A* is described in Section 4.2.1.1 (see also Figure 24). All mass spectra were recorded by a compact computer-based oscilloscope and were a-posteriori evaluated by the evaluation software CRISP (see Section 3.7.3). By that, they were converted to so-called stick spectra. To generate a stick spectrum, the raw spectrum is m/z-calibrated (converting sample number to a specific mass to charge ratio (m/z) value using Equation (23)) in CRISP using a wavelet scanning routine. Therefore, 20 data points of the raw spectrum left and right to the determined m/z value are summed up to generate an intensity value I_{stick} for this m/z value. In this way, an intensity value in the dimension of a peak area is obtained. Here, the intensity I_{stick} is given in mV·samples. The absolute intensity values are solely comparable to spectra which are generated in precisely the same way. As relative intensity values, i.e., spectral patterns, the stick spectra can be compared also with those from other mass spectrometers.

To distinguish between a valid signal and noise in the stick spectra, a detection limit (ion peak area threshold) of the ERICA-LAMS has to be determined. To determine the detection limit, i.e., the noise level, the data set of the first phase of the StratoClim campaign (Kalamata, Greece) was used. After mass calibration, the signal intensities for the usually unoccupied masses (m/z 2 up to m/z 6 for positive, m/z 2 up to m/z 11 for negative ions) were inspected. For this purpose, the normalized cumulative signal intensity distributions for each investigated m/z were calculated and the 99 % threshold determined according to Köllner (2019). The result was a threshold value of I_{stick} = 7 mV·samples for positive and negative ions (see Appendix B.14). Obtained signals with intensities above I_{stick} > 7 mV·samples are interpreted as signals above the noise level, i.e., valid signals. The detection limit in AMS instruments can also be determined by using three times the standard deviation of the signal from a filter measurement (e.g., Bahreini et al. (2003), Salcedo et al. (2006), and DeCarlo et al. (2006)). This method can be applied, besides other possible procedures (Drewnick et al., 2009) to determine the detection limit. Since CRISP may produce artifacts during data processing in the stick spectra, the detection limit cannot be reliably determined by this method. Therefore, this method is not applied for data provided by ERICA-LAMS. However, the 99 % threshold is a value very close to the value for three times the standard deviation of signals of unoccupied masses.

4.4.1.1 Sodium chloride (NaCl) and ammonium nitrate (NH_4NO_3) particles

As species that are present in the atmosphere NaCl and NH_4NO_3 particles were chosen for exemplary laboratory measurements (Ericsson, 1978; Nowak et al., 2010). Both species can be sufficiently well detected and it is possible to successfully ablate such particles. Furthermore, the natural isotopic abundance of the contained elements is known. Measuring pure substances permits to identify ions and fragment/cluster ions.

Figure 49 shows single particle raw mass spectra of a single NaCl particle (signal intensity I_{raw}) and the applied m/z calibration (signal intensity I_{stick}). Positive and negative ions were simultaneously detected by the bipolar ToF-MS of the ERICA-LAMS. The stick spectral lines coincide with the raw spectra. The signal at m/z +23 in the cation spectrum can be interpreted as Na^+ and at m/z +81 as $Na_2{}^{35}Cl^+$ with the corresponding isotopic signal for $Na_2{}^{37}Cl^+$ at m/z +83.

The spectral pattern (locations and relative intensities) of NaCl is comparable with results from another single particle mass spectrometer using a frequency quadrupled Nd:YAG laser for ablation (λ = 266 nm), e.g., the A-ATOFMS (Gross et al., 2000). In the anion spectrum the chlorine elemental peak at m/z -35 ($^{35}Cl^-$) shown with the corresponding isotopic signal at m/z -37 for $^{37}Cl^-$. Furthermore, the fragments and the corresponding isotopic signals for $NaCl_2^-$ (m/z -93 ($Na^{35}Cl_2^-$), -95 ($Na^{35}Cl^{37}Cl^-$) and -97 ($Na^{37}Cl_2^-$)) and $(NaCl)_2Cl^-$ (m/z -151 $(Na^{35}Cl)_2{}^{35}Cl^-$) and -153 ($(Na^{35}Cl)_2{}^{37}Cl^-$)) are present.

For NaCl, the fragment labels can be allocated to the stick spectra. By that the functionality of the ERICA-LAMS is proven.

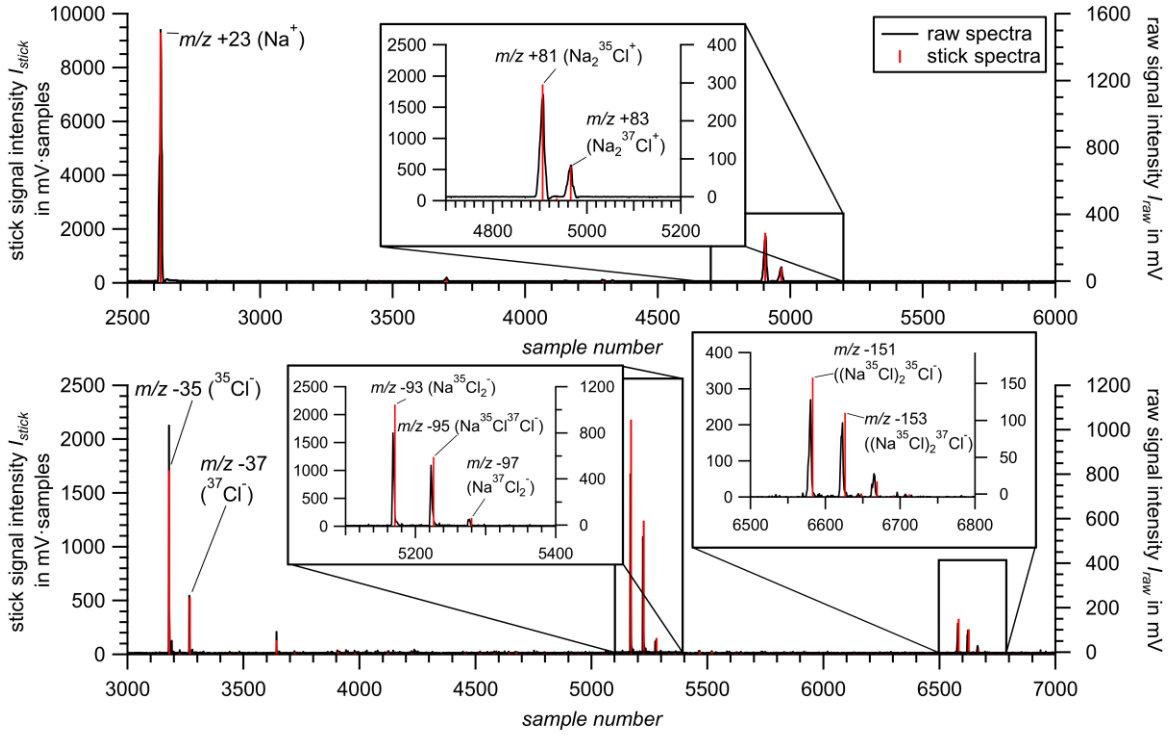

Figure 49: Laboratory generated ERICA-LAMS mass spectra: Stick mass spectrum (red sticks, left axis) and raw spectrum (voltage output versus sample number of the digitizer, 1.6 ns per sample, black line, right axis) of a laboratory generated sodium chloride particle. Top panel for cations, bottom panel for anions.

In the literature, the identified fragments for Na^+ (m/z +23), $Na_2{}^{35}Cl^+$ (m/z +81) with the corresponding isotopic signal for $Na_2{}^{37}Cl^+$ (m/z +83) can also be found for single particle mass spectrometers using λ = 266 nm (Figure 50, a) or λ = 193 nm (Figure 50, b) for particle ablation and ionization (Gross et al., 2000; Murphy et al., 2019).

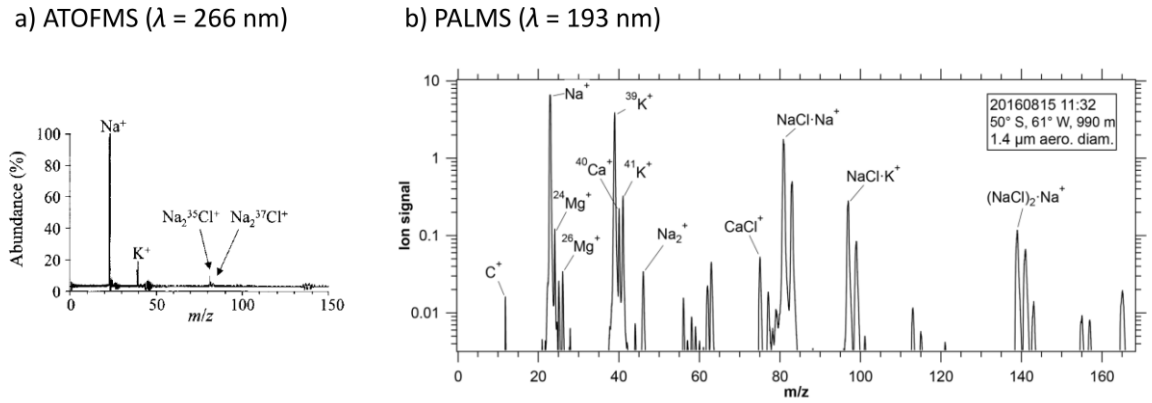

Figure 50: NaCl-containing single particle mass spectra from the literature: a) Laboratory generated single particle spectrum from a Na-enriched solution that was recorded by ATOFMS that uses a wavelength of λ= 266 nm for particle ablation. Reprinted with permission from Gross, D. S., Gälli, M. E., Silva, P. J., and Prather, K. A.: Relative Sensitivity Factors for Alkali Metal and Ammonium Cations in Single-Particle Aerosol Time-of-Flight Mass Spectra, Analytical Chemistry, 72, 416-422, doi: https://doi.org/10.1021/ac990434g, 2000. Copyright (2000) American Chemical Society. b) Spectrum of a as sea-salt classified particle that was recorded by PALMS that uses a wavelength of λ = 193 nm for particle ablation. Reprinted with permission (https://creativecommons.org/licenses/by/4.0/legalcode) from Murphy et al. (2019).

Figure 51 shows the single particle mass spectra as result of an m/z calibration for a pure ammonium nitrate particle as stick spectra. Here, the ions m/z +17 (NH_3^+) and +18 (NH_4^+) can be interpreted as ammonium and the ions at m/z +30 (NO^+), +46 (NO_2^+), -46 (NO_2^-), -62 (NO_3^-) as nitrate fragments. Furthermore, peaks appear at m/z -31, -125 and -188 that can be interpreted as ammonium nitrate cluster fragments (HNO^-, $(HNO_3)NO_3^-$ and $(HNO_3)_2NO_3^-$; Brands et al. (2011)).

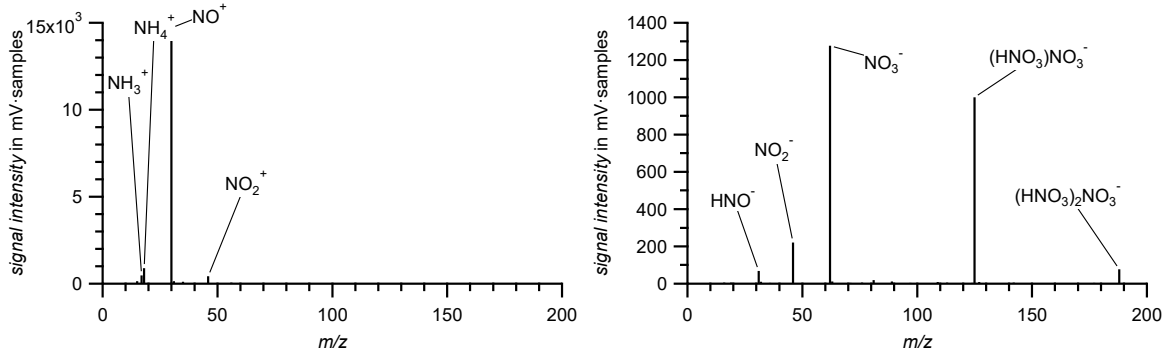

Figure 51: Laboratory generated ERICA-LAMS mass spectra (left: Cation, right: Anion) a laboratory generated ammonium nitrate particle.

The here presented fragments of sodium chloride, ammonium nitrate and the corresponding mass spectra are typical examples for what is used to evaluate the flight data in Chapter 5.

4.4.1.2 Gold particles

The sample inlet on the aircraft during the field deployment was gold-coated (see Section 3.8.3) to prevent chemical reaction on the metal surface (Dragoneas et al., 2020). The coating can also be used to identify particles that had wall contact during the sampling with the inherent possibility of introducing artefacts to the corresponding mass spectra. Such identified particles can either be ignored during data processing or used for an estimation of the number of particles that were touching and bouncing off from the inlet's surface. It has to be mentioned that a missing gold signature does not indicate that the sampled particle had no wall contact at all. In this case, however, the probability is considered very low that the particle will penetrate through the gold coating into the aluminum body

of the inlet, thereby creating aluminum signatures in the mass spectrum, which would be a sampling artifact. However, a single particle was detected that is assumed to be debris from the inlet coating (see Section 5.2.3.3). Gold does not generate a significant pattern in the mass spectrum up to m/z ±250. Due to a natural abundance of 100 % for the ^{197}Au isotope, the mass spectrum has to be extended up to at least m/z ±400 to identify the $^{197}Au_2^+$ signal at m/z +394 in the cation spectrum. Spencer et al. (2008) had shown that a genuine gold signal at m/z +197 in the anion spectrum is possible by using a light pulse of λ = 540 nm. In sulfate-containing or sulfuric acid coated particles, this peak can be interpreted as a cluster of $H(H_2SO_4)_2^-$.

To confirm that the ERICA-LAMS is able to identify gold signatures and to demonstrate their spectral pattern, gold spheres (d_{geo} = 200 nm and thus d_{va} = 3,860 nm; see Appendix B.2; Sigma-Aldrich, Inc.) were nebulized, dried, and measured in a dedicated laboratory experiment. The gold spheres were provided in a trisodium citrate buffer solution. In advance, this buffer solution was diluted by removing the supernatant aqueous phase above the gold precipitate and refilling it with purified water. For better results, this procedure was performed three times. Without this previous preparation of the suspension, the spectra were saturated by the sodium peak at m/z +23.

A typical bipolar spectrum recorded during the experiment is displayed in Figure 52. The Na^+-, K^+- and Ca^+-signals in the spectra result from the residual buffer solution. To confirm the signal on m/z +197 as Au^+ -cation, the mass spectrum was extended to view the Au_2^+-cation on m/z +394. In the negative spectrum, the signals are below the detection limit, so no characteristic peaks could be identified. Apparently, gold can be detected and distinguished from sulfate signals by the ERICA-LAMS. Thus, signals at m/z +197 and +394 can be used to identify gold fragment ions in the StratoClim data set (see Section 5.2.3.3).

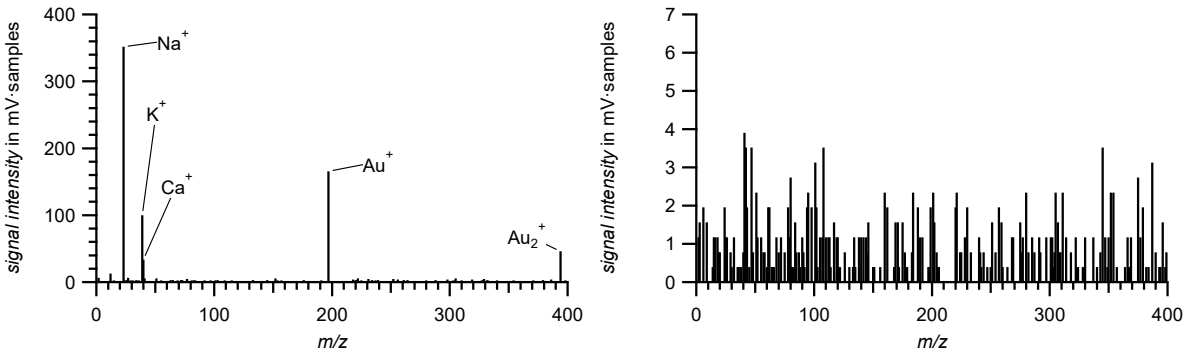

Figure 52: Laboratory generated ERICA-LAMS mass spectra (left: Cation, right: Anion) a laboratory generated gold particle. The signals of the anions are below the detection limit of 7 mV·samples.

4.4.1.3 Benz[a]anthracene particles

Another important particle type in the atmosphere is the class of polycyclic aromatic hydrocarbons (PAHs). PAHs are ubiquitous atmospheric pollutants which are well-recognized as carcinogenic, teratogenic, and genotoxic compounds. PAHs are released from incomplete combustion or pyrolysis of materials containing carbon and hydrogen, such as coal, oil, wood, and petroleum products. The sources can be natural or anthropogenic (Dat and Chang, 2017). Laboratory generated mass spectra of PAHs are rare in the literature. Since benz[a]anthracene (BaA) is known as a component of soot particles (Lima et al., 2005), this PAH type substance was tested with an example for single particle mass spectra shown in Figure 53. Clearly visible and typical for PAHs is the C_n^- and the C_nH_m-pattern in the cation and the anion spectra (Hinz et al., 1999). Also the molecular peak at m/z +228 (molecular weight of benz[a]anthracene M_w = 228 g mol^{-1}, NIST Chemistry WebBook, 2019), appears in the

spectrum (Silva and Prather, 2000). This shows the advantage of the λ = 266 nm ablation laser, which creates less fragmentation than a λ = 193 nm ablation laser (Brands et al., 2011).

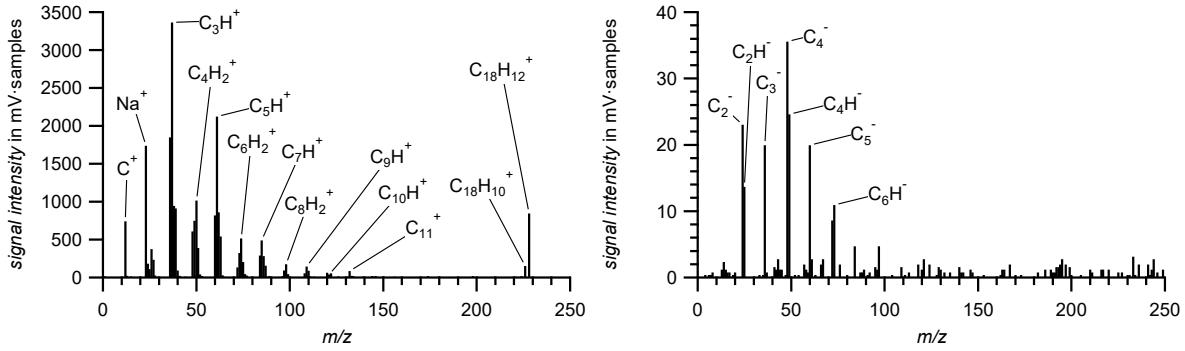

Figure 53: Laboratory generated ERICA-LAMS mass spectra (left: Cation, right: Anion) a laboratory generated benz[a]anthracene particle (d_{va} = 512 nm).

4.4.2 Resolution of the ERICA-LAMS mass spectra

The resolution R_{MS} is a measure for the performance of the mass spectrometer. It is defined as $R_{MS} = M/\Delta M$ (see Section 2.5). ΔM is determined by the FWHM of M. Thus, a larger resolution R_{MS} indicates a better separation of peaks in the mass spectrum. In addition, $M/\Delta M$ depends on the absolute value of M, i.e., the m/z value.

In Figure 54, details of two different raw cation spectra from two ambient aerosol particles are presented. Here the output voltage signal of the digitizer is displayed as function of the digitizer sample number (1.6 ns per sample). The trigger of the Q-switch delivers the start signal for the sample counting (see Section 3.7.3). The particles of the presented spectra were recorded during the StratoClim campaign (July and August 2017, (Bucci et al. (2020); see Chapter 5), at ground level at the airport of Kathmandu, Nepal. The signal intensities correspond to the isotopic abundance (Audi et al., 2003; *CRC Handbook of Chemistry and Physics*, 2018) of tin and lead. The occurrence of both species can be expected in a polluted environment as in Kathmandu, Nepal, and in particular at ground level of an operational airport.

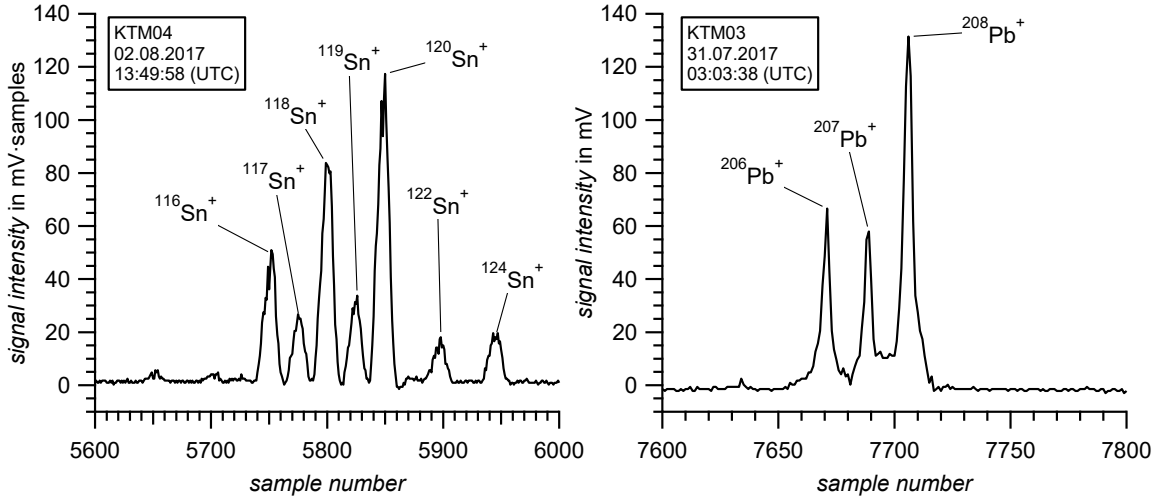

Figure 54: Details of cation raw spectra (voltage output against sample number of the spectrum, 1.6 ns per sample) of ambient particles in the boundary layer in Kathmandu, Nepal. Left: Tin isotopic pattern in spectrum of a particle recorded on ground level after landing at the hangar (flight KTM04, 02.08.2017, 13:49:58 UTC, 27.6950° N, 85.3627° E, d_{va} = 277 nm). Right: Lead isotopic pattern in spectrum of a particle recorded on the runway during take-off (flight KTM03, 31.07.2017, 03:03:38 UTC, 27.6858° N, 85.3541° E, d_{va} = 311 nm).

Out of these mass spectra the mass resolution R_{MS} of the ERICA-LAMS can be estimated to R_{MS} = 200 for positive ions of m/z 120 (left) and R_{MS} = 700 for m/z 200 (right). For negative ion spectra the mass resolution is about R_{MS} = 600 for both, m/z 100 and m/z 200.

The values of the resolution R_{MS} of other single particle mass spectrometers are comparable to the here presented ones. Brands (2009) states for the ALABAMA a value of R_{MS} = 200 for cations of m/z 108 and a value of R_{MS} = 600 for anions of m/z 120. The resolution of the A-ATOFMS (at m/z 165) is for both polarities R_{MS} = 600 (Gard et al., 1997). Without any specific m/z value, Gemayel et al. (2016) state for the LAAPTOF a R_{MS} of above R_{MS} > 600 for both polarities. The resolution for both ion polarities in the LAMPAS2 is typically in the range of R_{MS} = 300 (Trimborn et al., 2000).

4.4.3 Summary of the mass spectrometer performance of the ERICA-LAMS

To investigate the performance of the ERICA-LAMS, various types of known substances (NaCl, NH_4NO_3, gold, and benz[a]anthracene) were measured in laboratory experiments. All data were evaluated by the software CRISP and converted into stick spectra after a m/z calibration. Afterwards the detection limit (ion peak area threshold) was determined to 7 mV·samples for positive and negative species. Ammonium nitrate and sodium chloride particles were measured as test particles with compositions of particular atmospheric relevance. Mass spectra of these particle types are reported and can serve for comparison with other mass spectrometer using a wavelength of λ = 266 nm for laser ablation (Gross et al., 2000; Brands et al., 2011; Murphy et al., 2019). The comparison was successful and fragments/cluster labels could be allocated to the spectra according to the natural abundance. Furthermore, it was investigated, if gold particles are detectable and possible to ablate in the instrument. It was shown that to identify gold signals in the mass spectrum it has to be searched for the Au_2^+ peak, due to the lack of an isotopic pattern for gold. In the negative spectrum, pure gold signals do not show any characteristic peaks, so there is no room for misinterpretation with other fragments. Another measured particle type was benz[a]anthracene as a compound of PAH that also led to results that are comparable with other mass spectrometers (Silva and Prather, 2000).

Beside the proof of concept, the mass spectral resolution was determined by investigating the isotopic pattern of lead- and tin-containing particles. The result is a R_{MS} for positive ions of 200 (for m/z 120) and 700 (for m/z 200)). For negative ion spectra the mass resolution is about 600 for both m/z 100 and m/z 200.

Table 10 shows various parameters for some well described single particle mass spectrometers, such as the ALABAMA, the PALMS, the A-ATOFMS, the LAMPAS2, and the LAAPTOF in comparison to the ERICA-LAMS. Overall, the values of the determined parameters are comparable to the other instruments, especially to ALABAMA. The discussions and the references of the parameters of the other instruments can be found in the corresponding sections. However, the values of some of the parameters are not directly comparable with the values determined for the ERICA-LAMS, because the instrumental designs and methods of determination are different and the definitions of the parameters may differ from those presented here.

*Table 10: Comparison of the determined parameters with the parameters of other single particle mass spectrometers. The parameter τ_p is the pulse duration of the ablation laser, E_e is the ablation laser irradiance, and f_{rep} the repetition rate of the laser pulses. The discussions and the references of the parameters of the various instruments can be found in the corresponding sections (n/a: no applicable information found). References for ALABAMA: Brands (2009), Brands et al. (2011), and Köllner (2019). References for PALMS: Thomson et al. (2000), Lee et al. (2002), and Cziczo et al. (2006). References for A-ATOFMS: Gard et al. (1997), Su et al. (2004), and Pratt et al. (2009). Reference for LAMPAS2: Trimborn et al. (2000). References for LAAPTOF: Ahern et al. (2016), Gemayel et al. (2016), Marsden et al. (2016), Reitz et al. (2016), and Shen et al. (2018). * with newly developed aerodynamic lens (Clemen et al., 2020)*

		ERICA-LAMS	ALABAMA	PALMS	A-ATOFMS	LAMPAS2	LAAPTOF	Section
size range for particle detection in nm		174 – 3,173	270 -1,900 230-3,240*	~150 - 2,000	200 – 3,000	200 - 5,700	200 – 2,000	4.2.4
DE_{max} (max.)		100 %	35 % 100 %*	10 %	47.4 %	n/a	4.8 %	
λ detection in nm		405	405	532	532	532	405	4.1.2
$w_{0,dia}$ detection in µm		61 x 40	n/a	100 x 25	300	~30	51	
w_{part} detection in µm		100	n/a	~100	n/a	800	130	4.2.5
λ ablation in nm		266	266	193	266	337	193	4.1.3
E_{UV} in mJ		11	7	n/a	2	0.25	4	
τ_p in ns		6	6	2.5	5	3	8	
E_e in W cm^{-2}		$3.7 \cdot 10^9$	$3.7 \cdot 10^9$	$5 \cdot 10^9$	$3 \cdot 10^8$	$\sim 10^9$	$\sim 10^9$	
$w_{0,dia}$ ablation in µm		250	200	150	400	~30	~800 x ~600	
f_{rep} (max.) in s^{-1}		8	20	50	20	n/a	10	
w_{part} ablation in µm		60 - 480	300 - 700	n/a	340 - 380	n/a	n/a	4.2.5
AE	PSL	50 %	99.5 %	~95 %	> 80 %	n/a	94 %	4.3
	ambient	52 %	10 %	n/a	~30 %	n/a	~58 %	
α in mrad		0.1 - 2	n/a	8.7	n/a	n/a	n/a	4.2.5
TE (max.)		100 %	100 %	n/a	n/a	n/a	100%	
R_{MS} (max.)	Cations	700	200	n/a	600	300	>600	4.4.2
	Anions	600	600	n/a	600	300	>600	

4.5 Mass spectrometer performance of the ERICA-AMS

The aerosol mass spectrometer used here is in its properties and performance, as described above, very similar to the Aerodyne Inc. C-ToF-AMS (e.g., Drewnick et al. (2005) and Canagaratna et al. (2007)). This section presents the method of mass concentration determination by the ERICA-AMS, the determination of the Ionization Efficiency (IE), and the mass spectrometer resolution. The measurements with the ERICA-AMS presented in the following were conducted and evaluated by O. Appel, MPIC.

4.5.1 Determination of mass concentration by the ERICA-AMS

A detailed description of quantitative aerosol mass spectrometry can be found in Canagaratna et al. (2007). Data evaluation of ERICA-AMS measurements typically determines the mass concentrations of the aerosol species ammonium, nitrate, sulfate, organic and chloride. The separation of these aerosol species from the ensemble spectra is based on their fragmentation patterns (Allan et al., 2004). Only by this reproducible fragmentation, a quantitative determination of the mass concentrations of the different chemical species is possible. To determine the mass concentration C_s (in µg m^{-3}) of an aerosol species s from the ion signals, Equation (44) is used (see e.g., Canagaratna et al. (2007) and Schulz (2019)):

$$C_s = \sum_i I_{s,i} \cdot \frac{MW_{NO3}}{IE_{NO3} \cdot RIE_s \cdot CE} \cdot \frac{AB_{corr}}{\Phi_{ERICA} \cdot N_A} \cdot 10^{12} \quad (44)$$

Where $\sum_i I_{s,i}$ describes the sum of all ion fragments i of species s per second (in ions s^{-1}), MW_{NO3} the molecular mass of ammonium nitrate (MW_{NO3} = 62 g mol^{-1}), IE_{NO3} the ionization efficiency of nitrate (dimensionless), RIE_s the relative ionization efficiency of species s (dimensionless), CE the collection efficiency (dimensionless), AB_{corr} the air beam correction factor (dimensionless), Φ_{ERICA} the air volume sampling rate into the ERICA instrument (Φ_{ERICA} = 1.476 cm³ s^{-1}, see Section 3.2), and N_A the Avogadro's number. The factor 10^{12} is a dimensionless unit conversion factor.

The ionization efficiency IE_{NO3} is the number of ions detected per molecule introduced into the instrument (Drewnick et al., 2005). The factor IE_{NO3} can be determined by an appropriate calibration measurement (see Section 4.5.2).

The collection efficiency CE is a correction factor for possible particle losses within the instrument. These are in particular losses within the aerodynamic lens due to the transmission efficiency of the lens, due to insufficient particle beam focusing on the vaporizer, and due to particles bouncing off the vaporizer's surface (Huffman et al., 2005; Canagaratna et al., 2007). It has been shown that a value of CE = 0.5 is a good approximation for typical tropospheric aerosol (Canagaratna et al., 2007). However, there are approaches to make the bouncing and thus the parameter CE dependent on the chemical properties of the aerosol, i.e., acidity, ammonium nitrate mass fraction and relative humidity (Middlebrook et al., 2012).

The sum of the signals of N_2, O_2, Ar, and CO_2 is called Air Beam (AB). Since the concentrations of these species in air is constant, the air beam serves as a continuously measured internal standard. Fluctuations in the signal of the air beam indicate changes in the inlet flow or detection performance of the MCPs. For this, the air beam correction factor AB_{corr} is used for the conversion (Allan et al., 2003). The air beam correction factor is defined as:

$$AB_{corr} = \frac{I_{AB,calib}}{I_{AB}} \quad (45)$$

and is typically ~1. The air beam signal during calibration measurements is $I_{AB,calib}$ = 2.497·10^6 ions s^{-1} (averaged over four calibration measurements during StratoClim in KTM).

As described in Section 3.7.3.2, the ERICA-AMS data was evaluated by using the software named *Tofware* (Tofwerk AG). In the software, Equation (46) instead of Equation (44) is used to determine the mass concentration C_s of species s:

$$C_s = \sum_i I_{s,i} \cdot \frac{AB_{corr}}{f_{calib} \cdot \Phi_{ERICA} \cdot RIE_s \cdot CE} \tag{46}$$

Here, f_{calib} is the calibration factor, defined (in ions pg^{-1}) as:

$$f_{calib} = \frac{IE_{NO3} \cdot N_A}{MW_{NO3} \cdot 10^{12}} \tag{47}$$

Equation (47) contains the Avogadro's number N_A, the molecular mass of nitrate MW_{NO3} and the dimensionless unit conversion factor 10^{12}. Typically, the value for f_{calib} is around 2,000 ions pg^{-1} when running the instrument with a filament emission current of 1.6 mA and a ToF extraction frequency of 50 kHz.

As in the commercial AMS from Aerodyne Inc., each raw spectrum is converted into a stick spectrum by integrating over a time interval corresponding to each m/z according to the m/z calibration. The m/z calibration is performed as a six-point calibration using Equation (48) for each *buff* (definition for *buff* see Section 3.7.3.2). Typical values for the parameters are: A_{tof} ~ -53.619, B_{tof} ~ 679.13, and C_{tof} ~0.4991. The adopted isotopes are: CH^+, O_2^+, $^{182}W^+$, $^{184}W^+$, $^{186}W^+$ and SO_2^+ (see Table 11). The range between the integration regions is used to estimate the baseline, which is then subtracted from the peaks, respectively.

$$t_{tof} = A_{tof} + B_{tof} \cdot \left(\frac{m}{z}\right)^{C_{tof}} \tag{48}$$

Table 11: Isotopes and corresponding m/z values used for ERICA-AMS m/z calibration

isotope	m/z
CH^+	13.0078
O_2^+	31.9898
SO_2^+	63.9619
$^{182}W^+$	181.948
$^{184}W^+$	183.951
$^{186}W^+$	185.954

In Figure 55 an example of an ambient aerosol average spectrum is displayed (hardware specifications see Section 3.7.3.2). It was recorded during the fifth research flight in Kathmandu, Nepal (KTM05, 04.08.2017, 06:04:52 – 06:09:52 UTC), during the StratoClim field campaign (see Section 5.2.2). In the left panel, the integrated signals at open and closed shutter position as reference for the residual material in the vacuum are shown. The calculated difference of the shutter open signal and shutter closed signal is displayed in the right panel. Here the air beam peaks (m/z 28 (N_2^+), m/z 32 (O_2^+), m/z 40 (Ar^+)) as well as the most prominent aerosol peaks, in this case fragments of nitrate (m/z 30 (NO^+), m/z 46 (NO_2^+)) and sulfate (m/z 48 (SO^+), m/z 64 (SO_2^+)), are labeled.

The software then uses a so-called fragmentation table to attribute the several m/z-peaks to certain species (e. g., nitrate, sulfate, ammonium, organics, and chloride). The fragmentation table is similar

to the one used in the widespread analysis software SQUIRREL (see e.g., Allan et al. (2004)) with some instrument specific modifications. By a calibration with a test aerosol of ammonium nitrate, the ionization efficiency (IE, see Section 4.5.2) and thus the calibration factor f_{calib} can be determined. For quantitative measurements the single ion signal intensity SIS has to be known. Therefore, a manually operated program (*SingleIon.exe*, Tofwerk AG) determines the SIS before any measurement series, for instance for campaign flights. The acceleration voltage of the ToF-MS is set to obtain a SIS value of around 0.8 mV·ns. By that, the amount of one particular ion fragment of the aerosol species s I_s (in ions s^{-1}) can be calculated from the SIS value (in mV·ns), the extraction frequency $f_{extraction}$ = 5·10^4 s^{-1} and the measured signal intensity I_{AMS} (in mV·ns) as sum over all extractions k:

$$I_s = \sum_k \frac{I_{AMS,k}}{SIS} \cdot f_{extraction} \tag{49}$$

Using Equations (46), (47), and (49), the raw signal determined by the ERICA-AMS can be converted into a quantitative measure of an aerosol mass concentration C_s, taking the calibration measurements, device-specific and substance-specific constants, and the Avogadro's number into account.

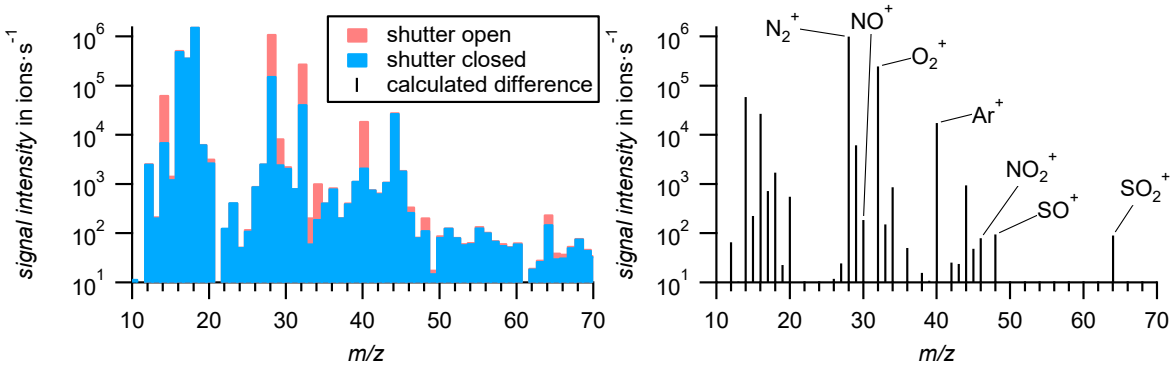

Figure 55: Example I of an ambient aerosol average spectrum (KTM05, 04.08.2017, 06:04:52 – 06:09:52 UTC). Left: The integrated signal intensities at open (red) and closed (blue) shutter position. Right: The calculated difference of open-closed from the left spectrum. The most prominent air and aerosol peaks are labeled (air beam peaks (m/z 28 (N_2^+), m/z 32 (O_2^+), and m/z 40 (Ar^+)), fragments of particulate nitrate (m/z 30 (NO^+), m/z 46 (NO_2^+)), and fragments of particulate sulfate (m/z 48 (SO^+), m/z 64 (SO_2^+)).

It was found that the air beam signal I_{AB} (sum of the air beam relating signals) is around 5 times higher than in comparable AMSes during deployment (Personal communication: O. Appel, MPIC, 2020). The reason is a relatively large skimmer directly after the aerodynamic lens in the first pumping stage (see Figure 13). This skimmer was designed for the single particle mass spectrometer LAAPTOF, where a wide opening ease the particle beam adjustment to the ablation laser focus. A high air beam value results in a high detection limit value for the organic fraction in the ERICA-AMS, since both are linked via the fragmentation table (Allan et al., 2004). To reduce the air beam signal, the current skimmer was replaced with a skimmer with a smaller hole in preparation for the ACCLIP (Asian summer monsoon Chemical and CLimate Impact Project) field campaign in summer 2021.

Detection limits are determined with signal fluctuations during a blank measurement using a particle filter in front of ERICA. According to for example Bahreini et al. (2003), the detection limit is defined as 3 times the standard deviation σ of the fluctuating signal. The detection limit decreases, i.e., the instrumental performance improves, with pumping time. After a pumping time of a few days and applying an averaging interval of t = 10 s, with the ERICA-AMS, a detection limit can be achieved of 0.1 µg m^{-3} for nitrate and 0.05 µg m^{-3} for sulfate, respectively (Personal communication: O. Appel,

MPIC, 2019). For other C-ToF-AMSes from Aerodyne Inc., minimum detection can reach limits for nitrate and sulfate values around 0.003 µg m^{-3} for an averaging interval of t = 30 s (Drewnick et al., 2009). For longer averaging times t, the detection limit will decrease with $1/\sqrt{t}$. The detection limit is significantly larger than for other C-ToF-AMSes, due to the low IE_{NO3} value and the short averaging interval t. Furthermore, a high air beam signal (I_{AB} = 2.5·10^6 ions s^{-1}) leads to a higher detection limit value for nitrate than for sulfate. Typical values of another C-ToF-AMS from Aerodyne Inc, achieves an air beam signal I_{AB} of around 4 – 6·10^5 ions s^{-1} (Personal communication: K. Kaiser, MPIC, 2020).

4.5.2 Ionization efficiency of the ERICA-AMS

To convert the total signal intensity of the different species into a sampled mass concentration, an ionization efficiency (IE) calibration has to be performed, ideally several times during a field campaign. The ionization efficiency is the number of ions detected per molecule introduced into the instrument (Drewnick et al., 2005). Currently, three different methods are commonly used. The first is a single particle-based method, using the chopper and the so-called Brute Force Single Particle (BFSP) mode of the AMS, to determine the signal intensity for a single particle. The second method is the event trigger single particle method. Here, the signal intensity of a single particle is detected with a fast acquisition card. The third method is based on a particle ensemble measurement, where the particles are size selected and measured by the AMS with a CPC used as reference in a setup similar to *Setup B* in Figure 24 (see Section 4.2.1.1). For ERICA-AMS, the latter method is applied, due to the lack of a chopper in the ERICA instrument. For this, the mass concentration of ammonium nitrate particles, size-selected by a DMA (d_{mob} = 350 nm), was measured by the ERICA-AMS. To consider a possible offset the signal during a filter measurement was subtracted. Taking the mass flow into the instrument into account the signal can be transferred into a mass concentration. The IE of nitrate IE_{NO3} is defined as ratio of the average number of determined ions per nitrate particle IPP_{NO3} and the average number of molecules per nitrate particle MPP_{NO3} (Hings, 2006):

$$IE_{NO3} = \frac{IPP_{NO3}}{MPP_{NO3}} \tag{50}$$

This parameter is included in the definition of the calibration factor f_{calib} (see Equation (47)).

Using a DMA for size selection, the size of the particles introduced into the instrument is known. By that, the average number of molecules per nitrate particle MPP_{NO3} can be calculated:

$$MPP_{NO3} = \frac{S \cdot N_A \cdot f_{NO3} \cdot \rho_{p,AN} \cdot {}^{\pi}/_{6} \cdot \left(\left({d_{mob}}^3 \cdot f_{SC} \right) + \left({d_{mob,DC}}^3 \cdot f_{DC} \right) \right)}{MW_{NO3}} \tag{51}$$

Here, d_{mob} is the electrical mobility diameter of the calibration particles (typically d_{mob} = 350 nm), $\rho_{p,AN}$ is the density of ammonium nitrate ($\rho_{p,AN}$ = 1.725 g cm^{-3}; see Appendix B.2), S is the Jayne shape factor that corrects for the actual particle density and shape (S = 0.8; see Appendix B.2; DeCarlo et al. (2004)), f_{NO3} is the NO_3 mass fraction in NH_4NO_3 (f_{NO3} = 0.775; see Hings (2006)), MW_{NO3} is the molecular weight of nitrate (MW_{NO3} = 62 g mol^{-1}), and N_A is the Avogadro constant (N_A = 6.02·10^{23} mol^{-1}). To account for the singly and doubly charged particles the parameters f_{SC} and f_{DC} are used (f_{SC} = 0.982 and f_{DC} = 0.018; see Section 4.2.3.3 and Appendix B.10).

The average number of ions per particle IPP_{NO3} can be determined from the measured nitrate signal, i.e., the sum of the nitrate fragment ions i, termed $\sum_i I_{NO3,i}$ (in ions s^{-1}), the particle number concentration $\bar{c}_{ref}$ (in particles cm^{-3}), and the volumetric inlet flow rate Φ_{ERICA} = 1.476 cm³ s^{-1} according to Hings (2006):

$$IPP_{NO3} = \frac{\sum_i I_{NO3,i}}{\bar{c}_{ref} \cdot \Phi_{ERICA}} \quad (52)$$

Before, during, and after the StratoClim Asian monsoon phase in Kathmandu, Nepal (see Section 5.2), four IE calibration measurements were conducted (see Table 12). The result for the calibration factor f_{calib} was in average f_{calib} = 1,965 ions pg^{-1}. In addition, the relative ionization efficiency (RIE) of ammonium RIE_{NH4} was determined based on measurements of ammonium nitrate particles and the relative ionization efficiency for sulfate RIE_{SO4} was determined based on measurements of ammonium sulfate particles according to Canagaratna et al. (2007). The averaged results are RIE_{NH4} = 4.368 and RIE_{SO4} = 0.972.

Table 12: IE calibration measurements for the StratoClim Asian monsoon phase in Kathmandu, Nepal. Presented are the dates of the measurement, the determined values for IE_{NO3}, f_{calib}, RIE_{NH4}, and RIE_{SO4} as well as the average values, the 1σ standard deviation and the relative uncertainties Δ^{rel}. In Kathmandu, Nepal, no ammonium sulfate calibration measurement was conducted.

Date	IE_{NO3}	f_{calib} in ions pg^{-1}	RIE_{NH4}	RIE_{SO4}	notes
29.06.2017	1.94·10^{-7}	1883	4.420	1.073	Mainz, before campaign
28.07.2017	2.01·10^{-7}	1956	4.361	n/a	Kathmandu, during campaign
08.09.2017	2.06·10^{-7}	2005	4.379	0.913	Mainz, after campaign
08.09.2017	2.07·10^{-7}	2014	4.312	0.931	Mainz, after campaign
	2.02·10^{-7}	1965	4.368	0.972	Average
	6.18·10^{-9}	60	0.045	0.088	1σ standard deviation
	0.03	0.03	0.01	0.09	Δ^{rel}

The default RIE value of RIE_{org} = 1.4 was used for organic compounds and for nitrate RIE_{NO3} = 1.1 was adopted (Canagaratna et al., 2007).

4.5.3 Resolution of the ERICA-AMS mass spectra

Analogously to the considerations for ERICA-LAMS the width of each mass peak is associated with a resolution $R_{MS} = M/\Delta M$. The data evaluation software *Tofware* displays a graph showing the resolution for the largest peaks in the mass spectrum. The acquired mass resolution of R_{MS} = 800 at m/z of 200 is comparable to the values of R_{MS} = 800 from typical commercial C-ToF-MS instruments (DeCarlo et al., 2006). The recorded data points and the fitting curve conducted by *Tofware* are presented in Figure 56.

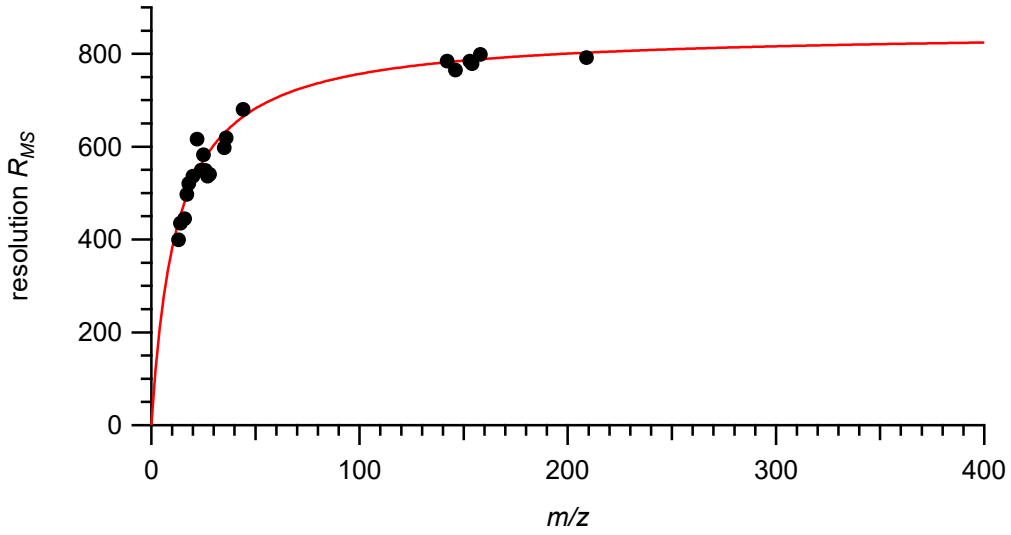

Figure 56: Resolution R_{MS} of the ERICA-AMS as function of m/z, fitted through the values from the largest peaks.

4.5.4 Interaction between the ERICA-LAMS and the ERICA-AMS

The serial assembly of the two instrumental parts lead to some interactions. Since the ERICA-LAMS is upstream in the particle beam, it is obviously unaffected by the ERICA-AMS. However, particles which are ablated in the ERICA-LAMS will be missing in the total mass of the ERICA-AMS.

In the following, the losses are estimated for two extreme cases, first very high, second very low particle number concentrations, during ambient aerosol sampling.

During laboratory and ambient aerosol measurements in the Planetary Boundary Layer (PBL), usually a particle number concentration over 100 cm^{-3} is detected by the detection units of the ERICA-LAMS. That leads to a maximum of 8 possible laser shots per second, due to the idle time of the ablation laser (see Section 3.4.1). Considering a theoretical maximum ablation efficiency of 100 % and a volumetric flow rate of Φ_{ERICA} = 1.476 cm^3 s^{-1}, losses around 5.4 % result (see also Section 3.5.1). This is a conservative estimation since some of the ablated particles would not have been detected by the ERICA-AMS due to their composition of refractory material. Also, small particles (d_{va} < 100 nm, see Section 4.2.4) cannot be detected by the detection units and will not lead to any losses at the ERICA-AMS. In these circumstances the losses introduced by the laser ablation are negligible for measurements at high particle number concentrations.

Low particle number concentrations are expected in pristine regions, like Arctic boundary layer during summertime. Here, particle number concentrations exceed rarely 5 cm^{-3} (Köllner et al., 2017) in the detectable size range. Considering the volumetric flow rate into the instrument, around 7 particles per second would be detected by the detection units. Due to a non-idle ablation laser, with a repetition rate of maximum 8 s^{-1}, the laser will shoot on almost every single particle. Theoretically, this can result in a loss of 100 % of particles for the ERICA-AMS. In practice, the ablation efficiency AE (see Section 4.3) is lower than unity. However, the ablation efficiency cannot be used to estimate the losses of the non-ablated particles. The reason is that the ablation efficiency might not be lower than unity because of the failure of the laser pulse when it hits the particle, but because of the ionization efficiency within the LDI process (see Section 2.3). For the same reasons as discussed above, this is a conservative estimate.

Apart from these losses due to the ablation of some particles, other loss processes also can become important. In the laboratory all particles can be charged especially if they come from particle generators involving DMAs (Forsyth et al., 1998; Kulkarni et al., 2011). As pointed out in Section 3.4.2 the flight path of these charged particles is affected by an electric field, such as the acceleration field (high voltage extraction) of the ERICA-LAMS in the ablation region. Here, charged particles get deflected when flying towards the ERICA-AMS vaporizer.

Also, atmospheric aerosol consists of charged particles. Since the atmospheric charge distribution is variable and can be size-dependent (Kulkarni et al., 2011), losses due to particle charges cannot be compensated for in the ERICA-AMS. To reduce such losses, the electric field of the ERICA-LAMS ion extraction is solely applied for a time interval of 10 ms, switched by HV switches, when a particle is within the ablation region (see Section 3.4.2). That keeps the losses in the lower percent range (see above) for high particle concentrations, because the ablation laser does not fire more than 8 times a second and particles can be in maximum deflected for only 80 ms per second. The deflection caused by the electric field depends on the particle size and charge and can be of the order of the vaporizer width. That means, not all charged particles will be lost even during application of the electric field. During the field deployment in Kalamata, Greece (see Section 5.1), the HV switches were not implemented yet. Here, the effect was observed for the first time after several IE calibrations lead to unreasonable mass concentration measurements with the ERICA-AMS. The problem was solved after implementing the HV switches (see Section 5.1.3). With this set up, in the future a measurement mode can be developed, where the amount of charged particle concentration might be estimated. For this the HV switches (see Section 3.7.2.4) would turn the electric field on and off alternately. Meanwhile, the ERICA-AMS would measure continuously the aerosol mass concentration. By calculating the difference, the amount of charged aerosol might be determined.

For low number concentrations of the ambient aerosol or a higher repetition rate of the ablation laser alternative sampling strategies have to be developed. For instance, the ERICA-LAMS could be switched off for a defined time interval of a few seconds to measure only the aerosol mass concentration with the ERICA-AMS. In another defined time interval, the ERICA-LAMS is switched on again for a few seconds. In this way, undistorted mass concentrations and single particle mass spectra would be obtained alternately. Such a feature, which automatically changes modes, is not yet implemented in the ERICA, but can be part of further instrumental development.

4.5.5 Summary of mass spectrometer performance of the ERICA-AMS

For data evaluation of the ERICA-AMS, the software *Tofware* is used. As in the commercial AMS, the raw spectra are converted into stick spectra by integrating over a time interval corresponding to one m/z each according to a six-point m/z calibration. By a calibration measurement with ammonium nitrate particles (usually d_{mob} = 350 nm), the ionization efficiency IE_{NO3} or f_{calib} can be determined. To convert a measured signal intensity I_{AMS} into the amount of one particular ion fragment I_S, also the single ion signal intensity SIS has to be determined and the extraction frequency $f_{extraction}$ has to be considered.

After these calibration measurements, the peak heights $I_{s,i}$ can be turned into a quantitative measure of the aerosol mass concentration for the different aerosol species C_s (ammonium, nitrate, sulfate, organics, and chloride) taking the calibration factor f_{calib}, volume flow into the instrument Φ_{ERICA}, the RIE of the species s RIE_s, the collection efficiency CE, and the air beam correction factor AB_{corr} into account. The detection limit (three times σ) was calculated by averaging the signal during a filter

measurement over t = 10 s to 0.10 µg m^{-3} for nitrate and 0.05 µg m^{-3} for sulfate. The by *Tofware* acquired mass resolution R_{MS} = 800 is comparable to other commercial C-ToF-MS instruments.

For the interaction of the ERICA-LAMS and the ERICA-AMS, the influences of the losses on ERICA-AMS mass concentration in two extreme cases, high and low particle number concentrations, were estimated, where the losses are negligible except under pristine conditions. To reduce losses by charged particles at the ERICA-AMS due to the electric field in the ERICA-LAMS ablation region, HV switches were implemented that generate an electric field only during ion extraction synchronously to the ablation laser pulse.

5 In-field performance during first aircraft measurements

The main goal of this Ph.D. thesis project was to design, build, and characterize ERICA (with emphasis on the ERICA-LAMS part), and to implement the instrument in the high-altitude research aircraft M-55 *Geophysica*. The analyses of the research flight data merely serve to provide a proof of concept for ERICA, as well as to document its feasibility and performance. As consequence, the scientific results of the field deployments of ERICA during StratoClim are not treated in detail and depth in the thesis as this is beyond its scope. However, a few key results from the ERICA-LAMS and also the ERICA-AMS are presented here with respect to the scientific context of the StratoClim project. The analyses for ERICA-AMS were performed by O. Appel (MPIC) and supported by the author.

The first in-field deployment of ERICA was during the StratoClim campaign (e.g., Rex et al. (2016), Brunamonti et al. (2018), and Bucci et al. (2020)) and was performed in two phases. The first phase took place in Kalamata, Greece, in August and September 2016 and was meant for the ERICA instrument as a test phase for the main field deployment in Kathmandu, Nepal, in July and August in 2017. First results of this campaign and its phases are presented in this chapter. The data sets of both phases were treated individually during evaluation. It can be noted that the first flight in Kalamata was the very first time that both polarities were measured for single particle mass spectra between 15 km and 20 km altitude in the stratosphere. Also, it was the first time that an AMS instrument was successfully deployed at such high altitudes.

5.1 Proof of concept: StratoClim mid-latitude phase in August/September 2016

The mid-latitude phase in 2016 of the StratoClim campaign was the first deployment of the ERICA instrument on *Geophysica* and was meant to be an operational test for the Asian monsoon phase one year later. The aim was to test that the instrument is able to operate continuously and autonomously during research flights under the ambient conditions at ground level and up to 20 km altitude. Furthermore, it is remotely controllable via a satellite communication (Section 3.8.1) during a research flight. Wherever possible, the recorded mass spectra were compared with results from other field campaigns, for which similarly working instruments were used.

The test phase took place in Kalamata, Greece, in the mid-latitudes at the Mediterranean Sea in August and September 2016. Base for this part of the campaign was the Kalamata International Airport (KLX; 37.07°N, 22.03°E), approximately 7 km west-northwestern to the city of Kalamata. In this phase, overall three research flights were performed. ERICA-LAMS recorded a total of 12,047 single particle mass spectra during the three flights while ERICA-AMS was operating continuously without interruptions or technical problems. In Table 13, the ambient conditions during the research flights and under which it is possible to measure with ERICA, such as GPS altitude, ambient pressure, and ambient temperature, are listed individually for each measurement flight. The altitude h_{amsl} is the actual elevation above mean sea level (amsl) determined by GPS. Overall, the altitude h_{amsl} ranged from 8 m to 20,239 m, the ambient pressure p_{stat} ranged from 56.0 hPa to 1,015.3 hPa, and the ambient temperature T_{out} from -72.7 °C to 32.0 °C (outside of the pressurized container; see Section 3.8.3). All data of the ambient conditions and the flight times that are listed in Table 13 were provided by the aircraft operation company MDB via the UCSE (see Section 3.8.4). The time series of the altitude, the ambient pressure, and temperature are provided in Appendix C.1. In total 12,047 single particle mass spectra were recorded during this test field deployment.

Table 13: Overview of the ambient conditions during the research flights in Kalamata, Greece. Listed are the flight number, the times, the maximum GPS altitude h_{amsl}, the ambient pressure p_{stat} range, the ambient temperature T_{out} range, and the number of recorded single particle mass spectra individually for each research flights during the mid-latitude phase of StratoClim 2016. The data of flight times, the altitude h_{amsl}, the ambient pressure p_{stat}, and the ambient temperature T_{out} were provided by UCSE.

Flight	**Date**	**Time (UTC)**	**Number of recorded spectra**	**max. h_{amsl} in m**	**p_{stat} in hPa**	**T_{out} in °C**
KLX01	30.08.2016	08:07:00 – 12:08:42	3,329	18,276	77.8 – 1,012.7	-71.6 – 31.7
KLX02	01.09.2016	06:28:27 – 10:56:22	6,314	20,030	58.5 – 1,015.3	-72.7 – 32.0
KLX03	06.09.2016	06:48:51 – 10:23:39	2,404	20,239	56.0 – 1,009.6	-71.7 – 25.5
Total (*KLX data set*)			12,047			

The implementation of the ERICA instrument design in its final configuration (Chapters 3 and 4) was the result of improvements after this test phase (see Section 5.1.3). During this test phase, in contrast to the conceptual description in Chapter 3, only two TMPs (SplitFlow 270 and HiPace® 80, both Pfeiffer Vacuum GmbH) were implemented because the vacuum pressures they produced were sufficient for the measurement operation. Furthermore, the HV-switch (Section 3.4.2) was not implemented yet and during LPM (Section 3.8.2) the vaporizer and the filament of the ERICA-AMS were not powered yet. Also, a different aerodynamic lens (LPL-2.5 from AeroMegt GmbH, see Shen et al. (2018)) and another O-ring type in the CPI (Section 3.2) were used. Thus, the particle beam characteristics presented in Sections 4.2.4 and 4.2.5, such as detection efficiencies, particle beam widths, particle beam divergence and transmission efficiencies cannot be applied for the mid-latitude phase. Due to timing issues of the communication between the TC and the acquisition software, the assignment of the determined *Upcount* values (see Section 3.7.3.1) to the single particle mass spectra failed. The problem was fixed immediately after the mid-latitude phase. Therefore, no calibrated particle size data and no information on measurement efficiencies are available for this test campaign. However, the obtained single particle mass spectra can provide information about the chemical composition of the detected aerosol particles.

Figure 57 shows the flight tracks of the three research flights performed by M-55 *Geophysica*. The major scientific aim of the flight patterns was to measure the Asian Monsoon outflow approaching from the east. Thus, the flight tracks were located towards the East from KLX. The flight tracks of each individual research flight are provided in Appendix C.1.

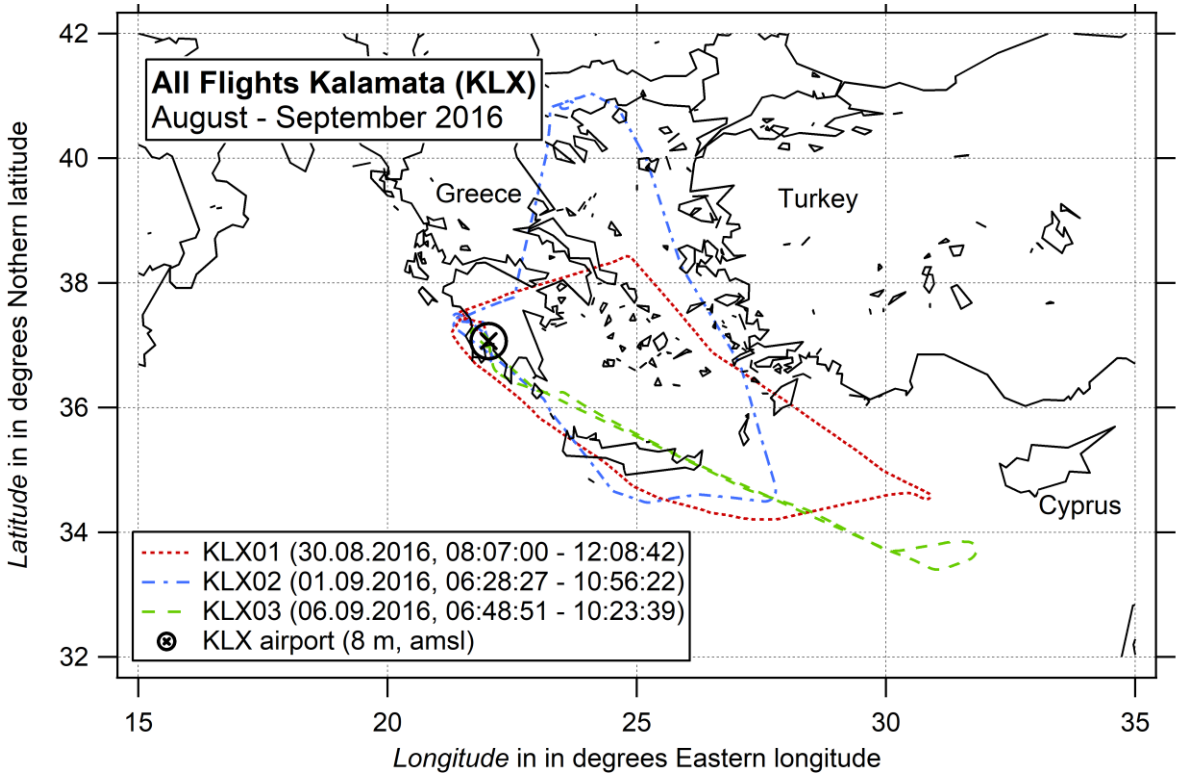

Figure 57: Flight tracks of the three research flights performed by Geophysica during the mid-latitudes phase of StratoClim 2016. The flight times, the number of recorded mass spectra and the conditions during the flights (max. h_{amsl}, p_{stat}, and T_{out}) are listed in Table 13 for each flight.

Figure 58, left panel, shows the vertical profile of the rate of recorded single particle mass spectra f_{spec} for all three research flights. The number of all recorded mass spectra $N_{spectra}$ was normalized to the retention time t_{flight} of the research aircraft in the respective altitude sections (bin size 500 m):

$$f_{spec} = \frac{N_{spectra}}{t_{flight}} \tag{53}$$

Figure 58 demonstrates the stable and steady performance (f_{spec} between 0.2 spectra s^{-1} and 0.5 spectra s^{-1}) of the instrument over the altitude range between 5,000 m to the ceiling height of 20,239 m. In the altitude range from ground level to 4,500 m, the rate f_{spec} is most likely higher due to the high particle number concentration in the boundary layer. The right panel in Figure 58 depicts the number of recorded mass spectra in the same altitude sections as for f_{spec}. The enhancement of recorded spectra in altitudes above 10,000 m results from the long flight duration. The boundary layer is visible in altitudes below 4,500 m. This graph and the underlying analyses demonstrate that ERICA-LAMS generated particle mass spectra over the entire altitude range from the ground to the aircraft's ceiling in the stratosphere irrespective of the ambient conditions.

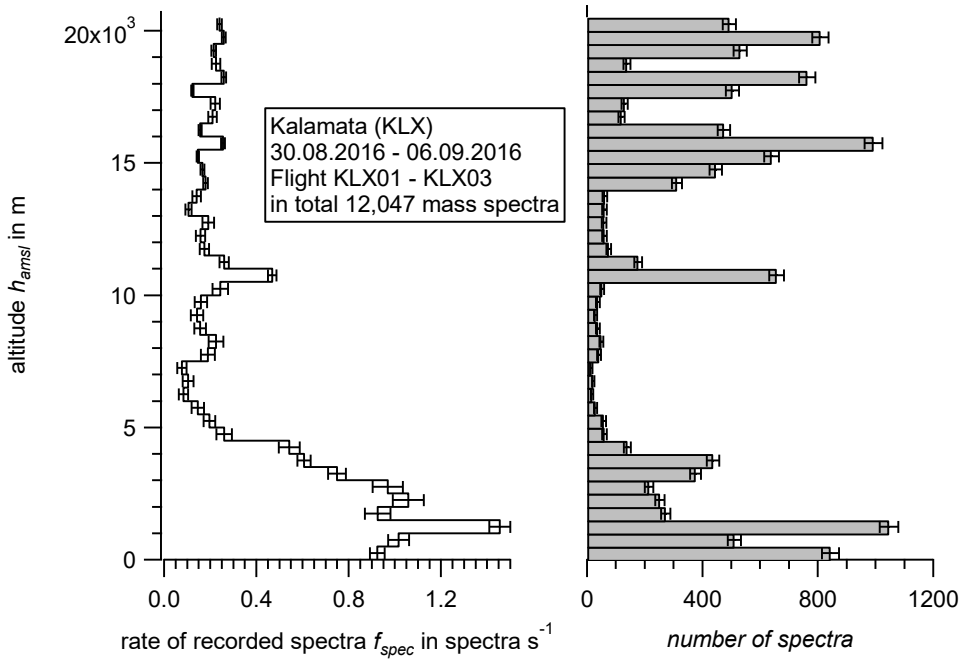

Figure 58: Vertical profile of the rate of recorded single particle mass spectra f_{spec} for all three research flights (left panel) and the number of recorded single particle mass spectra within all three flights (right panel). To calculate f_{spec}, the number of recorded mass spectra was normalized to the retention time of the research aircraft in the respective altitude sections (bin size 500 m). The uncertainties are based on counting statistics (see Appendix C.2.1).

5.1.1 Data preparation and particle type identification for the ERICA-LAMS by the clustering algorithm method

First of all, the raw binary-files of all flights recorded by the oscilloscope (in total 12,047) in a so-called b16-file format were converted to a so-called pbf-file format that can be read out by the evaluation software CRISP (see Section 3.7.3.1). For this, the *LAAP spectrum batch converter*, a GUI program, was used. The following procedure is the same routine as described for instance by Schmidt et al. (2017) to generate a stick spectral data set. First, all pbf-files were loaded in CRISP. Then, each raw spectrum was m/z calibrated (see Section 4.4.1) using the values listed in the Appendix C.3.1, Table 34, and, finally, converted into stick spectra for each individual particle.

To handle this high number of single particle mass spectra, an automated sorting routine (clustering algorithm) was used to pre-sort the mass spectra according to their spectral patterns. The resulting groups of mass spectra are named cluster. A commonly used clustering algorithm is the *k-means* algorithm (Hartigan and Wong, 1979; Rebotier and Prather, 2007). A detailed description of the implementation of the *k-means* algorithm in CRISP and its performance are parts in the Ph.D. theses of Klimach (2012) and Roth (2014) and can be found there. With this algorithm the number k of the clusters into which the data set is sub-divided is pre-defined. For the selection of the start clusters, the first particle spectrum in memory is used as a start reference. The other mass spectra are then checked one after the other until the specified distance criterion between the mass spectra is fulfilled. If this is the case, this spectrum is defined as the next reference. The procedure is repeated until the preset number k of clusters is reached. After that, all single particle mass spectra are compared to the found references and are assorted to the cluster of highest resemblance, here by the measure of the lowest Euclidean distance. For each of these clusters, a mean spectrum is calculated of all containing spectra and used as a new reference for the next iteration. This iteration is repeated until there are no changes of the assignments. After this clustering procedure, all mass spectra are assorted to one of the k

clusters. Appendix C.3.1, Table 35, shows the used parameters for clustering the *KLX data set* by the *k-means* algorithm. This data set consists of all 12,047 single particle mass spectra recorded throughout the three flights.

The number of start clusters was set to 15. Thus, the clustering of the data set delivered 15 clusters that were reduced to distinct four groups by combining the automatically identified clusters: *Inorganic*, meteoric dust (*Meteoric*), *Organic*, and *EC* (elemental carbon). One extra group combines all mass spectra that cannot be assigned to one of the four particle types mentioned above (total: 39; 0.32 % of the *KLX data set*). Therefore, the criteria in Table 14 were used to inspect the mean spectra of each cluster by comparing the signal intensities in a qualitative way of individual marker ions: intense (> 30 %), mid-intense (1 – 30 %), or weak (< 1 %) relative to the line with the highest intensity within the entire spectrum. Listed are the particle type denotation, the corresponding ion markers according to the post-clustering criteria for grouping and the corresponding chemical species. Each new line "m/z" in the table for one particle type needs to be considered as a "logical and" criterion, as well as the symbol ",". The symbol "/" indicates an "and/or" criterion. The references of the ion markers used for the chemical species are also provided in the Appendix C.4. The ion markers indicated "optional" are used as an additional information, but not as a stringent criterion.

The sorting aimed for particle types that are sufficiently assorted and suitable for referencing in later evaluations with respect to atmospheric locations or conditions. This was possible with meteoric dust particles, typically abundant in high altitudes, and elemental carbon, typically occurring in low and mid altitudes. Both types could be clearly identified due to their characteristic patterns after the clustering process. The mass spectra of the *Meteoric* particle type are characterized by intense signals at m/z +24 (Mg^+) and +56 (Fe^+) in the cation spectrum and m/z -97 (HSO_4^-), -99 ($H^{34}SO_4^-$) and -195 $H(HSO_4)_2$ in the anion spectrum (Murphy et al., 1998; Cziczo et al., 2001; Murphy et al., 2014; Schneider et al., 2019). The mass spectra of the *EC* particle type are characterized by m/z ±12 ($C^{\pm}$), +24 ($C_2^{\pm}$) and +36 ($C_3^{\pm}$) up to ±168 ($C_{14}^{\pm}$) in the cation and the anion spectra (Pratt and Prather, 2010). For the analyses of the flight data from Kalamata at least 5 of such carbon-fragments have to be present. The peak at m/z -26 was interpreted as $C_2H_2^-$ in case of a weak signal and as CN^- in case of a mid-intense signal (in both cases for a weak signal for all other organic lines). The remaining clusters were assorted into two particle types, *Inorganic* and *Organic*, that mainly differ in the content of intense signals of m/z +24 (C_2^+), +36 (C_3^+), and/or +48 (C_4^+) that typically correspond to organic molecules or fragments. These fragments can occur in the *Inorganic* (weak) and *Organic* particle type (intense) independently. The peak at m/z +12 can also interpreted as an organic fragment (C^+). However, a single peak at m/z +12 also occurs in the background spectrum, where only the residual gas phase in the vacuum chamber gets ionized. Thus, a single organic peak at m/z +12 is no evidence for an organic fragment of a particle that could be assigned to the organic chemical species.

Table 14: Criteria for post-clustering grouping to four particle type groups (Inorganic, Meteoric, Organic, and EC). See text for details.

Particle type denotation	**Ion markers**	**Chemical species**
Inorganic Originated from 4 clusters	m/z: +23 (Na^+)/ +24 (Mg^+)/ +27 (Al^+)/ +28 (Si^+)/ +39 (K^+)/ +40 (Ca^+)/ +48 (Ti^+)/ +52 (Cr^+)/ +56 (Fe^+/CaO^+)/ +59 (Co^+)/ +64 (TiO^+)/ +63 (Cu^+); *intense to mid-intense* m/z: -26 (CN^-)/ -35 (Cl^-)/-79 (PO_3^-); *mid-intense* / +30 (NO^+); *intense* / -46 (NO_2^-)/ -62 (NO_3^-); *weak* Optional m/z: +24 (C_2^+)/ +36 (C_3^+)/ +48 (C_4^+); *weak*	Metals Cyanide/Chloride/ Phosphate Nitrate Organics
Meteoric (Meteoric dust) Originated from 4 clusters	m/z: +24 (Mg^+), +25 ($^{25}Mg^+$), +26 ($^{26}Mg^+$); *intense* m/z: +54 ($^{54}Fe^+$), +56 (Fe^+); *intense* m/z: +27 (Al^+)/ +39 (K^+)/ +58 (Ni^+)/ +59 (Co^+); *weak* m/z: -97 (HSO_4^-); *dominant*, -99 ($H^{34}SO_4^-$); *mid-intense* / -195 ($H(HSO_4)_2^-$); *intense* / +30 (NO^+); *weak* / -46 (NO_2^-)/ -62 (NO_3^-); *weak* / -125 ((HNO_3)NO_3^-); *weak* / +18 (NH_4^+); *weak* m/z: +24 (C_2^+)/ +36 (C_3^+)/ +48 (C_4^+); *weak* m/z: -24 (C_2^-)/ -26 ($C_2H_2^-$); *weak* Optional m/z: -44 (SiO^-); *mid-intense*	Magnesium Iron other Metals Sulfate Nitrate Ammonium Organics Silicate
Organic Originated from 5 clusters	m/z: +23 (Na^+)/ +24 (Mg^+)/ +27 (Al^+)/ +28 (Si^+)/ +39 (K^+)/ +40 (Ca^+)/ +48 (Ti^+)/ +52 (Cr^+)/ +56 (Fe^+/CaO^+)/ +59 (Co^+)/ +64 (TiO^+)/ +63 (Cu^+); *mid-intense* m/z: -35 (Cl^-)/-79 (PO_3^-); *weak* / +30 (NO^+); *intense* / -46 (NO_2^-)/ -62 (NO_3^-); *weak* m/z: +24 (C_2^+)/ +36 (C_3^+)/ +48 (C_4^+); *intense*	Metals Chloride/ Phosphate Nitrate Organics
Elemental carbon (*EC*) Originated from 1 cluster	m/z: +12 (C^+)/ +24 (C_2^+)/ +36 (C_3^+) /… / +168 (C_{14}^+); *intense to mid-intense, at least 5 peaks* m/z: -12 (C^-)/ -24 (C_2^-)/ -36 (C_3^-) /… / -168 (C_{14}^-); *intense to mid-intense, at least 5 peaks*	Organics

The mean stick spectra of all four particle types (*Inorganic*, *Meteoric*, *Organic,* and *EC*) are presented in Figure 59. Ion markers that were used for the grouping and other characteristic peaks are tagged by the most likely fragment or ion species. It is obvious that all particle type anion spectra contain peaks that can be interpreted as sulfate fragments, especially HSO_4^- (m/z -97) is prominent. The signal at m/z -99 can be interpreted by the isotopic peak as $H^{34}SO_4^-$ (peak intensity ratio of the peak of HSO_4^- to the peak of $H^{34}SO_4^-$ = 22:1). Furthermore, in the mean spectra of the *Meteoric* and the *Organic* particle type, m/z -195 is visible and can be interpreted as another sulfate fragment peak, $H(HSO_4)_2^-$. In the *Organic* particle type all mass spectra that contain organic fragments (except the EC pattern) are summarized. In contrast to that the *Inorganic* particle type contains weak organic signals. Thus, also

fragments that are characteristic for other species like metals (e.g., m/z +43 interpreted as AlO^+) occur in the mean spectra of the *Organic* particle type. The *Organic* particle type partly consists of aged organic substances. The pattern of the *Meteoric* particle spectrum is comparable to the spectral pattern described in literature (Murphy et al., 1998; Cziczo et al., 2001; Murphy et al., 2014; Schneider et al., 2019). The peak in the anion mean spectrum at m/z -177 can be interpreted here as $[HSO_4SO_3]$. Not confirmed in the meteoric dust particle spectra but conceivable might be the fragment $[NH_4NO_3HSO_4]^-$ in the presence of NH_4NO_3. In the mean cation spectra of *Organic* particles, the peak at m/z +30 cannot clearly related to NO^+ or $CH_2H_2^+$as these are isobars. The *EC* mean spectra show the typical pattern (see Section 4.4) up to C_{11}^+ in the cation spectrum and C_9^- in the anion spectrum. Nitrate fragments (NO^+, NO_2^- and NO_3) only occur in the *Inorganic* mean spectra.

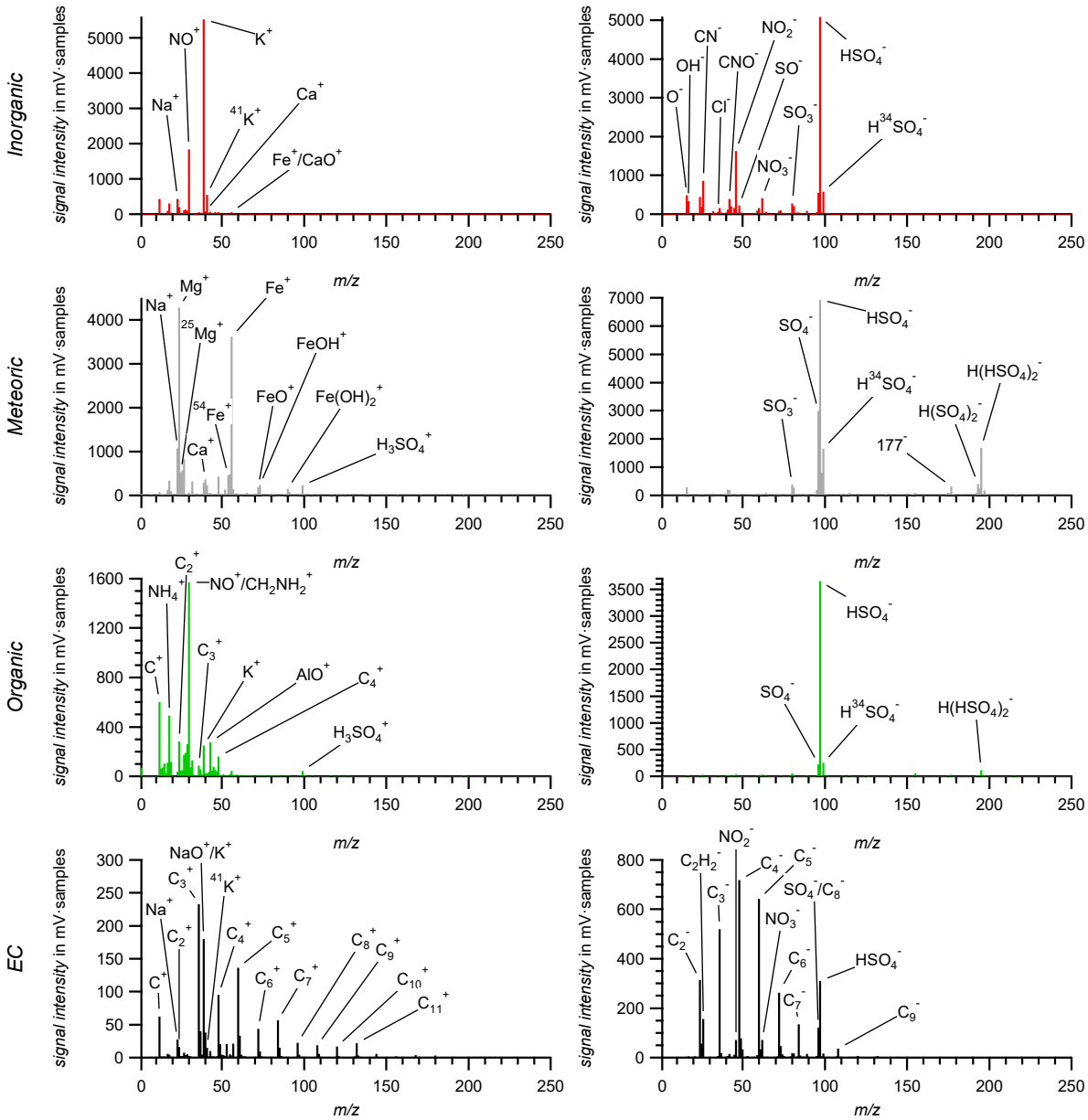

Figure 59: Mean stick spectra (left: cations, right: anions) of the four particle types: Inorganic (red), Meteoric (gray), Organic (green), and EC (black). Identified characteristic peaks are tagged with the most likely fragment/ion species.

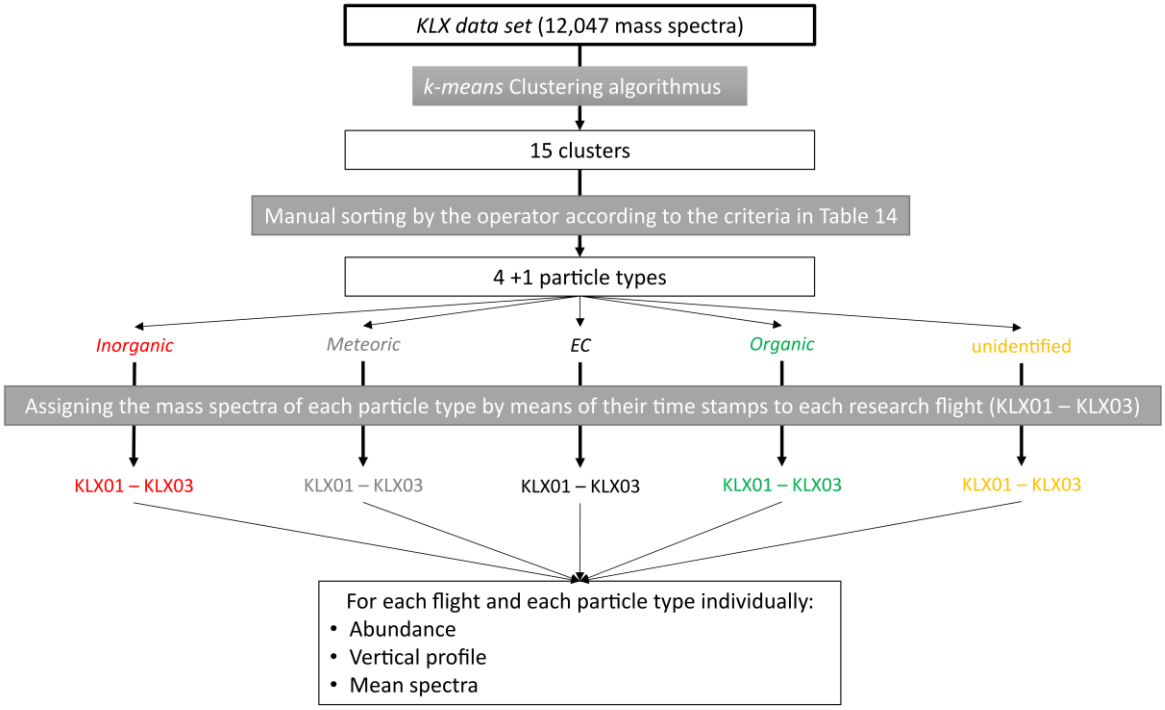

Figure 60: Flow chart of the data processing of the mass calibrated KLX data set. Data processing steps highlighted by gray boxes. Description see text.

After grouping the clusters, the single particle mass spectra were assigned to the measurement flights by means of their time stamps (see Section 3.7.3.1) within a particle type group. In this way, mean spectra of the four particle type groups are obtained individually for each flight. Thus, the flight-to-flight variability of the mean spectra of one particle type is low. Figure 60 summarizes the workflow of the data preparation of the *KLX data set*. These mean spectra are shown in Appendix C.5.

Figure 61 shows the abundance of the grouped particle types as pie-chart. The abundance, i.e., the particle number fraction f_{frac}, is calculated of the counted mass spectra of a specific particle type N_{type} divided by the total number of recorded mass spectra $N_{spectra}$:

$$f_{part} = \frac{N_{type}}{N_{spectra}} \tag{54}$$

It is obvious that the *Organic* particle number fraction is the largest fraction (57 %) followed by the *Inorganic* (20 %) and *Meteoric* (16 %) fractions. In Appendix C.6 the abundance of all four particle types is presented for each flight individually. It should be noted that the abundance strongly depends on the flight pattern of the research aircraft and the *Inorganic* and *Organic* particle types are defined broadly. To interpret the data in more detail, another parameter for instance the altitude or the particle size must be considered. This brings the results into a meteorological context. In CRISP, a routine is implemented where the time stamps of the single particle mass spectra can be correlated with an external data set (via its time series). In addition to that, the evaluation software CRISP includes a routine to extract data of a certain time interval, for instance single flights or other time intervals of interest (see Figure 60).

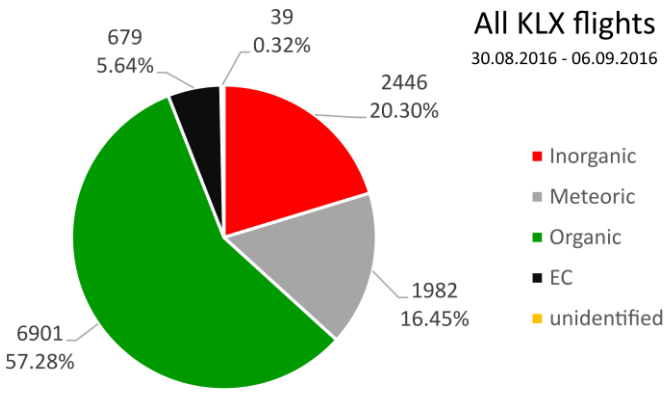

Figure 61: Abundance and number of spectra of the particle types: Inorganic (red), Meteoric (gray), Organic (green), EC (black), and unidentified (orange), based on the data set recorded during three research flights between 30.08.2016 and 06.09.2016 in the mid-latitude phase of StratoClim August/September 2016 from ground level up to 20,000 m. The data set consist of 12,047 single particle mass spectra.

5.1.2 Results of mid-latitudes phase using the clustering algorithm method

All single particle mass spectra are recorded together with the time of its ablation. This time stamp can be used to correlate the individual particle data to another parameter time series. This parameter can be for instance the altitude h_{amsl} that leads to a vertical distribution of the particle type. For this, the mass spectra were assorted into altitude sections (bin intervals 500 m). The bin widths were chosen to provide an acceptable level of statistical significance and resolution. To determine the particle number fraction f_{part} for one bin, the ratio of counts of particles of the specific particle type and all collected particles are calculated for each bin.

Figure 62 depicts the vertical distribution of the particle number fraction f_{part} for each particle type during research flight KLX02 as a cumulative distribution. In addition, the number of spectra in each altitude bin is displayed. It must be mentioned that some particle types are not detectable or cannot be ablated (see Section 3.5.1). Thus, the actual particle number fractions f_{part} might be somewhat distorted. However, it is possible to estimate a change in the composition of the aerosol. The *Inorganic* and *Organic* particle number fraction decreases above the estimated cold point tropopause (CPT). However, the *Organic* number fraction decreases only to 27 % at 20,000 m. To find the sources for these high values of particle number fractions of these broadly defined particle types are part of further investigations in the future. Flight KLX02 was chosen to visualize the proof-of-concept of the ERICA instrument for aircraft deployment. In higher altitudes (h_{amsl} > 17,500 m) the *Meteoric* particle type, i.e., meteoric dust particles, dominates the particle number fractions f_{part}. An enhancement of this fraction f_{part} was expected at higher altitudes (Murphy et al., 1998). By that it is shown that the ERICA-LAMS works qualitatively in high altitudes up to 20,000 m. As expected, at low altitudes the particle number fraction f_{part} of *EC* shows an enhancement. *EC* is created as primary aerosol by combustion processes as part of soot at low altitudes (Turpin et al., 1991; Seinfeld and Pandis, 2016). As shown in Pratt and Prather (2010), the *EC* particle number fraction is equally distributed in the altitude range of 1,000 – 6,000 m (for Wyoming and northern Colorado, approximately 41° N). Due to the lack of publications, the *EC* data at altitudes above 6,000 m cannot be compared with suitable references. However, a decrease of the *EC* fraction with altitude is reasonable considering the *EC* as primary aerosol. The occurrence of *EC* in higher altitudes can be explained by either local emitters like aircrafts (Blake and Kato, 1995; Pueschel et al., 1997) or vertical transport (Ditas et al., 2018). These

results of the single particle measurements also are indicative for the proper operation and functioning of the ERICA-LAMS.

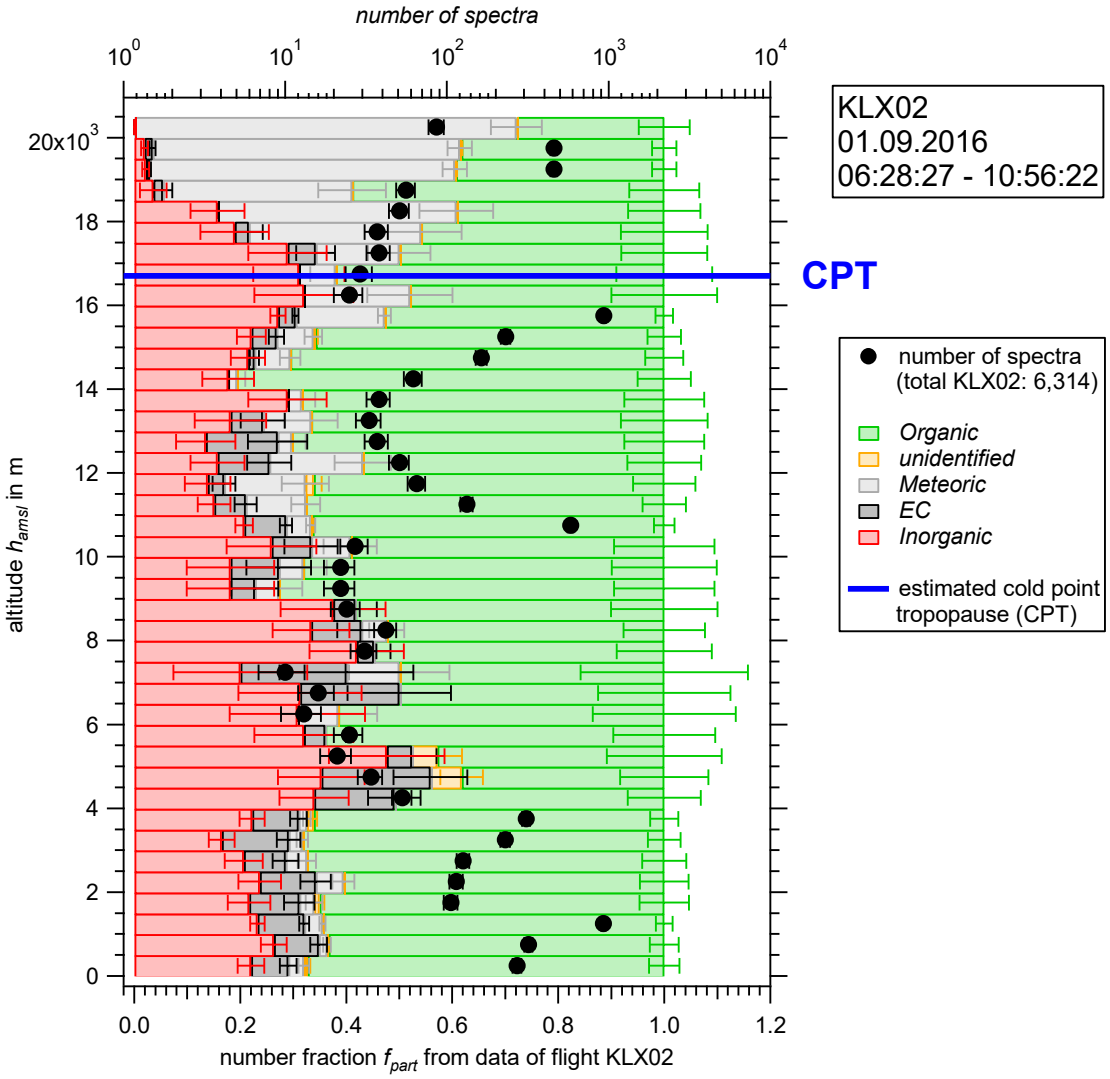

Figure 62: Cumulative vertically resolved fractions (bottom axis) during research flight KLX02 (01.09.2016, 06:28:27 – 10:56:22 UTC) of the described particle types, Inorganic (red), Meteoric (gray), Organic (green), EC (black), and unidentified (orange). Referring to the upper abscissa the black symbols designate total number of spectra in the corresponding altitude bins (black markers). The estimated cold point tropopause (CPT) at h_{amsl} = 16,700 m is marked by a blue line. The vertical resolution is in altitude bins of 500 m. The uncertainties are calculated from counting statistics according to Appendices C.2.2 and C.2.3. The uncertainty bars are in some cases smaller than the symbol.

In parallel to the measurements of the ERICA-LAMS, the ERICA-AMS was running uninterruptedly. Figure 63 displays the ERICA-AMS time series recorded during research flight KLX01 (Personal communication: O. Appel, MPIC, 2018). It depicts the mass concentration of the AMS typical aerosol types nitrate, sulfate, ammonium, chloride, and organics as described in Section 4.5.1. Each data point corresponds to 25 *buffs* which corresponds to 10 second measurement intervals (see Section 3.7.3.2). Thus, the shown time series is unsmoothed. The signal fluctuates due to the strong upscaling of weak raw signals caused by a non-valid IE calibration (see Section 5.1.3). In addition, the altitude profile of flight KLX01 is displayed. The graph excludes the outliers of unrealistically high and low values that exceed the displayed range. The instrument was automatically rebooted within 5 minutes after the preset altitude of 1,000 m was reached (Dragoneas et al., 2020) and was switched off by the pilot when reaching the parking position after landing. During the first hour of measurement, the values of the

mass concentrations, especially of the organic and chloride type, show unrealistic, negative values. The reason for this was a too short pumping time and that the filament and the vaporizer were switched off during the start preparation (see Section 5.1.3). Thus, the disturbing residual material was not sufficiently removed from the vacuum. The mass concentration values obtained for the organic components C_{Org} deviate from the expectations. For instance, in mid-latitudes, a mass concentration C_{Org} of around 1 – 5 µg m^{-3} was observed in altitudes up to 2,000 m in polluted areas by Morgan et al. (2010). The measurement during flight KLX02 shows negative values even two hours after take-off. All species (organics C_{Org}, nitrate C_{NO3}, sulfate C_{SO4}, ammonium C_{NH4}, and chloride C_{Cl}) are affected by a faulty IE-calibration (see Section 5.1.3). In addition, the high air beam signal (see Section 4.5.1) and the high residual humidity in the vacuum chamber biases the mass concentration values, due to the cross-relations in the fragmentation table (see Section 4.5.1). For this reason, the determined mass concentrations cannot be used for further analyses. The sulfate mass concentration C_{SO4} increases at high altitudes (> 17,000 m) as expected (Junge and Manson, 1961; Lazrus and Gandrud, 1974; Murphy et al., 2014). However, due to the faulty IE-calibration also this increase is only a qualitative measure. All in all, apart from the qualitative sulfate measurement, the measurement cannot be used for further evaluation. However, after the flights in Kalamata, Greece, these issues were revisited and resolved (which is described in Section 5.1.3).

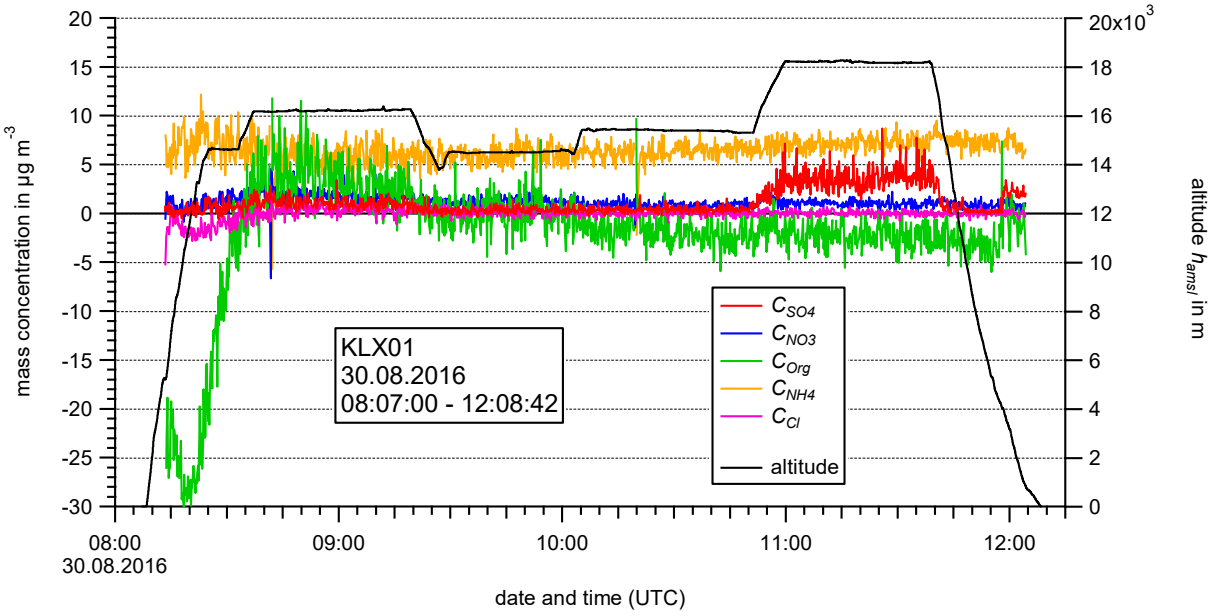

Figure 63: Continuous time series (KLX01, 30.08.2016, 08:07:00 – 12:08:42 UTC) of the particulate mass concentrations (nitrate (blue), sulfate (red), ammonium (orange), chloride (purple), and organics (green)) as measured with the ERICA-AMS. The aircraft altitude is shown as black line (right axis). Outliers of unrealistic high and low values are excluded and not shown in the graph. Data provided by O. Appel.

The ERICA-LAMS measurements provided here represent the very first bipolar particle mass spectra which were recorded at altitudes above 15,000 m and up to 20,000 m in the mid-latitude lower stratosphere. In addition, the data demonstrate that the instrument is capable to operate continuously and autonomously aboard an aircraft during research flights, including phases of aircraft vibrations and encounters with turbulence. In addition, the instrument operated during the field campaign in a temperature range between -72.7 °C and 32.0 ° (7 – 40 °C in the closed pressurized container). Thus, it has been demonstrated with the test flights in Kalamata, Greece, that ERICA is an aircraft-borne

instrument which is useful for ambient aerosol particle composition measurements once the above-mentioned problems of the ERICA-AMS part are resolved.

5.1.3 Improvements on the instrumental design and particle losses inside ERICA

After the deployment at KLX, it was found out that the behavior of the organic mass concentration signal can be improved by powering the filament and the vaporizer of the ERICA-AMS during the LPM (see Section 3.8.2) together with the TMPs a few hours before the research flight. The time schedule before a research flight permits only 2.5 to 4 hours in advance to access and power the instrument. An additional pump (HiPace® 30, Pfeiffer Vacuum GmbH, see Section 3.2; TMP6 in Figure 10) was implemented to improve the overall pumping rate. It was installed at the C-ToF chamber, so that the gas volume does not have to pass by the ion source (vaporizer and filament) and cannot be contaminated by molecules that degas from the vacuum chamber.

A further improvement was implemented by changing the design of the O-ring in the CPI (see Section 3.7.1.2). A high ambient pressure (1,000 mbar), i.e., at ground level, leads the O-ring been squeezed to keep the mass flow into the inlet constant. The squeezing of the O-ring shrinks the inner diameter of its aperture. At higher altitudes with correspondingly lower ambient pressure, the O-ring aperture opens to maintain the constant mass flow. Molleker et al. (2020) described that at high ambient pressures the commercially available O-ring (adopted for the Kalamata flights during the mid-latitude phase) is squeezed in a way that the aperture is warped such that the O-ring assumes a non-spherical shape (see photographs in Molleker et al. (2020)). This leads to impact losses of particles at the O-ring's perimeter and surface. For the quantitative measurements of the ERICA-AMS no procedure can compensate for this loss a-posteriori. Such particle losses at the warped O-ring during IE calibration lead to a wrong calibration factor. A new O-ring design improved the particle transmission through the CPI (Molleker et al., 2020). The new O-ring was manufactured in the laboratory and consists of a well-defined, softer rubber material mixture and the aperture’s inner diameter is smaller than the previously adopted commercial one. This results in less squeezing at high ambient pressure and therefore no distortion of the O-ring's shape. Also, it maintains the circular cross section of the opening during the squeezing as function of ambient pressure. The experiments described in Section 4.2 were conducted with the new O-ring.

Another reason for particle losses in connection with the ERICA-AMS measurements was the electrical extraction field of the ERICA-LAMS through which all particles must pass on their way to the vaporizer. Figure 64 shows the effect on positively charged particles deflected in the electrical field of the extraction plates. Negatively charged particles of course are deflected in the opposite direction. Altogether this leads to a spread of the particle beam such that an increased fraction of the particles actually misses the vaporizer and is thus lost for the AMS measurements. Owing to the occurrence of charged air molecules in the atmosphere ambient aerosol particles are either neutral (for the most part) or bear positive or negative charges, partially in dependency of altitude. To reduce these losses the electrical field is switched on only during particle ablation process by the HV-switch (10 ms; see Section 3.4.2).

Since the ablation laser is capable of firing only at a repetition rate of 8 s^{-1}, only very few of the passing aerosol particles are affected by the electrical field, if the high voltage is switched on only triggered simultaneously to the laser shot. In this context, also the procedure of the IE calibration for the ERICA-AMS plays an important role. This calibration is performed in the laboratory using ammonium nitrate aerosol particles emerging from a DMA (see Section 4.5.2) and thus all aerosol particles bear an electrical charge (e.g., see Section 4.2.3.3). If the electrical field of the ERICA-LAMS is switched on

continuously, i.e., at all times irrespective of the UV laser operation, during such calibrations each test particle will experience some deflection. In case not all particles are reaching the vaporizer, however, the calibration factor f_{calib} in Equation (47) resulting from comparison with the external CPC (see Section 4.5.2) will be inaccurate. As result, if this corrupted factor f_{calib} is used for ambient aerosol measurements, where not all particles are charged, the calculated mass loadings will be erroneous.

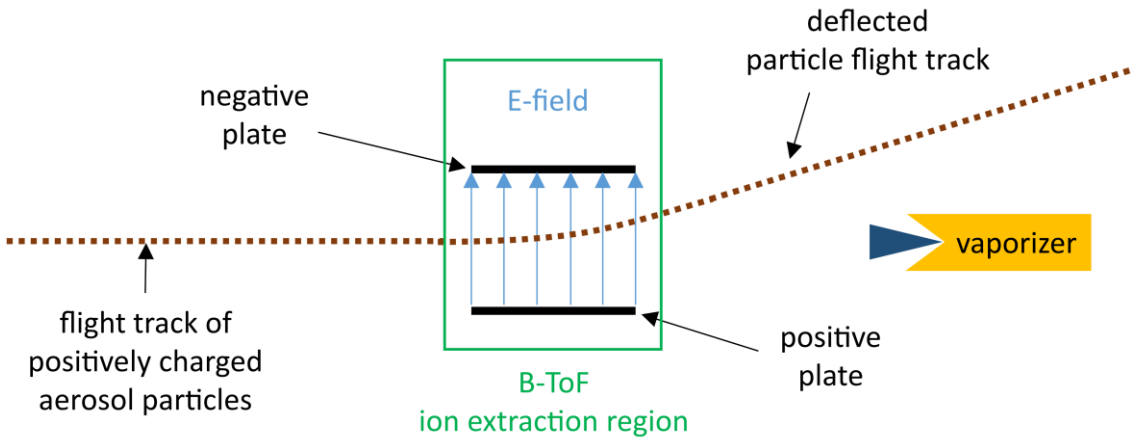

Figure 64: Principle of the effect on naturally positively charged particles as an example deflected in the electrical field of the extraction plates at the ERICA-LAMS.

In Section 4.5.4. the estimated losses inflicted upon the aerosol particle stream by the ablation laser are discussed. In addition to that, an experiment was performed comparing the measured mass concentration of ambient aerosol with operating pulsed HV switches and without any electric field. For this the ERICA instrument was running in two different modes: First, the ERICA-AMS was recording while the second detection laser was switched off. For this reason, no trigger was generated for the ablation laser and the HV switches. As a result, the ablation laser and the HV extraction field were not switched on at any time during this mode. Second, the ERICA-LAMS was running as described in Chapter 3 where the electrical extraction field was only switched on during the ablation laser shot for 10 ms. During this experiment, ambient aerosol particles were sampled from the atrium of the MPIC building (20.07.2018, 10:38 – 12:17 UTC) continuously by the ERICA-AMS. The ERICA-LAMS, i.e., the HV switches, was activated after 10 minutes and deactivated after another 10 minutes. This change was performed four times. The result was a loss of (5.4 ± 0.9) % of the sampled total mass at the ERICA-AMS in case of a running ERICA-LAMS at approximately 200 counts s^{-1} (DU1; Personal communication: O. Appel, MPIC, 2018). The size distribution of the sampled particles detected by the ERICA-LAMS detection unit is shown in Section 4.3.

The deployed aerodynamic lens (AeroMegt GmbH) had not been described in detail in the literature until that point. To exclude the lens as another possible source for particle losses, the lens was changed to the IPL-013 (Aerodyne Inc.) designed by Peck et al. (2016) which has been characterized by Xu et al. (2017). The change was carried out before the StratoClim Asian monsoon phase (see Section 5.2) and thus before the experiments that are presented in Section 4.2. Therefore, the particle beam parameters presented there represent the instrumental performance during the Asian monsoon phase.

With these implemented improvements as result from the experience gained from the Kalamata flights, the ERICA-AMS is capable to measure quantitatively due to a low background signal and a reduction of particle losses in the inlet system. Together with the properly functioning ERICA-LAMS the ERICA instrument was ready for the Asian monsoon phase.

5.2 StratoClim Asian monsoon phase in July/August 2017

The major goal of the StratoClim project was to produce more reliable projections of regional and global climate change by a better understanding of microphysical, chemical, and dynamical key processes in the upper troposphere and lower stratosphere (UT/LS) of the Asian monsoon. Therefore, the project bridges the gap between field observations and remote sensing observations, global models, and numerical models for detailed simulation of physical and chemical processes. The StratoClim field campaign in Nepal was set to investigate the influence of the characteristic major processes dominating particle and trace gas transport in the UT/LS by the Asian Monsoon Anticyclone (AMA) and to elucidate on the physical and chemical properties of the ATAL aerosol layer. The AMA is one of the major input regions of tropospheric air masses into the lowermost and possibly global stratosphere, e.g., Rex et al. (2016), Brunamonti et al. (2018), and Bucci et al. (2020).

*Table 15: Overview of the research flights during the Asian Monsoon phase of StratoClim and the number of recorded single particle mass spectra. Times (date and time), the maximum GPS altitude h_{amsl}, the ambient pressure p_{stat} range, and the ambient temperature T_{out} range are provided by UCSE. Local time in Kathmandu is UTC+5:45. *No ERICA-LAMS and ERICA-AMS data between 04:13:30 and 04:40:17 (1,607 s) and between 04:42:06 and 04:44:27 (141 s), due to two MCC reboots. ** No ERICA-LAMS data between 05:31:48 and 05:41:28 (581 s), due to ERICA-LAMS acquisition software reboot.*

Flight	**Date**	**Time (UTC)**	**Number of recorded spectra**	**max. h_{amsl} in m**	**p_{stat} in hPa**	**T_{out} in °C**
KTM01	27.07.2017	07:44:47 – 10:42:08	20,516	19,463	64.0 – 860.8	-79.5 – 32.0
KTM02	29.07.2017	03:00:13 – 07:27:12	18,605	20,477	54.7 – 863.7	-78.9 – 28.6
KTM03	31.07.2017	02:55:42 – 07:34:44	23,927	20,372	54.7 – 862.8	-80.2 – 27.2
KTM04	02.08.2017	08:27:28 – 12:29:14	14,028	20,447	54.5 – 857.4	-81.6 – 30.8
KTM05	04.08.2017	03:04:12 – 07:25:20	15,866*	20,274	55.9 – 858.7	-81.8 – 32.0
KTM06	06.08.2017	07:25:43 – 11:31:30	17,914	17,000	98.7 – 859.5	-81.4 – 30.6
KTM07	08.08.2017	03:41:35 – 07:15:43	13,625**	19,429	64.3 – 863.3	-85.8 – 28.2
KTM08	10.08.2017	08:43:40 – 12:28:41	13,608	19,158	67.6 – 858.2	-86.1 – 26.3
Total (*KTM flight data set*)			138,089			

The Asian monsoon phase took place in Kathmandu, Nepal, during July and August 2017 under subtropical and temperate conditions. Legs of the research flights reached the tropical zone. Base for this part of the StratoClim project was the Tribhuvan International Airport (KTM; 27.70°N, 85.36°E) in the city of Kathmandu, Nepal. During this phase, eight research flights were performed. During these

flights 138,089 single particle mass spectra were recorded (*KTM flight data set*). Including ground measurements before take-off and after landing 146,413 mass spectra were recorded (*KTM total data set*). Details on the flights, such as date, time, number of recorded spectra, maximum GPS altitude, ambient pressure, and ambient temperature, are presented in Table 15. Overall, the altitude h_{amsl} ranged from 1,338 m to 20,477 m, the ambient pressure p_{stat} ranged from 54.5 hPa to 863.7 hPa, and the ambient temperature T_{out} from -86.1 °C to 32.0 °C. The *KTM flight data set* contains the mass spectra that can be assigned to flights according to their time stamps from the *KTM total data set* that is used for data preparation (see Section 5.2.1). The presented results concerning the flights refer to the *KTM flight data set* (see Section 5.2.2).

During the research flights, the instrumental behavior was observed via a satellite communication (see Section 3.8.1). In flight KTM05 the MCC had to be rebooted twice due to an unexpected stop of the acquisition software of the ERICA-LAMS, which caused an interruption of the data recording of ERICA-LAMS and ERICA-AMS between 04:13:30 and 04:40:17 (1,607 s) and between 04:42:06 and 04:44:27 (141 s). In flight KTM07 a similar error occurred. Here only the ERICA-LAMS acquisition software (*LAAP acquisition software*, see Section 3.7.3.1) was reset, so only the recording of the ERICA-LAMS data between 05:31:48 and 05:41:28 (581 s) was missed. The ERICA-AMS continued recording data in that time interval. These three incidents demonstrate the usefulness of the implemented safety features and the redundancy concept. First, the *Iridium* satellite link enabled the ground operators to realize the occurrence of a problem online and to remotely restart the corresponding software modules. Second, the serial arrangement of ERICA-LAMS and ERICA-AMS (as evident from Figure 10) prevented a total loss of the measurements as ERICA-AMS continued normal operation during the failure period of ERICA-LAMS. Without these features about three quarters of the measurements from flight KTM 05 and one half of flight KTM 07 would have been lost.

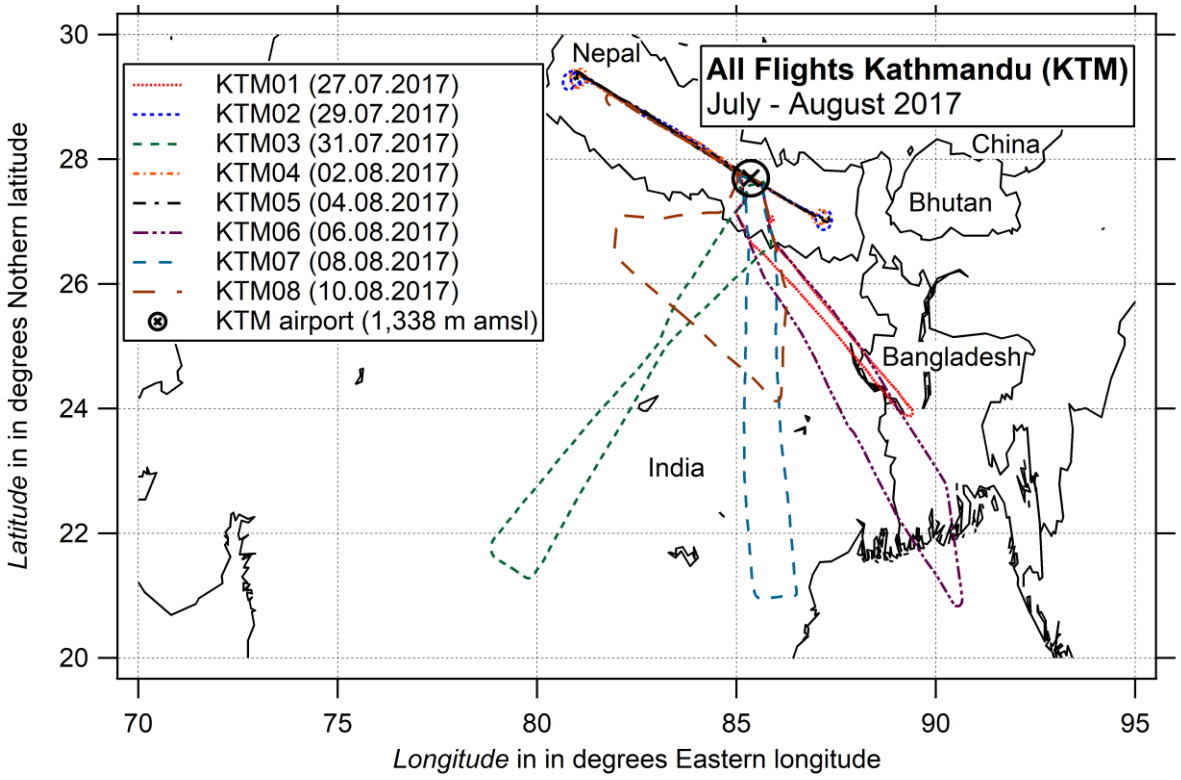

Figure 65: Flight tracks of the eight research flights performed by Geophysica during the Asian Monsoon phase of StratoClim 2017 from Tribhuvan International Airport (KTM) in Kathmandu, Nepal. The flight times, the number of recorded mass spectra and the conditions during the flights (max. h_{amsl}, p_{stat}, and T_{out}) are listed in Table 15 for each flight.

Figure 65 shows the flight tracks of the eight research flights during the Asian monsoon phase, based at Tribhuvan International Airport (KTM). The flight tracks were planned a few days in advance according to forecasts of the ground weather and the atmospheric situation above roughly 12 km. The time series of the altitude profile are displayed in Appendix C.8. All following altitude values refer to the GPS altitude recorded by UCSE.

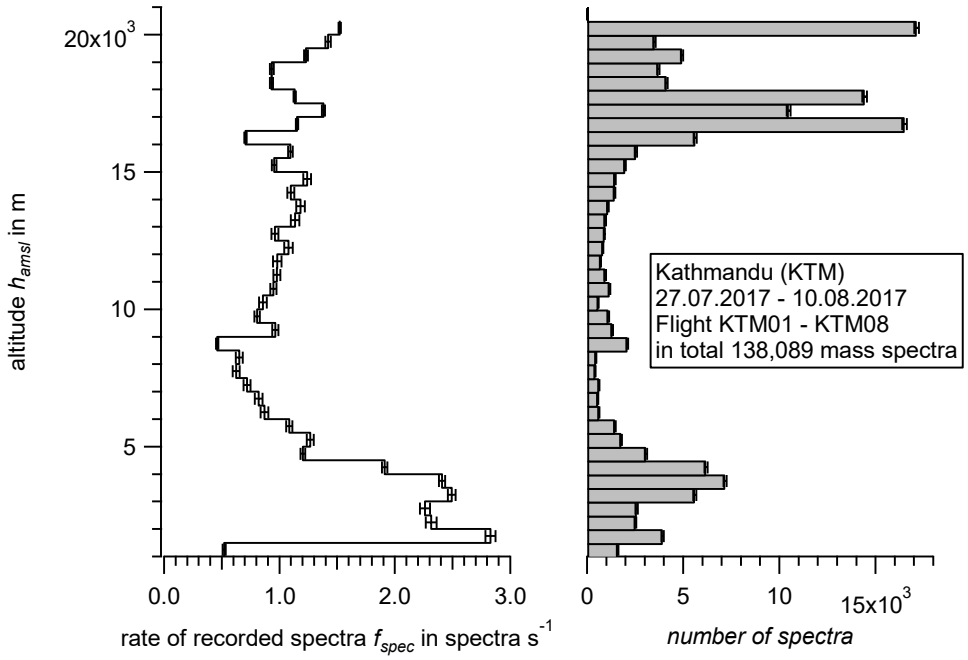

Figure 66: Vertical profile of the rate of recorded single particle mass spectra f_{spec} for all eight research flights (left panel) and the number of recorded single particle mass spectra within all eight flights (right panel). To calculate f_{spec}, the number of recorded mass spectra was normalized to the retention time of the research aircraft in the respective altitude sections (bin size 500 m). The uncertainties are based on counting statistics (see Appendix C.2.1).

Figure 66, left panel, shows the vertical profile of the rate of recorded single particle mass spectra f_{spec} for all eight research flights. It demonstrates the stable, steady performance (f_{spec} around 1.0 spectra s^{-1}) of the instrument for altitudes above 9,000 m. In the altitude below 4,500 m, the rate f_{spec}. is most likely higher due to the high particle number concentration in the boundary layer (see also Figure 58) and reaches values of 2.8 spectra s^{-1}. The right panel in Figure 66 depicts the number of recorded mass spectra in the same altitude bins. The enhancement of recorded spectra in altitudes above 16,000 m results from the long flight duration in these altitudes. The boundary layer regularly extends to altitude of around 4,500 m.

In the following sub-sections, the single particle data preparation and the results of the ERICA field deployment during the StratoClim Asian monsoon phase are presented. Furthermore, the interaction of ERICA-LAMS and ERICA-AMS is shown on the basis of flight KTM01. Since the author of this thesis had not evaluated the ERICA-AMS data, the focus of these sub-sections lies on the results of the single particle mass spectrometer ERICA-LAMS.

5.2.1 Data preparation and particle type identification for the ERICA-LAMS by the clustering algorithm method

As described in Section 5.1.1, the raw data of all eight flights has to be converted first into a CRISP compatible file format (pbf-file format) using the *LAAP spectrum batch converter* (see Section 3.7.3). The pbf-files were loaded in CRISP and were m/z calibrated (see Section 4.4.1) using the values listed in Appendix C.3.2, Table 36, and converted into stick spectra. The so prepared data set also includes single particle mass spectra recorded in between the research flights (in total 146,413 mass spectra), when the aircraft was on the ground before take-off and after landing (*KTM total data set*). This data set is basis for the following particle type determination.

Analogous to the data set recorded in Kalamata, Greece, the total data set was automatically sorted, i.e., clustered, by the *k-means* sorting algorithm (see Section 5.1.1). The parameters adopted for this clustering of the KTM data set are shown in Appendix C.3.2 ,Table 37. The number of initial clusters was set to 30.

In the region of the AMA an aerosol layer (Asian Tropopause Aerosol Layer, ATAL) was discovered by satellite measurements in an altitude range between roughly 13,000 – 18,000 m of unknown chemical composition (Vernier et al., 2015). It was suspected that it contains mainly sulfuric acid, sulfate and carbonaceous components (Vernier et al., 2015). However, the in-situ measurements of the ERICA-AMS in this altitude range showed an enhanced nitrate signal at the described altitudes (Personal communication: O. Appel, MPIC, 2018). Since the ERICA-LAMS is not sensitive to pure sulfuric acid (Section 3.5.1) and the majority (66 %) of the single particle mass spectra recorded during the flights contained sulfate fragment signals in the anions (m/z -96 (SO_4^-)/ -97 (HSO_4^-)), the described manual grouping by the operator was focused on the nitrate signals (m/z +30 (NO^+)/ -46 (NO_2^-)/ -62 (NO_3^-)/ -125 ($(HNO_3)NO_3^-$)).

By inspection of the output of the 30 automatically generated clusters it was found that 13 clusters showed typical nitrate fragments in the mean spectra. The a-posteriori grouping of the nitrate-containing clusters was organized by the operator such that differences in composition can be identified. For example, some of the nitrate-containing particles contained besides nitrate also ammonium and sulfate (termed particle type *NOSO*), but no organics, while others had additional organics (termed particle type *OrgNOSO*). Thus, the *OrgNOSO* particle type includes in addition to ammonium, nitrate, and sulfate also organic fragments (such as m/z: +24 (C_2^+)/ +36 (C_3^+)/ +48(C_4^+)). By this grouping subtle differences in particle composition can be highlighted. In case that in the mean spectrum of a cluster metal peaks occurred besides the ammonium, nitrate, sulfate, and organic fragments, the clusters were assorted either to the *KOrgNOSO* particle type or the *MetalOrgNOSO* particle type where "K" designates the predominant presence of the metal potassium. The peak at m/z -26 was interpreted as $C_2H_2^-$ in case of a weak ion marker signal intensity and as CN^- in case of a mid-intense signal. For both cases, the signal intensities of the organic fragments were weak. Furthermore, the peak at m/z -26 could not be clearly determined, if the signal intensities of the organic fragments were mid-intense (isobars). The *KOrgNOSO* particle type is distinguished by an intense peak at m/z +39 that can be interpreted as $^{39}K^+$ ion, since the intensity of the peak at m/z +41 corresponds to the isotopic ratio of $^{39}K^+/^{41}K^+$. Other metal ions occurred in this particle type in weak intensities. However, another particle type is characterized by mid-intense signals of metal ions, but a weaker potassium signal. This is the *MetalOrgNOSO* particle type. Thus, the particle type denotation of *KOrgNOSO*, *MetalOrgNOSO*, *OrgNOSO* and *NOSO* includes the main criteria in their names (K: potassium; Metals; Org: organics ion markers; NO: Nitrate ion markers; SO: Sulfate ion markers). The

particle types *Meteoric* and *EC* are denoted according to the typical and well-known pattern of the mass spectra (see Section 5.1.1 (Murphy et al., 1998; Cziczo et al., 2001; Pratt and Prather, 2010; Murphy et al., 2014; Schneider et al., 2019)) and were obtained by the clustering algorithm without the use of further start criteria. Both particle types were also obtained by the clustering algorithm for the *KLX data set* (see Section 5.1.1). The methodology thus appears consistent. Figure 67 shows an example for a stick spectrum of a single particle that was assigned to the *Meteoric* (meteoric dust) and Figure 68 that was assigned to the *EC* (elemental carbon) particle type.

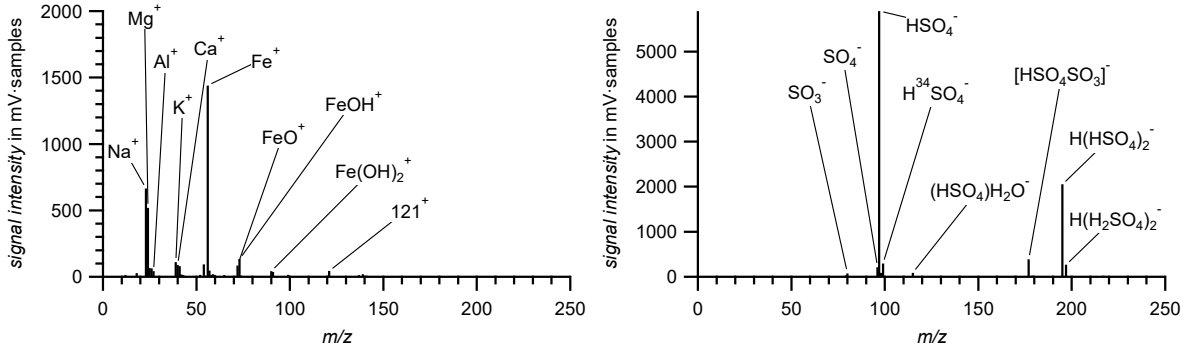

Figure 67: m/z calibrated stick spectrum of a single particle measured in 19,982 m altitude (28.6428° N, 82.9307° E) during StratoClim (flight KTM04, 02.08.2017, 11:51:45 UTC, d_{va} = 406 nm): Meteoric dust particle which is coated with sulfuric acid.

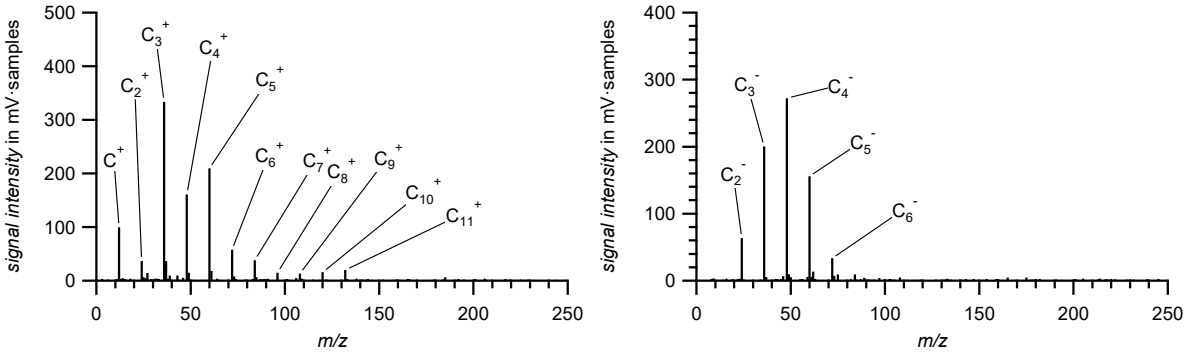

Figure 68: m/z calibrated stick spectrum of a single particle measured in 8,275 m altitude (27.3099° N, 85.7296° E) during StratoClim (flight KTM01, 27.07.2017, 08:13:11 UTC, d_{va} = 235 nm): EC particle without indication of any coating.

The ion markers of the particle type *Inorganic* are at least one of the following, typically inorganic fragments: Cyanide (CN^-), chloride (Cl^-) and phosphate (PO_3^-). Possibly corresponding metals (such as Na and K) also occurred in this particle type. Furthermore, signals at m/z ±2 and rarely at m/z ±1 are present that might be artefacts from ringing signals caused by the ablation laser light flash. This fact needs further investigation. Typical organic ion markers (e.g., C_2^+, C_3^+, or C_4^+) occurred solely with weak intensity. One group combines all mass spectra that cannot be assigned to one of the seven particle types, since the information of the negative polarity is missing. The total number of the *unidentified* particles from the Kathmandu flights is 219, which is 0.15% of *KTM total data set* (146,413 mass spectra). However, a signal occurred at m/z ±1 that might be also caused by the flashing light of the ablation laser.

The number of start clusters for the clustering algorithm was set to 30. Thus, the clustering of the data set delivered 30 clusters that were reduced to the described seven groups comprehended in Table 16 by combining the automatically identified clusters. Also, the number of origin clusters that were summarized to the particle types are listed. The criteria in Table 16 were used to inspect the mean

spectra of each cluster by comparing the signal intensities: Intense (> 30 %), mid-intense (1 – 30 %) or weak (< 1 %) relative to the line with the highest intensity within the entire spectrum. Listed are together with the particle type denotation, the corresponding ion markers according to the post-clustering grouping criteria and the corresponding chemical species. Each new line "m/z" in the table for one particle type needs to be considered as a "logical and" criterion, as well as the symbol ",". The symbol "/" indicates an "and/or" criterion. The criteria shown in Table 16 are based on observations after the automatic clustering process. Thus, only those fragments/ions and their combinations that were obtained in the resulting mass spectra were considered. In that sense the clustering is not yet a fully automated autonomous processing and still needs operator attendance. The references of the ion markers used for the chemical species are presented in the Appendix C.4.

Table 16: Criteria for post-clustering grouping to seven particle type groups (KOrgNOSO, MetalOrgNOSO, Meteoric, EC, Inorganic, NOSO, and OrgNOSO). See text for details. Continued on next page.

Particle type denotation	**Ion markers**	**Chemical species**
KOrgNOSO Originated from 9 clusters	m/z: +39 (K^+) *intense*, +41 ($^{41}K^+$); *mid-intense* m/z: +24 (C_2^+)/ +36 (C_3^+)/ +48 (C_4^+); *mid-intensem/z*: -24 (C_2^-)/ -26 (CN^-/$C_2H_2^-$); *mid-intense* m/z: +30 (NO^+); *intense* / -46 (NO_2^-)/ -62 (NO_3^-); *mid-intense* / -97 (HSO_4^-); *dominant*, -99 ($H^{34}SO_4^-$); *mid-intense* / -195 ($H(HSO_4)_2^-$); *weak* / +18 (NH_4^+); *mid-intense* m/z: +23 (Na^+)/ +25 ($^{25}Mg^+$)/ +27 (Al^+)/ +56 (Fe^+)/ +58 (Ni^+)/ +59 (Co^+); *weak* m/z: -16 (O^-)/-17 (OH^-); *weak*	Potassium Organics Nitrate Sulfate Ammonium Metals Oxygen/Hydroxy
MetalOrgNOSO Originated from 4 clusters	m/z: +23 (Na^+)/ +25 ($^{25}Mg^+$)/ +39 (K^+); *mid-intense* m/z: +27 (Al^+)/ +56 (Fe^+)/ +58 (Ni^+)/ +59 (Co^+); *mid-intense, at least 3 peaks present* m/z: +24 (C_2^+)/ +36 (C_3^+)/ +48 (C_4^+); *mid-intense* m/z: -24 (C_2^-)/ -26 (CN^-/$C_2H_2^-$); *mid-intense* m/z: +30 (NO^+); *intense* m/z: -46 (NO_2^-)/ -62 (NO_3^-); *mid-intense* m/z: -125 ($(HNO_3)NO_3^-$); *weak* m/z: -97 (HSO_4^-); *dominant*, -99 ($H^{34}SO_4^-$); *mid-intense* m/z: -195 ($H(HSO_4)_2^-$); *intense* m/z: +18 (NH_4^+); *mid-intense*	Metals Organics Nitrate Sulfate Ammonium
Meteoric (Meteoric dust) Originated from 4 clusters	m/z: +24 (Mg^+), +25 ($^{25}Mg^+$), +26 ($^{26}Mg^+$); *intense* m/z: +54 ($^{54}Fe^+$), +56 (Fe^+); *intense* m/z: +27 (Al^+)/ +39 (K^+)/ +58 (Ni^+)/ +59 (Co^+); *weak* m/z: -97 (HSO_4^-); *dominant*, -99 ($H^{34}SO_4^-$); *mid-intense* / -195 ($H(HSO_4)_2^-$); *intense* / +30 (NO^+); *weak* / -46 (NO_2^-)/ -62 (NO_3^-); *weak* / -125 ($(HNO_3)NO_3^-$); *weak* / +18 (NH_4^+); *weak* m/z: +24 (C_2^+)/ +36 (C_3^+)/ +48 (C_4^+); *weak* m/z: -24 (C_2^-)/ -26 ($C_2H_2^-$); *weak* Optional m/z: -44 (SiO^-); *mid-intense*	Magnesium Iron other Metals Sulfate Nitrate Ammonium Organics Silicate

Table 16: Continued.

Particle type denotation	Ion markers	Chemical species
EC (Elemental carbon) Originated from 1 cluster	m/z: +12 (C^+)/ +24 (C_2^+)/ +36 (C_3^+) /… / +168 (C_{14}^+); *intense to mid-intense, at least 5 peaks present* m/z: -12 (C^-)/ -24 (C_2^-)/ -36 (C_3^-) /… / -168 (C_{14}^-); *intense to mid-intense, at least 5 peaks present* Optional m/z: -97 (HSO_4^-), -99 ($H^{34}SO_4^-$); *mid-intense*	Organics Sulfate
Inorganic Originated from 6 clusters	m/z: +23 (Na^+)/ +24 (Mg^+)/ +27 (Al^+)/ +28 (Si^+)/ +39 (K^+)/ +40 (Ca^+)/ +48 (Ti^+)/ +52 (Cr^+)/ +56 (Fe^+/CaO^+)/ +59 (Co^+)/ +64 (TiO^+)/ +63 (Cu^+); *intense to mid-intense, at least 2 peaks present* m/z: -2 /-26 (CN^-)/ -35 (Cl^-)/-79 (PO_3^-); *mid-intense* m/z: +30 (NO^+); *weak* Optional m/z: +24 (C_2^+)/ +36 (C_3^+)/ +48 (C_4^+); *weak* Optional m/z: +2; *present*	Metals Cyanide/ Chloride/Phosphate Nitrate Organics
NOSO Originated from 4 clusters	m/z: +30 (NO^+); *dominant* / -46 (NO_2^-)/ -62 (NO_3^-); *mid-intense* / -125 ($(HNO_3)NO_3^-$); *mid-intense* m/z: -97 (HSO_4^-); *dominant*, -99 ($H^{34}SO_4^-$) *mid-intense* / -195 ($H(HSO_4)_2^-$); *weak* / +18 (NH_4^+); *intense* / -16 (O^-)/-17 (OH^-); *weak* Optional m/z: +24 (C_2^+)/ +36 (C_3^+)/ +48 (C_4^+); weak	Nitrate Sulfate Ammonium Oxygen/Hydroxy Organics
OrgNOSO Originated from 1 cluster	m/z: +24 (C_2^+)/ +36 (C_3^+)/ +48 (C_4^+); *mid-intense* m/z: +30 (NO^+); *dominant* / -46 (NO_2^-)/ -62 (NO_3^-); *weak* / +18 (NH_4^+); *mid-intense* / -97 (HSO_4^-); *intense*	Organics Nitrate Ammonium Sulfate

The particle types *KOrgNOSO* and *MetalOrgNOSO* have as criteria organics, nitrate, and sulfate as well as metals in common. However, for the particle type *KOrgNOSO* the signal at m/z +39 is dominant and only one additional metal species is defined, while for the assignment to the particle type *MetalOrgNOSO* more than two different metal species are allowed. The *Inorganic* particle type also contains metal fragments. In comparison to *KOrgNOSO* and *MetalOrgNOSO* only weak organic signals appear in the mean spectra of the six origin clusters. Similarly, the *NOSO* particle type differs from the *OrgNOSO* particle type by weak organic signals. However, these two particle types have nitrate, sulfate, and ammonium signals in common. For the assignment to the *MetalOrgNOSO*, *Meteoric*, or *Inorganic* particle type at least two metal species are required. The criteria of *MetalOrgNOSO* differ from those of the *Meteoric* particle type mainly by the intensity of the organic signals, which are defined as weak for *Meteoric*. Additionally, the simultaneous presence of Fe and Mg is necessary for the classification of a cluster to *Meteoric*. In contrast to the *Inorganic* particle type, the *Meteoric* particle type excludes the presence of cyanide, chloride, or phosphate signals.

The resulting mean stick spectra of all seven particle types are presented in Figure 69 and Figure 70: *KOrgNOSO*, *MetalOrgNOSO*, *Meteoric*, *EC*, *Inorganic*, *NOSO*, *OrgNOSO,* and *unidentified* mass spectra.

The number of spectra that are basis for the mean spectra of the particle types are depicted in the pie chart shown in Figure 71, right panel (*KTM total data set*).

Characteristic peaks that could be identified are tagged by the most likely fragment/ion species. Like in the mean spectra of the particle types that have been evaluated for the mid-latitude phase, it is obvious that all particle type anion spectra contain peaks that can be interpreted as sulfate fragments (m/z -97 (HSO_4^-) confirmed by m/z -99 ($H^{34}SO_4^-$)). *KOrgNOSO*, *MetalOrgNOSO* and *Meteoric* show a peak at m/z -195 that can be interpreted as another sulfate fragment peak ($H(HSO_4)_2^-$). In the *MetalOrgNOSO* and *Meteoric* particle types the peak in the anion mean spectrum at m/z -177 can be interpreted as $[HSO_4SO_3]^-$. In the presence of NH_4NO_3, like in *MetalOrgNOSO*, the peak can be interpreted as $[NH_4NO_3HSO_4]^-$ ion fragment. The *EC* mean spectrum shows the typical pattern (see Section 4.4) up to C_{12}^+ in the cation spectrum and up to C_9^- in the anion spectrum. In addition, sulfate signatures (HSO_4^-) are visible in the mean *EC* spectrum. There are ambiguities in the association of lines with specific ion fragments. The *MetalOrgNOSO* particle type combines all metal-containing mass spectra that come along with organic signature (C_2^+, C_3^+, or C_4^+). Thus, m/z +24, +48, +58, and +59 cannot be clearly identified as metal markers. The peak at m/z +24 can be interpreted as C_2^+ or Mg^+. Furthermore, the peak at m/z +48 can be seen as Ti^+ or Mg_2^+, as well as C_4^+- fragment ion, m/z +58 as Ni^+ or $CH_2NHCH_2CH_3^+$ and m/z +59 as Co^+ or $C_3H_7O^+$ (isobars). The peak at m/z +99 can also not be clearly identified as metallic ($ZnCl^+$) or inorganic ($H_3SO_4^+$). In the *Meteoric* particle type the peak at m/z +99 is likely related to the sulfate compound $H_3SO_4^+$. The peaks at m/z -155 in the mean spectrum of *MetalOrgNOSO* and *NOSO* are not identified as well as the peak at m/z -123 in the mean spectrum of *Inorganic*.

Similarities of the different particle types can be caused by internally mixed particles where for instance matrix and charge transfer effects (see Section 2.3) cause different spectral patterns. For example, highly ionizable metal species in the particle can cause organic signals to appear weak in the mass spectrum (e.g., Reilly et al. (2000) and Zhou et al. (2006)).

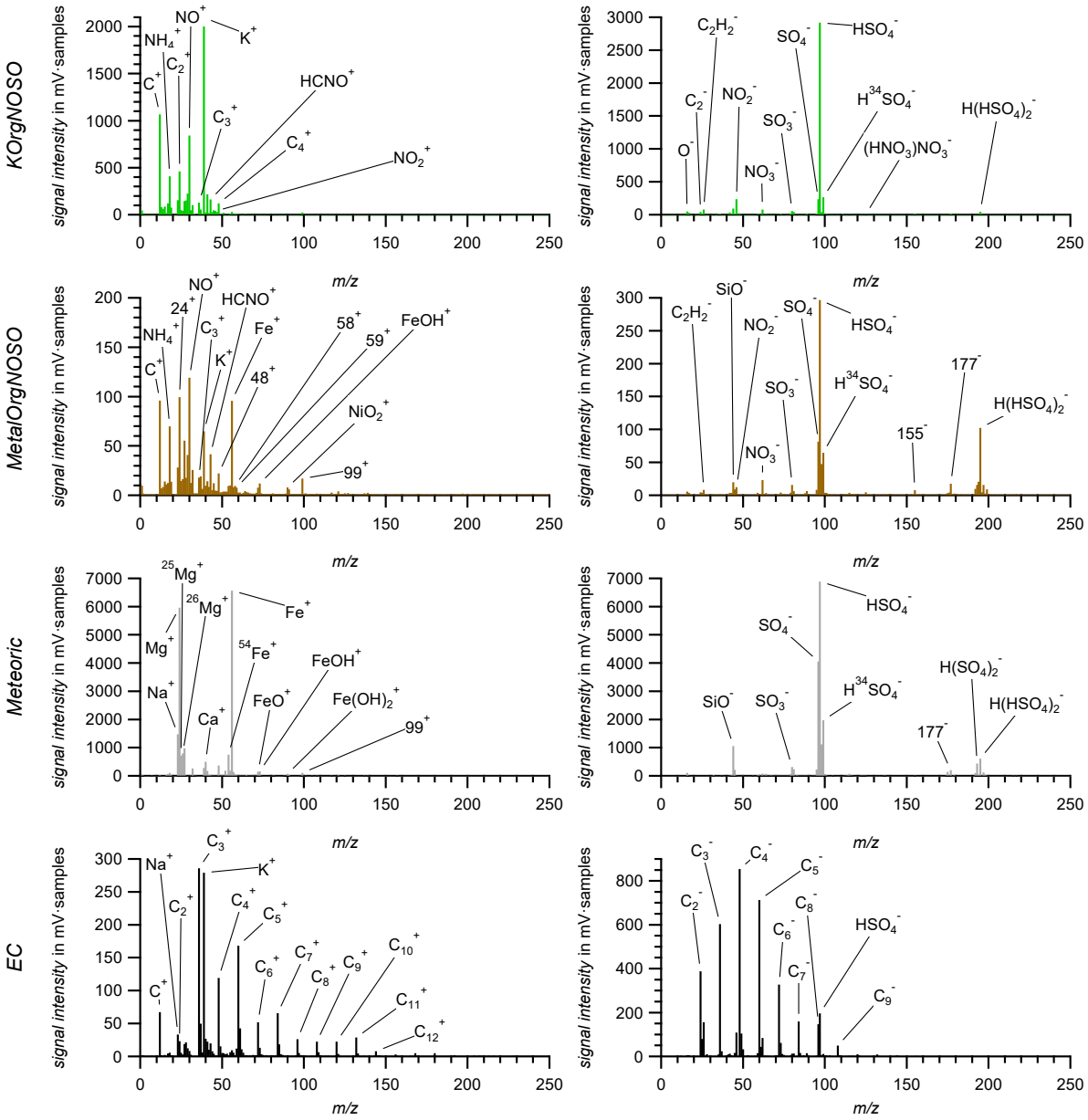

Figure 69: Mean stick spectra (based on the KTM total data set; left: cations, right: anions) of four particle types: KOrgNOSO (green), MetalOrgNOSO (brown), Meteoric (gray), and EC (black). Identified characteristic peaks are tagged with the most likely fragment/ion species. For lines at which only the m/z number are provided an unambiguous identification of the ions was not possible.

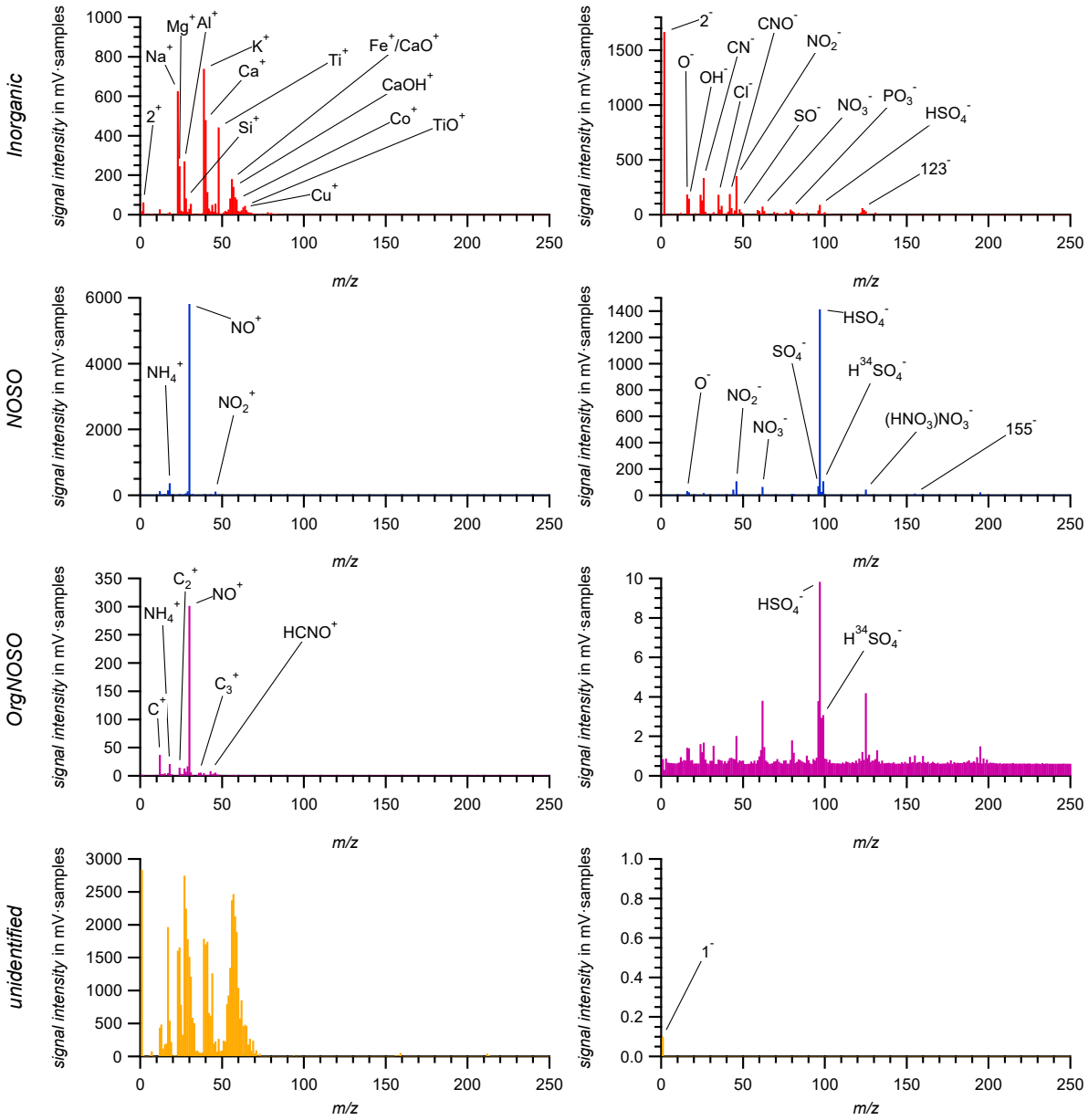

Figure 70: Mean stick spectra (based on the KTM total data set; left: cations, right: anions) of four particle types: Inorganic (red), NOSO (blue), OrgNOSO (purple), and unidentified mass spectra (orange). Identified characteristic peaks are tagged with the most likely fragment/ion species. For lines at which only the m/z number are provided an unambiguous identification of the ions was not possible.

Figure 71, left panel, shows the abundance, i.e., the particle number fraction f_{part}, of the described particle types of all eight research flights using the *KTM flight data set*. The pie chart was generated to obtain a first general overview of the relative abundances for all particle types resulting from the adopted grouping method. The fraction of the unidentified particles is the minority of 0.15 %. Almost one third of all recorded mass spectra were assorted to the *KOrgNOSO* particle type (32 %). Clear organic signatures can be found in 62 % of all mass spectra (*KOrgNOSO*, *MetalOrgNOSO,* and *OrgNOSO*). However, no particle type is overrepresented. Compared to the *KTM flight data set*, the abundance of the particle types *KOrgNOSO*, *MetalOrgNOSO*, *Meteoric*, and *EC* is slightly increased in the *KTM total data set*, while the particle types *Inorganic*, *NOSO* and *OrgNOSO* are slightly reduced in the *KTM total data set* (Figure 71, right panel). As noted in Section 5.1.1: The abundance strongly depends on the flight pattern of the aircraft during deployment and the definition of the particle types.

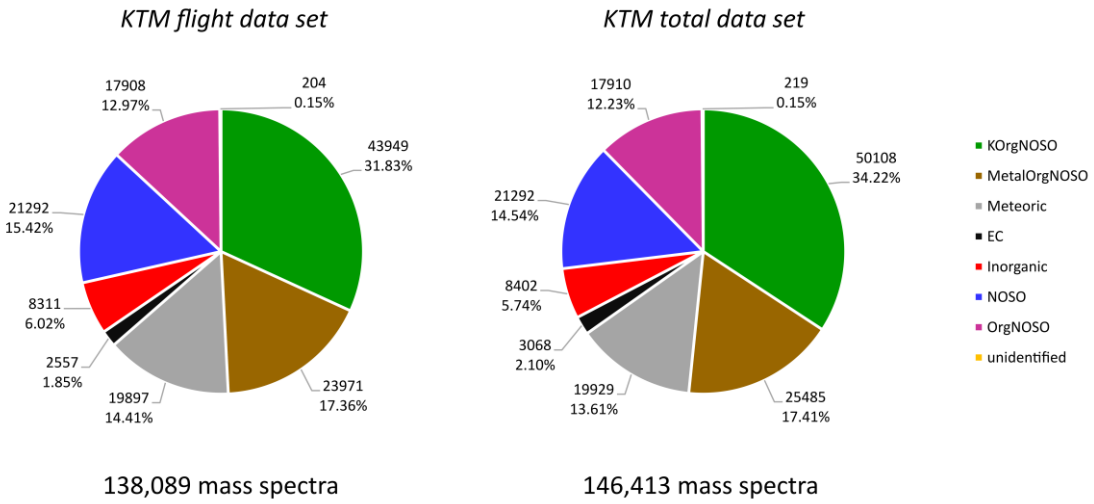

Figure 71: Abundance and number of spectra of the particle types: KOrgNOSO (green), MetalOrgNOSO (brown), Meteoric (gray), EC (black), Inorganic (red), NOSO (blue), OrgNOSO (purple), and unidentified mass spectra (orange) based on the data set recorded during the Asian Monsoon phase of StratoClim July/August 2017 at KTM. Left: KTM flight data set of 138,089 mass spectra. Right: KTM total data set of 146,413 mass spectra including mass spectra recorded before and after the research flights on ground level (used for data preparation).

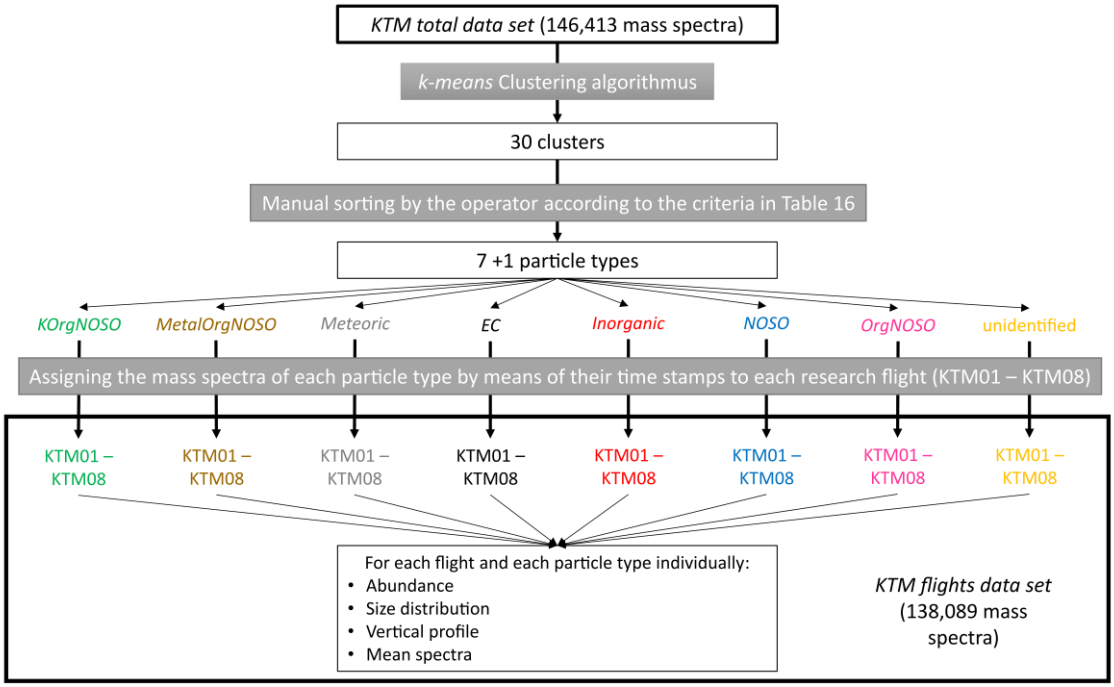

Figure 72: Flow chart of the data processing of the mass calibrated KTM total data set. Data processing steps highlighted by gray boxes. Description see text.

The *KTM flight data set* contains the mass spectra that can be assigned to flights according to their time stamps from the *KTM total data set*. Thus, the *KTM flight data set* is a fraction of the *KTM total data set.* Figure 72 summarizes the workflow of the data preparation. After grouping the clusters, the single particle mass spectra were assigned to the measurement flights by means of their time stamps (see Section 3.7.3.1) within a particle type group. In this way, mean spectra of the seven particle type groups are obtained individually for each flight. These mean spectra are shown in Appendix C.9. Due

to the data processing that assigns the mass spectra to the research flights after the clustering and grouping process the mean spectra of each particle type show a very similar pattern.

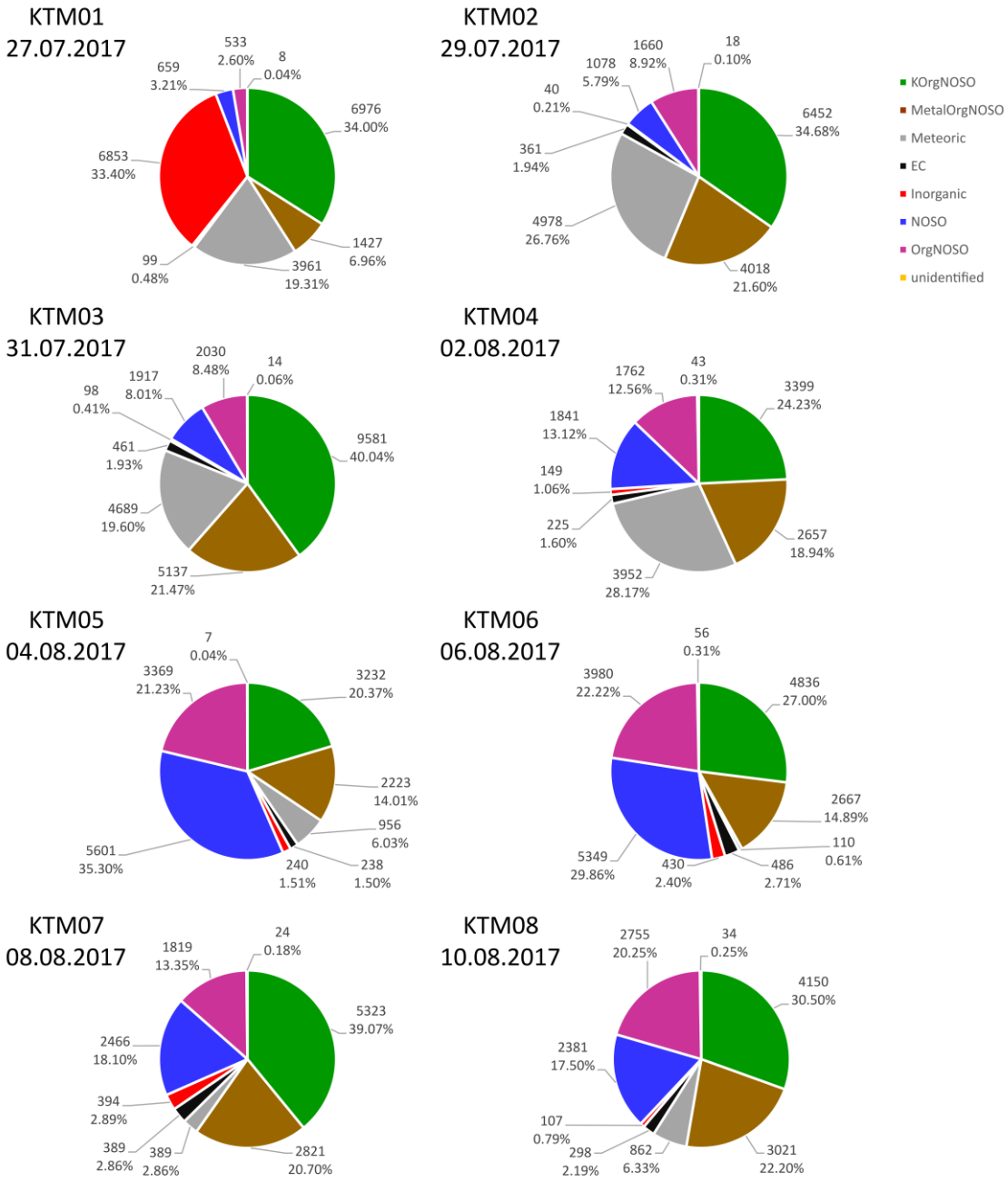

Figure 73: Abundance and number of spectra of the particle types: KOrgNOSO (green), MetalOrgNOSO (brown), Meteoric (gray), EC (black), Inorganic (red), NOSO (blue), OrgNOSO (purple), and unidentified mass spectra (orange) based on the KTM flight data set recorded during the Asian Monsoon phase of StratoClim at KTM for each of the eight research flights. The number of total recorded spectra of each flight is listed in Table 15.

Like the mean spectra, the abundance of particle types for each flight can be determined using the time stamps of the mass spectra. In Figure 73 the abundance of all particle types is presented for each flight individually. Compared to the other flights, the *Inorganic* particle type in flight KTM01 appears to be considerably increased. This particle type occurred mostly in the first part of the flight where the

step like flight pattern reached an altitude of only 17,000 m (see Figure 139 in Appendix C.8). In addition, the mean spectrum in flight KTM01 shows a significant deviation from the others (see Figure 155 in Appendix C.9). This fact requires further investigation. The *Meteoric* abundances appear increased in the flights KTM02, KTM03, and KTM04. In these three flights the major part of the single particle mass spectra were recorded in altitudes above 17,000 m (see Appendix C.11). According to the criteria in Table 16, the *MetalOrgNOSO* particle type might contain particles consisting of aged meteoric dust. In flights KTM05 to KTM08 the major part of the total number of mass spectra of each flight were recorded in altitudes below 17,000 m. That might be the reason why the *NOSO* and *OrgNOSO* particle type is dominant in flights KTM05 and KTM06 and the particle number fraction of the *MetalOrgNOSO* and *KOrgNOSO* particle type appears enhanced in flights KTM07 and KTM08.

In the following Section 5.2.2 the particle types were brought into a physical and meteorological context by using auxiliary data of altitude and particle size.

5.2.2 Results of Asian monsoon phase using the clustering algorithm method

Auxiliary data is necessary to bring the identified particle types into the context of meteorology and atmospheric physics. Here, the altitude and the particle size are used to generate vertical profiles and particle size distributions for each particle type. In the following sub-section, the particle types are characterized regarding their size and the altitude of occurrence.

5.2.2.1 Size distributions of the identified particle types

To calculate the arrival time of a particle in the ablation spot the particle flight time between both detection units is measured and stored with each particle spectrum as *Upcount* value (see Section 3.7.2.2). For 1.3 % of the spectra of the *KTM total data set* this *Upcount* recording failed. By calibration, the vacuum aerodynamic diameter (d_{va}) can be derived from the *Upcount*. Here, the method described in Section 4.2.2.1, is used. In the following the results refer to 144,517 mass spectra with valid size information as part of the *KTM total data set.*

Figure 74 shows the cumulative size-resolved aerosol composition of the identified particle types (*KOrgNOSO*, *MetalOrgNOSO*, *Meteoric*, *EC*, *Inorganic*, *NOSO*, *OrgNOSO,* and unidentified mass spectra) and the number of spectra based on the whole data set recorded within all eight research flights. To determine the particle number fraction f_{part} for one bin, the ratio of counts of particles of the specific particle type and all collected particles in that bin are calculated. The uncertainties indicate poorer statistics at the edges of the graph and an optimum around d_{va} = 300 nm. This fact is supported by the number of spectra that reflect the optimization of the detection unit to 218 nm (Section 4.1.1).

For d_{va} calibration, the PSL density of 1.05 g cm^{-3} was assumed (see Section 4.2.2). Thus, for different particle types this density assumption might be not fully appropriate. Particle types possessing higher densities would be shifted to smaller d_{va} values than presented and vice versa. However, particle types of same density values and same size appear in the same size bin in Figure 74. One major result from Figure 74 is that the ERICA-LAMS is capable of measuring the individual particle sizes under field conditions and that these can be related in a meaningful way to the particle chemical composition.

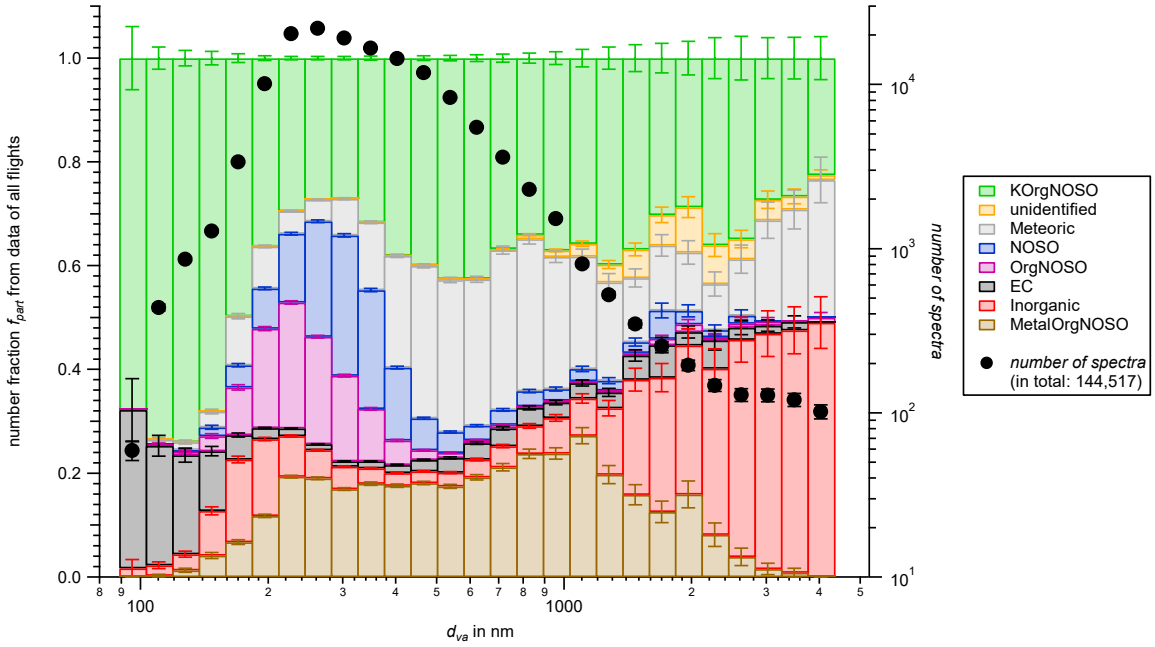

Figure 74: Cumulative size-resolved aerosol composition of the identified particle types: KOrgNOSO (green), MetalOrgNOSO (brown), Meteoric (gray), EC (black), Inorganic (red), NOSO (blue), OrgNOSO (purple), and unidentified mass spectra (orange) referring to the left axis. Referring to the right axis, the black symbols designate total number of spectra with valid size information (black markers) based on the whole KTM flights data set recorded during the Asian Monsoon phase of StratoClim 2017 within all eight research flights. The uncertainties are calculated from counting statistics according to Appendices C.2.2 and C.2.3. The uncertainty bars are in some cases smaller than the symbol.

The size distribution of the *Inorganic* particle number fraction f_{part} shows two modes that indicates different sources and particle sub-types. Indications for different sub-types are the variation of the mean spectra of flight KTM01 to the other flights (Appendix C.9). Furthermore, in the size range larger 1,700 nm, over 25 % of the particles are assorted to the *Inorganic* particle type which could be mineral dust (Alfaro et al., 1998; Hinds, 1999). To confirm that the signals are caused by mineral dust, further analysis of the mass spectra (*Inorganic*) in this size range is needed, e.g., by adopting the ion marker method (e.g., Köllner (2019)). The source of the mode at d_{va} = 200 nm is unknown and needs further investigation.

The *KOrgNOSO* fraction is larger than 20 % over the whole calibrated size range and shows two modes. Here also further investigation of the mass spectral signals and the time of occurrence is needed together with detailed meteorological analyses (e.g., by air parcel trajectories) to identify the particle source and sub-types, respectively. It can be stated that during all eight flights two modes of the *KOrgNOSO* particle type appear in the size distribution plots (Appendix C.10). One mode at lower sizes and one in the center of the distribution.

The lower mode of the *NOSO* particle type appears slightly shifted to higher particle sizes compared to the *OrgNOSO* particle type and might indicate two different particle types. The particle type with extra organic signal has its mode at lower size than the pure *NOSO* type. However, the small size difference between the two modes could also indicate that *NOSO* and *OrgNOSO* are the same particle type. It might appear as two individual particle types due to matrix effects (see Section 2.3) during the ablation process and the a-posteriori cluster analysis followed by grouping the individual clusters. Another hint that both originate from the same source is the simultaneous occurrence in the vertical profile (see Section 5.2.2.2). Also, the results from the ERICA-AMS indicate common occurrence of nitrate and

organics in the sampled aerosol particles. This result shows the limitation of the evaluation approach by the adopted clustering algorithm, where chemically identical particles can lead to mathematically different clusters. Assuming the same source for the *NOSO* and *OrgNOSO* particle type the types can be merged to the *NOSO+OrgNOSO* particle type. The size distribution for this type is shown in Figure 75. The maximum of the particle number fraction f_{part} occurs at particle sizes around d_{va} = 300 nm. At this particle size, the fraction f_{part} accounts for more than 42% of all particles measured at this size.

The fraction of the *EC* particle type is increasing with smaller particle sizes starting around d_{va} = 200 nm and was identified by the clustering method in one single cluster (out of initially 30). However, the particle type occurs in all size bins. Fresh *EC* particles are expected to be in the lower size range ($d_{va} < 200$ nm (Schmidt, 2015)). The reason might be that small EC particles are growing by acquiring a coating, for example of sulfuric acid solution. This coating might not affect the pattern (relative peak heights) of the mass spectrum in a way that both types (coated and uncoated) can be automatically be separated from each other by the clustering algorithm. A hint is given by the comparison of the single particle spectrum of *EC* (Figure 68) and the mean *EC* spectrum in Figure 69 where the additional sulfate peaks are depicted. This result shows, in contrast to the *NOSO*/*OrgNOSO* results above that also chemically different particles can lead to mathematically similar clusters when using a clustering algorithm.

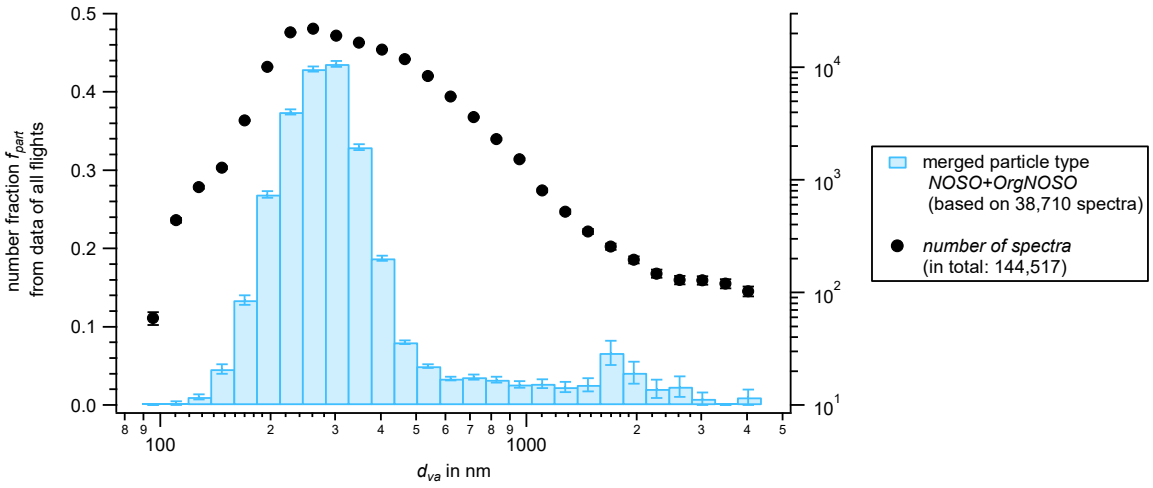

Figure 75 Particle size distribution of the merged particle type NOSO+OrgNOSO (light blue) from the KTM flights data set (left axis). Referring to the right axis, the black symbols designate total number of spectra with valid size information (black markers) based on the whole KTM flights data set recorded during the Asian Monsoon phase of StratoClim 2017 within all eight research flights. The uncertainties are calculated from counting statistics according to Appendices C.2.2 and C.2.3. The uncertainty bars are in some cases smaller than the symbol.

The major mode of the *Meteoric* fraction is at d_{va} = 700 nm that is comparable with previous single particle measurements in the stratosphere (Murphy et al., 2014; Schneider et al., 2019). Other modes occur at sizes larger than d_{va} = 5 µm and at d_{va} = 158 nm that mainly results from flight KTM01 and KTM08. To characterize these two modes further analysis is needed which is beyond the scope of this thesis.

For the *MetalOrgNOSO* particle type the most widespread criteria, i.e., multiple metal and organic ion markers were chosen (see Section 5.2.1, Table 16). Even though originating from only four clusters,

this widespread definition is reflected in a widespread size distribution extending from d_{va} = 200 nm to d_{va} = 2,000 nm. However, the variability of the relative peak heights of the mean spectra over all eight research flights is low (see Appendix C.9). The high fraction value at the mode of *Meteoric* and the mean spectra in Figure 69 indicate that parts of the *MetalOrgNOSO* particle types are either processed aerosol particles (aged meteoric dust) or mass spectra falsely assorted by the clustering algorithm, like discussed above for the *NOSO* and *OrgNOSO* fractions. The mean mass spectra of the *Meteoric* and the *MetalOrgNOSO* particle type show both peaks at m/z +24 (Mg^+) and +56 (Fe^+). Further investigation on the mass spectra is needed to find sub-types of the *MetalOrgNOSO* particle type.

For an unknown reason the unidentified particle type is not continuously distributed but shows a mode around d_{va} = 2,000 nm. The continuous distribution is reasonable, since the major criterion of the *unidentified* particle type is the lack of the anion spectrum that potentially can occur for any mass spectrum of any particle type.

The used clustering method provides a decent overview of different particle types. However, the problems of the algorithm, e.g., *NOSO* / *OrgNOSO* and *EC* / processed *EC*, would require a more elaborate evaluation method. Possible improvements can be an increase of initial cluster numbers and/or a change of the clustering algorithm (fuzzy c-means, minimum spanning tree (Klimach, 2012), the use of ion markers and decision trees). A combination of the listed methods is also conceivable.

5.2.2.2 Vertical profiles of the identified particle types

As described in Section 5.1.2 the altitude h_{amsl} can be used as an external parameter to show the vertically resolved fraction during the research flights. Figure 76 depicts the cumulative vertically resolved particle number fraction f_{part} during one single research flight, here exemplarily Flight KTM05, of the described particle types normalized to the total number of spectra of each altitude bin (bin size 500 m). Similar graphs for the vertical profiles of the other flights are provided in Appendix C.11. Furthermore, the number of recorded spectra is shown. Only one single flight is presented here, because the summation over all flights might blur the profile.

In terms of the *EC* and *Meteoric* fraction, the profile is similar to the previously presented (Section 5.1.2) from the mid-latitude campaign of StratoClim (Figure 62). The highest fraction of the *Meteoric* particle type is on the upper edge of the altitude range and the highest fraction of the *EC* type is at the lower altitudes. So, in two different consecutive phases of instrumental deployment the results of distinguishable particle types were consistent.

In Section 5.2.2.1 the possibility is described that the *MetalOrgNOSO* particle type might be a combination of various sub-types. The vertical profile indicates four to five different modes over the whole altitude range in flight KTM05. This is also the case for the *KOrgNOSO* particle type. The hypothesis (see Section 5.2.2.1) that the *MetalOrgNOSO* particle type contains mass spectra of the *Meteoric* type is supported by an abundance of the *MetalOrgNOSO* type at high altitudes (> 17,000 m). This mode might indicate aged meteoric dust particles (aged *Meteoric*). Further investigation of the mass spectra, for instance isolating the mass spectra in different altitude ranges, is needed to identify sub-types.

The fraction of the *KOrgNOSO* particle type decreases from around 80 % to 40 % with increasing altitude, especially between ground level and 6,500 m. As with the *MetalOrgNOSO* type, further investigation is needed to find the sub-types in this fraction.

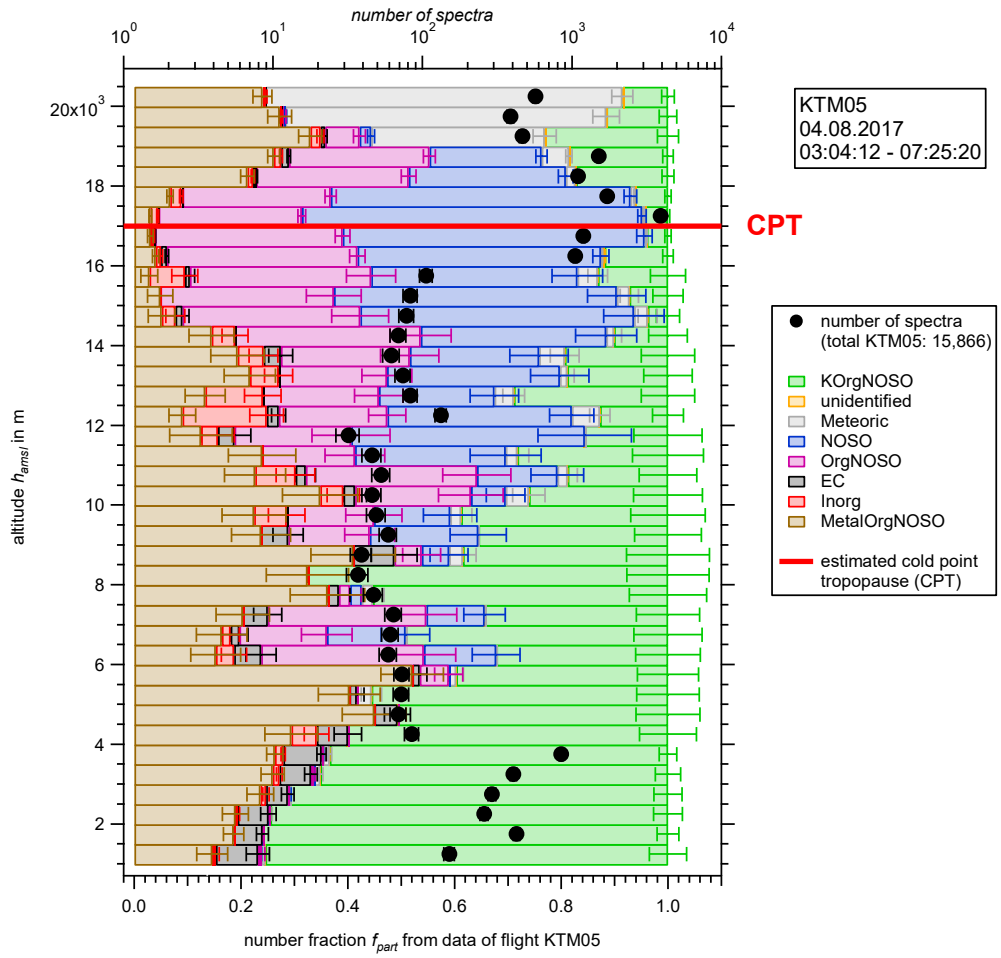

Figure 76: Vertical profile for the cumulative distribution of the particle number fractions f_{part} (bottom axis) during research flight KTM05 (04.08.2017; 03:04:12 – 07:25:20 UTC) of the described particle types: KOrgNOSO (green), MetalOrgNOSO (brown), Meteoric (gray), EC (dark gray), Inorganic (red), NOSO (blue), OrgNOSO (purple) and unidentified mass spectra (orange). Referring to the upper abscissa the black markers designate the total number of spectra in the corresponding altitude bins. The estimated CPT at h_{amsl} = 17,000 m is marked by a red horizontal line. The vertical resolution is in altitude bins of 500 m. The uncertainties are calculated from counting statistics according to Appendices C.2.2 and C.2.3. The uncertainty bars are in some cases smaller than the symbol.

The *Inorganic* particle type shows a mode around 11,000 m (see also Appendix C.11, Figure 175). However, only a few particles of this type were measured in this flight (number of *Inorganic* particles in KTM05: 237).

The *NOSO* and *OrgNOSO* particle type occur simultaneously. The simultaneous occurrence indicates, as discussed above that the two particle types might be a single type. However, two separate modes (7,000 m and > 8,000 m) indicate two physical or meteorological processes that has to be further investigated, e.g., by placing the composition measurements into the atmospheric context provided from meteorological and other data. For example, such modes could be a result of detrainment of aerosols or precursor gases from clouds, or of homogeneous new particle formation inside clouds or cloud free air. In Appendix C.11, Figure 180, the vertical profile of the merged particle type *NOSO+OrgNOSO* is shown individually for each flight. The ERICA-AMS measurements, besides others flight KTM05, confirm this layer by measuring an enhancement of nitrate concentration (Figure 77). Figure 76 and Figure 77 show that the layer of the *NOSO* and *OrgNOSO* particle type and the layer of enhanced nitrate mass concentration extends in altitude above the estimated local CPT. This behavior

indicates the vertical transportation processes inside the Asian summer Monsoon Anticyclone (AMA; Ploeger et al. (2015)).

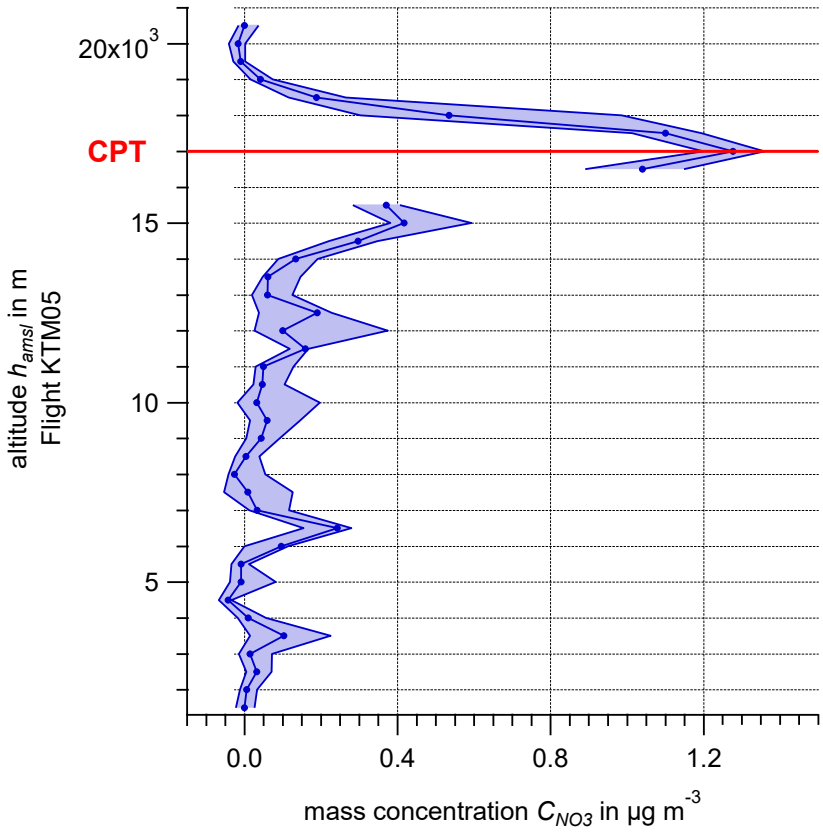

Figure 77: Vertical profile of the median nitrate mass concentration C_{NO3} measured with the ERICA-AMS during research flight KTM05 (04.08.2017; 03:04:12 – 07:25:20 UTC). The estimated CPT at h_{amsl} = 17,000 m is marked by a red horizontal line. The vertical resolution is in altitude bins of 500 m. Shaded areas indicate 25 and 75 percentiles. Data recorded during a cloud event are not shown in the graph. Data provided by O. Appel.

The conducted measurements of bipolar single particle mass spectra and particle ensemble measurements during the AMA in the ATAL are the first of their kind. Both instrument parts of ERICA indicate a prominent layer of nitrate-containing aerosol in the UT/LS region of the AMA. The first evidence of a solid layer of ammonium nitrate particles appeared as early as 1997 (Höpfner et al., 2019). Here, satellite measurements with CRISTA (CRyogenic Infrared Spectrometers and Telescopes for the Atmosphere) led to the discovery of such an ammonium nitrate layer in South Asia in the upper troposphere. Further satellite and balloon measurements also provided indications of a particle layer between 14-18 km altitude (e.g., Vernier et al. (2011), Thomason and Vernier (2013), and Vernier et al. (2015)). This Asian Tropopause Aerosol Layer (ATAL) is related to the AMA (Ploeger et al., 2015; Höpfner et al., 2019). In the AMA, air pollution accumulates and is distributed over a large area of the Northern Hemisphere (e.g., Park et al. (2007), Santee et al. (2017), and Lelieveld et al. (2018)). The air transported by the AMA during summer time influences the composition of the total lowermost stratosphere of the Northern Hemisphere (Ploeger et al., 2017; Yu et al., 2017). Lately it was under discussion, whether the ATAL consist predominantly of carbonaceous and sulfate-containing material, or mineral dust (e.g., Fadnavis et al. (2013), Vernier et al. (2015), Yu et al. (2015), and Vernier et al. (2011); Lau et al. (2018)) or nitrate (Gu et al., 2016). However, only very few measurements were available in ATAL. Indications of nitrate aerosol particles were provided by two balloon measurements (Vernier et al., 2018). Also, Höpfner et al. (2019) observed a layer above 15 km containing particulate

nitrate signature during the StratoClim Asian monsoon phase using the remote sensing instrument GLORIA (Gimballed Limb Observer for Radiance Imaging of the Atmosphere; Friedl-Vallon et al. (2014) and Riese et al. (2014)). GLORIA is an airborne imaging spectrometer that covers the mid-infrared spectral range from $\tilde{\nu}$ = 780 cm^{-1} to $\tilde{\nu}$ = 1,400 cm^{-1} and was part of the instrumental payload on *Geophysica* during the same flights when ERICA was operated. Figure 78 shows the vertical profiles of the nitrate mass concentration from ammonium nitrate retrievals measured by GLORIA during flight KTM03 on 31.07.2017 (Höpfner et al., 2019). The orange line shows the profile measured when the aircraft reached the second flight level and the green curve 10 minutes later on the same flight level (see Figure 141). In Figure 78, the increase in nitrate mass concentration is clearly visible at altitudes above 15 km.

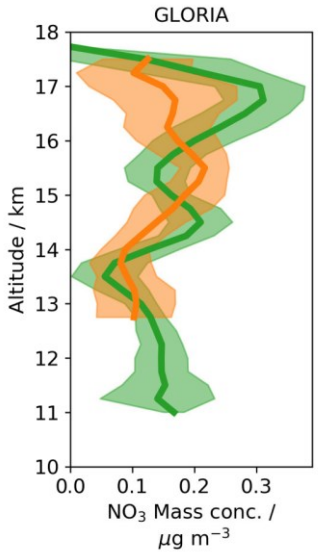

Figure 78: Airborne aerosol observation of GLORIA during flight KTM03 on 31.07.2017. The figure shows GLORIA NO_3 mass concentration profiles from ammonium nitrate retrievals. The data are mean profiles averaged during the flight between 3:50–3:55 UTC (orange) and between 4:05-4:10 UTC (green). Shaded areas indicate standard deviations. The estimated accuracy of the GLORIA data is 30%. The figure is adapted by permission from Springer Nature: Nature Geoscience, Höpfner et al. (2019), [COPYRIGHT] (2019).

Regarding the chemical composition, measurements with GLORIA showed a spectral signature at a wavenumber of $\tilde{\nu}$ = 831 cm^{-1}. This signature is characteristic for solid ammonium nitrate aerosol. This feature could not be replicated with aqueous ammonium nitrate or any other aerosol or trace gas (Höpfner et al., 2019).

To simulate solid ammonium nitrate aerosol particles in the atmosphere, an experiment was performed at the AIDA chamber (Aerosol Interaction and Dynamics in the Atmosphere; Möhler et al. (2008)) by Höpfner et al. (2019). For this purpose, pure ammonium nitrate solution and ammonium nitrate solution with added ammonium sulfate were injected into the chamber. The conditions in the chamber were similar to the conditions in the upper troposphere. No pure aqueous ammonium nitrate aerosol particles were observed down to -35 °C. To initialize particle crystallization of aqueous ammonium nitrate aerosol droplets a small amount of ammonium sulfate is needed. Without traces of ammonium sulfate present in the droplets these remain liquid to much lower temperatures than encountered during the flights. These experimental results support the satellite detection of solid ammonium nitrate particles within the AMA. Further evidence that the aerosol particles in the ATAL consist of an internal mixture of ammonium nitrate and ammonium sulfate was provided by the ERICA-LAMS. Figure 79 shows the mean spectrum of the *NOSO* particle type for particles recorded at altitudes

between 10 and 17 km during the entire StratoClim Asian monsoon phase. The data of this figure are the basis for the figure shown in the supplement of Höpfner et al. (2019). Clearly evident are signals that can be assigned to nitrate and sulfate fragments. In 91 % of the nitrate-containing mass spectra in the altitude range of 10,000 m and 17,000 m in flight KTM03, sulfate fragments are also found.

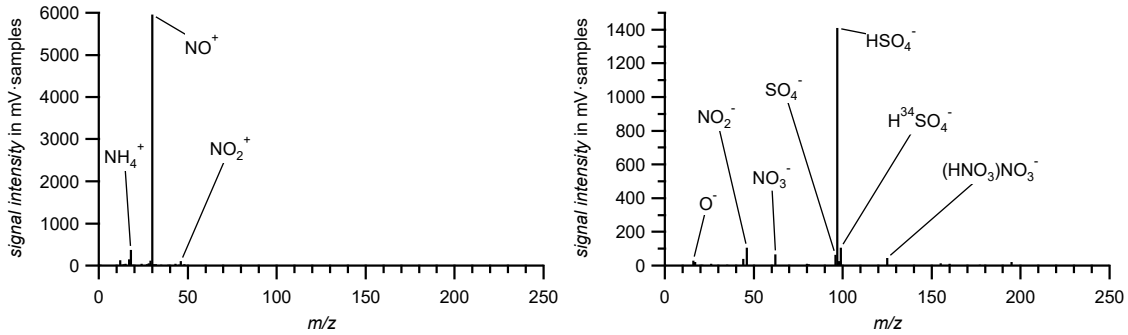

Figure 79: Mean spectrum of the NOSO particle type for 15,044 mass spectra recorded at altitudes between 10,000 m and 17,000 m during the entire StratoClim Asian monsoon phase 2017.

These analyses demonstrate the strength of concurrently operating such a combination of remote sensing and in-situ instruments on the same platform.

5.2.3 ERICA-LAMS results from application of the ion marker method: tungsten, mercury, and gold

Besides the mass spectra sorting method described above, another approach to evaluate single particle mass spectra is commonly used, e.g., by Köllner et al. (2017). In contrast to the sorting algorithm where the relative peak heights of all m/z peaks within single spectra are compared (see Section 5.1.1), the ion marker method is focused on the occurrence of specific single m/z peaks in the single particle mass spectra. These peaks are named ion marker.

By this approach the data set can be investigated for individual species, for instance metals. The search function for ion markers is implemented in the evaluation software CRISP (*ExploreData;* Klimach (2012)) and can be applied after the m/z calibration (see Section 4.4.1). Here, the single particle mass spectra can be checked for m/z peaks of pre-defined thresholds. The method to determine the threshold at which a peak can be interpreted as a valid signal is discussed in Section 4.4.1 and as result a value of 7 mV·samples for both polarities was determined (see Appendix B.14). For the described approach the specific marker ions have to be known in advance in contrast to the clustering method where the algorithm starts with a random mass spectrum (see Section 5.1.1).

The major advantage of this method compared to the clustering method is the independency from the signal intensity ratios of the peaks within a spectrum. To be counted as valid, only the ion marker peak threshold has to be exceeded for the investigated marker ion. The classification of single particle spectra to particle clusters is influenced by dominant ion peaks due to matrix effects and composition-dependent ionization efficiencies (see Section 2.3 and Köllner (2019)).

5.2.3.1 Identifying mass spectra by ion marker peaks and isotopic pattern

The laser ablation technique is highly sensitive to metal ions like Na, K, and Fe. Nevertheless, identifying metal ion species, especially at m/z values below 100 where m/z peaks can also be generated by non-metallic fragments such as organics (isobars), requires a sophisticated approach. One possible approach is the metal species identification by the abundance of the isotopes of the targeted metal

species. This approach is only possible for metals that contain stable isotopes. Furthermore, isotopic ratios close to 1 are not identifiable by this approach and other methods have to be applied.

During m/z calibration by CRISP the procedure creates a matrix, where each row represents a spectrum and each column represents a m/z value. Each cell contains the value for the intensity (Klimach, 2012). Out of this matrix the ratio of two m/z values can be calculated for each single spectrum. Subsequently, the data set can be checked by the *ExploreData* function for a defined value or value range. Thus, the appropriate mass spectra can be isolated. For the a-priori m/z calibration the parameters shown in Appendix C.3.3 (Table 38) were used. The calibration was applied to a data set of 150,565 single particle mass spectra containing research flights as well as ground measurements with ERICA between the flights (termed *enlarged KTM total data set*).

The whole data set was tested by this marker peak method to identify tungsten-containing particles. Tungsten was used as a marker since it was not expected naturally at high altitudes (> 8,000 m). Due to its extreme high melting (3,414 °C) and boiling point (5,555 °C) and because tungsten does not possess a measurable vapor pressure at standard conditions (*CRC Handbook of Chemistry and Physics*, 2018), the free element tungsten will not reach high altitudes in gaseous phase. It occurs naturally mainly in minerals (Brown and Pitfield, 2013). China, a country close to the sampled area, owns most of the tungsten ore resources and is also the world's largest supplier (Shedd, 2019). The element is technically used as component of hard material such as tungsten carbide (Holleman, 2019), in alloys such as W-Mo-alloys for aerospace application (Guan et al., 2011) and for light bulbs filaments (Brown and Pitfield, 2013). Therefore, tungsten-containing particles can be used as an anthropogenic marker for particles in the atmosphere and are of interest for this reason.

Natural W consists of one very long-lived radioisotope (^{180}W; half-life of $(1.8 \pm 0.2) \cdot 10^{18}$ years) and four stable (^{182}W, ^{183}W, ^{184}W and ^{186}W) isotopes. Table 17 shows the natural abundance of the natural tungsten isotopes (Audi et al., 2003). For the following evaluation the ratio of ^{184}W/^{183}W = 2.14 is used to identify tungsten-containing particles in the single particle mass spectra. In practice, a ratio interval between 1.5 and 2.7 is used for the evaluation. The usage of a range rather than a precise value is necessary due to the statistical deviation of the peak intensity of the m/z peaks.

Table 17: Natural tungsten isotopes and their natural abundances (Audi et al., 2003).

Isotope	Natural abundance
^{180}W	0.12 %
^{182}W	26.50 %
^{183}W	14.31 %
^{184}W	30.64 %
^{186}W	28.43 %

With the described procedure, 10 tungsten-containing particles were identified, which are 0.007 % of the *enlarged KTM total data set*. Figure 80 shows a bipolar single particle mass spectrum exemplarily. The spectrum depicts beside of W, furthermore Mo and Cd signals that both were also identified by their isotopes. In addition, Mg, Cr, and Fe could be identified in the same manner. Additionally, marker ions of light metals (Na and Al) and sulfate fragment ions (HSO_4^- and $[HSO_4SO_3]^-$) are present. Al (m/z +27) was verified by the marker ions at m/z +43 (AlO^+) and m/z -59 (AlO_2^-). The peak at m/z +23 is commonly taken as Na^+ (Roth, 2014), since at this m/z value organic substances generate no fragments. The particle was recorded during the second research flight during StratoClim in

Kathmandu (KTM02, on 29.07.2017) in 20,402 m (amsl) altitude. After size calibration (see Section 4.2.2) a particle size of d_{va} = 602 nm could be found. Dedicating this single particle to a certain source is difficult. However, an anthropogenic source such from aircraft engines where W-Mo-alloys are in use (Guan et al., 2011) is conceivable due to its heavy metal signals.

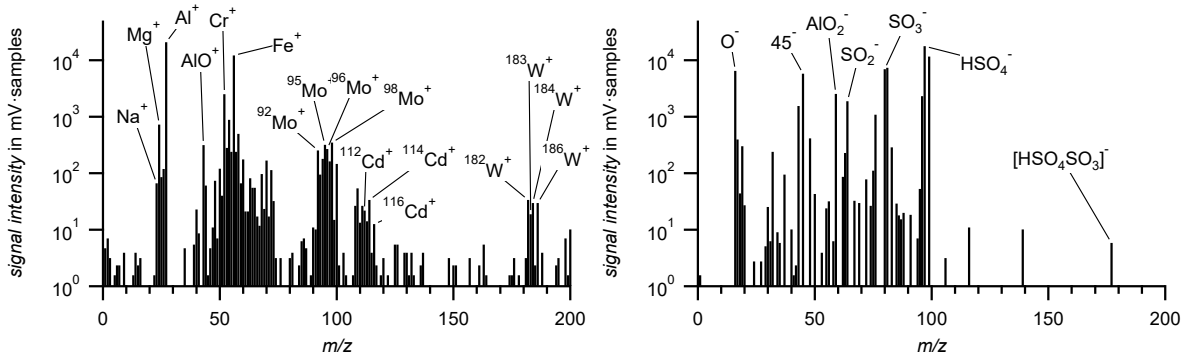

Figure 80: High mass metal and sulfate-containing particle detected in 20,402 m altitude (29.3846° N, 80.7619° E) during StratoClim flight KTM02 (29.07.2017, 06:09:34 UTC; d_{va} = 602 nm).

Despite the hypothesis states this particle of anthropogenic origin the source of the particle is unknown. Both, long-range transport to this altitude and emissions at these altitudes by aircraft or spacecraft are possible. Further investigation on meteorological parameters and other indicators would be needed to verify one of these and other possibilities. However, the ion marker method is useful to search for and identify elements that consists of more than one natural isotope.

The ion marker method can be applied in a sophisticated strategy to investigate a data set step wise. For instance, the determined tungsten-containing particles can be checked further for other ion marker peaks. Finally, a logic could be developed where most of the metal species can be grouped together. Due to isobars and monoisotopic species this logic is demanding to develop. This development was not within the scope of this work.

Beside metal ion marker peaks also for other specific ion marker peaks can be searched for. For instance, the ion marker peaks that are listed in Appendix C.4 can be applied. Here, nitrate-containing particles (m/z -46 (NO_2^-) and/or -62 (NO_3^-)) were investigated with respect to their sulfate content (m/z -96 (SO_4^-) and/or -97 (HSO_4^-), and/or -98 ($H_2SO_4^-$)). Therefore, the data set was filtered for nitrate ion marker peaks first. Then, the sulfate fragment containing particle number fraction was calculated. The result is that 95% of the particles with nitrate signature also contained sulfate. The described approach can also be applied to all mass spectra that were recorded above 5,000 m. Figure 81 shows the mean spectrum of nitrate-containing particles sampled at altitudes above 5,000 m where the nitrate and sulfate fragments are obvious. Here, the nitrate-containing mass spectra contain also 95 % of the described sulfate fragments. This might be an indication that nitrate-containing particles are internally mixed with sulfate compounds and that sulfate-containing particles were created first. This corresponds to the process described in Seinfeld and Pandis (2016), in which nitric acid gets absorbed on ammonium sulfate particles. This, however, remains speculative. The presence of metals demonstrates that the nitrate particles do not only form by homogeneous nucleation or that uptake of other materials by the nucleated particles might be important.

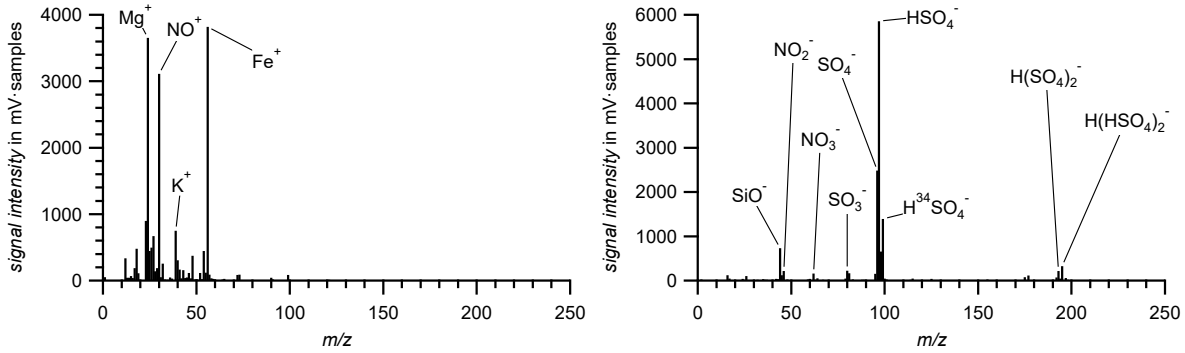

Figure 81: Mean stick spectra of 29,616 nitrate-containing particles sampled at altitudes above h_{amsl} > 5,000 m.

5.2.3.2 Mercury-containing particles in the atmosphere

Mercury is known as a global pollutant and of high interest due to its high toxicity and its ability to undergo long-range transport in the atmosphere. The global distribution of anthropogenic emissions of Hg shows an enhancement over South Asia. Thus, it was suspected to be found in the particle phase during the Asian monsoon phase as well (Kumari et al., 2015). Sources can be of natural or anthropogenic origin (Pirrone et al., 2010): Primary natural sources include volcanoes, geothermal sources, re-emission of already deposited Hg on water surfaces, land and vegetation, and biomass burning. Anthropogenic sources are coal and oil combustion, metal refining, incineration of waste, smelters, and manufacturing units (Kumari et al., 2015).

To check for mercury-containing particles in the *enlarged KTM data set* (in total 150,565 single particle mass spectra) the method presented in Section 5.2.3.1 was adopted. To identify the mass spectra of mercury-containing single particles the ion marker peaks m/z +199 ($^{199}Hg^+$), +200 ($^{200}Hg^+$), and +202 ($^{202}Hg^+$) were used. At least two of these three ion markers had to exceed the threshold of 7 mV·samples. As result 69 mass spectra (0.050 %) were found that represent mercury-containing particles as an upper limit. According to the method described above the ratio of the peaks m/z +199 ($^{199}Hg^+$) to +200 ($^{200}Hg^+$) was used to identify a lower limit (ratio between 1 and 3) that results in 48 (0.035 %) mass spectra. In KTM01 no mercury-containing particles were observed. One reason for the low number of mercury-containing particles might be the ionization energy of Hg of 10.4 eV. Another reason of the small fraction is the short atmospheric lifetime of particulate Hg compared to elemental gas phase Hg (Murphy et al., 2006). For further analysis the upper limit was used for better statistics.

Figure 82 shows the vertical profiles of the particle number fraction f_{part} of the mercury-containing particles, the median of the ambient temperature with interquartile ranges measured by UCSE (see Section 3.8.4), and ozone mixing ratio with interquartile ranges measured by the FOZAN-II (Fast OZone ANalyzer) in-situ instrument which also was operated on the M-55 *Geophysica* (Ulanovsky et al., 2001). To determine the particle number fraction f_{part} for one bin, the ratio of counts of mercury-containing particles and all collected particles are calculated for each bin. For the temperature and the ozone mixing ratio profile the same altitude bins were used as for the mass spectra evaluation (500 m). The particle number fraction f_{part} of mercury-containing particles shows an enhancement at altitudes above 16,000 m. Compared to previously shown fractions the value is low (see Sections 5.2.2.2 or 5.2.3.3). Due to poor statistics, f_{part} is difficult to quantify at low altitudes. However, it can be excluded that f_{part} is as high as at the upper flight altitudes, but it demonstrates the presence of mercury-containing particles in the UT/LS. The temperature profile combines the temperature measurements from all eight research flights, the ozone mixing ratio of all research flights except for KTM01 and

KTM06, where no data is available. The temperature profile depicts an averaged CPT at around 17,000 m (-81°C). Like f_{part} of mercury-containing particles the ozone mixing ratio increases at an altitude of 16,000 m. Ozone was identified as most important oxidizer for Hg in the atmosphere (Hynes et al., 2009). The coincidence shown in Figure 82 might support this result.

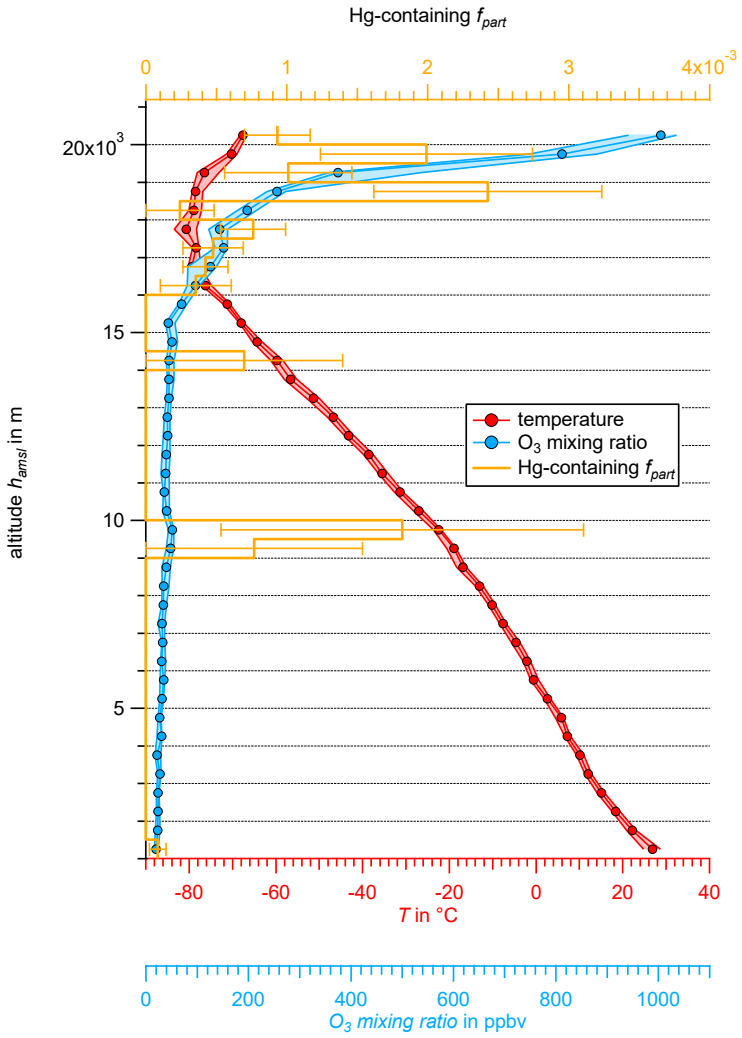

Figure 82: Vertical profiles of the particle number fraction f_{part} of the mercury-containing particles (orange, top abscissa; in total 69 mass spectra), the median of the ambient temperature (red, connected dots, bottom abscissa) with interquartile ranges (shaded area) provided by UCSE and ozone mixing ratio (blue, connected dots, bottom abscissa) with interquartile ranges (shaded area) provided by FOZAN-II. The altitude intervals are in bins of 500 m. The uncertainties are calculated from counting statistics according to Appendix C.2.3.

Murphy et al. (2006) also observed mercury-containing single particles in the UT/LS region. In addition, measurements of Slemr et al. (2009) had shown that the Hg vapor concentration decreases at altitudes around the tropopause and concluded that the depleted gaseous Hg reappears in the particulate phase. A reason might be condensation of elemental Hg (Hg^0) onto existing particles, nucleation, or chemical reaction, i.e., oxidation, by mainly ozone to $Hg^{(II)}$ according to Equation (55) in an aqueous phase. A homogenous reaction in the gas phase is unlikely (Hynes et al., 2009).

$$Hg^0 + O_3 \rightarrow Hg^{(II)}O + O_2 \qquad (55)$$

The low temperature in the altitude where the enhancement of the mercury-containing particle fraction occurs (< -75 °C) is far below the melting point of elemental Hg (-38.8°C; Holleman (2019)). In the case of condensation of Hg on particles it can be expected that the condensation core would be a particle type that occurs in higher abundance in the considered altitudes like *Meteoric* (see Section 5.2.1) with additional ion marker peaks that are characteristic for Hg, i.e., the isotopes of Hg. Figure 83 depicts the mean spectrum of the mercury-containing particles sampled above 15,000 m. The graph shows m/z values up to 250 since no peaks were observed above that value. The spectral pattern differs from the pattern of the *Meteoric* particle type (see Section 5.2.1). In addition, the spectrum-to-spectrum variability of the individual mass spectra is very high, resulting in no typical single particle mass spectrum of mercury-containing particles. Furthermore, only 9.5 % of the spectra contain ion marker peaks that are possibly caused by presence of iron (m/z +54 ($^{54}Fe^+$) and +55 ($^{55}Fe^+$)), but no iron oxide fragments were found. These arguments indicate that a condensation process might be unlikely, at least for the *Meteoric* particle type. Due to the lack of laboratory studies it cannot be excluded that matrix and charge transfer effects (see Section 2.3) could change the spectral pattern of *Meteoric* mass spectra in presence of Hg in the particle. The preference of Hg condensing on a specific particle type cannot be evaluated due to the small number of mercury-containing mass spectra. Better statistics furthermore would allow to investigate the mixed components of the mercury-containing particles.

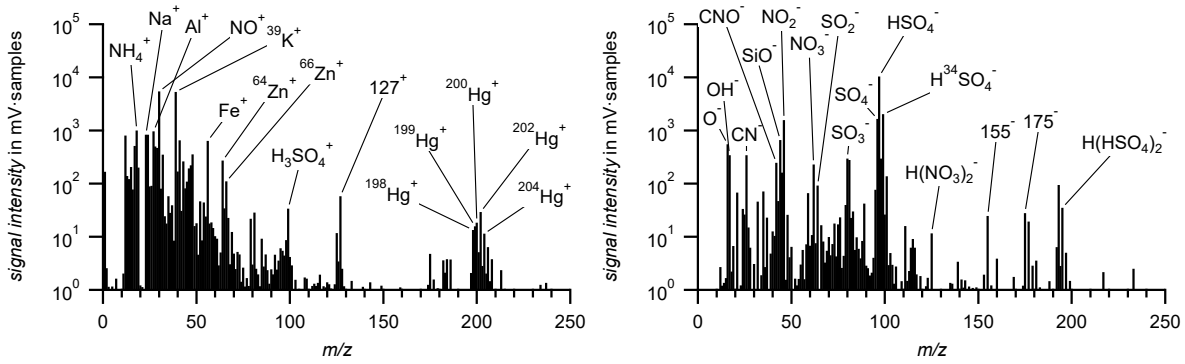

Figure 83: Mean stick spectra of mercury-containing particles sampled at altitudes larger 15,000 m (in total 63).

Nucleation as part of a New Particle Formation (NPF) event is not possible to be observed by the ERICA-LAMS. The NPF occurs in a size range smaller 20 nm that is much smaller than the observable size of d_{va} = 174 nm (d_{50}, see Section 4.2.4). However, particles that have grown on small Hg nuclei might be large enough to get detected and ablated. To confirm nucleation as sink for Hg vapor in the UT/LS region, other measurement techniques, such as particle sampler are needed. Here, the samples are evaluated by electron microscopy and elemental analysis (Ebert et al., 2016). These methods might deliver more detailed results. However, the size distribution of the mercury-containing fraction might indicate such NPF process in case the size distribution shows a mode close to the d_{50} value.

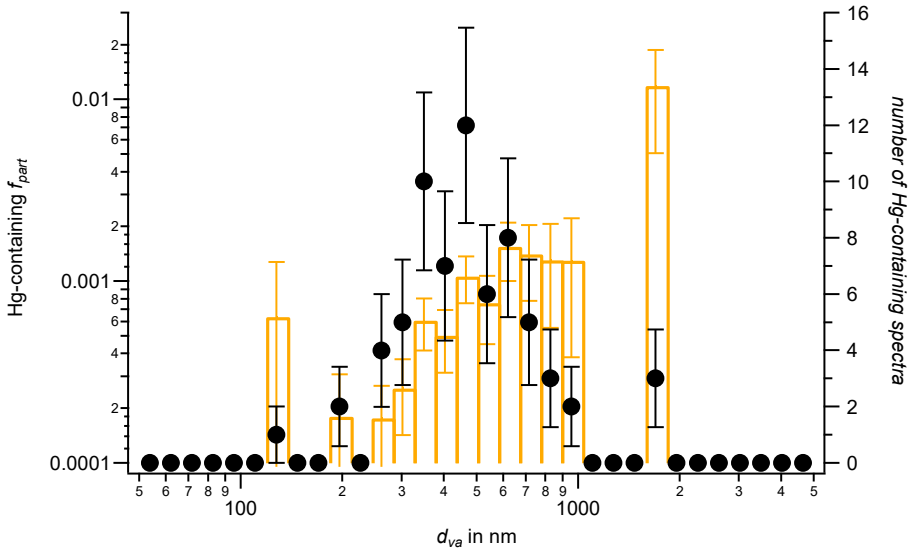

Figure 84: Size distribution as function of d_{va} of the mercury-containing particle fraction (orange, left ordinate) and the number of mercury-containing spectra (black markers, right ordinate; in total 69 mass spectra). The uncertainties are calculated from counting statistics according to Appendices C.2.2 and C.2.3.

Figure 84 shows the size distribution of the mercury-containing particles. Within the uncertainties the size of the fraction is consistently distributed between d_{va} = 325 nm and d_{va} = 1,020 nm. Particle sizes below d_{va} < 240 nm barely appear and in particular no peak or mode at the lower size detection limit can be seen. The reason might be the density of the particles. In addition, assuming mercury-containing particles possess higher density the size values (d_{va}) presented here are shifted to larger sizes (see Appendices B.1.4 and B.2) than the for calibration used PSL NIST size standards. Thus, the particle size of the measured mercury-containing particles is overestimated and the particles possess smaller values of d_{geo} than depicted in Figure 84.

To react in the aqueous phase, Hg has to be solved first. Elemental Hg has a Henry's Law constant of $1.1 \cdot 10^{-1}$ M·atm^{-1} (Sanemasa, 1975) and thus it is not highly soluble in water (Hynes et al., 2009). Also, HgO is known as sparingly soluble in water (10^{-4} mol·L^{-1}; Holleman (2019)). Therefore, it might be identified in the particle phase. In Figure 83 the species of Hg (like oxides or sulfides) cannot be identified, since no signals appear at m/z values higher than +206. Therefore, HgO cannot be proven but also cannot excluded that it is a component of the particle. An indication for HgO and thus for Equation (55) might be number of oxygen-containing particles within the set of mercury-containing particles. According to the analyses 43% of the mercury-containing particles also exhibit m/z -16 (O^-) lines. However, the source of the oxygen might also be particulate nitrate or sulfate. 70 % of the mercury-containing particles also contain fragments of nitrate (m/z +30 (NO^+), -46 (NO_2^-), and -62 (NO_3^-); at least two of these three ion marker peaks) and 92 % sulfate (m/z -97 (HSO_4^-) and -99 ($H^{34}SO_4^-$); at least one of these two ion marker peaks). The peaks at m/z +127, -155 and -177 are not identified.

A direct reaction of Hg with sulfuric acid to $Hg(SO_4)$ and with nitric acid to $Hg(NO_3)_2$ is unlikely at the conditions in the upper troposphere, since the syntheses in laboratory conditions need high temperatures and highly concentrated acid. However, the reaction might be possible but only slow, the products would be hydrolyzed in presence of water to sparingly soluble basic mercury salts according to Equation (56) (Holleman, 2019).

$$3\,HgSO_4 + 2\,H_2O \rightarrow HgSO_4 \cdot 2\,HgO + 2\,H_2SO_4 \quad (56)$$

The fact that oxidation products of Hg, such as HgO and basic mercury salts, are sparingly soluble leads to the conclusion that Hg might accumulate in a single particle after oxidation in the aqueous phase. The water content in the measured particles is unknown, but concentrated sulfuric acid tends to absorb water vapor (Greenewalt, 1926) also under conditions of the UT/LS (Seinfeld and Pandis, 2016). However, the oxidation process described in Equation (55) might also work in water free liquid concentrated sulfuric acid.

The poor statistics, hamper a final conclusion for a preferred process of the depleted Hg vapor. Therefore, further measurements are needed to enlarge the total number of mercury-containing spectra and improve on the statistics. In addition, other analysis methods have to be considered for a comprehensive evaluation, for example EDX and electron microscopic analyses on the aerosol particles that were collected for a posteriori analysis by an instrument in the payload of *Geophysica* (Ebert et al., 2016).

5.2.3.3 Gold-containing particles as artefacts from the gold-plated aircraft inlet

The ERICA instrument was mounted in a pressurized container and connected to an in-house build aircraft inlet system that protrudes out of the cowling of *Geophysica* to sample ambient air during the flights for the StratoClim campaign (see Section 3.8.3). The surface of the inlet was plated with a chemically inert gold-layer (Dragoneas et al., 2020). Murphy et al. (2004) have shown that ice crystals can produce submicron metal fragments when they impact the inlet while the aircraft is flying through ice clouds. However, the inlet was designed in a way that this effect is reduced to a minimum (Dragoneas et al., 2020). The recorded *KTM total data set* of 146,413 mass spectra was checked for Au ion marker peaks in order to proof the occurrence of gold-containing particles.

As discussed in Section 4.4.1.2, Au consists of one natural isotope only. However, it can be detected by the ERICA-LAMS. A possibility to identify gold-containing particles is to check for the Au_2^+ marker ion peak at m/z +394. Therefore, a m/z calibration up to m/z ±400 was necessary. Table 39 in Appendix C.3.3 shows the parameters of the m/z calibration used for the evaluation of gold-containing particles. For a-posteriori m/z calibration, the *KTM total data set* was checked for the Au ion markers m/z +197 and +394. The result was one single particle with the spectrum shown in Figure 85. It depicts the ion markers for Au (Au^+ and Au_2^+). Furthermore, the signals at m/z +63 ($^{63}Cu^+$), +65 ($^{65}Cu^+$), as well as m/z -115 ($Cu(CN)_2^-$) and -117 ($^{65}Cu(CN)_2^-$) indicate copper fragments as identified by the isotopic ratio. The latter two peaks and the peaks at m/z +72 (Na_2CN^+), +88 ($NaKCN^+$), -26 (CN^-), and -42 (CNO^-) indicate cyanide fragments besides m/z +23 (Na^+) and +39 (K^+) as the light metal fragments of sodium and potassium. Another light metal, Al, is indicated by peaks at m/z +27 (Al^+) and -75 (AlO_3^-). The peaks at m/z -204, -206, -249, -339, and -341 are not identified. The double signals at m/z -204 / m/z -206 and m/z -339 / m/z -341 might come from an element with an isotopic ratio of around 1 like Cu. Thus, it is very likely that the shown fragments might result from a particle that was spalled from the aircraft inlet. During the electroplating process the aluminum body of the aircraft inlet was first pickled by a basic zinc solution, then electroplated with a copper layer and afterwards with a gold-layer. At that, alkali cyanide solutions were used (Personal communication: M. Hobucher, MPIC, 2019). However, another particle source, for instance space debris (Opiela, 2009), cannot be fully excluded.

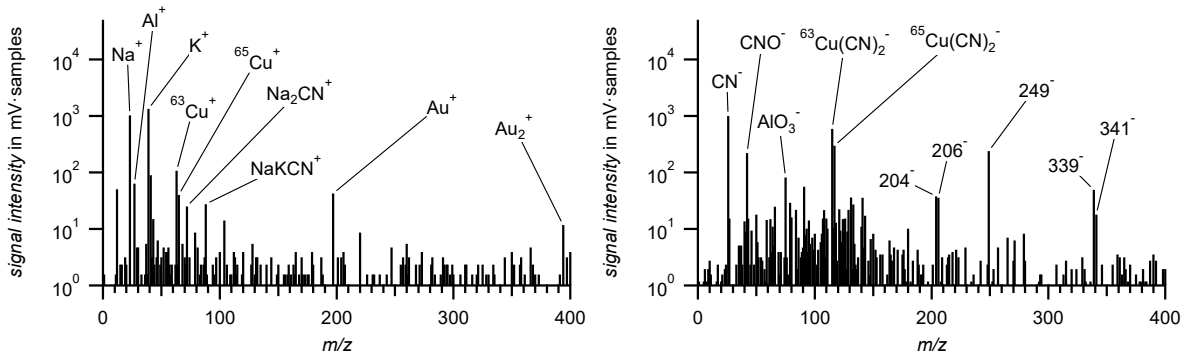

Figure 85: A gold-containing atmospheric single particle detected in 6,450 m altitude (27.7718° N, 84.987 ° E) during StratoClim (flight KTM05, 04.08.2017, 03:26:59 UTC; d_{va} = 379 nm).

Just one ablated particle out of over 140,000 particles in the whole data set seemed to be too few, so the approach of the ion marker method was broadened. High signals in the raw spectrum might lead to a mis-calibration of the m/z peak at m/z +394 (Au_2^+). Therefore, the data set was checked for two marker peaks: m/z +393 and +394. The result were 131 single particle mass spectra that were defined as lower limit of the number of gold-containing particles. Assuming another possible mis-calibration, the upper limit of gold-containing particles was defined by taking additionally peaks at m/z +196 and +197 into account. This approach led to 3,242 single particle mass spectra.

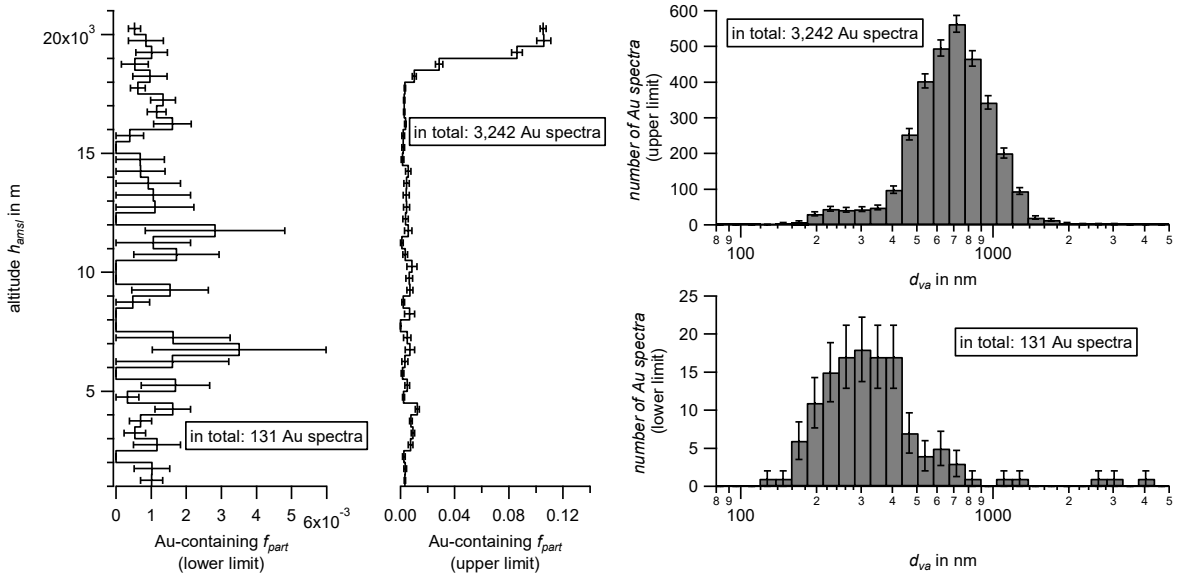

Figure 86: Vertical profiles (left-two panels) of the lower limit (left) and the upper limit (right) of the gold-containing particle fraction normalized to the total number of spectra contained in each bin. The right panels show the particle number size distributions (d_{va}) of the lower limit (bottom) and the upper limit (top) of the gold-containing particle numbers. The uncertainties are calculated from counting statistics according to Appendices C.2.2 and C.2.3.

Figure 86 shows the vertical profiles (left-two panels) of the lower limit (left) and the upper limit (right) of the gold-containing particle fraction over all research flights (bin size 500 m). For the lower limit, no accumulation at a certain altitude is obvious in contrast to the upper limit where enhanced values are found at altitudes above 17,000 m. The consistent distribution over the altitude of the lower limit fraction indicates a random occurrence of the gold-containing particles. Since the ion marker m/z +196 can be interpreted as $[(H_2SO_4)_2]^+$ ion (beside a mis-calibrated m/z +195) and thus as a fragment of sulfuric acid, the abundance at high altitudes where high concentrations of pure sulfuric acid are expected is reasonable (Junge and Manson, 1961; Lazrus and Gandrud, 1974; Murphy et al.,

2014). Thus, the upper limit might indicate an overestimation of the number of spalled Au particles from the aircraft inlet.

Shown at the right side of Figure 86 are the number size distributions (d_{va}) for the particles defining the lower and upper limit of the number of gold-containing particles. It is obvious that for the two limits the modes differ from d_{va} = 300 nm for the lower limit to d_{va} = 700 nm for the upper limit. This indicates that a different particle type may be responsible for the spectra of the upper limit than for the lower limit. A possible particle type that the mass spectra of the upper limit are part of might be the *Meteoric* particle type (see Section 5.2.2). This particle type also occurs at high altitudes and shows a similar size distribution pattern (see Section 5.2.2.1). In addition, ion marker peaks in the *Meteoric* particle type indicates sulfuric acid/sulfate content (see Section 5.2.1, Figure 69). Therefore, the upper limit might be an artefact caused by sulfuric acid- /sulfate-containing particles at high altitudes, possibly as part of the *Meteoric* particle type. However, this indicates that a combination of the clustering/grouping and the ion marker peak method is more powerful for data evaluation than just one of the methods alone.

In order to find the reason for the abrasion of the Au surface, the occurrence of Au particles can be compared with events such as flight patterns or meteorological events during the research flights. However, clouds are rather unlikely as a reason. It cannot be excluded that particles may adhere to the inlet surface during the flight and be released again later, containing Au fragments or not, resulting in delayed particle sampling. Nevertheless, the results of the evaluation for gold-containing particles show the possibility of the ERICA-LAMS to measure gold-containing particles during the StratoClim Asian monsoon phase and restrict possible contamination of the measurements by aircraft inlet fragments to an upper limit of 2.21 % in total, at least to 0.09 % (lower limit). This leads to the conclusion that the selected inlet design worked well for providing uncontaminated sample particles to ERICA.

5.2.4 Interaction of the ERICA-LAMS and the ERICA-AMS in StratoClim

Simultaneously to the single particle measurements with the ERICA-LAMS, mass spectra were also recorded with the ERICA-AMS during the StratoClim research flights. Especially with regard to sulfate-containing and sulfuric acid aerosol, the benefit of a simultaneous aerosol measurement by the two different measuring methods (LDI and flash vaporization/EI) is demonstrated. The research flight KTM01 was chosen for this demonstration. Figure 87 (left panel) shows the continuous and simultaneous performance of measurements by ERICA-LAMS and ERICA-AMS during this flight. Here, the time series of the sulfate mass concentration C_{SO4} (related to standard pressure) and the number of sulfate-containing single particle mass spectra (time bin size 90 s), are displayed. By applying the 7 mV·samples ion peak area threshold (see Appendix B.14) to m/z -96 (SO_4^-) and -97 (HSO_4^-), the sulfate-related marker signals (see Appendix C.4) were identified. The instrument started measuring after an automatically induced rebooted in an altitude of 5,305 m. In the time series in Figure 87 four sections of interest (a-d) are marked.

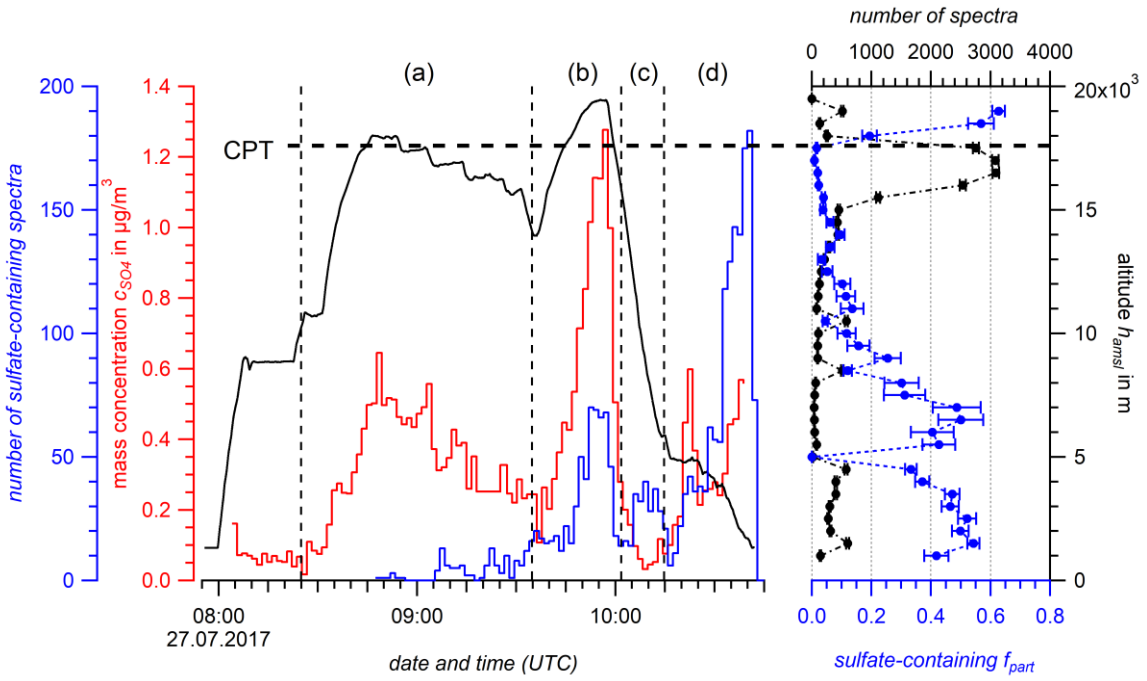

Figure 87: Left panel: Time series (flight KTM01 during StratoClim in Nepal, 27.07.2017, 08:00 – 10:45 UTC) of the sulfate-containing single particle mass spectra within 90 seconds as measured by the ERICA-LAMS (blue trace), the sulfate mass concentration (average time 90 s) as measured with the ERICA-AMS (red trace) and the aircraft altitude (black trace). Right panel: Vertical profile of the particle number fraction f_{part} of the sulfate-containing particles (blue) and the number of spectra in the corresponding altitude bins (in total: 20,516). The vertical resolution is in altitude bins of 500 m. The dashed horizontal line marks the estimated CPT (at h_{amsl} = 17,600 m). The uncertainties are calculated from counting statistics according to Appendices C.2.2 and C.2.3.

In the first section (a), the mass concentration of sulfate is increased, while the number of sulfate-containing particles detected is low. A possibility would be a sulfate-containing aerosol type in the for the ERICA-LAMS sub-detectable size range. Another possibility could be that pure sulfuric acid aerosol caused the increased sulfate mass concentration, which the ERICA-LAMS is not able to detect (Murphy, 2007). A third possibility would be that the here measured particle type consists of aged aerosol coated with sulfuric acid, which might reduce the ion yield at the ERICA-LAMS (Hatch et al., 2014). In the present case even to the extent that hardly any particles are detected at the ERICA-LAMS. However, in all three cases the ERICA-AMS would be suited to detect the sulfate components. The mean spectra of the sulfate-containing single particles indicate ammonium nitrate and mineral content (Figure 88, a).

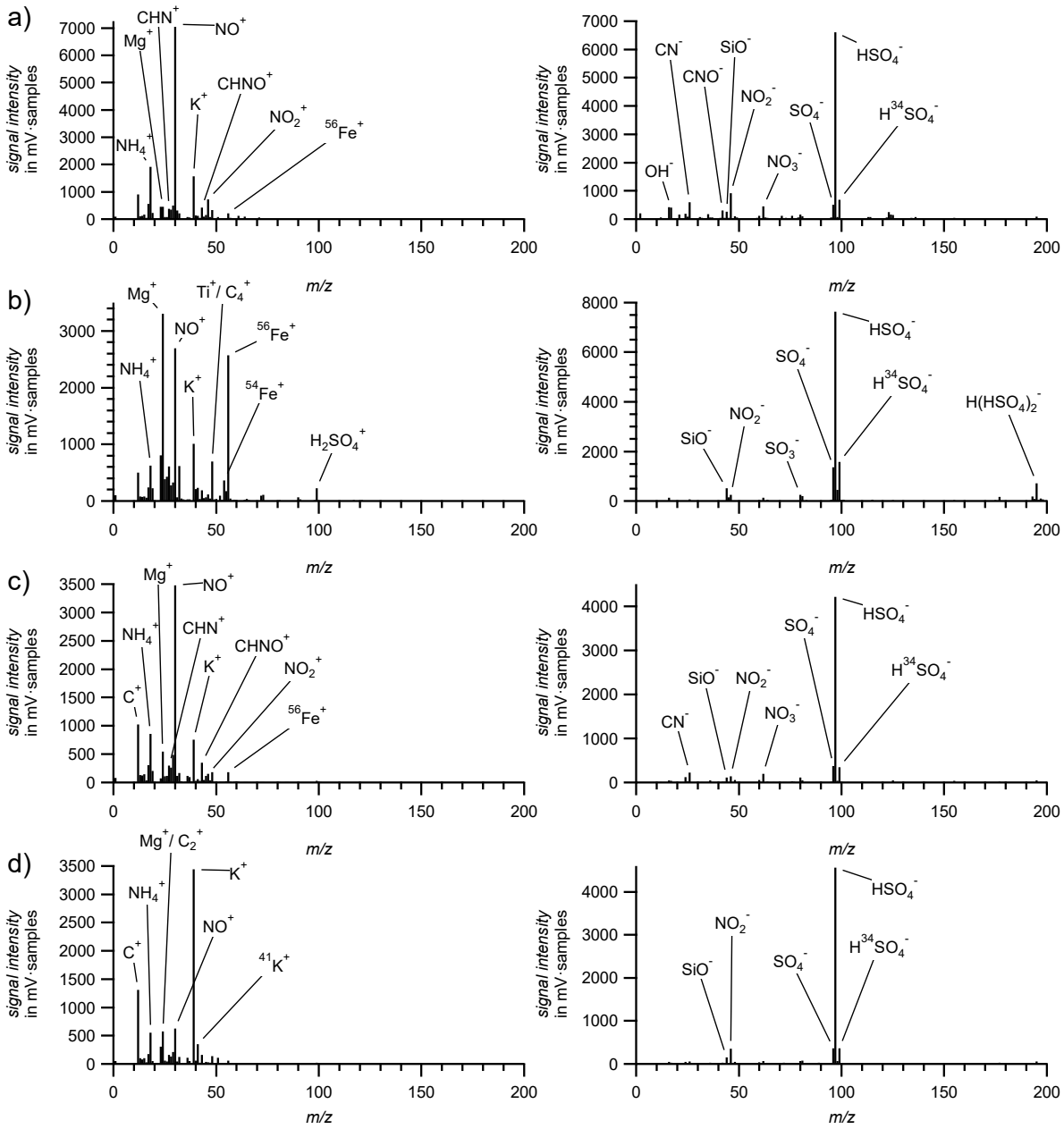

Figure 88: Mean spectra of the sulfate-containing single particle spectra recorded during flight KTM01 (27.08.2017) in various time intervals: a) 08:25:00 – 09:35:00 (169 mass spectra), b) 09:35:01 – 10:02:00 (603 mass spectra), c) 10:02:01 – 10:15:00 (247 mass spectra), and d) 12:15:01 – 10:42:00 (1363 mass spectra). All times are in UTC.

The data from ERICA-LAMS, as well as ERICA-AMS show an increase of the sulfate mass concentration as well as the amount of sulfate-containing single particles in the stratosphere (flight section b), i.e., at altitudes above the estimated CPT of 17,600 m altitude. This result can be expected due to the close proximity of the Junge-layer (Junge and Manson, 1961; Lazrus and Gandrud, 1974; Murphy et al., 2006; Ebert et al., 2016), which in the tropics is a few km above the ceiling of *Geophysica*. The enhancement of the sulfate-containing single particles measured by the ERICA-LAMS during flight section (b) is caused by condensed sulfuric acid on meteoric dust particles (Schneider et al., 2019). The mean spectrum (Figure 88, b) shows the typical structure of such a *Meteoric* particle type (see Section 5.2.1). Section (c) is characterized by an anticorrelation of sulfate mass concentration and the number of sulfate-containing single particles. However, the single particle mean spectrum is similar to the one of section (a) (Figure 88, c). That might indicate either that the same sulfate-containing aerosol type from

section (a) here has a thinner sulfate coating or that at these altitudes no pure sulfuric acid is present and thus not much mass is detected by the ERICA-AMS. Another simultaneous increase of mass concentration and sulfate-containing single particles is observed in section (d). Here, the mean spectrum shows a dominant peak at m/z +39 that is interpreted as K^+ indicating another aerosol type (Figure 88, d).

The right panel of Figure 87 shows the vertical profile of the number of single particle spectra indicating a higher proportion of the sampling time spent at the altitude range of 14,000 – 18,000 m. In addition, the particle number fraction f_{part} of the sulfate-containing particles is depicted. The parameter f_{part} is the ratio of the number of sulfate-containing particles to the number of all particles in each 500 m bin. The three different modes of the sulfate-containing f_{part} can be related to the sections (b), (c) and (d), as counted from top. In Figure 89, panel A, the vertical profile of the sulfate mass concentration C_{SO4} from ERICA-AMS is shown. As for the sulfate-containing single particles, an increase of the sulfate occurrence near the ground up to 6,500 m and above the estimated CPT (at h_{amsl} = 17,600 m) is clearly evident. Despite the high fraction of sulfate-containing single particles in the altitude range of 6,500 m to 11,000 m (Figure 87, right panel) the absolute concentration of particles is too low to generate a detectable signal at the ERICA-AMS. Above an altitude of about 13,000 m the sulfate mass concentration increases and reaches its maximum at an altitude of 18,500 m (Figure 89, panel A). This increase can be assigned to the Junge-layer (e.g., Junge and Manson (1961)).

The investigation conducted here shows that by using two complementary measuring techniques, the disadvantage of one component can be at least partially compensated for the advantage of the other component (see Section 1.2). The weakness of the ERICA-LAMS that is not able to detect pure sulfuric acid can be compensated by the ERICA-AMS. Vice versa, the weakness of the ERICA-AMS, which only detects non-refractory aerosol, is compensated by the ERICA-LAMS. Thus, the two methods, the ERICA-LAMS and the ERICA-AMS, used simultaneously contribute to a more comprehensive result than if only one of the two components had been adopted for aerosol analysis.

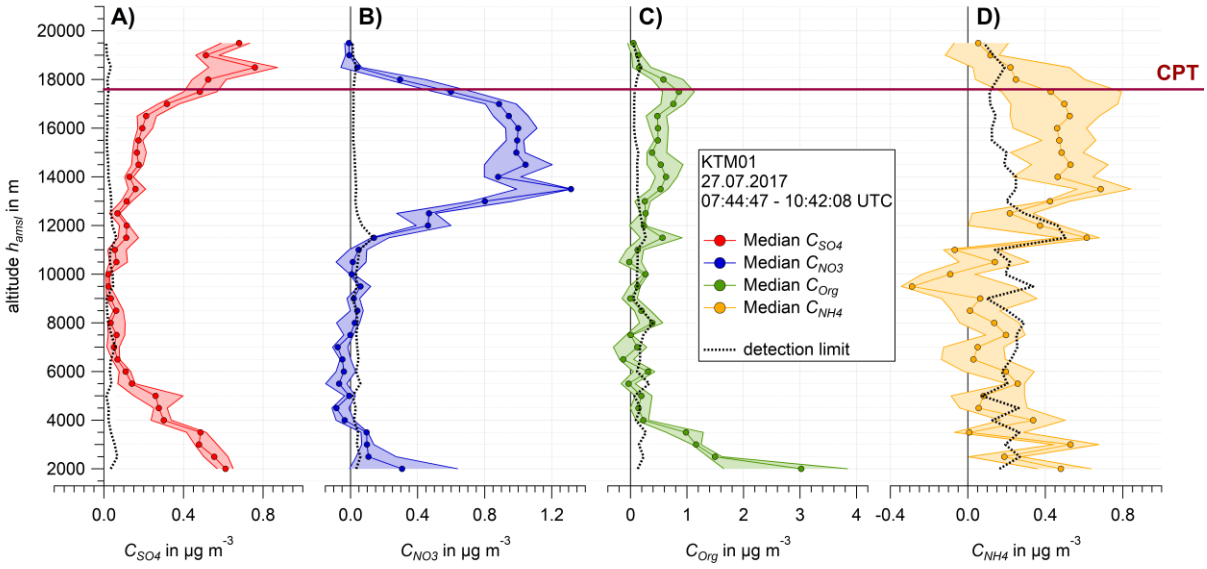

Figure 89: Vertical profiles of (A) sulfate (red), (B) nitrate (blue), (C) organics (green), and (D) ammonium (yellow) median mass concentration and interquartile ranges (shaded areas). For each species the calculated detection limit is depicted. The dark red horizontal line marks the estimated CPT (at h_{amsl} = 17,600 m). The data was provided by O. Appel.

In addition to the vertical profile of the sulfate mass concentration C_{SO4}, Figure 89 also shows the mass concentrations of nitrate C_{NO3} (Figure 89, panel B) and organics C_{Org} (Figure 89, panel C). Both species show increased mass concentration values near the ground (up to 3,500 m) and values around the detection limit until the values increase again at about 11,500 m for nitrate and at about 12,500 m for organics. Above the estimated CPT, the mass concentrations decrease down to the detection limit. The fourth species is particulate ammonium (Figure 89, panel D). Due to instrumental limitations (high air beam signal, see Section 4.5.1) the vertical profile is noisy. Up to an altitude of 12,500 m, the measured values of the ammonium mass concentration C_{NH4} fluctuate around the detection limit. Above that altitude, an increase of the mass concentration C_{NH4} is evident. Thus, all four species exhibit a layer feature above 12,500 m which extends to altitudes above the estimated CPT. This is the ATAL, which is discussed in Section 5.2.2.2. Besides the composition of nitrate and sulfate discussed in Section 5.2.2.2, the vertical profiles here show that the ATAL also consists of ammonium and organic components. This coincides with the results of the ERICA-LAMS where the particle type *NOSO* and *OrgNOSO* is present in the altitude range of the layer (see Appendix C.11, Figure 180, KTM01). Figure 87, right panel, indicates that in the altitude range of the ATAL, sulfate-poor aerosol was measured by the ERICA-LAMS. This result, which is not contradictory to the ERICA-AMS result, can be resolved by the fact that a different type of particle is present in this altitude range, which effectively reduces the fraction of sulfate-containing particles. By applying the clustering algorithm with consecutive manual particle type grouping (see Section 5.2.2), the *Inorganic* particle type was found also during flight KTM01. In this particular flight, no sulfate markers were found in the mean spectra of the *Inorganic* particle type (see Appendix C.9, Figure 155). This fact shows that for a comprehensive single particle analysis, both the ion marker method and the clustering method should be used. The *Inorganic* particle type might be related to refractory mineral dust material that cannot be measured by the ERICA-AMS. The mass concentrations of the respective species are up to a factor of 100 lower than in measurements carried out a year earlier in North-West India (Brooks et al., 2019). However, the numerical values, in the corresponding altitude ranges, are comparable with those of another measurement in the tropics above the Amazonian rain forest (Schulz et al., 2018). Altogether, the composition and the sources for this ATAL and the particles it consists of are subject of further investigations.

Flight KTM01 shows exemplarily that the gain in information benefits when both complementary methods (LDI and flash vaporization/EI) are used simultaneously. Furthermore, the single particle evaluation should not be limited to one evaluation method, clustering or markering. Since every evaluation method has its weaknesses, both methods should be combined and used in parallel. Of course, the data have to be carefully placed, for example by means of Chemical-Transport Models (CTM), into the meteorological context, as well as the distributions of dynamical tracers like CO, water vapor, ozone, and others.

6 Summary and outlook

The motivation for this work was to set up a novel aerosol mass spectrometer named ERICA, which combines two measurement techniques: The LDI technique and the thermal vaporization/electron impact ionization technique. Hereby, complementary information can be obtained. The aim was to compensate for the weaknesses of one technique by the strengths of the other technique (see Chapter 2). The major weaknesses of the ERICA-LAMS are the idle time of the ablation laser, the narrow particle size detection range, the inability to ionize pure sulfuric acid, and the only qualitative determination of the chemical composition of aerosols. However, these weaknesses can be at least partially compensated by the ERICA-AMS that terminates the particle beam. The ERICA-AMS can continuously and after calibration quantitatively measure the chemical composition of aerosols even in a wider size range than the ERICA-LAMS. Vice versa, the ERICA-LAMS compensates the weaknesses of the ERICA-AMS that is not capable of measuring refractory compounds. Furthermore, the ERICA-LAMS generates single particle bipolar mass spectra, whereas the ERICA-AMS provides cation information on particle ensembles only. Such an instrumental design is unique.

6.1 Summary of the ERICA instrumental properties

The design of the instrument including the inlet and vacuum system as well as the particle detection unit, the ERICA-LAMS and the ERICA-AMS, are presented in Chapter 3. The dimensions of the novel instrument are 600 mm x 740 mm x 1,400 mm (height x width x length) with a total weight of around 200 kg (or 360 kg when taking the pressurized container into account).

The inlet system of ERICA consists of the CPI and the aerodynamic lens. This aerodynamic lens focuses the sampled particles to a narrow beam. The particles are detected by their scattered light that comes from a laser diode (λ = 405 nm) and is reflected by an ellipsoidal reflector towards the PMT. Two units of this design allow the calculation of the point in time to trigger the ablation laser. The ablation laser is a frequency quadrupled Nd:YAG laser (λ = 266 nm) that ablates and ionizes the single particle. The ions are accelerated into a bipolar time-of-flight mass spectrometer. Non-ablated particles continue their flight towards the heated surface of the ERICA-AMS vaporizer (600 °C). Here, non-refractory particles get vaporized and in a following step ionized by an electron beam. The positive ions thus generated are accelerated into a C-shaped time-of-flight mass spectrometer. The background signal is measured while the particle beam is blocked by the shutter. To reduce the losses of mass at the ERICA-AMS by charged particles, the HV switches were implemented.

Additionally, the supply units, the instrument control units, and the data acquisition are treated in Chapter 3. The purpose of the control units and the GUI software (parameters and settings) are described. Furthermore, the calculation of the various triggers, the system data (e.g., particle counts and pressure values) and mass spectra recording as well as the data preparation for further evaluation are explained. In addition, the components needed for an autonomous operation aboard the research aircraft *Geophysica*, such as a satellite communication for instrumental system observation and to remote-control the instrument from the ground, are described as well as the low power mode and the pressurized container. This satellite communication enabled the ground operators to realize the occurrence of instrumental problems online and to remotely restart the corresponding software modules. Without this feature about three quarters of the measurements from flight KTM 05 and one half of flight KTM 07 would have been completely lost.

Table 18: Overview of the key parameters of the ERICA instrument.

Parameter	**Value(s)**
λ detection	405 nm
P_{max} (DL)	58 mW
$w_{0,dia}$ (DL, 1/e²-diameter)	61 µm x 40 µm
w_{part} (PSL, DU1)	~0.1 mm (d_{va} = > 218 nm)
α	0.1 mrad – 2 mrad
$r_{eff,L}$	0.1 mm – 0.4 mm (overall)
λ ablation	266 nm
E_{UV}	11 mJ
τ_p	6 ns
$w_{0,dia}$ (ablation laser, 1/e²-diameter)	250 µm
E_e	$3.7 \cdot 10^9$ W cm^{-2}
f_{rep} (max.)	8 s^{-1}
w_{part} ablation	60 µm – 480 µm
Range of the size calibration	80 nm – 5145 nm
Maximum DE_{max} (PSL)	100 %
Minimum DE_{max} (PSL)	1.5 %
d_{50} of DE_{max} (PSL, DU overall)	174 nm – 3173 nm
Maximum DE_{KTM} (ammonium nitrate)	86 %
Minimum DE_{KTM} (ammonium nitrate)	18 %
Maximum DE_{KTM} (PSL)	74 %
Minimum DE_{KTM} (PSL)	1.5 %
d_{50} of DE_{KTM} (PSL, DU2)	159 nm – 752 nm
Maximum TE	100 %
Minimum TE	5 %
d_{50} of TE (AN at vaporizer)	< 91 nm
Maximum AE	52 % (d_{va}~200 nm, ambient)
Minimum AE	< 3 % (d_{va} < 97 nm and d_{va}> 1035 nm)
R_{MS} (ERICA-LAMS) for m/z 200	cations: 700; anions: 600
R_{MS} (ERICA-AMS) for m/z 200	800
Dimensions (height x width x length)	600 mm x 740 mm x 1,400 mm
Weight	~200 kg (360 kg with container)
Total power consumption	1.2 kW (measuring mode)

Comprehensive laboratory measurements were conducted to characterize the key instrumental parameters (Chapter 4). With these the focused detection laser and ablation laser beams as well as the particle beam were investigated upon and the key parameters of each beam type were determined (see Table 18). In addition, the fraction of UV light intensity was measured. Furthermore, the particle size calibration was performed. Two different calibration approaches are discussed and the usage of a polynomial function seems most appropriate. After the first field campaign, improvements on the vacuum system were performed and the HV switches were implemented. The particle beam was adjusted to the ERICA-AMS vaporizer and the detection unit was adjusted to the particle beam. Afterwards, the detection efficiency was measured for various aerodynamic lens positions with PSL

and ammonium nitrate particles. A DMA/CPC system or an OPC served as reference device for these measurements, which provided the particle beam width, the effective detection radius of the detection unit and the vaporizer, the particle beam divergence, and the transmission efficiency of the aerodynamic lens for the two particle types as function of particle size. Furthermore, the detection efficiency was determined for two different aerodynamic lens positions (maximum detection efficiency and detection efficiency during the field campaign in Kathmandu, Nepal). To consider the doubly charged ammonium nitrate particles, the evaluation procedure was adapted in a way that goes beyond the published literature. A ground-based field experiment was conducted to determine the size resolved ablation efficiency. Furthermore, pure chemical substance solutions were nebulized and the created particles were sampled to validate the ERICA-LAMS mass spectra evaluation. Some of the key instrumental parameters for ERICA, obtained inter alia by instrument characterization measurements, are summarized in Table 18. Overall, the values of the determined parameters are comparable to five in the literature well described single particle mass spectrometers, especially to ALABAMA.

After the first aircraft-based field deployment in Kalamata, Greece, several technical improvements had to be implemented for ERICA to perform as successfully as described above. Finally, the Asian monsoon phase was conducted in Kathmandu, Nepal. Hereby, single particle and particle ensemble mass spectra were recorded in an altitude of up to 20,000 m. For the data evaluation of the field campaigns, the focus of this thesis is on the methods and results in connection with ERICA-LAMS.

6.2 Summary of selected results from the StratoClim aircraft campaign

The ERICA-LAMS measurements presented here represent the very first bipolar particle mass spectra which were recorded at altitudes up to 20,000 m in the temperate, subtropical, and tropical lower stratosphere. Within 11 flights of over 43 flight hours, in total 150,136 single particle mass spectra could be acquired. In addition, the data demonstrate that the instrument is capable of operating continuously and autonomously aboard an aircraft during research flights, including phases of highly demanding conditions. The test campaign in Kalamata, Greece, provided proof-of-concept of the ERICA-LAMS and uncovered some of the weaknesses of the ERICA-AMS, which were subsequently removed. With these implemented improvements, the ERICA-AMS is capable of measuring quantitatively due to a sufficient low background signal and a reduction of particle losses in the inlet system. So, both the ERICA-LAMS and the ERICA-AMS were ready for the Asian monsoon phase. The recorded data from the StratoClim field campaigns is of high quality and allows detailed analyses of the aerosol composition of the ATAL and the Asian Monsoon Anticyclone. Only 0.15 % of the data set sampled during the Asian monsoon phase could not be used for the evaluations. Due to a satellite communication link to the operators on the ground, the data loss could be limited to 39 minutes. However, the remaining data set allows first analyses that are summarized below.

The ERICA-LAMS data set sampled during the Asian monsoon phase was evaluated by two different approaches. The first was the particle type identification by clustering algorithm method and the second by using the ion marker peak method. Both methods have their strengths and weaknesses. The clustering method is typically used to identify different particle types according to their relative intensities without aiming for a chemical species. The identification of the peaks is performed after assorting the mass spectra by the algorithm. In the present case, the k-means algorithm was used by a followed manually grouping to reduce the number of particle types. By this approach, especially meteoric dust (*Meteoric*) particles and *EC* particles could be identified due to their specific mass spectral pattern. The individual clusters and the results from the ERICA-AMS of the Asian monsoon

data set indicated nitrate as a significant species. Thus, the grouping was performed to investigate the different nitrate-containing groups. This shows the advantage of the clustering method, where a particular structure in the data set is highlighted unbiased by an operator. In general, the analysis of the single particle mass spectra by the clustering method with a follow up grouping of the particle types depends strongly on the focus of the evaluation and might be to some degree dependent on the operator. Manual grouping results in particle types that may need to be resolved into sub-types by using additional data, such as altitude or particle size information, for further investigation. Relatively small peaks might be overseen when assorting the clusters to groups. Overall, it is the method of choice for starting to evaluate data sets.

The two StratoClim data sets, the data set from the mid-latitude and the Asian Monsoon phase, underwent this evaluation method. For the data sampled during the mid-latitude phase, four (*Inorganic*, *Meteoric*, *Organic,* and *EC*) and for the Asian Monsoon phase seven (*KOrgNOSO*, *MetalOrgNOSO*, *Meteoric*, *EC*, *Inorganic*, *NOSO,* and *OrgNOSO*) different particle types were identified. The derived vertical profiles of *Meteoric* and *EC* were compared to results from other publications and were thereby confirmed with satisfactory consistency. This shows the capability of the instrument to generate trustworthy data.

Both the ERICA-LAMS and the ERICA-AMS indicate the existence of a dominant feature, the ATAL layer of nitrate, containing aerosol in the UT/LS region of the AMA. The identified *NOSO* and *OrgNOSO* particle types show a layer of enhanced particle number fractions that reach above the estimated CPT. In the same altitude range the ERICA-AMS detected an enhanced nitrate mass concentration. The measurements conducted by the GLORIA remote sensing instrument confirmed this layer, named ATAL, and identified solid ammonium nitrate as the predominant aerosol component. By an experiment in the AIDA chamber it was found that solid ammonium nitrate needs sulfate for crystallization. The measurements by the ERICA-LAMS confirm that 91 % of the nitrate-containing particles show sulfate signatures in the investigated altitude range of 10,000 m – 17,000 m. The key results presented here are part of the publication by Höpfner et al. (2019) in Nature Geoscience. The conducted measurements of bipolar single particle mass spectra and particle ensemble measurements during the AMA in the ATAL are the first of their kind and it appears that the long-standing mystery of the ATAL chemical composition has been solved by the adopted methodology.

To demonstrate the benefit of a simultaneous aerosol measurement by the two different measuring methods (LDI and flash vaporization/EI), especially with regard to sulfate and sulfuric acid-containing aerosol, flight KTM01 serves as an example. The ERICA-LAMS is not able to detect pure sulfuric acid. However, this weakness can be compensated by the ERICA-AMS. The weakness of the ERICA-AMS, which only detects non-refractory aerosol, can be compensated by the ERICA-LAMS. Used simultaneously, the two methods, ERICA-LAMS and ERICA-AMS, contribute to a more comprehensive result than if only one component had been used for aerosol analysis. In addition, it is shown that the single particle evaluation should not be limited to one evaluation method, clustering or ion markering. Since each of these evaluation methods has its weaknesses, both methods should be combined and used in parallel. A comprehensive single particle analysis, both the ion marker and the clustering method should be used.

The ion marker method is used for searching the data set for specific known species like sulfate or organic fragments (Köllner et al., 2017). By an a-priori procedure the threshold for the ion marker peaks has to be determined (see Section 4.4.1). This threshold is also applied for identifying valid peaks during the grouping procedure after the clustering procedure. Here, the method was used to identify

metal species. The isotopic pattern of the species verified the metals, here W, Cd, Mo, and Hg. For monoisotopic elements the verification is limited to other ion marker peaks like dimeric fragments, e.g., Au_2^+, or confirming species such as oxides or hydroxides (Dall'Osto and Harrison, 2006; Roth, 2014). Since fragments of heavy metal species occur in the mass spectrum at values $m/z > 90$, these species are easier to determine than species that occur at $m/z < 90$. The latter species interfere with other organic fragments. These isobars are challenging and inspection of the relative intensities is obligatory. Searching for ion marker peaks for two different species independently might lead to an overall fraction over 100 % due to particles that contain both species. In addition to the search for metal species, the content of sulfate fragments in nitrate-containing mass spectra that were recorded above 5,000 m was found to be 95 %. This might be indicative of a nitrate/sulfate particle formation process where the sulfate-containing particle was created first.

Hg was also searched for in the single particle data set. Particulate Hg was found in the UT/LS region. Correlations with temperature and ozone mixing ratio gave hints that either a condensation, nucleation, or oxidation process leads to an enhanced fraction at high altitudes. By evaluating the mass spectra, the condensation process appeared unlikely, at least for the *Meteoric* particle type, compared to the nucleation or the oxidation process. However, no clear evidence for one of the processes was found. Further measurements and investigations using other analysis techniques are needed for a comprehensive analysis of the depletion of Hg vapor at high altitudes.

The evaluation for gold-containing particles by the ion marker peak method has shown that the minority (2.21 %; upper limit) of the particles might be caused by contact with the gold-plated aircraft inlet. Thus, these particles can be ignored for further investigation or can be further investigated in a separate study. However, the low fraction shows that the influence of the gold-plated inlet on the single particle measurements is minor and the isokinetic inlet performed sufficiently well. Furthermore, combining the clustering/grouping method and the ion marker method for data evaluation is more powerful than one method alone.

The presented case studies show the first results that are not final and merely serve to demonstrate the feasibility of ERICA for aircraft borne research flights such as during StratoClim, even up to altitudes of 20,000 m. These studies can be completed by various analysis methods.

The shown ion marker method can be applied by a sophisticated strategy in the future. In addition, a routine could be evolved where most of the metal species can be grouped together. This is demanding to develop, due to isobars and monoisotopic species. To investigate the Hg vapor depleting process, more specific results might be delivered by evaluating collected particle samples by electron microscopy and elemental analysis. In addition, more measurements, also by the ERICA-LAMS, are needed to improve on the statistics of mercury-containing particles to investigate the mixed components of the mercury-containing particles. The occurrence of Au particles can be investigated by correlation with incidences, such as the flight pattern or meteorological events, during research flights.

6.3 Outlook

For the future, some instrumental improvements are conceivable. For instance, the implemented HV switches can be used as a delayed extraction unit, where the electrical field is switched on shortly after the laser pulse. This might improve the mass spectra reproducibility due to reduced matrix effects. First tests of this technique were already performed with ALABAMA, whose TC has the same design as the one used for ERICA (Clemen et al., 2020). Another approach to improve the mass spectra reproducibility would be the implementation of beam shaping optics, i.e., changing the Gaussian beam profile to a top-hat profile. This would equalize the laser intensity distribution inside the ablation laser focus (Murphy, 2007; Voelkel and Weible, 2008). Thus, all hit particles would be ablated by the same laser intensity independent of their location in the ablation focal spot.

Although the ERICA-LAMS and ERICA-AMS combination was developed for the aircraft deployment within the ATAL, it can be used for many other purposes. An excimer laser can be implemented to provide laser pulses of $\lambda = 193$ nm. The larger dimensions of the laser supply units have to be considered as well as the fact that toxic gas is needed. However, it would be possible to ablate also pure sulfuric acid and ammonium sulfate particles (Murphy, 2007). The dimensions of the pressurized container restricted the dimensions of the ablation laser head. Thus, no wavelength separator was implemented. In further studies the effect of the remaining wavelengths in the ablation laser pulse to the mass spectra should be characterized. Another characterization of interest is the ablation laser's effect to the particles that are only partly ablated and the residuals reach the vaporizer of the ERICA-AMS. Therefore, a method has to be developed to ensure the linkage of the results to the very same particle.

In order to estimate the number concentration of the identified particle types and species, the fractions can be scaled up by using the data of the optical particle counter UHSAS as reference. A similar approach has been conducted in several field studies (e.g., Gunsch et al. (2018), Froyd et al. (2019), and Köllner (2019)).

A measurement mode could be implemented to estimate the amount of charged particle concentration. For this purpose, the electric field would be turned on and off alternately by the HV switches. Meanwhile, the ERICA-AMS would continuously measure the aerosol mass concentration. By calculating the difference of the mass concentration, the amount of charged aerosol might be calculated. By the same mode, the mass concentration could be measured by the ERICA-AMS unaffected by the ERICA-LAMS for predefined conditions, such as a low particle number concentration. This would lead to less losses at the ERICA-AMS and thus to more reliable results under such conditions.

After the successful field deployment in Kathmandu, Nepal, ERICA was transferred into another rack that can be mounted in NASA's DC-8 research aircraft. Here, ERICA was invited as part of the payload for the ND-MAX/ECLIF-2 (NASA/DLR-Multidisciplinary Airborne eXperiments/Emission and CLimate Impact of alternative Fuel) field campaign in January to February 2018 (Schneider et al., 2019). The campaign's base was located in Ramstein, Germany. Within eight research and three transit flights between Germany and the USA more than 270,000 single particle mass spectra were recorded during a total of 81 flight hours. Similar to StratoClim, another field campaign dedicated like StratoClim to the processes and effects of the Asian Monsoon Anticyclone (ACCLIP, acronym for: Asian summer monsoon Chemical and CLimate Impact Project) is planned in summer 2021 aboard the NSF/NCAR (National Science Foundation/National Center for Atmospheric Research) HIAPER research aircraft (High-performance Instrumented Airborne Platform for Environmental Research). Upon further invitation test flights with ERICA operating on HIAPER were performed in Boulder, Colorado, USA, in

January and February 2020. During eight flight hours around 50,000 single particle mass spectra were recorded. These invitations for two different US research aircrafts demonstrate that the developments in connection with the combination-mass spectrometer ERICA resulted in an instrument bearing high potential for future use.

The nearly flawless operation of ERICA during a total of 133 flight hours on three different research aircrafts during StratoClim, ND-MAX/ECLIF, and the ACCLIP test phase documents the high quality of the instrument and its reliable performance. Thus, design, implementation, and fully autonomous flight operation, especially on a high-altitude aircraft, of ERICA can be considered as veritable experimental success. For the first time, bipolar mass spectra were measured at stratospheric altitudes of 20 km, and for the first time an AMS type of instrument was operated at such altitudes. By means of ERICA, answers could be provided concerning the long-standing scientific question about the chemical composition of ATAL aerosol as described in the Nature Geoscience publication by Höpfner et al. (2019).

References

Ahern, A. T., Subramanian, R., Saliba, G., Lipsky, E. M., Donahue, N. M., and Sullivan, R. C.: *Effect of secondary organic aerosol coating thickness on the real-time detection and characterization of biomass-burning soot by two particle mass spectrometers*, Atmospheric Measurement Techniques, 9, 6117-6137, doi: 10.5194/amt-9-6117-2016, **2016**.

Alfaro, S. C., Gaudichet, A., Gomes, L., and Maillé, M.: *Mineral aerosol production by wind erosion: Aerosol particle sizes and binding energies*, Geophysical Research Letters, 25, 991-994, doi: 10.1029/98gl00502, **1998**.

Allan, J. D., Delia, A. E., Coe, H., Bower, K. N., Alfarra, M. R., Jimenez, J. L., Middlebrook, A. M., Drewnick, F., Onasch, T. B., Canagaratna, M. R., Jayne, J. T., and Worsnop, D. R.: *A generalised method for the extraction of chemically resolved mass spectra from Aerodyne aerosol mass spectrometer data*, Journal of Aerosol Science, 35, 909-922, doi: 10.1016/j.jaerosci.2004.02.007, **2004**.

Allan, J. D., Jimenez, J. L., Williams, P. I., Alfarra, M. R., Bower, K. N., Jayne, J. T., Coe, H., and Worsnop, D. R.: *Quantitative sampling using an Aerodyne aerosol mass spectrometer 1. Techniques of data interpretation and error analysis*, Journal of Geophysical Research: Atmospheres, 108, doi: 10.1029/2002jd002358, **2003**.

Allen, M. D. and Raabe, O. G.: *Slip Correction Measurements of Spherical Solid Aerosol Particles in an Improved Millikan Apparatus*, Aerosol Science and Technology, 4, 269-286, doi: 10.1080/02786828508959055, **1985**.

Anderson, J. O., Thundiyil, J. G., and Stolbach, A.: *Clearing the Air: A Review of the Effects of Particulate Matter Air Pollution on Human Health*, Journal of Medical Toxicology, 8, 166-175, doi: 10.1007/s13181-011-0203-1, **2012**.

Araújo, M., Silva, R., Lima, E., Pereira, D., and De Oliveira, P.: *Measurement of Gaussian laser beam radius using the knife-edge technique: Improvement on data analysis*, Applied Opttics, 48, 393-396, doi: 10.1364/AO.48.000393, **2009**.

Atkins, P. W. and De Paula, J.: *Physikalische Chemie*, 4th edition, Wiley-VCH, Weinheim, **2006**.

Audi, G., Bersillon, O., Blachot, J., and Wapstra, A. H.: *The Nubase evaluation of nuclear and decay properties*, Nuclear Physics A, 729, 3-128, doi: 10.1016/j.nuclphysa.2003.11.001, **2003**.

Bahreini, R., Dunlea, E. J., Matthew, B. M., Simons, C., Docherty, K. S., DeCarlo, P. F., Jimenez, J. L., Brock, C. A., and Middlebrook, A. M.: *Design and Operation of a Pressure-Controlled Inlet for Airborne Sampling with an Aerodynamic Aerosol Lens*, Aerosol Science and Technology, 42, 465-471, doi: 10.1080/02786820802178514, **2008**.

Bahreini, R., Ervens, B., Middlebrook, A. M., Warneke, C., de Gouw, J. A., DeCarlo, P. F., Jimenez, J. L., Brock, C. A., Neuman, J. A., Ryerson, T. B., Stark, H., Atlas, E., Brioude, J., Fried, A., Holloway, J. S., Peischl, J., Richter, D., Walega, J., Weibring, P., Wollny, A. G., and Fehsenfeld, F. C.: *Organic aerosol formation in urban and industrial plumes near Houston and Dallas, Texas*, Journal of Geophysical Research: Atmospheres, 114, doi: 10.1029/2008JD011493, **2009**.

Bahreini, R., Jimenez, J. L., Wang, J., Flagan, R. C., Seinfeld, J. H., Jayne, J. T., and Worsnop, D. R.: *Aircraft-based aerosol size and composition measurements during ACE-Asia using an Aerodyne aerosol mass spectrometer*, Journal of Geophysical Research: Atmospheres, 108, doi: 10.1029/2002jd003226, **2003**.

Bayazitoglu, Y. and Kakaç, S.: *Flow Regimes in Microchannel Single-Phase Gaseous Fluid Flow*. In: Microscale Heat Transfer Fundamentals and Applications, Kakaç, S., Vasiliev, L. L., Bayazitoğlu, Y., and Yener, Y. (Eds.), Springer Netherlands, Dordrecht, **2005**.

Blake, D. F. and Kato, K.: *Latitudinal distribution of black carbon soot in the upper troposphere and lower stratosphere*, Journal of Geophysical Research: Atmospheres, 100, 7195-7202, doi: 10.1029/94jd03118, **1995**.

Blanksby, S. J. and Ellison, G. B.: *Bond Dissociation Energies of Organic Molecules*, Accounts of Chemical Research, 36, 255-263, doi: 10.1021/ar020230d, **2003**.

Bläsner, M.: *Entwicklung eines bipolaren flugzeuggetragenen Aerosolmassenspektrometers*, PhD thesis, Dissertation, Mathematisch-Naturwissenschaftlichen Fakulät, Rheinische Friedrich-Wilhelms-Universität Bonn, Bonn, **2001**.

Bohren, C. F. and Huffman, D. R.: *Absorption and scattering of light by small particles*, New York a.o., **1998**.

Borrmann, S., Stefanutti, L., and Khattatov, V.: *Chemistry and aerosol measurements on the Geophysika stratospheric research aircraft: The airborne polar experiment*, Physics and Chemistry of the Earth, 20, 97-101, doi: 10.1016/0079-1946(95)00011-X, **1995**.

Borrmann, S., Thomas, A., Rudakov, V., Yushkov, V., Lepuchov, B., Deshler, T., Vinnichenko, N., Khattatov, V., and Stefanutti, L.: *Stratospheric aerosol measurements in the Arctic winter of 1996/1997 with the M-55 Geophysika high-altitude research aircraft*, Tellus B: Chemical and Physical Meteorology, 52, 1088-1103, doi: 10.3402/tellusb.v52i4.17085, **2000**.

Brands, M.: *Aufbau und Charakterisierung eines flugzeuggetragenen Einzelpartikel-Massenspektrometers*, PhD thesis, Dissertation, Fachbereich Physik, Mathematik und Informatik, Johannes Gutenberg-Universität Mainz, Mainz, **2009**.

Brands, M., Kamphus, M., Böttger, T., Schneider, J., Drewnick, F., Roth, A., Curtius, J., Voigt, C., Borbon, A., Beekmann, M., Bourdon, A., Perrin, T., and Borrmann, S.: *Characterization of a Newly Developed Aircraft-Based Laser Ablation Aerosol Mass Spectrometer (ALABAMA) and First Field Deployment in Urban Pollution Plumes over Paris During MEGAPOLI 2009*, Aerosol Science and Technology, 45, 46-64, doi: 10.1080/02786826.2010.517813, **2011**.

Brito, J., Freney, E., Dominutti, P., Borbon, A., Haslett, S. L., Batenburg, A. M., Colomb, A., Dupuy, R., Denjean, C., Burnet, F., Bourriane, T., Deroubaix, A., Sellegri, K., Borrmann, S., Coe, H., Flamant, C., Knippertz, P., and Schwarzenboeck, A.: *Assessing the role of anthropogenic and biogenic sources on PM1 over southern West Africa using aircraft measurements*, Atmospheric Chemistry and Physics, 18, 757-772, doi: 10.5194/acp-18-757-2018, **2018**.

Brock, C. A., Williamson, C., Kupc, A., Froyd, K. D., Erdesz, F., Wagner, N., Richardson, M., Schwarz, J. P., Gao, R. S., Katich, J. M., Campuzano-Jost, P., Nault, B. A., Schroder, J. C., Jimenez, J. L., Weinzierl, B., Dollner, M., Bui, T., and Murphy, D. M.: *Aerosol size distributions during the Atmospheric Tomography Mission (ATom): methods, uncertainties, and data products*, Atmospheric Measurement Techniques, 12, 3081-3099, doi: 10.5194/amt-12-3081-2019, **2019**.

Brockmann, J. E., Yamano, N., and Lucero, D.: *Calibration of the Aerodynamic Particle Sizer 3310 (APS-3310) with Polystyrene Latex Monodisperse Spheres and Oleic Acid Monodisperse Particles*, Aerosol Science and Technology, 8, 279-281, doi: 10.1080/02786828808959189, **1988**.

Brooks, J., Allan, J. D., Williams, P. I., Liu, D., Fox, C., Haywood, J., Langridge, J. M., Highwood, E. J., Kompalli, S. K., O'Sullivan, D., Babu, S. S., Satheesh, S. K., Turner, A. G., and Coe, H.: *Vertical and horizontal distribution of submicron aerosol chemical composition and physical characteristics across northern India during pre-monsoon and monsoon seasons*, Atmospheric Chemistry and Physics, 19, 5615-5634, doi: 10.5194/acp-19-5615-2019, **2019**.

Brown, T. and Pitfield, P.: *Tungsten*. In: Critical Metals Handbook, Gunn, G. (Ed.), John Wiley & Sons, Ltd., **2013**.

Brunamonti, S., Jorge, T., Oelsner, P., Hanumanthu, S., Singh, B. B., Kumar, K. R., Sonbawne, S., Meier, S., Singh, D., Wienhold, F. G., Luo, B. P., Boettcher, M., Poltera, Y., Jauhiainen, H., Kayastha, R., Karmacharya, J., Dirksen, R., Naja, M., Rex, M., Fadnavis, S., and Peter, T.: *Balloon-borne measurements of temperature, water vapor, ozone and aerosol backscatter on the southern slopes of the Himalayas during StratoClim 2016–2017*, Atmospheric Chemistry and Physics, 18, 15937-15957, doi: 10.5194/acp-18-15937-2018, **2018**.

Bucci, S., Legras, B., Sellitto, P., D'Amato, F., Viciani, S., Montori, A., Chiarugi, A., Ravegnani, F., Ulanovsky, A., Cairo, F., and Stroh, F.: *Deep convective influence on the UTLS composition in the Asian Monsoon Anticyclone region: 2017 StratoClim campaign results*, Atmospheric Chemistry and Physics Discussions, 2020, 1-29, doi: 10.5194/acp-2019-1053, **2020**.

Bukowiecki, N., Dommen, J., Prévôt, A. S. H., Richter, R., Weingartner, E., and Baltensperger, U.: *A mobile pollutant measurement laboratory—measuring gas phase and aerosol ambient concentrations with high spatial and temporal resolution*, Atmospheric Environment, 36, 5569-5579, doi: 10.1016/S1352-2310(02)00694-5, **2002**.

Cai, Y., Montague, D. C., Mooiweer-Bryan, W., and Deshler, T.: *Performance characteristics of the ultra high sensitivity aerosol spectrometer for particles between 55 and 800nm: Laboratory and field studies*, Journal of Aerosol Science, 39, 759-769, doi: 10.1016/j.jaerosci.2008.04.007, **2008**.

Canagaratna, M. R., Jayne, J. T., Jimenez, J. L., Allan, J. D., Alfarra, M. R., Zhang, Q., Onasch, T. B., Drewnick, F., Coe, H., Middlebrook, A., Delia, A., Williams, L. R., Trimborn, A. M., Northway, M. J., DeCarlo, P. F., Kolb, C. E., Davidovits, P., and Worsnop, D. R.: *Chemical and microphysical characterization of ambient aerosols with the aerodyne aerosol mass spectrometer*, Mass Spectrometry Reviews, 26, 185-222, doi: 10.1002/mas.20115, **2007**.

Carney, R. P., Kim, J. Y., Qian, H., Jin, R., Mehenni, H., Stellacci, F., and Bakr, O. M.: *Determination of nanoparticle size distribution together with density or molecular weight by 2D analytical ultracentrifugation*, Nature Communications, 2, 335, doi: 10.1038/ncomms1338, **2011**.

Chen, Y., Kozlovskiy, V., Du, X., Lv, J., Nikiforov, S., Yu, J., Kolosov, A., Gao, W., Zhou, Z., Huang, Z., and Li, L.: *Increase of the particle hit rate in a laser single-particle mass spectrometer by pulse delayed extraction technology*, Atmospheric Measurement Techniques, 13, 941-949, doi: 10.5194/amt-13-941-2020, **2020**.

Clemen, H.-C., Schneider, J., Klimach, T., Helleis, F., Köllner, F., Hünig, A., Rubach, F., Mertes, S., Wex, H., Stratmann, F., Kohl, R., Frank, F., Bingemer, H., Curtius, J., and Borrmann, S.: *Optimizing the detection, ablation and ion extraction efficiency of a single particle laser ablation mass spectrometer for application in environments with low aerosol particle concentrations*, Atmospheric Measurement Techniques Discussions, 2020, 1-48, doi: 10.5194/amt-2020-181, **2020**.

CRC Handbook of Chemistry and Physics. Rumble, J. R. (Ed.), CRC Press/Taylor & Francis, Boca Raton, FL., **2018**.

Cubison, M. J. and Jimenez, J. L.: *Statistical precision of the intensities retrieved from constrained fitting of overlapping peaks in high-resolution mass spectra*, Atmospheric Measurement Techniques, 8, 2333-2345, doi: 10.5194/amt-8-2333-2015, **2015**.

Cziczo, D. J., Thomson, D. S., and Murphy, D. M.: *Ablation, Flux, and Atmospheric Implications of Meteors Inferred from Stratospheric Aerosol*, Science, 291, 1772-1775, doi: 10.1126/science.1057737, **2001**.

Cziczo, D. J., Thomson, D. S., Thompson, T. L., DeMott, P. J., and Murphy, D. M.: *Particle analysis by laser mass spectrometry (PALMS) studies of ice nuclei and other low number density particles*, International Journal of Mass Spectrometry, 258, 21-29, doi: 10.1016/j.ijms.2006.05.013, **2006**.

Dall'Osto, M. and Harrison, R. M.: *Chemical characterisation of single airborne particles in Athens (Greece) by ATOFMS*, Atmospheric Environment, 40, 7614-7631, doi: 10.1016/j.atmosenv.2006.06.053, **2006**.

Dat, N.-D. and Chang, M. B.: *Review on characteristics of PAHs in atmosphere, anthropogenic sources and control technologies*, Science of the Total Environment, 609, 682-693, doi: 10.1016/j.scitotenv.2017.07.204, **2017**.

Davis, W. D.: *Abstract: Surface Ionization Mass Spectroscopy of Airborne Particulates*, Journal of Vacuum Science and Technology, 10, 278-278, doi: 10.1116/1.1317991, **1973**.

DeCarlo, P. F., Kimmel, J. R., Trimborn, A., Northway, M. J., Jayne, J. T., Aiken, A. C., Gonin, M., Fuhrer, K., Horvath, T., Docherty, K. S., Worsnop, D. R., and Jimenez, J. L.: *Field-Deployable, High-Resolution, Time-of-Flight Aerosol Mass Spectrometer*, Analytical Chemistry, 78, 8281-8289, doi: 10.1021/ac061249n, **2006**.

DeCarlo, P. F., Slowik, J. G., Worsnop, D. R., Davidovits, P., and Jimenez, J. L.: *Particle Morphology and Density Characterization by Combined Mobility and Aerodynamic Diameter Measurements. Part 1: Theory*, Aerosol Science and Technology, 38, 1185-1205, doi: 10.1080/027868290903907, **2004**.

Ditas, J., Ma, N., Zhang, Y., Assmann, D., Neumaier, M., Riede, H., Karu, E., Williams, J., Scharffe, D., Wang, Q., Saturno, J., Schwarz, J. P., Katich, J. M., McMeeking, G. R., Zahn, A., Hermann, M., Brenninkmeijer, C. A. M., Andreae, M. O., Pöschl, U., Su, H., and Cheng, Y.: *Strong impact of wildfires*

on the abundance and aging of black carbon in the lowermost stratosphere, Proceedings of the National Academy of Sciences, 115, E11595-E11603, doi: 10.1073/pnas.1806868115, **2018**.

Dockery, D. W.: *Health Effects of Particulate Air Pollution*, Annals of Epidemiology, 19, 257-263, doi: 10.1016/j.annepidem.2009.01.018, **2009**.

Dragoneas, A., Molleker, S., Appel, O., Hünig, A., Böttger, T., Hermann, M., Drewnick, F., Schneider, J., Weigel, R., and Borrmann, S.: *The realization of autonomous, aircraft-based, real-time aerosol mass spectrometry in the stratosphere*, prepared for submission to Atmospheric Measurement Techniques Discussions, doi: n/a, **2020**.

Drawin, H.-W.: *Zur spektroskopischen Temperatur- und Dichtemessung von Plasmen bei Abwesenheit thermodynamischen Gleichgewichts*, Zeitschrift für Physik, 172, 429-452, doi: 10.1007/BF01378304, **1963**.

Drewnick, F.: *Entwicklung und Charakterisierung eines Laser-massenspektrometrischen Verfahrens - Ein Beitrag zur Aerosolanalytik*, PhD thesis, Dissertation, Fakultät I - Allgemeine und Angewandte Naturwissenschaften, Universität Hohenheim, Hohenheim, **2000**.

Drewnick, F., Böttger, T., von der Weiden-Reinmüller, S. L., Zorn, S. R., Klimach, T., Schneider, J., and Borrmann, S.: *Design of a mobile aerosol research laboratory and data processing tools for effective stationary and mobile field measurements*, Atmospheric Measurement Techniques, 5, 1443-1457, doi: 10.5194/amt-5-1443-2012, **2012**.

Drewnick, F., Hings, S. S., Alfarra, M. R., Prevot, A. S. H., and Borrmann, S.: *Aerosol quantification with the Aerodyne Aerosol Mass Spectrometer: detection limits and ionizer background effects*, Atmospheric Measurement Techniques, 2, 33-46, doi: 10.5194/amt-2-33-2009, **2009**.

Drewnick, F., Hings, S. S., DeCarlo, P., Jayne, J. T., Gonin, M., Fuhrer, K., Weimer, S., Jimenez, J. L., Demerjian, K. L., Borrmann, S., and Worsnop, D. R.: *A New Time-of-Flight Aerosol Mass Spectrometer (TOF-AMS)—Instrument Description and First Field Deployment*, Aerosol Science and Technology, 39, 637-658, doi: 10.1080/02786820500182040, **2005**.

Drewnick, F., Schneider, J., Hings, S. S., Hock, N., Noone, K., Targino, A., Weimer, S., and Borrmann, S.: *Measurement of Ambient, Interstitial, and Residual Aerosol Particles on a Mountaintop Site in Central Sweden using an Aerosol Mass Spectrometer and a CVI*, Journal of Atmospheric Chemistry, 56, 1-20, doi: 10.1007/s10874-006-9036-8, **2007**.

Ebert, M., Weigel, R., Kandler, K., Günther, G., Molleker, S., Grooß, J. U., Vogel, B., Weinbruch, S., and Borrmann, S.: *Chemical analysis of refractory stratospheric aerosol particles collected within the arctic vortex and inside polar stratospheric clouds*, Atmospheric Chemistry and Physics, 16, 8405-8421, doi: 10.5194/acp-16-8405-2016, **2016**.

Eichler, H. J., Kronfeldt, H.-D., and Sahm, J.: *Das neue Physikalische Grundpraktikum*, 3rd edition, Springer, Berlin, Heidelberg, **2016**.

Ericsson, R.: *The influence of sodium chloride on the atmospheric corrosion of steel*, Materials and Corrosion, 29, 400-403, doi: 10.1002/maco.19780290604, **1978**.

Ettner-Mahl, M.: *Entwicklung und Charakterisierung eines Laserablationsmassenspektrometers zur Echtzeit-Analyse von atmosphärischen Aerosolpartikeln*, PhD thesis, Dissertation, Fachbereich Physik, Mathematik und Informatik, Johannes Gutenberg-Universität Mainz, Mainz, **2006**.

Fachinger, F., Drewnick, F., Gieré, R., and Borrmann, S.: *Communal biofuel burning for district heating: Emissions and immissions from medium-sized (0.4 and 1.5 MW) facilities*, Atmospheric Environment, 181, 177-185, doi: 10.1016/j.atmosenv.2018.03.014, **2018**.

Fadnavis, S., Semeniuk, K., Pozzoli, L., Schultz, M. G., Ghude, S. D., Das, S., and Kakatkar, R.: *Transport of aerosols into the UTLS and their impact on the Asian monsoon region as seen in a global model simulation*, Atmospheric Chemistry and Physics, 13, 8771-8786, doi: 10.5194/acp-13-8771-2013, **2013**.

Forsyth, B., Liu, B. Y. H., and Romay, F. J.: *Particle Charge Distribution Measurement for Commonly Generated Laboratory Aerosols*, Aerosol Science and Technology, 28, 489-501, doi: 10.1080/02786829808965540, **1998**.

Friedl-Vallon, F., Gulde, T., Hase, F., Kleinert, A., Kulessa, T., Maucher, G., Neubert, T., Olschewski, F., Piesch, C., Preusse, P., Rongen, H., Sartorius, C., Schneider, H., Schönfeld, A., Tan, V., Bayer, N., Blank, J., Dapp, R., Ebersoldt, A., Fischer, H., Graf, F., Guggenmoser, T., Höpfner, M., Kaufmann, M., Kretschmer, E., Latzko, T., Nordmeyer, H., Oelhaf, H., Orphal, J., Riese, M., Schardt, G., Schillings, J., Sha, M. K., Suminska-Ebersoldt, O., and Ungermann, J.: *Instrument concept of the imaging Fourier transform spectrometer GLORIA*, Atmospheric Measurement Techniques, 7, 3565-3577, doi: 10.5194/amt-7-3565-2014, **2014**.

Froyd, K. D., Murphy, D. M., Brock, C. A., Campuzano-Jost, P., Dibb, J. E., Jimenez, J. L., Kupc, A., Middlebrook, A. M., Schill, G. P., Thornhill, K. L., Williamson, C. J., Wilson, J. C., and Ziemba, L. D.: *A new method to quantify mineral dust and other aerosol species from aircraft platforms using single-particle mass spectrometry*, Atmospheric Measurement Techniques, 12, 6209-6239, doi: 10.5194/amt-12-6209-2019, **2019**.

Fuzzi, S., Baltensperger, U., Carslaw, K., Decesari, S., Denier van der Gon, H., Facchini, M. C., Fowler, D., Koren, I., Langford, B., Lohmann, U., Nemitz, E., Pandis, S., Riipinen, I., Rudich, Y., Schaap, M., Slowik, J. G., Spracklen, D. V., Vignati, E., Wild, M., Williams, M., and Gilardoni, S.: *Particulate matter, air quality and climate: lessons learned and future needs*, Atmospheric Chemistry and Physics, 15, 8217-8299, doi: 10.5194/acp-15-8217-2015, **2015**.

Galpin, T., Chartier, R. T., Levergood, N., and Greenslade, M. E.: *Refractive index retrievals for polystyrene latex spheres in the spectral range 220–420 nm*, Aerosol Science and Technology, 51, 1158-1167, doi: 10.1080/02786826.2017.1339014, **2017**.

Gard, E., Mayer, J. E., Morrical, B. D., Dienes, T., Fergenson, D. P., and Prather, K. A.: *Real-Time Analysis of Individual Atmospheric Aerosol Particles: Design and Performance of a Portable ATOFMS*, Analytical Chemistry, 69, 4083-4091, doi: 10.1021/ac970540n, **1997**.

Gemayel, R., Hellebust, S., Temime-Roussel, B., Hayeck, N., Van Elteren, J. T., Wortham, H., and Gligorovski, S.: *The performance and the characterization of laser ablation aerosol particle time-of-flight mass spectrometry (LAAP-ToF-MS)*, Atmospheric Measurement Techniques, 9, 1947-1959, doi: 10.5194/amt-9-1947-2016, **2016**.

Goetz, J. D., Giordano, M. R., Stockwell, C. E., Christian, T. J., Maharjan, R., Adhikari, S., Bhave, P. V., Praveen, P. S., Panday, A. K., Jayarathne, T., Stone, E. A., Yokelson, R. J., and DeCarlo, P. F.: *Speciated online PM1 from South Asian combustion sources – Part 1: Fuel-based emission factors and size distributions*, Atmospheric Chemistry and Physics, 18, 14653-14679, doi: 10.5194/acp-18-14653-2018, **2018**.

Greenewalt, C. H.: *Absorption of Water Vapor by sulfuric Acid Solutions1*, Industrial and Engineering Chemistry, 18, 1291-1295, doi: 10.1021/ie50204a031, **1926**.

GRIMM Aerosol Technik GmbH: *Handbuch Version Rev-A Aerosolspektrometer SERIE 1.129 SKY-OPC*. Ainring, Germany, **2008**.

Grimm Aerosol Technik GmbH: *SMPS (Sequenzial Mobility Particle Sizer) Series 5.400*. Ainring, Germany, **2005**.

Grimm Aerosol Technik GmbH: *User Manual - Condensation Particle Counter*. Ainring, Germany, **2003**.

Gross, D. S., Gälli, M. E., Silva, P. J., and Prather, K. A.: *Relative Sensitivity Factors for Alkali Metal and Ammonium Cations in Single-Particle Aerosol Time-of-Flight Mass Spectra*, Analytical Chemistry, 72, 416-422, doi: https://doi.org/10.1021/ac990434g, **2000**.

Gross, J. H.: *Mass spectrometry : a textbook*, 2nd edition, Springer, Berlin, Heidelberg, https://doi.org/10.1007/978-3-642-10711-5, **2011**.

Gross, J. H.: *Massenspektrometrie : Spektroskopiekurs kompakt*, Springer Spektrum, Berlin, Heidelberg, **2019**.

Gross, J. H.: *Massenspektrometrie: ein Lehrbuch*, Springer Spektrum, Berlin, **2013**.

Gu, Y., Liao, H., and Bian, J.: *Summertime nitrate aerosol in the upper troposphere and lower stratosphere over the Tibetan Plateau and the South Asian summer monsoon region*, Atmospheric Chemistry and Physics, 16, 6641-6663, doi: 10.5194/acp-16-6641-2016, **2016**.

Guan, J. L., Lu, H. W., Xiao, X. H., Wu, Y. C., and Chen, Z. D.: *Research on Precision Mirror Machining Technology for W-Mo Alloy*, Key Engineering Materials, 487, 303-307, doi: 10.4028/www.scientific.net/KEM.487.303, **2011**.

Gunsch, M. J., May, N. W., Wen, M., Bottenus, C. L. H., Gardner, D. J., VanReken, T. M., Bertman, S. B., Hopke, P. K., Ault, A. P., and Pratt, K. A.: *Ubiquitous influence of wildfire emissions and secondary organic aerosol on summertime atmospheric aerosol in the forested Great Lakes region*, Atmospheric Chemistry and Physics, 18, 3701-3715, doi: 10.5194/acp-18-3701-2018, **2018**.

Hartigan, J. A. and Wong, M. A.: *Algorithm AS 136: A K-Means Clustering Algorithm*, Journal of the Royal Statistical Society. Series C (Applied Statistics), 28, 100-108, doi: 10.2307/2346830, **1979**.

Hashida, M., Mishima, H., Tokita, S., and Sakabe, S.: *Non-thermal ablation of expanded polytetrafluoroethylene with an intense femtosecond-pulse laser*, Optics Express, 17, 13116-13121, doi: 10.1364/OE.17.013116, **2009**.

Haslett, S. L., Taylor, J. W., Evans, M., Morris, E., Vogel, B., Dajuma, A., Brito, J., Batenburg, A. M., Borrmann, S., Schneider, J., Schulz, C., Denjean, C., Bourrianne, T., Knippertz, P., Dupuy, R., Schwarzenböck, A., Sauer, D., Flamant, C., Dorsey, J., Crawford, I., and Coe, H.: *Remote biomass burning dominates southern West African air pollution during the monsoon*, Atmospheric Chemistry and Physics, 19, 15217-15234, doi: 10.5194/acp-19-15217-2019, **2019**.

Hatch, L. E., Pratt, K. A., Huffman, J. A., Jimenez, J. L., and Prather, K. A.: *Impacts of Aerosol Aging on Laser Desorption/Ionization in Single-Particle Mass Spectrometers*, Aerosol Science and Technology, 48, 1050-1058, doi: 10.1080/02786826.2014.955907, **2014**.

Healy, R. M., Sciare, J., Poulain, L., Crippa, M., Wiedensohler, A., Prévôt, A. S. H., Baltensperger, U., Sarda-Estève, R., McGuire, M. L., Jeong, C. H., McGillicuddy, E., O'Connor, I. P., Sodeau, J. R., Evans, G. J., and Wenger, J. C.: *Quantitative determination of carbonaceous particle mixing state in Paris using single-particle mass spectrometer and aerosol mass spectrometer measurements*, Atmospheric Chemistry and Physics, 13, 9479-9496, doi: 10.5194/acp-13-9479-2013, **2013**.

Heinen, H. J.: *On ion formation in laser desorption mass spectrometry with LAMMA*, International Journal of Mass Spectrometry and Ion Physics, 38, 309-322, doi: 10.1016/0020-7381(81)80076-9, **1981**.

Hinds, W. C.: *Aerosol technology: properties, behavior, and measurement of airborne particles*, 2nd edition, Wiley, New York, New York, USA, **1999**.

Hings, S.: *Characterisation and Field Deployment of a Novel Quantitative Time-of-Flight Aerosol Mass Spectrometer (ToF-AMS)*, PhD thesis, Dissertiation, Fachbereich Physik, Mathematik und Informatik, Johannes Gutenberg-Universität Mainz, Mainz, **2006**.

Hinz, K.-P., Greweling, M., Drews, F., and Spengler, B.: *Data processing in on-line laser mass spectrometry of inorganic, organic, or biological airborne particles*, Journal of the American Society for Mass Spectrometry, 10, 648-660, doi: 10.1016/s1044-0305(99)00028-8, **1999**.

Hinz, K.-P., Kaufmann, R., and Spengler, B.: *Simultaneous Detection of Positive and Negative Ions From Single Airborne Particles by Real-time Laser Mass Spectrometry*, Aerosol Science and Technology, 24, 233-242, doi: 10.1080/02786829608965368, **1996**.

Hiranuma, N., Adachi, K., Bell, D. M., Belosi, F., Beydoun, H., Bhaduri, B., Bingemer, H., Budke, C., Clemen, H. C., Conen, F., Cory, K. M., Curtius, J., DeMott, P. J., Eppers, O., Grawe, S., Hartmann, S., Hoffmann, N., Höhler, K., Jantsch, E., Kiselev, A., Koop, T., Kulkarni, G., Mayer, A., Murakami, M., Murray, B. J., Nicosia, A., Petters, M. D., Piazza, M., Polen, M., Reicher, N., Rudich, Y., Saito, A., Santachiara, G., Schiebel, T., Schill, G. P., Schneider, J., Segev, L., Stopelli, E., Sullivan, R. C., Suski, K., Szakáll, M., Tajiri, T., Taylor, H., Tobo, Y., Ullrich, R., Weber, D., Wex, H., Whale, T. F., Whiteside, C. L., Yamashita, K., Zelenyuk, A., and Möhler, O.: *A comprehensive characterization of ice nucleation by three different types of cellulose particles immersed in water*, Atmospheric Chemistry and Physics, 19, 4823-4849, doi: 10.5194/acp-19-4823-2019, **2019**.

Hiranuma, N., Brooks, S. D., Moffet, R. C., Glen, A., Laskin, A., Gilles, M. K., Liu, P., Macdonald, A. M., Strapp, J. W., and McFarquhar, G. M.: *Chemical characterization of individual particles and residuals of cloud droplets and ice crystals collected on board research aircraft in the ISDAC 2008 study*, Journal of Geophysical Research: Atmospheres, 118, 6564-6579, doi: 10.1002/jgrd.50484, **2013**.

Holleman, A. F.: *Lehrbuch der anorganischen Chemie*. Wiberg, E. and Wiberg, N. (Eds.), Berlin, **2019**.

Höpfner, M., Ungermann, J., Borrmann, S., Wagner, R., Spang, R., Riese, M., Stiller, G., Appel, O., Batenburg, A. M., Bucci, S., Cairo, F., Dragoneas, A., Friedl-Vallon, F., Hünig, A., Johansson, S., Krasauskas, L., Legras, B., Leisner, T., Mahnke, C., Möhler, O., Molleker, S., Müller, R., Neubert, T., Orphal, J., Preusse, P., Rex, M., Saathoff, H., Stroh, F., Weigel, R., and Wohltmann, I.: *Ammonium nitrate particles formed in upper troposphere from ground ammonia sources during Asian monsoons*, Nature Geoscience, doi: https://doi.org/10.1038/s41561-019-0385-8, **2019**.

Hudson, P. K., Murphy, D. M., Cziczo, D. J., Thomson, D. S., de Gouw, J. A., Warneke, C., Holloway, J., Jost, H.-J., and Hübler, G.: *Biomass-burning particle measurements: Characteristic composition and chemical processing*, Journal of Geophysical Research: Atmospheres, 109, doi: 10.1029/2003jd004398, **2004**.

Huffman, J. A., Jayne, J. T., Drewnick, F., Aiken, A. C., Onasch, T., Worsnop, D. R., and Jimenez, J. L.: *Design, Modeling, Optimization, and Experimental Tests of a Particle Beam Width Probe for the Aerodyne Aerosol Mass Spectrometer*, Aerosol Science and Technology, 39, 1143-1163, doi: 10.1080/02786820500423782, **2005**.

Hünig, A.: *Weiterentwicklung und Charakterisierung eines Einzelpartikel-Bioaerosolmassenspektrometers* Dipl.-Chem., Diploma thesis, Fachbereich Chemie, Pharmazie und Geowissenschaften, Johannes Gutenberg-Universität Mainz, Mainz, **2014**.

Hünig, A., Appel, O., Dragoneas, A., Molleker, S., Clemen, H.-C., Helleis, F., Klimach, T., Böttger, T., Drewnick, F., Schneider, J., and Borrmann, S.: *Design and characterization of a novel aerosol mass spectrometer combining laser ablation and flash vaporization techniques for aircraft application at high altitudes*, prepared for submission to Atmospheric Measurement Techniques Discussions, doi: n/a, **2020**.

Hynes, A. J., Donohoue, D. L., Goodsite, M. E., and Hedgecock, I. M.: *Our current understanding of major chemical and physical processes affecting mercury dynamics in the atmosphere and at the air-water/terrestrial interfaces*. In: Mercury Fate and Transport in the Global Atmosphere: Emissions, Measurements and Models, Pirrone, N. and Mason, R. (Eds.), Springer US, Boston, MA, **2009**.

IPCC: *Climate change 2013: The physical science basis. Contribution of working group I to the fifth assessment report of the intergovernmental panel on climate change*, IPCC, Cambridge, United Kingdom and New York, NY, USA, Report, 1535 pp., **2013**.

IUPAC: *Compendium of Chemical Terminology*, 2nd edition (the "Gold Book"), Blackwell Scientific Publications, Oxford, **1997**.

Jaenicke, R.: *Atmospheric Aerosols and Global Climate*. In: Climatic Variations and Variability: Facts and Theories: NATO Advanced Study Institute First Course of the International School of Climatology, Ettore Majorana Center for Scientific Culture, Erice, Italy, March 9–21, 1980, Berger, A. (Ed.), Springer Netherlands, Dordrecht, **1981**.

Jayne, J. T., Leard, D. C., Zhang, X., Davidovits, P., Smith, K. A., Kolb, C. E., and Worsnop, D. R.: *Development of an Aerosol Mass Spectrometer for Size and Composition Analysis of Submicron Particles*, Aerosol Science and Technology, 33, 49-70, doi: 10.1080/027868200410840, **2000**.

Jeong, C. H., McGuire, M. L., Godri, K. J., Slowik, J. G., Rehbein, P. J. G., and Evans, G. J.: *Quantification of aerosol chemical composition using continuous single particle measurements*, Atmospheric Chemistry and Physics, 11, 7027-7044, doi: 10.5194/acp-11-7027-2011, **2011**.

Jimenez, J. L., Bahreini, R., Cocker, D. R., Zhuang, H., Varutbangkul, V., Flagan, R. C., Seinfeld, J. H., O'Dowd, C. D., and Hoffmann, T.: *Correction to "New particle formation from photooxidation of diiodomethane (CH2I2)"*, Journal of Geophysical Research: Atmospheres, 108, doi: 10.1029/2003JD004249, **2003a**.

Jimenez, J. L., Bahreini, R., Cocker, D. R., Zhuang, H., Varutbangkul, V., Flagan, R. C., Seinfeld, J. H., O'Dowd, C. D., and Hoffmann, T.: *New particle formation from photooxidation of diiodomethane (CH2I2)*, Journal of Geophysical Research: Atmospheres, 108, doi: 10.1029/2002JD002452, **2003b**.

Jimenez, J. L., Jayne, J. T., Shi, Q., Kolb, C. E., Worsnop, D. R., Yourshaw, I., Seinfeld, J. H., Flagan, R. C., Zhang, X., Smith, K. A., Morris, J. W., and Davidovits, P.: *Ambient aerosol sampling using the Aerodyne Aerosol Mass Spectrometer*, Journal of Geophysical Research: Atmospheres, 108, doi: 10.1029/2001JD001213, **2003c**.

Junge, C. E. and Manson, J. E.: *Stratospheric aerosol studies*, Journal of Geophysical Research (1896-1977), 66, 2163-2182, doi: 10.1029/JZ066i007p02163, **1961**.

Kamphus, M., Ettner-Mahl, M., Brands, M., Curtius, J., Drewnick, F., and Borrmann, S.: *Comparison of two aerodynamic lenses as an inlet for a single particle laser ablation mass spectrometer*, Aerosol Science and Technology, 42, 970-980, doi: 10.1080/02786820802372158, **2008**.

Kamphus, M., Ettner-Mahl, M., Klimach, T., Drewnick, F., Keller, L., Cziczo, D. J., Mertes, S., Borrmann, S., and Curtius, J.: *Chemical composition of ambient aerosol, ice residues and cloud droplet residues in mixed-phase clouds: single particle analysis during the Cloud and Aerosol Characterization Experiment (CLACE 6)*, Atmospheric Chemistry and Physics, 10, 8077-8095, doi: 10.5194/acp-10-8077-2010, **2010**.

Kellner, R.: *Analytical chemistry : a modern approach to analytical science*, 2nd edition, Weinheim, **2004**.

Kimmel, J.: *Aerodyne ToF-AMS DAQ Users Manual*. Aerodyne Inc., **2011**.

Kissel, J. and Krueger, F. R.: *Ion formation by impact of fast dust particles and comparison with related techniques*, Applied Physics A, 42, 69-85, doi: 10.1007/BF00618161, **1987**.

Klimach, T.: *Chemische Zusammensetzung der Aerosole - Design und Datenauswertung eines Einzelpartikel-Laserablationsmassenspektrometers*, PhD thesis, Dissertation, Fachbereich Chemie, Pharmazie und Geowissenschaften, Johannes Gutenberg-Universität Mainz, Mainz, **2012**.

Köllner, F.: *Aerosol particles in the summertime arctic lower troposphere: Chemical composition, sources, and formation*, PhD thesis, Dissertation, Fachbereich Physik, Mathematik und Informatik, Johannes Gutenberg-Universität Mainz, Mainz, **2019**.

Köllner, F., Schneider, J., Willis, M. D., Klimach, T., Helleis, F., Bozem, H., Kunkel, D., Hoor, P., Burkart, J., Leaitch, W. R., Aliabadi, A. A., Abbatt, J. P. D., Herber, A. B., and Borrmann, S.: *Particulate*

trimethylamine in the summertime Canadian high Arctic lower troposphere, Atmospheric Chemistry and Physics, 17, 13747-13766, doi: 10.5194/acp-17-13747-2017, **2017**.

Kulkarni, P., Baron, P. A., and Willeke, K.: *Aerosol measurement : principles, techniques, and applications*, 3rd edition, Wiley, Hoboken, NJ, **2011**.

Kumari, A., Kumar, B., Manzoor, S., and Kulshrestha, U.: *Status of Atmospheric Mercury Research in South Asia: A Review*, Aerosol and Air Quality Research, 15, 1092-1109, doi: 10.4209/aaqr.2014.05.0098, **2015**.

Lau, W. K. M., Yuan, C., and Li, Z.: *Origin, Maintenance and Variability of the Asian Tropopause Aerosol Layer (ATAL): The Roles of Monsoon Dynamics*, Scientific Reports, 8, 3960, doi: 10.1038/s41598-018-22267-z, **2018**.

Lazrus, A. L. and Gandrud, B. W.: *Stratospheric sulfate aerosol*, Journal of Geophysical Research (1896-1977), 79, 3424-3431, doi: 10.1029/JC079i024p03424, **1974**.

Lee, S.-H., Murphy, D. M., Thomson, D. S., and Middlebrook, A. M.: *Chemical components of single particles measured with Particle Analysis by Laser Mass Spectrometry (PALMS) during the Atlanta SuperSite Project: Focus on organic/sulfate, lead, soot, and mineral particles*, Journal of Geophysical Research: Atmospheres, 107, AAC 1-1-AAC 1-13, doi: 10.1029/2000jd000011, **2002**.

Lelieveld, J., Barlas, C., Giannadaki, D., and Pozzer, A.: *Model calculated global, regional and megacity premature mortality due to air pollution*, Atmospheric Chemistry and Physics, 13, 7023-7037, doi: 10.5194/acp-13-7023-2013, **2013**.

Lelieveld, J., Bourtsoukidis, E., Brühl, C., Fischer, H., Fuchs, H., Harder, H., Hofzumahaus, A., Holland, F., Marno, D., Neumaier, M., Pozzer, A., Schlager, H., Williams, J., Zahn, A., and Ziereis, H.: *The South Asian monsoon—pollution pump and purifier*, Science, 361, 270-273, doi: 10.1126/science.aar2501, **2018**.

Lima, A. L. C., Farrington, J. W., and Reddy, C. M.: *Combustion-Derived Polycyclic Aromatic Hydrocarbons in the Environment—A Review*, Environmental Forensics, 6, 109-131, doi: 10.1080/15275920590952739, **2005**.

Lippmann, M., Yeates, D. B., and Albert, R. E.: *Deposition, retention, and clearance of inhaled particles*, British Journal of Industrial Medicine, 37, 337-362, doi: 10.1136/oem.37.4.337, **1980**.

Liu, P., Ziemann, P. J., Kittelson, D. B., and McMurry, P. H.: *Generating Particle Beams of Controlled Dimensions and Divergence: I. Theory of Particle Motion in Aerodynamic Lenses and Nozzle Expansions*, Aerosol Science and Technology, 22, 293-313, doi: 10.1080/02786829408959748, **1995a**.

Liu, P., Ziemann, P. J., Kittelson, D. B., and McMurry, P. H.: *Generating Particle Beams of Controlled Dimensions and Divergence: II. Experimental Evaluation of Particle Motion in Aerodynamic Lenses and Nozzle Expansions*, Aerosol Science and Technology, 22, 314-324, doi: 10.1080/02786829408959749, **1995b**.

Liu, P. S. K., Deng, R., Smith, K. A., Williams, L. R., Jayne, J. T., Canagaratna, M. R., Moore, K., Onasch, T. B., Worsnop, D. R., and Deshler, T.: *Transmission Efficiency of an Aerodynamic Focusing Lens System: Comparison of Model Calculations and Laboratory Measurements for the Aerodyne Aerosol Mass Spectrometer*, Aerosol Science and Technology, 41, 721-733, doi: 10.1080/02786820701422278, **2007**.

Lohmann, U. and Feichter, J.: *Global indirect aerosol effects: a review*, Atmospheric Chemistry and Physics, 5, 715-737, doi: 10.5194/acp-5-715-2005, **2005**.

Marsden, N., Flynn, M. J., Taylor, J. W., Allan, J. D., and Coe, H.: *Evaluating the influence of laser wavelength and detection stage geometry on optical detection efficiency in a single particle mass spectrometer*, Atmospheric Measurement Techniques Discussions, 2016, 1-25, doi: 10.5194/amt-2016-150, **2016**.

McKeown, P. J., Johnston, M. V., and Murphy, D. M.: *On-line single-particle analysis by laser desorption mass spectrometry*, Analytical Chemistry, 63, 2069-2073, doi: 10.1021/ac00018a033, **1991**.

MDB: *High-altitude M55 Geophysica aircraft - Investigators Handbook*. Myasishchev Design Bureau, Russia, **2002**.

Middlebrook, A. M., Bahreini, R., Jimenez, J. L., and Canagaratna, M. R.: *Evaluation of Composition-Dependent Collection Efficiencies for the Aerodyne Aerosol Mass Spectrometer using Field Data*, Aerosol Science and Technology, 46, 258-271, doi: 10.1080/02786826.2011.620041, **2012**.

Mie, G.: *Beiträge zur Optik trüber Medien, speziell kolloidaler Metallösungen*, Annalen der Physik, 330, 377-445, doi: 10.1002/andp.19083300302, **1908**.

Moffet, R. C. and Prather, K. A.: *In-situ measurements of the mixing state and optical properties of soot with implications for radiative forcing estimates*, Proceedings of the National Academy of Sciences, 106, 11872-11877, doi: 10.1073/pnas.0900040106, **2009**.

Möhler, O., Benz, S., Saathoff, H., Schnaiter, M., Wagner, R., Schneider, J., Walter, S., Ebert, V., and Wagner, S.: *The effect of organic coating on the heterogeneous ice nucleation efficiency of mineral dust aerosols*, Environmental Research Letters, 3, 025007, doi: 10.1088/1748-9326/3/2/025007, **2008**.

Molleker, S., Helleis, F., Klimach, T., Appel, O., Clemen, H.-C., Dragoneas, A., Gurk, C., Hünig, A., Köllner, F., Rubach, F., Schulz, C., Schneider, J., and Borrmann, S.: *Application of an O-ring pinch device as a constant pressure inlet (CPI) for airborne sampling*, Atmospheric Measurement Techniques, 2020, 1-13, doi: 10.5194/amt-2020-66, **2020**.

Morgan, W. T., Allan, J. D., Bower, K. N., Highwood, E. J., Liu, D., McMeeking, G. R., Northway, M. J., Williams, P. I., Krejci, R., and Coe, H.: *Airborne measurements of the spatial distribution of aerosol chemical composition across Europe and evolution of the organic fraction*, Atmospheric Chemistry and Physics, 10, 4065-4083, doi: 10.5194/acp-10-4065-2010, **2010**.

Murphy, D. M.: *The design of single particle laser mass spectrometers*, Mass Spectrometry Reviews, 26, 150-165, doi: 10.1002/mas.20113, **2007**.

Murphy, D. M., Cziczo, D. J., Hudson, P. K., and Thomson, D. S.: *Carbonaceous material in aerosol particles in the lower stratosphere and tropopause region*, Journal of Geophysical Research: Atmospheres, 112, doi: 10.1029/2006jd007297, **2007**.

Murphy, D. M., Cziczo, D. J., Hudson, P. K., Thomson, D. S., Wilson, J. C., Kojima, T., and Buseck, P. R.: *Particle Generation and Resuspension in Aircraft Inlets when Flying in Clouds*, Aerosol Science and Technology, 38, 401-409, doi: 10.1080/02786820490443094, **2004**.

Murphy, D. M., Froyd, K. D., Bian, H., Brock, C. A., Dibb, J. E., DiGangi, J. P., Diskin, G., Dollner, M., Kupc, A., Scheuer, E. M., Schill, G. P., Weinzierl, B., Williamson, C. J., and Yu, P.: *The distribution of sea-salt aerosol in the global troposphere*, Atmospheric Chemistry and Physics, 19, 4093-4104, doi: https://doi.org/10.5194/acp-19-4093-2019, **2019**.

Murphy, D. M., Froyd, K. D., Schwarz, J. P., and Wilson, J. C.: *Observations of the chemical composition of stratospheric aerosol particles*, Quarterly Journal of the Royal Meteorological Society, 140, 1269-1278, doi: 10.1002/qj.2213, **2014**.

Murphy, D. M., Hudson, P. K., Thomson, D. S., Sheridan, P. J., and Wilson, J. C.: *Observations of Mercury-Containing Aerosols*, Environmental Science & Technology, 40, 3163-3167, doi: 10.1021/es052385x, **2006**.

Murphy, D. M., Middlebrook, A. M., and Warshawsky, M.: *Cluster Analysis of Data from the Particle Analysis by Laser Mass Spectrometry (PALMS) Instrument*, Aerosol Science and Technology, 37, 382-391, doi: 10.1080/02786820300971, **2003**.

Murphy, D. M. and Thomson, D. S.: *Laser Ionization Mass Spectroscopy of Single Aerosol Particles*, Aerosol Science and Technology, 22, 237-249, doi: 10.1080/02786829408959743, **1995**.

Murphy, D. M., Thomson, D. S., and Mahoney, M. J.: *In Situ Measurements of Organics, Meteoritic Material, Mercury, and Other Elements in Aerosols at 5 to 19 Kilometers*, Science, 282, 1664-1669, doi: 10.1126/science.282.5394.1664, **1998**.

NASA: *ER-2 Airborne Laboratory Experimenter Handbook*. Center, D. F. R. (Ed.), National Aeronautics and Space Administration, Edwards, CA, **2002**.

NASA: *WB-57 Experimenter's Handbook*. Center, L. B. J. S. (Ed.), National Aeronautics and Space Administration, Houston, TX, **2017**.

NIST Chemistry WebBook, NIST Standard Reference Database Number 69. National Institute of Standards and Technology, Gaithersburg MD, **2019**.

Nowak, J. B., Neuman, J. A., Bahreini, R., Brock, C. A., Middlebrook, A. M., Wollny, A. G., Holloway, J. S., Peischl, J., Ryerson, T. B., and Fehsenfeld, F. C.: *Airborne observations of ammonia and ammonium nitrate formation over Houston, Texas*, Journal of Geophysical Research: Atmospheres, 115, doi: 10.1029/2010JD014195, **2010**.

Opiela, J. N.: *A study of the material density distribution of space debris*, Advances in Space Research, 43, 1058-1064, doi: 10.1016/j.asr.2008.12.013, **2009**.

Park, M., Randel, W. J., Gettelman, A., Massie, S. T., and Jiang, J. H.: *Transport above the Asian summer monsoon anticyclone inferred from Aura Microwave Limb Sounder tracers*, Journal of Geophysical Research: Atmospheres, 112, doi: 10.1029/2006jd008294, **2007**.

Patiny, L. and Borel, A.: *ChemCalc: A Building Block for Tomorrow's Chemical Infrastructure*, Journal of Chemical Information and Modeling, 53, 1223-1228, doi: 10.1021/ci300563h, **2013**.

Peck, J., Gonzalez, L. A., Williams, L. R., Xu, W., Croteau, P. L., Timko, M. T., Jayne, J. T., Worsnop, D. R., Miake-Lye, R. C., and Smith, K. A.: *Development of an aerosol mass spectrometer lens system for PM2.5*, Aerosol Science and Technology, 50, 781-789, doi: 10.1080/02786826.2016.1190444, **2016**.

Pirrone, N., Cinnirella, S., Feng, X., Finkelman, R. B., Friedli, H. R., Leaner, J., Mason, R., Mukherjee, A. B., Stracher, G. B., Streets, D. G., and Telmer, K.: *Global mercury emissions to the atmosphere from anthropogenic and natural sources*, Atmospheric Chemistry and Physics, 10, 5951-5964, doi: 10.5194/acp-10-5951-2010, **2010**.

Ploeger, F., Gottschling, C., Griessbach, S., Grooß, J. U., Guenther, G., Konopka, P., Müller, R., Riese, M., Stroh, F., Tao, M., Ungermann, J., Vogel, B., and von Hobe, M.: *A potential vorticity-based determination of the transport barrier in the Asian summer monsoon anticyclone*, Atmospheric Chemistry and Physics, 15, 13145-13159, doi: 10.5194/acp-15-13145-2015, **2015**.

Ploeger, F., Konopka, P., Walker, K., and Riese, M.: *Quantifying pollution transport from the Asian monsoon anticyclone into the lower stratosphere*, Atmospheric Chemistry and Physics, 17, 7055-7066, doi: 10.5194/acp-17-7055-2017, **2017**.

Pöschl, U.: *Atmospheric aerosols: Composition, transformation, climate and health effects*, Angewandte Chemie, International Edition, 44, 7520-7540, doi: 10.1002/anie.200501122, **2005**.

Prather, K. A., Bertram, T. H., Grassian, V. H., Deane, G. B., Stokes, M. D., DeMott, P. J., Aluwihare, L. I., Palenik, B. P., Azam, F., Seinfeld, J. H., Moffet, R. C., Molina, M. J., Cappa, C. D., Geiger, F. M., Roberts, G. C., Russell, L. M., Ault, A. P., Baltrusaitis, J., Collins, D. B., Corrigan, C. E., Cuadra-Rodriguez, L. A., Ebben, C. J., Forestieri, S. D., Guasco, T. L., Hersey, S. P., Kim, M. J., Lambert, W. F., Modini, R. L., Mui, W., Pedler, B. E., Ruppel, M. J., Ryder, O. S., Schoepp, N. G., Sullivan, R. C., and Zhao, D.: *Bringing the ocean into the laboratory to probe the chemical complexity of sea spray aerosol*, Proceedings of the National Academy of Sciences, 110, 7550-7555, doi: 10.1073/pnas.1300262110, **2013**.

Pratt, K. A., Mayer, J. E., Holecek, J. C., Moffet, R. C., Sanchez, R. O., Rebotier, T. P., Furutani, H., Gonin, M., Fuhrer, K., Su, Y., Guazzotti, S., and Prather, K. A.: *Development and Characterization of an Aircraft Aerosol Time-of-Flight Mass Spectrometer*, Analytical Chemistry, 81, 1792-1800, doi: 10.1021/ac801942r, **2009**.

Pratt, K. A., Murphy, S. M., Subramanian, R., DeMott, P. J., Kok, G. L., Campos, T., Rogers, D. C., Prenni, A. J., Heymsfield, A. J., Seinfeld, J. H., and Prather, K. A.: *Flight-based chemical characterization of biomass burning aerosols within two prescribed burn smoke plumes*, Atmospheric Chemistry and Physics, 11, 12549-12565, doi: 10.5194/acp-11-12549-2011, **2011**.

Pratt, K. A. and Prather, K. A.: *Aircraft measurements of vertical profiles of aerosol mixing states*, Journal of Geophysical Research: Atmospheres, 115, doi: 10.1029/2009JD013150, **2010**.

Pratt, K. A., Twohy, C. H., Murphy, S. M., Moffet, R. C., Heymsfield, A. J., Gaston, C. J., DeMott, P. J., Field, P. R., Henn, T. R., Rogers, D. C., Gilles, M. K., Seinfeld, J. H., and Prather, K. A.: *Observation of playa salts as nuclei in orographic wave clouds*, Journal of Geophysical Research: Atmospheres, 115, doi: 10.1029/2009jd013606, **2010**.

Pueschel, R. F., Boering, K. A., Verma, S., Howard, S. D., Ferry, G. V., Goodman, J., Allen, D. A., and Hamill, P.: *Soot aerosol in the lower stratosphere: Pole-to-pole variability and contributions by aircraft*, Journal of Geophysical Research: Atmospheres, 102, 13113-13118, doi: 10.1029/96jd03061, **1997**.

Qin, X., Bhave, P. V., and Prather, K. A.: *Comparison of Two Methods for Obtaining Quantitative Mass Concentrations from Aerosol Time-of-Flight Mass Spectrometry Measurements*, Analytical Chemistry, 78, 6169-6178, doi: 10.1021/ac060395q, **2006**.

Ready, J. F.: *Effects Due to Absorption of Laser Radiation*, Journal of Applied Physics, 36, 462-468, doi: 10.1063/1.1714012, **1965**.

Rebotier, T. P. and Prather, K. A.: *Aerosol time-of-flight mass spectrometry data analysis: A benchmark of clustering algorithms*, Analytica Chimica Acta, 585, 38-54, doi: 10.1016/j.aca.2006.12.009, **2007**.

Reilly, P. T. A., Lazar, A. C., Gieray, R. A., Whitten, W. B., and Ramsey, J. M.: *The Elucidation of Charge-Transfer-Induced Matrix Effects in Environmental Aerosols Via Real-Time Aerosol Mass Spectral Analysis of Individual Airborne Particles*, Aerosol Science and Technology, 33, 135-152, doi: 10.1080/027868200410895, **2000**.

Reitz, P., Zorn, S. R., Trimborn, S. H., and Trimborn, A. M.: *A new, powerful technique to analyze single particle aerosol mass spectra using a combination of OPTICS and the fuzzy c-means algorithm*, Journal of Aerosol Science, 98, 1-14, doi: 10.1016/j.jaerosci.2016.04.003, **2016**.

Rex, M., Schlager, H., Stroh, F., and Cairo, F.: *StratoClim FactSheet 2 Asian Monsoon Aircraft Campaign*. Alfred Wegener Institute Helmholtz Centre for Polar and Marine Research Potsdam, Germany, **2016**.

Riese, M., Oelhaf, H., Preusse, P., Blank, J., Ern, M., Friedl-Vallon, F., Fischer, H., Guggenmoser, T., Höpfner, M., Hoor, P., Kaufmann, M., Orphal, J., Plöger, F., Spang, R., Suminska-Ebersoldt, O., Ungermann, J., Vogel, B., and Woiwode, W.: *Gimballed Limb Observer for Radiance Imaging of the Atmosphere (GLORIA) scientific objectives*, Atmospheric Measurement Techniques, 7, 1915-1928, doi: 10.5194/amt-7-1915-2014, **2014**.

Roed, J., Andersson, K. G., Bell, K. F., Byrne, M. A., Fogh, C. L., Goddard, A. J. H., and Vollmair, D. V.: *Quantitative measurement of aerosol deposition on skin, hair and clothing for dosimetric assessment*, Risø National Laboratory, Roskilde, Report 87-550-2360-6, **1998**.

Roth, A.: *Untersuchung des Einflusses der Laserwellenlänge in der Einzelpartikel-Laserablations-Aerosol-Massenspektrometrie*Diplomarbeit, Fachbereich Chemie, Pharmazie und Geowissenschaften, Johannes Gutenberg Universität Mainz, Mainz, **2009**.

Roth, A.: *Untersuchungen von Aerosolpartikeln und Wolkenresidualpartikeln mittels Einzelpartikel-Massenspektrometrie und optischen Methoden* PhD thesis, Dissertation, Fachbereich Chemie, Pharmazie und Geowissenschaften, Johannes Gutenberg-Universität Mainz, Mainz, **2014**.

Roth, A., Schneider, J., Klimach, T., Mertes, S., van Pinxteren, D., Herrmann, H., and Borrmann, S.: *Aerosol properties, source identification, and cloud processing in orographic clouds measured by single particle mass spectrometry on a central European mountain site during HCCT-2010*, Atmospheric Chemistry and Physics, 16, 505-524, doi: 10.5194/acp-16-505-2016, **2016**.

Salcedo, D., Onasch, T. B., Dzepina, K., Canagaratna, M. R., Zhang, Q., Huffman, J. A., DeCarlo, P. F., Jayne, J. T., Mortimer, P., Worsnop, D. R., Kolb, C. E., Johnson, K. S., Zuberi, B., Marr, L. C., Volkamer, R., Molina, L. T., Molina, M. J., Cardenas, B., Bernabé, R. M., Márquez, C., Gaffney, J. S., Marley, N. A., Laskin, A., Shutthanandan, V., Xie, Y., Brune, W., Lesher, R., Shirley, T., and Jimenez, J. L.: *Characterization of ambient aerosols in Mexico City during the MCMA-2003 campaign with Aerosol Mass Spectrometry: results from the CENICA Supersite*, Atmospheric Chemistry and Physics, 6, 925-946, doi: 10.5194/acp-6-925-2006, **2006**.

Sánchez-Soberón, F., Rovira, J., Mari, M., Sierra, J., Nadal, M., Domingo, J. L., and Schuhmacher, M.: *Main components and human health risks assessment of PM10, PM2.5, and PM1 in two areas influenced by cement plants*, Atmospheric Environment, 120, 109-116, doi: 10.1016/j.atmosenv.2015.08.020, **2015**.

Sanemasa, I.: *The Solubility of Elemental Mercury Vapor in Water*, Bulletin of the Chemical Society of Japan, 48, 1795-1798, doi: 10.1246/bcsj.48.1795, **1975**.

Santee, M. L., Manney, G. L., Livesey, N. J., Schwartz, M. J., Neu, J. L., and Read, W. G.: *A comprehensive overview of the climatological composition of the Asian summer monsoon anticyclone based on 10 years of Aura Microwave Limb Sounder measurements*, Journal of Geophysical Research: Atmospheres, 122, 5491-5514, doi: 10.1002/2016jd026408, **2017**.

Schmale, J., Schneider, J., Jurkat, T., Voigt, C., Kalesse, H., Rautenhaus, M., Lichtenstern, M., Schlager, H., Ancellet, G., Arnold, F., Gerding, M., Mattis, I., Wendisch, M., and Borrmann, S.: *Aerosol layers from the 2008 eruptions of Mount Okmok and Mount Kasatochi: In situ upper troposphere and lower stratosphere measurements of sulfate and organics over Europe*, Journal of Geophysical Research: Atmospheres, 115, n/a-n/a, doi: 10.1029/2009JD013628, **2010**.

Schmidt, S.: *Analyse der chemischen Zusammensetzung von Eis- und Wolkenresiduen mittels Einzelpartikel-Massenspektrometrie und Charakterisierung von Aerosolpartikeln aus anthropogenen und natürlichen Quellen* PhD thesis, Dissertation, Fachbereich Chemie, Pharmazie und Geowissenschaften, Johannes Gutenberg-Universität Mainz, Mainz, **2015**.

Schmidt, S., Schneider, J., Klimach, T., Mertes, S., Schenk, L. P., Kupiszewski, P., Curtius, J., and Borrmann, S.: *Online single particle analysis of ice particle residuals from mountain-top mixed-phase clouds using laboratory derived particle type assignment*, Atmospheric Chemistry and Physics, 17, 575-594, doi: 10.5194/acp-17-575-2017, **2017**.

Schneider, J., Hings, S. S., Nele Hock, B., Weimer, S., Borrmann, S., Fiebig, M., Petzold, A., Busen, R., and Kärcher, B.: *Aircraft-based operation of an aerosol mass spectrometer: Measurements of tropospheric aerosol composition*, Journal of Aerosol Science, 37, 839-857, doi: 10.1016/j.jaerosci.2005.07.002, **2006**.

Schneider, J., Mertes, S., van Pinxteren, D., Herrmann, H., and Borrmann, S.: *Uptake of nitric acid, ammonia, and organics in orographic clouds: mass spectrometric analyses of droplet residual and*

interstitial aerosol particles, Atmospheric Chemistry and Physics, 17, 1571-1593, doi: 10.5194/acp-17-1571-2017, **2017**.

Schneider, J., Weigel, R., Klimach, T., Dragoneas, A., Appel, O., Hünig, A., Molleker, S., Köllner, F., Clemen, H.-C., Eppers, O., Hoppe, P., Hoor, P., Mahnke, C., Krämer, M., Rolf, C., Grooß, J. U., Zahn, A., Oversteiner, F., Ravegnani, F., Ulanovsky, A., Schlager, H., Scheibe, M., Diskin, G. S., DiGangi, J., Nowak, J., Zöger, M., and Borrmann, S.: *Aircraft-based observation of meteoric material in lower stratospheric aerosol particles between 15 and 68°N*, Earth and Space Science Open Archive, pre-print server, doi: 10.1002/essoar.10501338.1, **2019**.

Schoolcraft, T. A., Constable, G. S., Jackson, B., Zhigilei, L. V., and Garrison, B. J.: *Molecular dynamics simulations of laser disintegration of amorphous aerosol particles with spatially nonuniform absorption*, Nuclear Instruments and Methods in Physics Research Section B: Beam Interactions with Materials and Atoms, 180, 245-250, doi: https://doi.org/10.1016/S0168-583X(01)00424-4, **2001**.

Schoolcraft, T. A., Constable, G. S., Zhigilei, L. V., and Garrison, B. J.: *Molecular Dynamics Simulation of the Laser Disintegration of Aerosol Particles*, Analytical Chemistry, 72, 5143-5150, doi: 10.1021/ac0007635, **2000**.

Schröder, E.: *Massenspektrometrie: Begriffe und Definitionen*, Springer Berlin Heidelberg, Berlin, Heidelberg, **1991**.

Schulz, C.: *Secondary organic aerosol in the pristine Amazonian atmosphere: Chemical properties, formation pathways and interaction with clouds*, PhD thesis, Dissertation, Physik, Mathematik und Informatik, Johannes Gutenberg-Universität Mainz, Mainz, **2019**.

Schulz, C., Schneider, J., Amorim Holanda, B., Appel, O., Costa, A., de Sá, S. S., Dreiling, V., Fütterer, D., Jurkat-Witschas, T., Klimach, T., Knote, C., Krämer, M., Martin, S. T., Mertes, S., Pöhlker, M. L., Sauer, D., Voigt, C., Walser, A., Weinzierl, B., Ziereis, H., Zöger, M., Andreae, M. O., Artaxo, P., Machado, L. A. T., Pöschl, U., Wendisch, M., and Borrmann, S.: *Aircraft-based observations of isoprene-epoxydiol-derived secondary organic aerosol (IEPOX-SOA) in the tropical upper troposphere over the Amazon region*, Atmospheric Chemistry and Physics, 18, 14979-15001, doi: 10.5194/acp-18-14979-2018, **2018**.

Seinfeld, J. H. and Pandis, S. N.: *Atmospheric chemistry and physics : from air pollution to climate change*, 3rd edition, Wiley, Hoboken, NJ, **2016**.

Sensidyne: *Gilian Gillibrator2 Calibration System - Operation & Service Manual - Revision N - Document No. 850190M*. St. Petersburg, FL, **2016**.

Shedd, K. B.: *Tungsten Statistics and Information*, U.S. Geological Survey, Reston, Virginia, Report February 2019, **2019**.

Shen, X., Ramisetty, R., Mohr, C., Huang, W., Leisner, T., and Saathoff, H.: *Laser ablation aerosol particle time-of-flight mass spectrometer (LAAPTOF): performance, reference spectra and classification of atmospheric samples*, Atmospheric Measurement Techniques, 11, 2325-2343, doi: 10.5194/amt-11-2325-2018, **2018**.

Shen, X., Saathoff, H., Huang, W., Mohr, C., Ramisetty, R., and Leisner, T.: *Understanding atmospheric aerosol particles with improved particle identification and quantification by single-particle mass*

spectrometry, Atmospheric Measurement Techniques, 12, 2219-2240, doi: 10.5194/amt-12-2219-2019, **2019**.

Siegman, A. E.: *Lasers*, University Science Books, Sausalito, Californien, USA, **1986**.

Sierau, B., Chang, R. Y. W., Leck, C., Paatero, J., and Lohmann, U.: *Single-particle characterization of the high-Arctic summertime aerosol*, Atmospheric Chemistry and Physics, 14, 7409-7430, doi: 10.5194/acp-14-7409-2014, **2014**.

Silva, P. J. and Prather, K. A.: *Interpretation of Mass Spectra from Organic Compounds in Aerosol Time-of-Flight Mass Spectrometry*, Analytical Chemistry, 72, 3553-3562, doi: 10.1021/ac9910132, **2000**.

Sinha, M. P.: *Laser-induced volatilization and ionization of microparticles*, **1984**.

Skinner, D. R. and Whitcher, R. E.: *Measurement of the radius of a high-power laser beam near the focus of a lens*, Journal of Physics E: Scientific Instruments, 5, 237-238, doi: 10.1088/0022-3735/5/3/015, **1972**.

Slemr, F., Ebinghaus, R., Brenninkmeijer, C. A. M., Hermann, M., Kock, H. H., Martinsson, B. G., Schuck, T., Sprung, D., van Velthoven, P., Zahn, A., and Ziereis, H.: *Gaseous mercury distribution in the upper troposphere and lower stratosphere observed onboard the CARIBIC passenger aircraft*, Atmospheric Chemistry and Physics, 9, 1957-1969, doi: 10.5194/acp-9-1957-2009, **2009**.

Spencer, M. T., Furutani, H., Oldenburg, S. J., Darlington, T. K., and Prather, K. A.: *Gold Nanoparticles as a Matrix for Visible-Wavelength Single-Particle Matrix-Assisted Laser Desorption/Ionization Mass Spectrometry of Small Biomolecules*, The Journal of Physical Chemistry C, 112, 4083-4090, doi: 10.1021/jp076688k, **2008**.

Stark, H., Yatavelli, R. L. N., Thompson, S. L., Kimmel, J. R., Cubison, M. J., Chhabra, P. S., Canagaratna, M. R., Jayne, J. T., Worsnop, D. R., and Jimenez, J. L.: *Methods to extract molecular and bulk chemical information from series of complex mass spectra with limited mass resolution*, International Journal of Mass Spectrometry, 389, 26-38, doi: 10.1016/j.ijms.2015.08.011, **2015**.

Stefanutti, L., Sokolov, L., Balestri, S., MacKenzie, A. R., and Khattatov, V.: *The M-55 Geophysica as a Platform for the Airborne Polar Experiment*, Journal of Atmospheric and Oceanic Technology, 16, 1303-1312, doi: 10.1175/1520-0426(1999)016<1303:tmgaap>2.0.co;2, **1999**.

Streibel, T. and Zimmermann, R.: *Resonance-Enhanced Multiphoton Ionization Mass Spectrometry (REMPI-MS): Applications for Process Analysis*, Annual Review of Analytical Chemistry, 7, 361-381, doi: 10.1146/annurev-anchem-062012-092648, **2014**.

Su, Y., Sipin, M. F., Furutani, H., and Prather, K. A.: *Development and Characterization of an Aerosol Time-of-Flight Mass Spectrometer with Increased Detection Efficiency*, Analytical Chemistry, 76, 712-719, doi: 10.1021/ac034797z, **2004**.

Suess, D. T. and Prather, K. A.: *Mass spectrometry of aerosols*, Chemical Reviews, 99, 3007-3036, doi: 10.1021/cr980138o, **1999**.

Thomas, R. J.: *Particle size and pathogenicity in the respiratory tract*, Virulence, 4, 847-858, doi: 10.4161/viru.27172, **2013**.

Thomason, L. W. and Vernier, J. P.: *Improved SAGE II cloud/aerosol categorization and observations of the Asian tropopause aerosol layer: 1989–2005*, Atmospheric Chemistry and Physics, 13, 4605-4616, doi: 10.5194/acp-13-4605-2013, **2013**.

Thomson, D. S., Middlebrook, A. M., and Murphy, D. M.: *Thresholds for Laser-Induced Ion Formation from Aerosols in a Vacuum Using Ultraviolet and Vacuum-Ultraviolet Laser Wavelengths*, Aerosol Science and Technology, 26, 544-559, doi: 10.1080/02786829708965452, **1997**.

Thomson, D. S., Schein, M. E., and Murphy, D. M.: *Particle Analysis by Laser Mass Spectrometry WB-57F Instrument Overview*, Aerosol Science and Technology, 33, 153-169, doi: 10.1080/027868200410903, **2000**.

Tie, X., Wu, D., and Brasseur, G.: *Lung cancer mortality and exposure to atmospheric aerosol particles in Guangzhou, China*, Atmospheric Environment, 43, 2375-2377, doi: 10.1016/j.atmosenv.2009.01.036, **2009**.

Tigges, L., Wiedensohler, A., Weinhold, K., Gandhi, J., and Schmid, H. J.: *Bipolar charge distribution of a soft X-ray diffusion charger*, Journal of Aerosol Science, 90, 77-86, doi: 10.1016/j.jaerosci.2015.07.002, **2015**.

Timonen, H., Cubison, M., Aurela, M., Brus, D., Lihavainen, H., Hillamo, R., Canagaratna, M., Nekat, B., Weller, R., Worsnop, D., and Saarikoski, S.: *Applications and limitations of constrained high-resolution peak fitting on low resolving power mass spectra from the ToF-ACSM*, Atmospheric Measurement Techniques, 9, 3263-3281, doi: 10.5194/amt-9-3263-2016, **2016**.

Trimborn, A., Hinz, K. P., and Spengler, B.: *Online Analysis of Atmospheric Particles with a Transportable Laser Mass Spectrometer*, Aerosol Science and Technology, 33, 191-201, doi: 10.1080/027868200410921, **2000**.

Turpin, B. J., Huntzicker, J. J., Larson, S. M., and Cass, G. R.: *Los Angeles summer midday particulate carbon: primary and secondary aerosol*, Environmental Science & Technology, 25, 1788-1793, doi: 10.1021/es00022a017, **1991**.

Ulanovsky, A. E., Yushkov, V. A., Sitnikov, N. M., and Ravengnani, F.: *The FOZAN-II Fast-Response Chemiluminescent Airborne Ozone Analyzer*, Instruments and Experimental Techniques, 44, 249-256, doi: 10.1023/a:1017535608026, **2001**.

Vernier, J.-P., Fairlie, T. D., Deshler, T., Ratnam, M. V., Gadhavi, H., Kumar, B. S., Natarajan, M., Pandit, A. K., Raj, S. T. A., Kumar, A. H., Jayaraman, A., Singh, A. K., Rastogi, N., Sinha, P. R., Kumar, S., Tiwari, S., Wegner, T., Baker, N., Vignelles, D., Stenchikov, G., Shevchenko, I., Smith, J., Bedka, K., Kesarkar, A., Singh, V., Bhate, J., Ravikiran, V., Rao, M. D., Ravindrababu, S., Patel, A., Vernier, H., Wienhold, F. G., Liu, H., Knepp, T. N., Thomason, L., Crawford, J., Ziemba, L., Moore, J., Crumeyrolle, S., Williamson, M., Berthet, G., Jégou, F., and Renard, J.-B.: *BATAL: The Balloon Measurement Campaigns of the Asian Tropopause Aerosol Layer*, Bulletin of the American Meteorological Society, 99, 955-973, doi: 10.1175/bams-d-17-0014.1, **2018**.

Vernier, J.-P., Fairlie, T. D., Natarajan, M., Wienhold, F. G., Bian, J., Martinsson, B. G., Crumeyrolle, S., Thomason, L. W., and Bedka, K. M.: *Increase in upper tropospheric and lower stratospheric aerosol levels and its potential connection with Asian pollution*, Journal of Geophysical Research: Atmospheres, 120, 1608-1619, doi: 10.1002/2014JD022372, **2015**.

Vernier, J. P., Thomason, L., and Kar, J.: *CALIPSO detection of an Asian tropopause aerosol layer*, Geophysical Research Letters, 38, doi: 10.1029/2010gl046614, **2011**.

Vertes, A., Juhasz, P., Jani, P., and Czitrovszky, A.: *Kinetic energy distribution of ions generated by laser ionization sources*, International Journal of Mass Spectrometry and Ion Processes, 83, 45-70, doi: 10.1016/0168-1176(88)80087-9, **1988**.

Vetter, T.: *Berechnung der Mie-Streufunktionen zur Kalibrierung optischer Partikelzähler*, diploma, Diplomarbeit, Fachbereich Physik, Mathematik und informatik, Johannes Gutenberg-Universität Mainz, Mainz, **2004**.

Voelkel, R. and Weible, K. J.: *Laser beam homogenizing: limitations and constraints*, Proceedings SPIE, 7102, Optical Fabrication, Testing, and Metrology III, 71020J (25 September 2008), doi: 10.1117/12.799400, **2008**.

Vu, K. T., Dingle, J. H., Bahreini, R., Reddy, P. J., Apel, E. C., Campos, T. L., DiGangi, J. P., Diskin, G. S., Fried, A., Herndon, S. C., Hills, A. J., Hornbrook, R. S., Huey, G., Kaser, L., Montzka, D. D., Nowak, J. B., Pusede, S. E., Richter, D., Roscioli, J. R., Sachse, G. W., Shertz, S., Stell, M., Tanner, D., Tyndall, G. S., Walega, J., Weibring, P., Weinheimer, A. J., Pfister, G., and Flocke, F.: *Impacts of the Denver Cyclone on regional air quality and aerosol formation in the Colorado Front Range during FRAPPÉ 2014*, Atmospheric Chemistry and Physics, 16, 12039-12058, doi: 10.5194/acp-16-12039-2016, **2016**.

Wang, X. and McMurry, P. H.: *A Design Tool for Aerodynamic Lens Systems*, Aerosol Science and Technology, 40, 320-334, doi: 10.1080/02786820600615063, **2006**.

Wendisch, M., Pöschl, U., Andreae, M. O., Machado, L. A. T., Albrecht, R., Schlager, H., Rosenfeld, D., Martin, S. T., Abdelmonem, A., Afchine, A., Araùjo, A. C., Artaxo, P., Aufmhoff, H., Barbosa, H. M. J., Borrmann, S., Braga, R., Buchholz, B., Cecchini, M. A., Costa, A., Curtius, J., Dollner, M., Dorf, M., Dreiling, V., Ebert, V., Ehrlich, A., Ewald, F., Fisch, G., Fix, A., Frank, F., Fütterer, D., Heckl, C., Heidelberg, F., Hüneke, T., Jäkel, E., Järvinen, E., Jurkat, T., Kanter, S., Kästner, U., Kenntner, M., Kesselmeier, J., Klimach, T., Knecht, M., Kohl, R., Kölling, T., Krämer, M., Krüger, M., Krisna, T. C., Lavric, J. V., Longo, K., Mahnke, C., Manzi, A. O., Mayer, B., Mertes, S., Minikin, A., Molleker, S., Münch, S., Nillius, B., Pfeilsticker, K., Pöhlker, C., Roiger, A., Rose, D., Rosenow, D., Sauer, D., Schnaiter, M., Schneider, J., Schulz, C., Souza, R. A. F. d., Spanu, A., Stock, P., Vila, D., Voigt, C., Walser, A., Walter, D., Weigel, R., Weinzierl, B., Werner, F., Yamasoe, M. A., Ziereis, H., Zinner, T., and Zöger, M.: *ACRIDICON–CHUVA Campaign: Studying Tropical Deep Convective Clouds and Precipitation over Amazonia Using the New German Research Aircraft HALO*, Bulletin of the American Meteorological Society, 97, 1885-1908, doi: 10.1175/bams-d-14-00255.1, **2016**.

Wiedensohler, A.: *An approximation of the bipolar charge distribution for particles in the submicron size range*, Journal of Aerosol Science, 19, 387-389, doi: 10.1016/0021-8502(88)90278-9, **1988**.

Wieser, P., Greiner, W., Hildenbrandt, T., Kapr, T., and Schreiber, H.: *Lasermikrosonden-Massenspektrometrie atmosphärischer Aerosolpartikeln : Aerosol-Untersuchungen im Zusammenhang mit dem TULLA-Experiment*. In: KfK-PEF 87, Kernforschungszentrum Karlsruhe, Karlsruhe, **1991**.

Wiley, W. C. and McLaren, I. H.: *Time-of-Flight mass spectrometer with improved resolution*, Review of Scientific Instruments, 26, 1150-1157, doi: 10.1063/1.1715212, **1955**.

Willis, M. D., Burkart, J., Thomas, J. L., Köllner, F., Schneider, J., Bozem, H., Hoor, P. M., Aliabadi, A. A., Schulz, H., Herber, A. B., Leaitch, W. R., and Abbatt, J. P. D.: *Growth of nucleation mode particles in the summertime Arctic: a case study*, Atmospheric Chemistry and Physics, 16, 7663-7679, doi: 10.5194/acp-16-7663-2016, **2016**.

Willis, M. D., Köllner, F., Burkart, J., Bozem, H., Thomas, J. L., Schneider, J., Aliabadi, A. A., Hoor, P. M., Schulz, H., Herber, A. B., Leaitch, W. R., and Abbatt, J. P. D.: *Evidence for marine biogenic influence on summertime Arctic aerosol*, Geophysical Research Letters, 44, 6460-6470, doi: 10.1002/2017gl073359, **2017**.

Winker, D. M., Vaughan, M. A., Omar, A., Hu, Y., Powell, K. A., Liu, Z., Hunt, W. H., and Young, S. A.: *Overview of the CALIPSO Mission and CALIOP Data Processing Algorithms*, Journal of Atmospheric and Oceanic Technology, 26, 2310-2323, doi: 10.1175/2009jtecha1281.1, **2009**.

Wittig, A. E., Anderson, N., Khlystov, A. Y., Pandis, S. N., Davidson, C., and Robinson, A. L.: *Pittsburgh air quality study overview*, Atmospheric Environment, 38, 3107-3125, doi: 10.1016/j.atmosenv.2004.03.003, **2004**.

Wollny, A.: *Entwicklung eines bipolaren Flugzeitmassenspektrometers zur Analyse der chemischen Zusammensetzung von individuellen Aerosolpartikeln*, PhD thesis, Dissertation, Mathematisch-Naturwissenschaftlichen Fakultät, Rheinische Friedrich-Wilhelms-Universit¨at Bonn, Bonn, **2002**.

Wriedt, T.: *A Review of Elastic Light Scattering Theories*, Particle & Particle Systems Characterization, 15, 67-74, doi: 10.1002/(sici)1521-4117(199804)15:2<67::aid-ppsc67>3.0.co;2-f, **1998**.

Xu, W., Croteau, P., Williams, L., Canagaratna, M., Onasch, T., Cross, E., Zhang, X., Robinson, W., Worsnop, D., and Jayne, J.: *Laboratory characterization of an aerosol chemical speciation monitor with PM2.5 measurement capability*, Aerosol Science and Technology, 51, 69-83, doi: 10.1080/02786826.2016.1241859, **2017**.

Yoo, S.-H., Chae, S.-K., and Liu, B. Y. H.: *Influence of Particle Refractive Index on the Lower Detection Limit of Light Scattering Aerosol Counters*, Aerosol Science and Technology, 25, 1-10, doi: 10.1080/02786829608965374, **1996**.

Yu, P., Rosenlof, K. H., Liu, S., Telg, H., Thornberry, T. D., Rollins, A. W., Portmann, R. W., Bai, Z., Ray, E. A., Duan, Y., Pan, L. L., Toon, O. B., Bian, J., and Gao, R.-S.: *Efficient transport of tropospheric aerosol into the stratosphere via the Asian summer monsoon anticyclone*, Proceedings of the National Academy of Sciences, 114, 6972-6977, doi: 10.1073/pnas.1701170114, **2017**.

Yu, P., Toon, O. B., Neely, R. R., Martinsson, B. G., and Brenninkmeijer, C. A. M.: *Composition and physical properties of the Asian Tropopause Aerosol Layer and the North American Tropospheric Aerosol Layer*, Geophysical Research Letters, 42, 2540-2546, doi: 10.1002/2015gl063181, **2015**.

Zapp, K.-H., Wostbrock, K.-H., Schäfer, M., Sato, K., Seiter, H., Zwick, W., Creutziger, R., and Leiter, H.: *Ammonium Compounds*, Ullmann's Encyclopedia of Industrial Chemistry, doi: 10.1002/14356007.a02_243, **2000**.

Zawadowicz, M. A., Lance, S., Jayne, J. T., Croteau, P., Worsnop, D. R., Mahrt, F., Leisner, T., and Cziczo, D. J.: *Quantifying and improving the optical performance of the laser ablation aerosol particle time of flight mass spectrometer (LAAPToF) instrument*, Aerosol Science and Technology, 54, 761-771, doi: 10.1080/02786826.2020.1724867, **2020**.

Zelenyuk, A. and Imre, D.: *Single particle laser ablation Time-of-Flight mass spectrometer: An introduction to SPLAT*, Aerosol Science and Technology, 39, 554-568, doi: 10.1080/027868291009242, **2005**.

Zelenyuk, A., Imre, D., Wilson, J., Zhang, Z., Wang, J., and Mueller, K.: *Airborne Single Particle Mass Spectrometers (SPLAT II & miniSPLAT) and New Software for Data Visualization and Analysis in a Geo-Spatial Context*, Journal of the American Society for Mass Spectrometry, 26, 257-270, doi: 10.1007/s13361-014-1043-4, **2015**.

Zelenyuk, A., Yang, J., Choi, E., and Imre, D.: *SPLAT II: An Aircraft Compatible, Ultra-Sensitive, High Precision Instrument for In-Situ Characterization of the Size and Composition of Fine and Ultrafine Particles*, Aerosol Science and Technology, 43, 411-424, doi: 10.1080/02786820802709243, **2009**.

Zhigilei, L. V., Kodali, P. B. S., and Garrison, B. J.: *A Microscopic View of Laser Ablation*, The Journal of Physical Chemistry B, 102, 2845-2853, doi: 10.1021/jp9733781, **1998**.

Zhou, L., Rai, A., and Zachariah, M. R.: *Component and morphology biases on quantifying the composition of nanoparticles using single-particle mass spectrometry*, International Journal of Mass Spectrometry, 258, 104-112, doi: 10.1016/j.ijms.2006.07.006, **2006**.

Acronyms

Acronym	Description
AB	Air Beam
ACCLIP	Asian summer monsoon Chemical and CLimate Impact Project
AIDA	Aerosol Interaction and Dynamics in the Atmosphere
AMA	Asian Monsoon Anticyclone
AMS	Aerosol Mass Spectrometer
amsl	above mean sea level
ATAL	Asian Tropopause Aerosol Layer
BC	Black Carbon
BFSP	Brute Force Single Particle mode
BH	Bohren-Huffman
B-ToF-MS	Bipolar ToF Mass Spectrometer
CALIOP	Cloud-Aerosol Lidar with Orthogonal Polarization
CALIPSO	Cloud-Aerosol Lidar and Infrared Pathfinder Satellite Observations
CPC	Condensation Particle Counter
CPI	Constant-Pressure Inlet
CPICTRL	Constant-Pressure Inlet ConTRoL
CPT	Cold Point Tropopause
CRISP	Concise Retrieval of Information from Single Particles
CRISTA	CRyogenic Infrared Spectrometers and Telescopes for the Atmosphere
C-ToF-MS	C-shaped Time-of-Flight mass spectrometer
CTM	Chemical-Transport Models
DAQ	Data AQisition
DC	Double Charge
DETC	DETection Card
DL	Detection Laser
DM	Dichroitic Mirror
DMA	Differential Mobility Analyzer
DU	Detection Unit
EC	Elemental Carbon
ECLIF	Emission and CLimate Impact of alternative Fuel
EEPROM	Electrically Erasable Programmable Read-Only Memory
EI	Electron Impact Ionization

Acronym	Description
EP	Extraction Plate of the mass spectrometer
ERICA	ERC Instrument for Chemical composition of Aerosols
ERICA-AMS	ERICA Aerosol Mass Spectrometer
ERICA-LAMS	ERICA Laser Ablation Mass Spectrometer
FL	Flash Lamp
FLQS delay	Flash Lamp Q-Switch delay
FPGA	Field Programmable Gate Array
FSC	Fail-Safe Controller
FWHM	Full Width at Half Maximum
GLORIA	Gimballed Limb Observer for Radiance Imaging of the Atmosphere
GND	Ground
GPS	Global Positioning System
GUI	Graphic User Interface
HALO	High Altitude and Long-Range research aircraft
HDF5	Hierarchical Data Format, version 5
HIAPER	High-performance Instrumented Airborne Platform for Environmental Research
HV	High Voltage
IC	Integrated Circuit
IE	Ionization Efficiency
KLX	Kalamata International Airport in Kalamata, Greece
KTM	Tribhuvan International Airport in Kathmandu, Nepal
LAAP	Laser Ablation Aerosol Particle (AeroMegt GmbH)
LAAPTOF	Laser Ablation Aerosol Particle Time-Of-Fight mass spectrometer (AeroMegt GmbH)
LDI	Laser Desorption and Ionization
LPM	Low Power Mode
MCC	Main Control Computer
MCP	Multi-Channel-plate
MDB	Myasishchev Design Bureau
MoLa	Mobile Laboratory
MPIC	Max Planck Institute for Chemistry in Mainz, Germany
MS	Mass Spectrometer
MUPI	MUlti-Photon Ionization
NASA	National Aeronautics and Space Administration
NCAR	National Center for Atmospheric Research

Acronym	Description
ND-MAX	NASA/DLR-Multidisciplinary Airborne eXperiments
NIST	National Institute of Standards and Technology
NPF	New Particle Formation
NSF	National Science Foundation
OPC	Optical Particle Counter
PAH	Poly Aromatic Hydrocarbon
PBL	Planetary Boundary Layer
PID	Proportional-Integral-Derivative
PMT	PhotoMultiplier Tube
PPC	Pump and Pressure Controller
PSx	Pumping Stage x
PS	Power Supply
PSI	Paul Scherrer Institute
PSL	PolyStyrene Latex NIST certified size standard
PTC	Positive Temperature Coefficient
RAM	Random-Access Memory
RC	Resistor-Capacitor
REMPI	Resonance-Enhanced Multi-Photon Ionization
RIE	Relative Ionization Efficiency
RTD	Resistance Temperature Detector
S_0	Ground State
S_1	Exited State
SBD	Short Burst Data
SC	Single Charge
SIS	Single Ion Signal
SPMS	Single Particle Mass Spectrometer
SQUIRREL	SeQUential Igor data RetRiEvaL
SSD	Solid-State Drive
StratoClim	Stratospheric and upper tropospheric processes for better Climate predictions
SU	Shutter Unit
TC	Trigger Card
TEMPCTRL	TEMPerature ConTRoL
TMP	Turbo Molecular Pump
ToF-MS	Time-of-Flight Mass Spectrometry or Spectrometer

Acronym	Description
TPS	ToF Power Supply
UCSE	Unit for Connection with Scientific Equipment
UCSECTRL	UCSE ConTRoL unit
UHSAS	Ultra-High Sensitivity Aerosol Spectrometer
UPS	Uninterruptible Power Supply
USA	United States of America
UTC	Coordinated Universal Time
UT/LS	Upper Troposphere/Lower Stratosphere
UV	Ultra Violet
VAC	Volt Alternating Current
VDC	Volts of Direct Current

Variables, symbols, and units

Symbol	Typical unit	Description
A	number	amplitude of the Gaussian function
A_{tof}	s	m/z calibration coefficient
AB_{corr}	-	air beam correction factor
AE	-	ablation efficiency
AE_{frag}	J	appearance energy
a	m s^{-2}	acceleration of a particle
a_t	-	multiplying factor to calculate $r_{eff,L}$ from w_0
α	rad	particle beam divergence
B_{tof}	s $C^{0.5}$ $kg^{-0.5}$	m/z calibration coefficient
$\bar{C}_{AN}$	µg m^{-3}	mean mass concentration of ammonium nitrate
C_c	-	Cunningham slip correction factor
C_s	µg m^{-3}	mass concentration of an aerosol species s
C_{tof}	-	m/z calibration coefficient
CE	-	collection efficiency
c	m s^{-1}	speed of light (c = 299,792,458 m s^{-1})
cts_{Det}	number	counts at the detection units
c_{DC}	cm^{-3}	concentration of the doubly charged particles
c_{SC}	cm^{-3}	concentration of the singly charged particles
c_{ref}	cm^{-3}	reference number concentration
D	J	dissociation energy
DVI_{rel}	-	relative deviation of the measurement from the fitted curve
DE	-	detection efficiency
DE_{AN}	-	detection efficiency of ammonium nitrate particles at the detection units
DE_{AMS}	-	detection efficiency at the ERICA-AMS vaporizer
DE_{KTM}	-	detection efficiency for x_{pos} = 10.55 mm (setting in KTM)
DE_{PSL}	-	detection efficiency of PSL particles at the detection units
DE_{max}	-	maximum possible detection efficiency

Symbol	Typical unit	Description
d	m	travel distance of the ions in the drift tube
d_a	nm	aerodynamic diameter
$d_{eff,L}$	mm	effective detection laser beam width (diameter)
$d_{eff,V}$	mm	effective vaporizer width (diameter)
d_{50}	nm	diameter, where the transmission or detection is 50 %
d_{mob}	nm	electric mobility particle diameter
d_{nom}	nm	nominal particle diameter
d_{geo}	nm	geometric particle diameter
d_p	nm	particle diameter
d_{va}	nm	vacuum aerodynamic diameter
$d_{va,fit}$	nm	vacuum aerodynamic diameter of the fitted curve
$d_{va,particle}$	nm	vacuum aerodynamic diameter of the measured particle
dcs	-	duty cycle of the shutter (dcs = 12/25)
$\Delta^{abs}X$	unit of *X*	absolute uncertainty of the variable *X*
$\Delta^{rel}X$	-	relative uncertainty of the variable *X*
E	J	energy
E_e	W m^{-2}	irradiance
$E_{ionization}$	J	ionization energy
E_{ip}	J	ionization energy of the atoms
$E_{IR/green}$	J	ablation laser pulse energy of the green and IR light fraction
E_{photon}	eV	single photon energy
$E_{PositionX}$	J	ablation laser pulse energy at Position X (see Figure 19)
E_{total}	J	total ablation laser pulse energy of the green and IR light fraction
E_{UV}	J	ablation laser pulse energy of the UV light fraction
ΔE	J	Coulomb depression
F	N	force
F_{drag}	N	drag force
f_{calib}	ions pg^{-1}	calibration factor

Symbol	Typical unit	Description
f_{DC}	-	number fraction of doubly charged particles
$f_{extraction}$	s^{-1}	extraction frequency
f_{FC}	-	Franck-Condon factor
f_{Mie}	-	factor to calculate $r_{eff,L}$ from another particle sizes' $r_{eff,L}$ value by Mie theory
f_{NO3}	-	mass fraction of NO_3 in NH_4NO_3
f_{part}	-	particle fraction
f_{rep}	s^{-1}	repetition rate of the ablation laser
f_{SC}	-	number fraction of singly charged particles
f_{spec}	-	rate of recorded single particle mass spectra
f_{UV}	-	UV fraction of the ablation laser pulse
$\Phi_{AN,mass}$	$g\ s^{-1}$	mass flow of ammonium nitrate through the CPC
Φ_{ERICA}	$cm^3\ s^{-1}$	volumetric flow rate into the ERICA instrument
h	J s	Planck constant (h = 6.62607015 · 10^{-34} J s)
h_{amsl}	m	GPS altitude (above mean sea level)
H_e	$J\ m^{-2}$	radiant fluence
I_{AB}	ions s^{-1}	air beam signal during the flight measurements
$I_{AB,calib}$	ions s^{-1}	air beam signal during calibration measurements
I_{AMS}	mV·ns	measured signal intensity at the ERICA-AMS
I_{NO3}	ions s^{-1}	ion fragment signal of nitrate in the ERICA-AMS
I_{ir}	a.u.	irradiated intensity
I_{rel}	-	relative scattered light intensity from Mie theory
I_s	ions s^{-1}	ion fragment signal of species s in the ERICA-AMS
I_{sc}	a.u.	scattered light intensity
I_{stick}	mV · samples	stick mass spectrum signal intensity
I_{raw}	V	raw mass spectrum signal intensity
IE_{NO3}	-	ionization efficiency of nitrate
IPP_{NO3}	number	number of ions per nitrate particle
$K0$	nm	coefficient of the polynomial size calibration function

Symbol	Typical unit	Description
$K1$	nm μs^{-1}	coefficient of the polynomial size calibration function
$K2$	nm μs^{-2}	coefficient of the polynomial size calibration function
Kn	-	Knudsen number
k	nm	constant parameter in the size calibration function
k_B	J K^{-1}	Boltzmann constant (k_B = 1.380649 · 10^{-23} J K^{-1})
k_G	µs nm^{-1}	constant parameter in the size calibration function
L	m	characteristic length of the flow
λ	nm	wavelength
λ_{mfp}	nm	mean free path
M	units of m/z	mass of a peak
ΔM	units of m/z	mass spectrometer resolving power
M_w	g mol^{-1}	molecular weight
MW_{NO3}	g mol^{-1}	molecular mass of ammonium nitrate
MPP_{NO3}	number	number of molecules per nitrate particle
m	kg	mass of an ion
m_e	kg	the electron mass
m_p	kg	particle mass
m/z	dimensionless	mass-to-charge ratio; The *m* refers to the molecular or atomic mass number and *z* to the charge number of the ion (IUPAC, 1997)
μ	Pa s	fluid viscosity
N_A	mol^{-1}	Avogadro's number (N_A = 6.02214076·10^{23} mol^{-1})
N_{points}	number	number of measured points
N_{shots}	number	number of laser shots
$N_{spectra}$	number	number of acquired spectra
N_{trials}	number	number of trials
N_{type}	number	number of mass spectra of a specific particle type
n	-	refractive index
n_0	cm^{-3}	particle number density of the neutral particles

Symbol	Typical unit	Description
n_e	cm^{-3}	particle number density of the electrons
n_i	cm^{-3}	particle number density of the ions
n_p	number	number of particles
n_{PSL}	-	refractive index of PSL
P	W	power
P_0	W	offset of the power
P_{max}	W	maximum power
p	-	probability of success in binomial statistics
$p(x,y)$	-	probability function
p_g	Pa	pressure of the gas
p_{stat}	hPa	static pressure
pos_0	mm	central point of the Gaussian profile
pos	mm	position of the blade or aerodynamic lens
φ	-	DC charge fraction/SC charge fraction ratio
$Q(T)$	-	partition function of the ions
$Q_0(T)$	-	partition function of the neutral particles
q	-	probability of failure in binomial statistics
$\rho_{p,AN}$	$g\ cm^{-3}$	density of ammonium nitrate
$\rho_{p,Ao}$	$g\ cm^{-3}$	density of gold
ρ_p	$g\ cm^{-3}$	particle density
$\rho_{p,PSL}$	$g\ cm^{-3}$	density of PSL
R	$kg\ m^2\ s^{-2} mol^{-1}\ K^{-1}$	gas constant (R = 8.314462618 $kg\ m^2\ s^{-2} mol^{-1}\ K^{-1}$)
R_{MS}	-	resolution of a mass spectrometer
RIE_{NH4}	-	relative ionization efficiency of ammonium
RIE_{NO3}	-	relative ionization efficiency of nitrate
RIE_{org}	-	relative ionization efficiency of organic compounds
RIE_s	-	relative ionization efficiency of species s
RIE_{SO4}	-	relative ionization efficiency of sulfate
r	mm	$1/e^2$-radius

Symbol	Typical unit	Description
r_{eff}	mm	effective width (radius)
$r_{eff,L}$	mm	effective detection laser beam width (radius)
$r_{eff,V}$	mm	effective vaporizer width (radius)
$S_{ablation}$	-	particle beam and ablation laser focus overlap
$S_{detect,L}$	-	particle beam and detection laser beam overlap
$S_{detect,V}$	-	measure of the particle beam and vaporizer overlap
SIS	mV·ns	single ion signal at the ERICA-AMS
Stk	-	Stokes number
s_p	m	stop distance
s_{tof}	m	ion flight path length
σ	various	standard deviation of the probability density function
σ_{rel}	-	relative σ of the fractions for each chemical species
T	K	temperature
T_{out}	°C	ambient temperature
t	s	time or time interval
t_{flight}	s	flight time of the aircraft
Δt	s	time shift
t_{TC}	s	clock cycle time
t_{tof}	s	particle or ion flight time
TE	-	transmission efficiency of the aerodynamic lens
τ	µs	relaxation time
τ_p	ns	ablation laser pulse duration
U	V	voltage of the electric field
u_∞	m s^{-1}	undisturbed velocity of the fluid
upc	number	number of *Upcount*
upc_0	number	abscissa at the mode maximum of the Gaussian function
v	m s^{-1}	velocity of an ion
v_g	m s^{-1}	velocity of the gas molecules
v_p	m s^{-1}	particle velocity

Symbol	Typical unit	Description
w_0	m	beam waist 1/e²-radius of intensity of the Gaussian profile
$w_{0,dia}$	m	laser beam width ($1/e^2$-diameter)
w_{part}	m	particle beam width ($1/\sqrt{e}$-diameter)
$\bar{X}$	number	expected value in the binomial probability distribution
x_0	mm	mode of the aerodynamic lens scan
x_{pos}	mm	variable aerodynamic lens position
y_0	number	y-offset of the Gaussian function
Z	m $V^{-1}s^{-1}$	electrical mobility
z	C	charge of the ions
z_{asz}	mm	distance adjustment screws to ball joint along the particle axis
z_0	mm	focal length
z_{pos}	mm	razor blade to lens distance
z_R	mm	Rayleigh range

Appendix A: Supplementary information for Chapter 3

A.1 Diagram of the ERICA-LAMS mass spectrometer ion optics

The ERICA-LAMS time-of-flight mass spectrometer is described in Section 3.4.2.

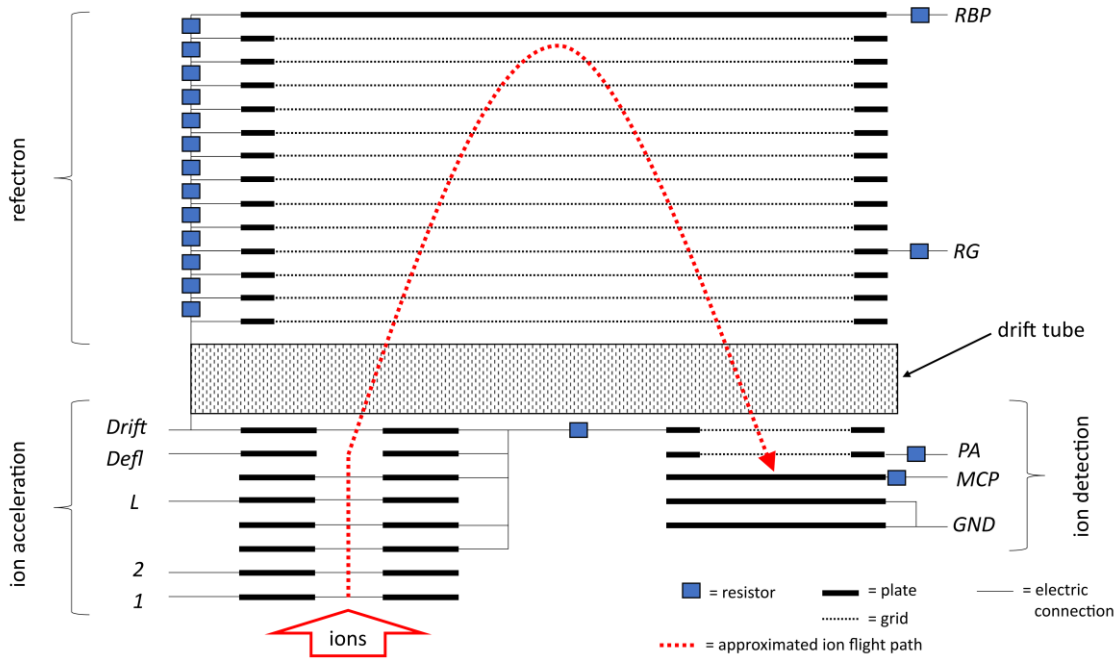

Figure 90: Diagram of the ion optics (not to scale) exemplarily for one polarity in the B-ToF-MS of the ERICA-LAMS (GND: Ground). The approximated ion path is shown in red. The set potential values of the various parameters (1, 2, L, Defl, Drift, RBP, RG, PA, and MCP,) are listed in Table 19.

Table 19: Pre-set voltage values in the ToF of the ERICA-LAMS (MS: Mass Spectrometer; GND: Ground).

Voltage parameter	**Potential value cation MS in Volt**	**Potential value for anion MS in V**
1	Shortcut to ground (GND)	Shortcut to ground (GND)
2	-4,990	4,990
L	-821	814
Defl	-2,154.936	2,080
Drift	-2,800	2,800
RBP	1,402	-1,400
RG	-840	780
PA	-3,000	1,200
MCP	1,400	1,786

A.2 Diagram of the ERICA-AMS mass spectrometer ion optics

The ERICA-AMS time-of-flight mass spectrometer is described in Section 3.5.2.

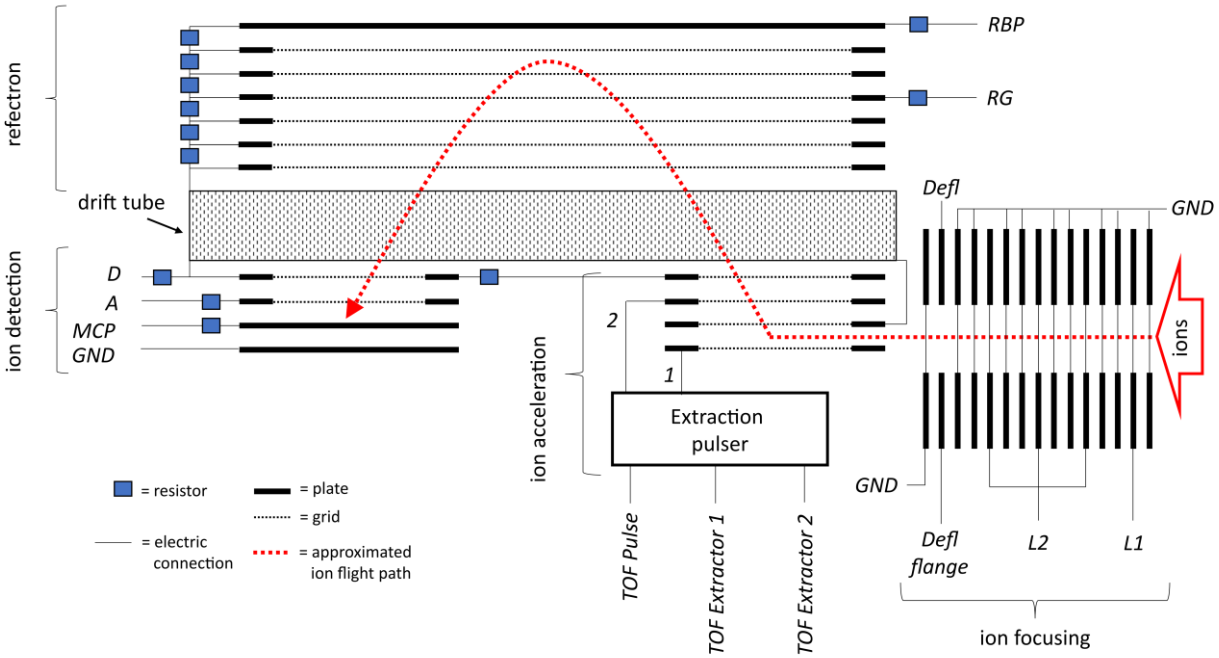

Figure 91: Diagram of the ion optics (not to scale) in the C-ToF-MS of the ERICA-AMS (GND: Ground). The approximated ion path is shown in red. The set potential values of the various parameters (L1, L2, Defl, Defl flange, TOF Pulse, TOF Extractor 1, TOF Extractor 2, RG, RBP, D, A, and MCP) are listed in Table 20.

Table 20: Pre-set voltage values in the ToF of the ERICA-AMS.

Voltage parameter	**Potential value in Volt**
L1	-135
L2	-106
Defl	-13
Defl flange	-3
TOF Pulse	700
TOF Extractor 1	80
TOF Extractor 2	700
RG	274
RBP	702
D	2,001
A	2,800
MCP	2,000

A.3 Temperature sensors and cooling fans

Table 21 shows the deployed 12 ambient (inside the pressurized container; rack1 to rack12) temperature and 32 surface temperature sensors deployed during StratoClim in the barrel aboard *Geophysica* and read out by the TEMPCTRL unit (see Section 3.7.1.5). The temperature sensors 60 to 63 are positioned outside the pressurized container. Figure 92 shows the positions of the ambient temperature sensors and cooling fans on the M-55 *Geophysica* rack.

Table 21: Table of deployed temperature sensors during StratoClim in the barrel aboard Geophysica. The 12 ambient (inside the pressurized container) temperature sensors are highlighted in bold letters (see also Figure 92). L: communication line on TEMPCTRL; S: sensor number on line L; #: set number on TEMPCTRL software; n/a: No sensor connected.

L	S	#	Name	L	S	#	name
1	0	8	**rack3**	4	0	32	detection recipient chamber
	1	9	battery pack		1	33	laser PS
	2	10	distribution box AC		2	34	**rack7**
	3	11	**rack2**		3	35	B-ToF chamber
	4	12	inverter		4	36	**rack6**
	5	13	**rack1**		5	37	*n/a*
	6	14	distribution box 27V		6	38	*n/a*
	7	15	MCC		7	39	*n/a*
2	0	16	**rack4**	5	0	40	container inside, bottom rear
	1	17	distribution box DC		1	41	Vicor1
	2	18	PPC		2	42	ACAC converter
	3	19	MD-1(B)		3	43	Vicor2
	4	20	**rack8**		4	44	heat exchanger
	5	21	MD-1(A)		5	45	container in bottom front
	6	22	LAMS amplifier		6	46	silicone oil circuit 1
	7	23	SplitFlow (TMP)		7	47	silicone oil circuit 2
3	0	24	**rack12**	7	0	56	container inside, top front
	1	25	**rack11**		1	57	container inside, mid front
	2	26	**rack10**		2	58	container inside, top mid rear
	3	27	**rack9**		3	59	container inside, top rear
	4	28	C-ToF chamber		4	60	container outside, top rear
	5	29	AMS amplifier		5	61	container outside, mid top rear
	6	30	**rack5**		6	62	container outside, mid bottom rear
	7	31	*n/a*		7	63	container outside, bottom rear

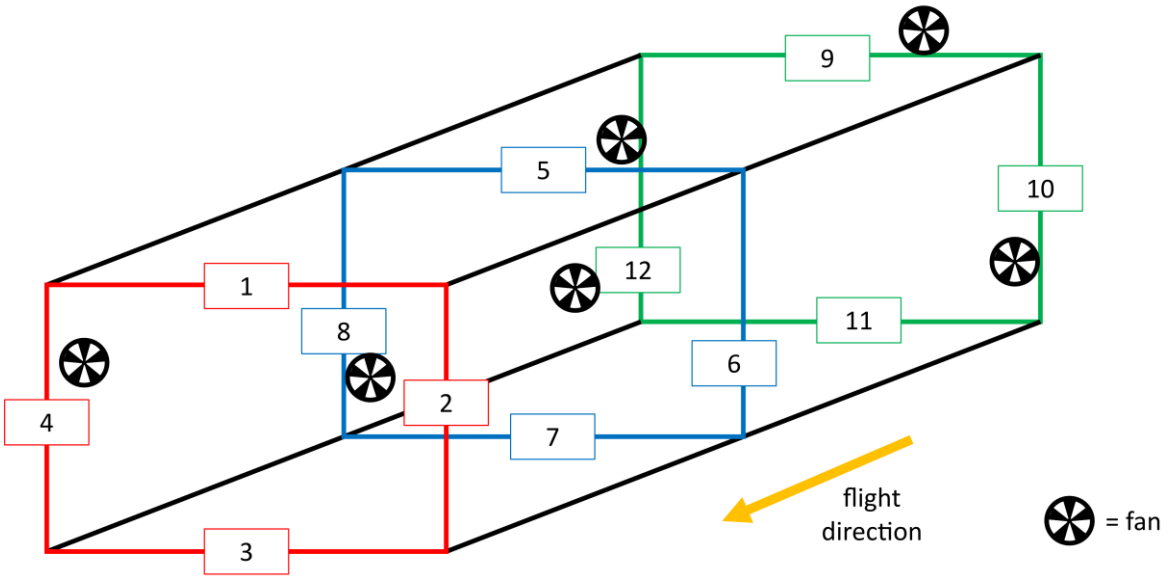

Figure 92: Positions of the temperature sensors on the M-55 Geophysica rack to observe ambient temperature distribution and the positions of the cooling fans to transfer the heat to the cold container walls for cooling the instrument (rack1 to rack13, see Table 21).

A.4 UCSE parameters

Table 22: Parameters recorded by UCSE and transmitted to UCSECTRL (MDB, 2002).

Parameter	Unit	Description
Date	-	yyyy-mm-dd (UTC)
Tout	°C	Out-boarding air temperature (T_{out})
Pstat	hPa	Static pressure (p_{stat})
Vtrue	km h^{-1}	true air speed
Halt	m	true altitude
Dr_ang	°	drift angle
Head	°	true heading
Pitch	°	pitch angle
Attack	°	attack angle
Sl_ang	°	slip angle
Uwind	m s^{-1}	absolute value of wind velocity
W_dir	°	wind direction
Roll	°	roll angle
Lat	°	latitude
Long	°	longitude
Gr_sp	km h^{-1}	ground speed
Tr_ang	°	track angle
Alt	m	GPS altitude (h_{amsl})
SS1	-	State word #1
SS2	-	State word #2
SRK	-	Word of one-time instruction
SYS_TIME	s	system time (seconds of day)

Appendix B: Supplementary information for Chapter 4

B.1 Uncertainty analysis

B.1.1 Detection laser and ablation laser characterization

The absolute uncertainties of the blade positions at x_{pos} and y_{pos} (termed $\Delta^{abs}x_{pos}$ and $\Delta^{abs}y_{pos}$) are based on reading errors of the translation stage (micrometer positioning system, $\Delta^{abs}x_{pos}$ = 0.0025 mm and $\Delta^{abs}y_{pos}$ = 0.0025 mm) and the absolute uncertainty of the measured laser power P (termed $\Delta^{abs}P$; values between 0.05 mW and 0.002 mW) reflect the fluctuation of the value at the bolometer display (Section 4.1.2).

B.1.2 Ablation laser characterization

Since the beam waist radius w_0 of the ablation laser result from a previous curve fitting, $\Delta^{abs}w_0$ is the resulting absolute uncertainty from the curve fitting procedures (between 0.004 mm and 0.035 mm). The absolute uncertainty of the blade positions at $\Delta^{abs}z_{pos}$ = 0.0025 mm is based on reading errors of the used caliper (Section 4.1.3).

B.1.3 UV light fraction of the ablation laser

The uncertainty of the measured laser pulse energy $\Delta^{abs}E_{UV}$ is based on reading errors of the used energy meter (Section 4.1.4). The values of $\Delta^{abs}E_{UV}$ are between 0.02 mJ and 0.07 mJ.

The uncertainty of the laser pulse energy for green and IR light $\Delta^{abs}E_{green/IR}$ and uncertainty of the fraction of the UV light $\Delta^{abs}f_{UV}$ is calculated based on Gaussian propagation of uncertainties:

$$\Delta^{abs}E_{green/IR} = \sqrt{(\Delta^{abs}E_{Position2})^2 + (\Delta^{abs}E_{Position5})^2} \quad (57)$$

$\Delta^{abs}E_{Position2}$ and $\Delta^{abs}E_{Position5}$ are the uncertainties of the laser pulse energy at Position 2 and Position 5, respectively, in the measurement setup (see Figure 19). $\Delta^{abs}E_{Position2}$ and $\Delta^{abs}E_{Position5}$ are based on reading errors of the used energy meter. The values for $\Delta^{abs}E_{Position2}$ are between 0.02 mJ and 0.07 mJ, and for $\Delta^{abs}E_{Position5}$ between 0.004 mJ and 0.009 mJ.

The UV fraction f_{UV} is calculated according Equation (58).

$$f_{UV} = \frac{E_{UV}}{E_{total}} \quad (58)$$

The total pulse energy E_{total} was measured at Position 1 (see Figure 19).

$\Delta^{abs}f_{UV}$ is calculated based on Gaussian propagation of uncertainties:

$$\Delta^{abs}f_{UV} = \sqrt{\left(\frac{\Delta^{abs}E_{UV}}{E_{total}}\right)^2 + \left(-\frac{\Delta^{abs}E_{total}\cdot E_{UV}}{{E_{total}}^2}\right)^2} \quad (59)$$

$\Delta^{abs}E_{total}$ is the absolute uncertainty of the total pulse energy E_{total} and is based on reading errors of the used energy meter. The values for $\Delta^{abs}E_{total}$ are between 0.04 mJ and 0.10 mJ.

B.1.4 Particle size

Manufacturers provide NIST Standard certificates for the used PSL particle charges containing the uncertainty of the modal geometric diameter of PSL particles $\Delta d_{geo,PSL}$. This value was multiplied by $\frac{\rho_{p,PSL}}{\rho_o}$ (see Appendix B.2) to derive the uncertainty of the modal $\Delta d_{va,PSL}$ value (see Table 5 and Table 7). The uncertainty of the PSL particle sizes is between 0.5 % - 14 % according to the NIST

certificates (see Section 4.2.1.2, Table 5 and Table 6). For ammonium nitrate particles the uncertainty of all sizes is conservatively estimated as 14 %. This value is the approximated maximum uncertainty of the particle size of PSL particles in the considered size range of d_{va} = 91 nm to d_{va} = 814 nm (see Section 4.2.1.2, Table 5 and Table 6; between 1.7 % and 14 % without size selection by a DMA).

B.1.5 Particle size calibration

For the particle size calibration (see Section 4.2.2), the *Upcount* histograms were curve fitted to the Gaussian function (Equation (26)). This delivers a value for the standard deviation σ_{upc} that functions as the absolute uncertainty of upc (termed $\Delta^{abs}upc$). Since the particle flight time $t_{ptof} = upc \cdot t_{TC}$, and clock cycle time t_{TC} = 40·10^{-3} µs (see Section 4.2.2.1) the absolute uncertainty of the particle flight time $\Delta^{abs}t_{ptof}$ can be estimated by Gaussian propagation of uncertainties to:

$$\Delta^{abs}t_{ptof} = \Delta^{abs}upc \cdot t_{TC} \tag{60}$$

The particle velocity v_p (see Section 4.2.2.2) is given by:

$$v_p = \frac{d_{DU}}{t_{ptof}} \tag{61}$$

where the distance between the focal points of the detection units DU1 and DU1 are 66.5 mm (see Section 3.3 and Appendix B.4). Thus, the absolute uncertainty of the particle velocity $\Delta^{abs}v_p$ can be estimated by Gaussian propagation of uncertainties to:

$$\Delta^{abs}v_p = \frac{d_{DU}}{{t_{ptof}}^2} \cdot \Delta^{abs}t_{ptof} \tag{62}$$

B.1.6 Detection efficiencies determined by aerodynamic lens scans

As described in Section 4.2.3, the detection efficiency DE for PSL and ammonium nitrate particles is determined for various aerodynamic lens positions by tilting the aerodynamic lens in discrete steps in the direction orthogonal to the detection laser axis. Here, the number of detected (*counts0* or *counts1*) particles per second cts_{Det} were counted. For each DE data point the 30 seconds averages $\overline{cts}_{Det}$ and $\bar{c}_{ref}$ were used.

The relative uncertainty of the volume flow into the ERICA instrument $\Delta^{rel}\Phi_{ERICA}$ equals the systematic uncertainty of the used soap bubble flow meter (Gilibrator2, Sensidyne, St. Petersburg, Fl, USA) and is conservatively estimated as $\Delta^{rel}\Phi_{ERICA}$ = 1 % (Sensidyne, 2016). The relative uncertainty of the volume flow into the CPC and the OPC $\Delta^{rel}\Phi_{ref}$ is a systematic uncertainty and assumed as $\Delta^{rel}\Phi_{ref}$ = 3 % (CPC; Grimm Aerosol Technik GmbH (2003)) and $\Delta^{rel}\Phi_{ref}$ = 5 % (OPC; GRIMM Aerosol Technik GmbH (2008)). Systematic uncertainties are generally not considered for the depicted uncertainty bars in the graphs in Chapter 4.

The absolute uncertainties of the aerodynamic lens positions at x_{pos} (termed $\Delta^{abs}x_{pos}$) are based on reading errors of the translation stage (micrometer positioning system, $\Delta^{abs}x_{pos}$ = 0.0025 mm).

The absolute uncertainty of the detection efficiency $\Delta^{abs}DE_{PSL\ or\ AN}$ (here not differentiated between the uncertainty of the detection efficiency for PSL particles $\Delta^{abs}DE_{PSL}$ and for ammonium nitrate particles $\Delta^{abs}DE_{AN}$; see Sections 4.2.3.1 and 4.2.3.2) is calculated based on Poisson statistics and Gaussian propagation of uncertainties:

$$\Delta^{abs}DE_{PSL\ or\ AN} = \left(\frac{\overline{cts}_{Det} \cdot {\Phi_{ERICA}}^{-1}}{\bar{c}_{ref}}\right) \cdot \sqrt{\left(\frac{\Delta^{abs}c_{ref}}{\bar{c}_{ref}}\right)^2 + \left(\frac{\Delta^{abs}cts_{Det}}{\overline{cts}_{Det}}\right)^2} \quad (63)$$

Here, the absolute uncertainties of the reference number concentration $\Delta^{abs}c_{ref}$ and of the number counts at the detection unit $\Delta^{abs}cts_{Det}$ are calculated based on Poisson statistics:

$$\Delta^{abs}c_{ref} = \frac{\bar{c}_{ref}}{\sqrt{\sum_{30\,s}(c_{ref} \cdot \Phi_{ref})}} \quad (64)$$

$$\Delta^{abs}cts_{Det} = \frac{\overline{cts}_{Det}}{\sqrt{\sum_{30\,s} cts_{Det}}} \quad (65)$$

Here, Φ_{ref} is the volume flow into the CPC (5 cm^3 s^{-1}) or OPC (20 cm^3 s^{-1}). Furthermore, the term $\sum_{30\,s}(c_{ref} \cdot \Phi_{ref})$ is the sum of the CPC or OPC counts and $\sum_{30\,s} cts_{Det}$ the sum of the counted particles, respectively, within 30 seconds. Thus, the argument in the square root is a sum of the number of counts used for Poisson statistics.

The detection efficiency at the ERICA-AMS vaporizer DE_{AMS} is determined by tilting the aerodynamic lens in discrete steps, like for the detection units described above and in detail in Section 4.2.3.3.

The absolute uncertainty of the detection efficiency at the ERICA-AMS $\Delta^{abs}DE_{AMS}$ is calculated based on Poisson statistics and Gaussian propagation of uncertainties (personal communication: O. Appel, MPIC, 2019):

$$\Delta^{abs}DE_{AMS} = \sqrt{\left(\sqrt{{\Delta^{rel}c_{CPC}}^2 + {\Delta^{rel}\gamma_{AMS}}^2} \cdot DE_{AMS}\right)^2 + {\Delta^{abs}\gamma_{AMS,noise}}^2} \quad (66)$$

Here, the relative uncertainties of the number concentration of the CPC $\Delta^{rel}c_{CPC}$ and the mass concentration of the ERICA-AMS $\Delta^{rel}\gamma_{AMS}$ are calculated based on Poisson statistics. Furthermore, $\Delta^{abs}\gamma_{AMS,noise}$ is the absolute uncertainty due to filter noise:

$$\Delta^{rel}c_{CPC} = \frac{1}{\sqrt{\sum_{t_{meas}}(c_{CPC} \cdot \Phi_{CPC})}} \quad (67)$$

$$\Delta^{rel}\gamma_{AMS} = \frac{1}{\sqrt{\sum_{t_{meas}} c_{CPC} \cdot \Phi_{ERICA} \cdot DE \cdot dcs}} \quad (68)$$

$$\Delta^{abs}\gamma_{AMS,noise} = \frac{1}{\sqrt{N_{points}}} \cdot \frac{\Delta^{abs}\gamma_{noise}}{\Phi_{AN,mass}} \quad (69)$$

Here Φ_{CPC} is the volume flow into the CPC (5 cm^3 s^{-1}), Φ_{ERICA} the volume flow into the ERICA instrument (Φ_{ERICA} = 1.476 cm^3 s^{-1}) and dcs is the duty cycle of the shutter (12/25; i.e., the fraction of time where aerosol particles actually reach the vaporizer). Furthermore, the term $\sum_{t_{meas}}(c_{CPC} \cdot \Phi_{CPC})$ is the sum of the CPC counts and $\sum_{t_{meas}} c_{CPC} \cdot \Phi_{ERICA} \cdot DE \cdot dcs$ is the sum of the estimated AMS counts within the measuring time t_{meas}. The estimated AMS count, needed for Poisson statistics, is

the measured mass divided by the mass of a single particle. Its size diameter is known, since only particles of a defined size pass through the DMA.

The parameter t_{meas} differs from measurement to measurement, but was typically around 30 s. Thus, the argument in the square root is a sum of the number of counts used for Poisson statistics. $\Delta^{abs}\gamma_{noise}$ is the averaged ERICA-AMS noise level (0.037 µg m^{-3}), $\Phi_{AN,mass}$ is the ammonium nitrate mass flow through the CPC and N_{points} is the number of measured points (number of *writes*, see Section 3.7.3.2).

The uncertainties of the maximum detection efficiency $\Delta^{rel}DE_{max}$ and the uncertainty of the detection efficiency during field deployment in KTM $\Delta^{rel}DE_{KTM}$ (see Section 4.2.4) are conservatively estimated to be 10 % based on reading errors from all plots used for evaluations like Figure 32.

All parameter estimations and curve fittings were performed with the *IGOR* Version software package using the appropriate functions. Correspondingly the uncertainties for the fits and parameters also are intrinsically calculated by the software. The absolute uncertainties of r_{eff}, σ, x_0 and TE (termed $\Delta^{abs}r_{eff}$, $\Delta^{abs}\sigma$, $\Delta^{abs}x_0$ and $\Delta^{abs}TE$) are directly derived from the curve fitting routine by using as one standard deviation. To represent the dimension of the particle beam at the specific position (DU1, DU2, ablation point, and ERICA-AMS vaporizer) the geometry of the instrument to the adjustment screws was considered and the uncertainties were calculated by multiplying the specific distance ratio factors (see Appendix B.4).

The absolute uncertainty for the effective vaporizer width was determined as $\Delta^{abs}r_{eff,V,SC}$ = 0.02 mm. This is, rounded up, the largest uncertainty $\Delta^{abs}r_{eff,V,SC}$ that occurred in the four measurements (see Section 4.2.3.3 and Appendix B.12).

B.1.7 Overlap parameter for detection units

The absolute uncertainty of the overlap parameter at the detection lasers $\Delta^{abs}S_{detect}$ (here not differentiated between $S_{detect,L}$ and $S_{detect,V}$; see Section 4.2.5) is calculated based on Gaussian propagation of uncertainties:

$$\Delta^{abs}S_{detect} = \sqrt{\left(\frac{\Delta^{abs}w_{part}}{2 \cdot r_{eff}}\right)^2 + \left(-\frac{\Delta^{abs}\, r_{eff} \cdot w_{part}}{2 \cdot {r_{eff}}^2}\right)^2} \qquad (70)$$

Here, r_{eff} is the effective radius and w_{part} the article beam width ($1/\sqrt{e}$-diameter). $\Delta^{abs}w_{part}$ equals $2 \cdot \Delta^{abs}\sigma$. The values of $\Delta^{abs}\, r_{eff}$ and $\Delta^{abs}\sigma$ were derived by the curve fitting procedure (see B.1.6). All parameters are in the dimension of the particle beam at the specific position (DU1, DU2, ablation point, and ERICA-AMS vaporizer) by multiplying the corresponding geometric factor (see Appendix B.4).

B.1.8 Overlap parameter for ablation region

The absolute uncertainty of the overlap parameter at the ablation laser $\Delta^{abs}S_{ablation}$ (see Section 4.2.5) is calculated based on Gaussian propagation of uncertainties:

$$\Delta^{abs}S_{ablation} = \sqrt{\left(\frac{\Delta^{abs}w_{part,abl}}{w_{0,dia}}\right)^2 + \left(-\frac{\Delta^{abs}w_{0,dia} \cdot w_{part,abl}}{{w_{0,dia}}^2}\right)^2} \qquad (71)$$

Here, $w_{0,dia}$ is the optical laser beam waist ($1/e^2$-diameter, see Section 4.1.3) and $w_{part,abl}$ the particle beam width at the ablation spot ($1/\sqrt{e}$-diameter). $\Delta^{abs}w_{part,abl}$ was calculated from $\Delta^{abs}\sigma$ at

DU2 by multiplying the geometric factor 1.840 (see Appendix B.4). $\Delta^{abs}\sigma$ was derived by the curve fitting procedure (see B.1.6).

B.1.9 Particle beam divergence

The absolute uncertainty of the particle beam divergence $\Delta^{abs}\alpha$ (see Section 4.2.5) is calculated based on Gaussian propagation of uncertainties:

$$\Delta^{abs}\alpha = \sqrt{\left(\frac{\Delta^{abs}\sigma}{z_{asd}}\right)^2 + \left(-\frac{\Delta^{abs}z_{asd}\cdot\sigma}{{z_{asd}}^2}\right)^2} \tag{72}$$

$\Delta^{abs}\sigma$ was derived by the curve fitting procedure (see B.1.6) and $\Delta^{abs}z_{asd}$ = 0.0025 mm is based on reading errors of the used caliper.

B.1.10 Ablation efficiency, number of spectra and number of shots

The absolute uncertainty of the ablation efficiency AE (see Section 4.3), termed $\Delta^{abs}AE$, is calculated using not Poisson counting but binomial statistics for taking the event (acquired spectrum) and the counter-event (acquired no spectrum) into account (Köllner, 2019).

$$\Delta^{abs}AE = \frac{\sqrt{N_{shots}\cdot AE\cdot(1-AE)}}{N_{shots}} = \frac{\sqrt{N_{spectra}\cdot(1-AE)}}{N_{shots}} \tag{73}$$

with the number of spectra, e.g., particles that are successfully ionized by the ablation laser and that create a mass spectrum, $N_{spectra}$, the number of laser shots N_{shots}, and the ablation efficiency AE. The parameter AE describes the fraction of the ablated and detected spectra and the term $(1-AE)$ describes the fraction of non-detected spectra. Thus, $N_{spectra} = N_{shots}\cdot AE$. The uncertainty $\Delta^{abs}AE$ describes the absolute uncertainty in percentage points.

Basis for the calculation of $\Delta^{abs}AE$ is the standard deviation $\sigma_X^{abs}$of the binomial probability distribution with the expected value $\bar{X} = N_{trials}\cdot p$, which is calculated as follows:

$$\sigma_X^{abs} = \sqrt{N_{trials}\cdot p\cdot q} \tag{74}$$

Here, N_{trials} is the number of trials, p is the probability of success and q is the probability of failure.

To calculate the absolute uncertainty of the number of spectra $\Delta^{abs}N_{spectra}$ for a given number of shots N_{shots}, binomial counting statistics is used. In contrast to that, Poisson statistics is used for an unknown number of shots N_{shots}.

To obtain the uncertainty of the ablation efficiency $\Delta^{abs}AE$, σ_X^{abs} is normalized to the number of shots N_{shots}.

The absolute uncertainty of the number of spectra $\Delta^{abs}N_{spectra}$ and absolute uncertainty of the number of shots $\Delta^{abs}N_{shots}$ which are based on Poisson statistics, are calculated as follows:

$$\Delta^{abs}N_{spectra} = \sqrt{N_{spectra}} \tag{75}$$

$$\Delta^{abs}N_{shots} = \sqrt{N_{shots}} \tag{76}$$

For instance, in the size bin d_{va} = 214 nm to d_{va} = 244 nm (see Figure 48) the number of shots is N_{shots} = 351 and the number of recorded spectra is $N_{spectra}$ = 182. Thus, the ablation efficiency, i.e., the hitting probability, is AE = 0.52. The resulting uncertainties for the parameters in this size bin are consequently: $\Delta^{abs}N_{shots}$ = 18.7, $\Delta^{abs}N_{spectra}$ = 13.5, and $\Delta^{abs}AE$ = 0.05.

B.2 Particle size calculation

The ERICA-instrument determines particle sizes in terms of the vacuum aerodynamic diameter (d_{va}). The geometric diameter d_{geo} of spheres (like determined e.g., from a suitable microscope), e.g., PSL and gold, is given by the specification of the manufacturer. The size measure when using a DMA is the electric mobility diameter d_{mob}. Thus, these sizes have to transferred to d_{va}.

The physical relationship between d_{va} and the volume equivalent diameter d_{ve} has been derived in the literature (Jimenez et al., 2003b, a; DeCarlo et al., 2004), where the parameters are: χ is the dynamic shape factor in the free-molecular regime (χ = 1.00 for spherical particles, Hinds (1999)), S is the Jayne shape factor, ρ_p is the density of the particles material in g cm^{-3} and ρ_o is the unit density of 1 g cm^{-3}:

$$d_{va} = d_{ve} \cdot \frac{1}{\chi} \cdot \frac{\rho_p}{\rho_o} = d_{mob} \cdot S \cdot \frac{\rho_p}{\rho_o} \tag{77}$$

For spherical particles DeCarlo et al. (2004) stated:

$$d_{mob} = d_{ve} = d_{geo} \tag{78}$$

Both equations were used to calculate d_{va} for PSL and gold spheres assuming χ equals 1 (DeCarlo et al., 2004):

$$d_{va,PSL} = d_{geo,PSL} \cdot \frac{\rho_{p,PSL}}{\rho_o} \tag{79}$$

$$d_{va,Au} = d_{geo,Au} \cdot \frac{\rho_{p,Au}}{\rho_o} \tag{80}$$

The particle density for PSL $\rho_{p,PSL}$ = 1.05 g cm^{-3} (Jayne et al., 2000) and for gold $\rho_{p,Au}$ = 19.32 g cm^{-3} (Carney et al., 2011).

Since ammonium nitrate particles are non-spherical, Equation (77) was used to calculate d_{va} (Jayne et al., 2000). Furthermore, the density $\rho_{p,AN}$ is $\rho_{p,AN}$ = 1.725 g cm^{-3} (Zapp et al., 2000) and S was assumed to be S = 0.8 (Jayne et al., 2000).

$$d_{va,AN} = d_{mob,AN} \cdot S \cdot \frac{\rho_{p,AN}}{\rho_o} \tag{81}$$

The aerodynamic diameter d_a is given as (Hinds, 1999):

$$d_a = d_{ve} \cdot \sqrt{\frac{\rho_p}{\rho_o \cdot \chi}} \tag{82}$$

Table 23 shows the calculated $d_{va,PSL}$ for various $d_{geo,PSL}$ according to Equation (79) and the calculated $d_{va,Au}$ for various $d_{geo,Au}$ according to Equation (80). Equation (27) , i.e., the size calibration function (see Section 4.2.2.1), can be solved for t_{ptof}. Substituting d_{va} (in nm) in the resulting Equation (83) provides t_{ptof}.

$$t_{ptof} = \frac{-K1 + \sqrt{K1^2 - 4 \cdot K2 \cdot (K0 - d_{va})}}{2\,K2} \tag{83}$$

Considering a clock cycle of 40 ns (see 3.7.2.2) the upc values can be determined from t_{ptof}. For the measurement with gold spheres (see Section 4.4.1.2) a gold particle size of d_{geo} = 200 nm was chosen.

Larger particles would exceed the *TriggTMax* value of 30,000 (see Section 3.7.2.2) and the detection efficiency for smaller particles, like for $d_{geo,Au}$ = $d_{geo,PSL}$ = 100 nm might be too low to be detected (see Section 4.2.5). The effect of the different density for the different particle types considering the same geometric diameters d_{geo} to the calculated d_{va} values is obvious.

Table 23: Geometric diameters of PSL particles $d_{geo,PSL}$ and the calculated vacuum aerodynamic diameters $d_{va,PSL}$ according to Equation (79) and the geometric diameters of gold spheres $d_{geo,Au}$ and the calculated vacuum aerodynamic diameters $d_{va,Au}$ according to Equation (80), the corresponding t_{ptof} values for gold spheres according to the size calibration function Equation (27), and the thus corresponding upc values for gold spheres. The particle size of the used gold spheres is highlighted by bold lettering.

$d_{geo,Au}$= $d_{geo,PSL}$	$d_{va,PSL}$	$d_{va,Au}$	t_{ptof} for gold spheres in µs	upc for gold spheres
80	84	1,544	802	20,049
100	105	1,930	874	21,860
200	210	**3,860**	**1,159**	**28,983**
300	315	5,791	1,378	34,461
400	420	7,721	1,563	39,082
600	630	11,581	1,874	46,840

B.3 Determination of the best position for the aerodynamic lens

To determine the optimum aerodynamic lens position, multiple lens position scans in x- and y-direction (see Figure 12) were performed using various particle sizes (d_{va}) of ammonium nitrate at the ERICA-AMS vaporizer. The figures below show the normalized detection efficiency DE_{AMS} as function of the aerodynamic lens position x_{pos} in Figure 93 and y_{pos} in Figure 94. The detection efficiency DE_{AMS} is determined by Equation (40) in Section 4.2.3.3, considering mass concentrations measured by the ERICA-AMS and the number concentrations measured by a CPC. DE_{AMS} for each measurement with the same particle size was normalized to the highest DE_{AMS} value. For the plots in Figure 93 and Figure 94 the geometric dimensions in the instrument were considered (see Appendix B.4).

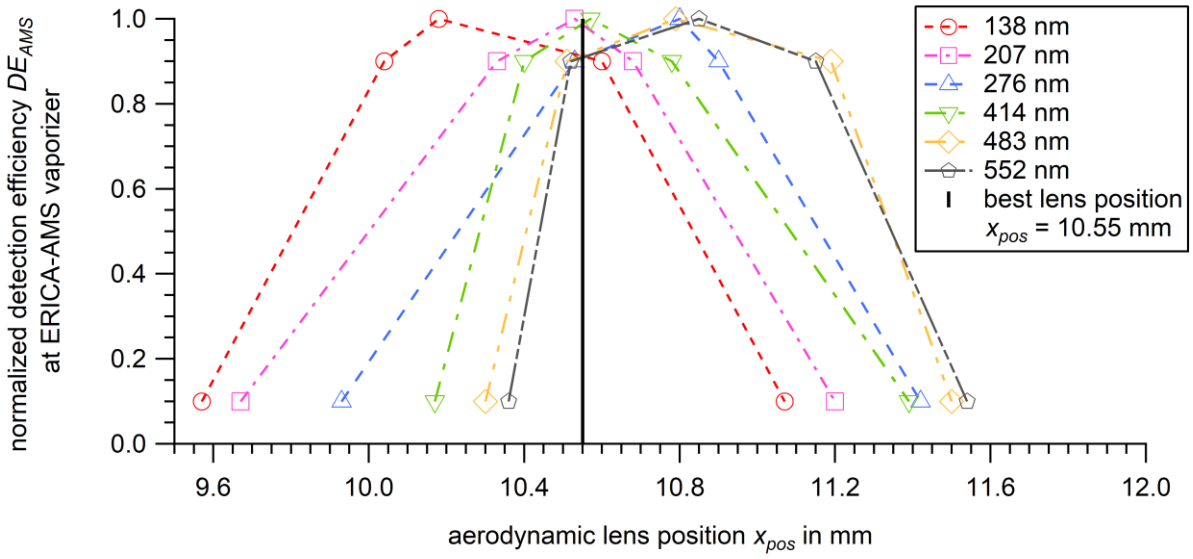

Figure 93: Detection efficiency as function of the aerodynamic lens position x_{pos} with various ammonium nitrate particle sizes (d_{va}) at the ERICA-AMS vaporizer. The black line marks the best aerodynamic lens position at x_{pos} = 10.55 mm.

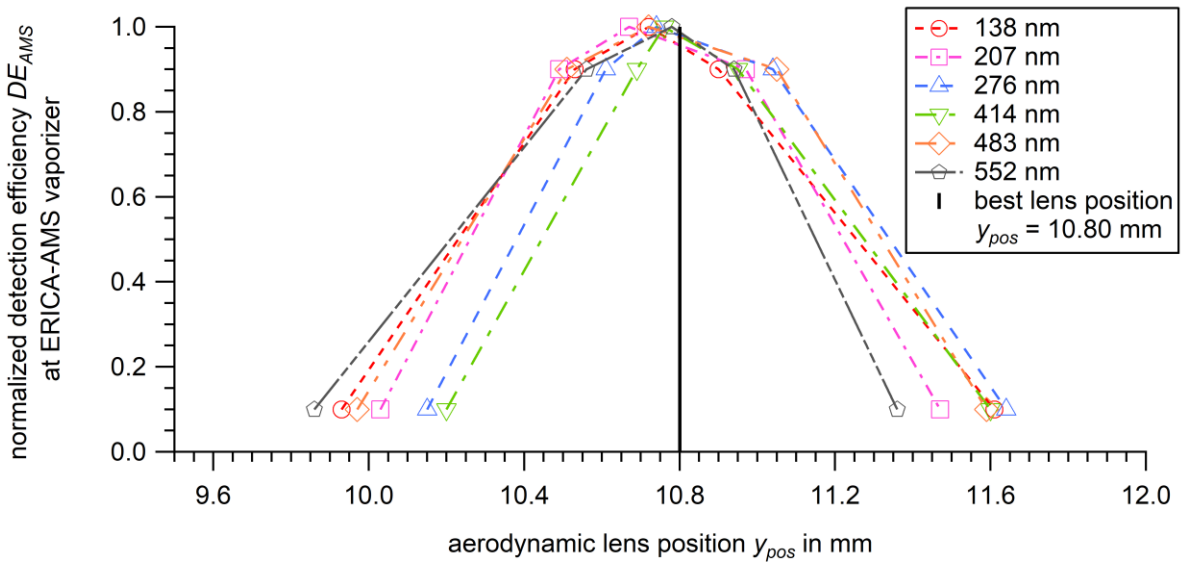

Figure 94: Detection efficiency as function of the aerodynamic lens position y_{pos} with various ammonium nitrate particle sizes (d_{va}) at the ERICA-AMS vaporizer. The black line marks the best aerodynamic lens position at x_{pos} = 10.80 mm.

Based on these scans the parameters x_{pos} and y_{pos} for the aerodynamic lens adjustment were set to 10.55 mm and 10.8 mm, respectively. This position defines the aerodynamic lens to ERICA-AMS vaporizer particle beam axis (z-axis in Figure 12). This axis is used for further detection unit and ablation laser adjustments described in Section 4.2.1 and set during ERICA-AMS regular operation (see Section 5.2).

B.4 Geometry and distance ratios in the ERICA instrument

The parameters r_{eff}, σ, x_0 and TE were determined by Equations (37), (39), and (41) and are thus in the dimension relative to the aerodynamic lens position x_{pos}. For the graphics and the calculations in Section 4.2.5 the parameters were rescaled to the dimension of the particle beam at the specific position (DU1, DU2, ablation point, and ERICA-AMS vaporizer) by the intercept theorem. Table 24 shows these factors according to the distances (see Section 3.3) in the ERICA instrument (see Figure 95). To rescale the ammonium nitrate spot on the adhesive strip to the position of the ERICA-AMS vaporizer the factor 3.452 is used (see Section 4.2.4). The *Multiplier* value is based on ratio of the DU2-ablation spot distance to the DU1-DU2 distance (see Section 3.7.2.2).

Table 24: Factors to rescale the parameters $r_{eff,L}$, $r_{eff,V}$, σ, x_0 and TE (also with SC and DC indices) to the dimension of the particle beam at the specific position: DU1, DU2, ablation point and ERICA-AMS vaporizer. Also, the calculation of the rescale factor of the ammonium nitrate spot on the adhesive strip to the position of the ERICA-AMS vaporizer and the calculation of the Multiplier is listed.

Position	Factor
DU1	$\frac{58.8\ mm}{133.7\ mm}$ = 0.44
DU2	$\frac{58.8\ mm+66.5\ mm}{133.7\ mm}$ = 0.937
ablation point	$\frac{246\ mm}{133.7\ mm}$ = 1.840
vaporizer	$\frac{547.3\ mm}{133.7\ mm}$ = 4.093
adhesive strip at the B-ToF-MS entry	$\frac{547.3\ mm}{158.55\ mm}$ = 3.452
Multiplier	$\frac{120,7\ mm}{66,5\ mm}$ = 1.815

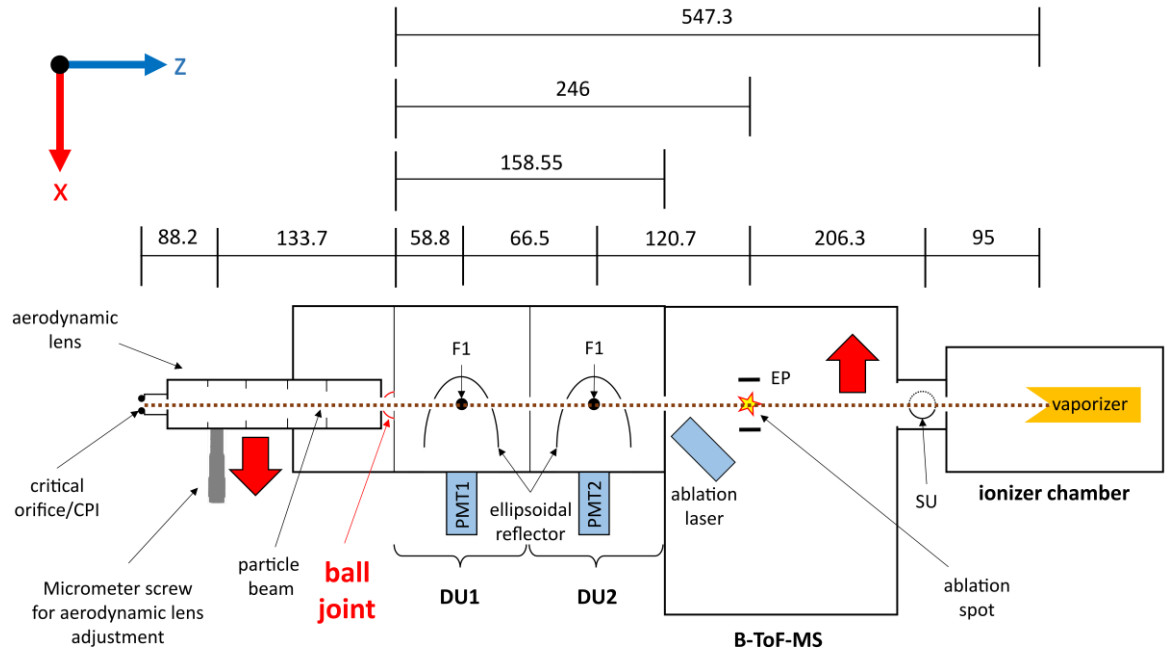

Figure 95: Scheme of the geometry and distances (in mm) in the ERICA instrument (not to scale; see also Figure 10). The red arrows indicate the directions of the movement of the lens and the particle beam during a scan with the aerodynamic lens in x-direction.

Figure 95 shows also the direction of the movement of the aerodynamic lens and the particle beam during a scan with the aerodynamic lens in x-direction (see Section 4.2.3). Due to the ball joint the movement of the particle beam is reverse to the movement of the aerodynamic lens.

B.5 Particle detection efficiency measurements for PSL particles at the detection units DU1 and DU2 by aerodynamic lens scans

The method to determine the particle detection efficiency of PSL particles at the ERICA-LAMS detection units by aerodynamic lens scans is described in Section 4.2.3.1. The values of the parameters x_0, σ, and $r_{eff,L}$ are in the dimension of the aerodynamic lens position x_{pos}. They can be rescaled by considering the distance ratios given by the geometry of the instrument (see Appendix B.4) and are discussed in Section 4.2.5. The results of the curve fits are summarized in Table 25.

Table 25: Rounded results of the curve fits from the particle detection efficiency measurements for PSL particles at the detection units DU1 and DU2 by means of aerodynamic lens scans.

	d_{va} in nm	x_0 in mm	$\Delta^{abs}x_0$ in mm	σ in µm	$\Delta^{abs}\sigma$ in µm	$r_{eff,L}$ in µm	$\Delta^{abs}r_{eff,L}$ in µm	TE	$\Delta^{abs}TE$
DU1	108	10.30	0.019	614.80	20.80	320.63	4.86	0.105	0.003
	218	10.25	0.001	105.83	1.74	335.78	1.34	0.729	0.003
	410	10.24	0.001	84.79	2.24	385.68	1.67	0.890	0.005
	629	10.19	0.002	121.97	4.08	402.20	3.13	0.899	0.008
	834	10.10	0.004	110.03	6.32	358.09	4.86	1.024	0.016
DU2	108	10.52	0.006	369.22	6.38	136.03	4.02	0.051	0.019
	218	10.46	0.001	83.27	1.25	142.46	1.06	0.729	0.001
	410	10.42	0.001	85.14	1.93	146.54	1.60	0.890	0.001
	629	10.37	0.003	118.81	3.00	146.82	2.60	0.899	0.002
	834	10.33	0.004	113.10	4.81	125.23	4.02	1.024	0.004

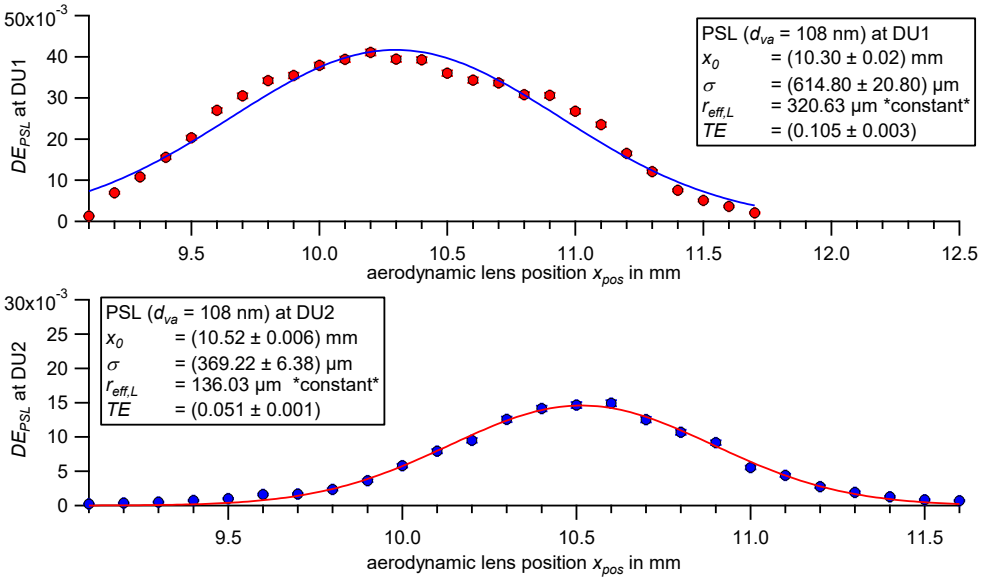

Figure 96: Scan of the aerodynamic lens position (x_{pos}) with PSL particles of d_{va} = 108 nm perpendicular to the laser beam at DU1 (top) and DU 2 (bottom). Displayed are the DE_{PSL} values of the measurement (markers) according to Equation (34) and the curve fit (line) according to Equation (37). The results are shown in the boxes. The uncertainty of the detection efficiency is based on counting statistics of DU and the CPC. The uncertainty of the lens position results from reading errors (see Appendix B.1.6). The uncertainty bars are in all cases smaller than the symbol.

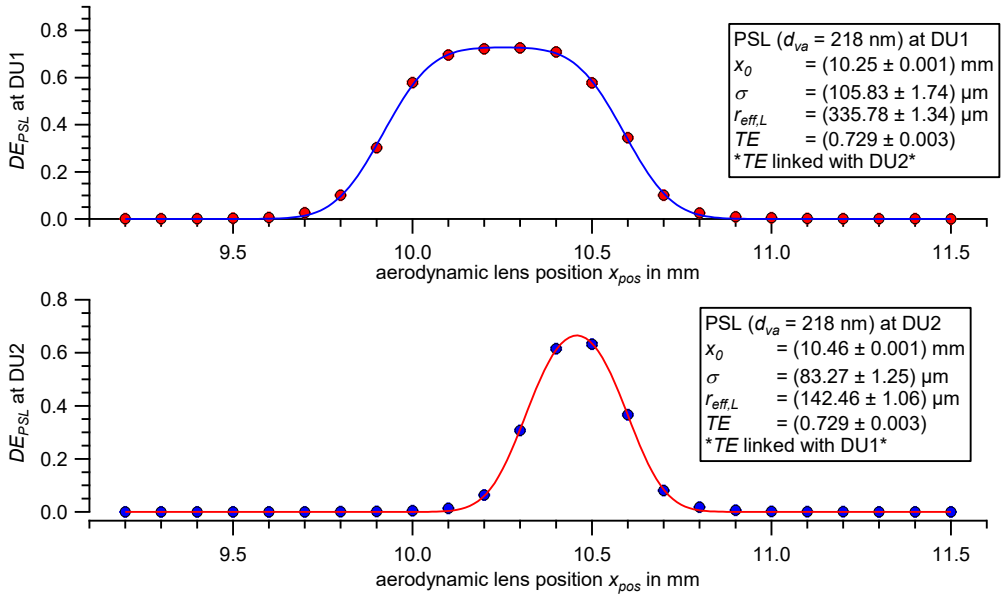

Figure 97: Scan of the aerodynamic lens position (x_{pos}) with PSL particles of d_{va} = 218 nm perpendicular to the laser beam at DU1 (top) and DU 2 (bottom). Displayed are the DE_{PSL} values of the measurement (markers) according to Equation (34) and the curve fit (line) according to Equation (37). The results are shown in the box. The uncertainty of the detection efficiency is based on counting statistics of DU and the CPC. The uncertainty of the lens position results from reading errors (see Appendix B.1.6). The uncertainty bars are in all cases smaller than the symbol.

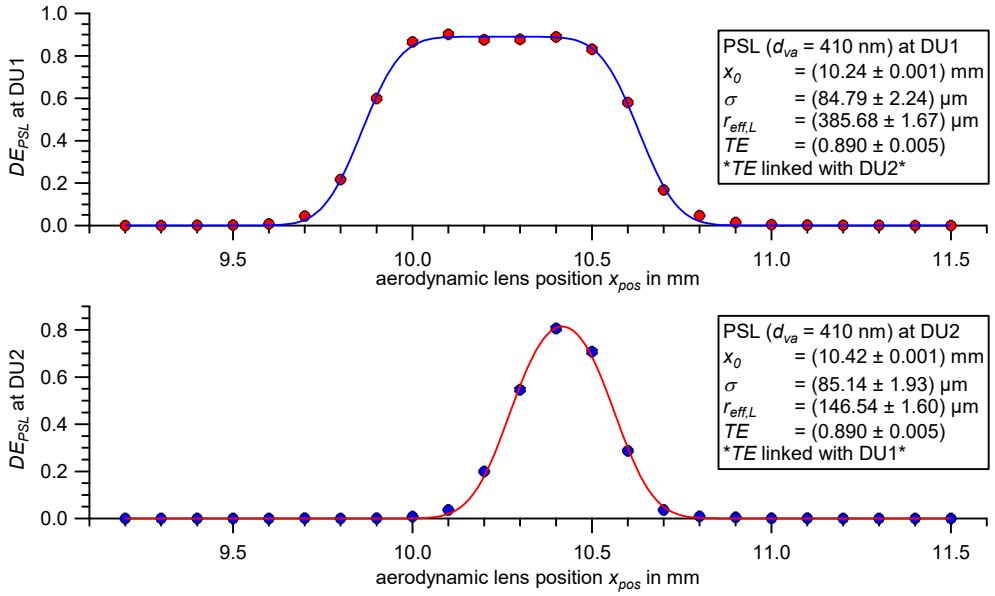

Figure 98: Scan of the aerodynamic lens position (x_{pos}) with PSL particles of d_{va} = 410 nm perpendicular to the laser beam at DU1 (top) and DU 2 (bottom). Displayed are the DE_{PSL} values of the measurement (markers) according to Equation (34) and the curve fit (line) according to Equation (37). The results are shown in the box. The uncertainty of the detection efficiency is based on counting statistics of DU and the CPC. The uncertainty of the lens position results from reading errors (see Appendix B.1.6). The uncertainty bars are in all cases smaller than the symbol.

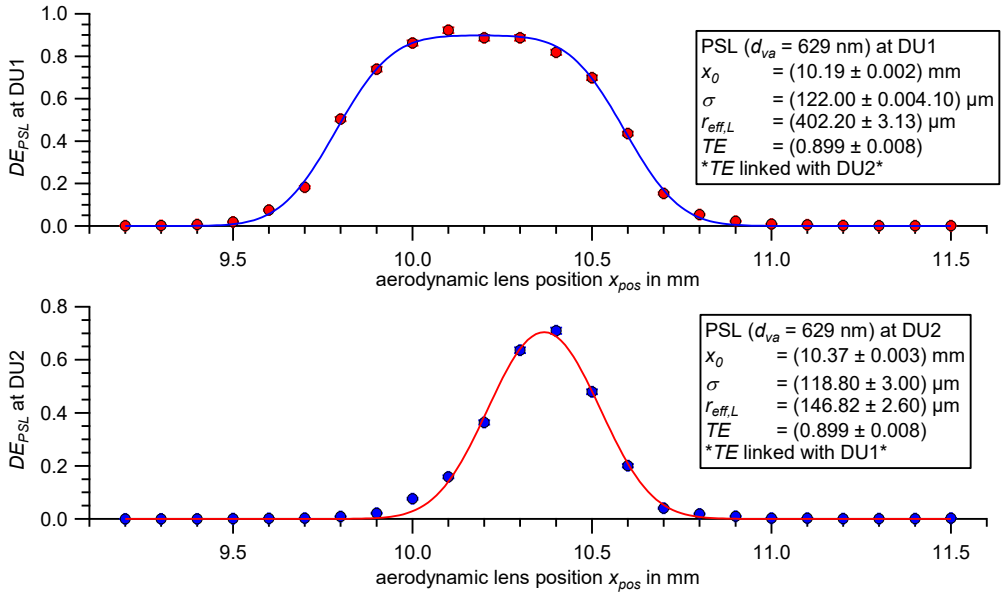

Figure 99: Scan of the aerodynamic lens position (x_{pos}) with PSL particles of d_{va} = 629 nm perpendicular to the laser beam at DU1 (top) and DU 2 (bottom). Displayed are the DE_{PSL} values of the measurement (markers) according to Equation (34) and the curve fit (line) according to Equation (37). The results are shown in the box. The uncertainty of the detection efficiency is based on counting statistics of DU and the CPC. The uncertainty of the lens position results from reading errors (see Appendix B.1.6). The uncertainty bars are in all cases smaller than the symbol.

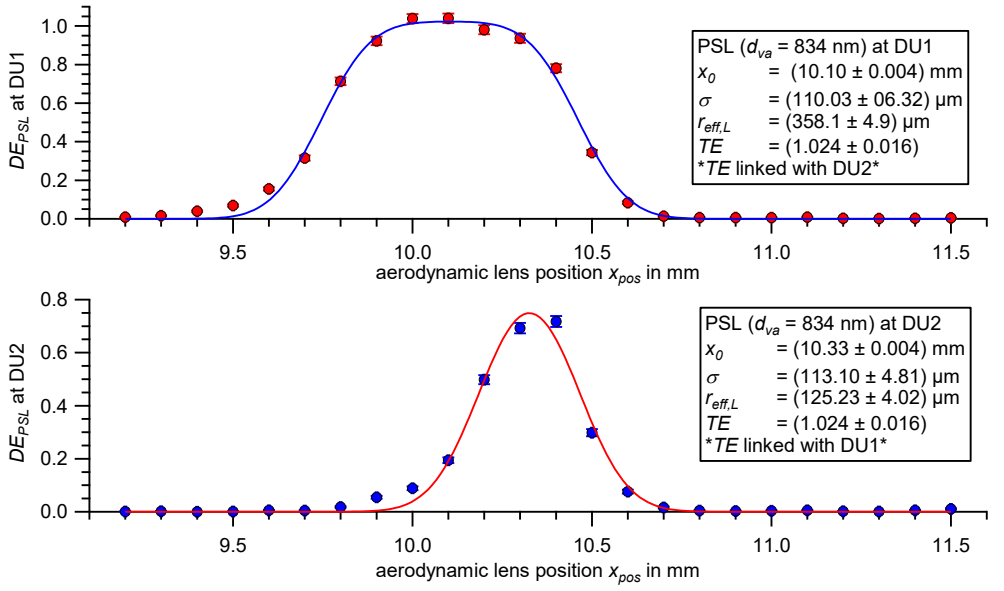

Figure 100: Scan of the aerodynamic lens position (x_{pos}) with PSL particles of d_{va} = 834 nm perpendicular to the laser beam at DU1 (top) and DU 2 (bottom). Displayed are the DE_{PSL} values of the measurement (markers) according to Equation (34) and the curve fit (line) according to Equation (37). The results are shown in the box. The uncertainty of the detection efficiency is based on counting statistics of DU and the CPC. The uncertainty of the lens position results from reading errors (see Appendix B.1.6). The uncertainty bars are in all cases smaller than the symbol.

B.6 Calculation of the relative Mie scattered light intensity

The relative Mie scattered light intensity I_{rel} is needed in Sections 2.2.2, 4.2.3, 4.2.4, and 4.2.5, and in Appendices B.7 and B.11. It was calculated by the program *BH-Mie-Rechner* programmed by Vetter (2004). The set parameters are presented in Table 26. Here, the design of the detection unit (see Section 3.3), the wavelength of the used detection laser (λ = 405 nm) and the refractive index for PSL particles n_{PSL} of approximately 1.65 (for λ = 405 nm; real part; see supplemental information of Galpin et al. (2017)) were considered. The frequently adopted refractive index for PSL is n_{PSL} = 1.59, however this is for a wavelength of λ = 633 nm (Yoo et al., 1996).

Table 26: Set values for the listed parameter in the software BH-Mie-Rechner from Vetter (2004) to calculate the relative Mie scattered light intensity I_{rel} as function of the particle size d_{va}. The results are used in the Sections 2.2.2, 4.2.3, 4.2.4, and 4.2.5, and Appendices B.7 and B.11.

Parameter	**Value**
Refractive index of the medium	1.0
Particle refractive index (real part)	1.65
Particle refractive index (imaginary part)	0.0
Wavelength	405 nm
Particle diameter range	0.04 – 6 µm
Particle diameter interval	0.04 µm
Detector angle range	14° – 164°
Detector angle interval	1°
Detector to particle distance	4.9 cm

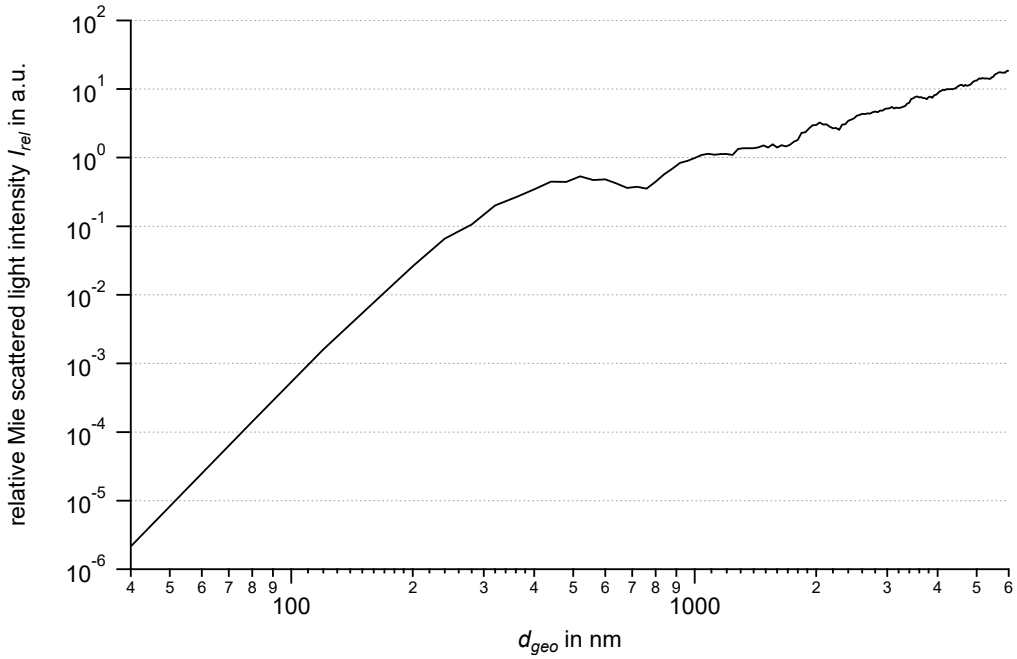

Figure 101: The relative Mie scattered light intensity I_{rel} for PSL particles (n_{PSL} = 1.65) as function of the particle size d_{geo} calculated with the software program BH-Mie-Rechner from Vetter (2004) using the settings in Table 26.

Figure 101 shows the relative Mie scattered light intensity I_{rel} for PSL particles as function of the particle size d_{geo} calculated with the software program *BH-Mie-Rechner* using the settings in Table 26. The curve is used in Appendix B.7 to calculate the effective laser radius $r_{eff,L}$ for PSL particle size d_{va}= 108 nm.

The refractive index for ammonium nitrate particles at a wavelength of λ = 405 nm is unknown and was assumed to be between n = 1.30 and n = 1.70. Figure 102 shows in double logarithmic representation the curve progressions with n as parameter of the relative Mie scattered light intensities I_{rel} as a function of the particle sizes between d_{geo} = 50 nm to d_{geo}= 400 nm. In the considered size range the curve progression approximates a power function. The curves are used in Appendix B.11 to calculate the effective laser radius $r_{eff,L,SC}$ for ammonium nitrate particle sizes d_{va}= 138 nm (d_{geo} = 100 nm) and d_{va} = 91 nm (d_{geo} = 66 nm).

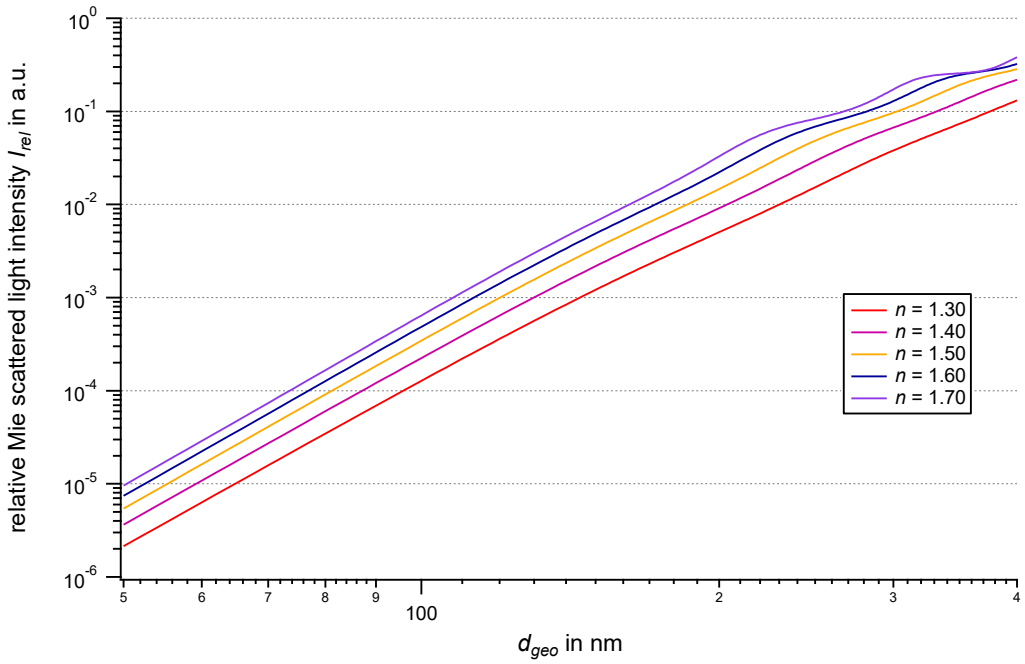

Figure 102: The relative Mie scattered light intensity I_{rel} as function of the particle size d_{geo} based on various refractive index n values (between n = 1.30 and n = 1.70) calculated with the software program BH-Mie-Rechner from Vetter (2004) using the settings in Table 26.

B.7 Calculation of the effective laser radius for PSL particles of d_{va} = 108 nm

As described in Section 4.2.3.1 the curve fitting of the measurement with PSL particles of d_{va} = 108 nm (d_{geo} = (103 ± 14) nm) was not performed by a *common curve fitting*, i.e., the parameter TE was not linked, because the large divergence of the particle beam will introduce losses at DU2 and thus the assumption of having the same TE is not applicable. TE and $r_{eff,L}$ strongly correlate already for DU1. Thus $r_{eff,L}$ has to be kept fixed at a value acquired using Mie Theory of light scattering. This was evident from the fact that the *common curve fitting* of the measurement does not converge with respect to $r_{eff,L}$ and TE. The result of the measurement is shown in Figure 96.

The relative Mie scattered intensity I_{rel} is the Mie scattered light intensity I_{sc} normalized to the irradiated intensity I_{ir} (Equation (84)). I_{rel} was determined by using the *BH-Mie-Rechner* (Bohren and Huffman, 1998; Vetter, 2004).

$$I_{rel} = {}^{I_{sc}}/_{I_{ir}} \tag{84}$$

The parameters adopted for the detailed calculations are shown in Appendix B.6. By that, for PSL particles of d_{geo} = 104 nm a Mie scattering intensity of $I_{rel,104nm}$= 7.10·10^{-4} a.u. and for PSL particles of d_{geo} = 208 nm $I_{rel,208nm}$= 3.42·10^{-2} a.u. was calculated.

The curve fitting of the aerodynamic lens position scan with PSL particles of d_{geo} = 208 nm (d_{va} = 218 nm) resulted an effective laser radius $r_{eff,L}$ = 336 µm for DU1 and $r_{eff,L}$ = 142 µm for DU2 (see Figure 97 in Appendix B.5). Considering the geometry of the instrument (see Appendix B.4) $r_{eff,L}$ = 148 µm for DU1 and $r_{eff,L}$ = 133 µm for DU2. The effective laser width $r_{eff,L}$ is a multiple (by factor a_t) of the beam waist 1/e²-radius w_0 = 30.3 µm (see Section 4.1.2):

$$r_{eff,L} = a_t \cdot w_0 \tag{85}$$

The factor a_t (see Equation (85)) is in average (mean of $a_{t,208nm}$ at DU1 and $a_{t,208nm}$ at DU2) $a_{t,208nm}$ = 4.687 for PSL particles of d_{geo} = 208 nm. The beam waist 1/e²-radius w_0 is w_0 = 30.3 µm (see Section 4.1.2). The radius r is the radius at the limit of detection $r_{eff,L}$ ($r = r_{eff,L}$).

The detection limit is for both particle sizes is the same:

$$I_{sc,208nm} = I_{sc,104nm} \tag{86}$$

As follows from Equation (84) and (86)

$$I_{ir,208nm}(r_{208nm}) \cdot I_{rel,208nm} = I_{ir,104nm}(r_{104nm}) \cdot I_{rel,104nm} \tag{87}$$

Considering a Gaussian laser profile (Eichler et al., 2016)

$$I(r) = I_0 \cdot exp\left[-\frac{2\,r^2}{{w_0}^2}\right] \tag{88}$$

where r is assumed as the edge of $r_{eff,L}$ and I_0 is the intensity in the center of the laser beam. Thus, $I_{ir}(a)$ is the intensity at the edge of $r_{eff,L}$

$$I_{ir}(a_t) = I_0 \cdot exp[-2\,{a_t}^2] \tag{89}$$

Inserted in Equation (87):

$$\begin{aligned} I_{0,208nm} \cdot exp\left[-2\,{a_{t,208nm}}^2\right] \cdot I_{rel,208nm} \\ = I_{0,104nm} \cdot exp\left[-2\,{\boldsymbol{a_{t,104nm}}}^2\right] \cdot I_{rel,104nm} \end{aligned} \tag{90}$$

The same laser and thus the same laser intensity in the center for both particle sizes is considered by

$$I_{0,208nm} = I_{0,104nm} \tag{91}$$

Solving Equation (90) for a_{104nm}:

$$
\begin{aligned}
exp\left[-2\ {a_{t,208nm}}^2\right] \cdot \frac{I_{rel,208nm}}{I_{rel,104nm}} &= exp\left[-2\ {a_{t,104nm}}^2\right] \\
-2\ {a_{t,208nm}}^2 + ln\left[\frac{I_{rel,208nm}}{I_{rel,104nm}}\right] &= -2\ {a_{t,104nm}}^2 \\
{a_{t,208nm}}^2 - \frac{1}{2} ln\left[\frac{I_{rel,208nm}}{I_{rel,104nm}}\right] &= {a_{t,104nm}}^2 \\
a_{t,104nm} = \sqrt{{a_{t,208nm}}^2 - \frac{1}{2} ln\left[\frac{I_{rel,208nm}}{I_{rel,104nm}}\right]} &= \mathbf{4.476}
\end{aligned}
\tag{92}
$$

After entering the values for the calculated parameters $a_{t,208nm}$, $I_{rel,208nm}$, and $I_{rel,104nm}$ in Equation (92), the result for factor $a_{t,104nm}$ is 4.476.

To calculate the factor $f_{Mie,104nm}$ that is used to calculate $r_{eff,L,104nm}$ out of $r_{eff,L,208nm}$, Equation (93) is used.

$$
f_{Mie,104nm} = \frac{r_{eff,L,104nm}}{r_{eff,L,208nm}} = \frac{a_{t,104nm} \cdot w_0}{a_{t,208nm} \cdot w_0} = \mathbf{0.955} \tag{93}
$$

Using that determined value for $f_{Mie,104}$, the $r_{eff,L}$ value for d_{geo} = 104 nm (d_{va} = 108 nm) is $r_{eff,L}$ = 320 µm at DU1 and $r_{eff,L}$ = 136 µm at DU2 (see Figure 96). The uncertainties are conservatively estimated as $\Delta^{abs} r_{eff,L}$ = 4.8 µm at DU1 and $\Delta^{abs} r_{eff,L}$ = 4.0 µm at DU2. These values are the approximated maximum uncertainties of $r_{eff,L}$ in the considered size range of d_{va} = 218 nm to d_{va} = 834 nm (see boxes in the figures in Appendix B.5) at DU1 and DU2. Considering the geometry of the instrument (see Section B.4), the values depicted in Figure 43 are $r_{eff,L}$ = 141 µm at DU1 and $r_{eff,L}$ = 127 µm at DU2 with the uncertainties $\Delta^{abs} r_{eff,L}$ = 2 µm at DU1 and $\Delta^{abs} r_{eff,L}$ = 4 µm at DU2.

B.8 Particle detection efficiency measurements for ammonium nitrate particles at the detection units DU1 and DU2 by aerodynamic lens scans

The method to determine the particle detection efficiency of ammonium nitrate particles at the ERICA-LAMS detection units DU1 and DU2 by aerodynamic lens scans is described in Section 4.2.3.2. Two *Series Of Measurements* (*SOM*; *A* see Appendix B.8.1 and *B*, see Appendix B.8.2) were conducted.

The values of the parameters $x_{0,SC}$, σ_{SC}, $r_{eff,L,SC}$, $x_{0,DC}$, σ_{DC}, and $r_{eff,L,DC}$ are in the dimension of the aerodynamic lens position x_{pos}. They can be rescaled by considering the distance ratios given by the geometry of the instrument (see Appendix B.4) and are discussed in Section 4.2.5. The results of the curve fits are summarized in Table 27. The highlighted values are not presented in the Sections 4.2.4 and 4.2.5 (see discussions in the Appendices B.8.1.1 and B.8.1.2).

Table 27: Rounded results of the curve fits from the particle detection efficiency measurements for ammonium nitrate particles at the detection units DU1 and DU2 by means of aerodynamic lens scans that are presented in B.8.1 and B.8.2. The highlighted values are not presented and evaluated in Section 4.2.5.

	d_{va} in nm	x_0 in mm	$\Delta^{abs}x_0$ in mm	σ in µm	$\Delta^{abs}\sigma$ in µm	$r_{eff,L}$ in µm	$\Delta^{abs}r_{eff,L}$ in µm	TE	$\Delta^{abs}TE$
DU1	91	**10.05**	**0.050**	**475.90**	**52.30**	171.12	20.00	**0.005**	**0.001**
	138	10.27	0.019	202.30	20.63	187.93	20.00	0.039	0.002
	213	10.25	0.001	127.47	4.89	203.02	6.24	0.855	0.028
	297	10.29	0.000	41.90	0.39	275.49	0.29	0.863	0.001
	335	10.27	0.001	40.71	1.24	290.28	0.92	0.861	0.004
	483	10.34	0.002	97.04	4.00	338.60	3.04	0.904	0.010
	548	10.39	0.005	144.17	9.66	369.19	7.84	0.913	0.022
	814	10.34	0.014	160.30	25.79	452.11	20.33	0.823	0.043
DU2	91	**10.50**	**262.000**	**-41.20**	**376000**	78.36	15.00	**0.000**	**0.004**
	138	10.43	0.012	84.31	12.08	86.05	15.00	0.039	0.002
	213	10.53	0.001	85.00	1.90	92.96	3.13	0.855	0.028
	297	10.53	0.000	34.43	0.32	85.23	0.24	0.863	0.001
	335	10.51	0.000	15.32	0.61	97.21	0.30	0.861	0.004
	483	10.57	0.003	95.23	3.00	110.75	2.52	0.904	0.010
	548	10.64	0.006	130.13	6.31	125.56	5.24	0.913	0.022
	814	10.56	0.016	112.66	14.41	113.46	12.32	0.823	0.043

B.8.1 Scans from Series Of Measurements (SOM) A

B.8.1.1 Measurements at Detection Unit DU1

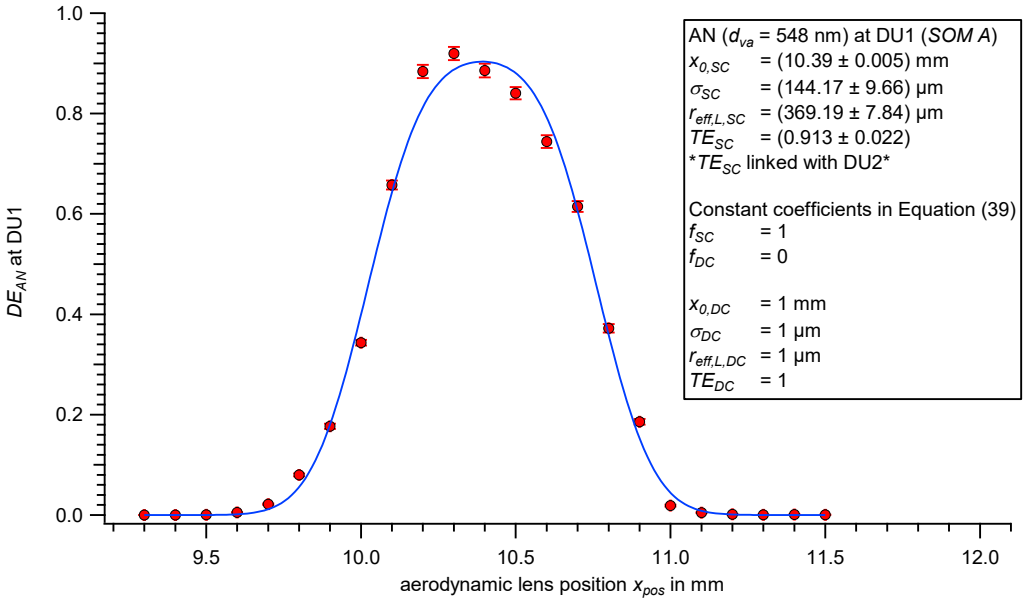

Figure 103: Scan of the aerodynamic lens position (x_{pos}) with ammonium nitrate particles of d_{va} = 548 nm (SOM A) perpendicular to the laser beam at DU1. Displayed are the DE_{AN} values of the measurement (markers) according to Equation (38) and the curve fit (line) according to Equation (39). The results and constants are shown in the box. The uncertainty of the detection efficiency DE_{AN} is based on counting statistics of DU and the CPC. The uncertainty of the lens position results from reading errors (see Appendix B.1.6). The uncertainty bars are in some cases smaller than the symbol.

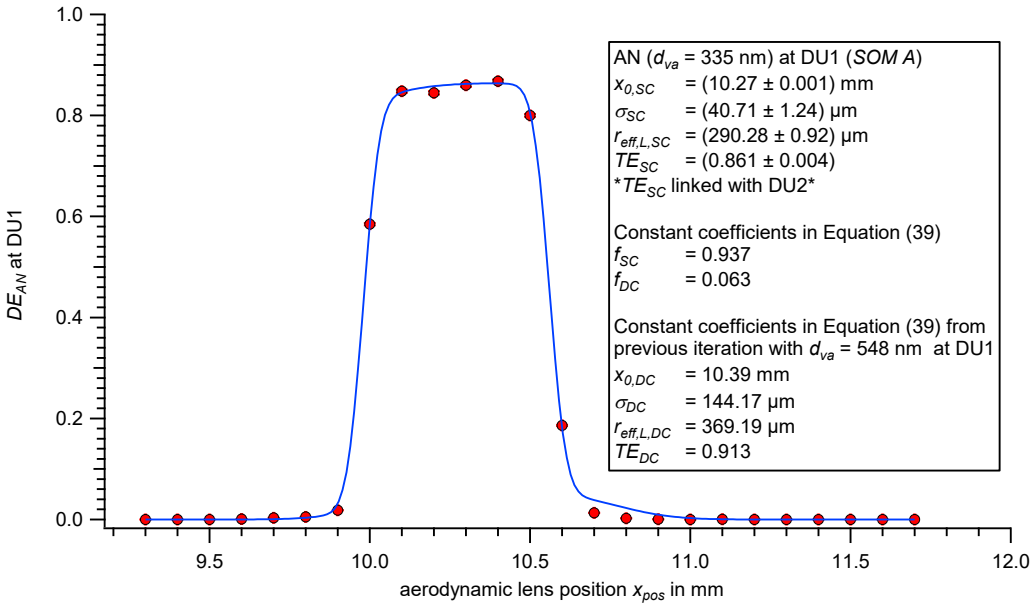

Figure 104: Scan of the aerodynamic lens position (x_{pos}) with ammonium nitrate particles of d_{va} = 335 nm (SOM A) perpendicular to the laser beam at DU1. Displayed are the DE_{AN} values of the measurement (markers) according to Equation (38) and the curve fit (line) according to Equation (39). The results and constants are shown in the box. The uncertainty of the detection efficiency DE_{AN} is based on counting statistics of DU and the CPC. The uncertainty of the lens position results from reading errors (see Appendix B.1.6). The uncertainty bars are in all cases smaller than the symbol.

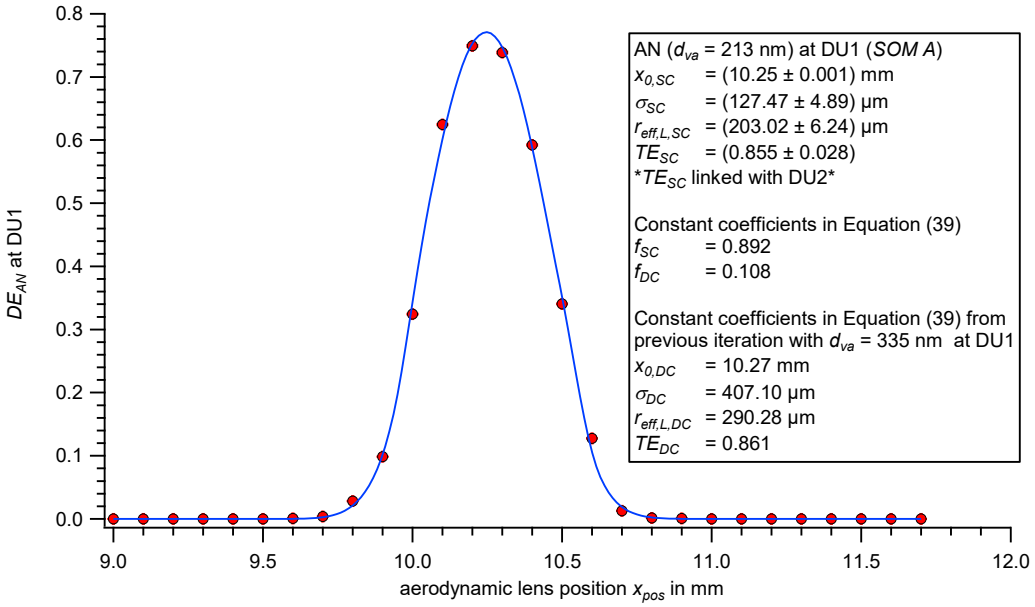

Figure 105: Scan of the aerodynamic lens position (x_{pos}) with ammonium nitrate particles of d_{va} = 213 nm (SOM A) perpendicular to the laser beam at DU1. Displayed are the DE_{AN} values of the measurement (markers) according to Equation (38) and the curve fit (line) according to Equation (39). The results and constants are shown in the box. The uncertainty of the detection efficiency DE_{AN} is based on counting statistics of DU and the CPC. The uncertainty of the lens position results from reading errors (see Appendix B.1.6). The uncertainty bars are in all cases smaller than the symbol.

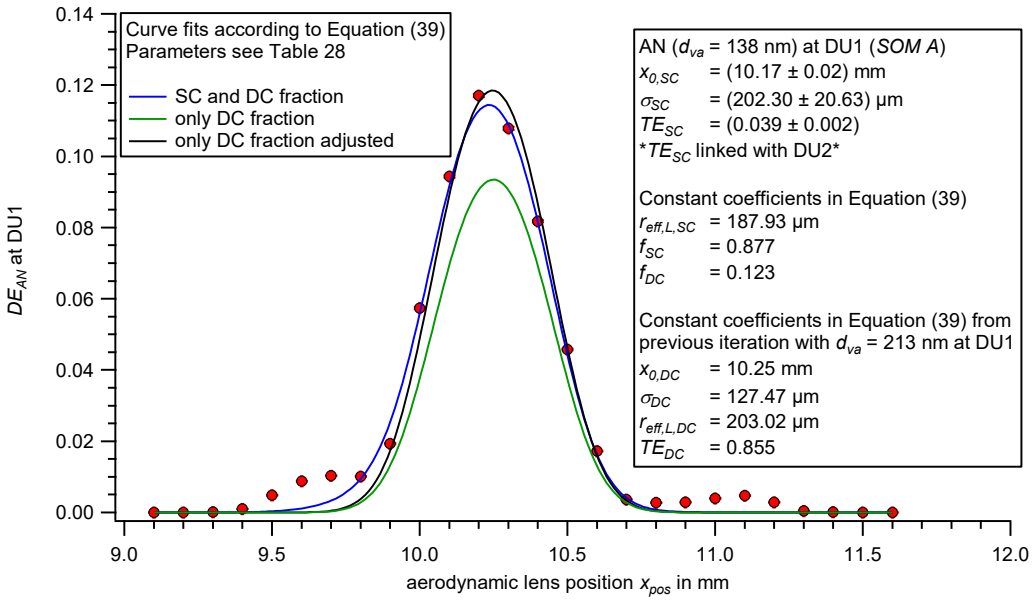

Figure 106: Scan of the aerodynamic lens position (x_{pos}) with ammonium nitrate particles of d_{va} = 138 nm (SOM A) perpendicular to the laser beam at DU1. Displayed are the DE_{AN} values of the measurement (markers) according to Equation (38) and the curve fits (lines) according to Equation (39). The results and constants considering the SC and DC fraction are shown in the box (blue line). The parameters for the curve fits which consider only the DC fraction (green and black line) are shown in Table 28. The uncertainty of the detection efficiency DE_{AN} is based on counting statistics of DU and the CPC. The uncertainty of the lens position results from reading errors (see Appendix B.1.6). The uncertainty bars are in all cases smaller than the symbol.

The results of the curve fits with ammonium nitrate particles of d_{va} = 138 nm at DU1 lead to contradictory results of the maximum possible detection efficiency DE_{max} (definition see Section 4.2.4) and an overlap parameter S_{detect} (definition see Section 4.2.5). At this particle size, the

maximum possible detection efficiency results in a value of only DE_{max}= 2.3 %, although the value of the overlap of the particle beam width w_{part} and the effective detection laser radius $r_{eff,L,SC}$ (definitions see Section 4.2.5) with a value of S_{detect} = 1.1 indicates a sufficient value for detection. This discrepancy might result from an insufficient curve fit (Equation (39)) due to a significant influence of the doubly charged fraction. This can be illustrated by plotting a curve fit where only the doubly charged fraction is considered (green line in Figure 106). The curve progression can be well explained by the doubly charged particles alone, when adjusting f_{DC} to 0.156 (black line in Figure 106). This leads to the parameters of the singly charged fraction being impossible to be determined reliably. Thus, the iterative evaluation cannot be meaningfully continued for the measurement with d_{va} = 91 nm (see Figure 107). As the parameters $x_{0,SC}$, σ_{SC}, and TE_{SC} cannot be reliably determined, they are not included in the evaluation in Sections 4.2.4 and 4.2.5.

The parameters for the curve fits in Figure 106 are shown in Table 28. The difference between the two f_{DC} values (only DC and only DC adjusted) of 27 % could be due to fluctuations in the CPC number concentration measurements used to determine the f_{DC} values (see Appendix B.10). Fluctuations of this magnitude are possible from measurement to measurement.

Table 28: Parameters used for the three different curve fits in Figure 106. Values of constant coefficients during the curve fitting routine are highlighted in bold writing (n/a: not applicable).

Parameters	SC and DC particle fraction	Only DC particle fraction	Only DC particle fraction adjusted to measurement
$x_{0,SC}$ in mm	10.27	n/a	n/a
σ_{SC} in µm	202.30	n/a	n/a
$r_{eff,L,SC}$ in µm	**187.93**	n/a	n/a
TE_{SC}	0.039	n/a	n/a
f_{SC}	**0.877**	**0**	**0**
f_{DC}	**0.123**	**0.123**	**0.156**
$x_{0,DC}$ in mm	**10.25**	**10.25**	**10.25**
σ_{DC} in µm	**127.47**	**127.47**	**127.47**
$r_{eff,L,DC}$ in µm	**203.02**	**203.02**	**203.02**
TE_{DC}	**0.855**	**0.855**	**0.855**

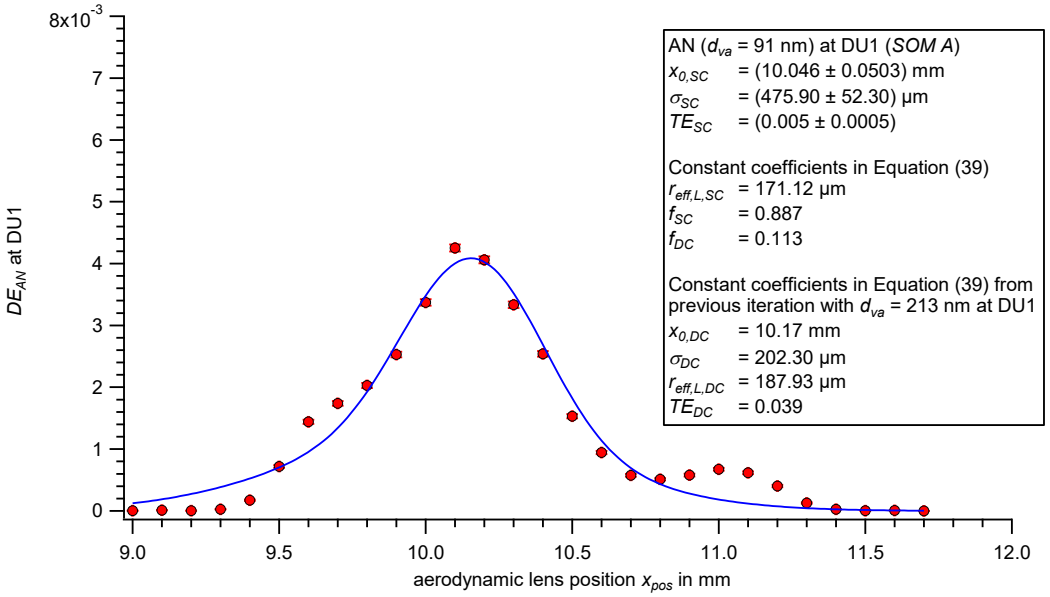

Figure 107: Scan of the aerodynamic lens position (x_{pos}) with ammonium nitrate particles of d_{va} = 91 nm (SOM A) perpendicular to the laser beam at DU1. Displayed are the DE_{AN} values of the measurement (markers) according to Equation (38) and the curve fit (line) according to Equation (39). The results and constants are shown in the box. The uncertainty of the detection efficiency DE_{AN} is based on counting statistics of DU and the CPC. The uncertainty of the lens position results from reading errors (see Appendix B.1.6). The uncertainty bars are in some cases smaller than the symbol.

B.8.1.2 Measurements at Detection Unit DU2

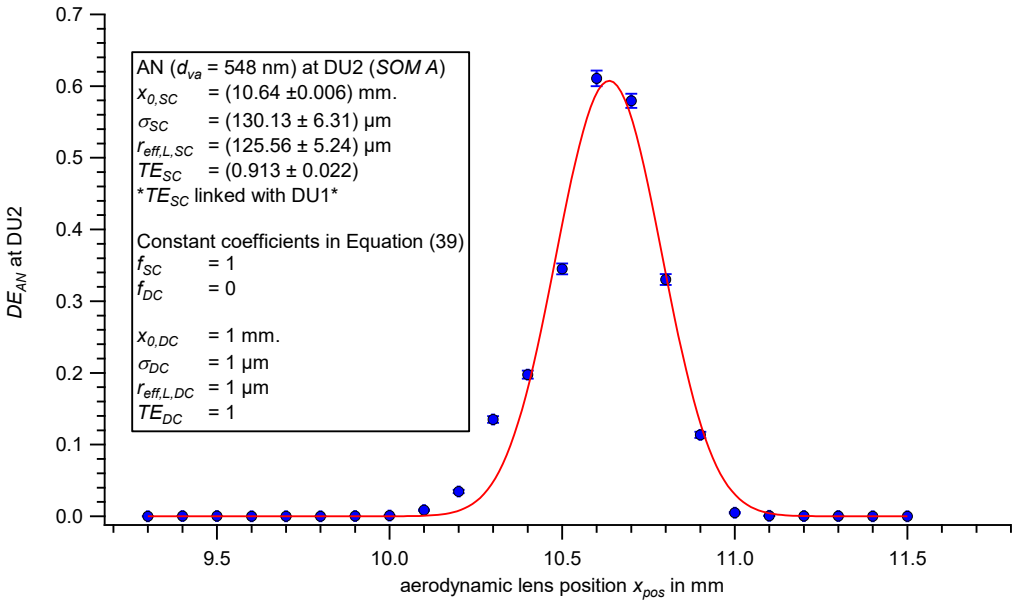

Figure 108: Scan of the aerodynamic lens position (x_{pos}) with ammonium nitrate particles of d_{va} = 548 nm (SOM A) perpendicular to the laser beam at DU2. Displayed are the DE_{AN} values of the measurement (markers) according to Equation (38) and the curve fit (line) according to Equation (39). The results and constants are shown in the box. The uncertainty of the detection efficiency DE_{AN} is based on counting statistics of DU and the CPC. The uncertainty of the lens position results from reading errors (see Appendix B.1.6). The uncertainty bars are in some cases smaller than the symbol.

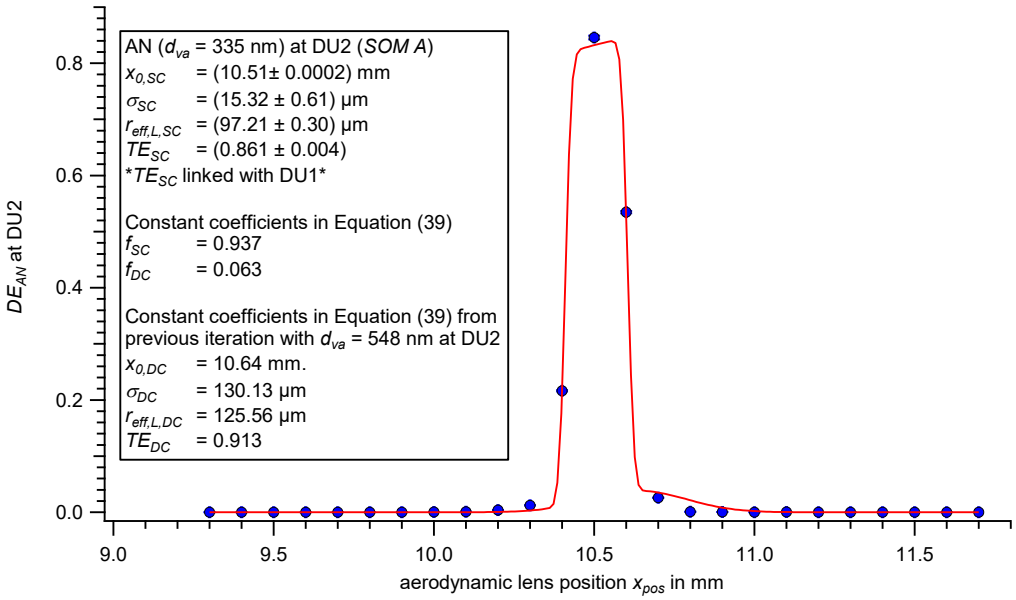

Figure 109: Scan of the aerodynamic lens position (x_{pos}) with ammonium nitrate particles of d_{va} = 335 nm (SOM A) perpendicular to the laser beam at DU2. Displayed are the DE_{AN} values of the measurement (markers) according to Equation (38) and the curve fit (line) according to Equation (39). The results and constants are shown in the box. The uncertainty of the detection efficiency DE_{AN} is based on counting statistics of DU and the CPC. The uncertainty of the lens position results from reading errors (see Appendix B.1.6). The uncertainty bars are in all cases smaller than the symbol.

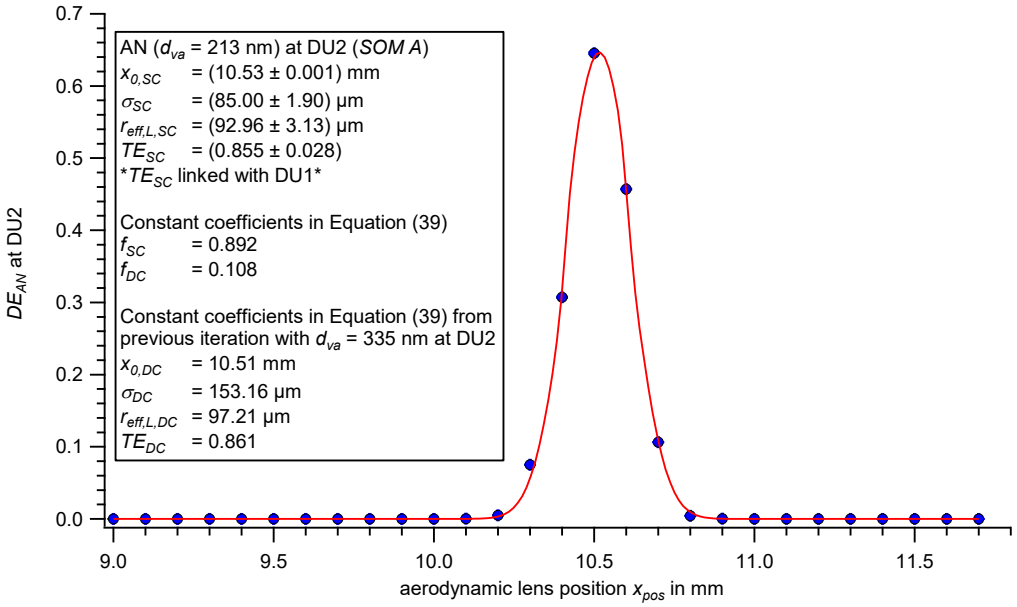

Figure 110: Scan of the aerodynamic lens position (x_{pos}) with ammonium nitrate particles of d_{va} = 213 nm (SOM A) perpendicular to the laser beam at DU2. Displayed are the DE_{AN} values of the measurement (markers) according to Equation (38) and the curve fit (line) according to Equation (39). The results and constants are shown in the box. The uncertainty of the detection efficiency DE_{AN} is based on counting statistics of DU and the CPC. The uncertainty of the lens position results from reading errors (see Appendix B.1.6). The uncertainty bars are in all cases smaller than the symbol.

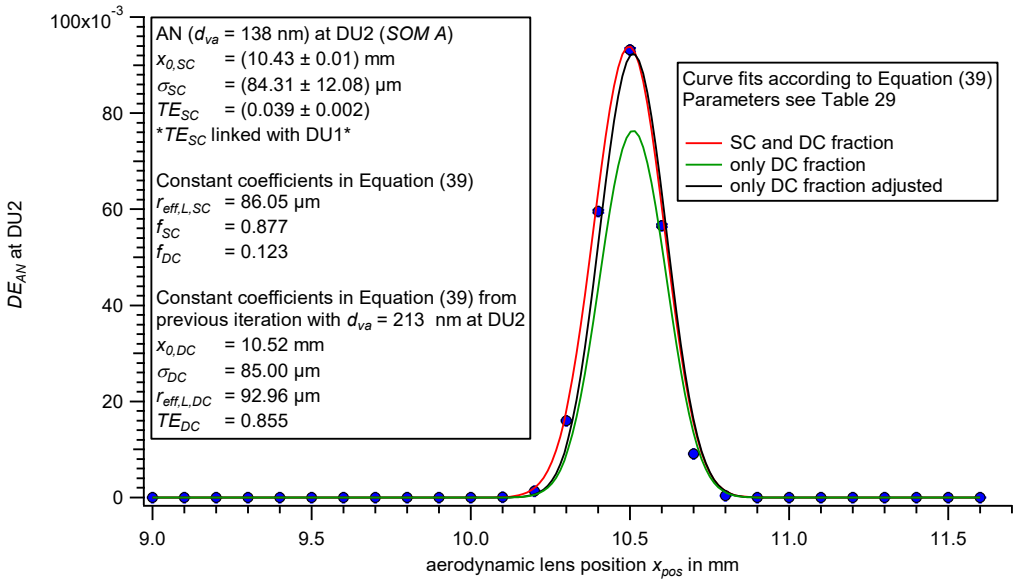

Figure 111: Scan of the aerodynamic lens position (x_{pos}) with ammonium nitrate particles of d_{va} = 138 nm (SOM A) perpendicular to the laser beam at DU2. Displayed are the DE_{AN} values of the measurement (markers) according to Equation (38) and the curve fits (lines) according to Equation (39). The results and constants considering the SC and DC fraction are shown in the box (red line). The parameters for the curve fits which consider only the DC fraction (green and black line) are shown in Table 29. The uncertainty of the detection efficiency DE_{AN} is based on counting statistics of DU and the CPC. The uncertainty of the lens position results from reading errors (see Appendix B.1.6). The uncertainty bars are in all cases smaller than the symbol.

As in Appendix B.8.1.1 the results of the curve fits with ammonium nitrate particles of d_{va} = 138 nm, here at DU2, lead also to contradictory results of DE_{max} (definition see Section 4.2.4) and S_{detect} (definition see Section 4.2.5). DE_{max} results in a value of only DE_{max}= 2.7 %, although the value of the overlap S_{detect} = 0.98 indicates a sufficient value for detection. As discussed in Appendix B.8.1.1,

this discrepancy might result from an insufficient curve fit that can be illustrated by plotting a curve fit where only the doubly charged fraction is considered (green line in Figure 111). By adjusting f_{DC} to 0.150 (black line in Figure 111), the curve progression can be well explained by the doubly charged particles alone. This leads to the parameters ($x_{0,SC}$, σ_{SC}, and TE_{SC}) of the singly charged fraction being impossible to be determined reliably. These parameters are not included in the evaluation in Sections 4.2.4 and 4.2.5, because the iterative evaluation cannot be meaningfully continued for the measurement with d_{va} = 91 nm (see Figure 112).

The parameters for the curve fits in Figure 111 are shown in Table 29. The difference between the two f_{DC} values (only DC and only DC adjusted) of 21 % could be due to fluctuations in the CPC number concentration measurements used to determine the f_{DC} values (see Appendix B.10). Fluctuations of this magnitude are possible from measurement to measurement.

Table 29: Parameters used for the three different curve fits in Figure 111. Values of constant coefficients during the curve fitting routine are highlighted in bold writing (n/a: not applicable).

Parameters	SC and DC particle fraction	Only DC particle fraction	Only DC particle fraction adjusted to measurement
$x_{0,SC}$ in mm	10.43	n/a	n/a
σ_{SC} in µm	84.31	n/a	n/a
$r_{eff,L,SC}$ in µm	**86.05**	n/a	n/a
TE_{SC}	0.039	n/a	n/a
f_{SC}	**0.877**	**0**	**0**
f_{DC}	**0.123**	**0.123**	**0.150**
$x_{0,DC}$ in mm	**10.53**	**10.53**	**10.53**
σ_{DC} in µm	**85.00**	**85.00**	**85.00**
$r_{eff,L,DC}$ in µm	**93.00**	**93.00**	**93.00**
TE_{DC}	**0.855**	**0.855**	**0.855**

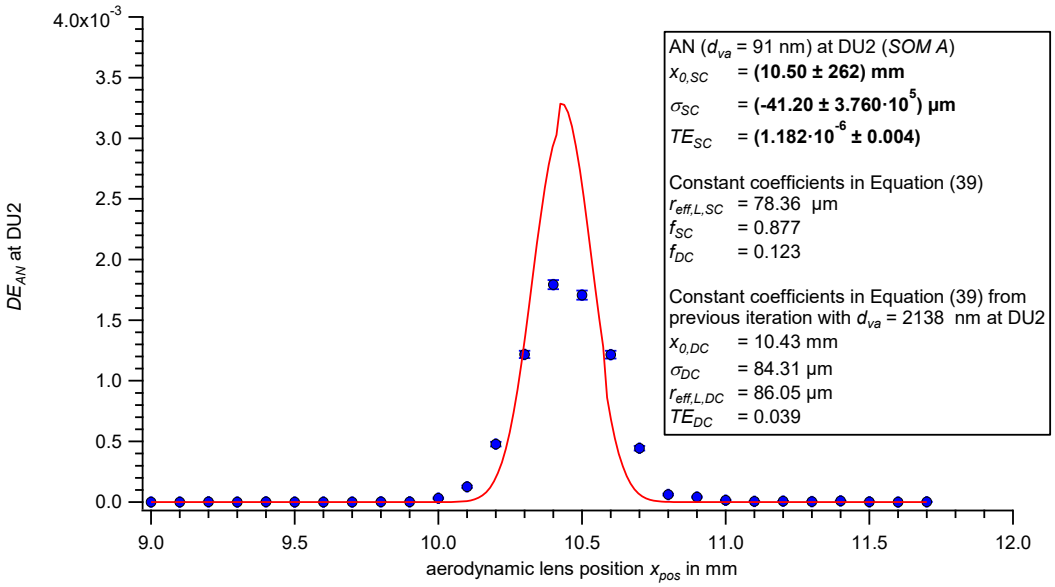

Figure 112: Scan of the aerodynamic lens position (x_{pos}) with ammonium nitrate particles of d_{va} = 91 nm (SOM A) perpendicular to the laser beam at DU2. Displayed are the DE_{AN} values of the measurement (markers) according to Equation (38) and the curve fit (line) according to Equation (39). The results and constants are shown in the box. The highlighted values inside the box are unreasonable. The uncertainty of the detection efficiency DE_{AN} is based on counting statistics of DU and the CPC. The uncertainty of the lens position results from reading errors (see Appendix B.1.6). The uncertainty bars are in some cases smaller than the symbol.

B.8.2 Scans from Series Of Measurements (SOM) B

B.8.2.1 Measurements at detection unit DU1

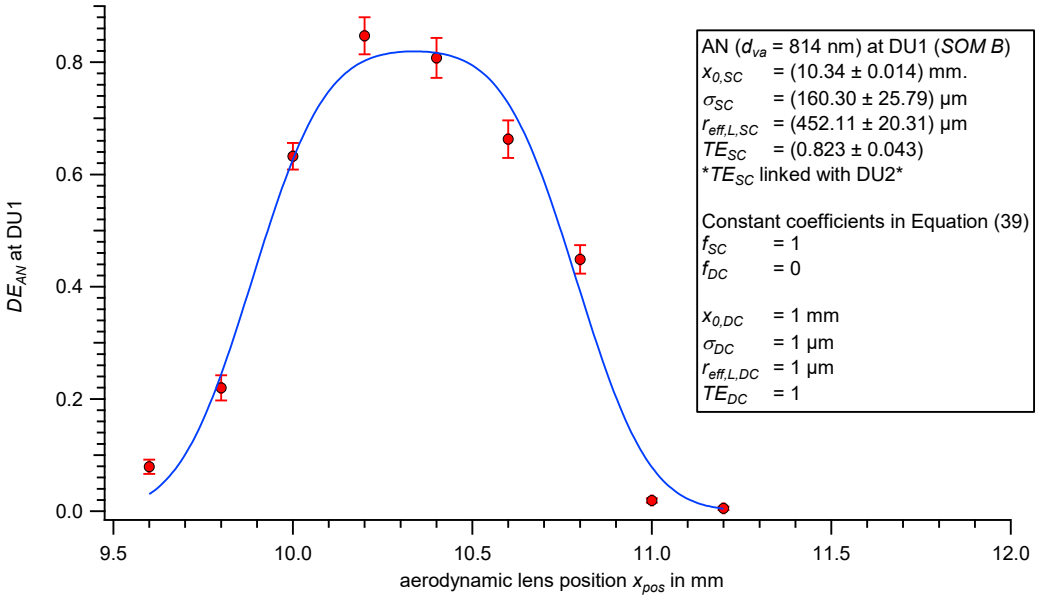

Figure 113: Scan of the aerodynamic lens position (x_{pos}) with ammonium nitrate particles of d_{va} = 814 nm (SOM B) perpendicular to the laser beam at DU1. Displayed are the DE_{AN} values of the measurement (markers) according to Equation (38) and the curve fit (line) according to Equation (39). The results and constants are shown in the box. The uncertainty of the detection efficiency DE_{AN} is based on counting statistics of DU and the CPC. The uncertainty of the lens position results from reading errors (see Appendix B.1.6). The uncertainty bars are in some cases smaller than the symbol.

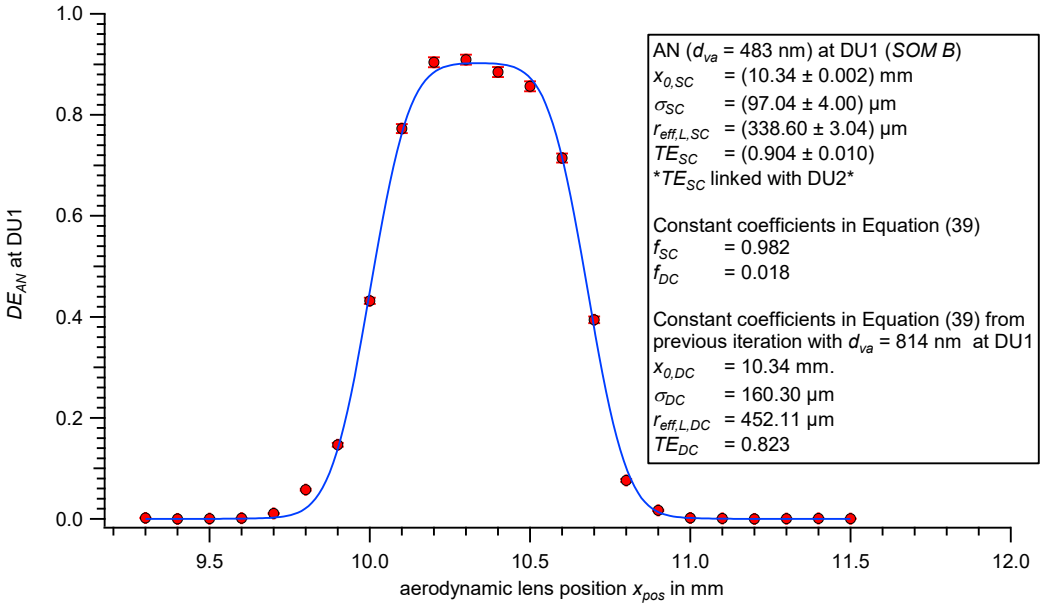

Figure 114: Scan of the aerodynamic lens position (x_{pos}) with ammonium nitrate particles of d_{va} = 483 nm (SOM B) perpendicular to the laser beam at DU1. Displayed are the DE_{AN} values of the measurement (markers) according to Equation (38) and the curve fit (line) according to Equation (39). The results and constants are shown in the box. The uncertainty of the detection efficiency DE_{AN} is based on counting statistics of DU and the CPC. The uncertainty of the lens position results from reading errors (see Appendix B.1.6). The uncertainty bars are in some cases smaller than the symbol.

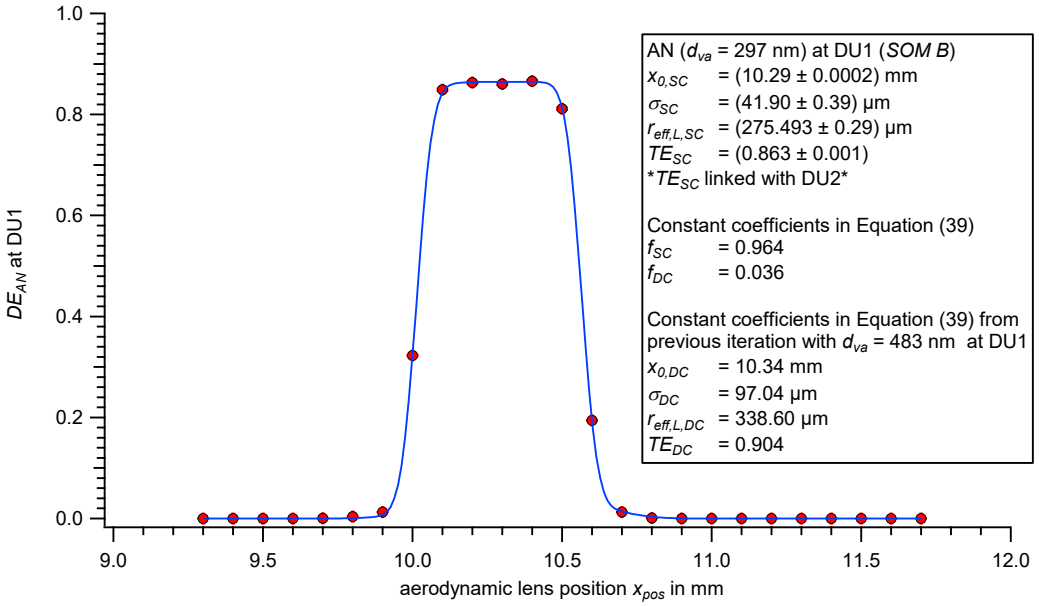

Figure 115: Scan of the aerodynamic lens position (x_{pos}) with ammonium nitrate particles of d_{va} = 297 nm (SOM B) perpendicular to the laser beam at DU1. Displayed are the DE_{AN} values of the measurement (markers) according to Equation (38) and the curve fit (line) according to Equation (39). The results and constants are shown in the box. The uncertainty of the detection efficiency DE_{AN} is based on counting statistics of DU and the CPC. The uncertainty of the lens position results from reading errors (see Appendix B.1.6). The uncertainty bars are in all cases smaller than the symbol.

B.8.2.2 Measurements at detection unit DU2

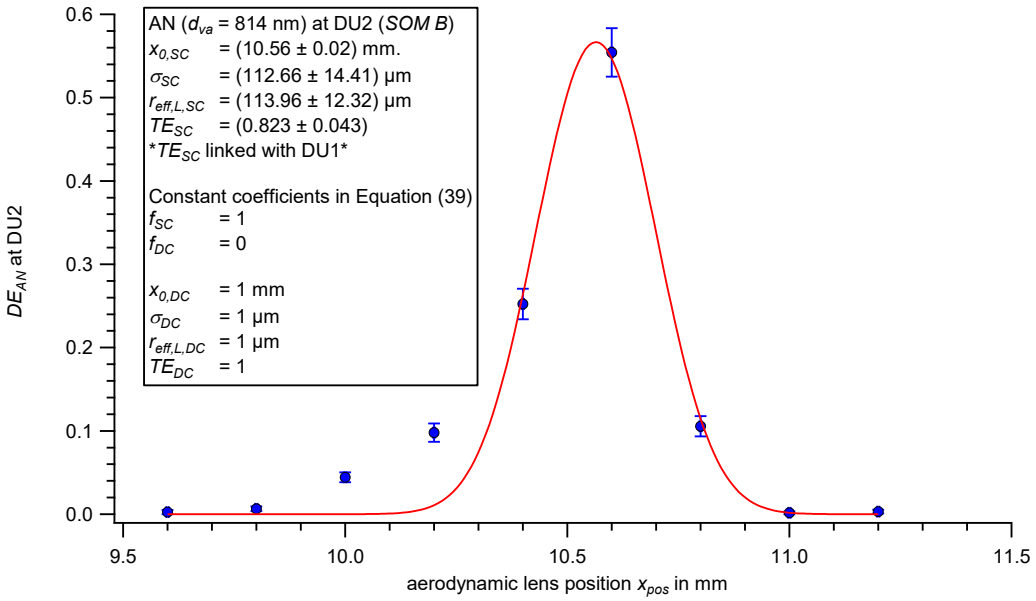

Figure 116: Scan of the aerodynamic lens position (x_{pos}) with ammonium nitrate particles of d_{va} = 814 nm (SOM B) perpendicular to the laser beam at DU2. Displayed are the DE_{AN} values of the measurement (markers) according to Equation (38) and the curve fit (line) according to Equation (39). The results and constants are shown in the box. The uncertainty of the detection efficiency DE_{AN} is based on counting statistics of DU and the CPC. The uncertainty of the lens position results from reading errors (see Appendix B.1.6). The uncertainty bars are in some cases smaller than the symbol.

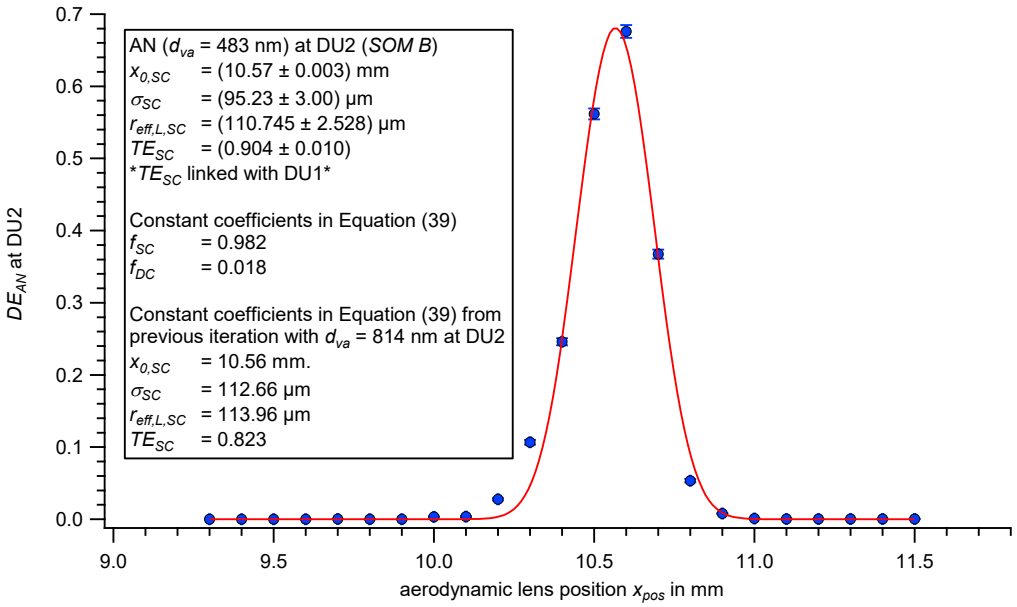

Figure 117: Scan of the aerodynamic lens position (x_{pos}) with ammonium nitrate particles of d_{va} = 483 nm (SOM B) perpendicular to the laser beam at DU2. Displayed are the DE_{AN} values of the measurement (markers) according to Equation (38) and the curve fit (line) according to Equation (39). The results and constants are shown in the box. The uncertainty of the detection efficiency DE_{AN} is based on counting statistics of DU and the CPC. The uncertainty of the lens position results from reading errors (see Appendix B.1.6). The uncertainty bars are in some cases smaller than the symbol.

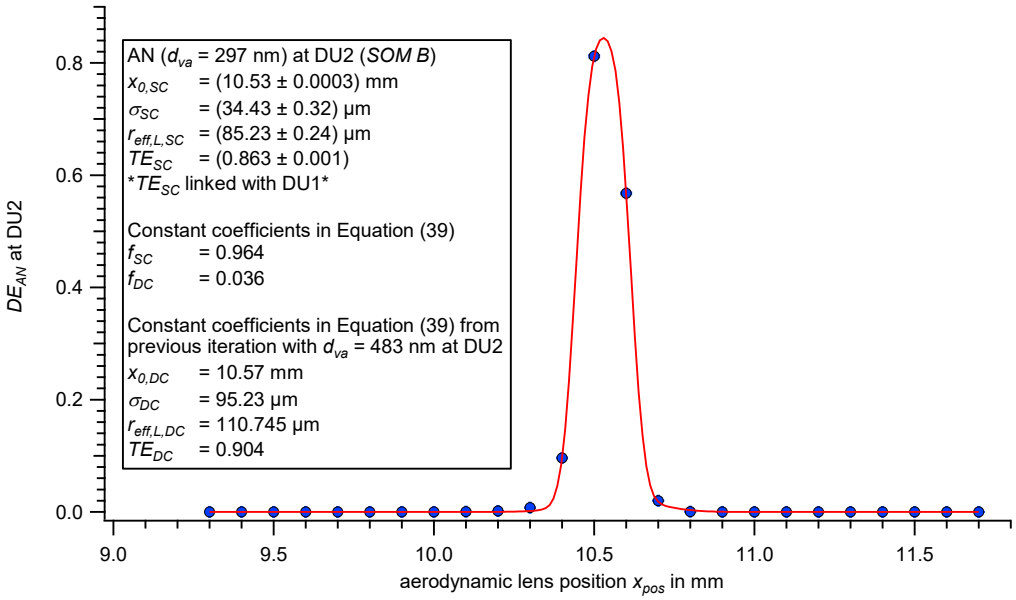

Figure 118: Scan of the aerodynamic lens position (x_{pos}) with ammonium nitrate particles of d_{va} = 297 nm (SOM B) perpendicular to the laser beam at DU2. Displayed are the DE_{AN} values of the measurement (markers) according to Equation (38) and the curve fit (line) according to Equation (39). The results and constants are shown in the box. The uncertainty of the detection efficiency DE_{AN} is based on counting statistics of DU and the CPC. The uncertainty of the lens position results from reading errors (see Appendix B.1.6). The uncertainty bars are in some cases smaller than the symbol.

B.9 Determination of the electrical mobility Z

The electrical mobility Z (in cm² V^{-1} s^{-1}), used in Section 4.2.3.2, is given by (Hinds, 1999):

$$Z = \frac{i \cdot e_0 \cdot C_c(d_{mob}) \cdot 10^{13}}{3 \cdot \pi \cdot \mu \cdot d_{mob}} \tag{94}$$

With the slip correction factor $C_c(d_{mob})$ (Hinds, 1999; Grimm Aerosol Technik GmbH, 2005):

$$C_c(d_{mob}) = 1.0 + 2.492 \cdot \frac{\lambda_{mfp}}{d_{mob}} + 0.84 \cdot \frac{\lambda_{mfp}}{d_{mob}} \cdot \exp\left(-0.43 \frac{d_{mob}}{\lambda_{mfp}}\right) \tag{95}$$

- i is the number of elementary charges,
- e_0 is the elementary charge 1.602·10^{-19} A s (Atkins and De Paula, 2006),
- d_{mob} is the mobility diameter in nm,
- μ is the fluid viscosity assumed as 1.81·10^{-4} Pa s for air (Hinds, 1999),
- λ_{mfp} mean free path assumed as 68 nm at room temperature and ambient pressure (Bayazitoglu and Kakaç, 2005).

The factor 10^{13} is a dimensionless unit conversion factor. For the conversion from d_{va} to d_{mob} and vice versa, Equation (77) in Appendix B.2 is used.

B.10 Determination of the parameters f_{SC} and f_{DC}

The parameters f_{SC} and f_{DC}, used for the fitting routine in Sections 4.2.3.2 and 4.2.3.3 according to Equations (39) and (41), and for the determination of DE_{AMS} in Section 4.2.3.3 according to Equation (40), are determined by CPC measurements and the ratio of the charge fraction of doubly charged (DC) particles to singly charged (SC) particles (DC charge fraction/SC charge fraction) φ for the respective particle size. The values of the DC charge fraction and the SC charge fraction were read out from Tigges et al. (2015).

The procedure is iterative, starting with the second largest *scan number* s (s = 4 in *SOM A* and s = 2 in *SOM B*; see Table 30). For the largest particle sizes used here (s = 5 in *SOM A* and s = 3 in *SOM B*) it is assumed that $f_{DC} = 0$ and f_{SC} = 1, since particle sizes larger than d_{va} > 1,000 nm (see Table 8) are only sparsely generated by the nebulizer.

The parameter $f_{DC,s}$ is the f_{DC} value for the *scan number* s and is iteratively calculated separately for each *SOM*:

$$f_{DC,s} = \frac{c_{DC,s}}{\bar{c}_{tot,s}} = \frac{\varphi_{s+1} \cdot c_{SC,s+1}}{\bar{c}_{tot,s}} \tag{96}$$

Here are:

- $f_{DC,s}$ the fraction of the doubly charged particles,
- φ_{s+1} the DC charge fraction /SC charge fraction ratio for *scan number* $s+1$, read out from Tigges et al. (2015),
- $c_{DC,s}$ the number concentration of the doubly charged particles for *scan number* s,
- $c_{SC,s+1}$ the number concentration of the singly charged particles for *scan number* $s+1$,
- $\bar{c}_{tot,s}$ the average of the total CPC number concentration for s*can number* s.

$c_{SC,s+1}$ cannot be measured directly. Since no higher than double charges have to be considered:

$$c_{SC,s+1} = (\bar{c}_{tot,s+1} - c_{DC,s+1}) \tag{97}$$

- $c_{DC,s+1}$ is the number concentration of the doubly charged particles for s*can number* $s+1$,
- $\bar{c}_{tot,s+1}$ is the average of the total CPC number concentration for *scan number* $s+1$.

Table 30: Scan numbers s of the measured ammonium nitrate particles for various particle sizes of singly charged species (SC) d_{va}, and the corresponding DC charge fraction /SC charge fraction ratio φ according to Tigges et al. (2015) and the calculated fraction of singly f_{SC} and doubly charged f_{DC} particles for the two Series Of Measurements (SOM) A and B.

scan number s	d_{va} **in nm**	φ	f_{SC}	f_{DC}	***SOM***
1	91		0.887	0.113	*A*
2	138	0.171	0.877	0.123	
3	213	0.302	0.892	0.108	
4	335	0.460	0.937	0.063	
5	548	0.631	1.000	0.000	
1	297		0.964	0.036	*B*
2	483	0.585	0.982	0.018	
3	814	0.747	1.000	0.000	

Since no higher than double charges have to be considered, the value for f_{SC} of the *size number s* ($f_{SC,s}$) is:

$$f_{SC,s} = 1 - f_{DC,s} \quad (98)$$

The results for the respective values according to the *scan number s* for f_{SC} and f_{DC} are summarized in Table 30 and transferred to Table 8.

B.11 Calculation of the effective laser radius for ammonium nitrate particle sizes d_{va} = 138 nm and d_{va} = 91 nm

Analogous to the calculation of the factor for the determination of the $r_{eff,L}$ values for the measurement with smaller PSL particles (see Appendix B.7), the factors for the measurements with ammonium nitrate particles with the sizes d_{va} = 138 nm (d_{geo} = 100 nm) and d_{va} = 91 nm (d_{geo} = 66 nm) were also determined. The starting point was the $r_{eff,L}$ values of DU1 and DU2 determined by means of *common curve fit* when measuring with d_{va} = 213 nm (d_{geo} = 154 nm; for conversion see Appendix B.2).

The calculation of the relative Mie scattered light intensity I_{rel} was performed for different refractive indices between n = 1.30 and n= 1.70 (Bohren and Huffman, 1998; Vetter, 2004) and is shown in Figure 102 in Appendix B.6. The refractive index of particulate ammonium nitrate particles at a wavelength of λ = 405 nm is unknown but was assumed to be in that range. The used parameters are also presented in Appendix B.6.

B.11.1 Calculation of the effective laser radius for ammonium nitrate particles of d_{va} = 138 nm

The curve fitting of the aerodynamic lens position scan with ammonium nitrate particles of d_{geo} = 154 nm (d_{va} = 213 nm) resulted an effective laser radius of $r_{eff,L,SC}$ = 203 µm for DU1 (Figure 105) and $r_{eff,L,SC}$ = 93 µm for DU2 (Figure 110). Considering the geometry of the instrument (see Appendix B.4) the values are $r_{eff,L,SC}$ = 89 µm for DU1 and $r_{eff,L,SC}$ = 87 µm for DU2.

The factor a_t (see Equation (85)) is in average (mean of $a_{t,154nm}$ at DU1 and $a_{t,154nm}$ at DU2) $a_{t,154nm}$ = 2.911 for ammonium nitrate particles of d_{geo} = 154 nm. The beam waist 1/e²-radius w_0 is w_0 = 30.3 µm (see Section 4.1.2). To calculate $a_{t,100nm}$, Equation (92) is used, where $a_{t,104nm}$ is substituted by $a_{t,100nm}$, $a_{t,208nm}$ by $a_{t,154nm}$, $I_{rel,104nm}$ by $I_{rel,100nm}$, and $I_{rel,208nm}$ by $I_{rel,154nm}$. The factor $f_{Mie,100nm}$ is calculated using Equation (93), where $f_{Mie,104nm}$ is substituted by $f_{Mie,100nm}$, $a_{t,104nm}$ is substituted by $a_{t,100nm}$, and $a_{t,208nm}$ by $a_{t,154nm}$. The results for the various refractive indices are shown in Table 31.

Table 31: Calculated factors to calculate the $r_{eff,L}$ values for the ammonium nitrate measurement with d_{geo} = 100 nm (d_{va} = 138 nm).

n	$I_{rel,154nm}$ in a.u.	$I_{rel,100nm}$ in a.u.	$a_{t,100nm}$	$f_{Mie,100nm}$
1.70	$7.579 \cdot 10^{-3}$	$6.427 \cdot 10^{-4}$	2.691	0.924
1.60	$5.596 \cdot 10^{-3}$	$4.848 \cdot 10^{-4}$	2.693	0.925
1.50	$3.901 \cdot 10^{-3}$	$3.443 \cdot 10^{-4}$	2.695	0.926
1.40	$2.494 \cdot 10^{-3}$	$2.243 \cdot 10^{-4}$	2.697	0.926
1.30	$1.391 \cdot 10^{-3}$	$1.277 \cdot 10^{-4}$	2.699	0.927

The average of the factors is $f_{Mie,100nm}$ = **0.926**. Using that value, the $r_{eff,L}$ value for d_{geo} = 100 nm (d_{va} = 138 nm) is $r_{eff,L,SC}$ = 188 µm at DU1 (see Figure 106) and $r_{eff,L,SC}$ = 86 µm at DU2 (see Figure 111). The uncertainties of the effective radius $\Delta^{abs}r_{eff,L,SC}$ are conservatively estimated as $\Delta^{abs}r_{eff,L,SC}$ = 20 µm at DU1 and $\Delta^{abs}r_{eff,L,SC}$ = 15 µm at DU2. These values are the approximated maximum uncertainties $\Delta^{abs}r_{eff,L,SC}$ in the considered size range of d_{va} = 213 nm to d_{va} = 814 nm (see boxes in the figures in Appendix B.8) at DU1 and DU2. Considering the geometry of the instrument (see Section B.4), the values depicted in Figure 43 are $r_{eff,L,SC}$ = 83 µm at DU1 and $r_{eff,L,SC}$ = 81 µm at DU2 with the uncertainties $\Delta^{abs}r_{eff,L,SC}$ = 9 µm at DU1 and $\Delta^{abs}r_{eff,L,SC}$ = 14 µm at DU2.

B.11.2 Calculation of the effective laser radius for ammonium nitrate particles of d_{va} = 91 nm

The calculation of the effective laser radius for ammonium nitrate particles of d_{va} = 91 nm was conducted similar to the calculation of the effective laser radius for particles of d_{va} = 138 nm (see Appendix B.11.1): The curve fitting of the aerodynamic lens position scan with ammonium nitrate particles of d_{geo} = 154 nm (d_{va} = 213 nm) resulted an effective laser radius of $r_{eff,L,SC}$ = 203 µm for DU1 (Figure 105) and $r_{eff,L,SC}$ = 93 µm for DU2 (Figure 110). Considering the geometry of the instrument (see Appendix B.4) the values are $r_{eff,L,SC}$ = 89 µm for DU1 and $r_{eff,L,SC}$ = 87 µm for DU2.

The factor a_t (see Equation (85)) is in average (mean of $a_{t,154nm}$ at DU1 and $a_{t,154nm}$ at DU2) $a_{t,154nm}$ = 2.911 for ammonium nitrate particles of d_{geo} = 154 nm. The beam waist 1/e²-radius w_0 is w_0 = 30.3 µm (see Section 4.1.2). To calculate $a_{t,66nm}$, Equation (92) is used, where $a_{t,104nm}$ is substituted by $a_{t,66nm}$, $a_{t,208nm}$ by $a_{t,154nm}$, $I_{rel,104nm}$ by $I_{rel,66nm}$, and $I_{rel,208nm}$ by $I_{rel,154nm}$. The factor $f_{Mie,66nm}$ is calculated using Equation (93), where $f_{Mie,104nm}$ is substituted by $f_{Mie,66nm}$, $a_{t,104nm}$ is substituted by $a_{t,66nm}$, and $a_{t,208nm}$ by $a_{t,154nm}$. The results for the various refractive indices are shown in Table 32.

Table 32: Calculated factors to calculate the $r_{eff,L}$ values for the ammonium nitrate measurement with d_{geo} = 66 nm (d_{va} = 91 nm).

n	$I_{rel,154nm}$ in a.u.	$I_{rel,66nm}$ in a.u.	$a_{t,66nm}$	$f_{Mie,66nm}$
1.70	$7.579 \cdot 10^{-3}$	$5.158 \cdot 10^{-5}$	2.446	0.840
1.60	$5.596 \cdot 10^{-3}$	$3.968 \cdot 10^{-5}$	2.450	0.841
1.50	$3.901 \cdot 10^{-3}$	$2.877 \cdot 10^{-5}$	2.454	0.843
1.40	$2.494 \cdot 10^{-3}$	$1.914 \cdot 10^{-5}$	2.458	0.844
1.30	$1.391 \cdot 10^{-3}$	$1.114 \cdot 10^{-5}$	2.462	0.846

The average of the factors is $f_{Mie,66nm}$ = **0.843**. Using that factor value, the $r_{eff,L,SC}$ value for d_{geo} = 66 nm (d_{va} = 91 nm) is $r_{eff,L,SC}$ = 171 µm at DU1 (see Figure 107) and $r_{eff,L,SC}$ = 78 µm at DU2 (see Figure 112). The uncertainties are conservatively estimated as $\Delta^{abs}r_{eff,L,SC}$ = 20 µm at DU1 and $\Delta^{abs}r_{eff,L,SC}$ = 15 µm at DU2. These values are the approximated maximum uncertainties $\Delta^{abs}r_{eff,L,SC}$ in the considered size range of d_{va} = 213 nm to d_{va} = 814 nm (see boxes in the figures in Appendix B.8) at DU1 and DU2. Considering the geometry of the instrument (see Section B.4), the values depicted in Figure 43 are $r_{eff,L,SC}$ = 75 µm at DU1 and $r_{eff,L,SC}$ = 73 µm at DU2 with the uncertainties $\Delta^{abs}r_{eff,L,SC}$ = 9 µm at DU1 and $\Delta^{abs}r_{eff,L,SC}$ = 14 µm at DU2.

B.12 Particle detection efficiency measurements for ammonium nitrate particles at the ERICA-AMS vaporizer by aerodynamic lens scans

The method to determine the particle detection efficiency of ammonium nitrate particles at the ERICA-AMS vaporizer by aerodynamic lens scans is described in Section 4.2.3.3. Two *Series Of Measurements* (*SOM*; *A* see Appendix B.12.1 and *SOM B*, see Appendix B.12.2) were conducted.

The values of the parameters $x_{0,SC}$, σ_{SC}, $r_{eff,V,SC}$, $x_{0,DC}$, σ_{DC}, and $r_{eff,V,DC}$ are in the dimension of the aerodynamic lens position x_{pos}. They can be rescaled by considering the distance ratios given by the geometry of the instrument (see Appendix B.4) and are discussed in Section 4.2.5. The results of the curve fits are summarized in Table 33. The highlighted values herein are not presented in Section 4.2.5.

TE_{SC} had to be set as a constant coefficient to TE_{SC} = 1 for the curve fitting of the measurements with the particle sizes between d_{va} = 814 nm and d_{va} = 483 nm (over both *SOM*). Tests with a free running variable TE_{SC} resulted in unrealistic values for the variables $x_{0,SC}$, σ_{SC}, $r_{eff,V,SC}$ and TE_{SC} and in unreasonably high values of the corresponding uncertainties, although the measurement results looked reasonable in terms of amplitude and shape (see Sections B.12.1 and B.12.2). By this approach, the uncertainties are in a meaningful range, but the values for the variable $r_{eff,V,SC}$ are unreasonably low. However, the iterative procedure was performed including the measurements with these particle sizes, but the results of the curve fittings are not presented in Sections 4.2.4 and 4.2.5.

As discussed in Section 4.2.3.3, the curve fitting of the measurement at the particle size of d_{va} = 91 nm only provided reasonable values if the value for $r_{eff,V,SC}$ = 1.98 mm was kept constant during the curve fitting. The absolute uncertainty for the effective vaporizer width was determined as $\Delta^{abs} r_{eff,V,SC}$ = 0.02 mm. This is, rounded up, the largest uncertainty $\Delta^{abs} r_{eff,V,SC}$ that occurred in the four measurements.

Table 33: Rounded results of the curve fits from the particle detection efficiency measurements for ammonium nitrate particles at the ERICA-AMS vaporizer by means of aerodynamic lens scans that are presented in B.12.1 and B.12.2. The highlighted values are not presented in Section 4.2.5.

d_{va} in nm	x_0 in mm	$\Delta^{abs} x_0$ in mm	σ in µm	$\Delta^{abs}\sigma$ in µm	$r_{eff,V}$ in µm	$\Delta^{abs} r_{eff,V}$ in µm	TE	$\Delta^{abs} TE$
91	10.49	0.009	267.58	13.50	484.45	20.00	0.883	0.017
138	10.40	0.008	210.33	18.10	469.55	15.80	1.048	0.039
213	10.48	0.007	89.20	11.10	475.50	8.16	1.038	0.025
297	10.47	0.007	34.88	8.21	506.08	4.03	1.053	0.016
335	10.45	0.004	45.10	4.48	487.43	4.51	1.053	0.015
483	**10.47**	**0.006**	**177.38**	**8.00**	**324.97**	**6.09**	**1.000**	
548	**10.51**	**0.007**	**269.08**	**7.05**	**232.61**	**4.56**	**1.000**	
814	**10.42**	**0.011**	**256.25**	**11.70**	**249.76**	**8.17**	**1.000**	

B.12.1 Scans from Series Of Measurements (SOM) A

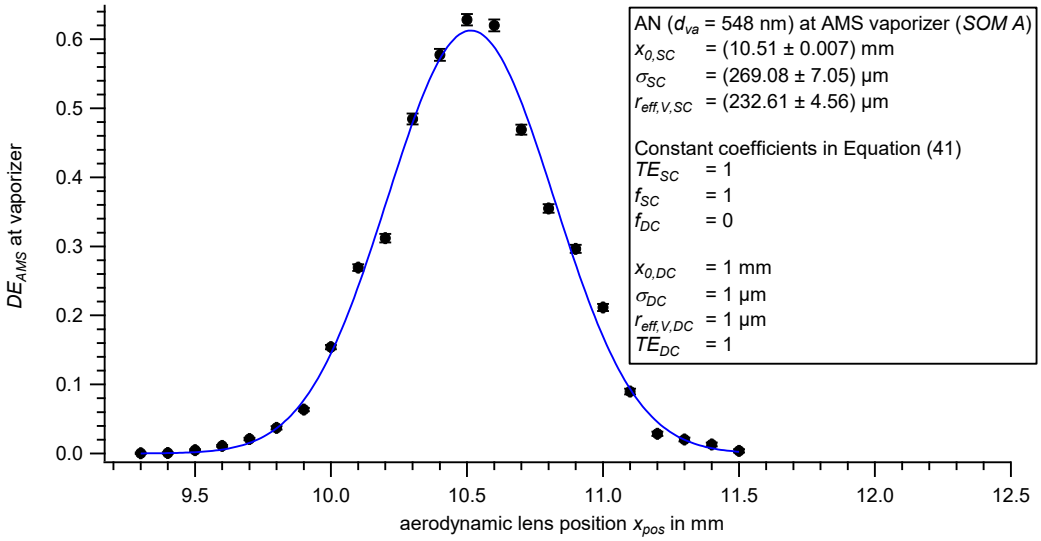

Figure 119: Scan of the aerodynamic lens position (x_{pos}) with ammonium nitrate particles of d_{va} = 548 nm (SOM A) at the ERICA-AMS vaporizer. The detection efficiency DE_{AMS} was evaluated from Equation (40) (markers) and curve fitted with a function according to Equation (41). The results and constants of the curve fits are shown in the box. The uncertainty of the detection efficiency is based on counting statistics of the CPC as well as the estimated counting statistic expected for the ERICA-AMS. The uncertainty of the lens position results from reading errors (see Appendix B.1.6). The uncertainty bars are in some cases smaller than the symbol.

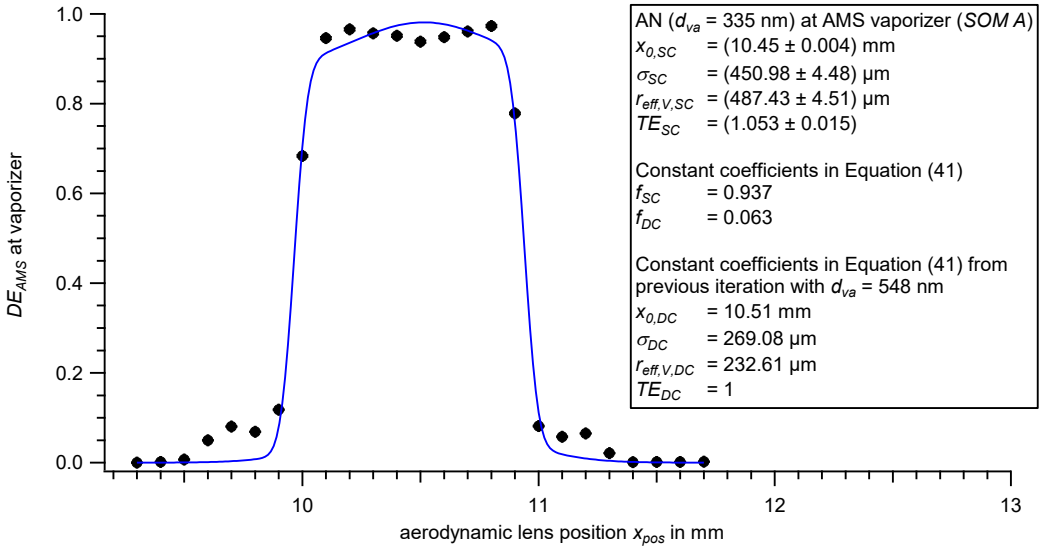

Figure 120: Scan of the aerodynamic lens position (x_{pos}) with ammonium nitrate particles of d_{va} = 335 nm (SOM A) at the ERICA-AMS vaporizer. The detection efficiency DE_{AMS} was evaluated from Equation (40) (markers) and curve fitted with a function according to Equation (41). The results and constants of the curve fits are shown in the box. The uncertainty of the detection efficiency is based on counting statistics of the CPC as well as the estimated counting statistic expected for the ERICA-AMS. The uncertainty of the lens position results from reading errors (see Appendix B.1.6). The uncertainty bars are in all cases smaller than the symbol.

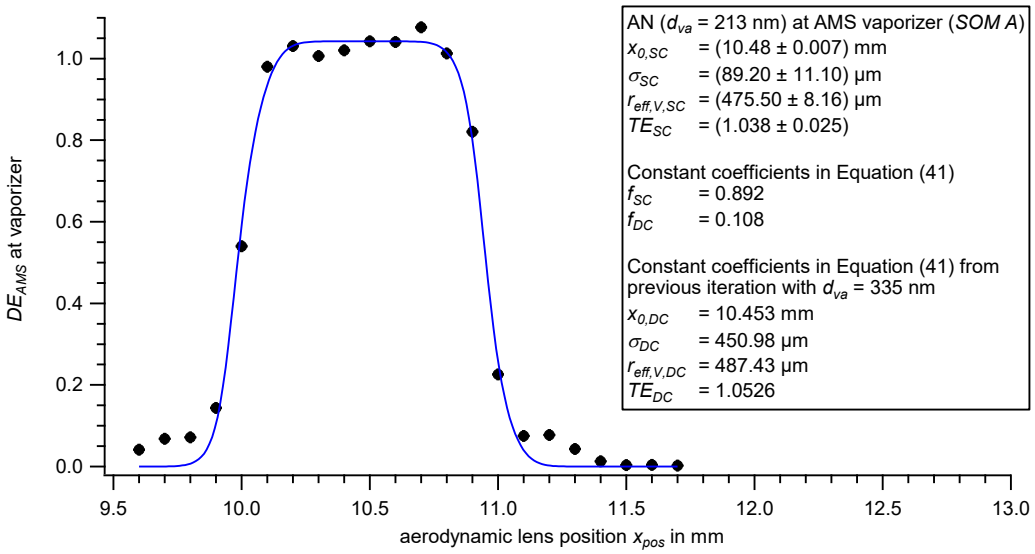

Figure 121: Scan of the aerodynamic lens position (x_{pos}) with ammonium nitrate particles of d_{va} = 213 nm (SOM A) at the ERICA-AMS vaporizer. The detection efficiency DE_{AMS} was evaluated from Equation (40) (markers) and curve fitted with a function according to Equation (41). The results and constants of the curve fits are shown in the box. The uncertainty of the detection efficiency is based on counting statistics of the CPC as well as the estimated counting statistic expected for the ERICA-AMS. The uncertainty of the lens position results from reading errors (see Appendix B.1.6). The uncertainty bars are in all cases smaller than the symbol.

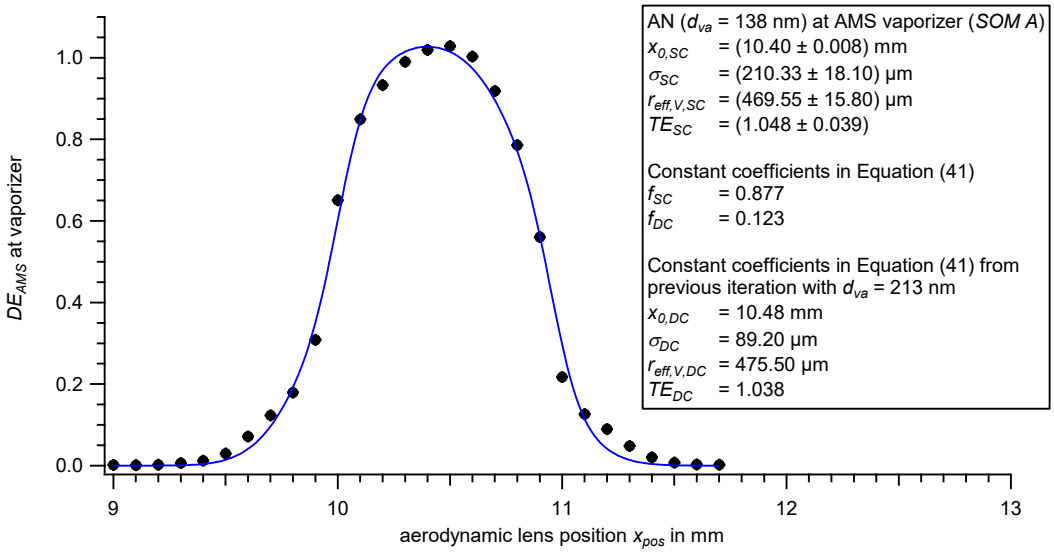

Figure 122: Scan of the aerodynamic lens position (x_{pos}) with ammonium nitrate particles of d_{va} = 138 nm (SOM A) at the ERICA-AMS vaporizer. The detection efficiency DE_{AMS} was evaluated from Equation (40) (markers) and curve fitted with a function according to Equation (41). The results and constants of the curve fits are shown in the box. The uncertainty of the detection efficiency is based on counting statistics of the CPC as well as the estimated counting statistic expected for the ERICA-AMS. The uncertainty of the lens position results from reading errors (see Appendix B.1.6). The uncertainty bars are in all cases smaller than the symbol.

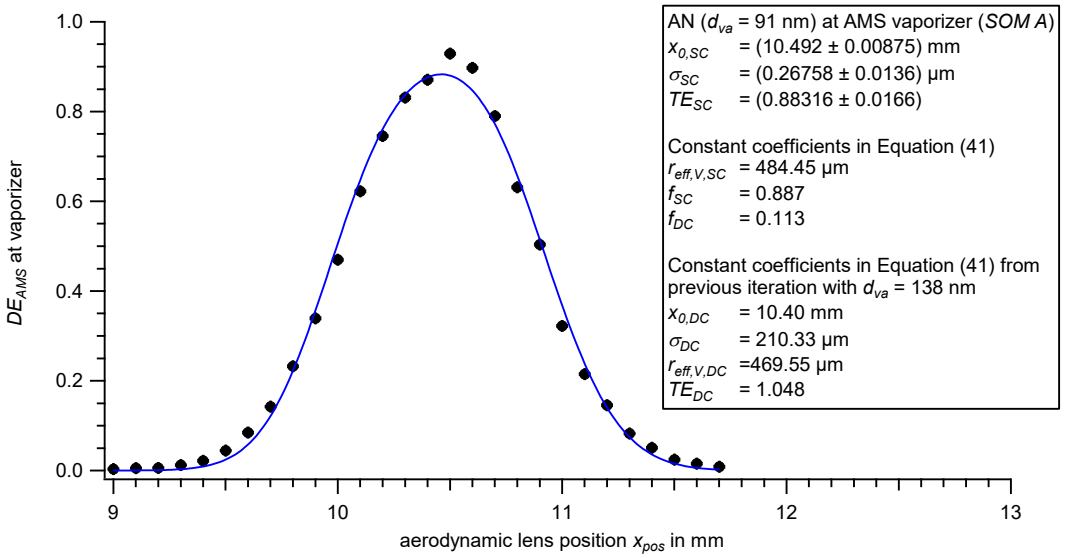

Figure 123: Scan of the aerodynamic lens position (x_{pos}) with ammonium nitrate particles of d_{va} = 91 nm (SOM A) at the ERICA-AMS vaporizer. The detection efficiency DE_{AMS} was evaluated from Equation (40) (markers) and curve fitted with a function according to Equation (41). The results and constants of the curve fits are shown in the box. The uncertainty of the detection efficiency is based on counting statistics of the CPC as well as the estimated counting statistic expected for the ERICA-AMS. The uncertainty of the lens position results from reading errors (see Appendix B.1.6). The uncertainty bars are in all cases smaller than the symbol.

B.12.2 Scans from Series Of Measurements (SOM) B

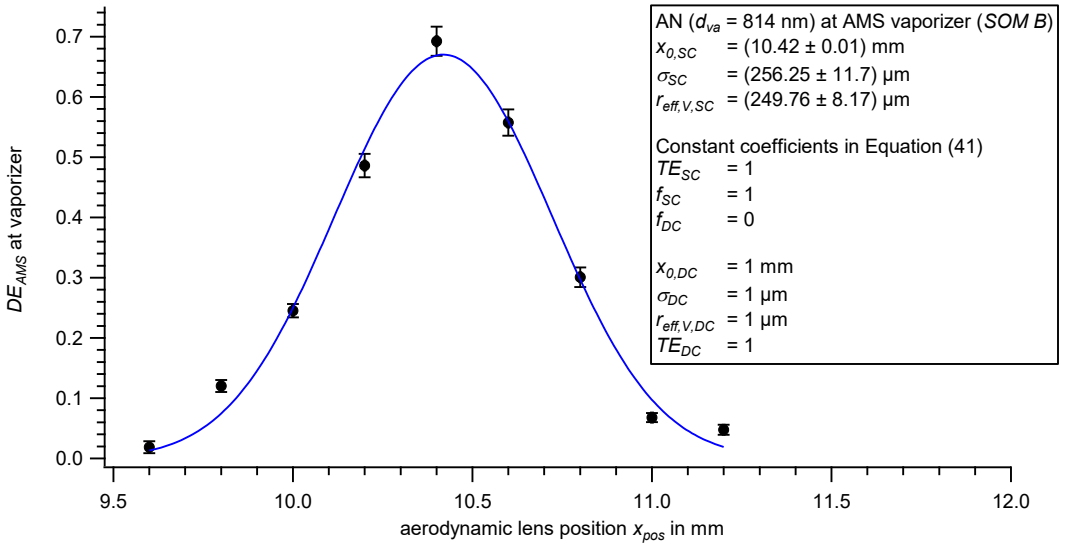

Figure 124: Scan of the aerodynamic lens position (x_{pos}) with ammonium nitrate particles of d_{va} = 814 nm (SOM B) at the ERICA-AMS vaporizer. The detection efficiency DE_{AMS} was evaluated from Equation (40) (markers) and curve fitted with a function according to Equation (41). The results and constants of the curve fits are shown in the box. The uncertainty of the detection efficiency is based on counting statistics of the CPC as well as the estimated counting statistic expected for the ERICA-AMS. The uncertainty of the lens position results from reading errors (see Appendix B.1.6). The uncertainty bars are in some cases smaller than the symbol.

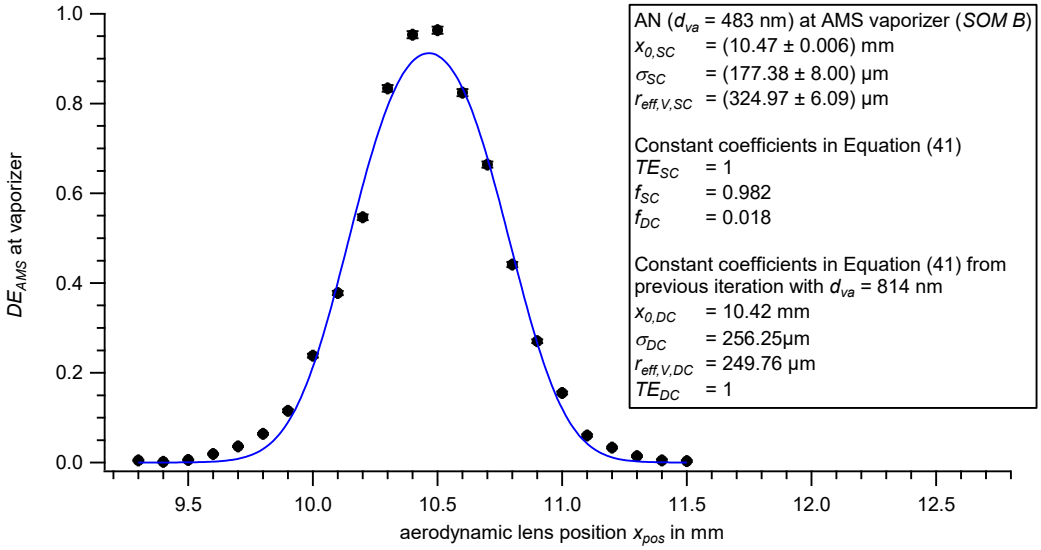

Figure 125: Scan of the aerodynamic lens position (x_{pos}) with ammonium nitrate particles of d_{va} = 483 nm (SOM B) at the ERICA-AMS vaporizer. The detection efficiency DE_{AMS} was evaluated from Equation (40) (markers) and curve fitted with a function according to Equation (41). The results and constants of the curve fits are shown in the box. The uncertainty of the detection efficiency is based on counting statistics of the CPC as well as the estimated counting statistic expected for the ERICA-AMS. The uncertainty of the lens position results from reading errors (see Appendix B.1.6). The uncertainty bars are in some cases smaller than the symbol.

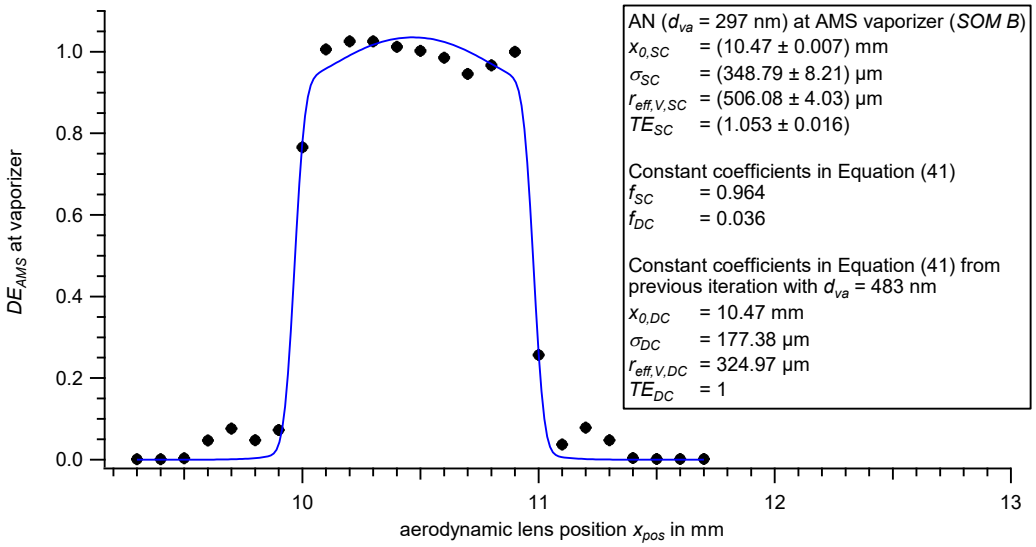

Figure 126: Scan of the aerodynamic lens position (x_{pos}) with ammonium nitrate particles of d_{va} = 297 nm (SOM B) at the ERICA-AMS vaporizer. The detection efficiency DE_{AMS} was evaluated from Equation (40) (markers) and curve fitted with a function according to Equation (41). The results and constants of the curve fits are shown in the box. The uncertainty of the detection efficiency is based on counting statistics of the CPC as well as the estimated counting statistic expected for the ERICA-AMS. The uncertainty of the lens position results from reading errors (see Appendix B.1.6). The uncertainty bars are in some cases smaller than the symbol.

B.13 Determination of maximum detection efficiency DE_{max} and the detection efficiency for the field deployment in Kathmandu DE_{KTM}

The parameters that are needed to determine DE_{max} and DE_{KTM} (see Section 4.2.4) were determined by curve fittings (see Sections 4.2.3.1, 4.2.3.2, and 4.2.3.3). The corresponding equations for all efficiencies are comprehended here:

Determination of DE_{max} for PSL particles at DU1 and DU2:

$$DE_{max} = \frac{1}{2} \cdot \left(erf\left(\frac{x_{pos} + r_{eff,L} - x_0}{\sqrt{2}\sigma} \right) - erf\left(\frac{x_{pos} - r_{eff,L} - x_0}{\sqrt{2}\sigma} \right) \right) \cdot TE \tag{99}$$

Determination of DE_{max} for ammonium nitrate particles at DU1 and DU2:

$$DE_{max} = \left(\frac{1}{2} \cdot \left(erf\left(\frac{x_{pos} + r_{eff,L,SC} - x_{0,SC}}{\sqrt{2}\ \sigma_{SC}} \right) - erf\left(\frac{x_{pos} - r_{eff,L,SC} - x_{0,SC}}{\sqrt{2}\ \sigma_{SC}} \right) \right) \cdot TE_{SC} \right) \tag{100}$$

Determination of DE_{max} for ammonium nitrate particles at the ERICA-AMS:

$$DE_{max} = \left(\frac{1}{2} \cdot \left(erf\left(\frac{x_{pos} + r_{eff,V,SC} - x_{0,SC}}{\sqrt{2}\,\sigma_{SC}} \right) - erf\left(\frac{x_{pos} - r_{eff,V,SC} - x_{0,SC}}{\sqrt{2}\,\sigma_{SC}} \right) \right) \cdot TE_{SC} \right) \tag{101}$$

Determination of DE_{KTM} for PSL particles at DU1 and DU2, where x_{pos} = 10.55 mm:

$$DE_{KTM} = \frac{1}{2} \cdot \left(erf\left(\frac{10.55\ + r_{eff,L} - x_0}{\sqrt{2}\sigma} \right) - erf\left(\frac{10.55\ - r_{eff,L} - x_0}{\sqrt{2}\sigma} \right) \right) \cdot TE \tag{102}$$

Determination of DE_{KTM} for ammonium nitrate particles at DU1 and DU2, where x_{pos} = 10.55 mm:

$$DE_{KTM} = \left(\frac{1}{2} \cdot \left(erf\left(\frac{10.55\ + r_{eff,L,SC} - x_{0,SC}}{\sqrt{2}\ \sigma_{SC}} \right) - erf\left(\frac{10.55\ - r_{eff,L,SC} - x_{0,SC}}{\sqrt{2}\ \sigma_{SC}} \right) \right) \cdot TE_{SC} \right) \tag{103}$$

Determination of DE_{KTM} for ammonium nitrate particles at the ERICA-AMS, where x_{pos} = 10.55 mm:

$$DE_{KTM} = \left(\frac{1}{2} \cdot \left(erf\left(\frac{10.55\ + r_{eff,V,SC} - x_{0,SC}}{\sqrt{2}\,\sigma_{SC}} \right) - erf\left(\frac{10.55\ - r_{eff,V,SC} - x_{0,SC}}{\sqrt{2}\,\sigma_{SC}} \right) \right) \cdot TE_{SC} \right) \tag{104}$$

B.14 Determination of ion peak area threshold for stick spectra

As described in Section 4.4.1 a detection limit (ion peak area threshold) of the ERICA-LAMS has to be determined to distinguish between a valid signal and noise in the stick spectra. For this, the data set of the first phase of the StratoClim campaign (Kalamata, Greece) was used. After mass calibration the signal intensities for the usually unoccupied masses by ions from ambient particles by laser ablation/ionization (m/z 2 up to m/z 6 for positive, m/z 2 up to m/z 11 for negative ions) were inspected. To determine the detection limit, the normalized cumulative signal intensity distributions for each investigated m/z were made and the overall 99 % threshold was determined (Köllner et al., 2017). For this purpose, a cumulative histogram of abundance as function of the signal intensity was generated for each inspected m/z value. Each of these histograms was normalized to the maximum abundance value. The result was I_{stick} = 7 mV·samples for positive and negative ions. That means that 99 % of the signal intensity values are below I_{stick} = 7 mV·samples. Figure 127 depicts the cumulative probability of signal intensities belonging to these non-occupied m/z values. Signals with intensities above I_{stick} > 7 mV·samples are interpreted as signals above the noise level.

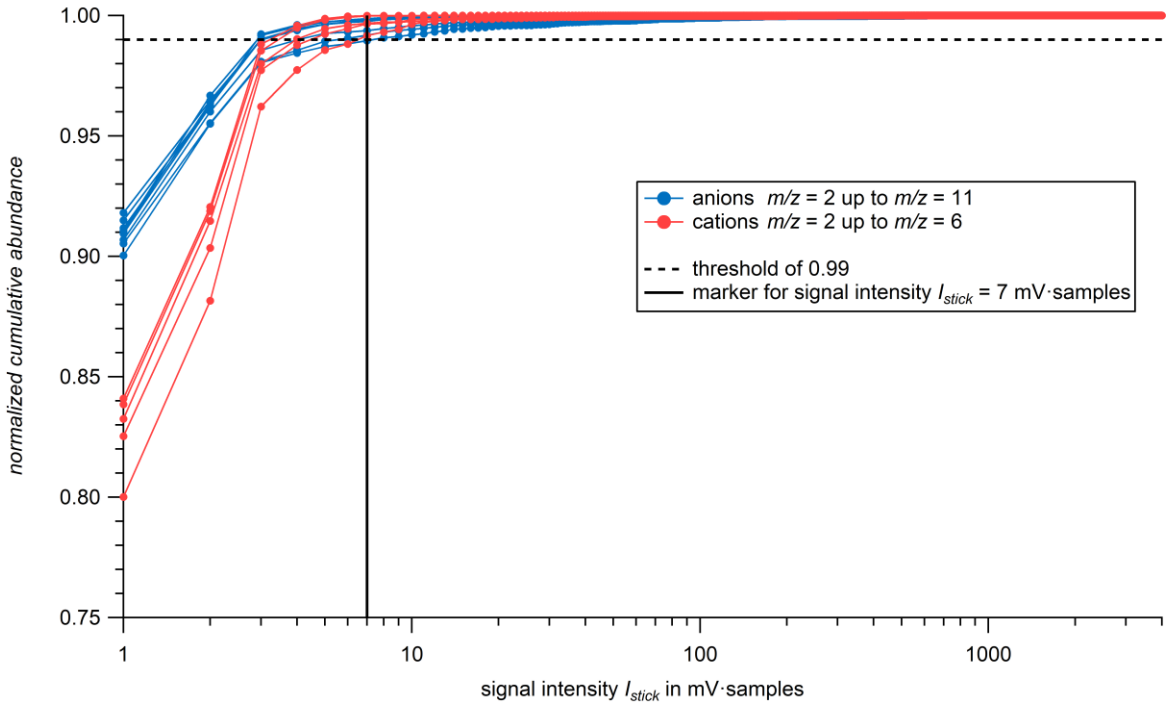

Figure 127: Normalized cumulative abundance of signal intensities I_{stick} for cations (red bundle, m/z 2 up to m/z 6) and anions (blue bundle, m/z 2 up to m/z 11). Each curve represents a different m/z value. Marked are the 0.99 threshold line (black, horizontal) and the value of I_{stick} = 7 mV·samples (black, vertical).

Appendix C: Supplementary information for Chapter 5

C.1 Mid-latitude phase – flight profiles and flight tracks

As described in Section 5.1 the mid-latitude phase of the StratoClim campaign was the first deployment of the ERICA instrument on *Geophysica*. It took place in Kalamata, Greece, in the mid-latitudes at the Mediterranean Sea in August and September 2016. Base for this part of the campaign was the Kalamata International Airport (KLX; 37.07°N, 22.03°E). Here, the time series of the altitude profiles and flight tracks are presented for each research flight. All following values of altitude h_{amsl}, pressure p_{stat}, and temperature T_{out} were provided by UCSE. The altitude h_{amsl} is the actual elevation above mean sea level (amsl) determined by GPS.

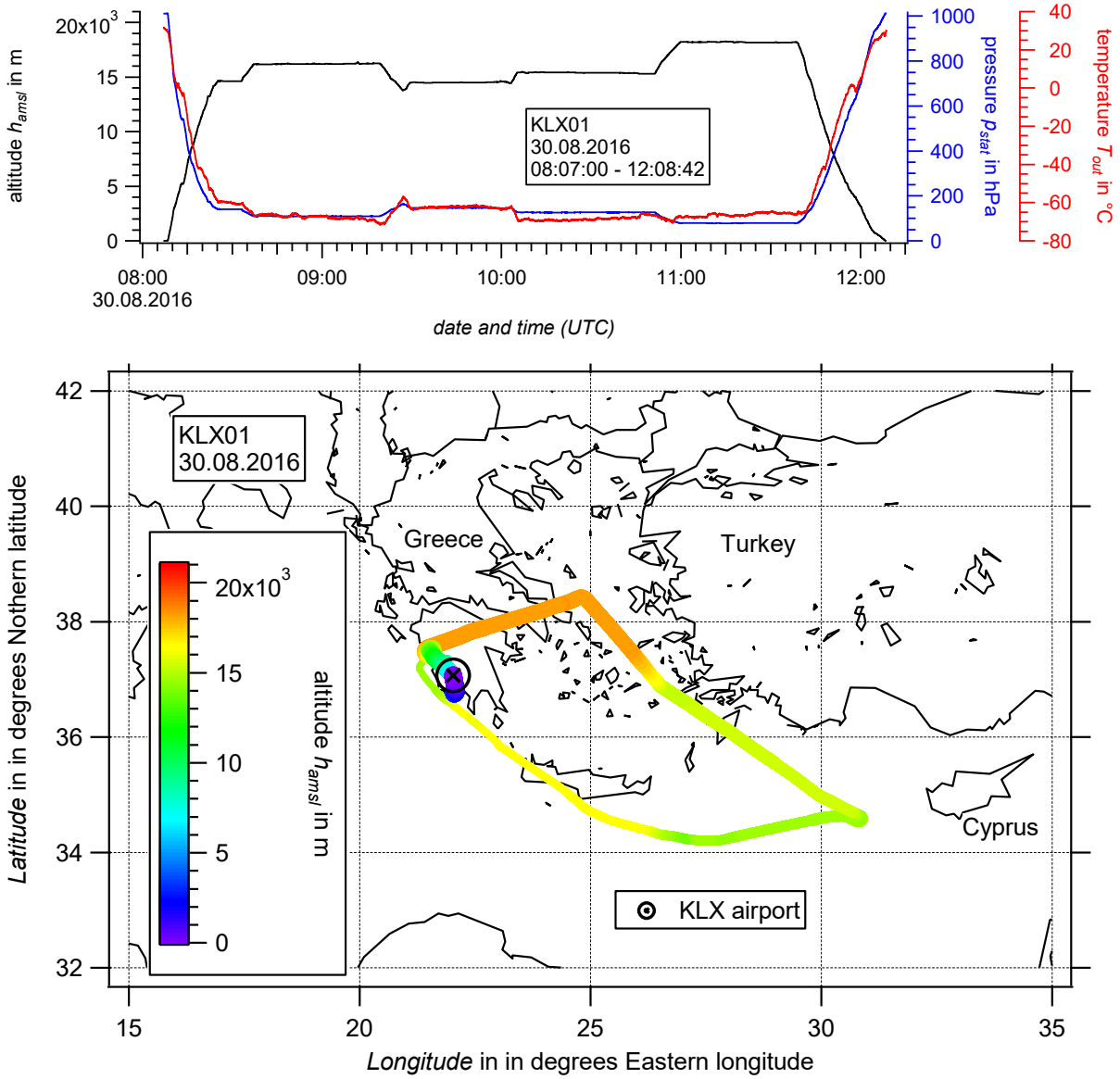

Figure 128: Timeseries of the GPS altitude h_{amsl}, static pressure p_{stat}, and ambient temperature T_{out} provided by UCSE (top) and flight track (bottom) of research flight KLX01 (30.08.2016, 08:07:00 – 12:08:42 UTC). The flight track is color-coded to depict the altitude (amsl). The increasing thickness of the line indicates the progress of flight time from takeoff (thinnest) until landing (thickest). The location of Kalamata International Airport (KLX) is marked by a black cross.

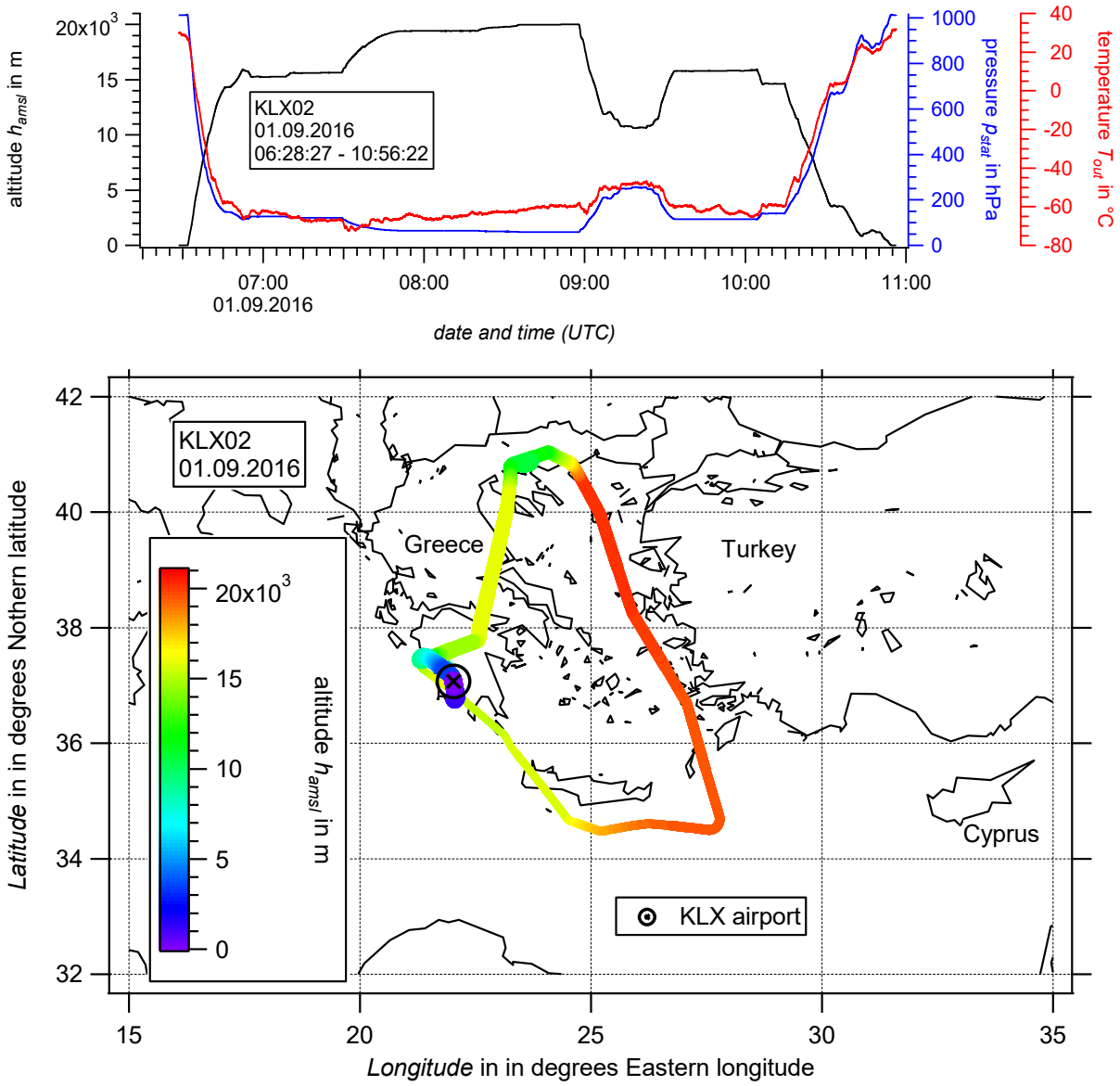

Figure 129: Timeseries of the GPS altitude h_{amsl}, static pressure p_{stat}, and ambient temperature T_{out} provided by UCSE (top) and flight track (bottom) of research flight KLX02 (01.09.2016, 06:28:27 – 10:56:22 UTC). The flight track is color-coded to depict the altitude (amsl). The increasing thickness of the line indicates the progress of flight time from takeoff (thinnest) until landing (thickest). The location of Kalamata International Airport (KLX) is marked by a black cross.

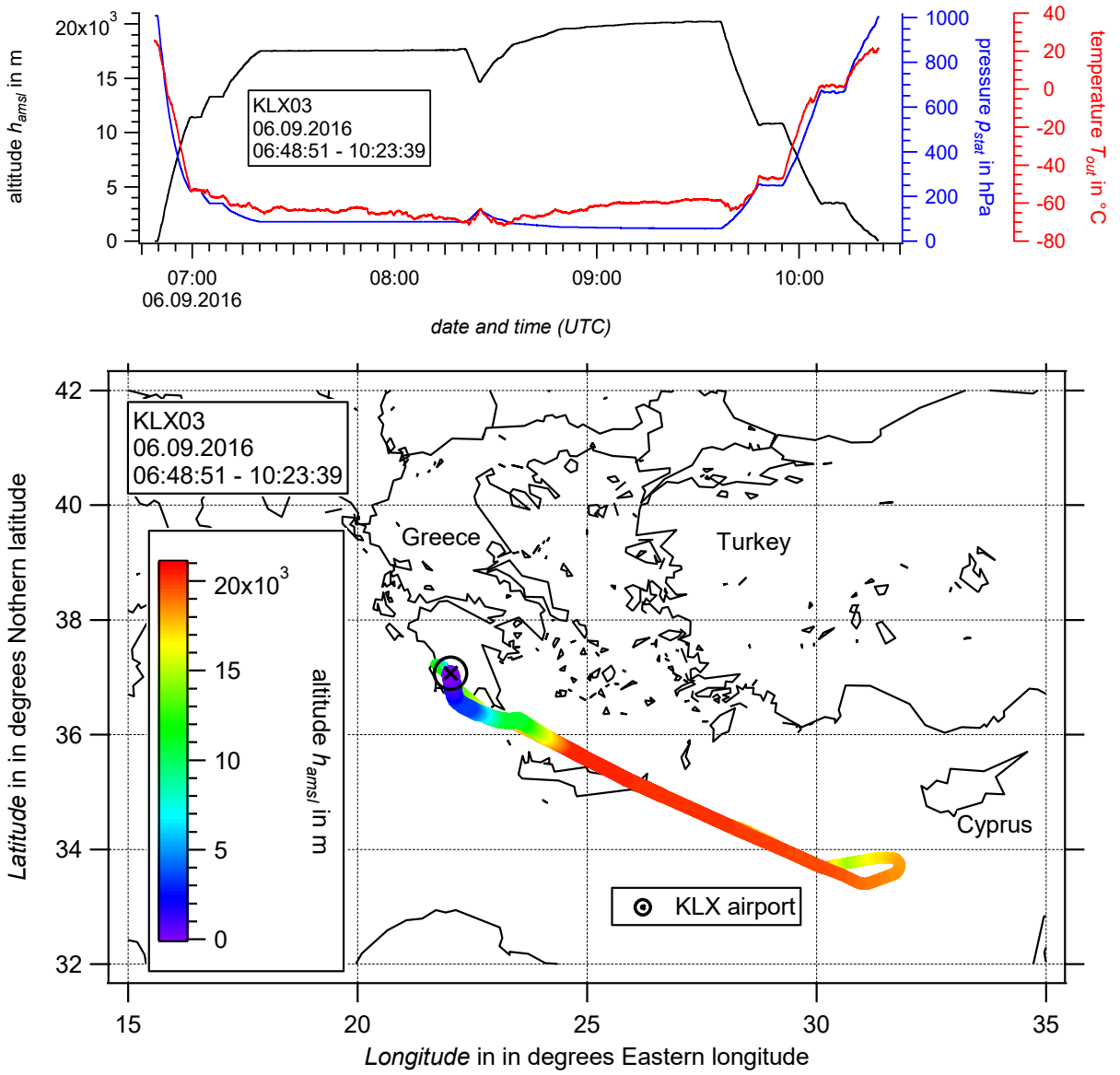

Figure 130: Timeseries of the GPS altitude h_{amsl}, static pressure p_{stat}, and ambient temperature T_{out} provided by UCSE (top) and flight track (bottom) of research flight KLX03 (06.09.2016, 06:48:51 – 10:23:39 UTC). The flight track is color-coded to depict the altitude (amsl). The increasing thickness of the line indicates the progress of flight time from takeoff (thinnest) until landing (thickest). The location of Kalamata International Airport (KLX) is marked by a black cross.

C.2 Uncertainty calculation for vertical profiles and size distribution

C.2.1 Rate of recorded mass spectra

The absolute uncertainty of the of recorded single particle mass spectra normalized to the research flight time for each altitude bin (see Section 5.1 and 5.2) is calculated based on Gaussian propagation of uncertainties:

$$\Delta^{abs} f_{spec} = \frac{\sqrt{N_{spectra}}}{t_{flight}} \tag{105}$$

The parameter f_{spec} is the rate of recorded mass spectra and $N_{spectra}$ is the total number of recorded single particle mass spectra in the specific altitude bin. $\sqrt{N_{spectra}}$ conform with the absolute uncertainty of the number of spectra $\Delta^{abs} N_{spectra}$ is calculated based on Poisson statistics (see Appendix C.2.2). The uncertainty of the flight time of the aircraft in the specific altitude bin t_{flight} is not considered in Equation, since the uncertainty of the time measurement can be neglected compared to the measured time.

C.2.2 Number of spectra

The absolute uncertainty of the number of spectra $\Delta^{abs} N_{spectra}$ is calculated based on Poisson statistics:

$$\Delta^{abs} N_{spectra} = \sqrt{N_{spectra}} \tag{106}$$

$N_{spectra}$ can be either the (total) number of spectra or the number of spectra of a specific particle type (e.g., gold-containing particles in Section 5.2.3.3 and Hg- containing particles in Section 5.2.3.2) in total or for specific bins (altitude or size; e.g., see Sections 5.1.2, 5.2.2.1, and 5.2.2.2).

C.2.3 Particle number fraction

The absolute uncertainty of the measured particle number fraction $\Delta^{abs} f_{part}$ for each altitude (see Sections 5.1.2 and 5.2.2.2) or size bin (see Section 5.2.2.1) is calculated using binomial statistics (see also Appendix B.1.10):

$$\Delta^{abs} f_{part} = \frac{\sqrt{N_{spectra} \cdot f_{part} \cdot (1 - f_{part})}}{N_{spectra}} \tag{107}$$

Here, $N_{spectra}$ is the number of recorded single particle mass spectra in the specific bin (altitude or size) and f_{part} is the particle fraction of the determined particle type. The parameter f_{part} can be seen as the probability of recording a spectrum of the defined criterion (cluster or particle type/species).

The parameter f_{part} can be either the fraction of the particle type for the sum over all flights (e.g., Section 5.2.2.1) or for a single flight (e.g., Section 5.2.2.2). The particle type can be determined either by clustering algorithm/grouping method (see Sections mentions above) or ion marker peak method (see Section 5.2.3). Also, the uncertainties of the vertical profile fractions and size distribution fractions presented in Appendices C.7, C.11, and C.10 are based on binomial statistics.

The uncertainty $\Delta^{abs} f_{part}$ represents solely the lower limit of the uncertainty. When calculating the uncertainties of clustering by means of counting statistics, the algorithm does not take any mis-assignments of the manual grouping into account (Roth, 2014). According to Roth (2014), uncertainties of between 13 % and 48 % result for the assigned particle types, taking the mis-assignments into account. These uncertainties are not considered in the uncertainty bars.

C.3 Parameters for m/z calibration and clustering

C.3.1 Mid-latitude flights from Kalamata, Greece

Table 34 shows the overview of the parameters set in CRISP for the m/z calibration and Table 35 shows the overview of the parameters for clustering the data set by the *k-means* algorithm for the mid-latitude phase (see Section 5.1.1). The details of the algorithm and the procedures, as well as the meaning of the individual parameters are described Klimach (2012).

Table 34: Overview of the parameters for the m/z calibration set in CRISP. The values were applied for cation and anion spectra for the data evaluation of the KLX data set before processing by clustering algorithm.

Parameter	**Value for cations**	**Value for anions**
startA	18	18
IntA	20	20
stepA	0.2	0.2
startB	542	538
IntB	10	10
stepB	0.2	0.2
MaxStep	60	60
MinSum	10	1
anz	250	250
width	5	5
BG offset	12	10

Table 35: Overview of the parameters for clustering the KLX data set by the k-means algorithm. The parameters are described in detail in Klimach (2012).

Type of clustering	k-means
Source for clustering	anion + cation
Pre-processing type	Power each mz
Pre-processing power	0.5
Normalization type	sum
Normalization time	before concatenation
Initialization type	find different start cluster
Number of clusters	15
Start cluster difference	0.8
Distance mode	Euclidean

C.3.2 Subtropical flights from Kathmandu, Nepal

Table 36 shows the overview of the parameters for the m/z calibration set in CRISP for the m/z calibration and Table 37 shows the overview of the parameters for clustering the *KTM total data set* by the *k-means* algorithm for the Asian monsoon phase (see Section 5.2.1). The meaning of the parameters are described in detail in Klimach (2012).

Table 36: Overview of the parameters for the m/z calibration set in CRISP. The values were applied for cation and anion spectra for the data evaluation of the KTM data set before processing by clustering algorithm.

Parameter	**Value for cations and anions**
startA	11
IntA	30
stepA	0.2
startB	531
IntB	20
stepB	0.2
MaxStep	60
MinSum	1
anz	250
width	5
BG offset	10

Table 37: Overview of the parameters for clustering the KTM total data set by the k-means algorithm. The parameters are described in detail in Klimach (2012).

Type of clustering	k-means
Source for clustering	anion + cation
Pre-processing type	Power each mz
Pre-processing power	0.5
Normalization type	sum
Normalization time	before and after concatenation
Initialization type	find different start cluster
Number of clusters	30
Start cluster difference	0.8
Distance mode	euclidean

C.3.3 Case studies from Kathmandu, Nepal

The mass spectra of the *KTM total data set* used for the tungsten- (see Section 5.2.3.1) and mercury-investigation (see Section 5.2.3.2) were synchronized to UCSE time in advance. Table 38 shows the settings for the therefore used m/z calibration. The meaning of the parameters are described in detail in Klimach (2012).

Table 38: Overview of the parameters for the m/z calibration set in CRISP for investigating tungsten-containing and mercury-containing particles. The values were applied for cation and anion spectra for the data evaluation of the KTM data set.

Parameter	Value for cations	Value for anions
startA	11	11
IntA	30	30
stepA	0.2	0.2
startB	531	531
IntB	20	20
stepB	0.2	0.2
MaxStep	60	60
MinSum	10	1
anz	400	400
width	5	5
BG offset	12	10
Number of spectra	150,565	

To investigate whether gold particles are spalled from the inlet only mass spectra recorded during research flights were considered (see Section 5.2.3.3). Table 39 shows the settings for the therefore used m/z calibration.

Table 39: Overview of the parameters for the m/z calibration set in CRISP for investigating gold-containing particles. The values were applied for cation and anion spectra for the data evaluation of the KTM data set.

Parameter	Value for cations	Value for anions
startA	13	13
IntA	26	26
stepA	0.2	0.2
startB	531	531
IntB	20	20
stepB	0.2	0.2
MaxStep	60	60
MinSum	10	1
anz	400	400
width	5	5
BG offset	12	10
Number of spectra	146,413	

These parameters are provided here to enable reprocessing -if needed- of the mass spectra under the same conditions as for this thesis.

C.4 Ion marker peaks identification

To identify the chemical species for the particle types (Section 5.1 and 5.2) ion marker peaks were used. For that purpose the searching tools from the NIST Chemistry WebBook (https://webbook.nist.gov/chemistry/mw-ser/, 2019) and the searching tool *ChemCalc* (Patiny and Borel, 2013) were applied. The resulting ions/fragments were checked for plausibility by comparing these with other marker ions in the entire mass spectrum, especially in case of isobars. Typically, this was an iterative process. The isotopic ratios were given by Audi et al. (2003). As described in the Sections 5.1.1 and 5.2.1, the peak at m/z -26 was interpreted as $C_2H_2^-$ in case of a weak signal and as CN^- in case of a mid-intense signal. Furthermore, if the signal intensities of the organic fragments were mid-intense, the peaks could not be clearly determined. In addition, for the interpretation of other ion marker peaks both above mentioned data bases were used in general.

Table 40 lists the chemical species and their corresponding ion marker peaks that were used for the particle type determination of the clustered data sets. Additionally, the references for the species are presented. Beside the references listed here, also other references were consulted like e.g., Hinz et al. (1999), Gross et al. (2000), Silva and Prather (2000), Cziczo et al. (2001), Lee et al. (2002), Hudson et al. (2004), Spencer et al. (2008), Pratt et al. (2011), Prather et al. (2013), Murphy et al. (2014), Sierau et al. (2014), Roth et al. (2016), Schmidt et al. (2017), Shen et al. (2018), and Froyd et al. (2019).

For validation of the chemical species, namely sodium chloride, ammonium nitrate, and gold, dedicated laboratory experiments were conducted for this thesis (see Section 4.4.1).

Table 40: Chemical species and corresponding ion marker peaks used for the particle type determination of the clustered data sets in Sections 5.1.1 and 5.2.1. Additionally, the references for the species are provided (data base; ** laboratory study; *** field study). Continued on next page.*

Chemical species	**Ion marker peaks (m/z values)**	**Reference**
Metals	+23 (Na^+) +24 (Mg^+), +25 ($^{25}Mg^+$), +26 ($^{26}Mg^+$) +27 (Al^+) +28 (Si^+) +39 (K^+), +41 ($^{41}K^+$) +40 (Ca^+), +56 (CaO^+) +48 (Ti^+), +64 (TiO^+) +52 (Cr^+) +54 ($^{54}Fe^+$), +56 (Fe^+) +58 (Ni^+) +59 (Co^+) +63 (Cu^+)	NIST Chemistry WebBook (2019)*, Patiny and Borel (2013)*, Audi et al. (2003)*, Schmidt (2015)**, dedicated laboratory experiments for this thesis (Section 4.4.1)**, Roth (2014)***
Cyanide	-26 (CN^-)	NIST Chemistry WebBook (2019)*, Schmidt (2015)**, Pratt et al. (2010)***, Roth (2014)***
Chloride	-35 (Cl^-)	Brands (2009)**, dedicated laboratory experiments for this thesis (Section 4.4.1)**

Table 40: Continued.

Chemical species	**Ion marker peaks (m/z values)**	**Reference**
Phosphate	-79 (PO_3^-)	NIST Chemistry WebBook (2019)*, Schmidt (2015)**, ,Pratt and Prather (2010)***
Silicate/Carbon sulfide	-44 (SiO^-)	NIST Chemistry WebBook (2019)*, Schneider et al. (2019)
Ammonium	+18 (NH_4^+)	Brands et al. (2011)**, dedicated laboratory experiments for this thesis (Section 4.4.1)**
Nitrate	+30 (NO^+); -46 (NO_2^-), -62 (NO_3^-), -125 ((HNO_3)NO_3^-)	Brands et al. (2011)**, Roth (2014)**, dedicated laboratory experiments for this thesis (Section 4.4.1)**
Sulfate	-97 (HSO_4^-), -99 ($H^{34}SO_4^-$), -195 ($H(HSO_4)_2^-$)	Patiny and Borel (2013)*,Murphy et al. (1998)***, Pratt and Prather (2010)***
Oxygen/Hydroxy	-16 (O^-), -17 (OH^-)	NIST Chemistry WebBook (2019)*
Organics	+12 (C^+), +24 (C_2^+), +36 (C_3^+), +48 (C_4^+); -24 (C_2^-), -26 ($C_2H_2^-$) as individually and independently occurring organic peaks (in contrast to the "consecutive row" for organics of EC, see below)	NIST Chemistry WebBook (2019)* , Brands et al. (2011)**, Köllner (2019)***
Organics of EC	+12 (C^+), +24 (C_2^+), +36 (C_3^+), … , +168 (C_{14}^+); -12 (C^-), -24 (C_2^-), -36 (C_3^-), … , -168 (C_{14}^-) in a picket fence pattern like a "consecutive row" of at least 5 peaks	Brands (2009)**, Schmidt (2015)**, Brands et al. (2011)***
gold	+197 (Au^+), +394 (Au_2^+)	dedicated laboratory experiments for this thesis (Section 4.4.1.2)**

C.5 Mid-latitude phase – mean spectra

As described in Section 5.1.1 the data set of the single particle mass spectra was evaluated by using the *k-means* clustering algorithm. The resulting 15 clusters were reduced to four groups by combining the automatically identified clusters: *Inorganic*, *Meteoric*, *Organic,* and *EC*. Here, the mean spectra of each particle type are presented individually for each research flight. The number of spectra that are basis for the mean spectra are depicted in the pie charts shown in Appendix C.6, Figure 135.

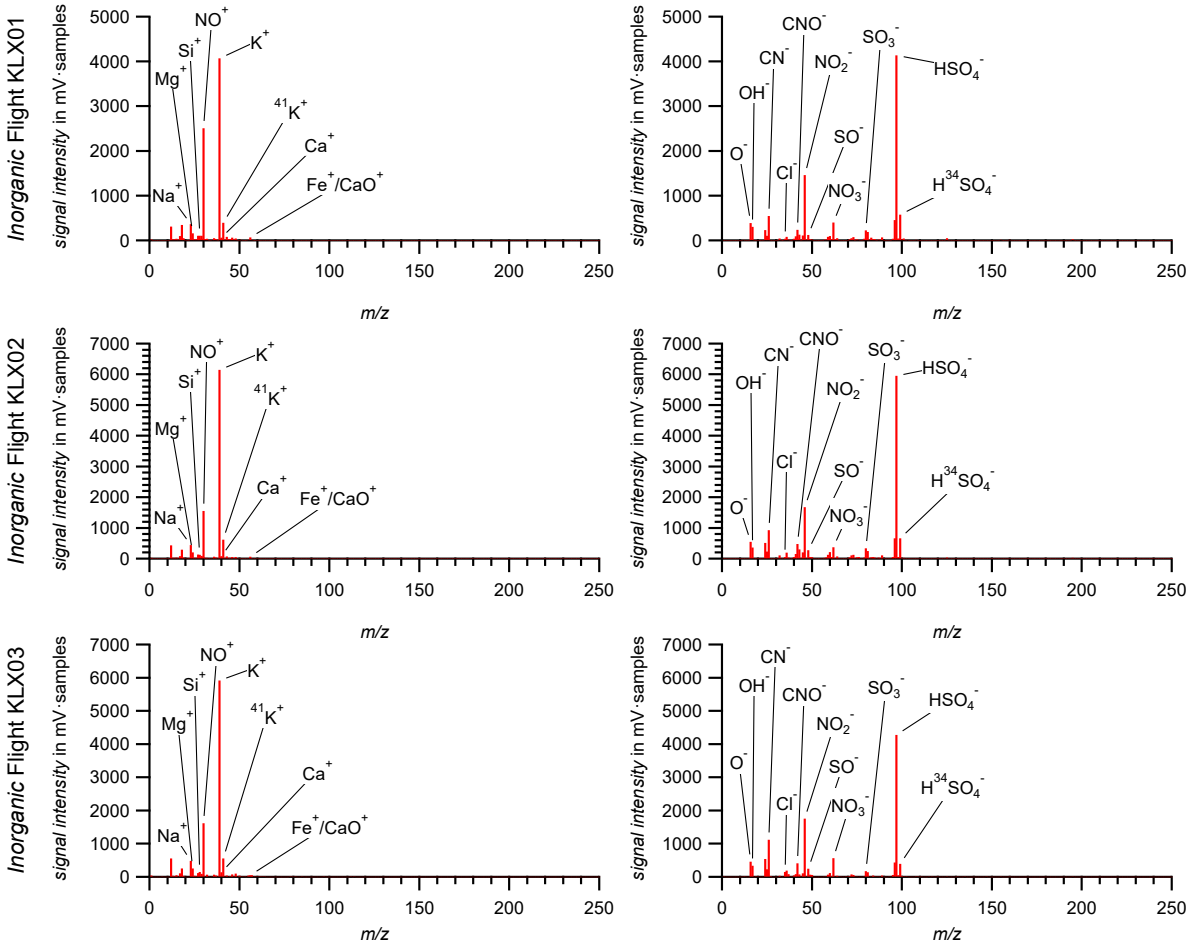

Figure 131: Mean stick spectra (left: cations, right: anions) of the Inorganic particle type (red) individually for all research flights in the mid-latitude phase of StratoClim. Identified characteristic peaks are tagged with the most likely fragment/ion species.

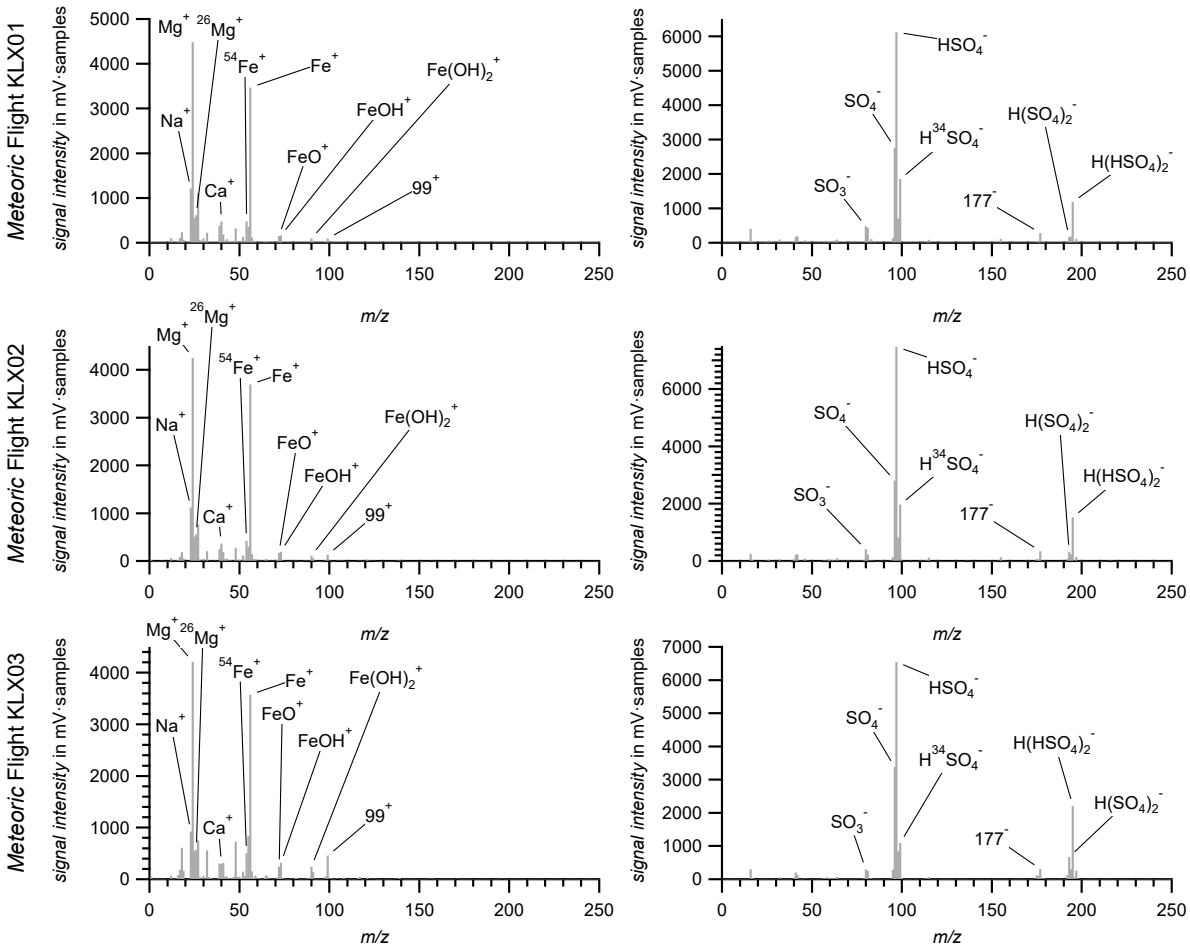

Figure 132: Mean stick spectra (left: cations, right: anions) of the Meteoric particle type (gray) individually for all research flights in the mid-latitude phase of StratoClim. Identified characteristic peaks are tagged with the most likely fragment/ion species. For lines at which only the m/z number are provided an unambiguous identification of the ions was not possible.

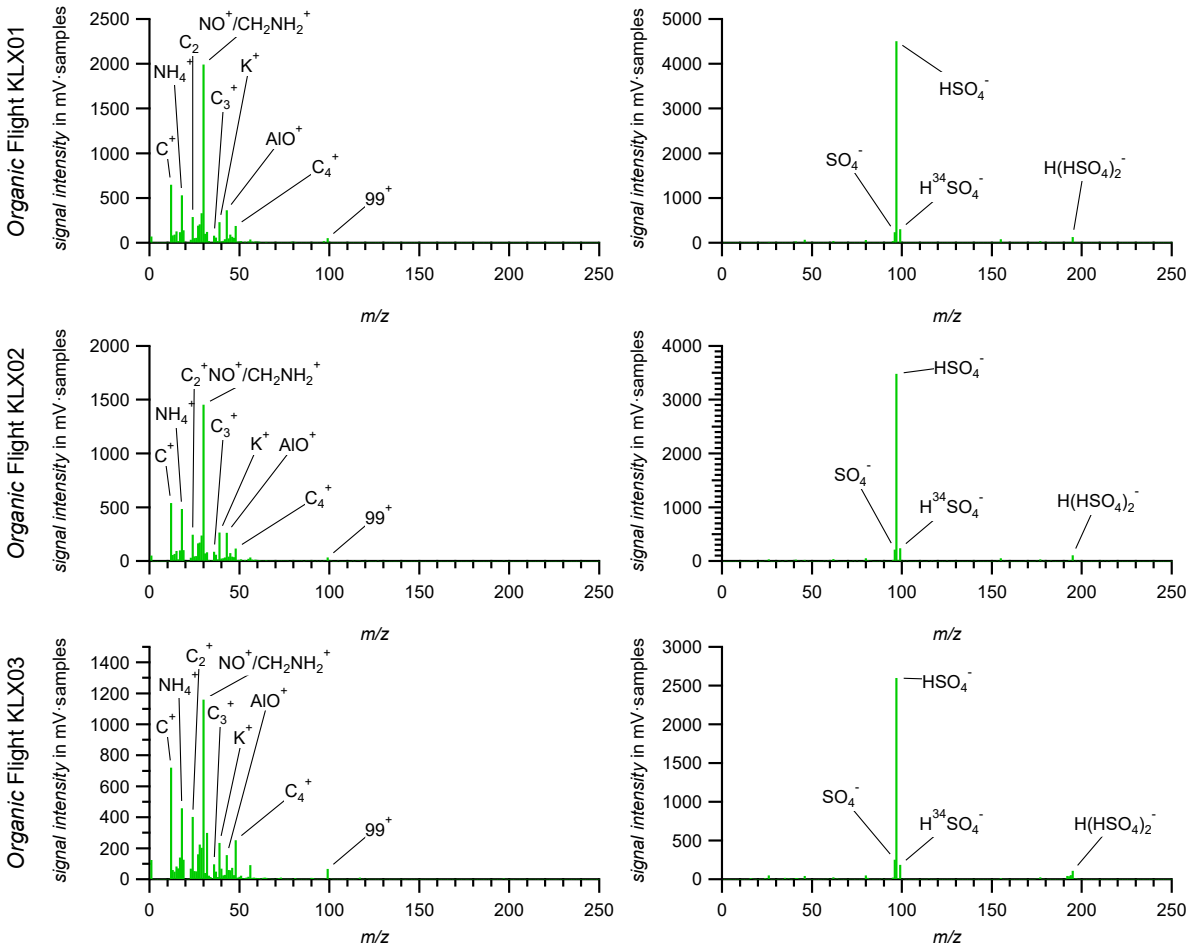

Figure 133: Mean stick spectra (left: cations, right: anions) of the Organic particle type (green) individually for all research flights in the mid-latitude phase of StratoClim. Identified characteristic peaks are tagged with the most likely fragment/ion species. For lines at which only the m/z number are provided an unambiguous identification of the ions was not possible.

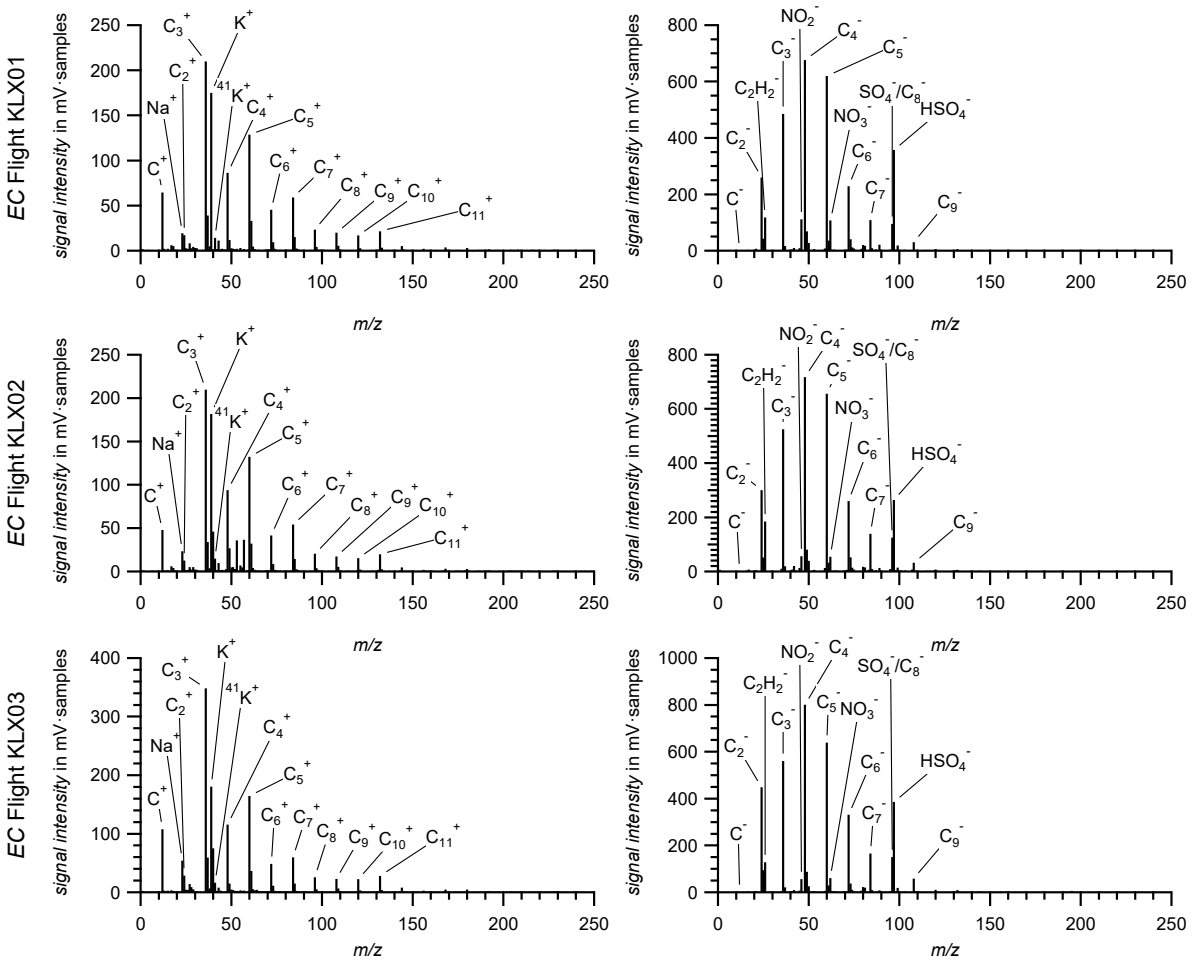

Figure 134: Mean stick spectra (left: cations, right: anions) of the elemental carbon (EC) particle type (black) individually for all research flights in the mid-latitude phase of StratoClim. Identified characteristic peaks are tagged with the most likely fragment/ion species.

C.6 Mid-latitude phase – data overview in pie charts

As described in Section 5.1.1 the data set of the single particle mass spectra was evaluated by using the clustering algorithm. The resulting 15 clusters were reduced to distinct five groups by combining the automatically identified clusters: *Inorganic*, *Meteoric*, *Organic*, *EC,* and unidentified mass spectra. Here, the abundance of each particle type is presented individually for each research flight.

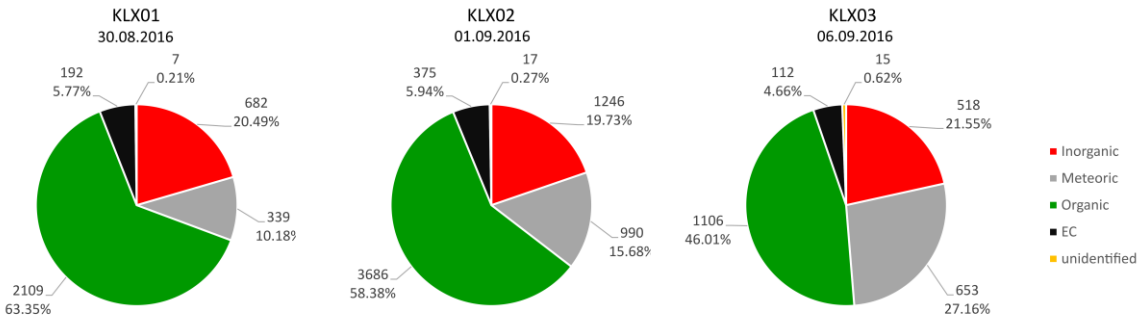

Figure 135: Abundance of the grouped particle types, Inorganic (red), Meteoric (gray), Organic (green), EC (black), and unidentified (orange), based on the data set recorded during three research flights between 30.09.2016 and 09.06.2016 in the mid-latitude phase of StratoClim individually for each flight. The total data set consist of 12,047 single particle mass spectra.

C.7 Mid-latitude phase – vertical profiles

As described in Section 5.1.1 the data set of the single particle mass spectra was evaluated by using the clustering algorithm. The resulting 15 clusters were reduced to distinct four groups by combining the automatically identified clusters: *Inorganic*, *Meteoric*, *Organic,* and *EC.* Here, the vertical profiles of each particle type are presented individually for each research flight. All following altitude values h_{amsl} refer to the GPS altitude provided by UCSE. The GPS altitude is the actual elevation above mean sea level (amsl). To determine the particle number fraction f_{part} for a bin, for each bin the ratio is calculated from the number of particles of the specific particle type and the number of all collected particles. The uncertainties are calculated from counting statistics according to Appendices C.2.2 and C.2.3.

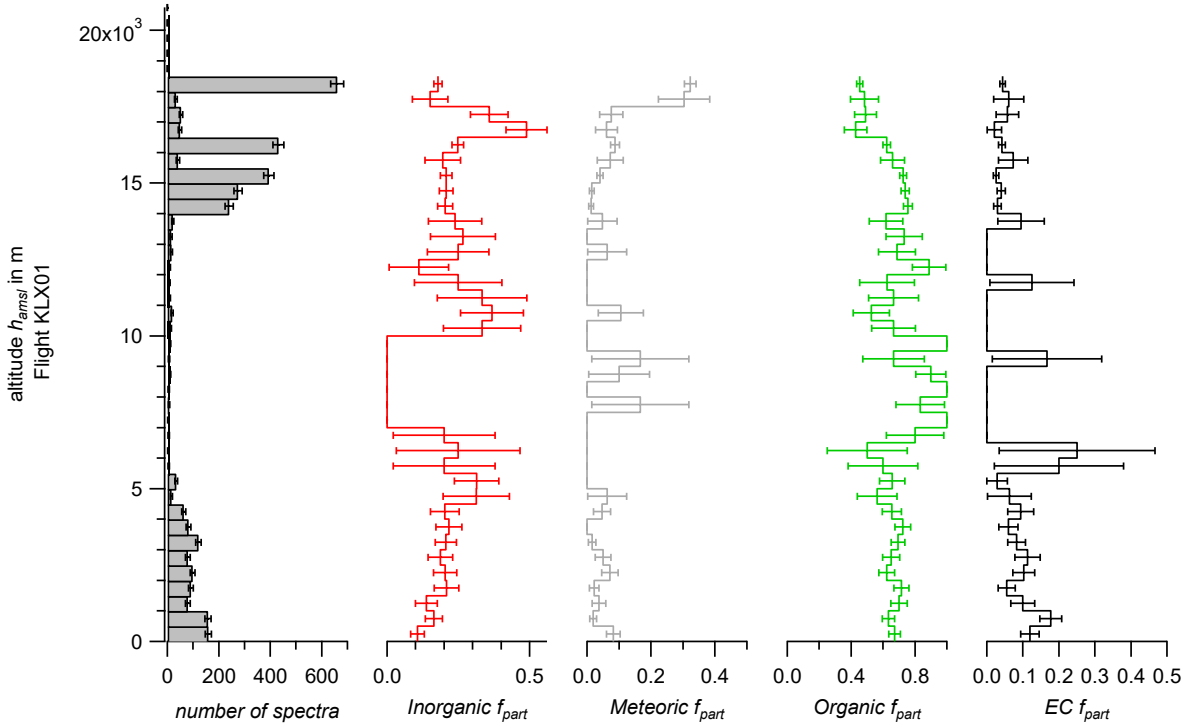

Figure 136: Vertically resolved particle number fractions f_{part} during research flight KLX01 (30.08.2016, 08:07:00 – 12:08:42 UTC) of the particle types: Inorganic (red), Meteoric (gray), Organic (green), and EC (black), normalized to the number of recorded spectra in each bin. The left panel shows the total number of spectra in each bin (black solid bars; in total for KLX01: 3,329). The uncertainties are calculated from counting statistics according to Appendices C.2.2 and C.2.3.

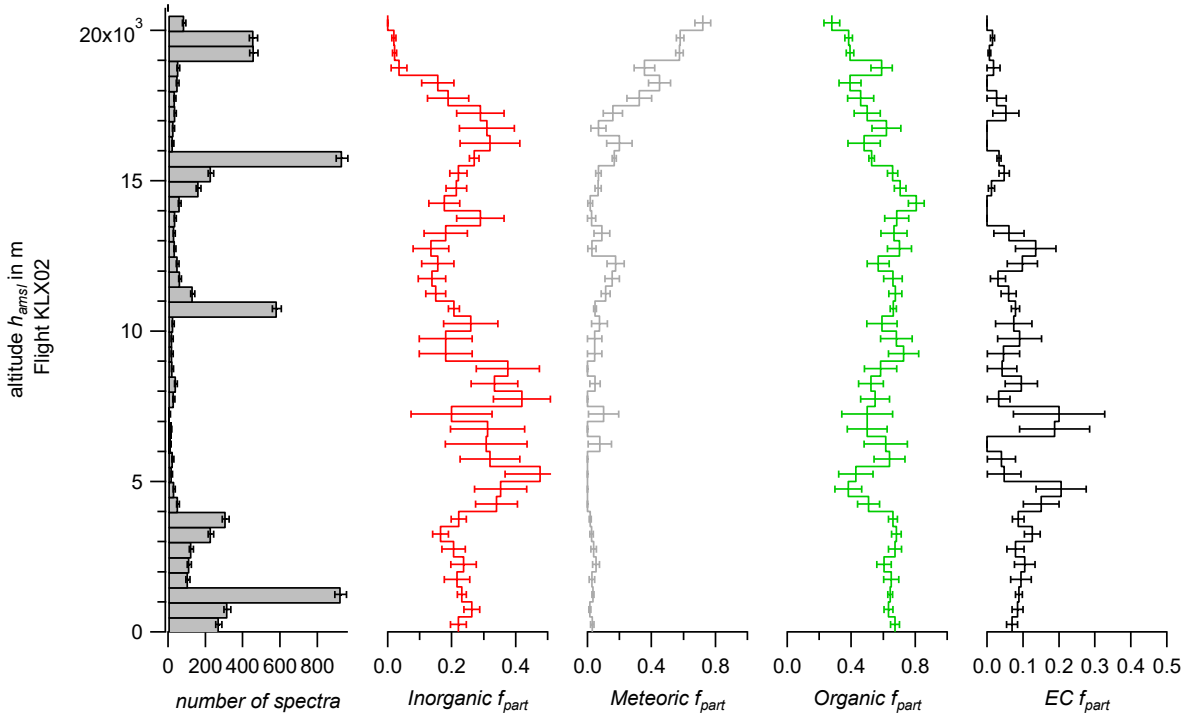

Figure 137: Vertically resolved particle number fractions f_{part} during research flight KLX02 (01.09.2016, 06:28:27 – 10:56:22 UTC) of the particle types: Inorganic (red), Meteoric (gray), Organic (green), and EC (black), normalized to the number of recorded spectra in each bin. The left panel shows the total number of spectra in each bin (black solid bars; in total for KLX02: 6,314). The uncertainties are calculated from counting statistics according to Appendices C.2.2 and C.2.3.

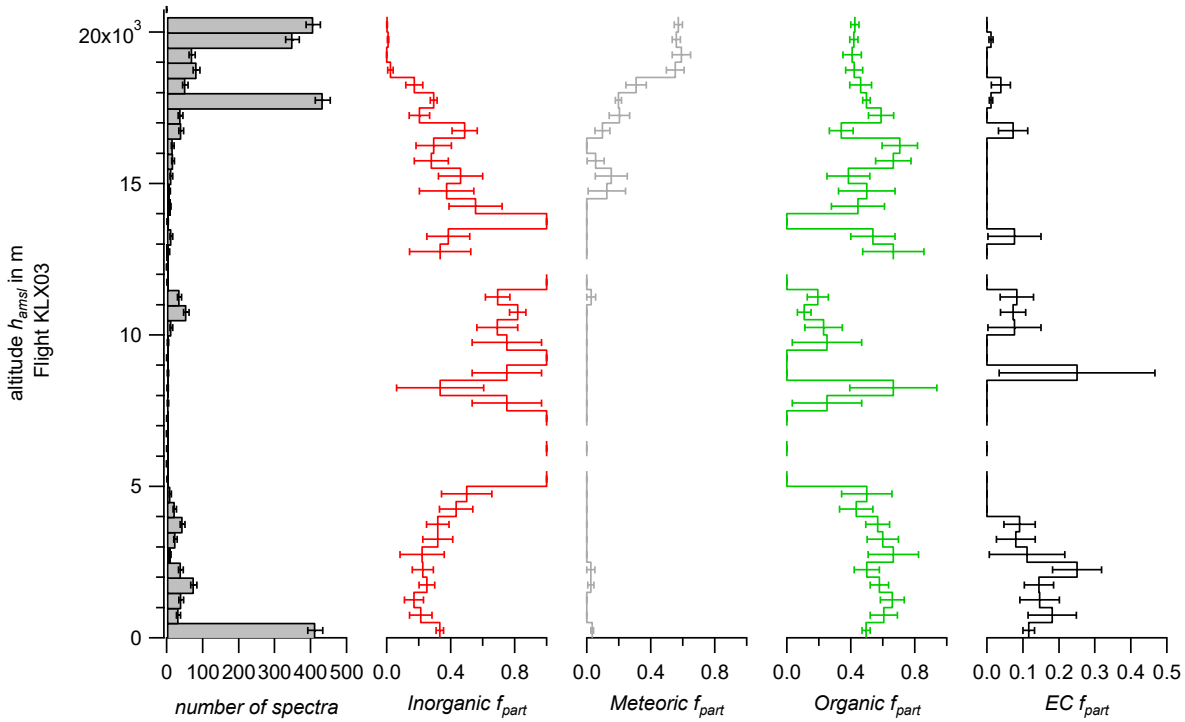

Figure 138: Vertically resolved particle number fractions f_{part} during research flight KLX03 (06.09.2016, 06:48:51 – 10:23:39 UTC) of the particle types: Inorganic (red), Meteoric (gray), Organic (green), and EC (black), normalized to the number of recorded spectra in each bin. The left panel shows the total number of spectra in each bin (black solid bars; in total for KLX03: 2,404). The uncertainties are calculated from counting statistics according to Appendices C.2.2 and C.2.3.

C.8 Asian monsoon phase – flight profiles and flight tracks

As described in Section 5.2 the Asian Monsoon phase of the StratoClim campaign took place in Kathmandu, Nepal, in Southern Asia as part of the subtropical and temperate zone in July and August 2017. Base for this part of the campaign was the Tribhuvan International Airport (KTM; 27.70°N, 85.36°E). Here, the time series of the altitude profiles and flight tracks are presented for each research flight. All following values of altitude h_{amsl}, pressure p_{stat}, and temperature T_{out} were provided by UCSE. The altitude h_{amsl} is the actual elevation above mean sea level (amsl) determined by GPS.

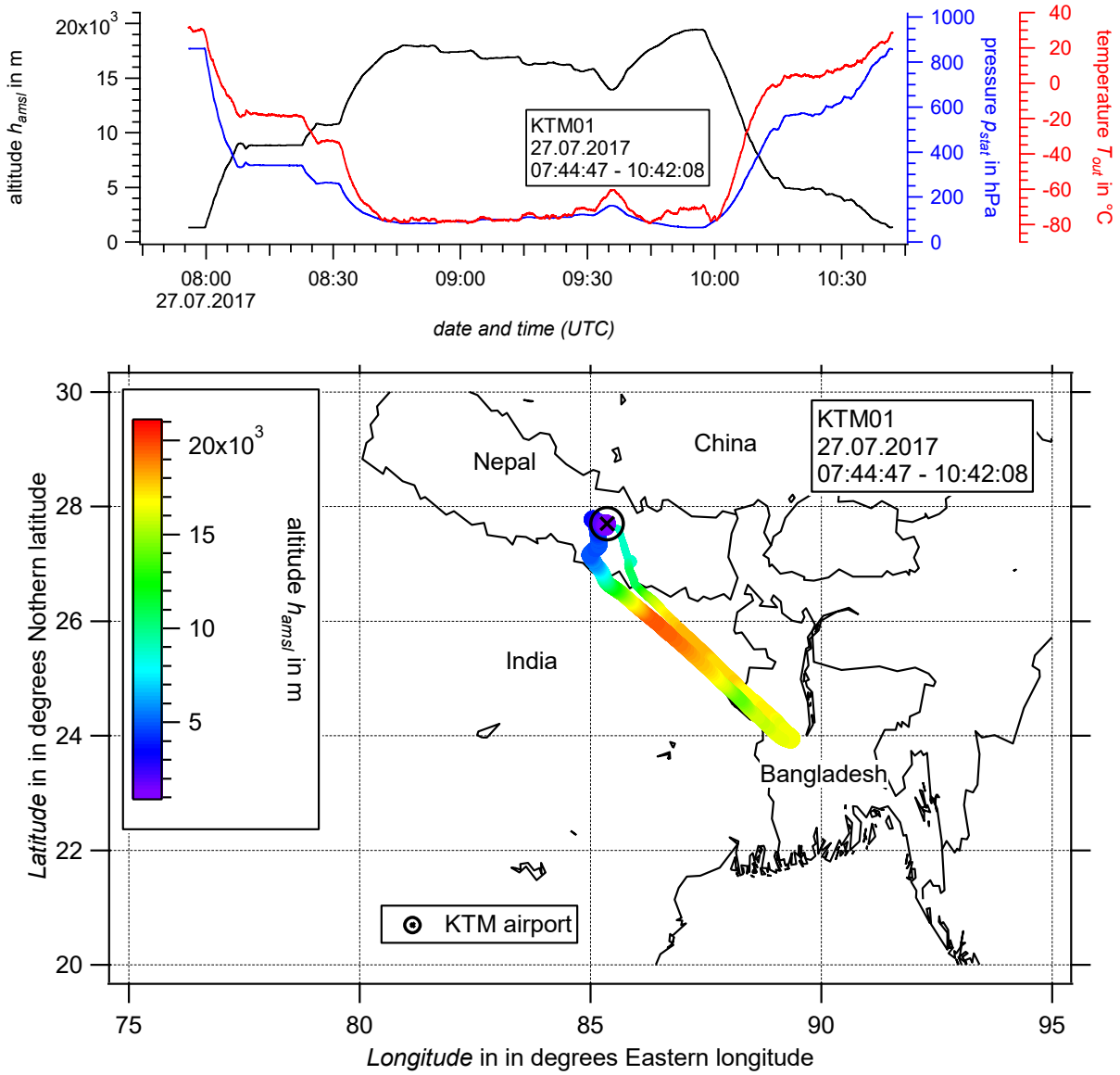

Figure 139: Timeseries of the GPS altitude h_{amsl}, static pressure p_{stat}, and ambient temperature T_{out} provided by UCSE (top) and flight track (bottom) of research flight KTM01 (27.07.2016, 07:44:47 – 10:42:08 (UTC)). The flight track is color-coded to depict the altitude (amsl). The increasing thickness of the line indicates the progress of flight time from takeoff (thinnest) until landing (thickest). The location of Tribhuvan International Airport (KTM) is marked by a black cross.

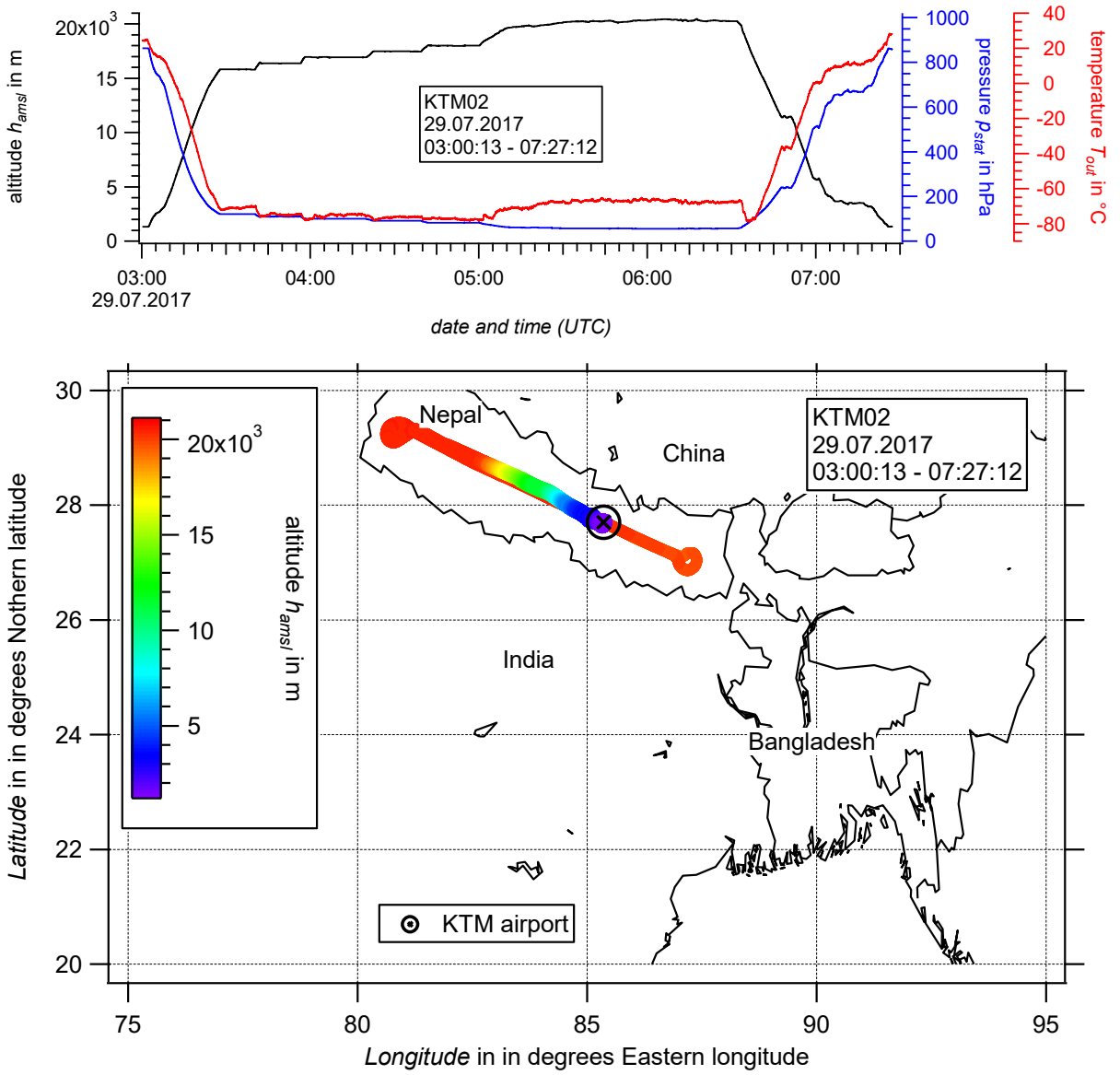

Figure 140: Timeseries of the GPS altitude h_{amsl}, static pressure p_{stat}, and ambient temperature T_{out} provided by UCSE (top) and flight track (bottom) of research flight KTM02 (29.07.2016, 03:00:13 – 07:27:12 (UTC)). The flight track is color-coded to depict the altitude (amsl). The increasing thickness of the line indicates the progress of flight time from takeoff (thinnest) until landing (thickest). The location of Tribhuvan International Airport (KTM) is marked by a black cross.

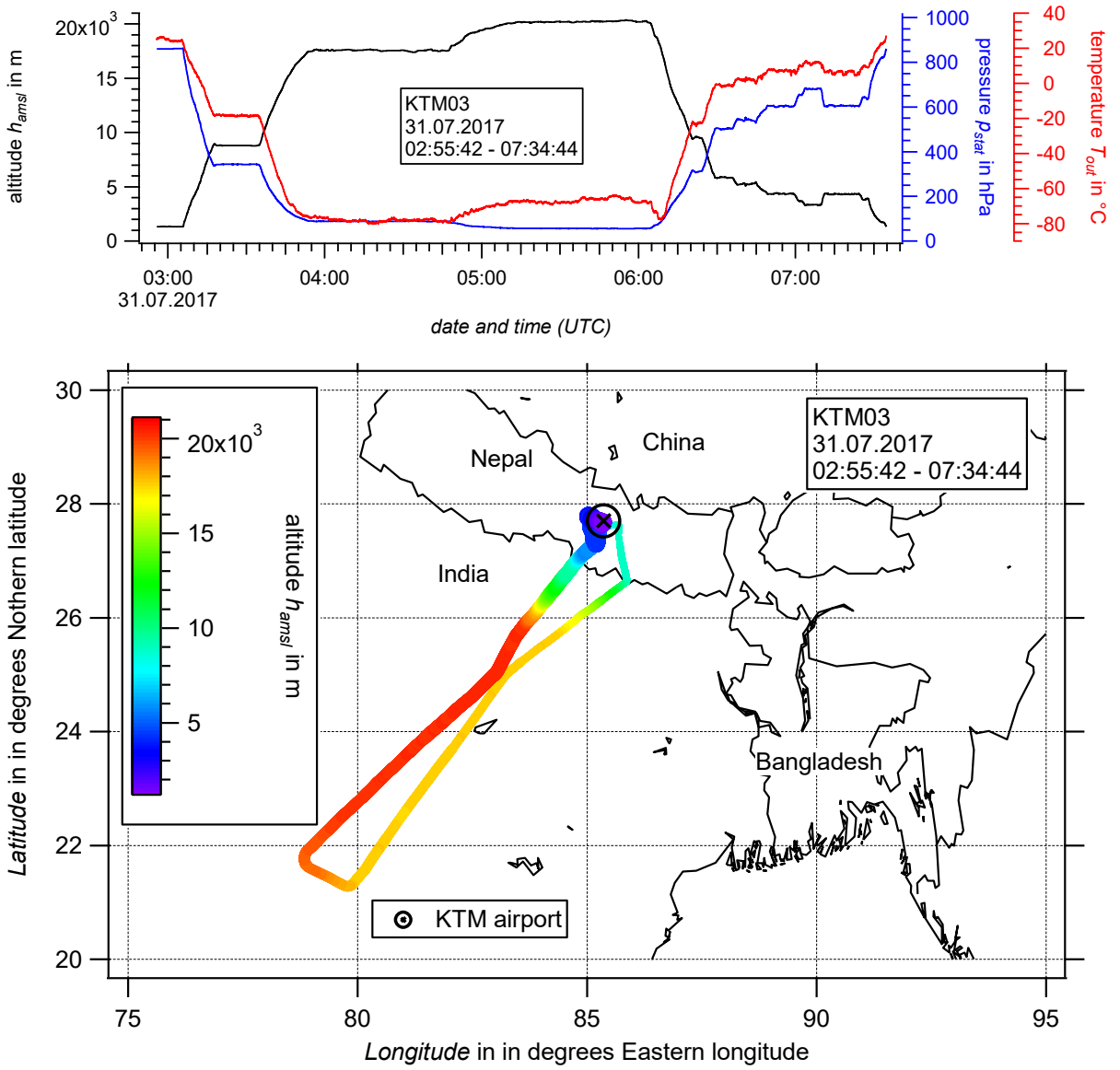

Figure 141: Timeseries of the GPS altitude h_{amsl}, static pressure p_{stat}, and ambient temperature T_{out} provided by UCSE (top) and flight track (bottom) of research flight KTM03 (31.07.2016, 02:55:42 – 07:34:44 (UTC)). The flight track is color-coded to depict the altitude (amsl). The increasing thickness of the line indicates the progress of flight time from takeoff (thinnest) until landing (thickest). The location of Tribhuvan International Airport (KTM) is marked by a black cross.

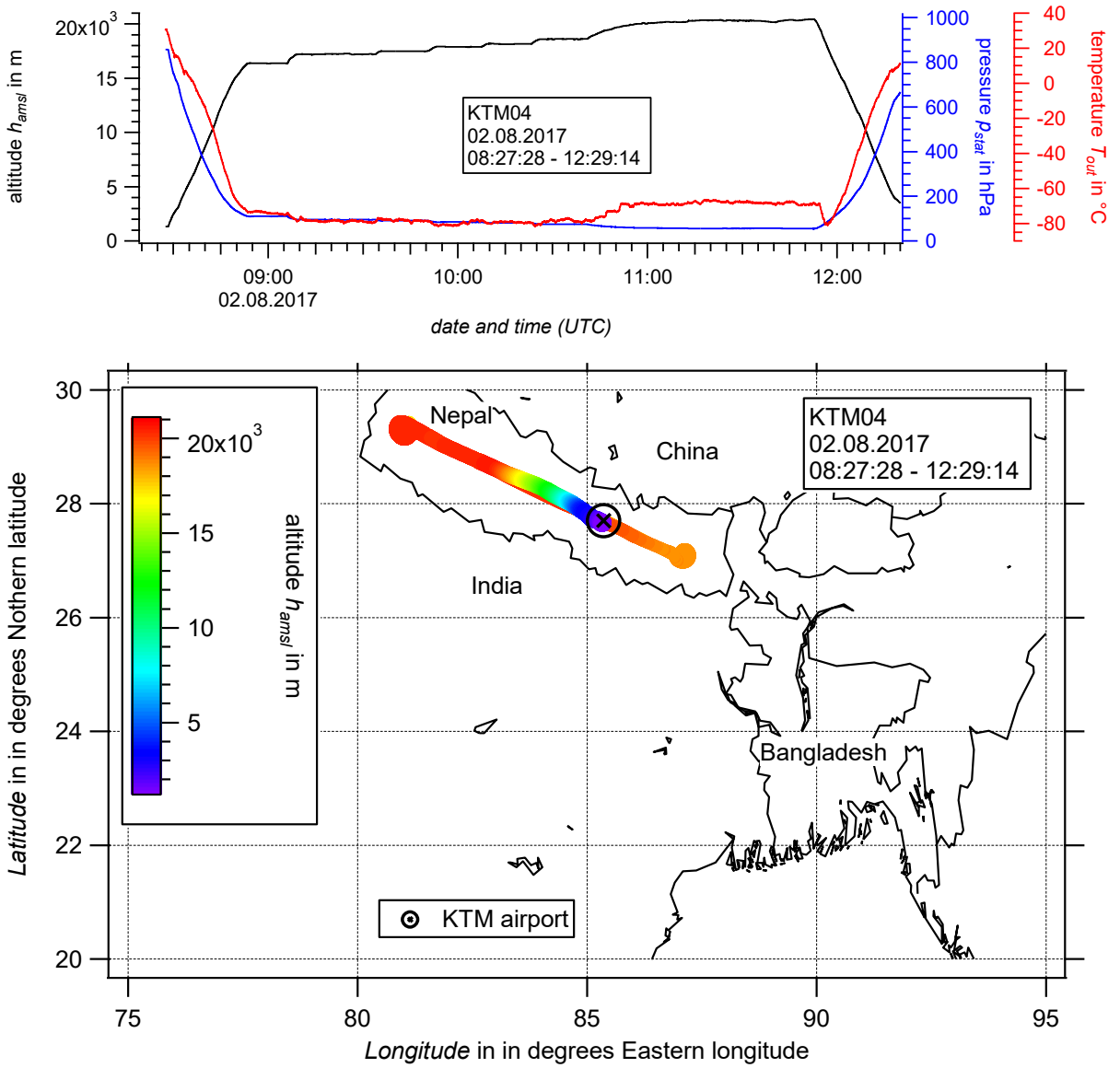

Figure 142: Timeseries of the GPS altitude h_{amsl}, static pressure p_{stat}, and ambient temperature T_{out} provided by UCSE (top) and flight track (bottom) of research flight KTM04 (02.08.2016, 08:27:28 – 12:29:14 (UTC)). The flight track is color-coded to depict the altitude (amsl). The increasing thickness of the line indicates the progress of flight time from takeoff (thinnest) until landing (thickest). The location of Tribhuvan International Airport (KTM) is marked by a black cross.

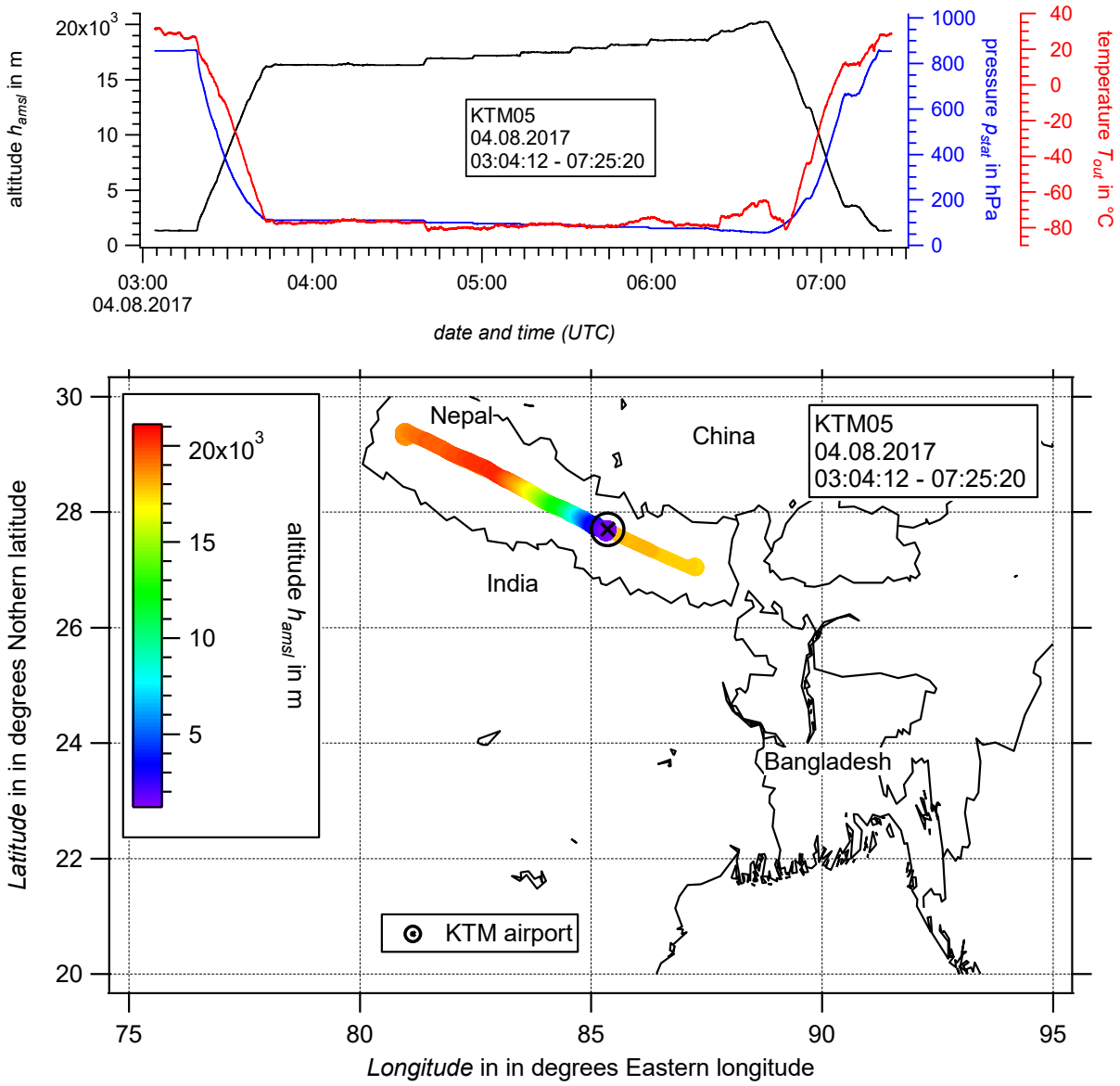

Figure 143: Timeseries of the GPS altitude h_{amsl}, static pressure p_{stat}, and ambient temperature T_{out} provided by UCSE (top) and flight track (bottom) of research flight KTM05 (04.08.2016, 03:04:12 – 07:25:20 (UTC)). The flight track is color-coded to depict the altitude (amsl). The increasing thickness of the line indicates the progress of flight time from takeoff (thinnest) until landing (thickest). The location of Tribhuvan International Airport (KTM) is marked by a black cross.

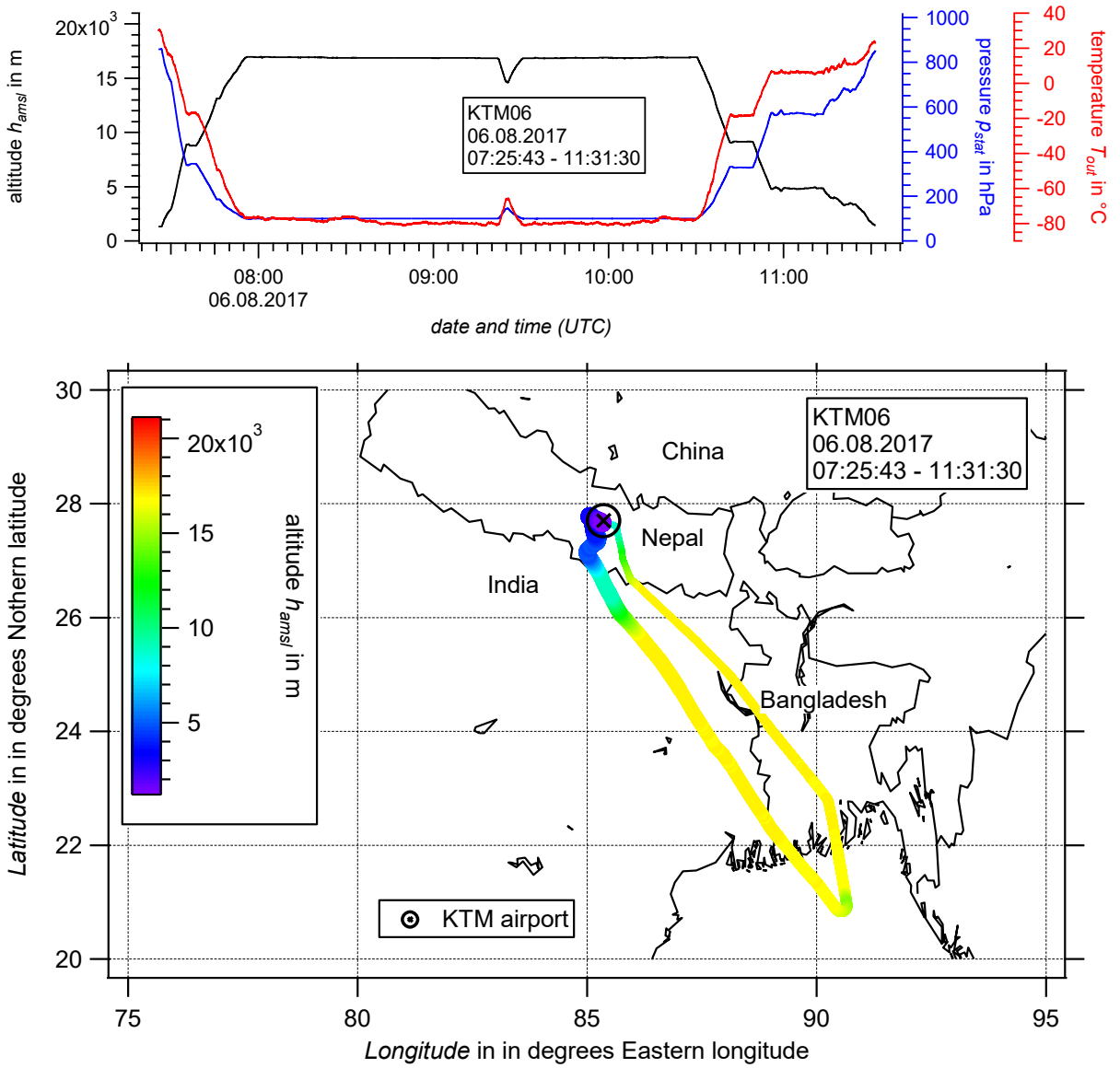

Figure 144: Timeseries of the GPS altitude h_{amsl}, static pressure p_{stat}, and ambient temperature T_{out} provided by UCSE (top) and flight track (bottom) of research flight KTM06 (06.08.2016, 07:25:43 – 11:31:30 (UTC)). The flight track is color-coded to depict the altitude (amsl). The increasing thickness of the line indicates the progress of flight time from takeoff (thinnest) until landing (thickest). The location of Tribhuvan International Airport (KTM) is marked by a black cross.

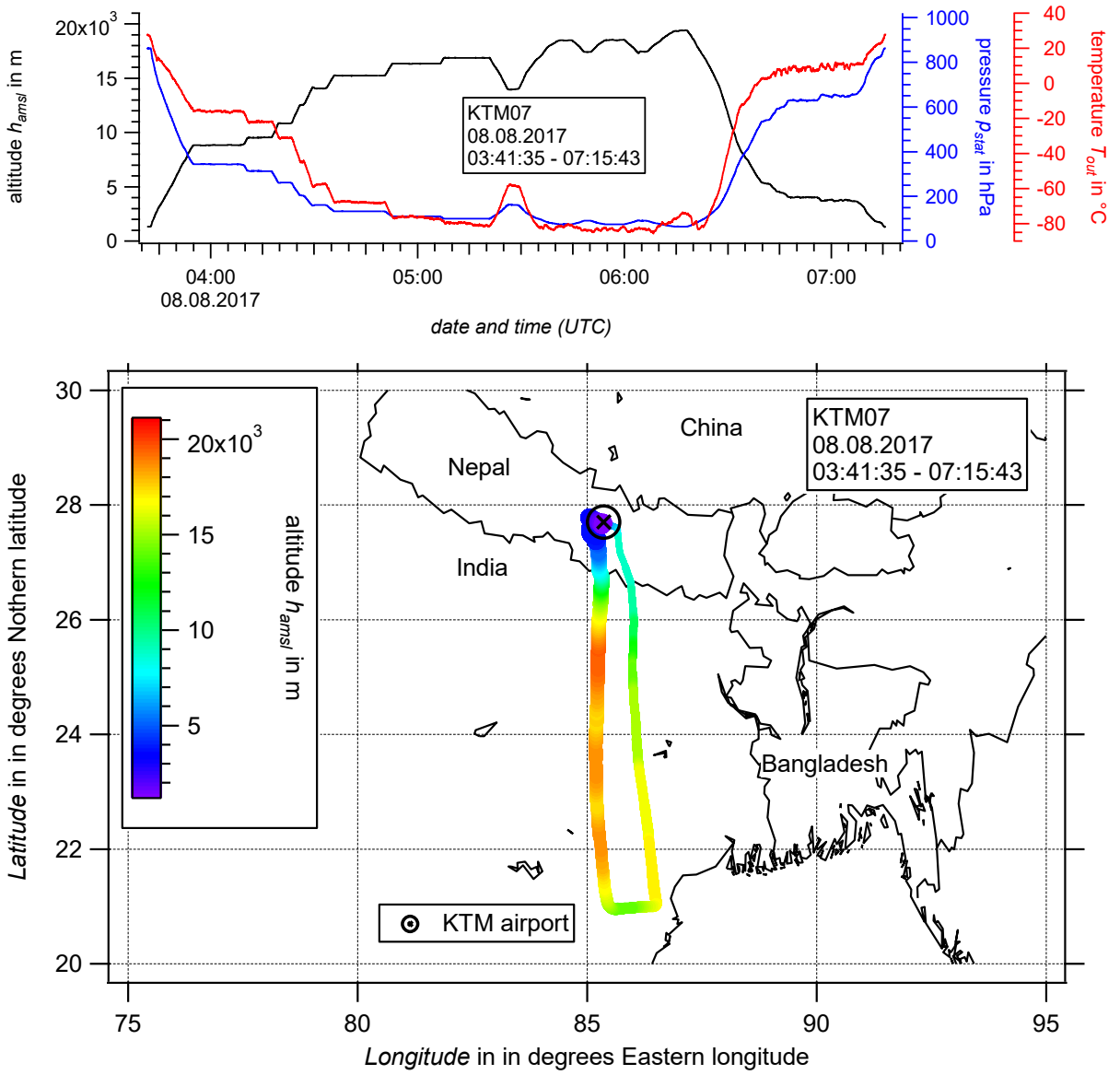

Figure 145: Timeseries of the GPS altitude h_{amsl}, static pressure p_{stat}, and ambient temperature T_{out} provided by UCSE (top) and flight track (bottom) of research flight KTM07 (08.08.2016, 03:41:35 – 07:15:43 (UTC)). The flight track is color-coded to depict the altitude (amsl). The increasing thickness of the line indicates the progress of flight time from takeoff (thinnest) until landing (thickest). The location of Tribhuvan International Airport (KTM) is marked by a black cross.

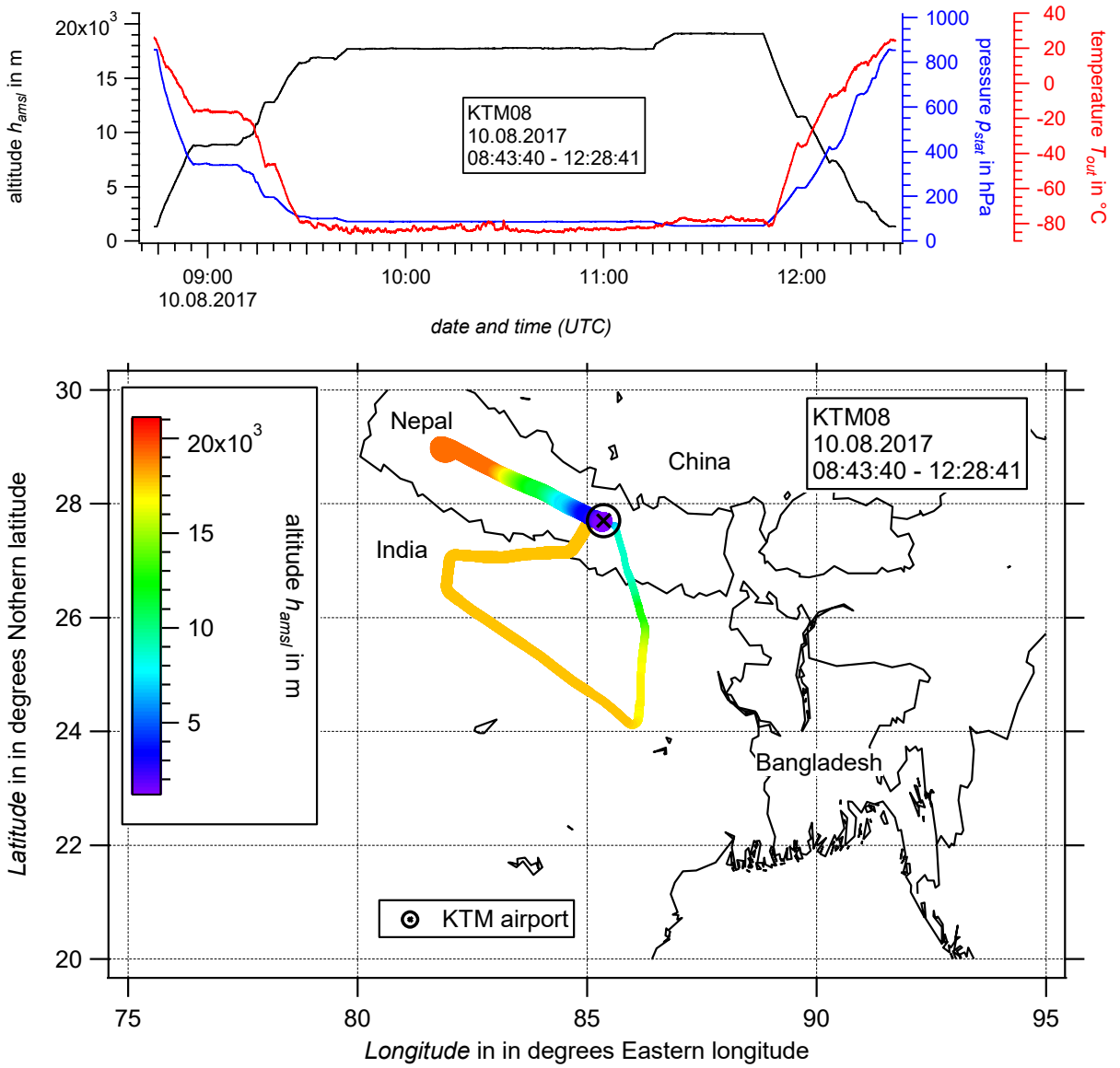

Figure 146: Timeseries of the GPS altitude h_{amsl}, static pressure p_{stat}, and ambient temperature T_{out} provided by UCSE (top) and flight track (bottom) of research flight KTM08 (10.08.2016, 08:43:40 – 12:28:41 (UTC)). The flight track is color-coded to depict the altitude (amsl). The increasing thickness of the line indicates the progress of flight time from takeoff (thinnest) until landing (thickest). The location of Tribhuvan International Airport (KTM) is marked by a black cross.

C.9 Asian monsoon phase – mean spectra

As described in Section 5.2.1 the data set of the single particle mass spectra was evaluated by using the *k-means* clustering algorithm. The initial and thus resulting 30 clusters were reduced to seven groups by combining the automatically identified clusters in a meaningful way: *KOrgNOSO*, *MetalOrgNOSO*, *Meteoric*, *EC*, *Inorganic*, *NOSO* and *OrgNOSO*. In the following, the mean spectra of each particle type are presented individually for each research flight. The mean spectra are generated after the clustering and subsequent manual assignment procedure. Each individual particle mass spectrum of a particle type is assigned to the respective flight by means of the time stamp (see also Figure 72). Thus, the flight-to-flight differences of the mean spectra within the individual particle types are small. The flight-to-flight variability is apparently lower for the *NOSO*, *OrgNOSO*, *Meteoric,* and *EC* particle types than for the other three particle types. This indicates for all these four particle types that the aerosol on which the mass spectra are based might be freshly formed and thus be non-aged. An exception is flight KTM01 for the *OrgNOSO* particle type. Here, the anion spectrum contains organic and nitrate fragments as well as sulfate fragments. In the cation spectrum the organic fragment $C_4H_9^+$ occurs, which does not occur in the other *OrgNOSO* mean spectra. For the particle types *Inorganic*, *MetalOrgNOSO*, and *KOrgNOSO* the variability is more pronounced. For example, the *Inorganic* particle type in flight KTM01 does not contain sulfate fragments in the mean spectrum compared to the other flights. The stronger variability can either indicate aged aerosol or different aerosol types and sources combined in one particle type. This requires further investigation, which is beyond the scope of this thesis.

The number of spectra that are basis for the mean spectra are depicted in the pie charts for each individual flight shown in Figure 73 (see Section 5.2.1).

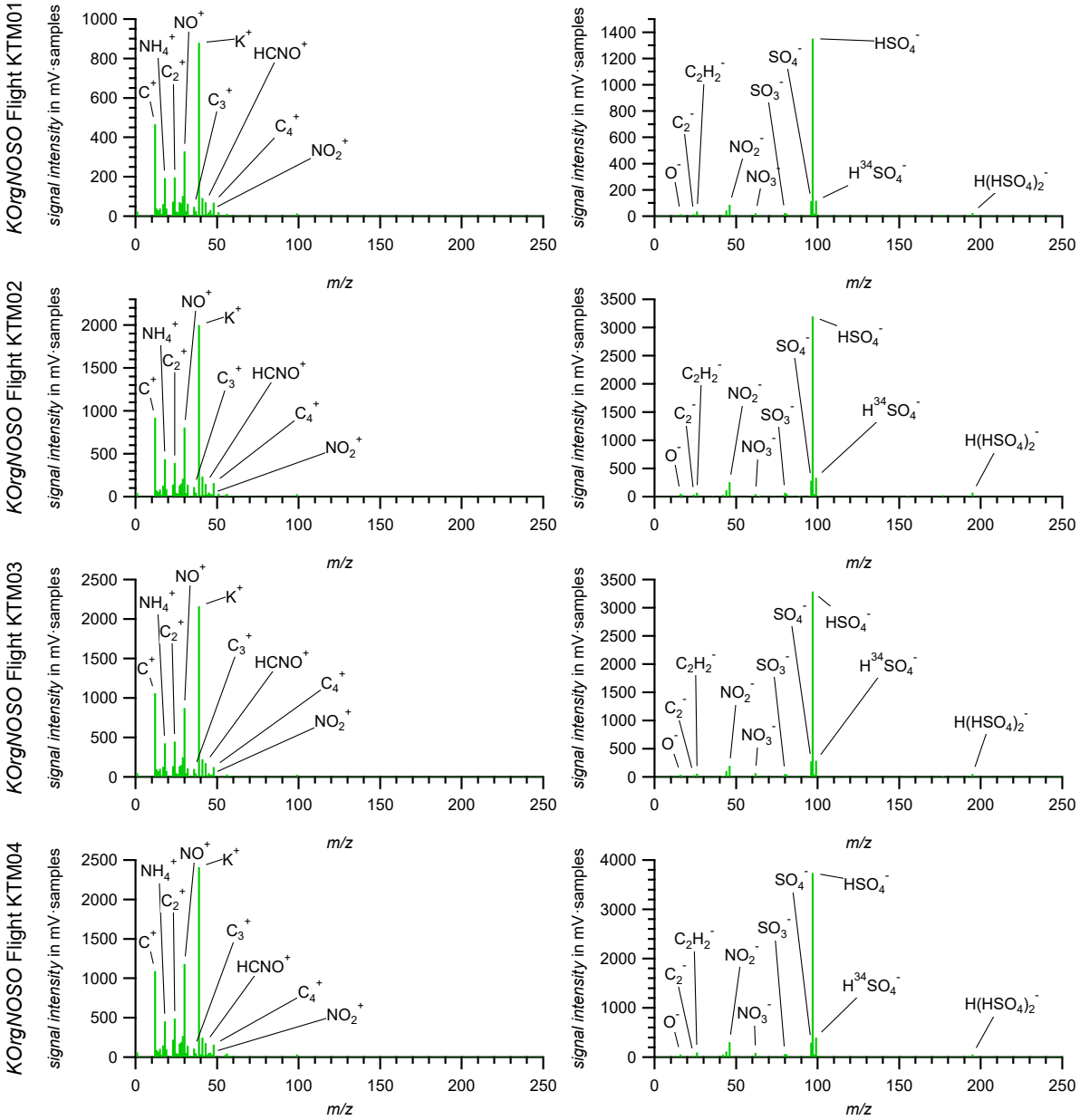

Figure 147: Mean stick spectra (left: cations, right: anions) of the KOrgNOSO particle type (green) for research flights KTM01 – KTM04 in the Asian monsoon phase of StratoClim. Identified characteristic peaks are tagged with the most likely fragment/ion species.

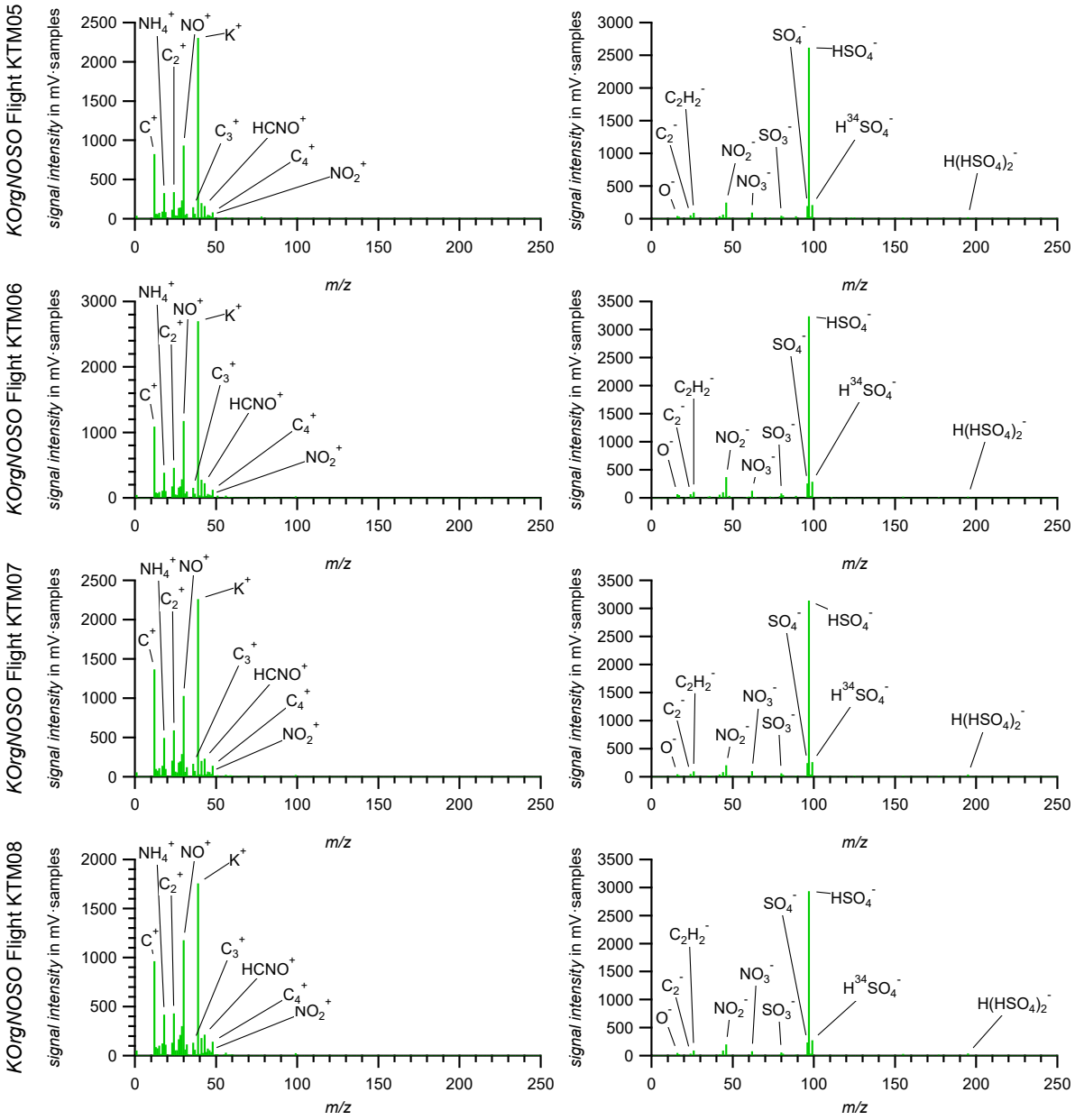

Figure 148: Mean stick spectra (left: cations, right: anions) of the KOrgNOSO particle type (green) for research flights KTM05 – KTM08 in the Asian monsoon phase of StratoClim. Identified characteristic peaks are tagged with the most likely fragment/ion species.

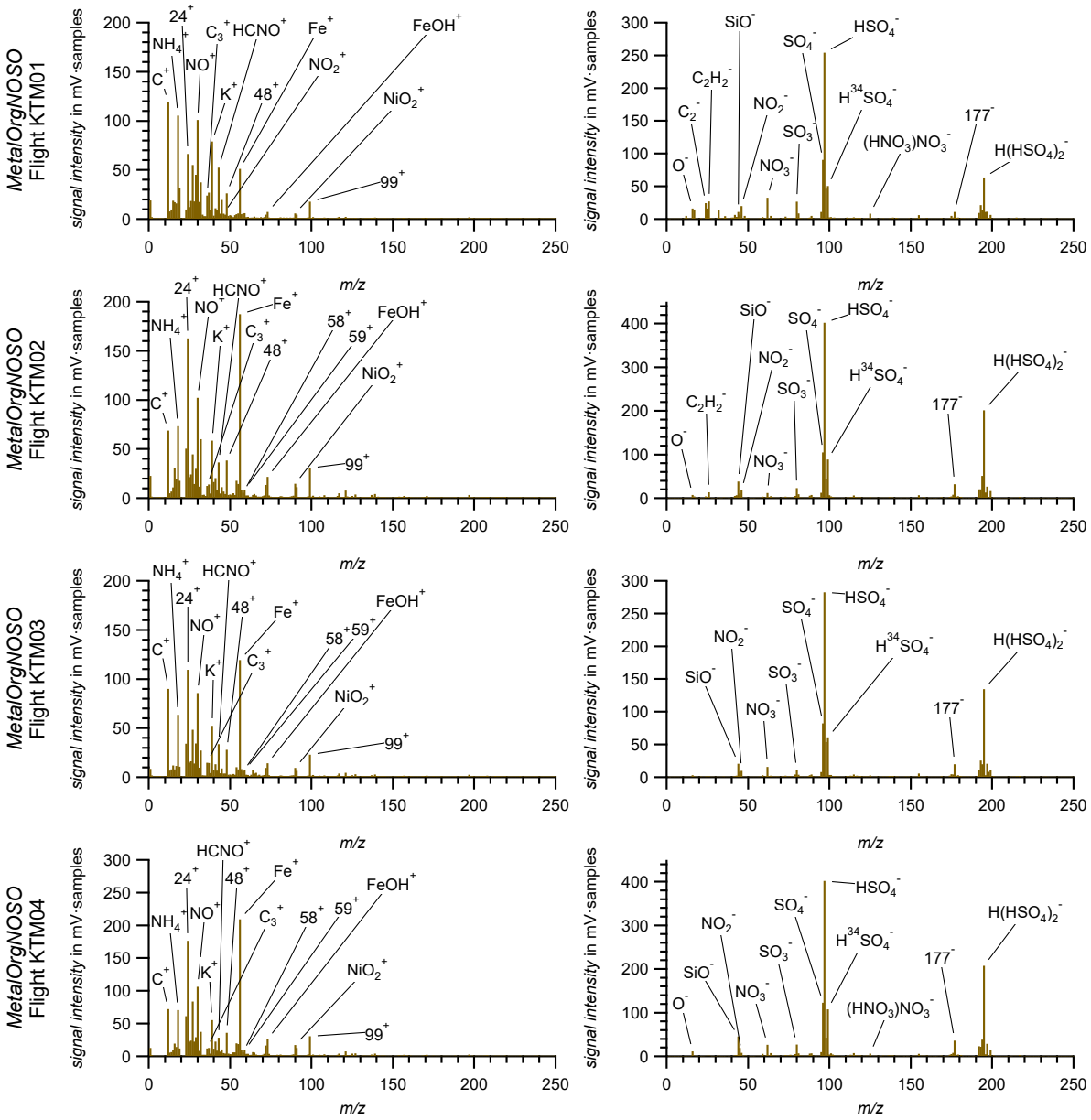

Figure 149: Mean stick spectra (left: cations, right: anions) of the MetalOrgNOSO particle type (brown) for research flights KTM01 – KTM04 in the Asian monsoon phase of StratoClim. Identified characteristic peaks are tagged with the most likely fragment/ion species. For lines at which only the m/z number are provided an unambiguous identification of the ions was not possible.

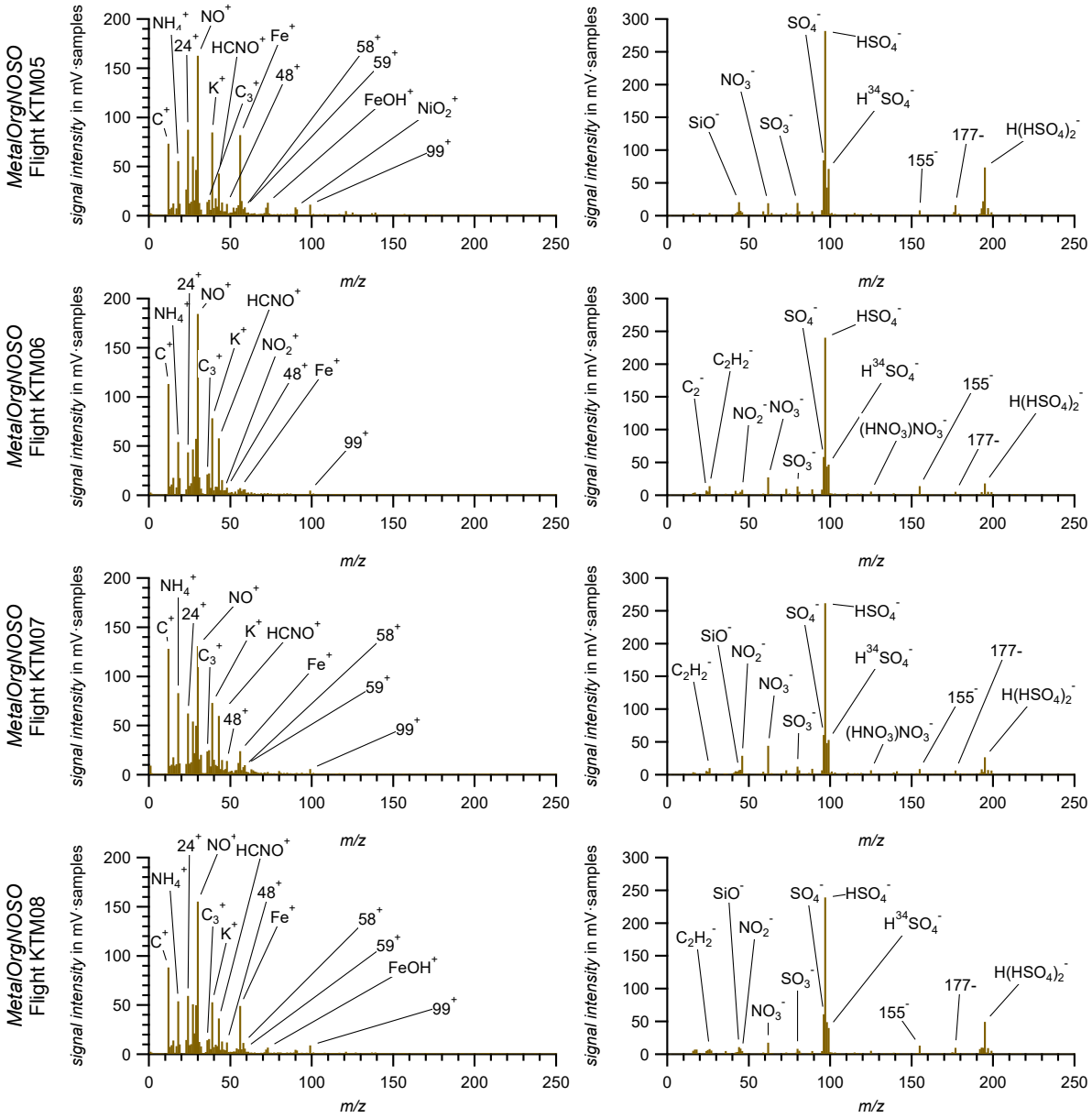

Figure 150: Mean stick spectra (left: cations, right: anions) of the MetalOrgNOSO particle type (brown) for research flights KTM05 – KTM08 in the Asian monsoon phase of StratoClim. Identified characteristic peaks are tagged with the most likely fragment/ion species. For lines at which only the m/z number are provided an unambiguous identification of the ions was not possible.

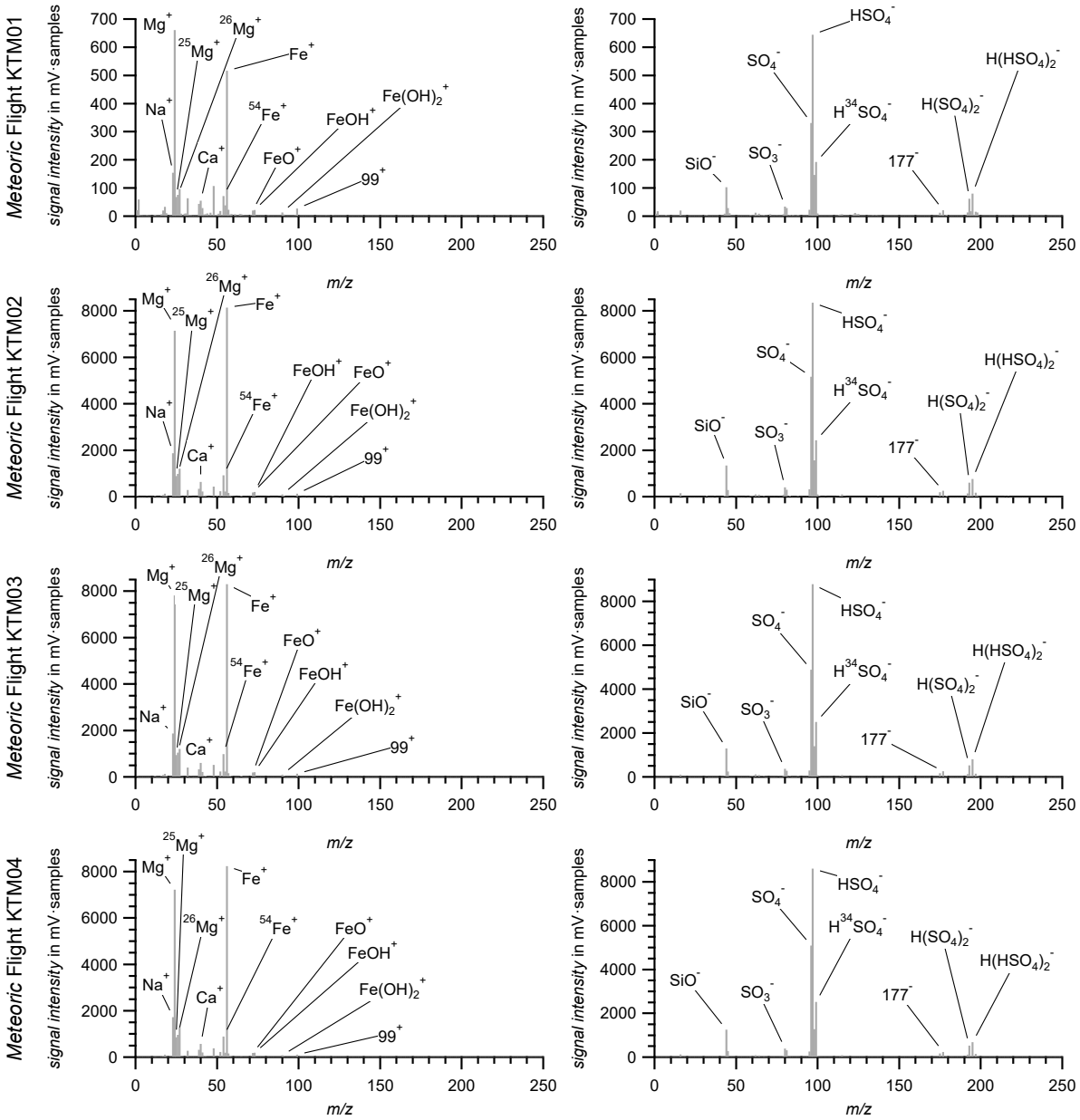

Figure 151: Mean stick spectra (left: cations, right: anions) of the Meteoric particle type (gray) for research flights KTM01 – KTM04 in the Asian monsoon phase of StratoClim. Identified characteristic peaks are tagged with the most likely fragment/ion species. For lines at which only the m/z number are provided an unambiguous identification of the ions was not possible.

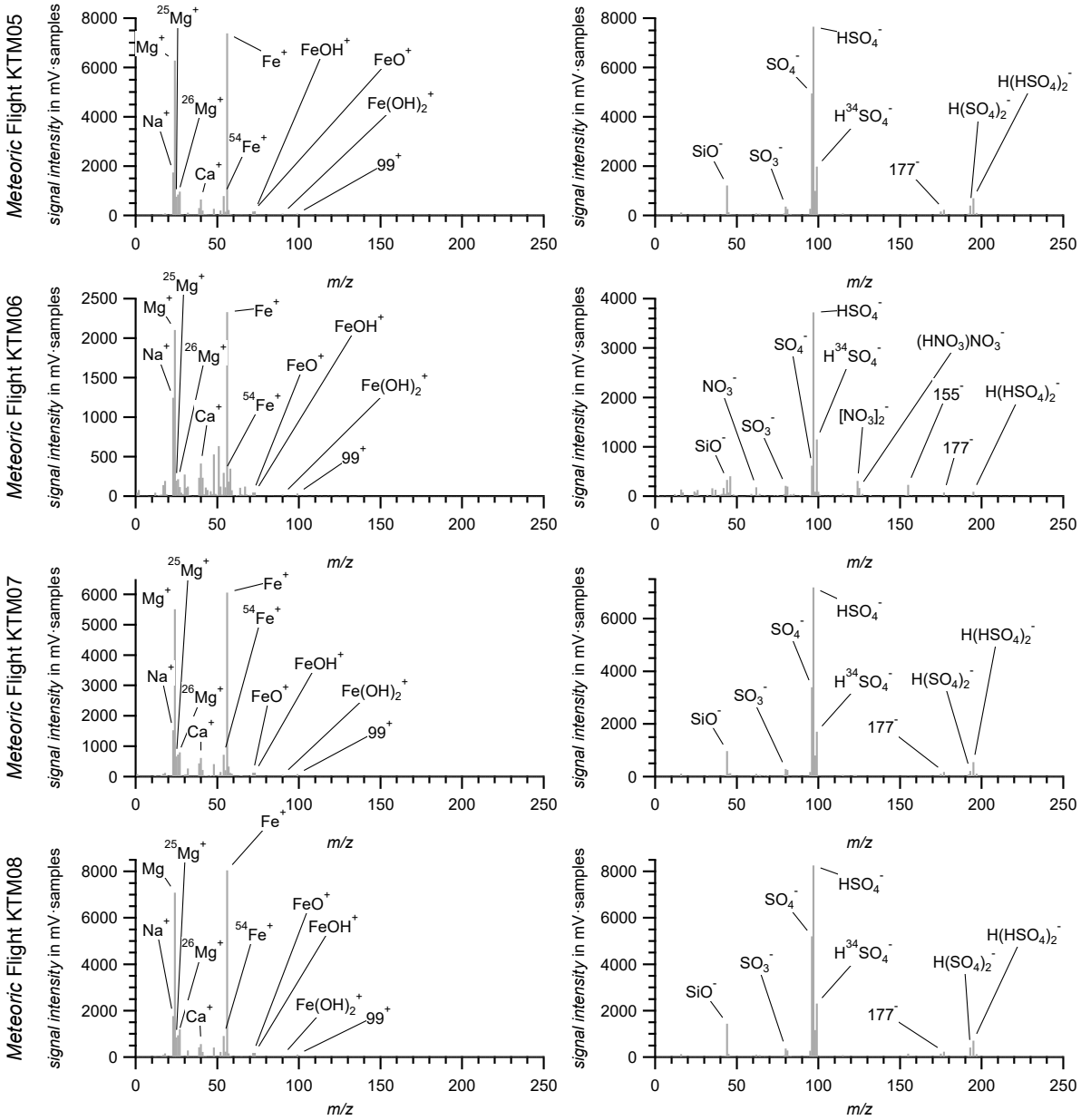

Figure 152: Mean stick spectra (left: cations, right: anions) of the Meteoric particle type (gray) for research flights KTM05 – KTM08 in the Asian monsoon phase of StratoClim. Identified characteristic peaks are tagged with the most likely fragment/ion species. For lines at which only the m/z number are provided an unambiguous identification of the ions was not possible.

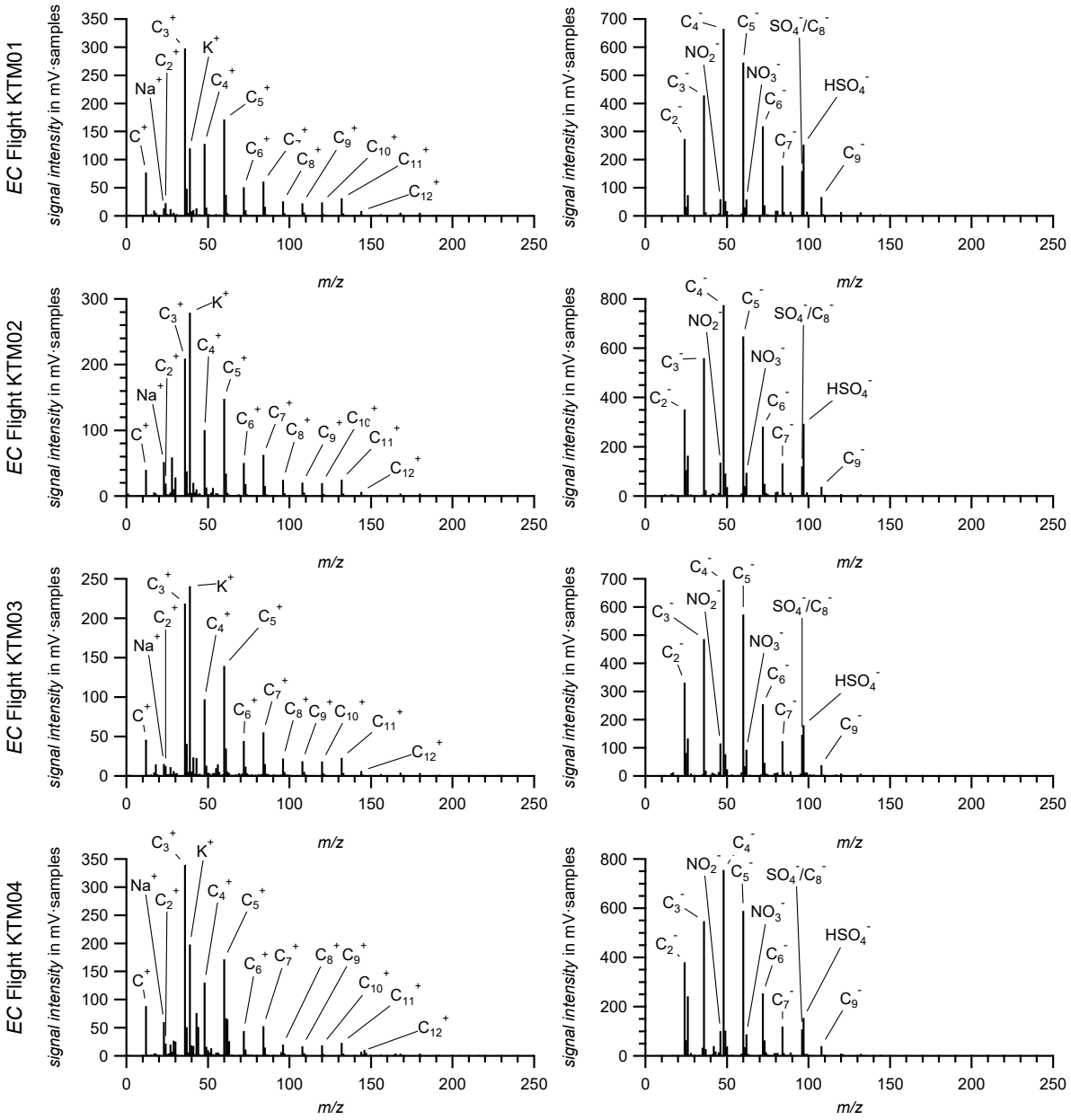

Figure 153: Mean stick spectra (left: cations, right: anions) of the EC particle type (black) for research flights KTM01 – KTM04 in the Asian monsoon phase of StratoClim. Identified characteristic peaks are tagged with the most likely fragment/ion species.

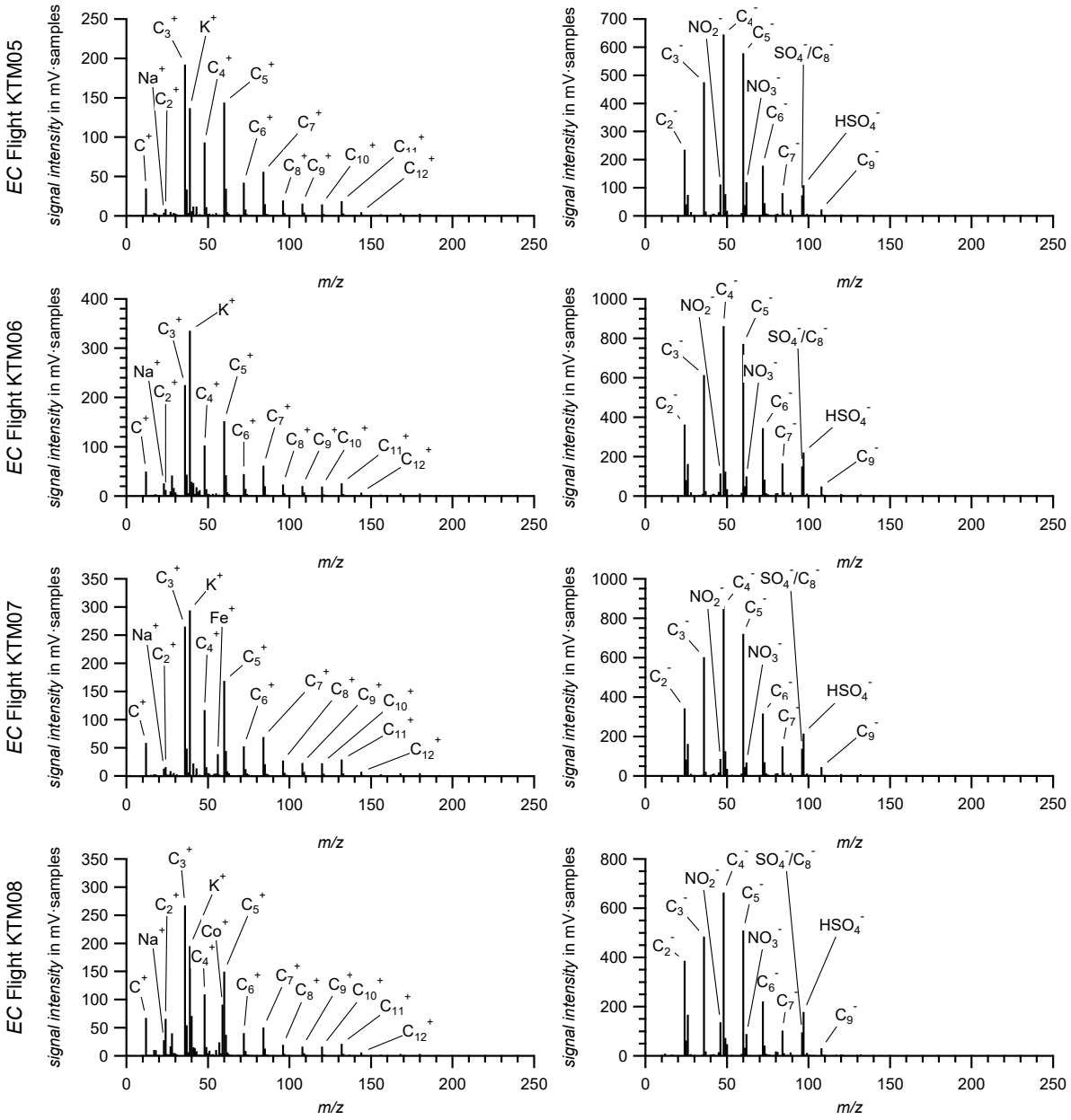

Figure 154: Mean stick spectra (left: cations, right: anions) of the EC particle type (black) for research flights KTM05 – KTM08 in the Asian monsoon phase of StratoClim. Identified characteristic peaks are tagged with the most likely fragment/ion species.

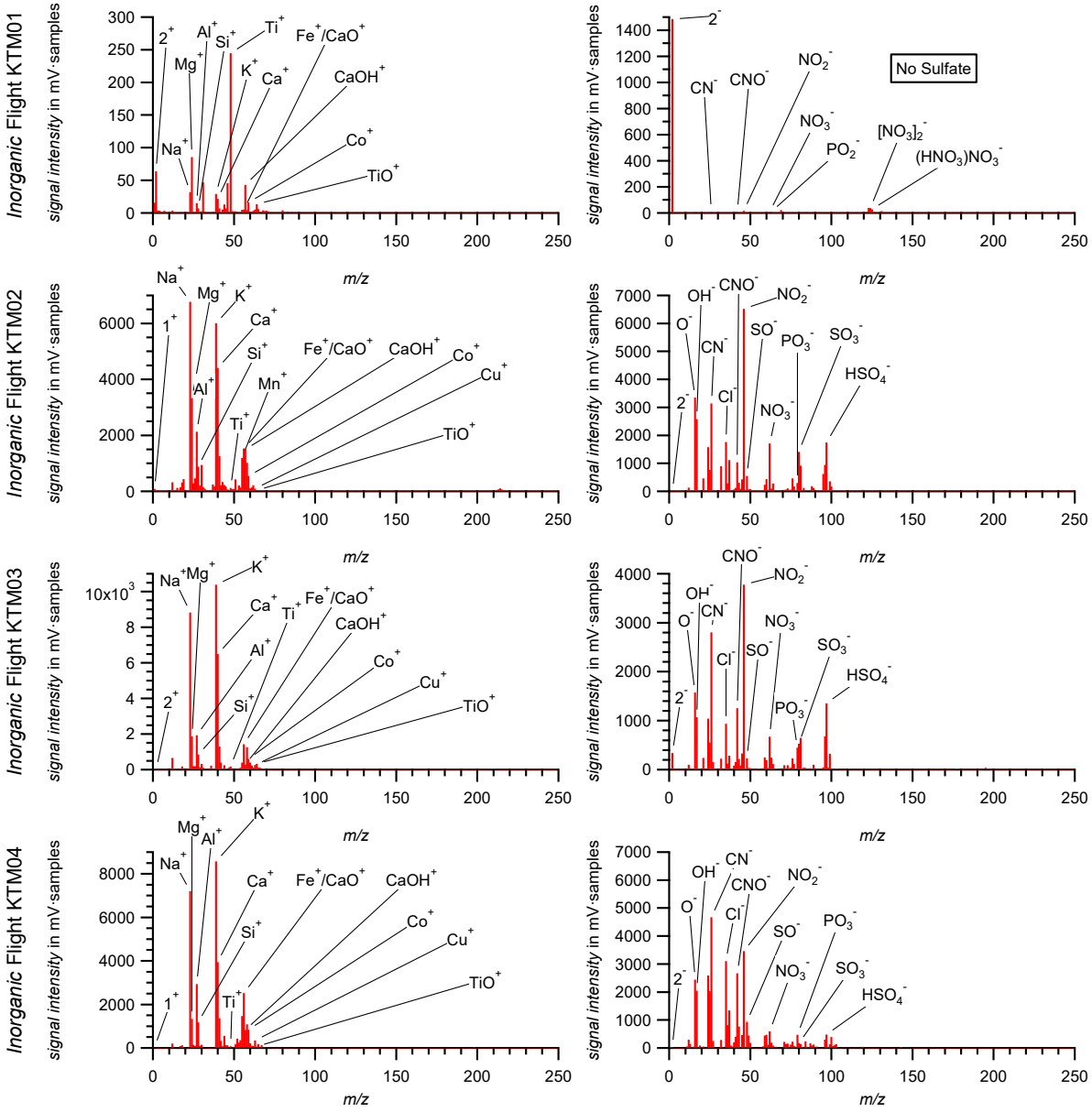

Figure 155: Mean stick spectra (left: cations, right: anions) of the Inorganic particle type (red) for research flights KTM01 – KTM04 in the Asian monsoon phase of StratoClim. Identified characteristic peaks are tagged with the most likely fragment/ion species. For lines at which only the m/z number are provided an unambiguous identification of the ions was not possible.

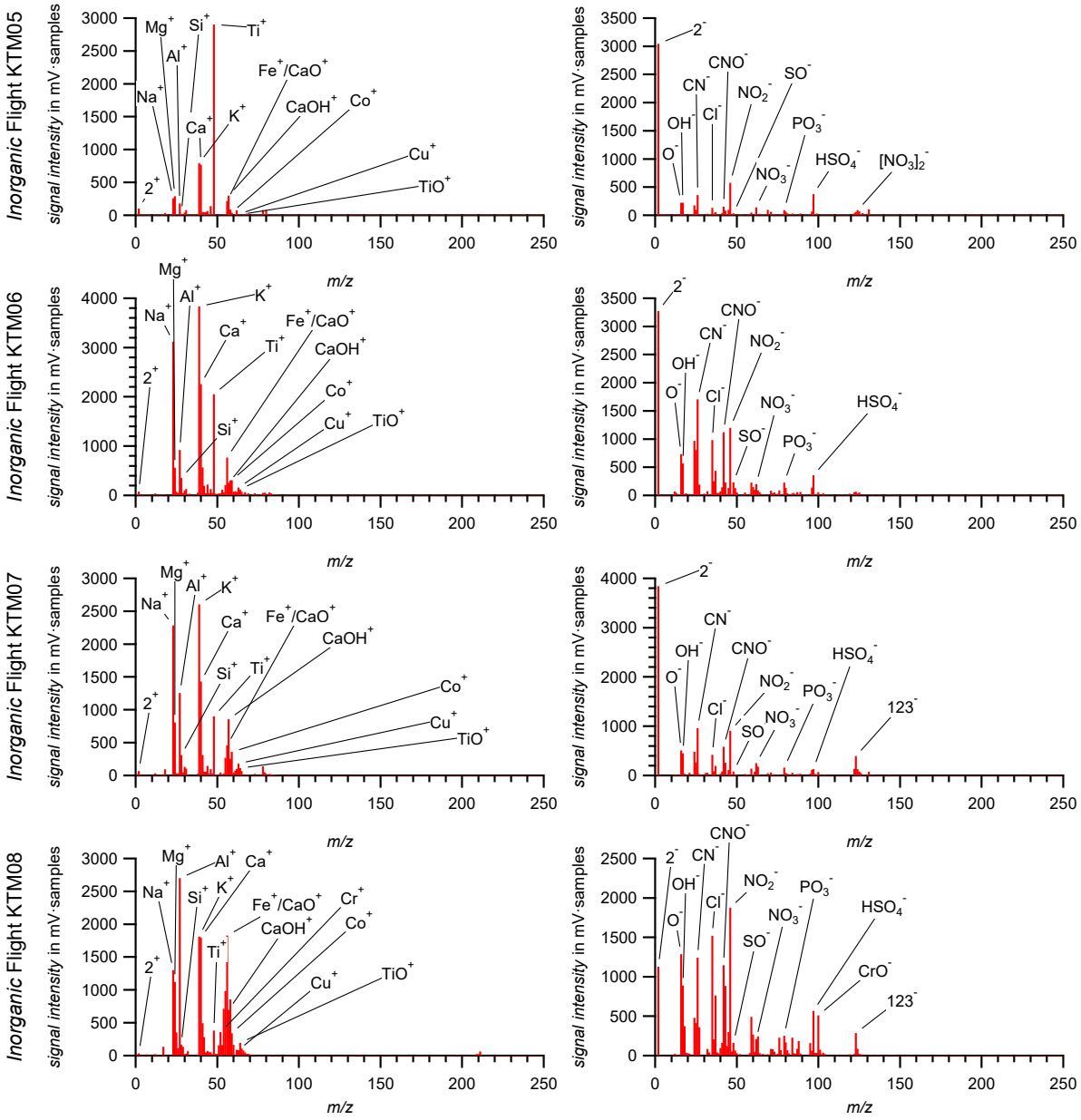

Figure 156: Mean stick spectra (left: cations, right: anions) of the Inorganic particle type (red) for research flights KTM05 – KTM08 in the Asian monsoon phase of StratoClim. Identified characteristic peaks are tagged with the most likely fragment/ion species. For lines at which only the m/z number are provided an unambiguous identification of the ions was not possible.

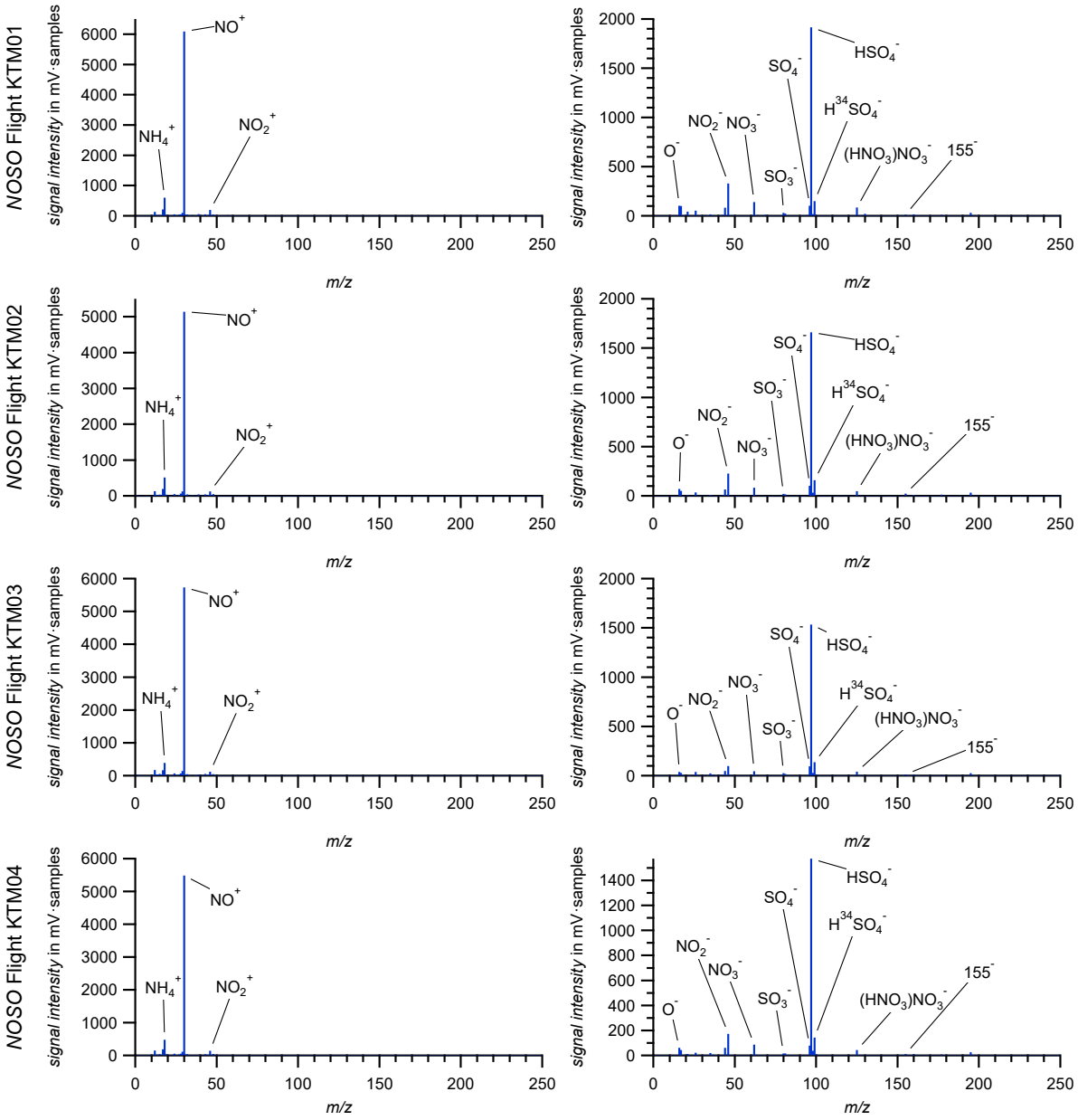

Figure 157: Mean stick spectra (left: cations, right: anions) of the NOSO particle type (blue) for research flights KTM01 – KTM04 in the Asian monsoon phase of StratoClim. Identified characteristic peaks are tagged with the most likely fragment/ion species. For lines at which only the m/z number are provided an unambiguous identification of the ions was not possible.

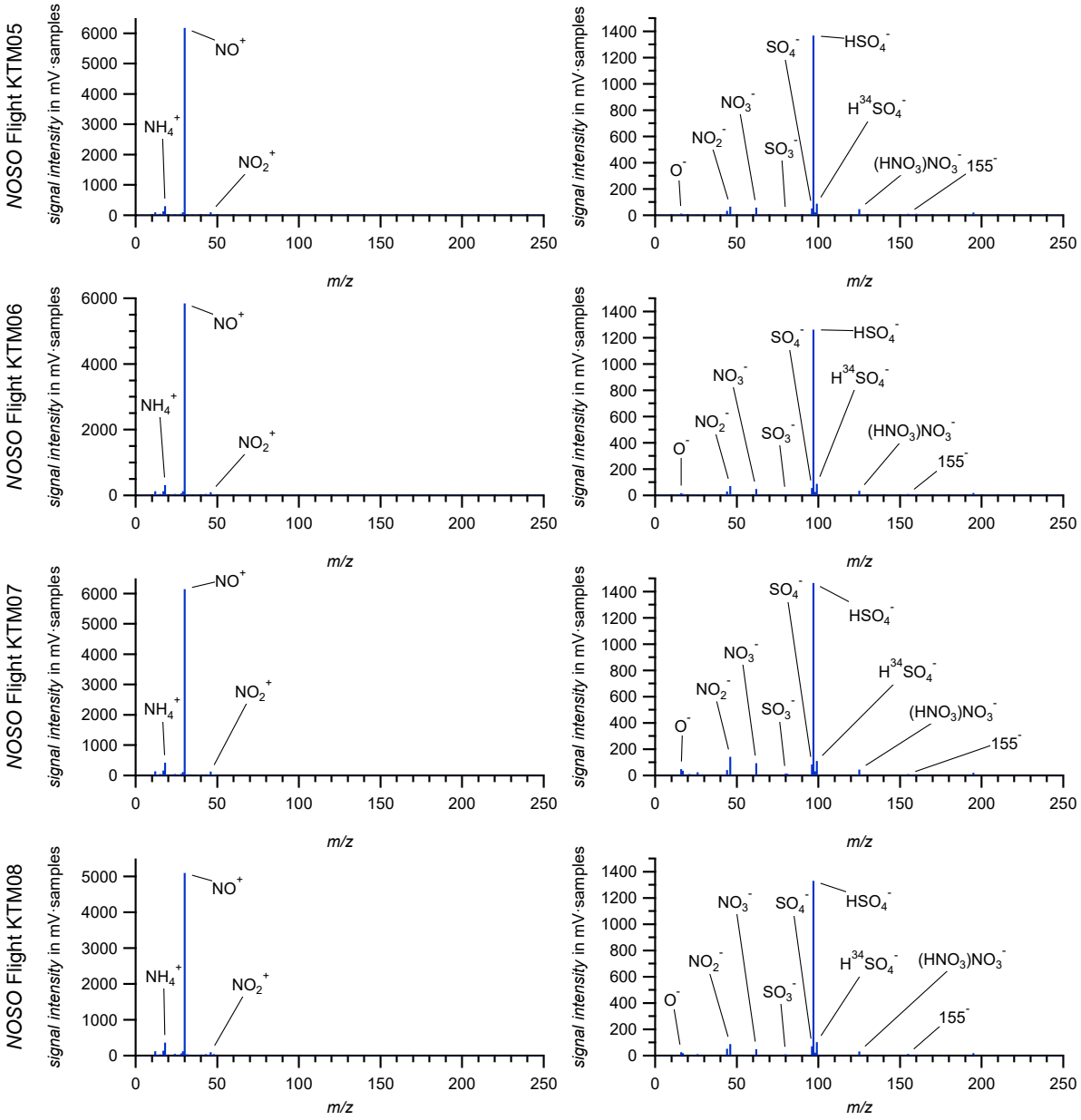

Figure 158: Mean stick spectra (left: cations, right: anions) of the NOSO particle type (blue) for research flights KTM05 – KTM08 in the Asian monsoon phase of StratoClim. Identified characteristic peaks are tagged with the most likely fragment/ion species. For lines at which only the m/z number are provided an unambiguous identification of the ions was not possible.

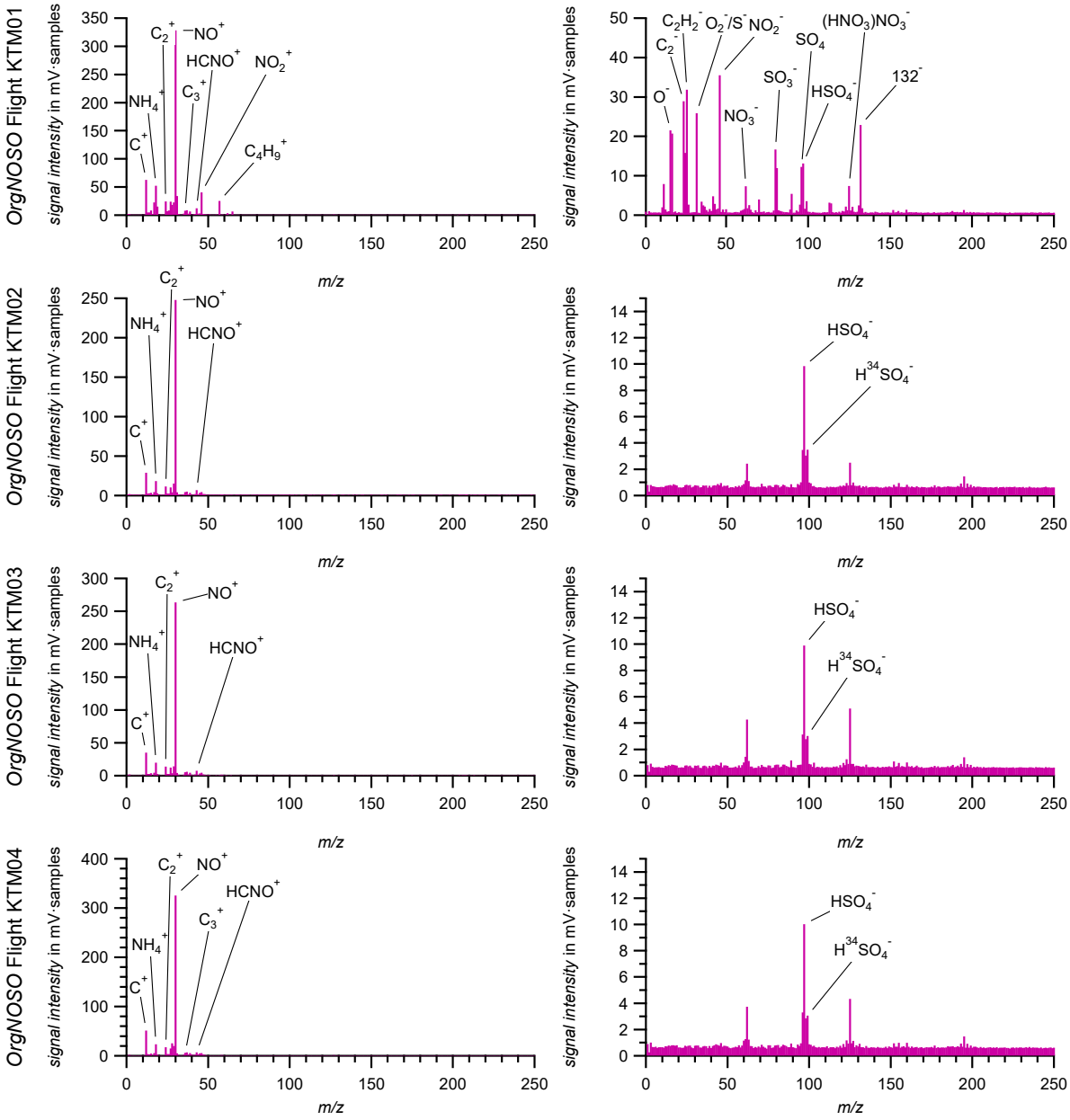

Figure 159: Mean stick spectra (left: cations, right: anions) of the OrgNOSO particle type (purple) for research flights KTM01 – KTM04 in the Asian monsoon phase of StratoClim. Identified characteristic peaks are tagged with the most likely fragment/ion species. For lines at which only the m/z number are provided an unambiguous identification of the ions was not possible.

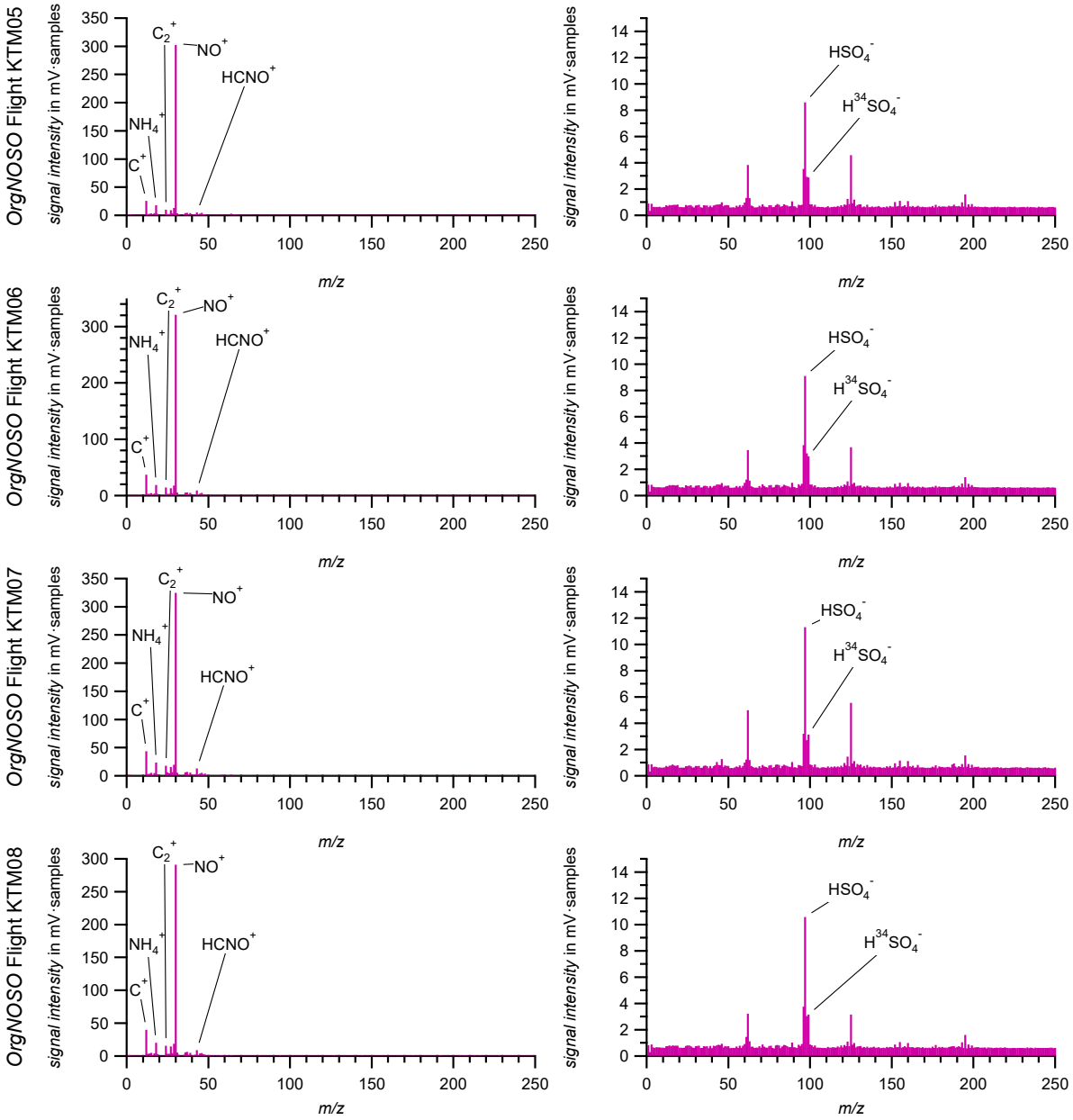

Figure 160: Mean stick spectra (left: cations, right: anions) of the OrgNOSO particle type (purple) for research flights KTM05 – KTM08 in the Asian monsoon phase of StratoClim. Identified characteristic peaks are tagged with the most likely fragment/ion species.

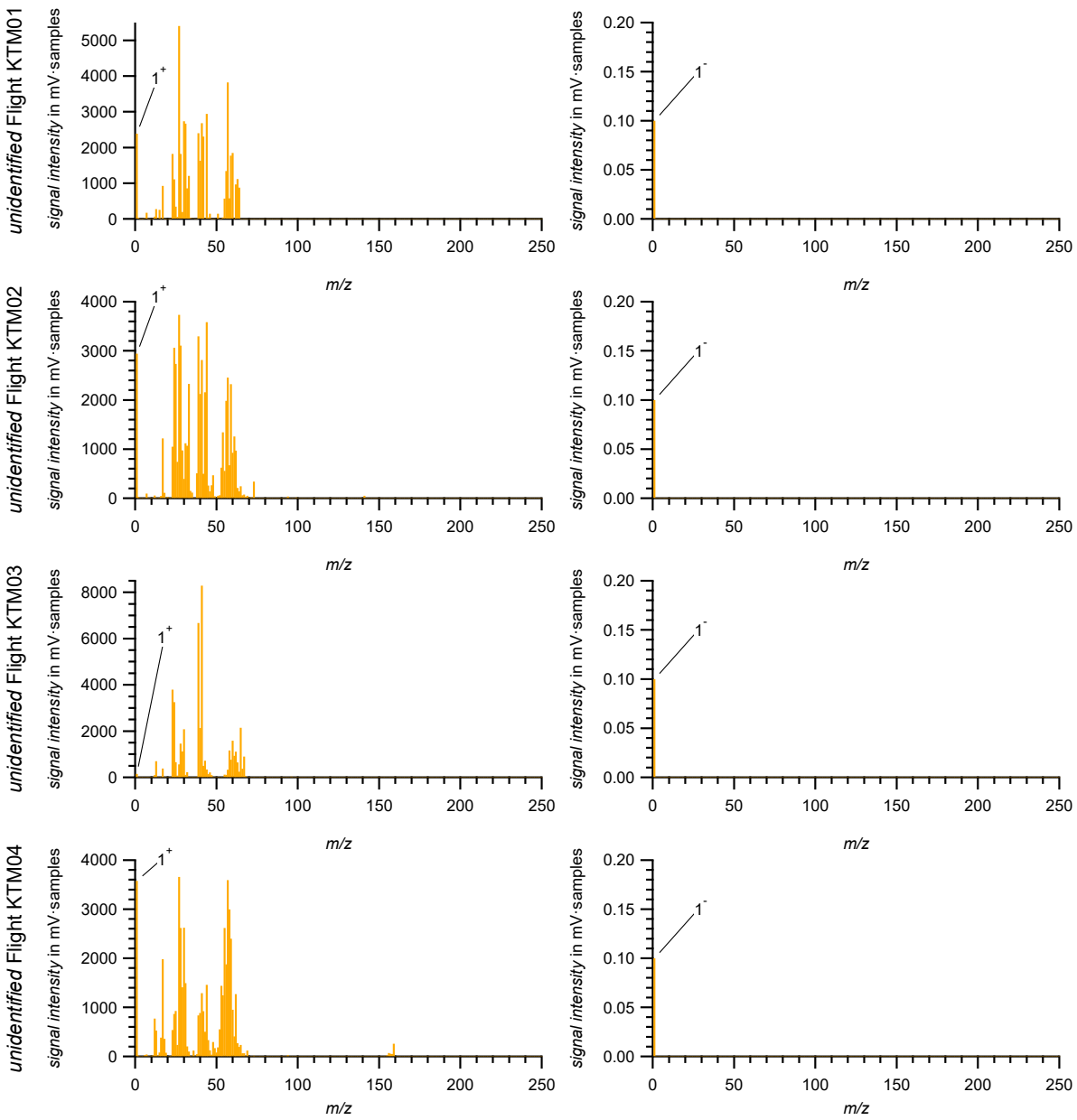

Figure 161: Mean stick spectra (left: cations, right: anions) of the unidentified particle type (orange) for research flights KTM01 – KTM04 in the Asian monsoon phase of StratoClim.

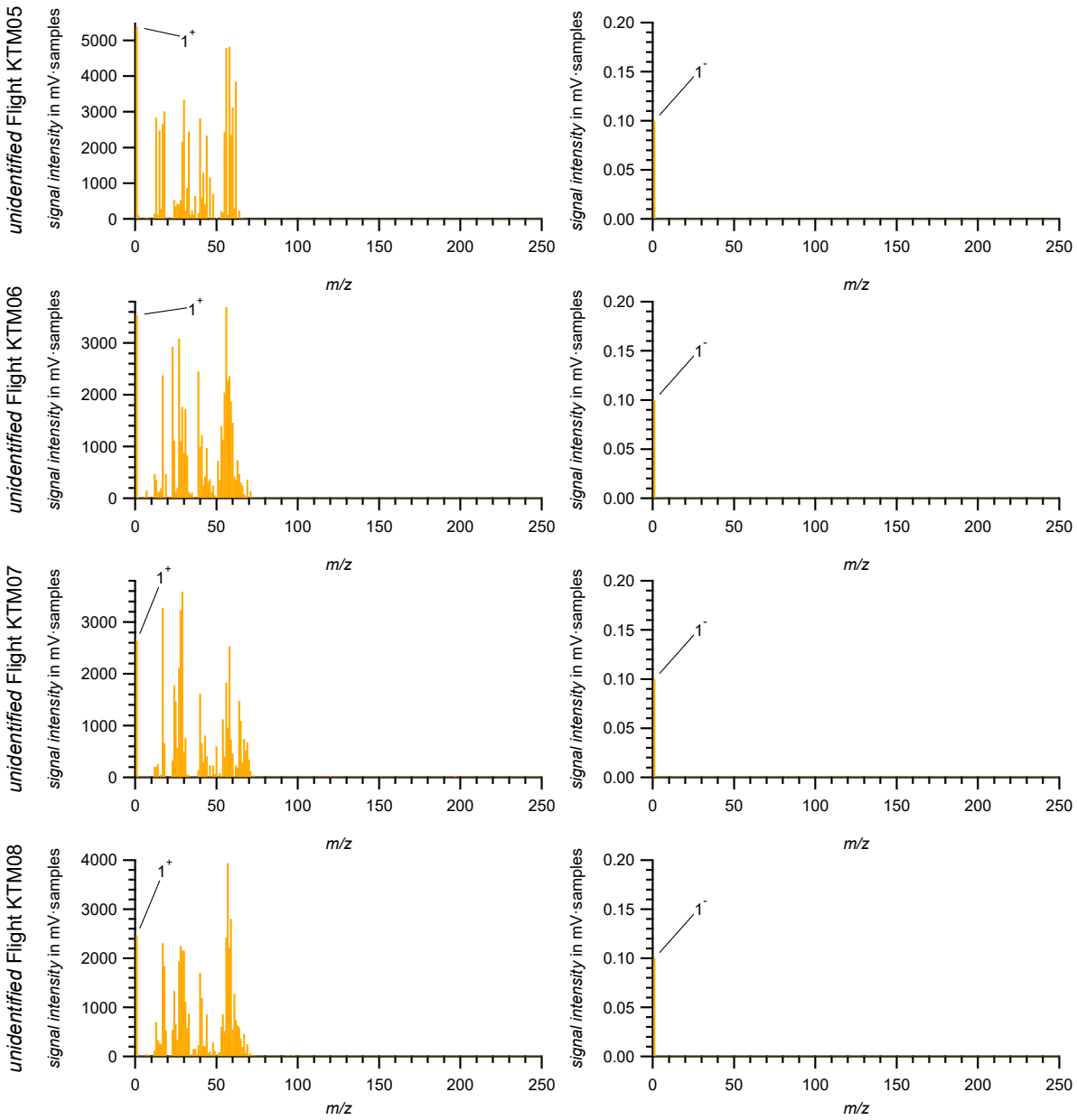

Figure 162: Mean stick spectra (left: cations, right: anions) of the unidentified particle type (orange) for research flights KTM05 – KTM08 in the Asian monsoon phase of StratoClim.

C.10 Asian monsoon phase – size distributions

This appendix shows the cumulative size-resolved aerosol compositions of the seven particle types and unidentified particles individually for each research flight (see Section 5.2.2.1). The identification process for the particle types is described in Section 5.2.1. To determine the particle number fraction f_{part} for a bin, for each bin the ratio is calculated from the number of particles of the specific particle type and the number of all collected particles in that.

Figure 163 to Figure 170 show for each flight the cumulative size-resolved aerosol composition of the identified particle types: *KOrgNOSO* (green), *MetalOrgNOSO* (brown), *Meteoric* (gray), *EC* (black), *Inorganic* (red), *NOSO* (blue), *OrgNOSO* (purple), and unidentified mass spectra (orange) referring to the left axis. Referring to the right axis, the black symbols designate total number of spectra with valid size information (black markers) based on the data set of the referring research flight (KTM01 to KTM08). The uncertainties are calculated from counting statistics according to Appendices C.2.2 and C.2.3. The uncertainty bars are in some cases smaller than the symbol. For further in-depth analyses similar graphs can be generated from the data in dependency of, e.g., flight altitude, meteorological and other conditions.

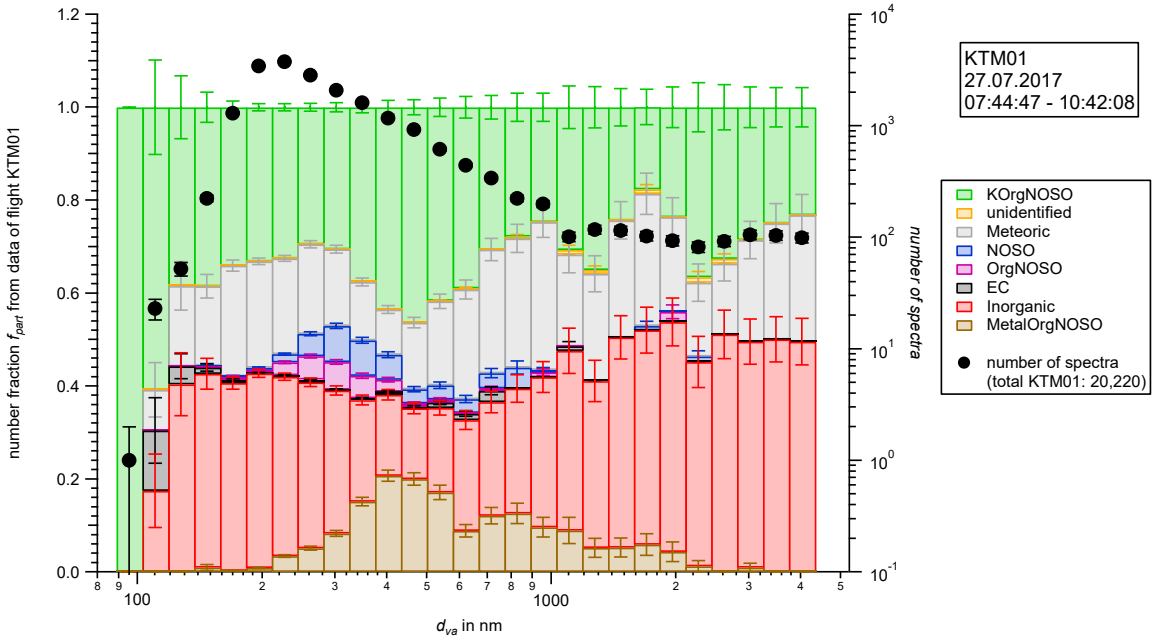

Figure 163: Cumulative size-resolved aerosol composition of the identified particle types of research flight KTM01 (27.07.2017; 07:44:47 – 10:42:08 UTC). See text for description.

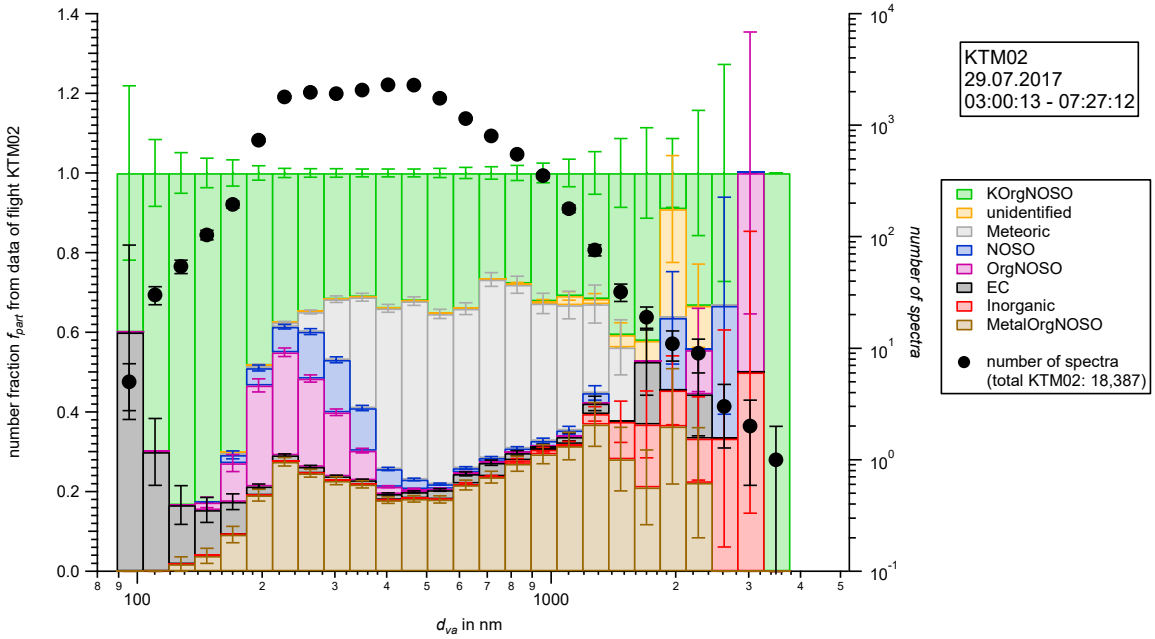

Figure 164: Cumulative size-resolved aerosol composition of the identified particle types of research flight KTM02 (29.07.2017; 03:00:13 – 07:27:12 UTC). See text for description.

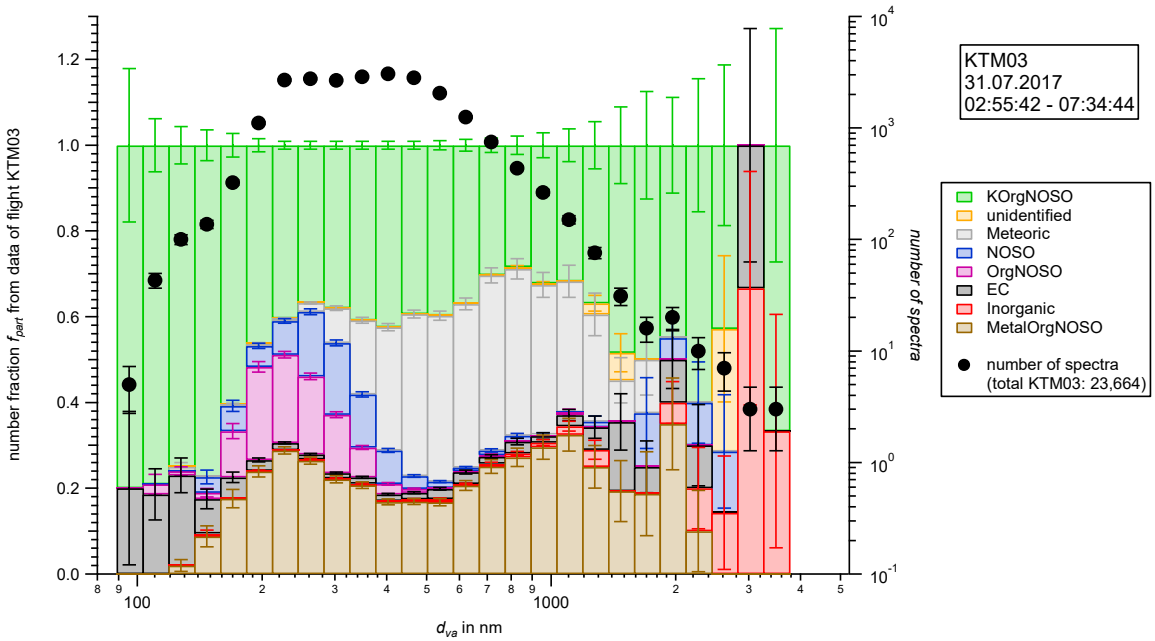

Figure 165: Cumulative size-resolved aerosol composition of the identified particle types of research flight KTM03 (31.07.2017; 02:55:42 – 07:34:44 UTC). See text for description.

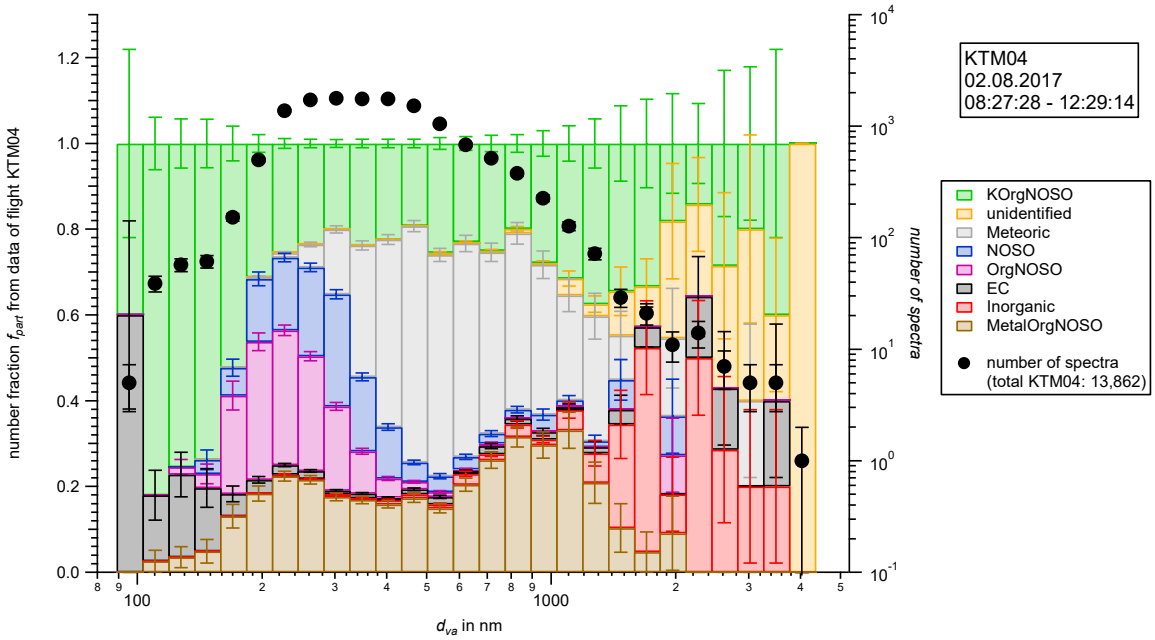

Figure 166: Cumulative size-resolved aerosol composition of the identified particle types of research flight KTM04 (02.08.2017; 08:27:28 – 12:29:14 UTC). See text for description.

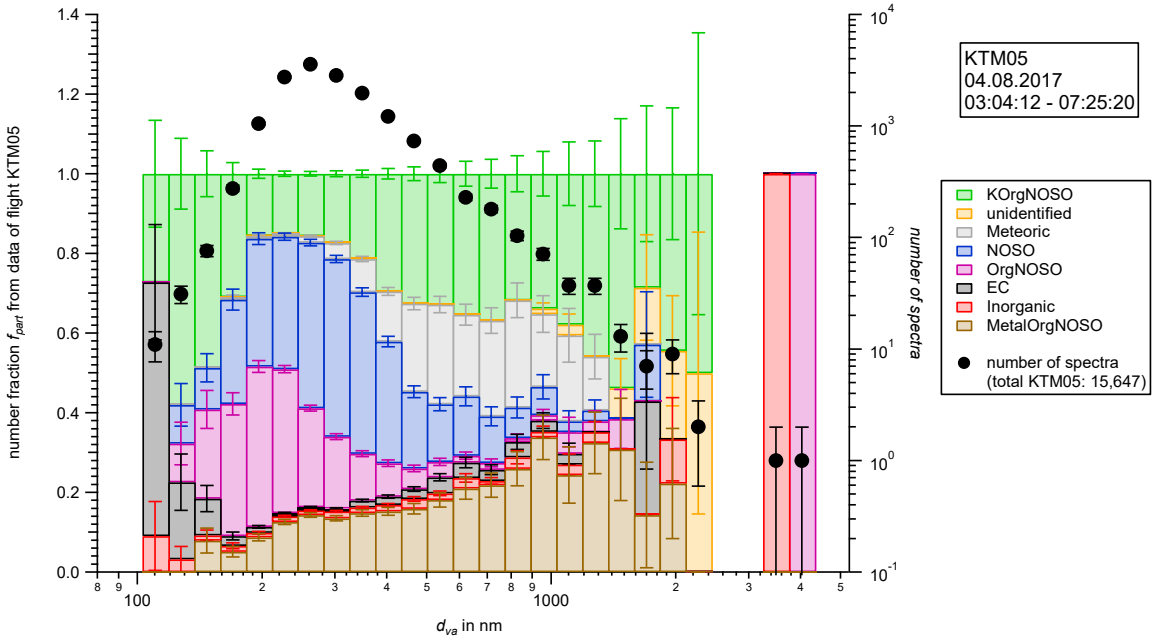

Figure 167: Cumulative size-resolved aerosol composition of the identified particle types of research flight KTM05 (04.08.2017; 03:04:12 – 07:25:20 UTC). See text for description.

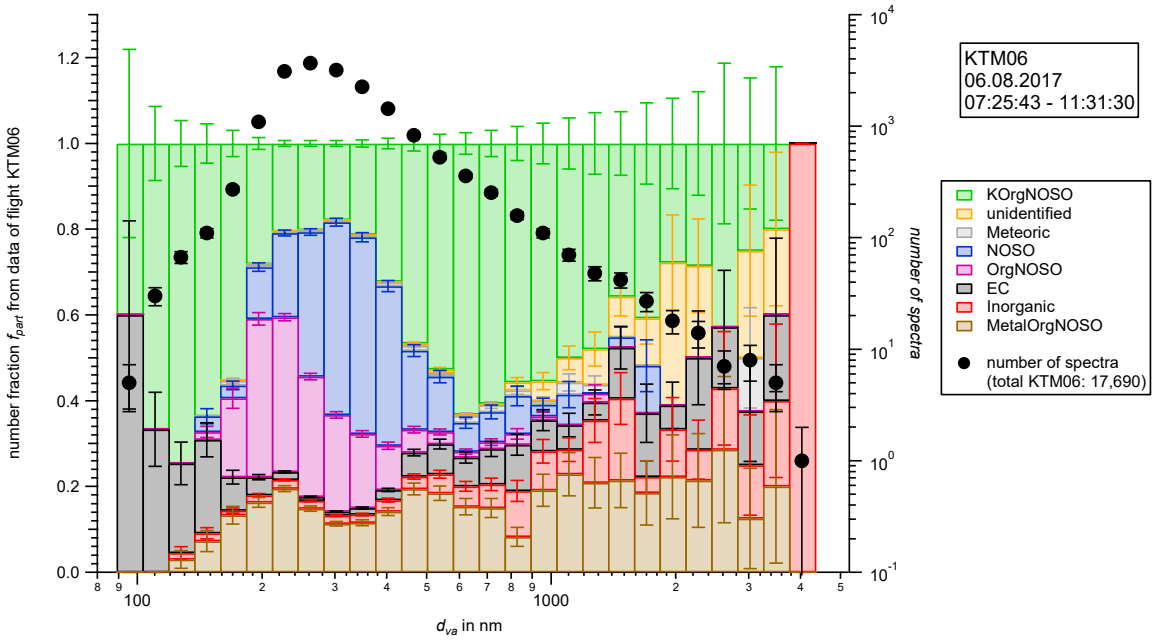

Figure 168: Cumulative size-resolved aerosol composition of the identified particle types of research flight KTM06 (06.08.2017; 07:25:43 – 11:31:30 UTC). See text for description.

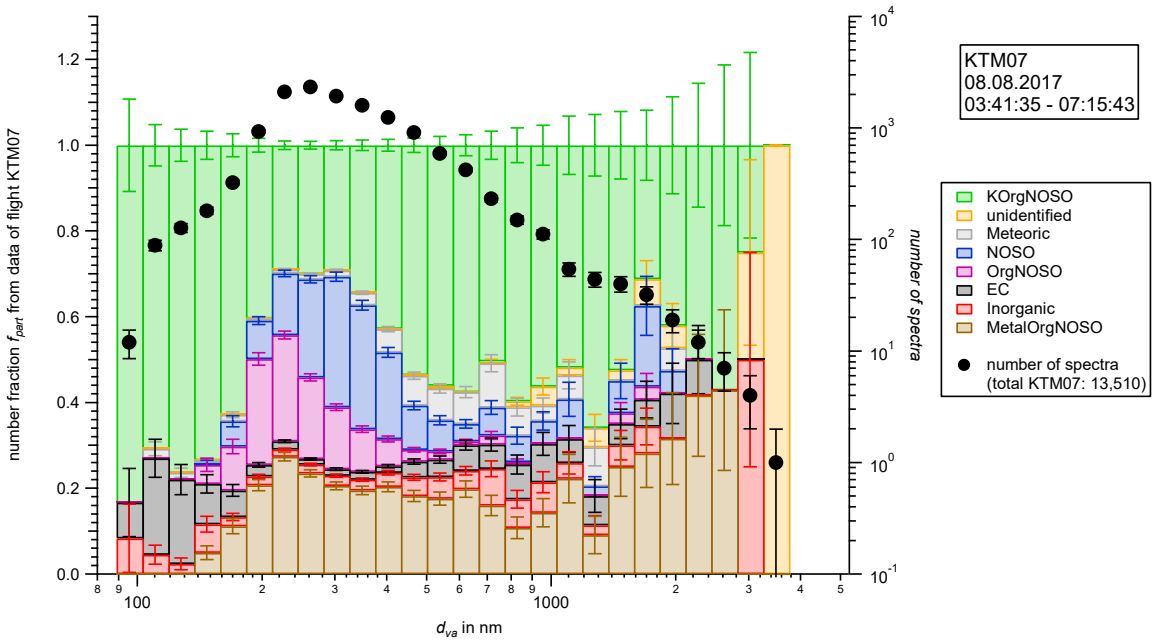

Figure 169: Cumulative size-resolved aerosol composition of the identified particle types of research flight KTM07 (08.08.2017; 03:41:35 – 07:15:43 UTC). See text for description.

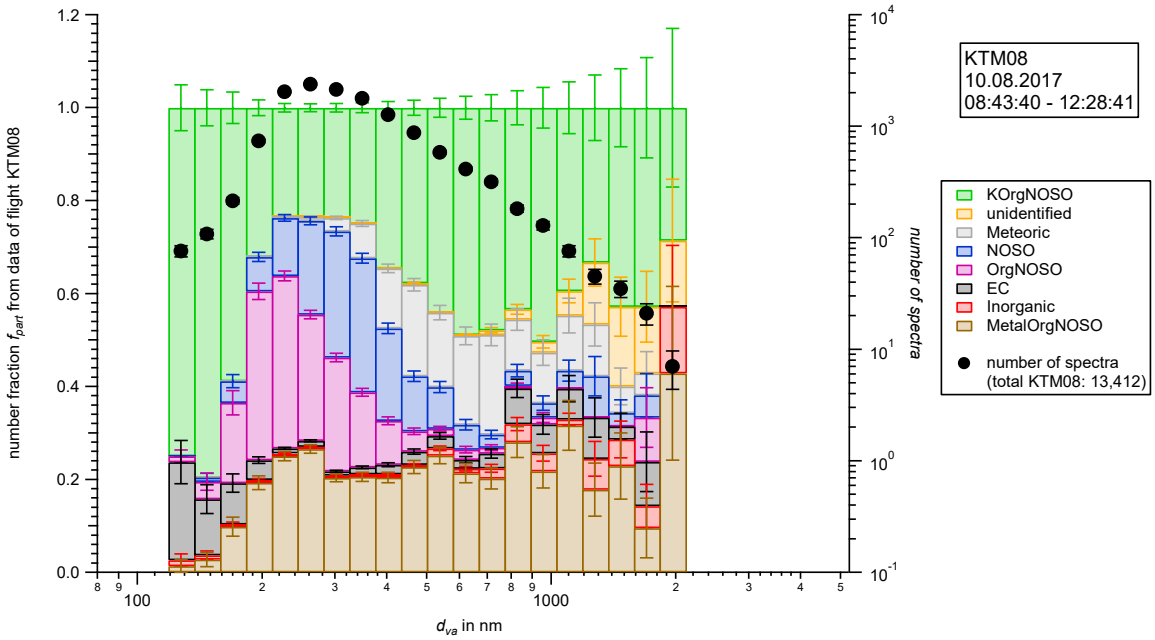

Figure 170: Cumulative size-resolved aerosol composition of the identified particle types of research flight KTM08 (10.08.2017; 08:43:40 – 12:28:41 UTC). See text for description.

C.11 Asian monsoon phase – vertical profiles

This appendix shows the vertically resolved particle number fraction f_{part} of the particle types (*KOrgNOSO*, *MetalOrgNOSO*, *Meteoric*, *EC*, *Inorganic*, *NOSO*, *OrgNOSO,* and unidentified) individually for each research flight (altitude bin size = 500 m, see also Section 5.2.2.2). To determine the particle number fraction f_{part} for each bin the ratio is calculated from the number of particles of the specific particle type and the number of all collected particles in that particular bin. All following altitude values h_{amsl} refer to the GPS (amsl). Figure 179 shows the vertically resolved particle number fractions f_{part} of unidentified particles (orange). In flight KTM04 and KTM06 the f_{part} of unidentified particles reaches maximum values of 20 % and 18 %, respectively. This appears to be increased because only a small total number of mass spectra was recorded in the corresponding height bins. Here, 10 unidentified mass spectra from a total of 50 mass spectra in flight KTM04 and 15 unidentified mass spectra from a total of 82 mass spectra in flight KTM06 were recorded. Figure 180 shows the vertically resolved particle number fractions f_{part} of the merged particle types of *NOSO* and *OrgNOSO* (*NOSO+OrgNOSO*; light blue) for each individual research flight, normalized to the total number of recorded spectra in each bin. The uncertainties are calculated from counting statistics according to Appendices C.2.2 and C.2.3.

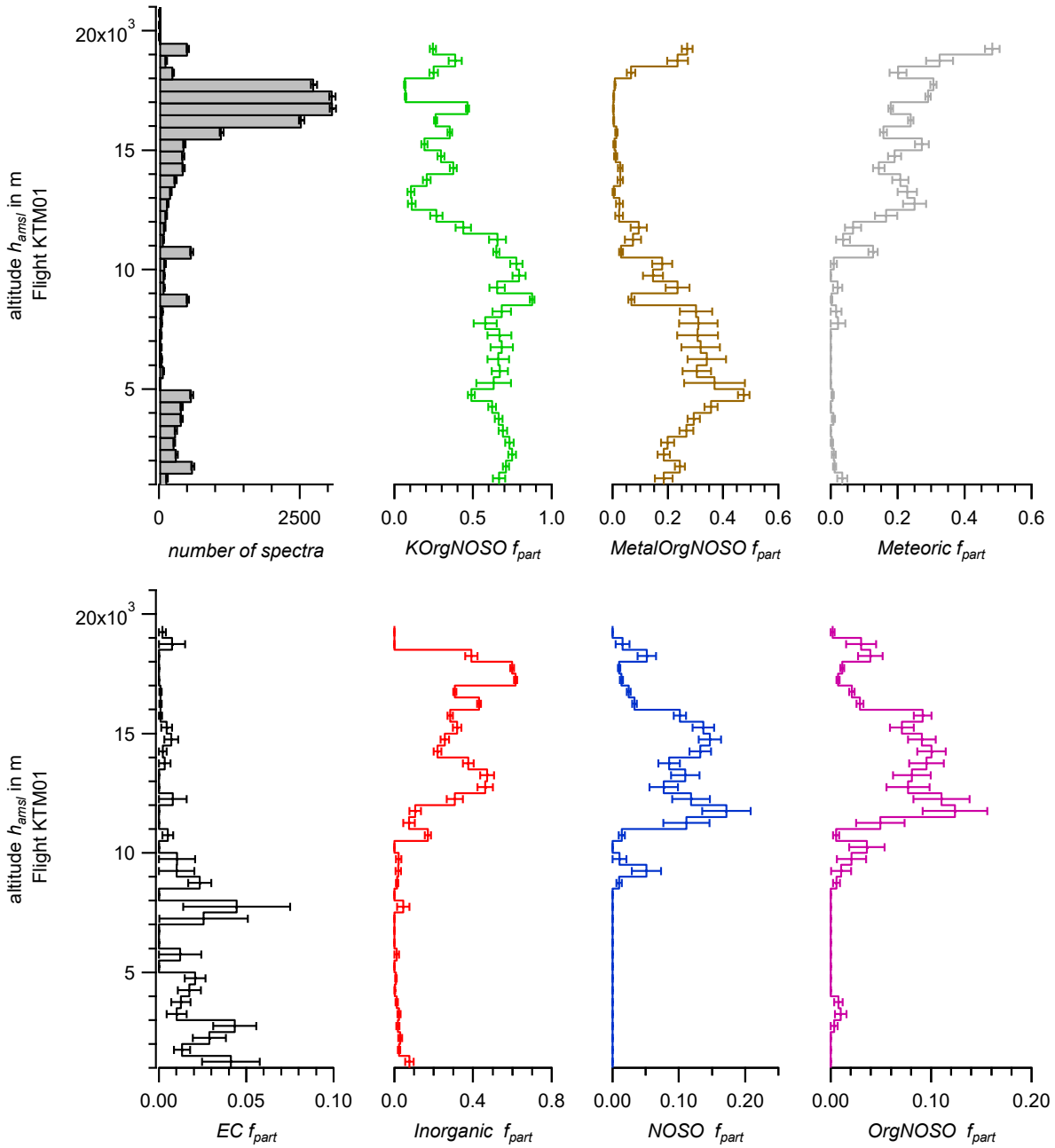

Figure 171: Vertically resolved particle number fractions f_{part} during research flight KTM01 (27.07.2017, 07:44:47 – 10:42:08 UTC) of the particle types: KOrgNOSO (green), MetalOrgNOSO (brown), Meteoric (gray), EC (black), Inorganic (red), NOSO (blue), and OrgNOSO (purple), normalized to the number of recorded spectra in each bin. The top left panel shows the total number of spectra in each bin (black solid bars; in total for KTM01: 20,516). The uncertainties are calculated from counting statistics according to Appendices C.2.2 and C.2.3.

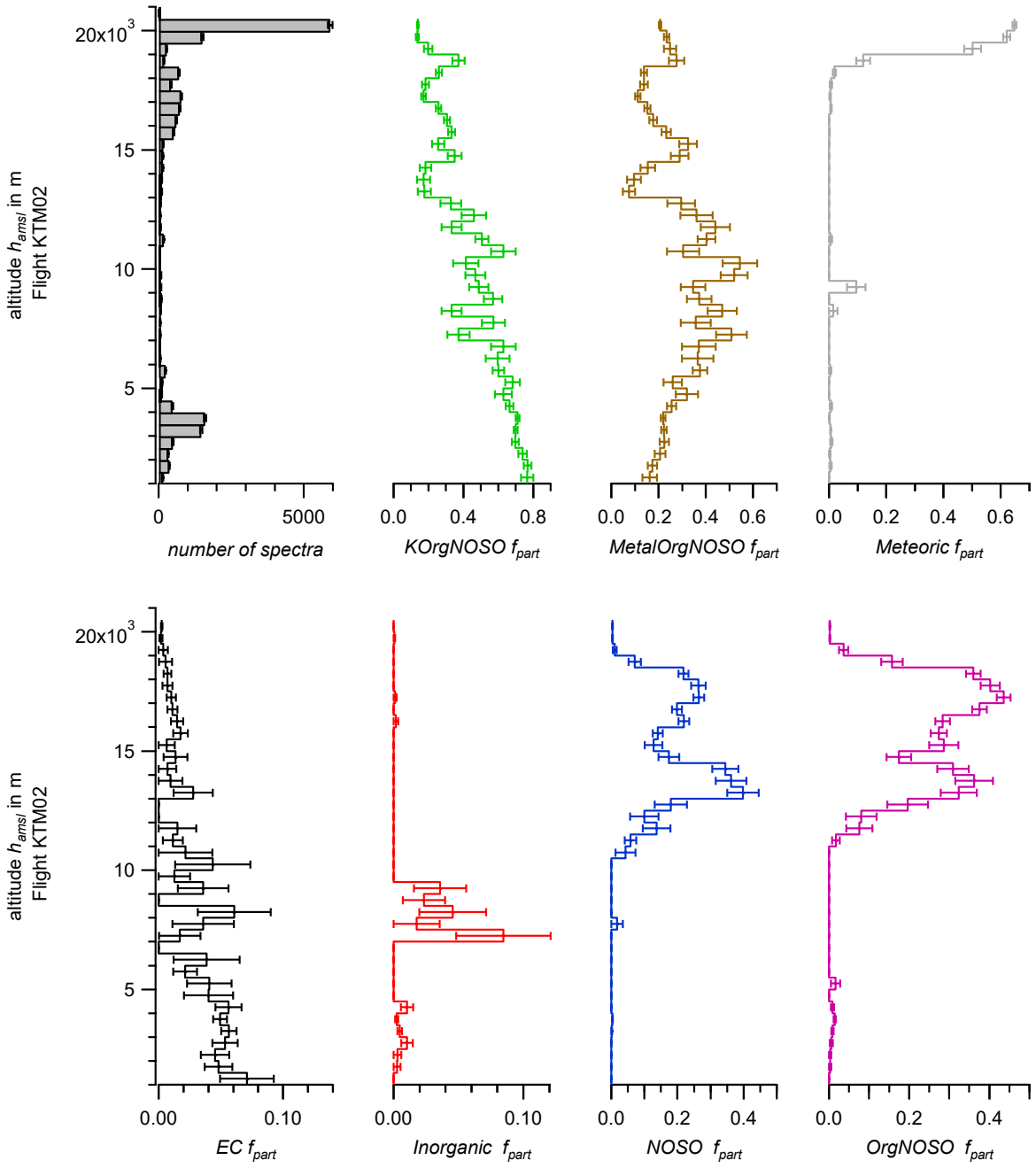

Figure 172: Vertically resolved particle number fractions f_{part} during research flight KTM02 (29.07.2017, 03:00:13 – 07:27:12 UTC) of the particle types: KOrgNOSO (green), MetalOrgNOSO (brown), Meteoric (gray), EC (black), Inorganic (red), NOSO (blue), and OrgNOSO (purple), normalized to the number of recorded spectra in each bin. The top left panel shows the total number of spectra in each bin (black solid bars; in total for KTM02: 18,605). The uncertainties are calculated from counting statistics according to Appendices C.2.2 and C.2.3.

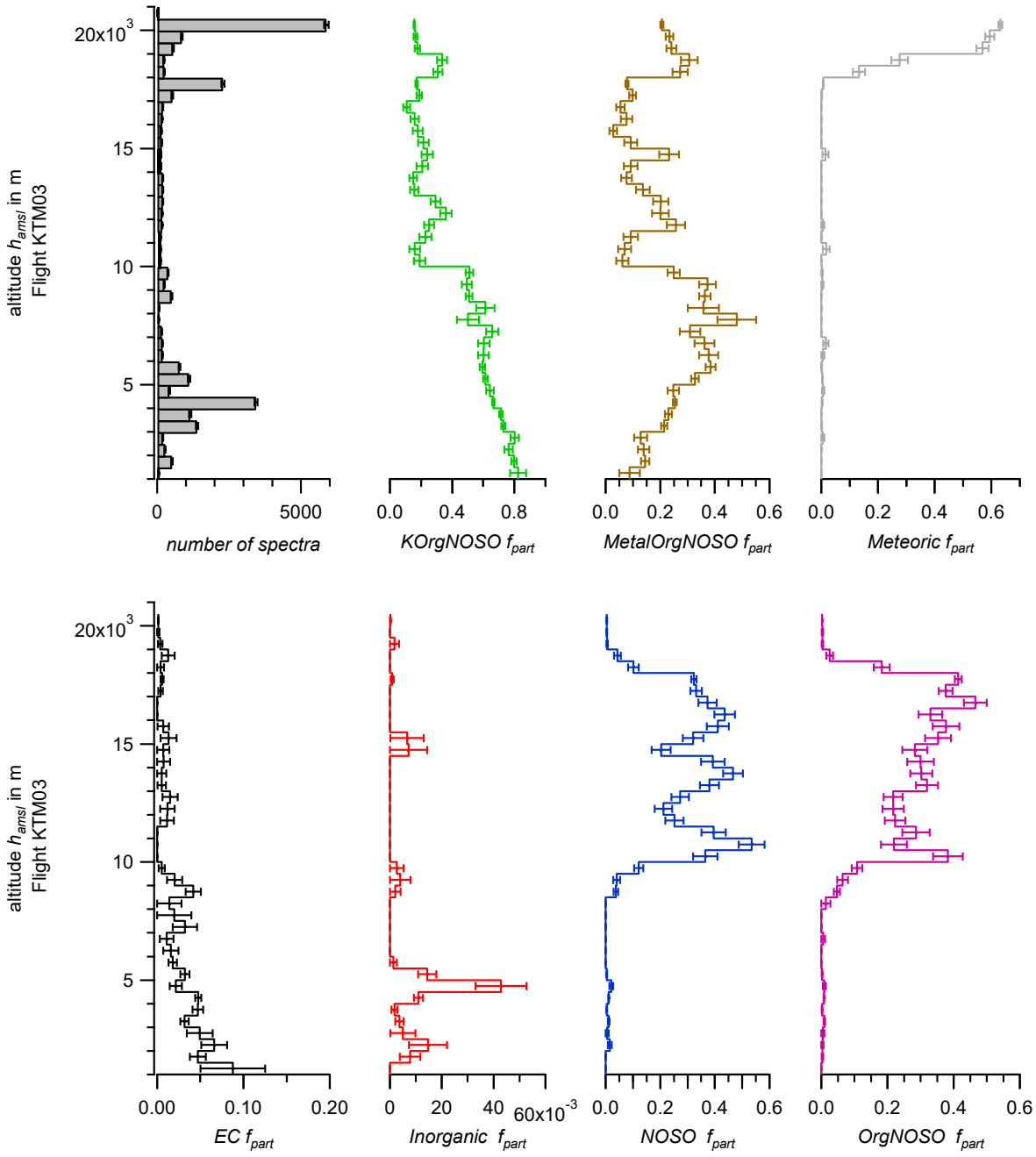

Figure 173: Vertically resolved particle number fractions f_{part} during research flight KTM03 (31.07.2017, 02:55:42 – 07:34:44 UTC) of the particle types: KOrgNOSO (green), MetalOrgNOSO (brown), Meteoric (gray), EC (black), Inorganic (red), NOSO (blue), and OrgNOSO (purple), normalized to the number of recorded spectra in each bin. The top left panel shows the total number of spectra in each bin (black solid bars; in total for KTM03: 23,927). The uncertainties are calculated from counting statistics according to Appendices C.2.2 and C.2.3.

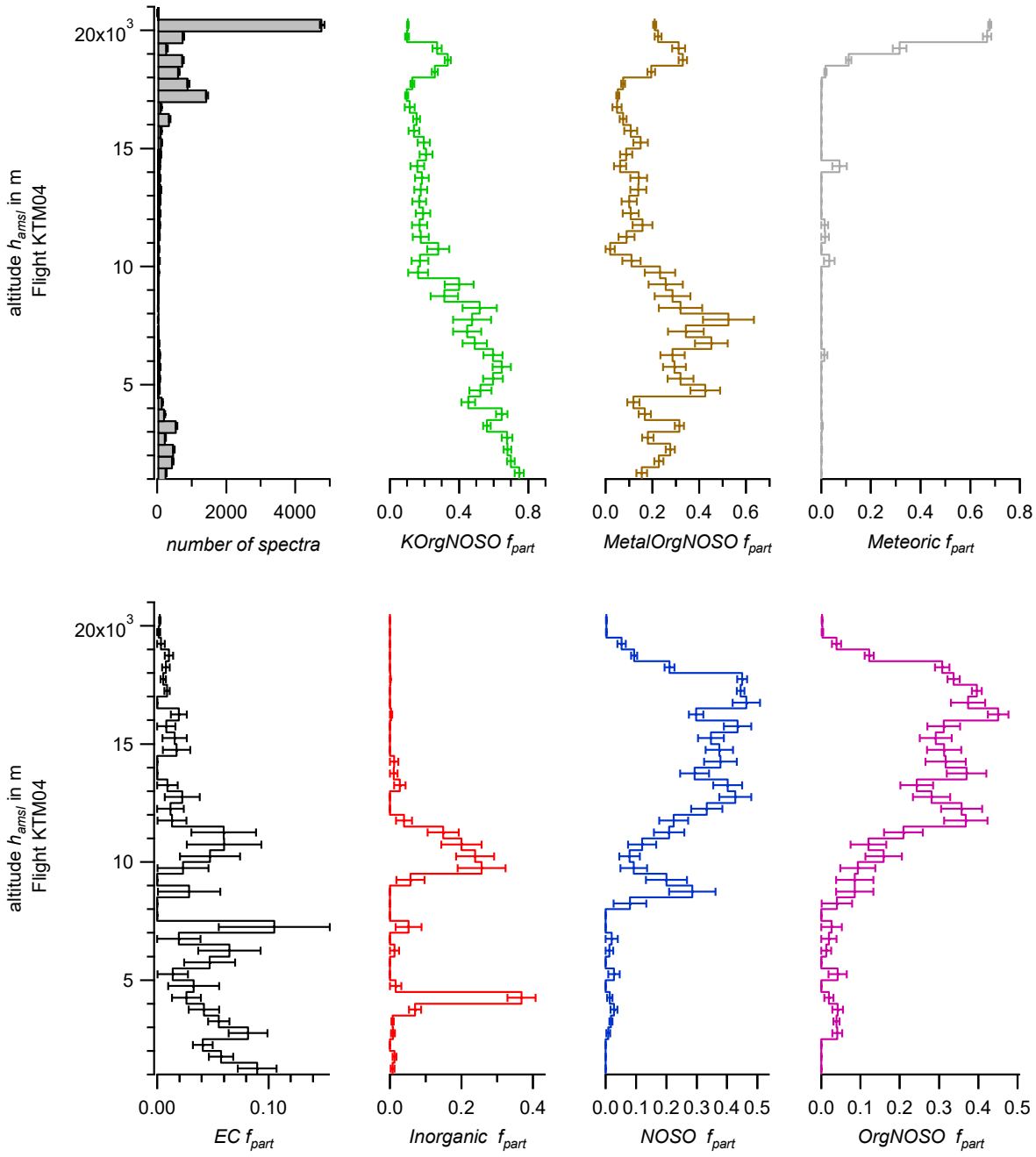

Figure 174: Vertically resolved particle number fractions f_{part} during research flight KTM04 (02.08.2017, 08:27:28 – 12:29:14 UTC) of the particle types: KOrgNOSO (green), MetalOrgNOSO (brown), Meteoric (gray), EC (black), Inorganic (red), NOSO (blue), and OrgNOSO (purple), normalized to the number of recorded spectra in each bin. The top left panel shows the total number of spectra in each bin (black solid bars; in total for KTM04: 14,028). The uncertainties are calculated from counting statistics according to Appendices C.2.2 and C.2.3.

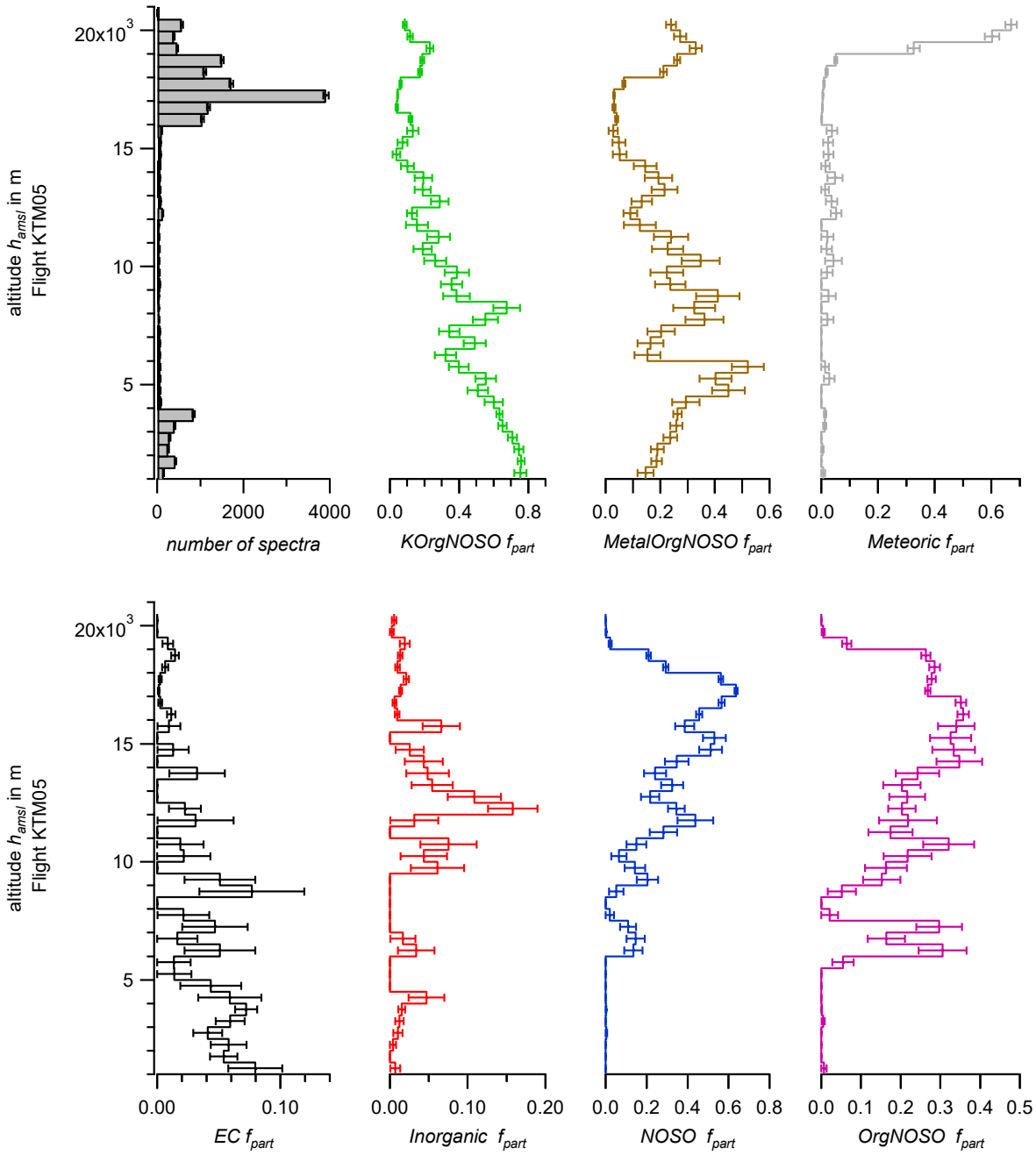

Figure 175: Vertically resolved particle number fractions f_{part} during research flight KTM05 (04.08.2017, 03:04:12 – 07:25:20 UTC) of the particle types: KOrgNOSO (green), MetalOrgNOSO (brown), Meteoric (gray), EC (black), Inorganic (red), NOSO (blue), and OrgNOSO (purple), normalized to the number of recorded spectra in each bin. The top left panel shows the total number of spectra in each bin (black solid bars; in total for KTM05: 15,866). The uncertainties are calculated from counting statistics according to Appendices C.2.2 and C.2.3.

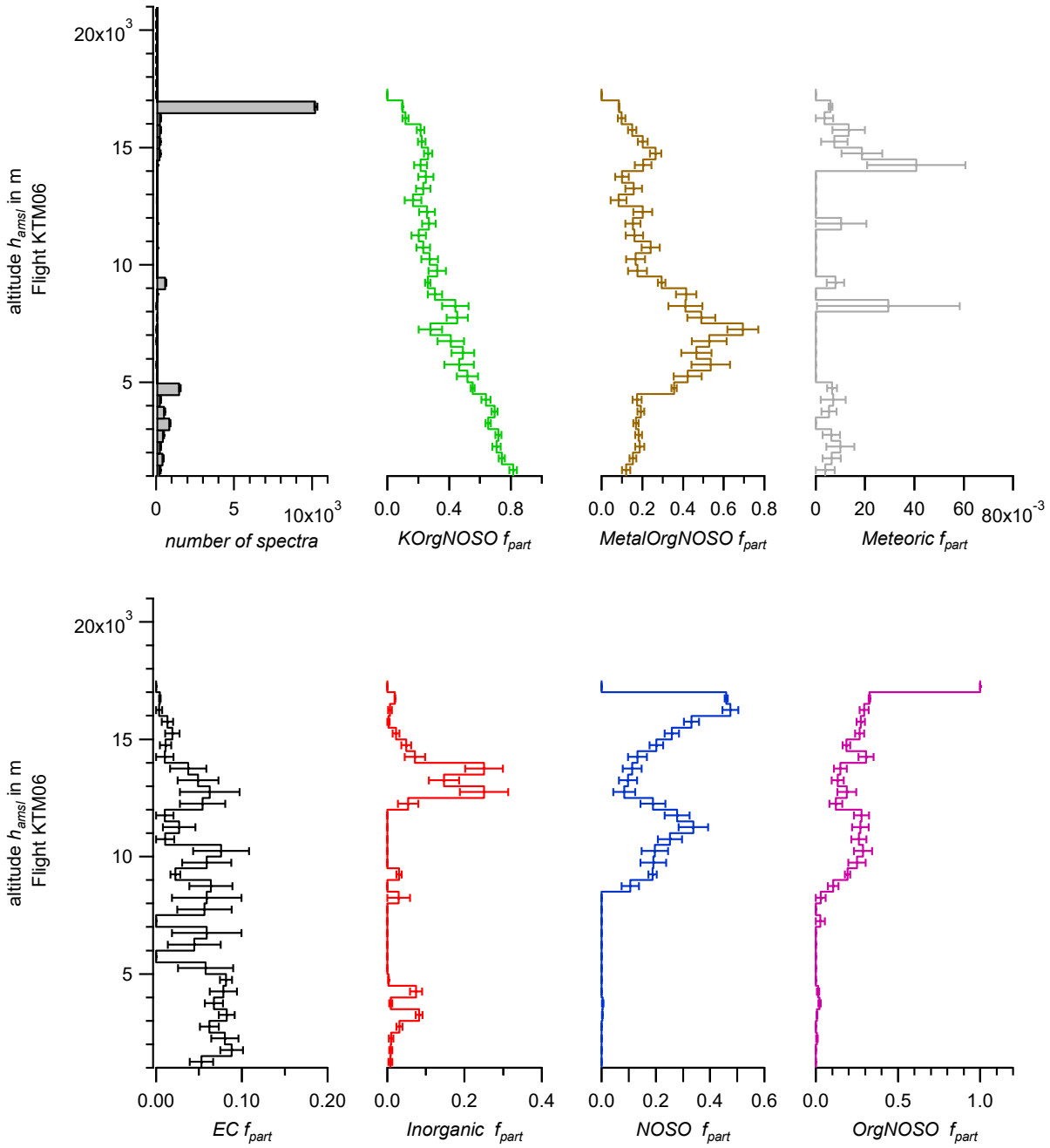

Figure 176: Vertically resolved particle number fractions f_{part} during research flight KTM06 (06.08.2017, 07:25:43 – 11:31:30 UTC) of the particle types: KOrgNOSO (green), MetalOrgNOSO (brown), Meteoric (gray), EC (black), Inorganic (red), NOSO (blue), and OrgNOSO (purple), normalized to the number of recorded spectra in each bin. The top left panel shows the total number of spectra in each bin (black solid bars; in total for KTM06: 17,914). The uncertainties are calculated from counting statistics according to Appendices C.2.2 and C.2.3.

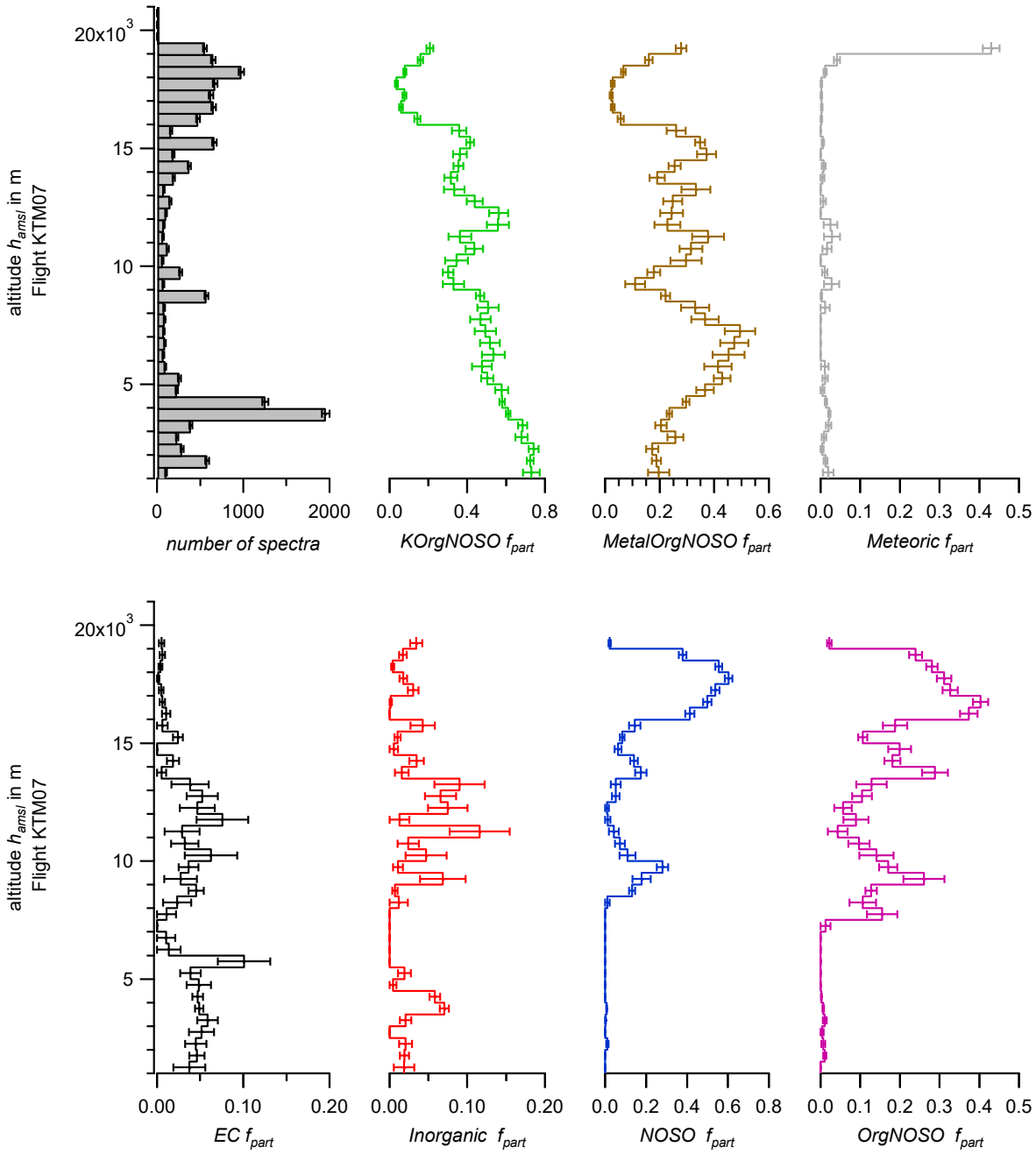

Figure 177: Vertically resolved particle number fractions f_{part} during research flight KTM07 (08.08.2017, 03:41:35 – 07:15:43 UTC) of the particle types: KOrgNOSO (green), MetalOrgNOSO (brown), Meteoric (gray), EC (black), Inorganic (red), NOSO (blue), and OrgNOSO (purple), normalized to the number of recorded spectra in each bin. The top left panel shows the total number of spectra in each bin (black solid bars; in total for KTM07: 13,625). The uncertainties are calculated from counting statistics according to Appendices C.2.2 and C.2.3.

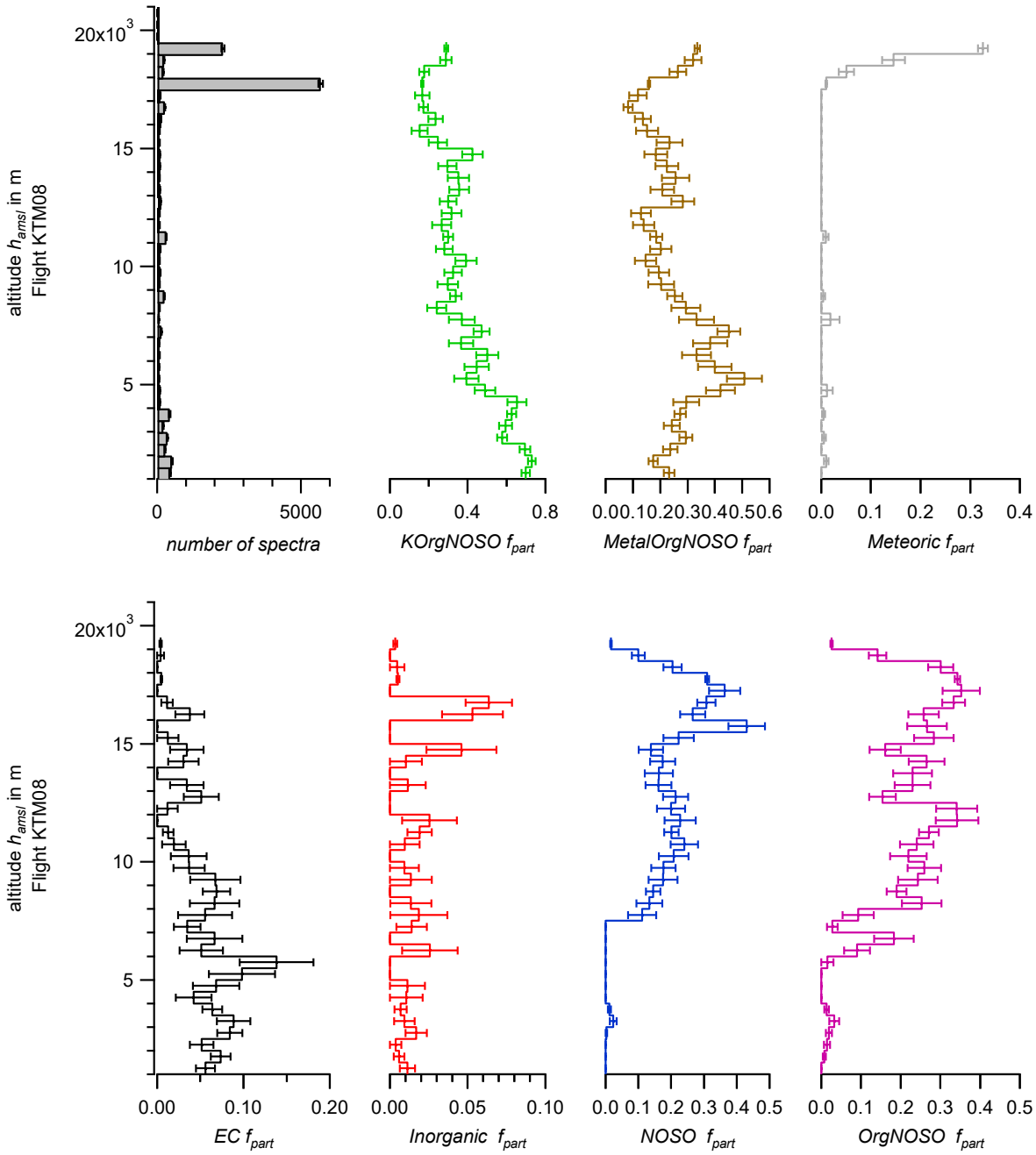

Figure 178: Vertically resolved particle number fractions f_{part} during research flight KTM08 (10.08.2017, 08:43:40 – 12:28:41 UTC) of the particle types: KOrgNOSO (green), MetalOrgNOSO (brown), Meteoric (gray), EC (black), Inorganic (red), NOSO (blue), and OrgNOSO (purple), normalized to the number of recorded spectra in each bin. The top left panel shows the total number of spectra in each bin (black solid bars; in total for KTM08: 13,608). The uncertainties are calculated from counting statistics according to Appendices C.2.2 and C.2.3.

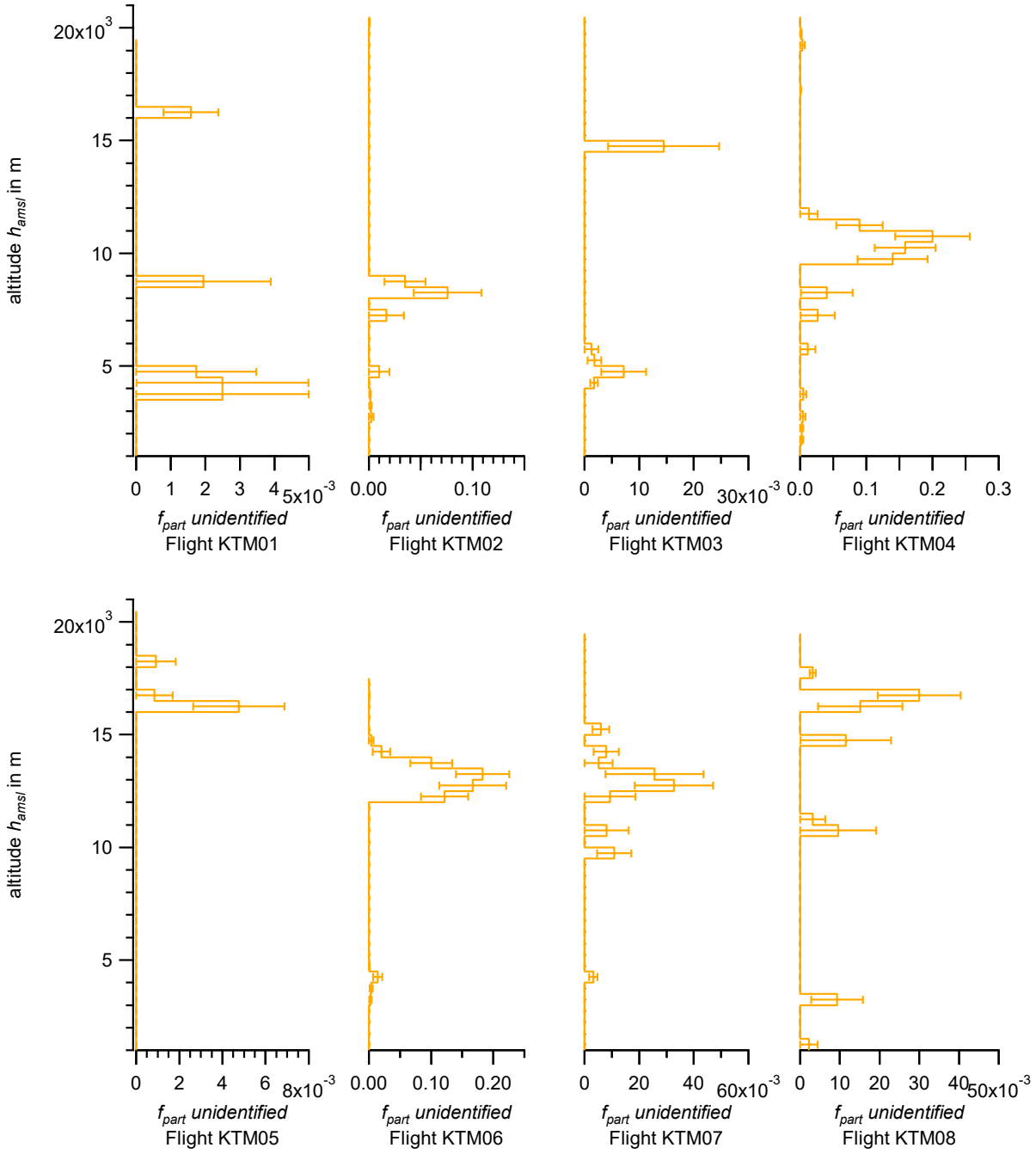

Figure 179: Vertically resolved particle number fractions f_{part} of unidentified particles (orange) for each individual research flight, normalized to the total number of spectra for each bin. The uncertainties are calculated from counting statistics according to Appendix C.2.3.

Figure 180 shows the vertically resolved particle number fractions f_{part} of the merged particle types of *NOSO* and *OrgNOSO* (*NOSO+OrgNOSO*; light blue) for each individual research flight, normalized to the total number of spectra for each bin. In flight KTM02, KTM05, KTM07, and KTM08 the particle number fractions have their maximum at the estimated CPT. These maxima reach f_{part} values of above f_{part} > 0.8. The observed maximum fraction of close to 1 in flight KTM06 might be enhanced due to a low number of recorded spectra (see Figure 176). Except for flight KTM06, where no data is available in such altitudes, the observed layer extends above the altitude of the estimated local CPT. This might indicate a transportation process by the AMA (Ploeger et al., 2015).

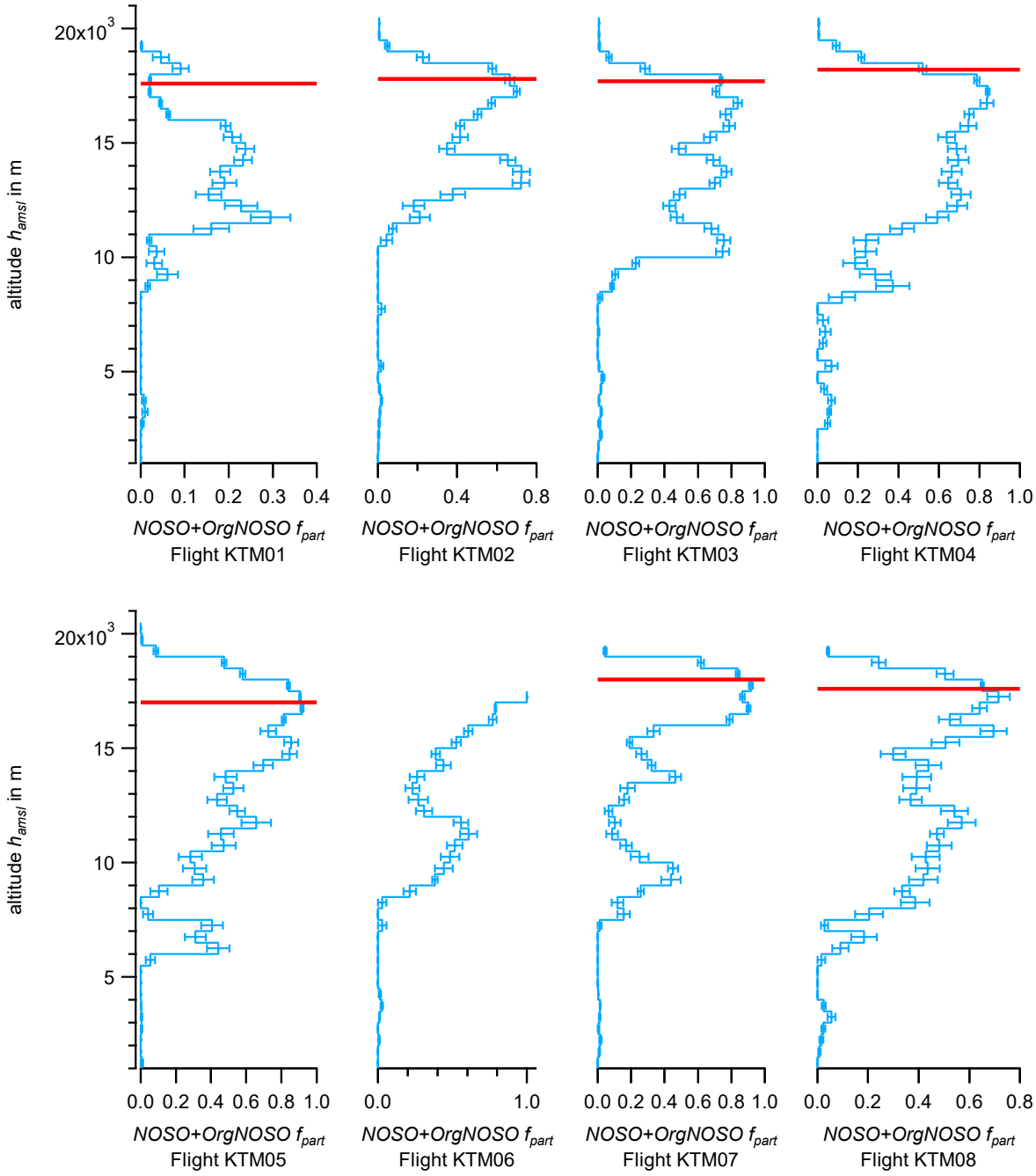

Figure 180: Vertically resolved particle number fractions f_{part} of the merged particle types of NOSO and OrgNOSO (NOSO+OrgNOSO; light blue) for each individual research flight, normalized to the total number of spectra for each bin. The red horizontal line marks the estimated cold point tropopause (see Table 41). The uncertainties are calculated from counting statistics according to Appendix 14.2.3.

Table 41 lists the altitudes of the estimated cold point tropopause (CPT). The CPT values were determined from the temperature profiles (GPS altitude h_{amsl} against temperature T_{out}). The altitude value was read at the lowest temperature value and rounded to the nearest 100 m. In flight KTM06 the CPT was not reached.

Table 41: Altitudes (amsl) of the estimated cold point tropopause (CPT). Determination of the values see text.

Flight	Altitude of the estimated CPT in m
KTM01	17,600
KTM02	17,800
KTM03	17,700
KTM04	18,200
KTM05	17,000
KTM06	n/a
KTM07	18,000
KTM08	17,600

Publications

Peer-reviewed publications:

Höpfner, M., Ungermann, J., Borrmann, S., Wagner, R., Spang, R., Riese, M., Stiller, G., Appel, O., Batenburg, A. M., Bucci, S., Cairo, F., Dragoneas, A., Friedl-Vallon, F., **Hünig, A**., Johansson, S., Krasauskas, L., Legras, B., Leisner, T., Mahnke, C., Möhler, O., Molleker, S., Müller, R., Neubert, T., Orphal, J., Preusse, P., Rex, M., Saathoff, H., Stroh, F., Weigel, R., and Wohltmann, I.: *Ammonium nitrate particles formed in upper troposphere from ground ammonia sources during Asian monsoons*, Nature Geoscience, doi: 10.1038/s41561-019-0385-8, 2019.

Molleker, S., Helleis, F., Klimach, T., Appel, O., Clemen, H.-C., Dragoneas, A., Gurk, C., **Hünig, A.**, Köllner, F., Rubach, F., Schulz, C., Schneider, J., and Borrmann, S.: *Application of an O-ring pinch device as a constant pressure inlet (CPI) for airborne sampling*, Atmospheric Measurement Techniques, 2020, 1-13, doi: 10.5194/amt-2020-66, 2020.

In review:

Clemen, H.-C., Schneider, J., Klimach, T., Helleis, F., Köllner, F., **Hünig, A.**, Rubach, F., Mertes, S., Wex, H., Stratmann, F., Kohl, R., Frank, F., Bingemer, H., Curtius, J., and Borrmann, S.: *Optimizing the detection, ablation and ion extraction efficiency of a single particle laser ablation mass spectrometer for application in environments with low aerosol particle concentrations*, Atmospheric Measurement Techniques Discussions, 2020, 1-48, doi: 10.5194/amt-2020-181, 2020.

In preparation:

Hünig, A., Appel, O., Dragoneas, A., Molleker, S., Clemen, H.-C., Helleis, F., Klimach, T., Böttger, T., Drewnick, F., Schneider, J., and Borrmann, S.: *Design and characterization of a novel aerosol mass spectrometer combining laser ablation and flash vaporization techniques for aircraft application at high altitudes*, prepared for submission to Atmospheric Measurement Techniques Discussions, doi: n/a, 2020.

Dragoneas, A., Molleker, S., Appel, O., **Hünig, A.**, Böttger, T., Hermann, M., Drewnick, F., Schneider, J., Weigel, R., and Borrmann, S.: *The realization of autonomous, aircraft-based, real-time aerosol mass spectrometry in the stratosphere*, prepared for submission to Atmospheric Measurement Techniques Discussions, doi: n/a, 2020.

Schneider, J., Weigel, R., Klimach, T., Dragoneas, A., Appel, O., **Hünig, A.**, Molleker, S., Köllner, F., Clemen, H.-C., Eppers, O., Hoppe, P., Hoor, P., Mahnke, C., Krämer, M., Rolf, C., Grooß, J. U., Zahn, A., Oversteiner, F., Ravegnani, F., Ulanovsky, A., Schlager, H., Scheibe, M., Diskin, G. S., DiGangi, J., Nowak, J., Zöger, M., and Borrmann, S.: *Aircraft-based observation of meteoric material in lower stratospheric aerosol particles between 15 and 68°N*, Earth and Space Science Open Archive, pre-print server, doi: 10.1002/essoar.10501338.1, 2019.

Conference contributions:

[Not included in the electronic version]

External contributions to the thesis work

[Not included in the electronic version]

Danksagung

[Not included in the electronic version]

[Not included in the electronic version]

Curriculum Vitae

[Not included in the electronic version]

Declaration

I hereby declare that I wrote the dissertation submitted without any unauthorized external assistance and used only sources acknowledged in the work. All textual passages, which are appropriated verbatim or paraphrased from published and unpublished texts as well as all information obtained from oral sources are duly indicated and listed in accordance with bibliographical rules. In carrying out this research, I complied with the rules of standard scientific practice as formulated in the statutes of Johannes Gutenberg University Mainz to insure standard scientific practice. External contributions to data and analyses presented in this study are specified in detail on page 292.

Mainz, July 17, 2020

_____

Andreas Hünig